Black Sea Journal of Engineering and Science

Volume 8 | Issue 1

ISSN: 2619 - 8991

BS Journals

BLACK SEA JOURNAL OF ENGINEERING AND SCIENCE

(BSJ ENGIN SCI)

Black Sea Journal of Engineering and Science (BSJ Eng Sci) is a double-blind peer-reviewed, open-access international journal published electronically 6 times (January, March, May, July, September, and November) in a year by since January 2018. It publishes, in English and Turkish, full-length original research articles, innovative papers, conference papers, reviews, mini-reviews, rapid communications or technical note on advances in a wide range of scientific disciplines from all fields of engineering and science and from any source.

ISSN 2619 - 8991

Phone: +90 362 408 25 15

Fax: +90 362 408 25 15

Email: bsjsci@blackseapublishers.com

Web site: http://dergipark.gov.tr/bsengineering

Sort of publication: Periodically 6 times (January, March, May, July, September, and November) in a year

Publication date and place: January 15, 2025 - Samsun, TURKEY

Publishing kind: Electronically

EDITORIAL DECLERATION

Dear authors and readers,

First of all, we would like to thank you for being our travel companion by writing, evaluating, and reading us about this broadcasting life we started six years ago. With these thoughts, we are especially thankful for researchers and academicians honoring with the articles, valuable scientists involved in editorial boards, and reviewers for their contributions to the evaluation processes through their opinions/ideas/contributions/criticisms. With this article, we wanted to inform you, our valuable stakeholders, about the development of The Black Sea Journal of Engineering and Science (BSJ Eng Sci). The statistics of the BSJ Eng Sci for the last seven years are given below. Hope you will be with us in future issues.

Year	Articles	Cites	Cite Index*	CNA	CNC	CCI
2018	20	11	0.55	20	11	0.55
2019	22	15	0.68	42	26	0.62
2020	29	41	1.41	71	67	0.94
2021	32	50	1.56	103	117	1.14
2022	24	105	4.38	127	222	1.75
2023	78	146	1.87	205	368	1.80
2024	151	192	1.27	356	560	1.57

CNA= cumulative number of articles, CNC= cumulative number of cite, CCI= cumulative cite index

*: according to Scholar Google

Rejection rate:

- 2020: 09%
- 2021: 18%
- 2022: 25%
- 2023: 14%
- 2024: 16%

Average review time (days): 64

Average time from send to publish (days): 95

EDITOR BOARDS

REVIEWERS OF THE ISSUE*

Prof. Dr. Abdurrahman EYMEN, Erciyes University, Department of Geotechnical Engineering, Geographic Information Systems, TÜRKİYE

Prof. Dr. Beyza ÖZKÖK, Yıldız Technical University, Department of Quantitative Methods, Operations Research in Mathematics, TÜRKİYE

Prof. Dr. Ergül TÜRKMEN, Amasya University, Department of Mathematics, Algebra and Number Theory, TÜRKİYE

Prof. Dr. Gürkan Alp Kağan GÜRDİL, Ondokuz Mayıs University, Department of Agricultural Machinery, Biomaterial, TÜRKİYE

Prof. Dr. Hamza MENKEN, Mersin University, Department of Mathematics, Algebra and Number Theory, TÜRKİYE

Prof. Dr. Hidayet OĞUZ, Necmettin Erbakan University, Department of Energy Systems Engineering, Agricultural Energy Systems, TÜRKİYE

Prof. Dr. Kemal KARABAĞ, Akdeniz University, Department of Agricultural Biotechnology, Animal Biotechnology, TÜRKİYE

Prof. Dr. Muhammet KURULAY, Istanbul Technical University, Department of Mathematical Engineering, Algorithms and Calculation Theory, TÜRKİYE

Prof. Dr. Özgür AVŞAR, Eskişehir Technical University, Department of Civil Engineering, Structural Dynamics, TÜRKİYE

Prof. Dr. Ramazan ACAR, Selçuk University, Department of Field Crops, Pasture-Meadow Forage Plants, TÜRKİYE

Prof. Dr. Umman Tugba GÜRSOY, İstanbul University, Department of Numerical Methods, Operations Research in Mathematics, TÜRKİYE

Assoc. Prof. Dr. Ahmet ÖZTEL, Bartın University, Department of Business Administration, Quantitative Decision Methods, TÜRKİYE

Assoc. Prof. Dr. Alev KELLECI AKBAY, İskenderun Technical University, Department of Mathematics, Algebraic and Differential Geometry, TÜRKİYE

Assoc. Prof. Dr. Aylin ÖZODABAŞ, Bilecik Şeyh Edebali University, Department of Civil Engineering, Construction Materials, TÜRKİYE

Assoc. Prof. Dr. Canan AKIN, Giresun University, Department of Mathematics, Algebra and Number Theory, TÜRKİYE

Assoc. Prof. Dr. Cem TIRINK, Iğdır University, Department of Animal Science, Biometry, TÜRKİYE

---

* The ranking is arranged alphabetically within the academic title

Volume 8, Issue 1 (2025)

Table of Contents

Research Articles

Black Sea Journal of Engineering and Science
doi: 10.34248/bsengineering.1557319

Open Access Journal
e-ISSN: 2619 – 8991

Research Article
Volume 8 - Issue 1: 1-10 / January 2025

EFFECTS OF LOADING TYPE AND LOADING RATE ON GLULAM SIPO TIMBER BEAMS FOR FLEXURAL LOADING

Minel Ahu KARA ALAŞALVAR[1]*

[1]*Gazi University, Graduate School of Natural and Applied Sciences, 06500, Ankara, Türkiye*

Abstract: Glulam wood elements are a high-performance structural material created by bonding layers of wood with structural adhesives. This study investigates the behavior of glulam beams made from the tropical timber species Sipo, which has limited representation in existing literature, under different loading types and rates in bending tests. Six Sipo glulam beams were tested: three under four-point bending and three under three-point bending. To assess the behavior at various loading rates, loads were applied at rates of 10 mm/min, 20 mm/min, and 30 mm/min. The results included load-displacement curves, ultimate load capacities, initial stiffness, and energy dissipation capacities. The study revealed differences between values obtained from three-point and four-point bending tests. Generally, beams subjected to three-point bending yielded higher values than those tested under four-point bending at the same loading rates. Notably, a significant reduction in values was observed for both testing methods at the loading rate of 20 mm/min.

Keywords: Glulam, Bending tests, Strength, Tropical timber

***Corresponding author:** Gazi University, Graduate School of Natural and Applied Sciences, 06500, Ankara, Türkiye
E mail: minelahukara@gmail.com (M. A. KARA ALAŞALVAR)
Minel Ahu KARA ALAŞALVAR https://orcid.org/0000-0003-1138-1446

Received: September 27, 2024
Accepted: November 15, 2024
Published: January 15, 2025

Cite as: Kara Alaşalvar MA. 2025. Effects of loading type and loading rate on glulam sipo timber beams for flexural loading. BSJ Eng Sci, 8(1): 1-10.

1. Introduction

Wood has long been one of the natural and renewable materials used in construction. Over the centuries, the use of wood has been observed in various structures, including wooden houses, bridges, waterfront structures, and utility poles. The simplicity of production, lightweight nature, reusability, and environmental compatibility of wood make it a preferred material for lightweight structures. With the advancement of technology, wood continues to maintain its importance today. Modern technological innovations have enhanced the durability of wood, leading to the emergence of many new wood products such as plywood, particleboard, and other panel products. The glue-lamination process has significantly improved dimensional and surface laminations in wood, resulting in increased load-carrying capacity (Issa and Kmeid, 2005).

One of the oldest engineered wood products is glulam. Glulam is an engineering product created by laminating two or more layers of wood boards in parallel to the direction of the fibers. Compared to other building materials, glulam offers significant advantages. First, it allows for the production of large and wide components, making it possible to obtain long elements even from small trees, which is particularly beneficial for structural elements spanning wide spaces. Another advantage lies in architectural design; the production process allows for the creation of various architectural elements that would be challenging to achieve with other materials due to the bending of the wood. Additionally, the drying of the timber before production minimizes potential drying defects. One of the most important benefits of glulam is the ability to produce variable cross-sections. In glulam beams, large quantities of lower-quality timber can be used in the laminated sections that experience less stress. Generally, higher-grade laminations are positioned near the upper and lower edges of the beams, where higher stresses occur, while lower-grade laminations are utilized in the interior sections of the beams (toward the center). Furthermore, different species can be selected to meet the structural requirements of the laminations (Stark et al., 2010).

Glulam technology enables the production of various structural elements, including bending, axial, curved, and tapered straight members (Stark et al., 2010). Notably, recent studies in the literature focus on glulam beams. Wang et al. (2024) investigated the reinforcement of glulam beams with epoxy resin-bonded prestressing tendons, analyzing the effects of prestressing force levels and bonded types on the flexural behavior of these beams. The study involved four-point bending tests on 12 beams prepared using unreinforced, unbonded, or bonded prestressing techniques, revealing a significant increase of up to 78.8% in flexural capacity and 13.5% in stiffness compared to unreinforced beams (Wang et al., 2024). Das et al. (2023) explored the applicability of the Albizia procera species in glulam beam production, finding its physical and mechanical properties superior

to those of solid Albizia procera timber (Das et al., 2023). Li et al. (2024) discuss the limitations in load-bearing capacity and stiffness of beam joints in long-span wooden structural elements that are joined using self-drilling screws. To address these limitations, they propose inclined self-drilling screw connections made from engineered bamboo. High strength engineered bamboo plates were employed to enhance the joints of the glued laminated timber (glulam) beams. Within the scope of the experimental study, 13 glulam beams were designed, and four-point bending tests were conducted on the samples. The results indicated that the mechanical properties of beams connected with parallel self-drilling screws were superior to those connected with staggered self-drilling screws. Additionally, it was found that the bending capacity of glulam beams combined with parallel-engineered bamboo scrimber plates increased with the number of self-drilling screws used (Li et al., 2024). Zhang et al. (2023) proposed a design for a hollow rectangular cross-section glulam beam with high bending behavior and stability. To enhance the load-bearing capacity, the beam's bottom was reinforced with fiber reinforced polymer (FRP elements). The study investigated the bending behavior of the beam through experimental, theoretical, and finite element methods. The results showed that the reinforced Glulam beams exhibited increased load-bearing capacity, and that the strengthening effect of CFRP elements was superior to that of BFRP elements (Zhang et al., 2023). Mercimek et al. (2024) conducted a four-point bending test on 26 glulam beams to investigate how various factors—including the number of laminated layers, the distance between finger joint connections, the direction of the finger joints, the use or non-use of reinforcement, and the spacing of CFRP strips—affect the bending behavior of glulam beams. The results obtained from the experimental study were compared with numerical analyses conducted using the finite element software ABAQUS. The study concluded that the developed reinforcement method incorporating CFRP strips enhanced the load-bearing capacity of finger-jointed glulam beams and positively influenced the overall load-displacement behavior (Mercimek et al., 2024). Mei et al. (2024) conducted a study on glulam beams reinforced with connected steel rods. The research aimed to evaluate the reinforcement ratio and pre-tensioning level, as well as to assess the impact of unconnected steel rods on the bending capacity of the beams. Theoretical models of both unconnected reinforced and pre-tensioned glulam beams were presented. Consequently, minimum and maximum reinforcement ratios were determined based on beam cracking and variations in sectional stresses. The study also involved relevant analyses to develop a bending capacity prediction model (Mei et al., 2024). İşleyen et al. (2023) investigated the overall behavior of glulam beams reinforced with CFRP strips and the performance of timber under rapid dynamic impact loading in conjunction with reinforcement. In the study, CFRP strip elements were placed in the lower section of the glulam beams and between multiple L-layers of laminated beam components. Additionally, fan-type anchors were applied to delay the separation of CFRP strip elements from the surface. The reinforced glulam elements were compared with reference samples that did not receive reinforcement. The CFRP-reinforced glulam beams were also modeled using ABAQUS finite element software (İşleyen et al., 2023). Wang et al. (2024) conducted a study utilizing birch plywood panels to bond two glulam beam halves for creating a long span. In this study, four-point bending tests were applied to the samples using birch plywood in the mid-span region of the glulam beams. Numerical and analytical modeling were performed, revealing that the developed models aligned well with the obtained test results (Wang et al., 2024). Zhao et al. (2023) conducted a study on a self-balancing system known as a glulam beam series for large-span glulam structures. Five-point bending tests were performed on the prepared samples. The study found that as the diameter increased, the damage mode of the samples changed, ranging from failure of the lower steel cables to damage in the upper glulam beams. Various parameter analyses were considered to develop numerical models, and a series of design recommendations were presented, taking into account both load capacity and economic impacts (Zhao et al., 2023). Yang et al. (2016) conducted an experimental and theoretical study investigating the bending behavior of glulam beams reinforced with FRP and steel elements. In the study, Douglas fir was used, and the test samples were prepared both as reinforced and unreinforced, undergoing four-point bending tests. The effects of reinforcement materials, reinforcement ratios, and configurations on bending behavior were examined. The results indicated that the reinforced beams exhibited improved bending capacity, overall bending stiffness, and tensile deformation at failure compared to the unreinforced control beams (Yang et al., 2016). He et al. (2022) conducted four-point bending tests on 18 glulam wooden beams, either unreinforced or reinforced with CFRP. The study investigated the effects of the elastic modulus of CFRP and the configuration of CFRP on bending performance. The results indicated that the reinforced glulam beams exhibited a more ductile bending failure characteristic compared to the unreinforced beams (He et al., 2022). Uzel et al. (2018) compared the bending behavior of glulam beams made from Pinus sylvestris with that of solid wood beams. The variables considered in the study included the number of laminations, types of adhesives used, and the reinforcement grids applied to the laminated surfaces. The results indicated that the highest ultimate load capacity was observed in beams made with five laminated layers, utilizing polyurethane adhesives and steel wire reinforcement grids (Uzel et al., 2018). İşleyen et al. (2021a) conducted a study on the reinforcement of

laminated timber beams. In this context, they examined glulam beams by determining the variables associated with the application of CFRP strips in different configurations and CFRP fan-type anchors at the ends of the strips. The study involved testing reinforced laminated timber beams, both anchored and unanchored with CFRP strips, using a three-point bending test. The results included load-displacement graphs of the specimens, from which various interpretations were made (İşleyen et al., 2021a). In another study, İşleyen et al. (2021b) experimentally investigated the behavior under bending loads of three-layer laminated timber beams reinforced with CFRP strips, both anchored and unanchored, featuring different adhesive lengths. The findings indicated that increasing the adhesive length of the CFRP strips and employing CFRP fan-type anchors at the strip ends enhanced the ultimate load capacity, initial stiffness values, displacement ductility ratios, and energy dissipation capacity of the timber beams (İşleyen et al., 2021b). Ghoroubi et al. (2022) conducted an experimental study on the general load-displacement behavior, stress distributions, and shear stress-shear displacement behavior in the connection zones where wooden structural elements are bonded with adhesive or mechanical anchors. The experimental work examined the overall load-displacement behavior of wooden connection areas combined with adhesive and mechanical anchors at lengths of 180, 240, and 350 mm. The study proposed a generalized material model for the shear stress-shear displacement interface at wooden-to-wood connection points (Ghoroubi et al., 2022).

Based on the conducted investigations, it has been determined that there are studies on glulam beams in the literature, with recent research increasingly focusing on the reinforcement of glulam beams. Furthermore, in the experimental studies found in the literature, the loading types applied to glulam beams under bending are generally uniform (either three-point or four-point loading), allowing for an examination of the mechanical properties of the glulam beams. Additionally, when reviewing the experimental studies in the literature, it is observed that there are a limited number of studies where both three-point and four-point bending tests are applied together, and most of these studies primarily concentrate on solid wood elements. In recent literature, studies involving both loading types on massive wood elements have been examined. Notably, research by Hein and Brancheriau (2018) focused on Eucalyptus species, while Brancheriau et al. (2002) investigated six different wood types. Additionally, Yoshihara (2013) explored solid wood, MDF, and five-plywood wood elements, and Babiak et al. (2018) analyzed spruce and oak wood samples. In this context, examining the behavior of glulam beams under different loading types during bending tests is crucial for comprehensively evaluating and interpreting their load-displacement behaviors, initial stiffness, and energy dissipation capacities, thereby contributing to the literature. The study investigates the overall load-displacement behavior and other related mechanical properties of glulam beams under various bending loads (three-point and four-point bending) and differentiates loading rates (10 mm/min, 20 mm/min, and 30 mm/min) to experimentally reveal the influence of loading rates on the overall load-displacement graph of the glulam beams.

In this study, six glulam wood beam elements were prepared using Sipo wood species. Three of the glulam beams were subjected to four-point bending tests, while the other three underwent three-point bending tests. Additionally, the specimens were subjected to different loading rates (10 mm/min, 20 mm/min, and 30 mm/min) under a constant load. By comparing the overall behaviors of the specimens under different loading types and rates, the results were interpreted through general load-displacement graphs, ultimate load capacity, displacement at ultimate load, initial stiffness, and energy dissipation capacity values.

2. Materials and Methods

2.1. Test specimens and materials

In the experimental study, laminated wood beam test specimens were produced using Sipo wood through the glulam engineering technique. As part of the testing program, six glulam Sipo wood beam elements were prepared (Table 1). These specimens were tested under three-point and four-point bending loads, which were monotonically increased until failure occurred. The variables examined in this study included loading type and loading rate. The behaviors of the glulam beams under different loading types and rates were characterized through their overall load-displacement graphs. In this context, it is aimed to make a significant contribution to the literature by revealing the general load-displacement behavior, initial stiffness and energy dissipation capacity of the tropical sipo tree species selected in the study and used as a glulam beam, which is included in a few studies in the literature.

Table 1. Properties of test specimens

Specimen	Dimensions (mm)	Number of glulam layer
1 2 3 4 5 6	72 x 90 x 1450	3

The wooden beams were prepared with dimensions of 72 x 90 x 1450 mm. The laminated wooden beams were produced in three layers, each with a thickness of 24 mm. The experimental study utilized the tropical wood species known as Sipo, which has been less frequently studied in the literature. Care was taken to select wood for the experimental work that did not contain defects

such as knots, cracks, or fiber irregularities. The physical and mechanical properties of Sipo wood are presented in Table 2. Furthermore, in the production of Sipo glulam, PVA d3/d4 (polyvinyl acetate) adhesive from the manufacturer *"Follmann"* was used, with attention to ensuring that the materials to be bonded were dry and free of dust and grease. Three wooden elements, each 24 mm thick, were bonded together using polyvinyl acetate adhesive, completing the production of the glulam wooden beams.

Table 2. Physical and mechanical properties of sipo wood (Gérard et al., 2017)

Properties	Value	Unit
Density	0,62	g/cm^3
Coefficient of volumetric shrinkage	0,42%	per %
Crushing strength	56	MPa
Static bending strength	91	MPa
Longitudinal modulus of elasticity	13,240	MPa

Note: at 12% moisture content, with 1MPa=1 N/mm^2

In the experimental study, the four-point bending test setup applied to glulam beams is illustrated in Figure 1, while the three-point bending test setup is shown in Figure 2. The experimental study program for the test specimens is presented in Table 3.

2.2. Bending Test Setup

In the experimental study, bending tests were conducted using a servo-hydraulic loading system of MTS-322 brand with a capacity of 500 kN. A hydraulic actuator system with a capacity of 500 kN was employed to apply loads to the test specimens, and deformations were measured. At this point, the first group of tests, consisting of specimens numbered 1, 2, and 3, underwent four-point bending tests at a constant loading rate; the loading rates were set at 10 mm/min for specimen 1, 20 mm/min for specimen 2, and 30 mm/min for specimen 3. The four-point static bending load was monotonically increased until the specimens failed. In the second group of tests, consisting of specimens numbered 4, 5, and 6, three-point bending tests were similarly conducted at a constant loading rate; the loading rates were 10 mm/min for specimen 4, 20 mm/min for specimen 5, and 30 mm/min for specimen 6. The three-point static bending load was monotonically increased until the specimens failed. The tests were conducted based on load-displacement graphs.

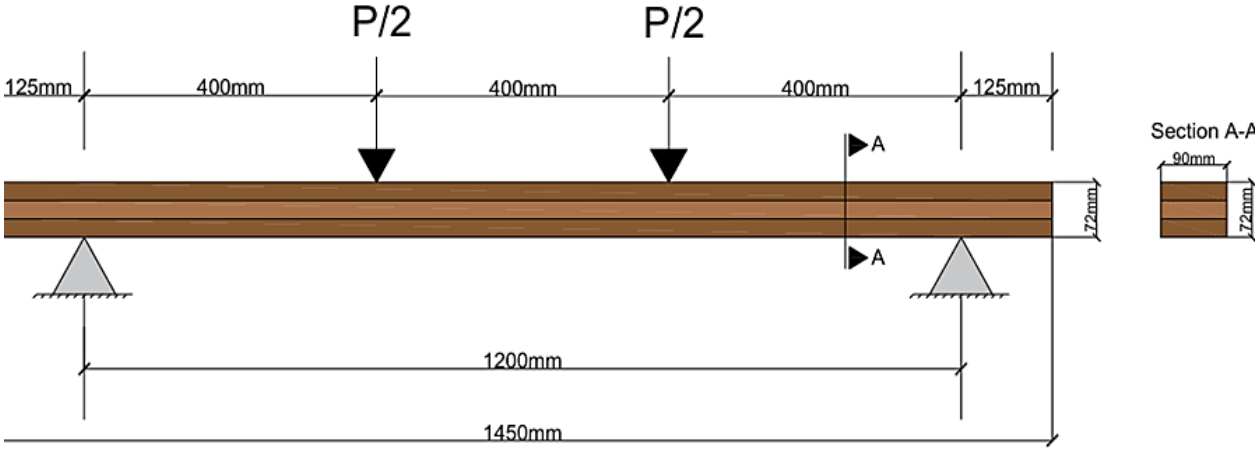

Figure 1. The four-point bending test setup applied to glulam beams.

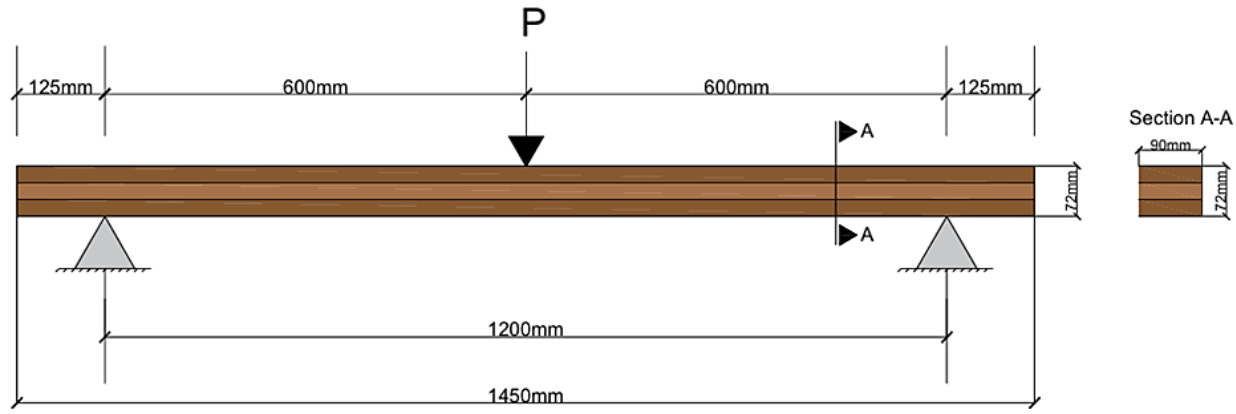

Figure 2. The three-point bending test setup applied to glulam beams.

Table 3. Experimental study program

Specimen	Loading type	Loading rate
1	Four point bending	10 mm/min
2		20 mm/min
3		30 mm/min
4	Three point bending	10 mm/min
5		20 mm/min
6		30 mm/min

3. Results and Discussion

The ultimate load capacity, displacement at ultimate load, initial stiffness, max. displacement, and energy dissipation capacity values were interpreted from the load-displacement graphs of the experimental specimens. The results obtained from the experimental study and the calculated values are presented in Table 4. The test specimens' initial stiffness values were calculated by proportioning the 10 kN load value to the displacement at that point, where no slope change occurred in the load-displacement graphs. It was observed that the ultimate load-bearing capacity of the test specimens decreased by 15%, falling below 85% of their ultimate carrying capacity, which were identified as the failure points of the specimens in the experimental study. The initial stiffness values of the experimental specimens were calculated using the slope of the linear portion of the load-displacement graphs in the initial region. The energy dissipation capacity values were obtained by calculating the area under the load-displacement graphs. In calculating the energy dissipation capacities of the experimental specimens, the area under the graphs was calculated by taking the region up to the point of failure. The points and approaches used in the calculations are illustrated on a typical load-displacement graph in Figure 3. The data obtained from the experimental study are illustrated with graphs and shown in Figure 4. Load-displacement graphs obtained as a result of the experimental study are given in Figure 5. Photographs illustrating the failure states of the specimens after the experimental study are shown in Figure 6.

Table 4. Experimental results

Specimen	Ultimate load capacity(kN)	Displacement at ultimate load (mm)	Initial Stiffness (kN/mm)	Max. displacement (mm)	Energy dissipation capacity (kN.mm)	Failure mode
1	18,27	15,83	1,15	15,84	142,48	Cracking and separation in the tension zone
2	18,13	15,22	1,19	15,23	134,91	Separation and fractures in the tension zone
3	41,12	33,38	1,23	33,41	726,53	Cracking and separation in the tensile zone
4	23,75	36,76	0,65	36,89	508,65	Cracks in the tension zone
5	18,57	28,86	0,64	28,88	288,28	Cracks in the tension zone
6	19,84	21,44	0,93	21,47	214,11	Cracks in the tension zone

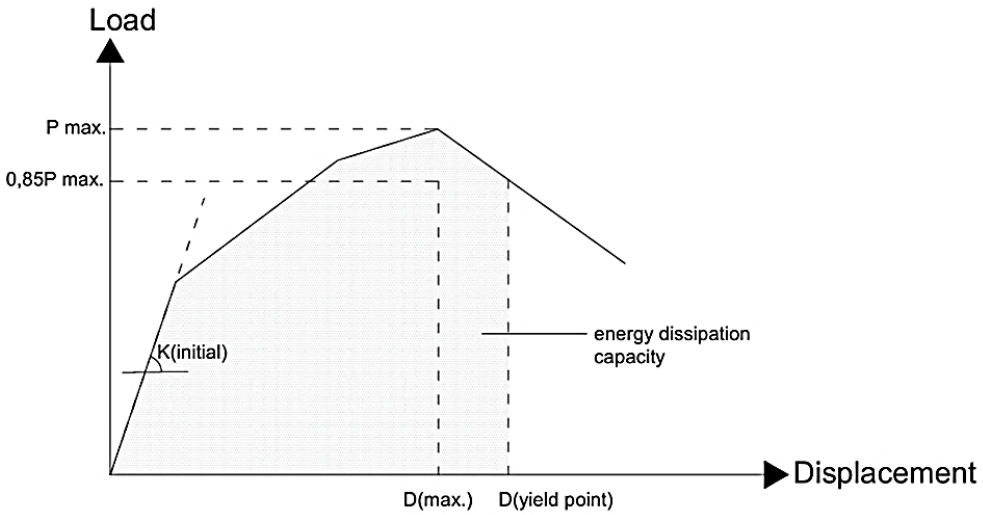

Figure 3. The approach used for calculating initial stiffness and energy dissipation capacity.

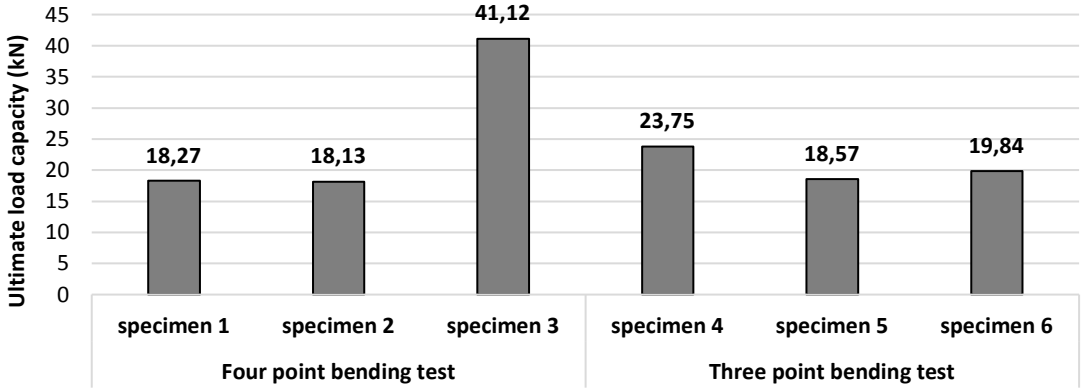

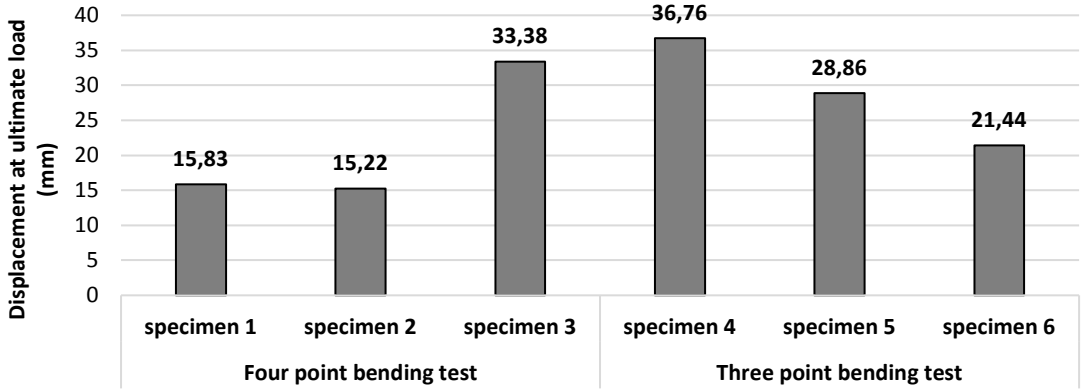

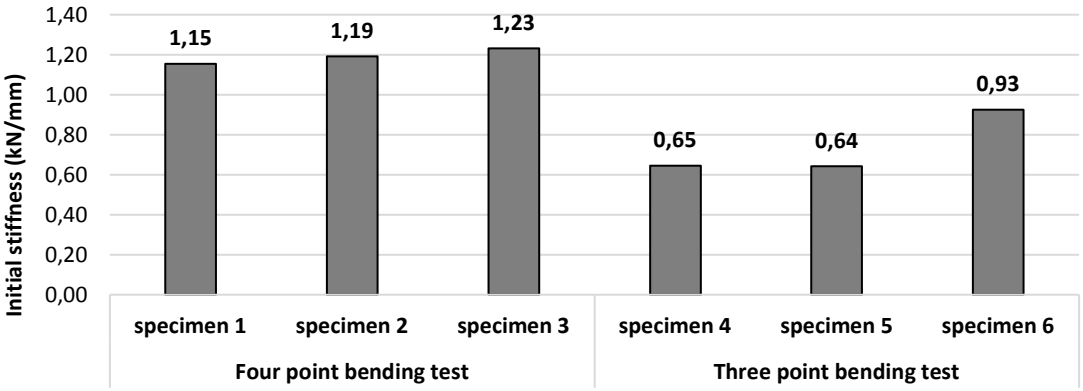

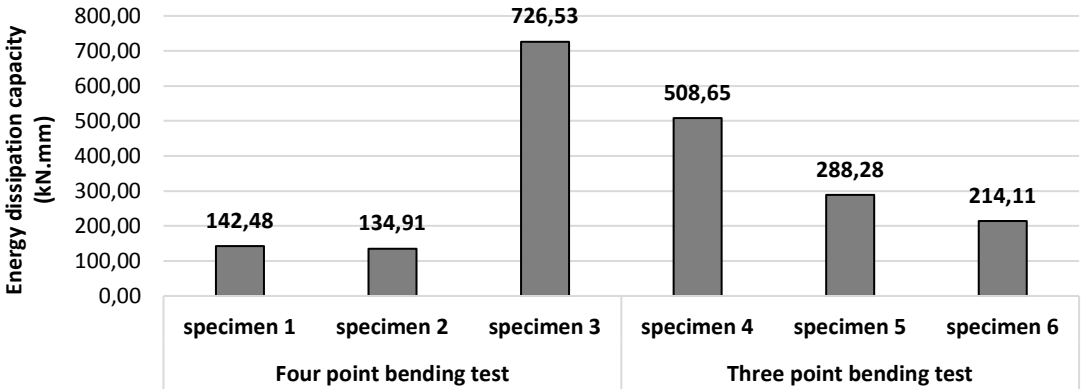

Figure 4. Graphs of the ultimate load capacity, displacement at ultimate load, initial stiffness and energy dissipation capacity values for test samples.

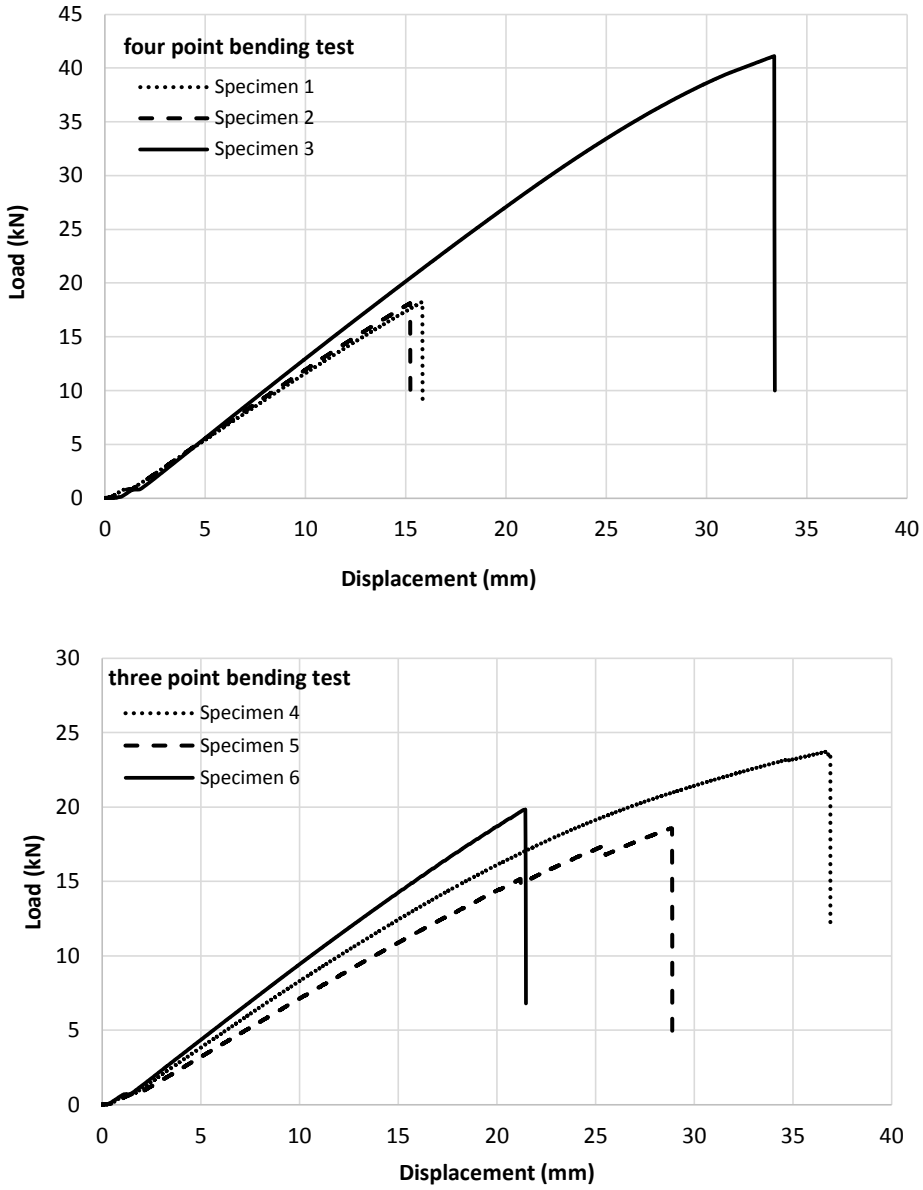

Figure 5. Load-displacement graphs of specimens.

Figure 6. Failure modes of specimens.

3.1. Loading Type Effect

When comparing the results of bending tests on glulam beams under different loading types, the ultimate load-bearing capacity of specimens tested using a three-point bending test was found to be higher than that of those tested with a four-point bending test, except for specimen 3. Notably, specimen 4, tested at the same loading rate (10 mm/min), showed approximately 30% greater ultimate load-bearing capacity than specimen 1, which underwent the four-point test. Similarly, for specimens 2 and 5, tested at 20 mm/min, specimen 5 exhibited about 3% higher ultimate load-bearing capacity compared to specimen 2, which was subjected to the four-point test. A similar result was found in a study by Hein and Brancheriau (2018). In their research on Eucalyptus specimens, they conducted both three-point and four-point bending tests and found that the average wood strength obtained from the three-point bending test (76.8 MPa) was higher than that obtained from the four-point bending test (73 MPa). They also emphasized that the volume of wood under maximum stress was greater in the four-point bending test, which led to longer exposure of the beam to the effects of internal cracks or defects at the moment of failure (Hein and Brancheriau, 2018).

The results obtained from the experimental study showed a contrasting outcome when comparing specimens 3 and 6 at the same loading rate (30 mm/min). Specimen 6, tested using the three-point bending method, exhibited approximately 52% lower results than specimen 3, which underwent the four-point bending test. These findings regarding the ultimate load-bearing capacities of the specimens were consistent for the displacement at ultimate load, maximum displacement, and energy dissipation capacity values as well.

In this context, when comparing specimens 1 and 4 at the same loading rate (10 mm/min), specimen 4, tested using the three-point bending method, showed approximately 132% significantly greater displacement at ultimate load compared to specimen 1, which was subjected to the four-point test. Similarly, at a loading rate of 20 mm/min, specimen 5 exhibited around 90% greater displacement at ultimate load compared to specimen 2. Conversely, for specimens 3 and 6 at the same loading rate (30 mm/min), specimen 6 showed approximately 35% lower displacement at ultimate load than specimen 3, which underwent the four-point bending test.

At the same loading rate (10 mm/min), specimen 4, tested using the three-point bending method, exhibited approximately 43% lower initial stiffness compared to specimen 1, which was subjected to the four-point bending test. Similarly, at a loading rate of 20 mm/min, specimen 5 showed around 46% lower initial stiffness compared to specimen 2. For specimens 3 and 6 at the same loading rate (30 mm/min), specimen 6, tested with the three-point method, resulted in approximately 24% lower initial stiffness than specimen 3, which underwent the four-point bending test.

At the same loading rate (10 mm/min), specimen 4, tested using the three-point bending method, demonstrated approximately four times greater energy dissipation capacity compared to specimen 1, which was subjected to the four-point bending test. Similarly, at a loading rate of 20 mm/min, specimen 5 exhibited more than twice the energy dissipation capacity of specimen 2. In contrast, for specimens 3 and 6 at the same loading rate (30 mm/min), specimen 6, tested with the three-point method, resulted in approximately one-third less energy dissipation capacity than specimen 3, which underwent the four-point bending test.

The experimental study revealed differences between the values obtained from three-point and four-point bending tests on glulam beams, with generally higher values recorded for specimens subjected to the three-point bending test compared to those tested using the four-point method at the same loading rates. This finding aligns with the results of Babiak et al. (2018), who conducted similar tests on spruce and oak wood specimens, noting discrepancies between the two testing methods. They suggested that these differences could be attributed to shear stresses (Babiak et al., 2018).

3.2. Loading Rate Effect

When comparing different loading rates in four-point bending tests conducted on glulam beams, specimen 1 reached an ultimate load capacity of 18.27 kN. Specimen 2, at a loading rate of 20 mm/min, resulted in approximately 0.7% lower maximum force than specimen 1. However, when specimen 3 was tested at a loading rate of 30 mm/min, it demonstrated a significantly higher ultimate load capacity, approximately 127% greater than that of specimen 2. Examining the displacements at ultimate load, specimen 1 exhibited a displacement of 15.83 mm. Specimen 2, under the same loading rate of 20 mm/min, showed about 4% less displacement at ultimate load compared to specimen 1. Conversely, specimen 3, tested at 30 mm/min, displayed approximately 119% greater displacement at ultimate load than specimen 2. In terms of initial stiffness, specimen 2 demonstrated about 3% greater initial stiffness compared to specimen 1, while specimen 3 showed approximately 3% greater initial stiffness than specimen 2. Regarding energy dissipation capacities, specimen 2 had an energy dissipation capacity about 5% lower than that of specimen 1, whereas specimen 3 exhibited a significantly higher energy dissipation capacity, nearly six times that of specimen 2.

In three-point bending tests conducted on glulam beams with varying loading rates, specimen 4 achieved an ultimate load capacity of 23.75 kN at a loading rate of 10 mm/min. Specimen 5, tested at 20 mm/min, exhibited approximately 22% lower ultimate load compared to specimen 4, while specimen 6, at 30 mm/min, showed about 7% higher maximum force than specimen 5. When comparing displacements at ultimate load, it was

observed that displacements gradually decreased with increasing loading rates. Specifically, specimen 5 had approximately 21% lower displacement than specimen 4, and specimen 6 exhibited about 25% lower displacement at ultimate load compared to specimen 5. In terms of initial stiffness, specimen 4 had a stiffness of 0.65 kN/mm, while specimen 5 was close at 0.64 kN/mm. However, specimen 6 demonstrated approximately 45% greater initial stiffness than specimen 5. Regarding energy dissipation capacities, the highest energy dissipation capacity was recorded for specimen 4 at 508.65 kN.mm. Specimen 5 had about 43% lower energy dissipation compared to specimen 4, while specimen 6 showed approximately 26% lower energy dissipation than specimen 5.

When evaluating the test results in terms of the effects of loading rates, both three-point and four-point bending tests showed significant impacts on the mechanical properties of the specimens. In this context, Gerhards (1977) noted that loading rate has a significant effect on wood. He indicated that loading speed is the most influential factor on the tensile strength perpendicular to the grain in dry wood, followed by the compressive strength parallel to the grain, as well as bending and shear strengths. He also mentioned that the effects of these last three properties do not differ significantly (Gerhards, 1977). In examining the effects of loading rates on glulam wood beams, both three-point and four-point bending tests revealed that as the loading rate increased from 10 mm/min to 20 mm/min, the ultimate load capacity of the specimens decreased. However, an increase from 20 mm/min to 30 mm/min resulted in a significant increase in ultimate load capacity, particularly for specimen 3. In the four-point bending test, the initial stiffness increased in parallel with the loading rate. In contrast, in the three-point bending test, the initial stiffness decreased when the loading rate increased from 10 mm/min to 20 mm/min, but increased again when the loading rate rose from 20 mm/min to 30 mm/min. The energy dissipation capacities also showed that in the four-point bending test, there was a decrease in energy dissipation at the loading rate of 20 mm/min, correlating with the ultimate load results. However, the highest value was obtained at the loading rate of 30 mm/min. In the three-point bending test, energy dissipation capacities gradually decreased with increasing loading rates.

When examining the experimental results based on the loading rate, it was found that, with the exception of the loading rate of 20 mm/min, an increase in loading rate led to an enhancement in the ultimate load, displacement at ultimate load, initial stiffness, and energy dissipation capacity in four-point bending tests. However, when assessing the three-point bending test results based on loading rates, no significant outcomes were observed regarding ultimate load, displacement at ultimate load, initial stiffness, and energy dissipation capacity with increasing loading rates. Similar findings were reported by Büyüksarı (2017), who conducted three-point bending tests on oak wood at different loading rates and noted that the loading rate had no statistically significant effect on the bending strength of oak. Nonetheless, it was mentioned that the strength and elastic modulus values generally decreased with a reduction in loading speed (Büyüksarı, 2017).

4. Conclusion

In the experimental study, test samples made from six sipo glulam wood elements were subjected to bending tests. The aim was to investigate and reveal the behavior of glulam samples under different loading types (four-point and three-point bending tests) and various loading rates (10 mm/min, 20 mm/min, and 30 mm/min). In this context, general load-displacement curves for the glulam samples were constructed based on the experimental data; from these graphs, the ultimate load capacity, displacement at ultimate load, initial stiffness, and energy dissipation capacities of the samples were determined. The results obtained from the study can be summarized as follows:

- There are differences observed in the values obtained from the three-point and four-point bending tests applied to the glulam beams.
- Generally, the samples subjected to the three-point bending test yielded higher values compared to those tested using the four-point bending test at the same loading rates. However, this result was not applicable to the sample tested with the four-point bending method at a loading rate of 30 mm/min.
- The different loading rates (10 mm/min, 20 mm/min, and 30 mm/min) applied to the glulam beams affected the results obtained from both the three-point and four-point bending tests.
- In the four-point bending test, an increase in the loading rate led to enhancements in the ultimate load, displacement at ultimate load, initial stiffness, and energy dissipation capacity of the samples. However, this result was not applicable at the loading rate of 20 mm/min, where decreases were observed in the ultimate load, displacement at ultimate load, and energy dissipation capacity.
- In the three-point bending test, no significant results were obtained regarding the ultimate load, displacement at ultimate load, initial stiffness, and energy dissipation capacity with increasing loading rates. It was noted that the displacement at ultimate load and energy dissipation capacity values decreased as the loading rate increased.
- In both the four-point and three-point bending tests, a significant decrease in the values of the samples was observed at the loading rate of 20 mm/min.
- In the case of the four-point bending test conducted at a loading rate of 30 mm/min, the values were found to be at their highest level.

Author Contributions

The percentages of the author contributions are presented below. The author reviewed and approved the final version of the manuscript.

	M.A.K.A
C	100
D	100
S	100
DCP	100
DAI	100
L	100
W	100
CR	100
SR	100
PM	100
FA	100

C=Concept, D= design, S= supervision, DCP= data collection and/or processing, DAI= data analysis and/or interpretation, L= literature search, W= writing, CR= critical review, SR= submission and revision, PM= project management, FA= funding acquisition.

Conflict of Interest

The author declared that there is no conflict of interest.

Ethical Consideration

Ethics committee approval was not required for this study because of there was no study on animals or humans.

Acknowledgements

The author would like to thank the "Department of Civil Engineering at Ankara University" for the use of the "Structural Mechanics Laboratory".

References

Babiak M, Gaff M, Sikora A, Hysek Š. 2018. Modulus of elasticity in three-and four-point bending of wood. Compos Struct, 204: 454-465.

Brancheriau L, Bailleres H, Guitard D. 2002. Comparison between modulus of elasticity values calculated using 3 and 4 point bending tests on wooden samples. Wood Sci Technol, 36(5): 367-383.

Büyüksari Ü. 2017. Effect of loading rate on mechanical properties of micro-sized oak wood. Maderas, 19(2): 163-172.

Das AK, Islam MN, Ghosh CK, Ghosh RK. 2023. Physical and mechanical properties of Albizia procera glulam beam. Heliyon, 9(8).

Gérard J, Guibal D, Paradis S, Cerre JC. 2017. Tropical timber atlas: technological characteristics and uses. Éditions Quæ. RD 10 78026 Versailles Cedex, Paris, France, pp: 834-836

Gerhards CC. 1977. Effect of duration and rate of loading on strength of wood and wood-based materials, USDA Forest Service Research Paper, U.S. Department of Agriculture Forest Service Forest Products Laboratory Madison, Wis, USA, pp: 1-24.

Ghoroubi R, Mercimek Ö, Sakin S, Anil Ö. 2022. Experimental investigation of bonding behavior of anchoraged timber-to-timber joint. Arch Civ Mech Eng, 22: 1-16.

He M, Wang Y, Li Z, Zhou L, Tong Y, Sun X. 2022. An experimental and analytical study on the bending performance of CFRP-reinforced glulam beams. Front Mater, 8: 802249.

Hein PRG, Brancheriau L. 2018. Comparison between three-point and four-point flexural tests to determine wood strength of Eucalyptus specimens. Maderas, 20(3): 333-342.

Issa CA, Kmeid Z. 2005. Advanced wood engineering: glulam beams. Constr Build Mater, 19(2): 99-106.

İşleyen ÜK, Ghoroubi R, Mercimek Ö, Anıl Ö, Erdem RT. 2023. Investigation of impact behavior of glulam beam strengthened with CFRP. Struct, 51: 196-214.

İşleyen ÜK, Ghoroubi R, Mercimek Ö, Anil Ö, Erdem RT. 2021a. Behavior of glulam timber beam strengthened with carbon fiber reinforced polymer strip for flexural loading. J Reinf Plast Compos, 40(17-18): 665-685.

İşleyen ÜK, Ghoroubi R, Mercimek Ö, Anıl Ö, Togay A, Erdem RT. 2021b. Effect of anchorage number and CFRP strips length on behavior of strengthened glulam timber beam for flexural loading. Adv Struct Eng, 24(9): 1869-1882.

Li H, Ren Y, Zuo T, Xu X, Wang Y, Tian P. 2024. Experimental study of flexural behavior of glulam Douglas Fir beams spliced with engineered bamboo cover plates and inclined self-tapping screws. Struct, 65: 106658.

Mei L, Ren J, Lin X, Wu M, Guo N, Yang W, Sheng Y. 2024. Analytical model for prestressed glulam beams reinforced with unbonded steel bars. Eng Struct, 307: 117862.

Mercimek Ö, Ghoroubi R, Akkaya ST, Türer A, Anıl Ö, İşleyen, ÜK. 2024. Flexural behavior of finger joint connected glulam wooden beams strengthened with CFRP strips. Struct 66: 106853.

Stark NM, Cai Z, Carll C. 2010. Wood-based composite materials panel products, glued-laminated timber, structural composite lumber, and wood–nonwood composite materials. In: Ross RJ, editor. Wood handbook: wood as an engineering material. Forest Products Laboratory, United States Department of Agriculture Forest Service Madison, Wisconsin, USA, pp: (11-1)-(11-26).

Uzel M, Togay A, Anil Ö, Söğütlü C. 2018. Experimental investigation of flexural behavior of glulam beams reinforced with different bonding surface materials. Constr. Build Mater, 158: 149-163.

Wang Y, He M, Li Z. 2024. Flexural behavior of glulam beams reinforced by bonded prestressing tendons. Eng Struct, 315:118436.

Wang T, Wang Y, Ringaby J, Crocetti R, Wålinder M, Blomqvist L. 2024. Glulam beams adhesively bonded by birch plywood plates in moment-resisting beam-to-beam connections. Eng Struct, 302:117471.

Yang H, Liu W, Lu W, Zhu S, Geng Q. 2016. Flexural behavior of FRP and steel reinforced glulam beams: Experimental and theoretical evaluation. Constr Build Mater, 106: 550-563.

Yoshihara H. 2013. Comparison of results obtained by static 3- and 4-point bending and flexural vibration tests on solid wood, MDF, and 5-plywood. HF, 67(8): 941-948.

Zhao J, Liu H, Chen Z, Zhao S, Yang S, He F. 2023. Investigation on the mechanical behavior of glulam beam string. Struct, 52: 582-597.

Zhang X, Zhang Y, Xie X. 2023. Experimental and analytical investigation of the flexural behaviour of stiffened hollow glulam beams reinforced with fibre reinforced polymer. Struct, 50: 810-822.

Black Sea Journal of Engineering and Science
doi: 10.34248/bsengineering.1560496

Open Access Journal
e-ISSN: 2619 – 8991

Research Article
Volume 8 - Issue 1: 11-18 / January 2025

TECHNICAL EXAMINATION OF PASTURE AREAS IN LAND CONSOLIDATION PROJECTS AND LEGAL FRAMEWORK: THE CASE OF BALIKESİR PROVINCE, TÜRKİYE

Tayfun ÇAY[1], Ömer ACAR[2*]

[1]*Konya Technical University, Faculty of Engineering and Natural Sciences, Department of Geomatics Engineering, 42250, Konya, Türkiye*
[2]*Kahramanmaraş Sütçü İmam University, Göksun Vocational School, Department of Architecture and Urban Planning, 46600, Kahramanmaraş, Türkiye*

Abstract: Among the natural resources, pasture areas are of great importance for animal husbandry and animal production. In addition, they have many benefits, from preventing soil and water erosion to protecting genetic resources. Many studies are being carried out to protect, improve, and make these areas sustainable. In rural areas, land consolidation studies are carried out to obtain the highest yield from the unit area with the least cost. Inland consolidation studies, the geometric shapes of the parcels are corrected, their planning is done so that they will have direct access to roads, irrigation, and drainage networks, and land reclamation is carried out. Pasture lands within the regulation border are also evaluated within this scope. In Türkiye, until April 28, 2018, consolidation studies were carried out by the Ministry of Food, Agriculture and Livestock and the General Directorate of State Hydraulic Works, while after this date, they were carried out by the General Directorate of State Hydraulic Works. In addition to the changes in the implementing institution in the consolidation projects, changes were made to the legislation. The changes made within this scope also include the evaluation of pasture areas. In this study, the Manyas Left Bank Irrigation and Fertile Pumped Irrigation L.C. and F.D.S. Project, the works carried out in Bereketli and Simavlı villages will be evaluated. The General Directorate of State Hydraulic Works carries out the project. Different applications regarding pasture areas within the project's scope were made in two villages. The main difference in the application is the cutting from pasture areas. No cutting was done in Simavlı Village pastures, but Bereketli pastures were cut. Within the scope of our study, these differences were revealed, and their status before and after the project was evaluated. Of the two villages in the same project area, no deduction was made from pasture parcels in Simavlı Village, while deductions were made in Bereketli Village. In Simavlı Village, most of the pasture parcels were left out of the regulation in order to reduce the rate of participation in standard facilities and to avoid expropriation costs.

Keywords: Land consolidation, Pasture, Rural area arrangement, Technical analysis

***Corresponding author:** Kahramanmaraş Sütçü İmam University, Göksun Vocational School, Department of Architecture and Urban Planning, 46600, Kahramanmaraş, Türkiye
E mail: oacar@ksu.edu.tr (Ö. ACAR)
Tayfun ÇAY https://orcid.org/0000-0002-4661-5583
Ömer ACAR https://orcid.org/0000-0002-2382-8594

Received: October 03, 2024
Accepted: November 17, 2024
Published: January 15, 2025

Cite as: Çay T, Acar Ö. 2025. Technical examination of pasture areas in land consolidation projects and legal framework: the case of Balikesir province, Türkiye. BSJ Eng Sci, 8(1): 11-18.

1. Introduction

Rapid industrialization and urbanization have put pressure on rural areas, causing their shrinkage/deterioration (Kucukmehmetoglu and Geymen, 2009; Aydoğdu et al., 2012; Gürbüz et al., 2012; İkincikarakaya et al., 2013; Denizdurduran et al., 2017; Sumiahadi et al., 2020; Yin et al., 2022). Rural areas where food needs are met for living things must be protected and their sustainability ensured (Diesendorf, 2000; Marten, 2001; Capone et al., 2014; Bacior and Prus, 2018; Akın, 2021). One of the essential criteria for sustainable rural development is the efficient and effective use of agricultural lands for their planned purpose (Steiner et al., 2000; Reidsma et al., 2011; Akdeniz et al., 2023).

Land consolidation studies are among the methods applied to ensure this (Pašakarnis and Maliene, 2010; Kaya and Şişman, 2020; Ertunç and Janus, 2021; Zang et al., 2021; Akdeniz and Acar, 2023). Land consolidation refers to the arrangement made in rural areas in line with the objectives of combining small and fragmented agricultural lands with irregular geometric shapes and making them suitable for modern agriculture, increasing agricultural production, using water resources more effectively, protecting and improving soil, ensuring food security, and increasing the living standards of farmers and their families (Çay, 2001; Crecente et al., 2002; Vitikainen, 2004; Demirel, 2005; Lerman and Cimpoieş, 2006; Pašakarnis and Maliene, 2010; Munnangi et al., 2020; Çay and Acar, 2022; Acar and Akdeniz, 2023).

The first land consolidation study in Türkiye was carried out by the General Directorate of Soil and Water in 1961, based on the provisions of the Turkish Civil Code No. 743 and Law No. 7457 on the Organization and Duties of the

General Directorate of Soil Conservation and Agricultural Irrigation Works of the Ministry of Agriculture (Çevik, 1974; Demirtaş and Sarı, 2003; Çay and İşcan, 2005; Acar and Bengin, 2018). From 1961 to 2023, consolidation works were carried out by different institutions at different times and according to different legislations, including the Land Consolidation Regulation, the Soil and Agricultural Reform Law, the Agricultural Reform Law on Land Arrangement in Irrigation Areas, the Soil Protection and Land Use Law, the Law on the Organization and Duties of the General Directorate of State Hydraulic Works, and the Land Consolidation Regulation (Küsek, 2014; Duru et al., 2017; Güzel, 2021; Akkul, 2022). Between 1961 and 2022, consolidation works were completed on 6.78 million hectares, and 82% of the completed works were carried out by the General Directorate of Agricultural Reform (TRGM), 11% by the General Directorate of State Hydraulic Works (DSI), and 7% by other institutions (GTHB, 2016; DSI, 2017; GTHB; 2017; DSI, 2022a). On April 28, 2018, land consolidation works carried out by different institutions under different laws were transferred to DSI to ensure that a single institution managed them. Before April 28, 2018, TRGM was carrying out land consolidation works according to the provisions of Law No. 3083, while DSI was carrying out them according to the provisions of Law No. 5403.

There were differences in the arrangement of pasture areas in the projects carried out by both institutions. While deductions were made from pasture areas in TRGM projects, no deductions were made from pasture areas in DSI projects. The legislative change made with the transfer process started to allow deductions from pasture areas in projects carried out by DSI. The 3rd paragraph of Article 15 of the Land Consolidation and In-Farm Development Services Implementation Regulation published in the Official Gazette dated February 2, 2019 (Official Gazette, 2019) states: "*Meadows and pastures and other immovable properties registered in the public common property register shall be included in the consolidation by making a deduction for the common participation share and shall benefit from the irrigation, drainage, and road system as much as possible.*" Land consolidation projects were examined according to the changes made in the land consolidation legislation. Some consolidation projects carried out by DSI in Bandırma District of Balıkesir were completed before the transfer process, and some were completed after the transfer process. Of the two arrangement areas evaluated, Simavlı Village was registered before the transfer process, and Bereketli Village was registered after the transfer process according to the legislation applied.

Within the scope of our study, these differences were revealed, and their status before and after the project was evaluated. Of the two villages in the same project area, no deduction was made from pasture parcels in Simavlı Village, while deductions were made in Bereketli Village. In Simavlı Village, most of the pasture parcels were left out of the regulation in order to reduce the rate of participation in standard facilities and to avoid expropriation costs.

2. Materials and Methods

Manyas Left Bank Irrigation and Bereketli Pumped Irrigation L.C., and the 25th Regional Directorate of the General Directorate of State Hydraulic Works of the Ministry of Agriculture and Forestry carry out F.D.S. Project in Balıkesir province. Project data in the study area were obtained from the 25th Regional Directorate. It is carried out in 23 villages, 7 in Bandırma district, 5 in Gönen district, and 11 in Manyas district, in an area of approximately 200 km^2. Simavlı Village, where suspension work started before 28.04.2018, and Bereketli Village, where suspension work started after 28.04.2018, were evaluated in the project area (Figure 1). The consolidation work carried out in Simavlı Village started within the scope of the provisions of Law No. 5403 and was evaluated within this scope. The arrangement works were completed without making any deductions from the pasture areas. The consolidation works carried out in Bereketli Village were carried out by the provisions of Law No. 6200, and the arrangement works were completed by making deductions from the pasture areas. In both consolidation projects, the cadastral status (before consolidation) and parcellation plan (after consolidation) were analyzed using LiTop software. Netcad 8.5, LiCad, and ArcGIS software were used to create thematic maps. The inclusion rates of pasture areas in the regulation, cadastral status and parcellation plan, utilization status of irrigation and drainage system, interruption rate, and location change criteria were evaluated in the study area.

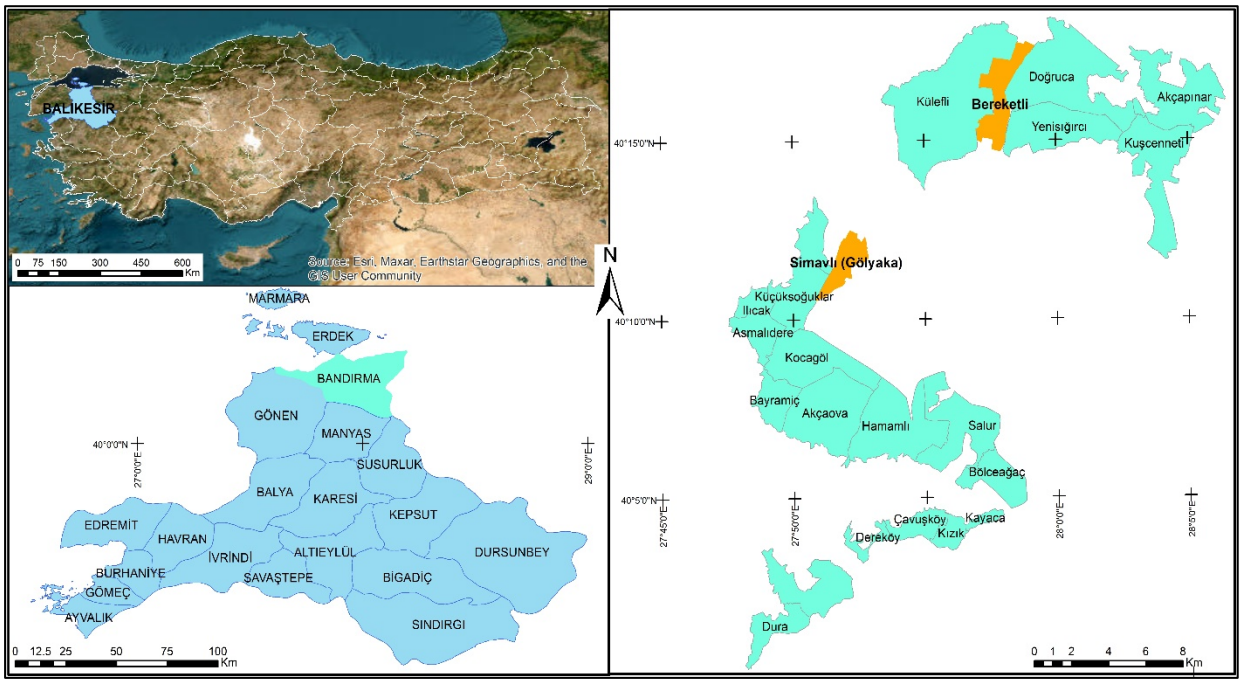

Figure 1. Study area.

3. Results and Discussion

In the arrangement study in Simavlı (Gölyaka) Village, 468 parcels are located within the arrangement border (Figure 2). Although there are 54 pasture parcels in Simavlı village, the number of pasture parcels subject to arrangement is 2 (Figure 2).

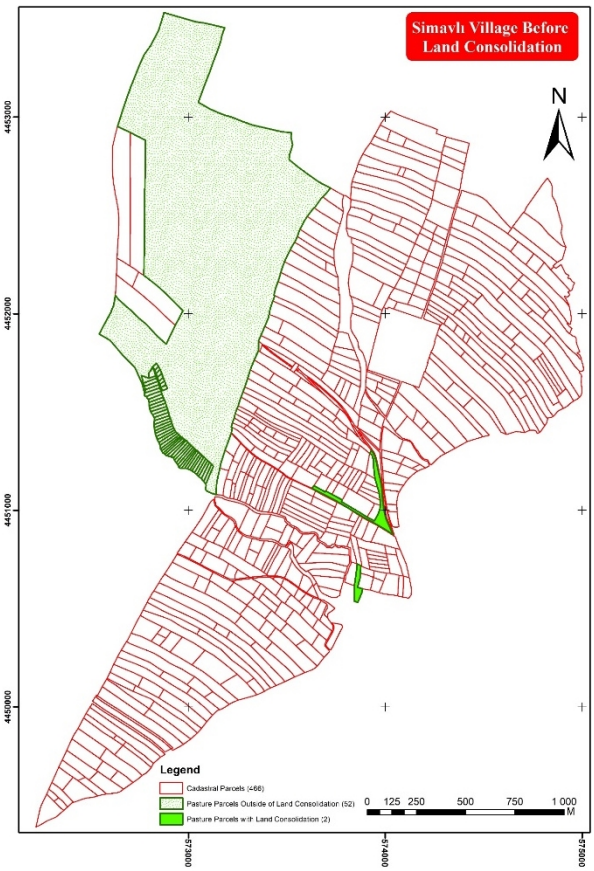

Figure 2. Simavli village cadastral status map

The separation diameter was arranged in the pasture parcel numbered 201, and 2319.15 m² of it was included in the project, and 2330.85 m² of it was left out of consolidation. The total title deed area of 54 pasture parcels is 142.54 hectares, and the total area of pasture parcels included in the project is 1.72 hectares. 98.79% of the pasture parcels in the project area were left out of the project. Pasture parcel numbered 311 was primarily preserved in its current location, and the part of pasture parcel numbered 201 included in the arrangement was planned to be close to the large pasture parcel in Figure 2. In the project, a subdivision plan was prepared for pasture areas as three parcels (Figure 3). The participation share rate for common facilities in the regulation area was calculated as 9.80%, and no deduction was made from pasture parcels (Table 1). Before and after consolidation, the pasture area remained at 17219.14 m², and the pasture parcels did not undergo any changes in area. Within the project's scope, all pasture parcels included/not included in the regulation benefit from irrigation and drainage systems. The first suspension of Simavlı Village was made on 02.06.2017. The project was completed, and registration procedures were carried out on 21.12.2022. In the regulation area, where the first suspension was made before the transfer process, the implementation was completed with the initiative of the authorized administration without making any arrangements according to the new legislation. There is no provision in Law No. 7139 regarding the status of the projects that have been started to be arranged.

In the study conducted in Simavlı Village, land consolidation studies were carried out by the provisions of Law No. 5403. In the projects conducted by D.S.İ, no deductions were made from pasture areas. Especially if

the deduction rate was 10% or more, it caused pasture areas to be excluded from the regulation. If the pasture parcels outside the regulation border were included in the project, the deduction rate would be 11.79%. In this case, D.S.İ. should expropriate the part exceeding 10%, i.e., 1.79%. The expropriation process is not preferred because it will both burden the institution financially and cause time losses due to possible problems during the expropriation process. If deductions were made from pasture areas as is the practice today in Simavlı Village, the deduction rate to be calculated in the project area would be 8.51%, and all pasture parcels would be subject to regulation, allowing for regulation in their geometric shapes.

In the regulation study carried out in Bereketli Village, 509 parcels are located within the regulation border (Figure 4). 6 of these parcels consist of pasture parcels registered as Public Common Property, and all of the pasture parcels are subject to regulation.

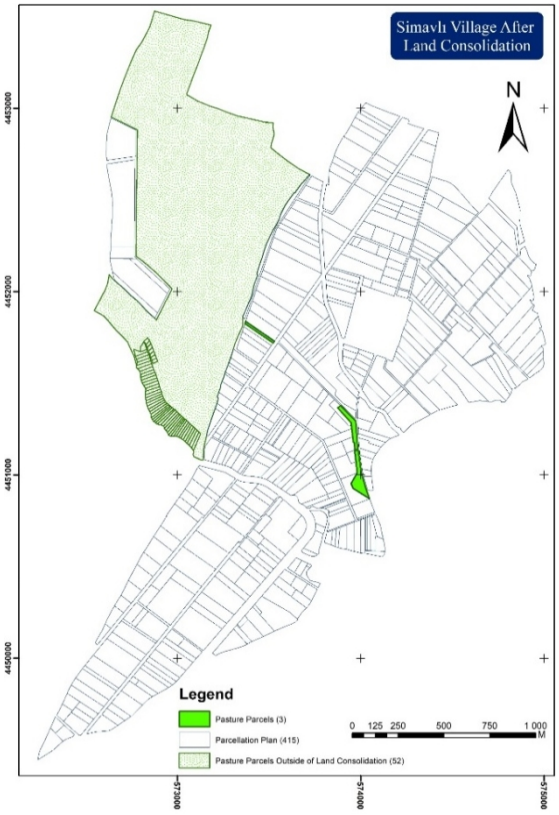

Figure 3. Simavlı village subdivision plan

Table 1. Simavlı village LC-8 list (DSİ, 2022b)

Province: Balıkesir
District: Bandırma
Neighborhood: Simavlı

Republic of Türkiye, Ministry of Agriculture and Forestry, General Directorate of State Hydraulic Works, State Hydraulic Works 25th Regional Directorate, Manyas Left Bank Irrigation and Bereketli Pumped Irrigations Lc, New Block Parcel Sequential List

Land Deduction: 0.098028
LC-8

Landowner			Before land consolidation						Project Values			After Land Consolidation						
			Parcel			Consolidation										AS		
EN	LN	FN	BN	PN	RA (m^2)	AA (m^2)	EA (m^2)	IA (m^2)	PVN	DA	E/PC	EBN	BN	PN	PA (m^2)	A (m^2)	E/PC	PI
1.		TF	-	311	14900	14900	0	14900	8195	0	8195	118	118.	3.	5739.59	5736.59	3155.13	0.550001
						14900	0	14900	8195	0	8195					5736.59	3155.13	
1.		TF	-	311	14900	14900	0	14900	8195	0	8195	118	118.	8.	9163.4	9163.4	5039.87	0.550000
						14900	0	14900	8195	0	8195					9163.4	5039.87	
1.		TF	-	201	4650	4650	2330.85	2319.15	1275.53	0	1275.53	119	135.	4.	2319.15	2319.15	1275.53	0.550000
						4620	2330.85	2319.15	1275.53	0	1275.53					2319.15	1275.53	

Total New Entitlement	9470.53
Total New Parcel Area	17219.14
Total Entitlement	9470.53
Total Deduction Amount (Entitlement)	0
Total Deduction Amount (m^2)	0
Total Parcel Value Number	9470.53
Total Included Area	17219.15
Total Excluded Area	2330.85
Total Allocated Area	17219.14

EN= enterprise number, LN= last name, FN= first name, BN= block number, PN= parcel number, RA= registered area, AA= allocated area, EA= excluded area, IA= included area, PVN= parcel value number, DA= deduction amount, E/PC= entitlement/payment claim, TF= treasury of finance, AS= allocated share, EBN= existing block number. BN= block number, PN= parcel number, PA= parcel area, PI= parcel index

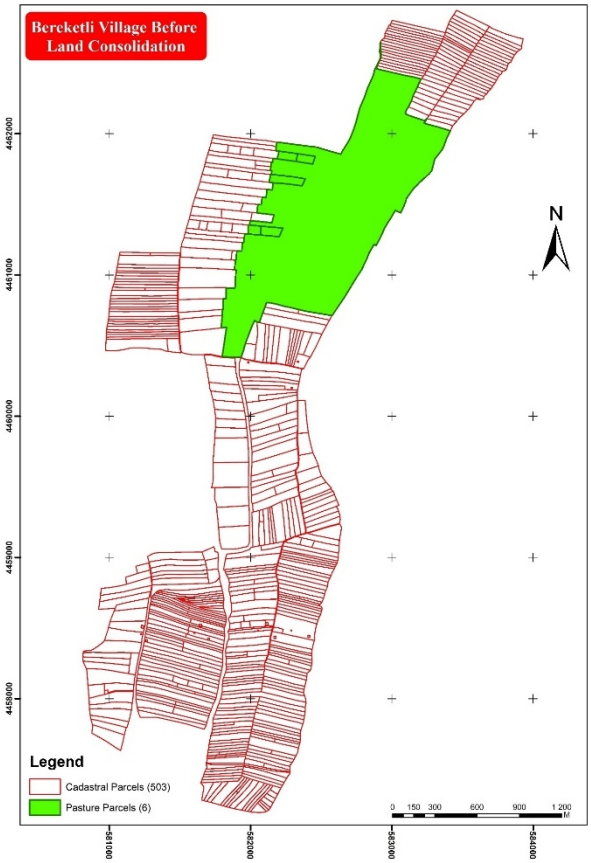

Figure 4. Bereketli village cadastral status map.

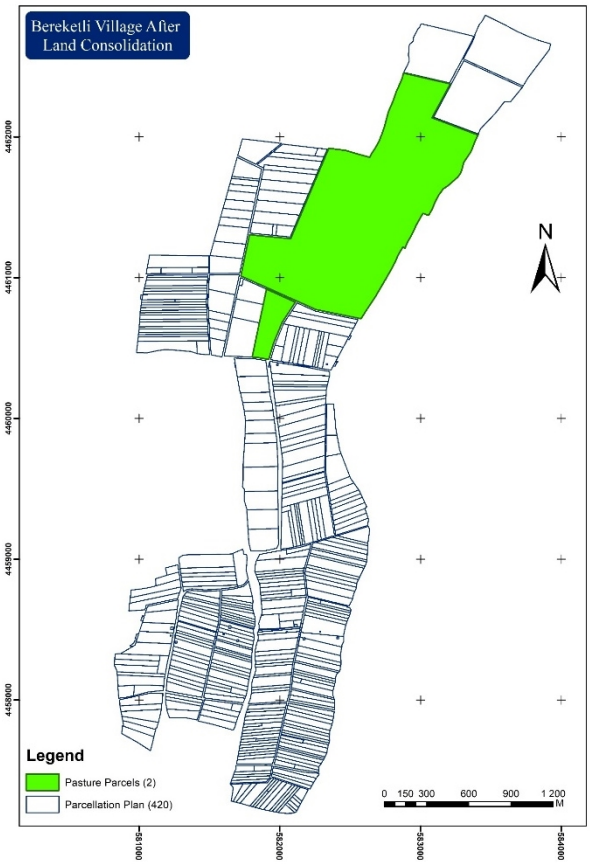

Figure 5. Bereketli village subdivision plan.

The total area of pasture parcels in the regulation area is 141.62 hectares. The deduction amount within the project's scope was calculated as 3.96%, and deductions were made from all parcels included in the regulation at this rate (Table 2). The total deduction amount made in pasture parcels is 5.61 hectares. After the project, pasture parcels were distributed as 136.01 hectares. Pasture areas, six parcels before consolidation, were combined after the project, and a subdivision plan was prepared as two parcels (Figure 5).

The subdivision plan was prepared in the project by preserving the pasture areas primarily in their location before consolidation. It is seen that their geometric shape is more regular than before consolidation. All pasture parcels benefit from irrigation and drainage systems within the project's scope. The first suspension of the arrangement work in Bereketli village was made on 10.11.2018. The project was completed, and registration procedures were completed on 04.01.2023. In the study conducted in Bereketli Village, land consolidation studies were carried out by the provisions of law no. 6200. With the transfer of authority to DSI in land consolidation studies, deductions were made from pasture areas. Pasture areas were included in the consolidation studies, and in-field development services were provided. If the project were intended to be carried out without deductions from pasture areas, the deduction rate to be calculated would be 4.90% when pasture areas were included, and 1% more deductions would be made from private lands, which would prevent the shrinkage of 5.61 hectares of pasture area.

Table 2. Bereketli village LC-8 list (DSİ, 2023)

Province: Balıkesir
District: Bandırma
Neighborhood: Bereketli

Republic of Türkiye, Ministry of Agriculture and Forestry, General Directorate of State Hydraulic Works, State Hydraulic Works 25th Regional Directorate, Manyas Left Bank Irrigation and Bereketli Pumped Irrigations Lc, New Block Parcel Sequential List

Land Deduction: 0.039606

LC-8

Landowner			Before land consolidation						Project Values			After Land Consolidation						
			Parcel				Consolidation									AS		
EN	LN	FN	BN	PN	RA (m²)	AA (m²)	EA (m²)	IA (m²)	PVN	DA	E/PC	EBN	BN	PN	PA (m²)	A (m²)	E/PC	PI
305.		PCP	-	50	5700	5700	0	5700	3135	124.16	3010.84	106	104.	1.	1287077.13	5474.25	3010.84	0.550000
305.		PCP	-	51	9047.38	9047.38	0	9047.38	4976.06	197.08	4778.98	106				8689.05	4778.98	
305.		PCP	-	61	13238.72	13238.72	0	13238.72	7281.3	288.38	6992.91	106				12714.39	6992.91	
305.		PCP	-	70	6900	6900	0	6900	3795	150.3	3644.7	106				6626.72	3644.7	
305.		PCP	-	71	7486.35	7486.35	0	7486.35	4117.49	163.08	3954.42	106				7189.85	3954.42	
305.		PCP	-	151	1373855.54	1373855.54	0	1373855.54	755620.55	29927.11	725693.44	104				1246382.9	685510.59	
						1416227.99	0	1416227.99	778925.39	30850.12	748075.28					1287077.1	707892.43	
305.		PCP	-	151	1373855.54	1373855.54	0	1373855.54	755620.55	29927.11	725693.44	104	128.	4.	73059.72	73059.72	40182.85	0.550000

Total New Entitlement	748075.28
Total New Parcel Area	1360136.85
Total Entitlement	748075.28
Total Deduction Amount (Entitlement)	30850.12
Total Deduction Amount (m²)	56091.14
Total Parcel Value Number	778925.39
Total Included Area	1416227.99
Total Excluded Area	0
Total Allocated Area	1360136.85

EN= enterprise number, LN= last name, FN= first name, BN= block number, PN= parcel number, RA= registered area, AA= allocated area, EA= excluded area, IA= included area, PVN= parcel value number, DA= deduction amount, E/PC= entitlement/payment claim, PCP= public common property, AS= allocated share, EBN= existing block number. BN= block number, PN= parcel number, PA= parcel area, PI= parcel index

4. Conclusion

Land consolidation studies have been carried out in our country since 1961. These studies carried out with many different laws and regulations, were last transferred to DSI with the statute made in 2019 and are currently implemented according to the regulation issued in 2021.

This research examined the approaches applied during the transition to the latest regulation. In this context, the applications made in Simavlı and Bereketli Villages of Bandırma District of Balıkesir Province, whose projects continue during the transition period, were evaluated.

No deduction was made from pasture parcels in the land consolidation study carried out in Simavlı village. There are 54 pasture parcels in the arrangement area in Simavlı village. When pasture areas are included in the arrangement, the participation share rate for common facilities is 11.79%, necessitating expropriation. 52 pasture parcels are excluded from the regulation to reduce the participation rate from common facilities. By excluding 52 pasture parcels from the regulation, the rate of participation share from common facilities was reduced by 2%. This situation caused 52 pasture parcels not to benefit from land consolidation and in-field development services. Because pasture parcels were not included in the arrangement, the block plan where 52 pasture parcels are located was terrible, and the private lands located there were also affected by this situation. As a result, it is seen that not subjecting pasture parcels to deduction does not mean protecting pastures; on the contrary, it means that pastures in project areas such as Simavlı do not benefit from land consolidation and in-field development services.

In the land consolidation work carried out in Bereketli Village, deductions were made from pasture areas. A deduction of 3.96% was made from the pasture areas included in the arrangement in Bereketli Village as a participation share in common facilities. If the project had been completed without deductions from pastures, the deduction rate would have increased to 4.9%. Since the project was completed by deductions from pasture parcels in this area, the pasture area decreased from 141.62 ha to 136.01 ha, and 5.61 ha of pasture area was allocated to shared facilities.

While no deductions were made in Simavlı Village, which is included in the same project, deductions were made in Bereketli Village. In the regulation made with Law No. 7139, it was stated that all projects should be evaluated within the scope of this law on the date of the law announcement within the scope of the transfer process. Instead, an article could have been added stating that projects to be made after the law announcement date should be subject to this law and projects whose tenders were made before the law announcement date should be completed according to the provisions of the legislation, they were subject to.

According to the current legislation, pasture areas are cut. Pasture areas are essential areas for animal husbandry. These areas need to be protected, and grass quality needs to be improved. However, pasture quality

varies in each region, and pasture quality may even be lost. Therefore, each region should be evaluated on its own. Social surveys conducted before land consolidation should be more critical, and livelihood determination should be more comprehensive. Decisions should be made considering the people's livelihood in the project area. Pasture commissions in provincial directorates of agriculture should give opinions on whether to make cuts, and project-specific decisions should be made based on these opinions. It may be more beneficial to make a legislative change in order not to make deductions from pasture areas where animal husbandry is intensive. Pasture quality is good, and to make deductions in areas where agricultural production is intensive.

Author Contributions

The percentages of the authors' contributions are presented below. The author reviewed and approved the final version of the manuscript.

	T.Ç.	Ö.A.
C	50	50
D	50	50
S	50	50
DCP	50	50
DAI	50	50
L	50	50
W	50	50
CR	50	50
SR	50	50
PM	50	50
FA	50	50

C=Concept, D= design, S= supervision, DCP= data collection and/or processing, DAI= data analysis and/or interpretation, L= literature search, W= writing, CR= critical review, SR= submission and revision, PM= project management, FA= funding acquisition.

Conflict of Interest

The authors declared that there is no conflict of interest.

Ethical Consideration

Ethics committee approval was not required for this study because of there was no study on animals or humans.

References

Acar Ö, Akdeniz HB. 2023. Arazi toplulaştırma projelerinin parsel şekil değişimine etkisinin analizi: Manyas/Salur mahallesi örneği, Türkiye. In: Ayaz T, Öztürk F, editors. Tarımsal Eski Sorunlara Yeni Yaklaşımlar. Iksad Publishing House, Ankara, Türkiye pp: 81–101. https://doi.org/10.5281/zenodo.8373721

Acar Ö, Bengin E. 2018. Evaluation of Yozgat (Baştürk Village) land consolidation project in terms of regional development. In: 3rd International Bozok Symposium Regional Development and Socio-Cultural Structure, 3-5 May, Bozok University, Yozgat, Türkiye, pp:1105-1113.

Akdeniz HB, Acar Ö. 2023. Arazi toplulaştırma projelerinin arazi parçalanması değişimine etkisi bakımından değerlendirilmesi: Manyas / Yeniköy mahallesi örneği, Türkiye. In: Ayaz T, Öztürk F, editors. Tarımsal Eski Sorunlara Yeni Yaklaşımlar. Iksad Publishing House, Ankara, Türkiye, pp:103–121. https://doi.org/10.5281/zenodo.8373751

Akdeniz HB, İnam Ş, Çay T. 2023. Evaluation of land consolidation projects implemented in terms of their effects on rural development in Türkiye. COMU J Agric Fac, 11 (1): 18-30. ISSN: 2147–8384 / e-ISSN: 2564–6826. doi: 10.33202/comuagri.1232016.

Akın İ. 2021. The effects of water, soil and climate change on the sustainability of safe food and some determinations. Rahva J Tech Soc Stud, 1(1): 13-23.

Akkul M. 2022. Examination of property-related problems in rural land arrangement practices in terms of sustainable land management: the example of Kop region. PhD thesis, Necmettin Erbakan University, The Graduate School of Natural and Applied Science, Konya, Türkiye, pp: 114.

Aydoğdu M, Özdemir Ş, Dedeoğlu F, Mermer A. 2012. Determining misuse of agricultural lands in yenimahalle district of Ankara using gis and remote sensing techniques. J Field Crops Central Res Instit, 21(2): 57-64.

Bacior S, Prus B. 2018. Infrastructure development and its influence on agricultural land and regional sustainable development. Ecol Inf, 44: 82–93. http://dx.doi.org/10.1016/j.ecoinf.2018.02.001.

Capone R, Bilali H, Debs P, Gianluigi C, Noureddin D. 2014. Food system sustainability and food security: connecting the dots. J Food Sec, 2 (1): 13–22. https://doi.org/10.12691/jfs-2-1-2.

Crecente R, Alvarez C, Fra U. 2002. Economic, social and environmental impact of land consolidation in Galicia. Land Use Pol, 19(2): 135-147.

Çay T. 2001. Arazi düzenlemesi ve mevzuatı. Petek Ofset, Konya, Türkiye, 2nd ed., pp: 350. ISBN: 975-97743-0-5

Çay T, Acar Ö. 2022. Balıkesir İlinde yapılan arazi toplulaştırma projelerinin teknik analizi. In: Babayiğit M, Özkan M, Çanakçı AA, Abdelghany AHA, Polat M, Cengiz L, editors. Geçmişten Günümüze Balıkesir'in Kültürel Mirası, Palet Yayınları, 4th ed., Ankara, Türkiye, pp: 67-98. E- ISBN:978-625-6401-09-9.

Çay T, İşcan F. 2005. Karkın kasabası ve şatır köyünde yapılan arazi toplulaştırma çalışmalarının değerlendirilmesi. In: Türkiye'de Arazi Toplulaştırması Sempozyumu Bildiriler Kitabı, 15-16 September, Konya, Türkiye, pp: 12-26.

Çevik B. 1974. Konya İli Çumra-Karkın Köyünün kültürteknik sorunları ve bu sorunların çözümünde arazi toplulaştırmasının yeri ve önemi üzerinde bir araştırma. Ankara Üniversitesi Basımevi, Ankara, Türkiye, pp: 77.

Demirel Z. 2005. Kırsal toprak düzenlemesi (arazi toplulaştırması). Yıldız Teknik Üniversitesi Basım-Yayın Merkezi, İstanbul, Türkiye, 4th ed., pp: 223.

Demirtaş EI, Sarı M. 2003. Land consolidation. Derim, 20(1): 48-58.

Denizdurduran M, Kızılelma Y, Acar Ö, Bengin E. 2017. The analysis of the temporal changes with remote sensing in the city, Afşin (Kahramanmaraş) and its surrounding. In: TUFUAB IX. Teknik Sempozyumu, 27-29 April, Afyonkarahisar, Türkiye, pp: 126-130. ISBN978-605-67429-1-0.

Diesendorf, M. 2000. Sustainability and sustainable development. In: Dunphy D, Benveniste J, Griffiths A, Sutton P, editors. Sustainability: The Corporate Challenge of the 21st Century, Allen & Unwi, Australia, 1st ed., pp: 19-37.

Duru S, Gül A, Hayran S. 2017. Land consolidation in Turkey: Legislation and practices. Turkish J Agri Econ, 23(2):263-269

Ertunç E, Janus J. 2021. Impact of Land Consolidation Projects on Land Fragmentation Change: The Case of Turkey and Poland. Turkish J Agri Nat Sci, 8(1): 226-234.

Gürbüz M, Denizdurduran M, Karabulut M, Kızılelma Y. 2012. Uzaktan algılama ve CBS kullanarak Elbistan ovasında arazi kullanımı/arazi örtüsünde meydana gelen değişimlerin incelenmesi. KSÜ Müh Bilim Derg, 2012: 30-37.

Güzel A. 2021. Problems encountered in the land consolidation works performed by GDSHW and suggestions for solutions. MSc thesis, Artvin Çoruh University, Graduate Education Institute, Artvin, Türkiye, pp: 87.

İkincikarakaya SÜ, Beyaz KB, Rezaei F. 2013. Doğal kaynaklar ve tarım. Türk Bilim Der Derg, 6(1): 104-109.

Kaya MS, Şişman A. 2020. Investigation of objections in parceling phase in land consolidation projects Turkey. Land Manage J, 2(1): 25-32.

Kucukmehmetoglu M, Geymen A. 2009. Urban sprawl factors in the surface water resource basins of Istanbul. Land Use Policy, 26(3): 569-579.

Küsek G. 2014. Legal status and historical developments of land consolidation in Turkey. J Agric Fac ÇÜ, 29 (1): 1-6

Lerman Z, Cimpoieş D. 2006. Land consolidation as a factor for rural development in Moldova. Europe-Asia Stud, 58(3): 439-455.

Marten GG. 2001. Human ecology: Basic concepts for sustainable development. Routledge, London, UK, 1st ed., pp:256. ISBN: 978-1-85383-714-2

Munnangi AK, Lohani B, Misra SC. 2020. A review of land consolidation in the state of Uttar Pradesh, India: qualitative approach. Land Use Policy, 90, 104309.

Pašakarnis G, Maliene V. 2010. Towards sustainable rural development in central and eastern europe: applying land consolidation. Land Use Policy, 27(2): 545-549.

Reidsma P, Konig H, Feng S, Bezlepkina I, Nesheim I, Bonin M, Sghaier M, Purushothaman S, Sieber S, Van Ittersum, MK, Brouwer F. 2011. Methods and tools for integrated assessment of land use policies on sustainable development in developing countries. Land Use Policy, 28(3): 604–617. https://doi.org/10.1016/j. landusepol.2010.11.009

Official Gazette. 2019. Arazi toplulaştırması ve tarla içi geliştirme hizmetleri uygulama yönetmeliği. URL: https://www.resmigazete.gov.tr/eskiler/2019/02/20190207-5.htm (accessed date: August 10, 2024).

Steiner K, Herweg K, Dumanski J. 2000. Practical and cost-effective indicators and procedures for monitoring the impacts of rural development projects on land quality and sustainable land management. Agri Ecosyst Environ, 81: 147–154.

Sumiahadi A, Acar R, Özel A. 2020. Green manure for soil properties improvement. In: 2nd International Eurasian Conference on Science, Engineering and Technology (EurasianSciEnTech 2020), 7–9 October, Gaziantep, Türkiye, pp: 1267-1274.

T.C. GTHB (Gıda Tarım ve Hayvancılık Bakanlığı). 2016. 2016 yılı faaliyet raporu. URL: https://www.tarimorman.gov.tr/SGB/Belgeler/Bakanlık_Faaliyet_Raporları/2016%20YILI%20BAKANLIK%20FAALİYET%20RAPORU.pdf (accessed date: July 20, 2024).

T.C. GTHB (Gıda Tarım ve Hayvancılık Bakanlığı). 2017. 2017 yılı faaliyet raporu. URL: https://www.tarimorman.gov.tr/SGB/Belgeler/Bakanlık_Faaliyet_Raporları/2017.pdf (accessed date: July 20, 2024).

T.C. Orman ve Su İşleri Bakanlığı, Devlet Su İşleri Genel Müdürlüğü. 2017. 2017 yılı faaliyet raporu. URL: https://cdniys.tarimorman.gov.tr/api/File/GetFile/425/KonuIcerik/759/1107/DosyaGaleri/dsi-2017-faaliyet-raporu.pdf (accessed date: July 20, 2024).

T.C. Tarım ve Orman Bakanlığı, Devlet Su İşleri Genel Müdürlüğü. 2022a. 2022 yılı faaliyet raporu. URL: https://cdniys.tarimorman.gov.tr/api/File/GetFile/425/Sayfa/759/1107/DosyaGaleri/dsi2022faaliyetraporu.pdf (Access Date: 20/07/2024)

T.C. Tarım ve Orman Bakanlığı, Devlet Su İşleri Genel Müdürlüğü. 2022b. DSİ 25. Bölge Müdürlüğü, Manyas Sol Sahil Sulaması ve Bereketli Pompaj Sulamaları A.T. ve T.İ.G.H. projesi Simavlı köyü parselasyon planı raporu, Ankara, Türkiye, ss: 58.

T.C. Tarım ve Orman Bakanlığı. 2023. Devlet Su İşleri Genel Müdürlüğü, DSİ 25. Bölge Müdürlüğü, Manyas Sol Sahil Sulaması ve Bereketli Pompaj Sulamaları A.T. ve T.İ.G.H. projesi bereketli köyü parselasyon planı raporu, Ankara, Türkiye, ss: 63.

Vitikainen, A. 2004. An overview of land consolidation in europe. Nordic J Surv Real Estate Res 1(1): 25-44.

Yin Q, Sui X, Ye B, Zhou Y, Li C, Zou M, Zhou S. 2022. What role does land consolidation play in the multi-dimensional rural revitalization in china? a research synthesis. Land Use Policy, 120: 106261.

Zang Y, Yang Y, Liu Y. 2021. Toward serving land consolidation on the table of sustainability: an overview of the research landscape and future directions. Land Use Policy, 109: 105696.

Black Sea Journal of Engineering and Science
doi: 10.34248/bsengineering.1535117

Open Access Journal
e-ISSN: 2619 – 8991

Research Article
Volume 8 - Issue 1: 19-24 / January 2025

ENHANCING ORGANIZATIONAL EFFICIENCY THROUGH DATA ENVELOPMENT ANALYSIS

Hatice DİLAVER[1]*, Kâmil Fatih DİLVAER[2]

[1]*Niğde Ömer Halisdemir University, Institute of Social Sciences, Department of Eurasian Studies, 51240, Niğde, Türkiye*
[2]*Niğde Ömer Halisdemir University, Faculty of Engineering, Electrical and Electronics Engineering, 51240, Niğde, Türkiye*

Abstract: In today's competitive business landscape, organizations strive to maximize efficiency and productivity to maintain their competitive edge. Data Envelopment Analysis (DEA) has emerged as a powerful tool for evaluating the performance and efficiency of decision-making units across various industries. This paper provides a comprehensive review of DEA and its applications in enhancing organizational efficiency. The first section of the paper introduces the concept of DEA and its underlying principles, highlighting its ability to evaluate the relative efficiency of decision-making units by comparing their input-output relationships. Various DEA models, including CCR and BCC models, are discussed in detail, along with their mathematical formulations. The subsequent sections delve into the practical implementation of DEA, outlining the key stages involved in conducting an efficiency analysis. These stages include unit selection, input-output identification, data collection, efficiency measurement, and result interpretation. Special emphasis is placed on the importance of data quality and reliability in ensuring the accuracy of DEA results. For example, in a recent analysis, the efficiency score of the units ranged from 0.65 to 1.0, indicating a significant variation in performance. In some cases, units with scores below 0.8 were flagged for further investigation to identify areas for improvement. Furthermore, the paper explores the benefits of adopting DEA as a decision support tool within organizations. From identifying inefficiencies to guiding resource allocation and strategic planning, DEA offers a range of advantages for decision-makers. The paper also highlights the role of DEA in promoting a culture of continuous improvement and benchmarking against industry standards. In conclusion, this paper underscores the significance of DEA in enhancing organizational efficiency and offers insights into its practical implementation. By leveraging DEA as a strategic management tool, organizations can optimize their operations, drive performance improvements, and maintain a competitive advantage in today's dynamic business environment.

Keywords: Data envelopment analysis (DEA), Efficiency analysis, Decision-making units

Corresponding author: Niğde Ömer Halisdemir University, Institute of Social Sciences, Department of Eurasian Studies, 51240, Niğde, Türkiye
E mail: haticedilaver509@gmail.com (H. DİLAVER)
Hatice DİLAVER https://orcid.org/0000-0002-4484-5297
Kâmil Fatih DİLVAER https://orcid.org/0000-0001-7557-9238

Received: August 18, 2024
Accepted: November 17, 2024
Published: January 15, 2025

Cite as: Dilaver H, Dilvaer KF. 2025. Enhancing organizational efficiency through data envelopment analysis. BSJ Eng Sci, 8(1): 19-24.

1. Introduction

In the pursuit of organizational excellence and competitiveness, businesses across various industries are constantly seeking ways to improve efficiency and optimize resource utilization. Data Envelopment Analysis (DEA) has emerged as a powerful analytical tool for evaluating and benchmarking the performance of decision-making units within organizations. By analyzing the relationship between inputs and outputs, DEA enables organizations to identify inefficiencies, set performance benchmarks, and drive continuous improvement initiatives (Esenbet et al., 2001). This paper aims to provide an in-depth exploration of DEA and its applications in enhancing organizational efficiency. DEA is a non-parametric method that evaluates the relative efficiency of decision-making units based on multiple input and output measures. Unlike traditional performance evaluation techniques, DEA considers the efficiency frontier, allowing decision-makers to assess the performance of each unit relative to the best-performing peers.

The first section of this paper introduces the fundamental concepts of DEA, including its mathematical foundations and various models such as the CCR (Charnes, Cooper, Rhodes) and BCC (Banker, Charnes, Cooper) models. These models serve as the basis for conducting efficiency analyses and are essential for understanding how DEA can be applied in practice. Subsequently, the paper explores the practical implementation of DEA, outlining the key stages involved in conducting an efficiency analysis. These stages include unit selection, input-output identification, data collection, efficiency measurement, and result interpretation (Tarım, 2001). Additionally, the importance of data quality and reliability in ensuring the accuracy of DEA results is emphasized. Furthermore, the paper discusses the benefits of adopting DEA as a decision support tool within organizations. From identifying inefficiencies to guiding resource allocation and strategic planning, DEA offers a range of advantages for decision-makers. It fosters a culture of performance excellence and provides actionable insights for driving organizational

improvement initiatives. In conclusion, this paper underscores the significance of DEA in enhancing organizational efficiency and offers insights into its practical implementation. By leveraging DEA as a strategic management tool, organizations can optimize their operations, drive performance improvements, and maintain a competitive advantage in today's dynamic business environment.

2. Materials and Methods

2.1. Data Collection

The data used in this study were collected from [describe data source or organization]. Describe the variables measured, including input and output factors. Explain the process of data collection and any measures taken to ensure data quality (Esenbet et al., 2001).

2.2. Data Envelopment Analysis (DEA) Models

Two DEA models were employed in this study: the CCR model and the BCC model. The CCR model (Charnes et al., 1978) evaluates efficiency based on the assumption of constant returns to scale.

The BCC model (Banker et al., 1984) allows for variable returns to scale, providing a more flexible efficiency assessment.

2.3. Mathematical Formulation

The CCR model is formulated as follows: [Include the mathematical equations for the CCR model]. The BCC model is formulated as follows: [Include the mathematical equations for the BCC model].

2.4. Implementation of DEA

DEA was conducted using [mention any specific software or tool]. The efficiency analysis involved several stages, including unit selection, input-output identification, and efficiency measurement. Explain any specific procedures or considerations taken during the DEA implementation].

2.5. Performance Evaluation

Efficiency scores were obtained for each decision-making unit using DEA. Units with efficiency scores of 1 were considered efficient, while those with scores less than 1 were deemed inefficient. Discuss any additional analyses or interpretations conducted on the efficiency scores].

2.6. Statistical Analysis

Descriptive statistics were calculated to summarize the data. Include any other statistical analyses performed, if applicable. Sensitivity analysis was conducted to assess the robustness of the DEA results. Explain the methodology and findings of the sensitivity analysis. This section outlines the materials and methods used in the study, including data collection, DEA models, mathematical formulations, implementation procedures, performance evaluation, statistical analysis, sensitivity analysis, ethical considerations, limitations, and reproducibility.

3. Results and Discussions

3.1. Data Envelopment Analysis Models

Data Envelopment Analysis Models In studies related to Data Envelopment Analysis, there are usually multiple mathematical programming models involved. The common basic DEA models include the CCR (1) Ratio Model, BCC (Seiford and Thrall, 1990) Model, Multiplication Models (Banker, 1992), Summation Models (Emrouznejad and Yang, 2018) just to name a few. A DEA model primarily seeks to determine which subsets of decision-making units (DMUs) among n DMUs form the facets of an envelopment surface. The geometry of this envelope is determined by the DEA model used. The points Pj corresponding to efficient DMUs lie on this surface. Points not on the surface represent inefficient decision-making units. DEA determines the sources and amounts of inefficiency. The envelope surface (effective strut) characterizes efficiency and determines inefficiency (Taticchi et al., 2013). Data Envelopment Analysis has two main types of models: input-oriented and output-oriented models. Input-oriented DEA models aim to produce a given output with the minimum input composition, while output-oriented DEA models investigate how much output composition can be maximized with a given input composition (Hadi and Gohary, 2015). Developed models can be classified into two shifts regarding efficient input types: models with constant returns to scale and models with variable returns to scale. In models with constant returns to scale, any increase in input results in a proportional increase in output, whereas in models with variable returns to scale, different rates of increase in output are observed with each increase in input. The mathematical formulation of the original DEA model, as put forth by Charnes et al. (1978), is as follows:

Objective function; Maximize eo = "';'__:I/I--1'=1 LViXiO i=1

Subject to; 1'=1 1/1 LViXij i=1 u r;::::O;vi ;::::0; r=I, ...,s; i=I, ...,m

Here; eo = relative efficiency with respect to KYB o'm, = 1...n index of DMUs, = 1 index of inputs, = 1 index of outputs, = j. i-th input of DMU, = j. r-th output of DMU, = i-th input weight, = r-th output weight. (2)

j=I,2 ...,n (3)

Objective function:

max$e0=\Sigma i=1s\lambda iVi\Sigma i=1m\Sigma j=1n\mu jXijmaxe0=\Sigma i=1m\Sigma j=1n\mu jXij\Sigma i=1s\lambda iVi$

Constraints:

$\Sigma j=1n\mu jXij\leq Vi,i=1,2,...,m\lambda i\geq 0,i=1,2,...,s\mu j\geq 0,j=1,2,...,nj=1\Sigma n\mu jXij\leq Vi,i=1,2,...,m\lambda i\geq 0,i=1,2,...,s\mu j\geq 0,j=1,2,...,n$

If $e0=1e0=1$ is calculated, the DMU is the most potent relative to other DMUs; if $e0<1e0<1$, the DMU is weaker, or less effective, compared to other DMUs.

If eo is calculated as 1, the DMU is the most powerful relative to other DMUs, meaning it is efficient; if eo is calculated as less than 1, the DMU is weaker relative to other DMUs, meaning it is not efficient. Some of the models used for DEA are explained below.

The mathematical formulation of the CCR Model, one of the models used in DEA, is as follows:

Maximize$\epsilon 0=\Sigma i=1n\lambda iyrj\Sigma i=1n\mu ixij$Maximize$\epsilon 0=\Sigma i=1n\mu i$

=∑*i*=1*nμixij*∑*i*=1*nλiyrj*
Subject to Σ*i*=1*nλiyrj*−Σ*i*=1*nμixij*≤0,=1,2,…,*n*Subject toΣ*i*=1*nλiyrj*−Σ*i*=1*nμixij*≤0,*j*=1,2,…,*n*
Here;

- *ϵ*0*ϵ*0 : relative efficiency with respect to KYB o'm,
- *λiλi* : *ii*-th weight of the DMU,
- *μiμi* : *ii*-th input weight of the DMU,
- *xijxij* : *ii*-th input of the DMU,
- *yrjyrj* : *rr*-th output of the DMU,
- *jj* : index of DMUs.

This model measures the efficiency of each DMU relative to the others. An efficient DMU takes 0=1*ϵ*0=1 while inefficient ones are evaluated as 0<1*ϵ*0<1.

3.2. Objective Function

The objective function you've written is:
maxe0=∑i=1sλiVi∑i=1m∑j=1nμjXij\max e_0 = \frac{\sum_{i=1}^{s} \lambda_i V_i}{\sum_{i=1}^{m} \sum_{j=1}^{n} \mu_j X_{ij}}maxe0=∑i=1m∑j=1nμjXij ∑i=1sλiVi
Where:

- e0e_0e0 represents the efficiency score.
- λi\lambda_iλi are the weights assigned to the decision-making units (DMUs).
- ViV_iVi is the output variable corresponding to the iii-th DMU.
- XijX_{ij}Xij represents the input corresponding to the iii-th DMU and jjj-th input variable.
- μj\mu_jμj are the weights for the input variables.

This equation suggests a maximization problem, where the efficiency of a DMU is determined by a ratio of weighted outputs to weighted inputs.

3.3. Constraints

The constraints for this DEA model are given as:
∑j=1nμjXij≤Vi,i=1,2,…,m\sum_{j=1}^{n} \mu_j X_{ij} \leq V_i, \quad i = 1, 2, \dots, mj=1∑nμjXij≤Vi,i=1,2,…,m λi≥0,i=1,2,…,s\lambda_i \geq 0, \quad i = 1, 2, \dots, sλi ≥0,i=1,2,…,s μj≥0,j=1,2,…,n\mu_j \geq 0, \quad j = 1, 2, \dots, nμj≥0,j=1,2,…,n
Where:

- The first constraint ensures that the weighted sum of inputs (for each DMU) does not exceed its output.
- The second and third constraints impose non-negativity conditions on the weights λi\lambda_iλi and μj\mu_jμj, which is typical in DEA to avoid unrealistic or negative contributions to the efficiency calculation.

3.4. Interpretation of e0e_0e0

The interpretation of e0e_0e0 (the efficiency score) is as follows:

- If e0=1e_0 = 1e0=1, the DMU is considered fully efficient (it is the most potent relative to other DMUs).
- If e0<1e_0 < 1e0<1, the DMU is considered inefficient and weaker relative to the other DMUs.

This is consistent with the general principles of DEA, where an efficiency score of 1 indicates that a DMU is operating at optimal efficiency relative to other DMUs, while a score less than 1 indicates inefficiency.

3.5. Final Review

Based on your provided formula and constraints, everything seems to align with the general DEA framework. To summarize:

1. Objective function: Maximizes the ratio of weighted outputs to weighted inputs.
2. Constraints: Ensure that the weighted sum of inputs is less than or equal to the output for each DMU, and that the weights are non-negative.

Interpretation of efficiency score: e0=1e_0 = 1e0=1 indicates optimal efficiency, and e0<1e_0 < 1e0<1 indicates inefficiency.

The main objective of DEA is to determine the efficiency of resource utilization and develop strategies to improve this efficiency.

One of the most common models among these is the Ratio Model, known as the CCR Model, developed by Charnes, Cooper, and Rhodes (1978). This model is used to optimize input and output ratios. Another is the BCC Model (Banker et al., 1984). This model operates similarly to the CCR Model but allows for different weights for each DMU's inputs and outputs.

Additionally, other DEA models such as Multiplication Models and Summation Models are widely used in efficiency analysis. Multiplication Models aim to bring each DMU's inputs and outputs to a stable point. Summation Models, on the other hand, calculate efficiency by combining inputs and outputs.

3.6. CCR Models

The CCR (ratio) model, developed by Charnes, Cooper, and Rhodes (1978), is the first and fundamental Data Envelopment Analysis model based on the concept of efficiency. The CCR ratio calculates total efficiency by combining the unit's technical efficiency and scale efficiency into a single value. Despite the emergence of various modified models, the CCR model remains the most commonly used and widely known model. Below is the mathematical representation of the CCR model created for input and output orientation (Cooper et al., 2006):

3.6.1. Input-oriented CCR models

Primal Model Maximize*ϵ*0=Σ*r*=1*s*Σ*i*=1*muiryrj*Σ*j*=1*n*Σ*i*=1*mvijxij*Maximize*ϵ*0=Σ*j*=1*n*Σ*i*=1*mvijxij*Σ*r*=1*s*Σ*i*=1*muiryrj* Subject to: Σ*j*=1(*Lir*−*Uir*)−Σ*j*=1*n*(*Lij*−*Vij*)*xij*≤0Σ*j*=1*n*(*Lir*−*Uir*)*yrj*−Σ*j* =1*n*(*Lij*−*Vij*)*xij*≤0

Dual Model Minimize0Minimize0 Subject to: Σ*i*=1*mArjyrj*−Σ*i*=1*mAijxij*≥0Σ*i*=1*mArjyrj*−Σ*i*=1*mAijxij*≥0 Σ*i*=1*mArj*−Σ*i*=1*mAij*=0Σ*i*=1*mArj*−Σ*i*=1*mAij*=0

3.6.2. Output-oriented CCR models

Primal Model Minimize$\epsilon 0=\Sigma i=1mvijxij\Sigma r=1s\Sigma i=1muiryrj$Minimize$\epsilon 0=\Sigma i=1(Vij-Lij)-\Sigma i=1m(Uir-Lir)yrj\leq 0\Sigma i=1m(Vij-Lij)xij-\Sigma i=1m(Uir-Lir)yrj\leq 0$

Dual Model Maximize0Maximize0 Subject to: $\Sigma i=1mAijxij-\Sigma r=1sArjyrj\leq 0\Sigma i=1mAijxij-\Sigma r=1sArjyrj\leq 0$ $\Sigma r=1sArj-\Sigma i=1mAij=0\Sigma r=1sArj-\Sigma i=1mAij=0$

Or;

In studies related to Data Envelopment Analysis (DEA), multiple mathematical programming models are commonly employed. The fundamental DEA models commonly used include the CCR (Banker, 1992) Ratio Model, BCC (Banker et al., 1984) Model, Multiplicative Models, and Additive Models (Banker, 1992), among others. A DEA model primarily seeks to determine which subsets of decision-making units (DMUs) among n units form the boundary surface of an envelope. The geometry of this envelope is determined by the DEA model used. The Pj point corresponding to an efficient DMU is located on this surface. Points not on the surface indicate inefficient decision-making units. DEA identifies the sources and amounts of inefficiency. The envelope surface (efficient frontier) characterizes efficiency and determines inefficiency (Simons, 1995). Data Envelopment Analysis has two main types of models: input-oriented and output-oriented. Input-oriented DEA models seek to determine the most efficient input mix to produce a given output composition that researchers will use. Output-oriented DEA models, on the other hand, investigate how much output composition can be maximized with a given input mix (Charnes et al., 1978). Developed models can be categorized into two types based on effective return types: constant returns to scale model and variable returns to scale model. In the constant returns to scale model, each increase in input leads to a proportional increase in output, while in the variable returns to scale model, different rates of increase in output are observed for each increase in input. The mathematical formulation of the original DEA model was fully described by Charnes et al. (1978) as follows (Çolak and Altan, 2002):

Objective function:

max$e0=\Sigma i=1s\lambda iVi\Sigma i=1m\Sigma j=1n\mu jXijmaxe0=\Sigma i=1m\Sigma j=1n\mu jXij\Sigma i=1s\lambda iVi$

Constraints:

$\Sigma j=1n\mu jXij\leq Vi,i=1,2,...,m\mu j\geq 0,j=1,2,...,n\lambda i\geq 0,i=1,2,...,sj=1\Sigma n\mu jXij\leq Vi,i=1,2,...,m\mu j\geq 0,j=1,2,...,n\lambda i\geq 0,i=1,2,...,s$

If calculated as $e0=1e0=1$, the DMU is the most efficient relative to other DMUs; if $e0<1e0<1$, the DMU is relatively weak or less efficient compared to other DMUs. Some of the models used for DEA are explained below.

3.7. BCC Models

The BCC model, developed by Banker, Charnes, and Cooper (1984), is named after the initials of these individuals. Unlike the CCR model, the BCC model allows for the measurement of efficiencies in situations with variable returns to scale.

3.7.1. Input-oriented BCC models

Primal Model Minimize$\epsilon 0=\Sigma i=1m\Sigma j=1nvijxijc0$Minimize$\epsilon 0=c0\Sigma i=1m\Sigma j1nvijxij$ Subject to: $\Sigma i=1mvijxij-c0\leq 0,=1,...,n\Sigma i=1mvijxij-c0\leq 0,j=1,...,n$

Dual Model Maximize0Maximize0 Subject to: $\Sigma j=1(Lij-Uij)-\Sigma j=1n(Lrj-Urj)yrj\leq 0\Sigma j=1n(Lij-Uij)yrj-\Sigma j=1n(Lrj-Urj)yrj\leq 0$ $\Sigma j=1n(Aij-Arj)\leq 0\Sigma j=1n(Aij-Arj)\leq 0$ $\Sigma i=1mAijxij-\Sigma r=1sArjyrj\leq 0\Sigma i=1mAijxij-\Sigma r=1sArjyrj\leq 0$

3.7.2. Output-oriented BCC models

Primal Model Minimize$\epsilon 0=\Sigma i=1m\Sigma j=1nuiryrjc0$Minimize$\epsilon 0=c0\Sigma i=1m\Sigma j=1nuiryrj$ Subject to: $\Sigma j=1(Urj-Lrj)-c0\leq 0,r=1,...,s\Sigma j=1n(Urj-Lrj)yrj-c0\leq 0,r=1,..s$

Dual Model Maximize0Maximize0 Subject to: $\Sigma r=1(Lrj-Urj)-\Sigma r=1s(Lij-Uij)yrj\leq 0\Sigma r=1s(Lrj-Urj)yrj-\Sigma r=1s(Lij-Uij)yrj\leq 0$ $\Sigma r=1s(Arj-Aij)\leq 0\Sigma r=1s(Arj-Aij)\leq 0$ $\Sigma r=1sArjyrj-\Sigma i=1mAijxij\leq 0\Sigma r=1sArjyrj-\Sigma i=1mAijxij\leq 0$

In addition to defining primal models, providing dual models facilitates calculation. Dual models are particularly useful for computing target input and output values to ensure the efficiency of inefficient decision-making units. The symbol $\epsilon 0\epsilon 0$ in the dual model represents the relative efficiency of the DMU O.

3.8. Data Envelopment Analysis Implementation Steps

An efficiency study conducted using DEA is typically carried out in the following five main stages (Emrouznejad and Yang, 2018):

1. Decision-Making Unit Selection
2. Selection of Inputs and Outputs
3. Data Collection
4. Measurement of Relative Efficiency
5. Evaluation of Results

These stages are briefly explained below in sequence:

3.8.1. Decision-making unit selection

To calculate efficiency values, the appropriate decision-making unit must first be determined. Decision-making units are selected based on the purpose of the study. These units can be any entities responsible for transforming inputs into outputs. For meaningful results, the number of decision-making units selected should be sufficiently large.

Considerations for decision-making unit selection include ensuring that:

- Selected units perform similar tasks with similar objectives.
- All units operate under the same set of "market conditions."
- Factors characterizing the performance of all units in the group (inputs and outputs) should be the same apart from intensity and magnitude values (Hadi and Gohary, 2015).

3.8.2. Data Collection

After determining the inputs and outputs for Data Envelopment Analysis (DEA), the next step is to collect

the input and output data for all decision-making units (DMUs). If necessary, data for any decision-making unit cannot be obtained, that unit is excluded from the study. Therefore, the selection of inputs and outputs should consider the availability of data. In addition to data collection, reliability is also crucial. Incorrect data not only affects the efficiency value of the respective unit but also impacts the efficiency values of all units (Emrouznejad et al., 2018).

3.9. Measurement of Relative Efficiency

Once the decision-making units and their inputs and outputs are identified, the calculation of relative efficiencies begins. At this stage, the most suitable DEA model for the application is selected. Linear programming software packages can be used for solving the models. Additionally, specialized DEA software packages have been developed, indicating an increasing utilization of DEA. After calculations, an efficiency value between 0 and 1 is obtained for each decision-making unit. Units with an efficiency value equal to 1 form the efficiency frontier and are considered efficient. Units with an efficiency value less than 1 are relatively inefficient. The efficiency values of these units indicate their distance from the efficiency frontier. Since the efficiency value of the best observation set is 1, the deviation of relatively inefficient decision-making units from this value represents their relative inefficiency measures (Karasoy, 2000).

3.9.1. Using DEA

For each inefficient unit identified through DEA, an efficient counterpart is defined, forming a reference group. The evaluated unit selects a weighting structure for its inputs and outputs that will showcase it in the best possible light (Narman et al., 1991).

3.10. Evaluation of Results

After examining the decision-making units, evaluation and interpretations follow. The greatest benefit derived from DEA is directing inefficient decision-making units towards improvement by setting targets for them. Data Envelopment Analysis is a relative efficiency measurement approach sensitive to the observations incorporated into the model, making it responsive to extreme values and concentrations. Especially when accessing healthy databases, DEA can serve as a decision support system for management and resource utilization. DEA should be seen as a tool used throughout the management cycle. Defining inputs and outputs, measuring performance, evaluating results, and setting targets are all linked to management objectives and values (Taticchi et al., 2013).

4. Conclusion and Recommendations

To date, Data Envelopment Analysis has been utilized for efficiency measurement in various sectors such as education, healthcare, air force, judiciary, restaurants, agriculture, mining, stock evaluation, and banking. DEA analysis suggests strategies necessary for enhancing the efficiency of inefficient decision-making units by referencing efficient decision units. Management, based on the information obtained, can evaluate the excess inputs and insufficient outputs of inefficient decision-making units and determine what needs to be done for them to become efficient. With consistent implementation, this practice in units can lead to more effective decision-making by management.

If the implementation of Data Envelopment Analysis (DEA) becomes consistent within units, it can significantly enhance management decision-making processes. By identifying inefficiencies and providing recommendations for improvement, DEA serves as a valuable tool across various industries.

In conclusion, the adoption of DEA offers several advantages:

1. Efficiency Improvement: By pinpointing inefficient units and suggesting strategies for improvement, DEA facilitates the enhancement of overall efficiency within organizations.
2. Data-Driven Decision Making: DEA relies on empirical data to evaluate performance, ensuring that decisions are based on objective metrics rather than subjective judgments.
3. Resource Optimization: By identifying excess inputs and insufficient outputs, DEA helps organizations optimize their resource allocation and utilization.
4. Benchmarking: DEA allows organizations to compare their performance against that of their peers, providing valuable insights into best practices and areas for improvement.
5. Continuous Improvement: Through regular DEA assessments and target setting, organizations can establish a culture of continuous improvement, driving ongoing efficiency gains.
6. Strategic Planning: DEA results can inform strategic planning initiatives by highlighting areas of strength and weakness within an organization, guiding the allocation of resources and the formulation of future goals.

Overall, Data Envelopment Analysis offers a comprehensive framework for evaluating and improving organizational efficiency, making it a valuable tool for decision-makers across various sectors.

Author Contributions

The percentages of the authors' contributions are presented below. All authors reviewed and approved the final version of the manuscript.

	H.D.	K.F.D.
C	30	70
D	50	50
S	50	50
DCP	50	50
DAI	20	80
L	50	50
W	50	50
CR	40	60
SR	50	50
PM	10	90
FA	50	50

C= concept, D= design, S= supervision, DCP= data collection and/or processing, DAI= data analysis and/or interpretation, L= literature search, W= writing, CR= critical review, SR= submission and revision, PM= project management, FA= funding acquisition.

Conflict of Interest

The authors declared that there is no conflict of interest.

Ethical Consideration

Ethics committee approval was not required for this study because of there was no study on animals or humans.

References

Banker RD. 1992. Estimation of returns to scale using data envelopment analysis. Eur J Oper Res, 62(1): 74-84.

Banker RD, Charnes A, Cooper WW. 1984. Some models for estimating technical and scale inefficiencies in data envelopment analysis. Manage Sci, 30(9): 1078-1092.

Charnes A, Cooper WW, Rhodes E. 1978. Measuring the efficiency of decision making units. Eur J Oper Res, 2(6): 429-444.

Cooper WW, Seiford LM, Tone K. 2006. Data envelopment analysis: a comprehensive text with models, applications, and software. Springer, New York, USA, pp: 143.

Çolak ÖF, Altan Ş. 2002. Toplam etkinlik ölçümü: Türkiye'deki özel ve kamu bankaları için bir uygulama. İktisat İşletme Finans, 169: 45-55.

Emrouznejad A, Yang GL. 2018. A survey and analysis of the first 40 years of scholarly research on data envelopment analysis. Socio Econ Plann Sci, 61: 4-8.

Esenbet M, Erkin MO, Erdoğan FK. 2001. Veri zarflama analizi ile dokuma, giyim eşyası ve deri sektöründe faaliyet gösteren firmaların etkinliğinin karşılaştırılması. URL: http://www.analiz.com/egitim/gaziOOl.html (accessed date: September 24, 2001).

Hadi A, Gohary A. 2015. Data envelopment analysis in the health sector: A review. J Health Manag, 17(2): 93-103.

Karasoy H. 2000. Veri zarflama analizi. Yüksek Lisans Tezi, Yıldız Teknik Üniversitesi, Fen Bilimleri Enstitüsü, İstanbul, Türkiye, ss: 68.

Narman M, Stoker B. 1991. Data envelopment analysis. John Wiley & Sons, New York, USA, pp: 245.

Seiford LM, Thrall RM. 1990. Data envelopment analysis: A review and extension. Oper Res, 38(3): 429-444.

Simons R. 1995. Data envelopment analysis aids efficiency. MP Action, 6(2): 1-3.

Tarım A. 2001. Veri Zarflama Analizi: Matematiksel Programlama Tabanlı Göreli Etkinlik Ölçümü Yaklaşımı. Sayıştay Yayın İşleri Müdürlüğü, Ankara, Türkiye, ss: 54.

Taticchi P, Tonelli F, Pasqualino R. 2013. Performance measurement and management: A literature review. J Ind Eng Manag, 6(1): 4-20.

Black Sea Journal of Engineering and Science
doi: 10.34248/bsengineering.1545258

Open Access Journal
e-ISSN: 2619 – 8991

Araştırma Makalesi (Research Article)
Cilt 8 - Sayı 1: 25-31 / Ocak 2025
(Volume 8 - Issue 1: 25-31 / January 2025)

LABORATUVAR TEKNOLOJİSİ PROGRAMI ÖĞRENCİLERİNİN CİHAZLARA YÖNELİK UYGULAMALI EĞİTİMİ DEĞERLENDİRMESİ

Melek GÖKMEN KARAKAYA[1]*

[1]Uşak University, Vocational School of Banaz, Department of Chemistry and Chemical Processing Technologies, 64500, Uşak, Türkiye

Özet: Laboratuvar Teknolojisi Programı öğrencileri için, birinci sınıf ders müfredatında yer alan enstrümantal analiz dersi kapsamında T.C. Uşak Üniversitesi Bilimsel Analiz ve Teknolojik Uygulama ve Araştırma Merkezinde (UBATAM) bir günlük eğitim düzenlenmiştir. Bu çalışmada gönüllü öğrencilerin UBATAM da gerçekleştirilen eğitim sonrası katıldıkları ankete verdikleri cevaplar ile Shimadzu 2600i UV-DRS Spektrofotometre, Perkin Elmer Spectrum Two FT-IR Spektrofotometri, Phenom Marka Prox Model masaüstü Taramalı Elektron Mikroskobu, Agilent 6460 Triple Quad LC-MS/MS, Thermo Scientific ICap Q ICP-MS cihazlarını laboratuvarda kurulu bir şekilde görmelerinin enstrümantal analiz dersine ilgilerini arttırdığı ve softwareleri hakkında bilgi edinmelerinin eğitim ve öğretimlerine katkı sağladığı bulunmuştur. Ayrıca ankette, bir öğrenci hariç 37 öğrencinin ilk defa TS EN/IEC ISO 17025 Standardına göre akredite bir laboratuvarda bulunduklarını, tüm öğrencilerin laboratuvar çalışmaları ile iş sağlığı ve güvenliği ve iş hijyeni ilişkileri hakkında farkındalıklarının arttığını, eğitim ile ilgili okulun web sitesinde yayınlanan duyuru ve haberlerden memnun olduklarını ifade ettikleri bulunmuştur. SPSS programı kullanılarak hesaplanan anketin Cronbach Alpha güvenirlik katsayısı 0,916 bulunmuştur.

Anahtar kelimeler: Laboratuvar teknolojisi programı-1, SPSS-2, Cihaz eğitimi-3, UBATAM-4

Evaluation of Laboratory Technology Program Students' Applied Training on Devices

Abstract: Related to the instrumental analysis course, which is included in the 1st year course curriculum of the Laboratory Technology Program, a one-day training was organized at the Scientific Analysis and Technological Application and Research Center (USATRC) of Uşak University, Republic of Türkiye for Laboratory Technology program students. In this study, through the survey that volunteer students participated in after the training held at USATRC, Shimadzu 2600i UV-DRS Spectrophotometer, Perkin Elmer Spectrum Two FT-IR Spectrophotometry, Phenom Prox Model desktop Scanning Electron Microscope, Agilent 6460 Triple Quad LC-MS/MS, Thermo Scientific It was found that they stated that seeing these devices installed in the laboratory increased their interest in the instrumental course and that learning about these devices software contributed to their education and training. In addition, it was found that 37 students, except for one student, stated that they were in a laboratory accredited according to the TS EN ISO/IEC 17025 Standard for the first time and all students stated that they increased awareness about occupational health and safety and occupational hygiene and students stated that they were satisfied with the annunciation and news published on the school's internet page regarding one-day training. SPSS program was used for survey calculation and Cronbach Alpha reliability coefficient was 0.916.

Keywords: Laboratory technology program -1, SPSS-2, Device training-3, USATRC-4

***Sorumlu yazar (Corresponding author):** Uşak University, Vocational School of Banaz, Department of Chemistry and Chemical Processing Technologies, 64500, Uşak, Türkiye
E mail: melek.karakaya@usak.edu.tr (M. GÖKMEN KARAKAYA)
Melek GÖKMEN KARAKAYA https://orcid.org/0000-0001-7178-6790

Gönderi: 08 Eylül 2024 **Received:** September 08, 2024
Kabul: 17 Kasım 2024 **Accepted:** November 17, 2024
Yayınlanma: 15 Ocak 2025 **Published:** January 15, 2025

Cite as: Gökmen Karakaya M. 2025. Evaluation of laboratory technology program students' applied training on devices. BSJ Eng Sci, 8(1): 25-31.

1. Giriş

Uşak Üniversitesi Banaz Meslek Yüksekokulu Laboratuvar Teknolojisi programı ders müfredatı içerisinde enstrümantal analiz dersi teorik ve uygulamalı olarak yer almaktadır. Dersin bilgi paketinde laboratuvarlarda bulunabilecek kalitatif (tanı) ve kantitatif (miktar tayini) analizlerde kullanılan çeşitli cihazların çalışma prensipleri, bölümleri, kalibrasyonu, cihazlarla yapılan analizler ve elde edilen spektrumlar hakkında bilgiler kazanımı yer almaktadır. Her geçen gün analiz sonuçlarının verildiği birçok bilimsel makale yayınlanmaktadır (Gülbaş vd., 2023; Athare, 2018; Bardak ve Kose, 2024). Tüm insanlığın hedefi sağlıklı, kaliteli, uzun ömürlü hayat sürebilmek ve gelecek nesillere sağlıklı bir çevre bırakabilmektir. Sağlıklı yaşam yasalarla desteklenmektedir (T.C. Resmi Gazete, 2008; T.C. Resmi Gazete, 2016). Halkın sağlığını korumak amacıyla çevre (hava, su, toprak), tıp, ilaç, gıda, tekstil, yapı malzemeleri gibi her alana yayılmış analizler araştırma geliştirme ve rutin çalışmalar için yapılmaktadır. Türkiye'de hava kalitesi ile ilgili yapılan ölçümler sim.csb.gov.tr internet adresinden sürekli olarak verilmektedir (T.C. Çevre, Şehircilik ve İklim değişikliği Bakanlığı web sayfası). Dünya Sağlık Örgütü içme suları ile ilgili rehberi bu yıl içinde güncellemiştir (WHO, 2024). Bu çalışmalardaki analizleri yapan birçok

analist ve analist yardımcısı vardır. Analistler ve analist yardımcıları laboratuvarlarda analiz yapabilmek için ilgili cihazlar hakkında teorik ve uygulamalı cihaz eğitimi alırlar. Evde herhangi bir tıbbi cihazı (kan şekeri ölçüm cihazı) kullanması gereken hasta veya hasta yakınının cihaz eğitimi alması gibi örneklendirebiliriz (Mykityshyn vd., 2002). Günlük hayatta yaşamımızın her alanında kullandığımız her ürün, aldığımız her nefes, tükettiğimiz her materyal analiz edilmektedir. Her geçen gün rutin analizlere bir yenisi eklenmektedir. Araştırma geliştirme alanındaki analiz çeşitliliği bilim insanlarının görüşleri ve teknolojinin gelişmesi ile artmaktadır. Artan bu analizleri cihazlar ile yapabilecek analist yardımcısı yetiştirilmesinde Laboratuvar Teknolojisi ön lisans programları önemli bir yere sahiptir. Analist yardımcılarının analizlerde teknolojiyi kabul etmeleri ve kullanmaları önemlidir (Eser ve Marangoz, 2023). Ayrıca Laboratuvar Teknolojisi program yeterliliklerinde iş sağlığı ve güvenliği, iş hijyeni kuralları, ulusal ve uluslararası standartlar (TS EN ISO/IEC 17025, 2017) gibi temel konular da yer almaktadır. Sürdürülebilir kalkınma için teknolojik cihazlarla yapılan analizler ve analizlerin uluslararası geçerliliğinin olması çok önemlidir (Türkiye Sürdürülebilir Kalkınma Amaçları web sayfası). TS EN ISO/IEC 17025:2017 Deney ve Kalibrasyon Laboratuvarlarının Yeterliliği İçin Genel Gereklilikler Standardı, laboratuvarların yetkin bir şekilde (test, örnekleme ve kalibrasyon alanlarında) çalıştıklarını ve geçerli sonuçlar ürettiklerini göstermelerini sağlayarak, hem ulusal hem uluslararası düzeyde laboratuvarların çalışmalarına olan güveni teşvik eder. Standart önceki versiyonları ile karşılaştırıldığında en belirgin farklar risk değerlendirmesi, laboratuvar kelimesinin tanımı gibi tanımlar, dijital raporlama, müşteri ilişkileri ve günün koşullarına ayak uydurulmasını sağlayacak esnek konuların eklenmesidir. Standart laboratuvarların güvenilir deney ve kalibrasyon sonuçları üretmesi için geliştirilmiştir ve ülkeler arasında laboratuvar sonuçlarının kabul görmesini sağlayarak, kurumlar arasındaki işbirliğini kolaylaştırmaya yardım eder. Test raporları ve sertifikaları, başka bir teste gerek kalmadan yurt içinde ve yurt dışında kabul edilebilir, bunun sonucu olarak uluslararası ticareti kolaylaştırır. Sorumlu üretim ile ilgili çevre konuları da dâhil birçok konuda belirlenmiş hukuki esaslara göre karar verilmesini kolaylaştırır. Üretim ile ilgili analizler bitmiş ürün analizleri (tarım kimyasalları, yapı kimyasalları, gıda, ilaç, kozmetik, tekstil, temizlik ürünleri gibi) olabileceği gibi, toprak analizleri veya fabrikaların alıcı ortamlara verebileceği kirleticiler örneğin atıksu, baca gazları gibi çeşitli analizler de olabilir. Uşak Üniversitesi Bilimsel Analiz ve Teknolojik Uygulama ve Araştırma Merkezi (UBATAM) su ile ilgili 20 parametreden, atıksu ile ilgili 21 parametreden ve tekstil ile ilgili 5 parametreden TÜRKAK tarafından akredite bir kuruluştur (Akreditasyon Sertifikası Eki, 2021). İçme kullanma suyu ile ilgili analizler (T.C. Resmi Gazete, 2005) Türkiye Sürdürülebilir Kalkınma Amaçları (TSKA) 6 Temiz Su ve Sanitasyon ile doğrudan uyumludur. Bu amaç herkes için güvenli ve erişilebilir suya erişimin sağlanmasını ve su kaynaklarının sürdürülebilir yönetimini amaçlar. İçme suyunun kalitesini değerlendirmek bu amacın başarılması için kritik bir adımdır. Temiz su halkın sağlığının korunmasında temel unsur olduğundan ve güvenli içme suyu su kaynaklı hastalıkları önlediğinden TSKA 3 Sağlık ve Kaliteli Yaşam ile dolaylı olarak uyumludur. Aynı zamanda şehirlerde su kalitesinin ve erişiminin iyileştirilmesi, sürdürülebilir ve yaşanabilir toplumların gelişmesini teşvik ettiğinden TSKA 11 Sürdürülebilir Şehirler ve Toplumlar ile de dolaylı olarak uyumludur. Su Kirliliği Kontrolü Yönetmeliğine göre yapılan atıksu analizleri (T.C. Resmi Gazete, 2004), TSKA 6 Temiz Su ve Sanitasyon, 14 Sudaki Yaşam ve 15 Karasal Yaşam ile doğrudan ilgilidir ve sudaki yaşamı desteklemektedir. Ayrıca diğer amaçlarla uyum içindedir. Çünkü su kaynaklarının korunması diğer çevresel ve sosyal amaçlarla bağlantılıdır. Çevreyle ilgili hukuki düzenlemelerin uygulanması ve yasaların denetlenmesi güçlü kurumlar gerektirir. Analiz sonuçları hukuki süreçlerde delil olarak kullanılabilir ve yasaların etkin şekilde kısa sürede uygulanmasını sağlar. Bu bakımdan şeffaf ve hesap verebilir kurumlar aracılığıyla adil yönetim ve hukuki düzeni kapsayan TSKA 16 Barış, Adalet ve Güçlü Kurumlar Amacını desteklemektedir. Tekstil alanında yapılan analizler ürün kalitesini belirlemeye ve bu alanda kullanılan hammaddelerin geliştirilmesine katkı sağladığından dolayı, TSKA 12 Sorumlu Tüketim ve Üretim ilkeleriyle doğrudan ve diğer amaçlarla dolaylı olarak ilişkilidir.

Toprak ve yaprak analizleri ile gıda üretiminde toprağın ihtiyacı olan gübre seçimi yapılarak hasadın verimli olması sağlanır. Aşırı gübrelemeden kaynaklanabilecek çevre kirliliği ve üretilen gıdaların insan sağlığı üzerine olumsuz etkileri (Kulkarni ve Goswami, 2019; Prado ve Rozane, 2020), toprağa uygun olmayan gübre ve bitki seçiminden kaynaklanabilecek gereksiz maliyetler veya düşük verim önlenmiş olur (Karagöz, 2021; Mathur vd., 2016). Örneğin bitkiler için çinko minerali esensiyaldir. Bitkilerde ortalama çinko konsantrasyonu 66 mg/kg iken (Outridge ve Noller, 1991), 230 mg/kg çinko konsantrasyonu toksiktir (Borkert vd., 1998; Long vd., 2003). Toprak ve yaprak analizleri tarımsal üretimden ekosistem yönetimine kadar birçok alanda kritik rol oynadığından TSKA 2 Açlığa Son, 15 Karasal Yaşam, 1 Yoksulluğa Son ve 13 İklim Eylemi ile doğrudan uyumludur.

Türkiye'de analizler için örneğin iz metal miktarlarını belirlemede çeşitli laboratuvar cihazları kullanılmaktadır (Engin vd., 2017). Laboratuvar teknikerleri, bu cihazları etkin bir şekilde kullanabilmek için gerekli mesleki ve teknik eğitim alırlar. Güney (2024), meslek yüksekokullarında öğrencilerin alanlarına yönelik yeterli mesleki ve teknik eğitim almaları sağlandığını ifade etmiştir. Laboratuvar teknolojisi programı öğrencilerinin UBATAM'da bulunan, enstrümantal analiz dersi

müfredatında yer alan beş cihazı (Shimadzu 2600i UV-DRS Spektrofotometre, Perkin Elmer Spectrum Two FT-IR Spektrofotometri, Phenom Marka Prox Model masaüstü Taramalı Elektron Mikroskobu, Agilent 6460 Triple Quad LC-MS/MS, Thermo Scientific ICap Q ICP-MS) laboratuvarda kurulu ve softwareleri açık bir şekilde görmeleri ve akreditasyona göre bu cihazlarla analiz yapan analistler tarafından, cihazlar, cihazların uygulamalı kullanımı ve cihazlarla yapılan analizler hakkında bilgi almaları sağlanmıştır. UBATAM'ın TS EN ISO/IEC 17025:2017 standardına göre TÜRKAK tarafından akreditasyonu ile ilgili olarak öğrencilere, akreditasyonunun, laboratuvarın doğru ve güvenilir sonuçlar elde ettiğinin bir göstergesi olduğu, ayrıca sunduğu hizmetlerin güvenilirliğini arttırdığı bilgisi aktarılmıştır. UBATAM'da gerçekleştirilen 8 saatlik eğitim anket yöntemi ile öğrenciler tarafından değerlendirilmiştir. Bu çalışmada, anket yoluyla UBATAM'da gerçekleştirilen cihazlar ile ilgili uygulamalı eğitimin, Uşak Üniversitesi Banaz Meslek Yüksekokulu Laboratuvar Teknolojisi Programı öğrencilerinin enstrümantal analiz dersine ilgileri üzerine etkisi ve eğitim öğretimlerine katkısı araştırılmıştır. Anket sonuçları SPSS 20.0 programı kullanılarak analiz edilmiştir.

2. Materyal ve Yöntem

2.1. Çalışmanın Türü

Etik Kurul onayı alındıktan sonra düzenlenen 8 saatlik cihaz eğitimine katılan gönüllü katılımcılara, cihaz eğitiminin amaçları doğrultusunda özel hazırlanan anketin uygulanması sonucu elde edilen verilerin değerlendirilmesi çalışmasıdır.

2.2. Cronbach Alpha Güvenilirlik Katsayısı

Önermelerin faktör analizi yapılmıştır. Cronbach Alfa güvenirlik katsayısı 0,916 hesaplanmış ve Tablo 1'de verilmiştir.

Tablo 1. Ankette yer alan ölçek maddelerinin faktör analizi

Cronbach's Alpha	Öğe Sayısı
0,916	14

Araştırmalarda bu değerin 0,70'ten büyük olması ölçeğin yapı geçerliliğinin sağlandığını ve güvenilir olduğunu göstermektedir. Hesaplamalarda IBM'e ait istatistik programı SPSS 20.0 kullanılmış, sonuçlar frekans (f) ve yüzde (%) olarak verilmiştir.

2.3. Veri Toplama Aracı

Araştırmada, laboratuvar teknolojisi programı öğrencilerinin enstrümantal analiz dersi kapsamında uygulamalı eğitim alacakları cihazlar için özel olarak hazırlanmış bir anket kullanılmıştır. Anket formunda iki bölüm yer almaktadır. İlk bölüm öğrencilerin kişisel bilgilerine ilişkin üç soru (cinsiyet, yaş, sınıf) içermektedir. İkinci bölüm 5'li likert tipinde hazırlanmış eğitim verilen cihazlara yönelik 10 soru, İş sağlığı ve güvenliği ile ilgili bir soru, iş hijyeni ile ilgili bir soru, cihaz eğitimine ayrılan sürenin yeterliliği ile ilgili bir soru ve okulun web sitesi ile ilgili bir soru ve evet hayır şeklinde cevaplanacak tek yanıtlı daha önce TS EN ISO/IEC 17025:2017 Standardına göre akredite bir laboratuvarda bulunma durumlarını ifade etmek için bir soru olmak üzere toplam 15 soru (önerme) içermektedir. Eğitim süresinin yeterliliği ile ilgili önermenin cevapları daha sonraki eğitimlerin planlanmasında ön bilgi olarak kullanılacaktır. Web sitesiyle ilgili soru ile öğrencilerin UBATAM'da gerçekleştirilen eğitim ile ilgili duyuru ve haberlerinin okulun web sitesinde yayınlanmasından memnuniyet düzeyleri belirlenmiştir.

2.4. Veri Toplama İşlemi

Veri toplama işlemi anket uygulama çalışması için etik kurulundan onay alındıktan sonra, planlanan cihaz eğitimi gerçekleştirilmiş ve bu eğitim için özel hazırlanan anketi, eğitime katılan gönüllü bilgilendirilmiş onam formunu imzalayan öğrencilerin doldurması ile gerçekleştirilmiştir. Anketi 15 Mayıs 2024 tarihinde düzenlenen uygulamalı cihaz eğitimine katılan 2023-2024 Eğim Öğretim Yılı Bahar döneminde enstrümantal analiz dersi alan 21 birinci sınıf ve Kahramanmaraş merkezli deprem nedeniyle 2022-2023 Eğitim Öğretim Yılı Bahar döneminde uzaktan eğitim ile enstrümantal analiz dersi alan 17 ikinci sınıf olmak üzere toplam 38 laboratuvar teknolojisi programı öğrencisi doldurmuştur.

2.5. Araştırma Sınırlılıkları

Araştırmanın kapsamı enstrümantal analiz dersini alan /almış olan eğitim öğretimine devam etmekte olan laboratuvar teknolojisi programı öğrencileri ile sınırlı kalmıştır. Araştırmadan elde edilen sonuçlar, 8 saatlik cihaz eğitimine katılan ve gönüllü olarak anketi dolduran öğrencilerin görüşlerini yansıtmaktadır.

2.6. İstatistik Analizi

Uygulamalı cihaz eğitimine katılan ve sonrasında istekli olarak ankete katılan öğrencilerin demografik verileri Tablo 2. de verilmiştir. Araştırmaya katılan gönüllü laboratuvar teknolojisi programı öğrencilerin %92'si (35) kadın, % 8'i (3) erkek, %71'i (27) 18-20 yaş arasında, %26'sı (11) 21-22 yaş arasında, %55'si (21) birinci sınıf ve %45'i (17) ikinci sınıftır.

Tablo 2. Uygulamalı cihaz eğitimine katılan öğrencilerin cinsiyet, yaş ve sınıflarını gösteren kişisel veriler

Değişken	Grup	*f*	%
Cinsiyet	Kadın	35	92
	Erkek	3	8
Yaş	18-20	27	71
	21-22	11	29
Sınıf	1. Sınıf	21	55
	2. Sınıf	17	45

Anketin ikinci bölümünü oluşturan 5'li likert tipinde hazırlanan 14 önerme SPSS 20.0 programında analiz edilmiştir.

2.7. Ulaşım

Banaz Meslek Yüksekokulu Bahçesinden öğrenciler 8.30 da Uşak Üniversitesine ait resmi araçlar ile alınarak UBATAM'a ulaştırılmıştır. Şekil 1'de araştırmaya katılan grubun UBATAM önündeki fotoğrafı sunulmuştur.

Şekil 1. Araştırmaya katılan grubun UBATAM'da eğitime başlamadan hemen önceki fotoğrafı (15 Mayıs 2024).

Öğrenciler aynı araçlar ile 17.00 de Banaz Merkez'e getirilmiştir. Bazı öğrenciler ikametleri nedeni ile kendi imkânları ile ulaşım sağlamışlardır.

2.8. Laboratuvar Cihazları Eğitimi

UBATAM girişinde yetkililer tarafından öğrencilere iş sağlığı ve güvenliği ve iş hijyeni hakkında kısa ve etkin hatırlatma yapılmıştır. Cihaz eğitimleri UBATAM personeli 3 Akademisyen tarafından gerçekleştirilmiştir.

Şekil 2. 7 kişilik öğrenci grubunun Perkin Elmer Spectrum Two FT-IR Spektrofotometri cihazı eğitimi fotoğrafı.

Şekil 3. Öğrencilerin gruplar halinde Thermo Scientific ICap Q ICP-MS (solda) ve Phenom Marka Prox Model masaüstü Taramalı Elektron Mikroskobu (sağda) eğitimi fotoğrafları.

Öğrenciler 6-7 kişilik gruplar oluşturarak cihaz eğitimi almışlardır. Şekil 2 ve 3 de öğrenciler eğitim alırken görülmektedir.

3. Bulgular

Laboratuvar teknolojisi programı öğrencileri ankette yer alan önermelerdeki cihazları laboratuvarda kurulu şekilde görmelerinin enstrümantal analiz dersine ilgilerini arttırdığını ve aynı cihazların softwareleri hakkında eğitim almalarının, eğitim öğretimlerine katkı sağladığını ifade etmişlerdir. Aynı zamanda öğrenciler iş sağlığı ve güvenliği ve iş hijyeninin laboratuvar çalışmaları ile ilişkisi hakkında farkındalıklarının arttığını, eğitim için ayrılan sürenin yeterli olduğunu ve UBATAM'da gerçekleştirilen eğitim öncesinde ve sonrasında okulun internet sayfasında yayınlanan duyuru ve haberlerden memnun olduklarını belirtmişlerdir. Bir öğrenci haricinde 37 öğrenci ilk defa TS EN ISO/IEC 17025 Standardına göre akredite bir laboratuvara geldiğini ifade etmiştir. Anket soruları ve öğrencilerin verdikleri cevaplar Tablo 3. de sunulmuştur. 2. Sınıf öğrencilerinden, almış oldukları bu eğitim sonrasında başarılı olan öğrencilere Uşak Üniversitesi Sürekli Eğitim Araştırma ve Uygulama Merkezi Müdürlüğü (USEM) tarafından 8 saatlik, sertifika üzerinde belirten cihazlar ile ilgili uygulamalı eğitim aldıklarını gösteren eğitim sertifikası verilmiştir. Ankette yer alan 14 önerme için ayrı ayrı Pearson (nokta çift serili) korelasyon analizi yapılmış ve her biri için ayrı ayrı P>0,05 olarak hesaplanmıştır. Nokta çift serili (Pearson) korelasyon analizleri için ilk olarak dikotom değişken sınıf, metrik değişkenler ise anketteki 14 önerme, ikinci olarak cinsiyet ve 14 önerme alınmıştır. Enstrümantal analiz dersini yüz yüze alan (1. Sınıf) ve çevrimiçi alan (2. Sınıf) öğrencilerin ankete verdikleri cevaplar karşılaştırıldığında, aralarında anlamlı bir fark olmadığı görülmüştür. Öğrencilerin sınıfı ile yaşları arasında Pearson korelasyon analizi yapıldığında r= ,525 ve P= ,001 olarak hesaplanmıştır. Beklenildiği gibi sınıf ile yaş değişkenleri arasında pozitif yönlü istatistiksel olarak anlamlı bir ilişki olduğu hesaplanmıştır. Araştırmaya katılan öğrencilerin yaş ve sınıf değişkenleri için Pearson korelasyon grafiği Şekil 4 de verilmiştir.

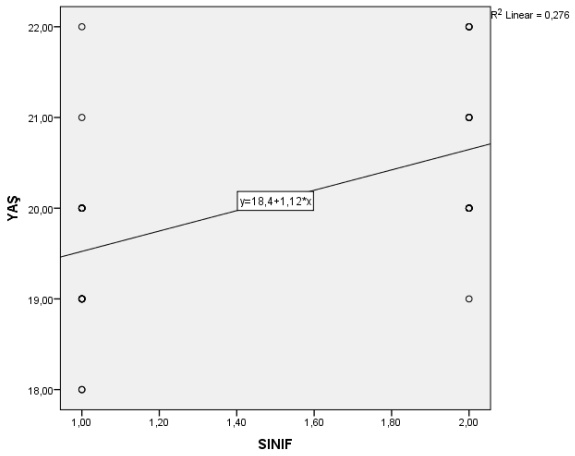

Şekil 4. Öğrencilerin yaş ve sınıf değişkenleri arasındaki ilişkiyi gösteren Pearson korelasyon grafiği.

Tablo 3. Uygulamalı cihaz eğitimine katılan öğrencilerin ankette yer alan önermelere vermiş oldukları cevaplar

	Önermeler	Kesinlikle katılmıyorum % (*f*)	Katılmıyorum % (*f*)	Fikrim yok % (*f*)	Katılıyorum % (*f*)	Kesinlikle katılıyorum% (*f*)
1	Shimadzu 2600i UV-DRS Spektrofotometre cihazını laboratuvarda kurulu şekilde görmek derse ilgimi arttırdı.	-	-	-	32 (12)	68 (26)
2	Analistin Shimadzu 2600i UV-DRS Spektrofotometre cihazının software eğitimi, eğitim öğretimime katkı sağladı.	-	-	-	40 (14)	60 (24)
3	Perkin Elmer Spectrum Two FT-IR Spektrofotometri cihazını laboratuvarda kurulu şekilde görmek derse ilgimi arttırdı.	-	-	-	29 (11)	71 (27)
4	Analistin Perkin Elmer Spectrum Two FT-IR Spektrofotometri cihazının software eğitimi eğitim öğretimime katkı sağladı.	-	-	-	32 (12)	68 (26)
5	Phenom Marka Prox Model masaüstü Taramalı Elektron Mikroskobu cihazını laboratuvarında kurulu şekilde görmek derse ilgimi arttırdı.	-	-	-	32 (12)	68 (26)
6	Analistin Phenom Marka Prox Model masaüstü Taramalı Elektron Mikroskobu cihazının software eğitimi eğitim öğretimime katkı sağladı.	-	-	-	32 (12)	68 (26)
7	Agilent 6460 Triple Quad LC-MS/MS cihazını laboratuvarında kurulu şekilde görmek derse ilgimi arttırdı	-	-	-	34 (13)	66 (25)
8	Analistin Agilent 6460 Triple Quad LC-MS/MS cihazının softwarei hakkında bilgi vermesi eğitim öğretimime katkı sağladı.	-	-	-	26 (10)	74 (28)
9	Thermo Scientific ICap Q ICP-MS cihazını laboratuvarında kurulu şekilde görmek derse ilgimi arttırdı.	-	-	-	34 (13)	66 (25)
10	Analistin Thermo Scientific ICap Q ICP-MS cihazının softwarei hakkında bilgi vermesi eğitim öğretimime katkı sağladı.	-	-	3 (1)	21 (8)	76 (29)
11	İş Sağlığı ve Güvenliğinin laboratuvarda önemi ile ilgili farkındalığım arttı.	-	-	-	24 (9)	76 (29)
12	İş Hijyeninin laboratuvar çalışması ile ilişkisi hakkında farkındalığım arttı.	-	-	-	18 (7)	82 (31)
13	UBATAM da cihaz eğitimi için ayrılan süre yeterli.	-	-	-	34 (13)	66 (25)
14	UBATAM eğitimi öncesinde ve sonrasında okulun internet sayfasındaki duyuru ve haberlerden memnunum.	-	-	-	32 (12)	68 (26)

4. Tartışma

Meslek yüksekokulu öğrencilerinin teknolojik gelişmeleri takip edebilecek şekilde eğitim almaları önemlidir. Bu çalışmada öğrenciler, uluslararası standartlara göre akredite laboratuvarda aldıkları sekiz saatlik eğitimi değerlendirmişlerdir. Bu çalışmada değerlendirilen eğitim UBATAM'da ön lisans öğrencilerine verilen ve sertifika ile belgelenen kurumumuzun ilk uygulamalı cihaz eğitimi olmuştur (UÜ, 2024). Eğitim veren yetkililerin iş yükü çok ve eğitim maliyetli olmasına rağmen öğrencilerden ücret talep edilmemiştir. Öğrencilerin uygulama becerileri kazanmaları ön plana alınmıştır. Genel uygulama becerilerine yönelik Güney (2024) Teknik Bilimler Meslek yüksekokulunda yapmış olduğu bir çalışmada müfredat kapsamında ayrıca bir eğitim verilmeden öğrencilerin bataryalı elektrikli araçlar alanında pratik becerilerini değerlendirmiş ve öğrencilerin yeterli mesleki ve teknik eğitim almış olduğunu tespit etmiştir. Bölümümüzde Laboratuvar Teknolojisi programı öğrencilerinin bir laboratuvar teknikerinin günümüzün taleplerini karşılayabilecek çeşitli analizleri yapabilmeleri için gereken, müfredat kapsamında yer alan, yüksek teknoloji ile üretilmiş cihazları görmeleri, softwareleri de dâhil cihazlarla ilgili uygulamalı eğitim almaları sağlanmıştır. Eğitim sonrasında eğitimi başarı ile tamamlayan ikinci sınıf öğrencilerine eğitim sertifikası verilmiştir. Bu çalışmada, gerçekleştirilen uygulamalı cihaz eğitiminin eğitimi alan öğrenciler tarafından değerlendirme sonuçları sunulmuştur. Öğrencilerin, bu eğitimin kendilerine mesleki alanda katkı sağladığını ifade ettikleri bulunmuştur. Bu nedenle programa kayıtlı her öğrenciye bu şansın verilmesi amacıyla uygulamalı cihaz eğitimi yıllık faaliyet planına eklenmiştir.

4. Sonuç

Cihaz eğitiminin en iyi sonuç alınabilecek şekilde sürdürülebilmesi için eğitim planı hazırlanarak gerekli resmi yazışmalar önceden yapılmıştır. Eğitim programı bu plana göre sürdürülmüştür. Bu çalışma Uşak Üniversitesi Banaz Meslek Yüksekokulu Kimya ve Kimyasal İşleme Teknolojileri Bölümü Laboratuvar Teknolojisi Programı öğrencileri (eğitime katılımcı olarak) ile UBATAM'da (cihaz eğitimi veren birim) gerçekleştirilmiş ve UZEM tarafından katılımcı ikinci sınıf başarılı öğrencilere eğitim sertifikası verilmiştir. Anket çalışması, cihaz eğitimine katılan gönüllü 21 birinci sınıf ve 17 ikinci sınıf laboratuvar teknolojisi programı öğrencilerinden oluşan 38 kişiye uygulanmıştır. Test sonuçları SPSS 20.0 programlarında değerlendirilmiş ve aşağıdaki sonuçlar elde edilmiştir. Bu çalışma ile öğrencilere eğitim öğretim yıllarında son teknoloji ile üretilmiş laboratuvar cihazları ile ilgili, TS EN ISO/IEC 17025 Standardına göre akredite bir laboratuvarda, analistler tarafından verilen uygulamalı cihaz eğitiminin, öğrencilerin enstrümantal analiz dersine ilgilerini arttırdığı ve eğitim öğrenimlerine katkı sağladığı ortaya çıkmıştır. Gerçekleştirilen eğitim ile laboratuvar çalışmaları ile İş Sağlığı ve Güvenliği ve İş Hijyeni ilişkileri hakkında öğrencilerin farkındalıklarının arttığı ve eğitim ile ilgili duyuru ve haberlerin bölümün internet sayfasında yayınlanmasından öğrencilerin memnun oldukları bulunmuştur. Planlanan eğitim süresinin yeterli olduğu, 37 öğrencinin ilk defa uluslararası akredite bir laboratuvara giriş yaptığı belirlenmiş ve öğrencilerin cihaz eğitimi ile ilgili görüşleri ile cinsiyetleri ve sınıfları arasında anlamlı bir ilişki olmadığı hesaplanmıştır.

Katkı Oranı Beyanı

Yazarın katkı yüzdeleri aşağıda verilmiştir. Yazar makaleyi incelemiş ve onaylamıştır.

	M.GK.
K	100
T	100
Y	100
VTI	100
VAY	100
KT	100
YZ	100
KI	100
GR	100

K= kavram, T= tasarım, Y= yönetim, VTI= veri toplama ve/veya işleme, VAY= veri analizi ve/veya yorumlama, KT= kaynak tarama, YZ= Yazım, KI= kritik inceleme, GR= gönderim ve revizyon.

Çatışma Beyanı

Yazar bu çalışmada hiçbir çıkar ilişkisi olmadığını beyan etmektedirler.

Etik Onay Beyanı

T.C. Uşak Üniversitesi Fen ve Mühendislik Bilimleri Bilimsel Araştırma ve Yayın Etiği Kurul'undan bu araştırma kapsamında uygulanacak yöntemlerin etik olarak uyguluk onayı alınmıştır (Onay tarihi: 12 Mart 2024, Onay numarası: 2024-6).

Destek ve Teşekkür Beyanı

Uşak Üniversitesi (UÜ) Bilimsel Analiz ve Teknolojik Uygulama ve Araştırma Merkezine (UBATAM), UBATAM Müdürü Doç. Dr. Erkan HALAY'a, Öğr. Gör. Dr. Mehmet KAYHAN'a, Öğr. Gör. Dr. Süleyman GÖKÇE'ye, UÜ Sürekli Eğitim Araştırma ve Uygulama Merkezi Müdürlüğüne (USEM) ve UÜ Banaz Meslek Yüksekokulu Müdürlüğüne teşekkür ederim.

Kaynaklar

Akreditasyon Sertifikası Eki. 2021. URL: https://ubatam.usak.edu.tr/duyuru/690 ve URL: https://secure.turkak.org.tr/pdf/AB1285T.pdf?r=4476d9ad16fc437ba71d430407d0542e (erişim tarihi: 29 Ekim 2024).

Athare AE. 2018. Synthesis and characterisation of ZnO nanoparticals by XRD, EDX, SEM, FTIR and UV-DRS. Int J Sci Res Sci Eng Technol, 4: 627-631.

Bardak F, Kose E. 2024. 2-Klorokinolinin moleküler ve spektroskopik özelliklerinin kuantum kimyasal hesaplama yöntemleriyle araştırılması. AKÜ Fen Müh Bilim Derg, 24(3): 504-518.

Borkert CM, Cox FR, Tucker MR. 1998. Zinc and copper toxicity in peanut, soybean, rice, and corn in soil mixtures. Commun Soil Sci Plant Anal, 29(19–20): 2991–3005.

Engin MS, Uyanik A, Cay S. 2017. Investigation of trace metals distribution in water, sediments and wetland plants of Kızılırmak Delta, Turkey. Int J Sediment Res, 32(1): 90-97.

Eser N, Marangoz AY. 2023. Teknoloji kabul modeli çerçevesinde metaverse ve tüketiciler. Bilişim Teknol Derg, 16(4): 285-297.

Gülbaş HE, Bozkurt S, Halay E. 2023. Synthesis and characterization of dicarboxamide derivative: Cu+ 2 selective turn-on fluorometric and colorimetric chemosensor. J Heterocycl Chem, 60(7): 1223-1229.

Güney B. 2024. Development and evaluation of students' practice skills in vocational and technical education of electric vehicles. BSJ Eng Sci, 7(4): 724-735.

ISO/IEC 17025: 2017. 2017. General requirements for the competence of testing and calibration laboratories. URL: https://www.iso.org/obp/ui/#iso:std:iso-iec:17025:ed-3:v1:en (erişim tarihi: 22 Ağustos 2024).

Karagöz İ. 2021. Fertilization and fertilizer types. Appl Soil Chem, 2021: 123-148.

Kulkarni S, Goswami A. 2019. Effect of excess fertilizers and nutrients: a review on impact on plants and human population. In Proceedings of International Conference on Sustainable Computing in Science, Technology and Management (SUSCOM), February 26-28, Jaipur, India, pp: 2094-2099.

Long XX, Yang XE, Ni WZ, Ye ZQ, He ZL, Calvert DV, Stoffella JP. 2003. Assessing zinc thresholds for phytotoxicity and potential dietary toxicity in selected vegetable crops. Commun Soil Sci Plant Anal, 34(9-10): 1421-1434.

Mathur MA, Dias, MF, Mathur MP. 2016. Importance of green technology in fertilizer quality improvement. Procedia Eng, 138: 308-313.

Mykityshyn A, Fisk AD, Rogers WA. 2002. Learning to use a

home medical device: Mediating age-related differences with training. Hum Factors, 44(3): 354-364.

Outridge PM, Noller BN. 1991. Accumulation of toxic trace elements by freshwater vascular plants. In Reviews of Environmental Contamination and Toxicology: Continuation of Residue Reviews. Springer, New York, USA, pp: 1-63.

Prado RdM, Rozane DE. 2020. Leaf analysis as diagnostic tool for balanced fertilization in tropical fruits. In: Srivastava, AK, Hu, C, Editors. Fruit crops: Diagnosis and management of nutrient constraints. Elsevier, Amsterdam, Netherlands, pp: 131–141.

T.C. Çevre, Şehircilik ve İklim değişikliği Bakanlığı, Ulusal Hava Kalite İzleme Ağı. URL: https://www.mevzuat.gov.tr/mevzuat?MevzuatNo=12188&MevzuatTur=7&MevzuatTertip=5 (erişim tarihi: 22 Ağustos 2024).

T.C. Resmi Gazete. 2004. Su Kirliliği Kontrolü Yönetmeliği, No:25687. URL: https://www.mevzuat.gov.tr/mevzuat?MevzuatNo=7221&MevzuatTur=7&MevzuatTertip=5 (erişim tarihi: 29 Ekim 2024).

T.C. Resmi Gazete. 2005. İnsani Tüketim Amaçlı Sular Hakkında Yönetmelik, No:25730 URL: https://www.mevzuat.gov.tr/mevzuat?MevzuatNo=7510&MevzuatTur=7&MevzuatTertip=5 (erişim tarihi: 29 Ekim 2024).

T.C. Resmi Gazete. 2008. Hava Kalitesi Değerlendirme ve Yönetimi Yönetmeliği, No:26898. URL: https://www.resmigazete.gov.tr/eskiler/2016/10/20161020-3.htm (erişim tarihi: 22 Ağustos 2024).

T.C. Resmi Gazete. 2016. İnsani Tüketim Amaçlı Sular Hakkında Yönetmelikte Değişiklik Yapılmasına Dair Yönetmelik, No:29863. URL: https://www.resmigazete.gov.tr/eskiler/2016/10/20161020-3.htm (erişim tarihi: 22 Ağustos 2024).

Türkiye Sürdürülebilir Kalkınma Amaçları. URL: https://turkiye.un.org/tr/sdgs (erişim tarihi: 22 Ağustos 2024).

Uşak Üniversitesi (UÜ) Sürekli Eğitim Araştırma ve Uygulama Merkezi (USEM). 2024. Haberler. URL: https://usem.usak.edu.tr/duyuru/12952 (erişim tarihi: 22 Ağustos 2024).

World Health Organization. 2024. Guidelines for drinking-water quality: Fourth edition incorporating the first and second addenda. Geneva: Licence: CC BY-NC-SA 3.0 IGO. URL: https://www.who.int/publications/i/item/9789240045064 (erişim tarihi: 22 Ağustos 2024).

Black Sea Journal of Engineering and Science
doi: 10.34248/bsengineering.1549943

Open Access Journal
e-ISSN: 2619 – 8991

Research Article
Volume 8 - Issue 1: 32-40 / January 2025

EVALUATION OF DIFFERENT SWAB WETTING CHEMICALS AFFECTING THE YIELD OF DNA OBTAINED FROM BIOLOGICAL EVIDENCE ON CARTRIDGE CASINGS

Fatma Ebru YÜKSEK[1], Eda Nur AY[1], Yakup GÜLEKÇİ[1]*

[1]*Kütahya Health Sciences University, Faculty of Engineering and Natural Sciences, Department of Forensic Sciences, 43100, Kütahya, Türkiye*

Abstract: Cartridge casings made from transition metals can be examined ballistically and also serve as significant evidence by containing touch DNA. However, the success rate of profiles obtained from this type of evidence is generally low. To enhance the success of DNA profiling from suspects' biological evidence, using swabs moistened with chemicals can be beneficial. Typically, swabs are moistened with water, whose hypotonic nature disrupts cell integrity, causing the release of DNA. However, water is not the only agent used for moistening swabs; various buffer solutions are also utilized. The ability of swabs to transfer touch DNA depends on the type of buffer solution used. Sodium dodecyl sulfate (SDS), a strong anionic detergent, denatures non-covalently linked secondary and tertiary structures increasing the release of bound DNA. Another buffer solution used for swab moistening is the Te+4 buffer, which contains EDTA and Tris. EDTA chelates metal ions, inactivating enzymes that could potentially damage DNA, while Tris adjusts the pH to an optimal level. This study aims to compare the effectiveness of microfiber and cotton swabs moistened with SDS, Te+4 buffer, and water in recovering genetic material from blood and epithelial cells deposited on brass cartridge casings. The study also evaluates the impact of firing on the quality of DNA profiles by analyzing the RFU difference obtained on cartridge case and cartridges. Although the number of complete profiles obtained from water- and SDS-wetted swabs are equal, the average RFU value of SDS-wetted swabs is approximately twice that of water-wetted swabs. The minimum number of complete profiles belongs to swabs wetted with Te^{+4} buffer. SDS is particularly advantageous over water when used on casings with epithelial cells. Microfiber swabs are more effective in eliminating degradative factors caused by firing, thus enhancing profiling success. Comparisons of the RFU values indicate that casings yield lower values compared to cartridges, supporting the negative impact of the high heat, pressure, and residues generated during firearm discharge.

Keywords: Ballistics, Swab wetting chemical, DNA profiling, Identification, Touch DNA

***Corresponding author:** Kütahya Health Sciences University, Faculty of Engineering and Natural Sciences, Department of Forensic Sciences, 43100, Kütahya, Türkiye
E mail: yakup.gulekci@ksbu.edu.tr (Y. GÜLEKÇİ)
Fatma Ebru YÜKSEK https://orcid.org/0000-0002-1666-5416
Eda Nur AY https://orcid.org/0000-0001-9070-253X
Yakup GÜLEKÇİ https://orcid.org/0000-0001-9643-6850

Received: September 14, 2024
Accepted: November 17, 2024
Published: January 15, 2025

Cite as: Yüksek FE, Ay EN, Gülekçi Y. 2025. Evaluation of different swab wetting chemicals affecting the yield of DNA obtained from biological evidence on cartridge casings. BSJ Eng Sci, 8(1): 32-40.

1. Introduction

Touch DNA, which plays a crucial role in forensic investigations due to its polymorphic nature, is obtained by analyzing cells deposited when a suspect or victim contacts or holds target surfaces at a crime scene (Aditya et al., 2011). The exact origin of the limited amount of DNA resulting from such contact remains unclear. Numerous studies suggest that touch DNA may consist of shed corneocytes (Burrill et al., 2019). It can also include endogenous or transferred nucleated epithelial cells (Lacerenza et al., 2016), fragmented cells and nuclei (Zoppis et al., 2014), and cell-free DNA (Wang et al., 2017; Kanokwongnuwut et al., 2018).

Obtaining an adequate number of cells for identification from touch DNA is more challenging than obtaining DNA found in bodily fluids such as blood (Aditya et al., 2011). Factors such as the individual's cell transfer efficiency, gender, pre-contact activities, and duration of contact also influence the amount of DNA collected (Goray et al., 2016; Kanokwongnuwut et al., 2018; Sessa et al., 2019; van Oorschot et al., 2019).

Another parameter influencing the success of DNA profiling from touch DNA collected from a surface is the surface type itself. Certain materials interact with cells, affecting the efficiency of DNA collection. For example, transition metals and alloys can alter DNA's double helix structure, complicating the amplification of desired strands (Bonsu et al., 2020). Metal ions can form ion-metal bonds with various molecules within the DNA, hindering its collection from surfaces. Additionally, metals as polymerase chain reaction (PCR) inhibitors result in low STR amplification yields (Horsman-Hall et al., 2009).

Cartridge casings made from transition metals like copper, brass, and nickel disperse at the crime scene when a firearm is discharged (Combs et al., 2015; Bonsu et al., 2020). These casings can be examined ballistically and can also serve as significant evidence containing

touch DNA (Sterling, 2017; Nandi et al., 2021). However, factors such as the high heat and pressure generated during firing, and ion-metal interactions from the metals, which act as PCR inhibitors, make DNA recovery from casings challenging (Horsman-Hall et al., 2009; Thanakiatkrai and Rerkamnuaychoke, 2019; Bonsu et al., 2020). Despite these challenges, DNA evidence remains highly important due to its reliability and definitive results in personal identification, leading to the development of various methods to enhance DNA yield. These methods include swabbing (Thomasma and Foran, 2013), tape lifting (Milnthorp et al., 2015), soaking (Prasad et al., 2022), and vacuuming (Prasad et al., 2022). Swabs moistened with a solution can improve the profiling success of biological evidence transfer from suspects (Schulte et al., 2023). Wetting swabs to collect trace biological stains has become a standard practice, as it facilitates the rehydration of the stain and the transfer of cells onto the swab, maximizing the amount of biological material collected (Bonsu et al., 2020). Water is typically used for moistening swabs (Lee et al., 1998). However, the hypotonic nature of water can compromise cell integrity, potentially leading to the release of DNA that may become trapped within the swab fibers, thereby reducing recovery efficiency (Martin et al., 2006; Benschop et al., 2010).

Sampling from metal surfaces using swabs moistened with water can cause oxidative damage to the DNA template during collection (Holland et al., 2019; Kuffel et al., 2021). Additionally, copper found in brass cartridges can degrade DNA upon contact with water (MacDonald et al., 2015).

Various buffer solutions are used as wetting agents instead of water to mitigate these issues. Buffer solutions chemically facilitate the dissolution of nucleic acids from surfaces, enhance absorption onto the swab, and minimize the degradation potential of DNA by binding to metal cations released from surfaces (Bonsu et al., 2020). The effectiveness of buffers in extracting touch DNA from surfaces varies depending on the type of buffer solution used (Thomasma and Foran, 2013; Adamowicz et al., 2014). These solutions typically contain detergents (such as Triton X-100, sodium dodecyl sulfate (SDS)), a chelating agent (like EDTA), or phosphate-buffered saline (PBS) (Bonsu et al., 2020).

Detergents are molecules that contain both hydrophobic and hydrophilic parts, allowing them to disperse easily in water and interact with cell membranes, altering their properties. A three-stage model has been developed to describe how detergents dissolve cell membranes. In the initial stage, detergent molecules distribute between aqueous and lipid components. Interaction with the lipid compartment leads to the development of vesicle bilayers. The detergent-saturated vesicle bilayers coexist with lipid-detergent mixed aggregates, increasing the lipid-detergent ratio. As the ratio increases, detergent-enriched bilayer fragments are forced to transform into a smaller structure where unimers with hydrophilic and hydrophobic segments are combined (Kedar et al., 2010). Although this provides a general understanding of how detergents function, each detergent may act uniquely (Ahyayauch et al., 2010).

Due to containing both hydrophobic and hydrophilic structures, detergents solubilize cell components such as lipids, fats, and proteins in buffer solutions (Thomasma and Foran, 2013; Salager, 2002). Detergents that assist in cell lysis can cause precipitation at higher concentrations and may interfere with commercial DNA extraction kits (van Oorschot et al., 2003; Bonsu et al., 2020). SDS, a strong anionic detergent, denatures secondary and non-disulfide-linked tertiary structures to increase the release of bound DNA (Farrell, 2010).

Another buffer solution used for swab moistening is Te+4 buffer, which consists of EDTA and Tris. EDTA binds to metal ions as a chelating agent, depleting the metals available to metal-dependent enzymes. The resulting ion depletion inactivates enzymes like deoxyribonucleases (DNases) that catalyze the hydrolytic cleavage of phosphodiester bonds, potentially damaging DNA (Farrell, 2010). Tris maintains the environmental pH at a level where DNases are inactive (Li, 2015).

The type of swab used is as crucial as the wetting agent in determining DNA profile quality. Cotton swabs are the most commonly used swab type globally for collecting biological material or stains (Aloraer, 2017). Microfiber swabs, specially designed to easily release collected materials into extraction fluids, are becoming increasingly popular (Ambers et al., 2018).

This study compares the effectiveness of microfiber and cotton swabs moistened with SDS, Te+4 buffer, and water in recovering genetic material from blood and touch DNA on brass cartridge casings. Additionally, the study evaluates the impact of firing on DNA profile quality. Thus, the wetting chemical and swab type that will maximize DNA profile quality for both biological materials will be determined.

2. Materials and Methods

To prevent contamination, all consumables, magazines, and cartridge cases were cleaned with Zefiran IM (Molteni, Switzerland) before the start of the study. Consumables were autoclaved at 121°C for 20 minutes (Labor İldam, Türkiye). A male participant over the age of 18 contaminated 9x19 mm MKE brand brass cartridge cases with epithelial cells and blood. The participant washed his hands with soap and water one hour before applying epithelial cells to the cartridge cases. The epithelial cell contamination on the cartridge cases was achieved by having the participant press the cases with his thumb and index finger during routine activities, without any additional procedures apart from washing his hands (Figure 1). During the epithelial cell contamination process, care was taken to ensure that finger contact with the cartridge case did not exceed 10 seconds. Under sterile conditions, 10 µL of blood collected from the participant was evenly distributed on

the outer wall of the cartridge cases using a micropipette (Figure 2). The cartridge cases, loaded into the weapon by the participant, were fired by a professional shooter using a Sarsılmaz Kılınç Mega 2000 model firearm at a designated shooting range with obtained permissions. The tarpaulin spread over the area where the cartridge cases fell was changed after each shot. A researcher wearing double gloves collected the cartridge cases, changing gloves after picking up each one. The cartridge cases, placed in paper evidence bags, were then transported to the laboratory. The collected cartridge cases were subjected to DNA analysis on the same day. Each cartridge case was stored under sterile conditions in the laboratory until analysis.

Figure 1. Cartridges cases contaminated with epithelial cells.

Figure 2. Cartridge cases contaminated with blood.

2.1. Preparation of Swab Wetting Chemicals

To investigate the effect of swab-wetting chemicals on DNA yield from cartridge cases, 2% SDS (Multicell, Canada), Te+4 buffer (Multicell, Canada), and distilled water (Merck, Germany) were used. The swabs included COPAN brand (Italy), FLOQ swabs, and BeyanLab brand (Türkiye) cotton swabs. For distilled water, 1 liter was placed in a sterile jar and autoclaved at 121°C for 20 minutes. To prepare 2% SDS, 2 grams of SDS powder was measured and distilled water was added to reach a total volume of 100 mL. A magnetic stirrer (Velp Scientifica-Arex) was used to dissolve the SDS. The Te+4 buffer (10mM Tris – 1mM EDTA) was used as received in solution form and required no further preparation. From each swab-wetting chemical, 400 µL was drawn using a micropipette and applied to the swab head to ensure the entire surface was moistened.

2.2. Control Sample

A control sample was obtained by contaminating an identical cartridge case with blood, similar to those used in the experiment. This cartridge case was not fired, and the day after the sample was prepared, a cotton swab was used to collect the sample for DNA analysis. Blood, which is rich in DNA, was chosen as a positive control to verify the accuracy of the analyses that the kit worked correctly and was able to produce the expected results.

2.3. DNA Isolation

DNA analyses were conducted on 12 cartridge cases (6 contaminated with blood and 6 with epithelial cells) that had been fired, and on 6 cartridges (3 contaminated with blood and 3 with epithelial cells) that had not been fired (Table 1).

Table 1. Types of swabs used for sampling from cartridge cases and cartridges

Types of Swabs Used for Sampling from Cartridge Cases		
Biological Material Type	Swab Wetting Chemical (400 µL)	Swab Type
Blood	SDS	Cotton Swab
		Microfiber Swab
	Te^{+4} Buffer	Cotton Swab
		Microfiber Swab
	Distilled Water	Cotton Swab
		Microfiber Swab
Epithelial Cells	SDS	Cotton Swab
		Microfiber Swab
	Te^{+4} Buffer	Cotton Swab
		Microfiber Swab
	Distilled Water	Cotton Swab
		Microfiber Swab
Types of Swabs Used for Sampling from Cartridges		
Biological Material Type	Swab Wetting Chemical (400 µL)	Swab Type
Blood	SDS	Cotton swab
	Te^{+4} Buffer	
	Distilled Water	
Epithelial Cells	SDS	Microfiber swab
	Te^{+4} Buffer	
	Distilled Water	

Due to the low number of cells transferred to the cartridges through touch, the organic isolation method (phenol-chloroform), preferred for isolating trace amounts of samples as high amounts of DNA were obtained, was selected (Eychner et al., 2016; Semizoğlu, 2013). While isolating DNA using the organic isolation method (Semizoğlu, 2013), modifications were made by adding 10 µL of proteinase-K to the samples moistened with SDS, Te+4 Buffer, and distilled water, and 3 µL for the isolation negative control. The isolation negative control is a mixture where all steps required for organic isolation are followed, but no DNA-containing cells are added to the tube. After evaporating the alcohol from the microcentrifuge tubes, 30 µL of Te+4 buffer was added, and the tubes were spun briefly (approximately 5 seconds) to ensure that the Te+4 buffer containing DNA was not left on the sidewalls or the inner lid. The resulting isolates were stored at -80 °C until the STR amplification stage.

2.4. Amplification of STRs

The amplification of STR regions was performed using the GlobalFiler™ PCR Amplification Kit with 24 loci (Applied Biosystems, Waltham, USA). For each sample, 7.5 µL of the reaction mix (Applied Biosystems, Waltham, USA), 2.5 µL of the primer mix (Applied Biosystems, Waltham, USA), and 15 µL of DNA isolate were used. A total of 25 µL of the mixture was prepared, and the samples were placed into a GeneAmp® 9700 PCR system (Applied Biosystems, Waltham, USA). Samples were kept in the initial incubation phase at 95 °C for one minute. This was followed by ten seconds of denaturation at 94 °C followed by 30 cycles of elongation at 59 °C for ninety seconds. Finally, after a final extension at 60 °C for ten minutes, PCR was completed. The STR amplification parameters were set according to the manufacturer's recommendations. Since electrophoresis was performed on the same day, the samples were stored at +4°C after amplification.

2.5. Electrophoresis Analysis

For each sample analyzed on the ABI 3500 Genetic Analyzer (Applied Biosystems, Waltham, USA), a mixture was prepared consisting of 9.6 µL Hi-Di™ formamide (Applied Biosystems, Waltham, USA), 0.4 µL GeneScan™ 600 LIZ™ Size Standard v2.0 (Applied Biosystems, Waltham, USA), and 1 µL of PCR product (Applied Biosystems, Waltham, USA). A total of 10 µL of the formamide/size standard mixture was placed into the ABI PRISM 3500 instrument (Applied Biosystems, Waltham, USA), and 1 µL of the PCR product was added on top.

The samples were run using 36 cm capillaries with POP-4 polymer, with an injection time of 15 seconds at 1.2 kV and a run time of 1550 seconds at 13 kV. The DS-36 Matrix standard and GS POP-4 (1ml) – C Filter were selected for the analysis. After the PCR products were processed under the appropriate conditions on the ABI PRISM 3500 Genetic Analyzer (Applied Biosystems, Waltham, USA), the raw data obtained were analyzed using GeneMapper IDx version 1 software (Applied Biosystems, Waltham, USA) for genotype determination. The RFU threshold was set at 200 (SWGDAM, 2021). The concept of a complete profile was defined based on the number of alleles possessed by the participant.

3. Results

The success of the swab types and wetting chemicals was evaluated by averaging the RFU values observed in the DNA profiles. The success percentages of showing full profiles for cartridge cases and cartridges were calculated based on the specific swab type and biological materials. No contamination was detected in the isolation negative control samples. The average RFU values of the profiles obtained from the positive control samples ranged between 5,000 and 10,000. A total of eight swabs showed complete profiles (Table 2).

Table 2. Samples showing complete profiles

Biological Material	Wetting Chemical	Cartridge Case*(n=12)		Cartridge* (n=6)	
		Swab Type			
		Cotton Swab	Microfiber Swab	Cotton Swab	Microfiber Swab
Blood	SDS	✓	✓	✓	
	Te+4 Buffer	X	✓	✓	
	Distilled Water	✓	✓	✓	
Epithelial Cell	SDS	X	—		—
	Te+4 Buffer	X	X		X
	Distilled Water	X	—		X

*: The ✓ symbol indicates a complete profile, while the — symbol represents that the sample showed a partial profile, X symbol represents no results were obtained from the DNA analyses.

After firing the cartridges contaminated with epithelial cells and blood, samples were collected using cotton swabs. For cartridge cases contaminated with epithelial cells, no complete profile was obtained regardless of the swab wetting chemical used. However, complete profiles were obtained from cartridge cases contaminated with blood using cotton swabs moistened with SDS and distilled water. Comparing the profiles, the average RFU value obtained with SDS was higher than that obtained with distilled water (Table 3).

Microfiber swabs were used to collect samples from cartridges contaminated with epithelial cells and blood and then fired. For cartridge cases contaminated with epithelial cells, no alleles were observed when microfiber swabs were moistened with Te+4 buffer. Partial DNA profiles were obtained from swabs moistened with distilled water and SDS, but these were unsuitable for comparison due to significant degradation of key alleles. In terms of RFU values, SDS (16001-17000) was found to be more successful than distilled water (13001-14000) (Table 3). Complete DNA profiles were obtained from all swab wetting chemicals used on cartridge cases contaminated with blood (Table 2). However, when examining RFU values, the highest amount of DNA was observed with SDS treatment (Table 3). In the DNA profiles obtained from microfiber swabs moistened with distilled water, the morphological appearance of alleles at specific loci deviated from the expected standards, disrupting the heterozygote peak balance. Therefore, after SDS, the next most successful chemical was Te+4 buffer at the stage of sampling blood cartridge case with microfiber swabs.

In the swab samples collected from cartridges contaminated with blood using cotton swabs, all wetting chemicals produced complete profiles, and no degradation was observed (Table 2). Based on RFU values, the least successful swab was the one moistened with distilled water (6001-7000). The RFU value of the swab moistened with Te+4 buffer (83001-84000) was

approximately twice that of the one moistened with SDS (17001-18000) (Table 3).

In the DNA profile of the swab moistened with SDS, N-binding (split peaks) was observed in each gene region (Figure 3).

Table 3. Average RFU Ranges of Profiles

Biological Material	Wetting Chemical	Cartridge Case (n=12)		Cartridge (n=6)	
		Cotton Swab	Microfiber Swab	Cotton Swab	Microfiber Swab
Blood	SDS	16001-17000	29001-30000	17001-18000	
	Te+4 Buffer	0	4001-5000	83001-84000	
	Distilled Water	13001-14000	11001-12000	6001-7000	
Epithelial Cell	SDS	0	1201-1300		1101-1200
	Te+4 Buffer	0	0		0
	Distilled Water	0	0-200		0

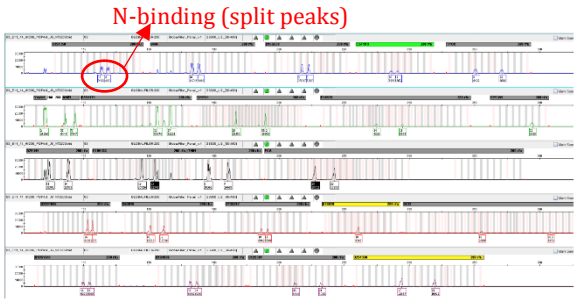

Figure 3. DNA profile image of blood collected from a cartridge using a cotton swab moistened with SDS.

Microfiber swabs were used to collect samples from cartridges contaminated with epithelial cells. A usable profile for comparison was obtained only from the swab moistened with SDS (Figure 4). However, since the profile was partial, it could not be matched to an unidentified individual.

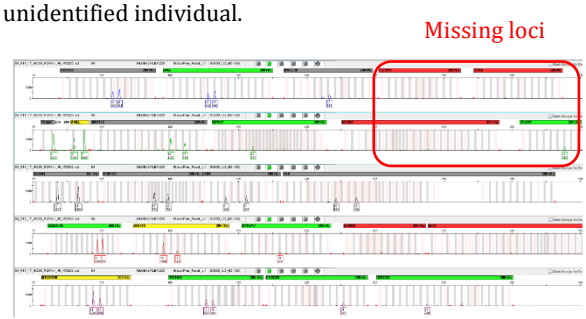

Figure 4. Partial and Degraded DNA Profile Image of Epithelial Cells Collected from a Cartridge Using a Microfiber Swab Moistened with SDS

In the phase where blood samples were collected using cotton swabs, swabs taken from cartridges showed a higher percentage of complete profiles (100%) compared to cartridge cases (67%) (Table 4). The RFU values of profiles obtained after firing were lower compared to those that were not fired (Table 3). The likelihood of obtaining a complete profile from cartridge cases contaminated with blood was higher than those contaminated with epithelial cells.

No allele loss was observed in swabs with a full profile, whereas no alleles were observed in swabs with a RFU value of zero, resulting in a loss of 45 alleles (Table 5). The 18 profiles obtained from the study is shown in supplement 1 and the detailed representation of missing alleles on the profile is shown in supplement 2.

Table 4. Percentage full profile rates by biological material and swab type

Biological Material	Wetting Chemical	Cartridge Case* (n=12)		Cartridge* (n=6)	
		Swab Type			
		Cotton Swab	Microfiber Swab	Cotton Swab	Microfiber Swab
Blood	SDS	67%	100%	100%	
	Te+4 Buffer				
	Distilled Water				
Epithelial Cell	SDS	0%	0%		0%
	Te+4 Buffer				
	Distilled Water				

Table 5. Number of missing allel by profile

Biological Material	Wetting Chemical	Cartridge Case (n=12)		Cartridge (n=6)	
		Swab Type			
		Cotton Swab	Microfiber Swab	Cotton Swab	Microfiber Swab
Blood	SDS	0	0	0	
	Te+4 Buffer	45	0	0	
	Distilled Water	0	0	0	
Epithelial Cell	SDS	45	15		9
	Te+4 Buffer	45	45		45
	Distilled Water	45	38		45

4. Discussion

Distilled water is commonly preferred as a swab wetting chemical. However, in cases where the number of cells obtained from trace or degraded samples is limited, water may be insufficient, necessitating the use of alternative chemicals. In this context, chemicals such as Te+4 buffer and SDS can support more efficient cell collection and analysis. Furthermore, it has been demonstrated in various studies that the material and design of swabs significantly affect DNA collection efficiency (Brownlow et al., 2012; Dadhania et al., 2013). Therefore, it is thought that alternative wetting chemicals and swab designs could revolutionize genetic analyses.

SDS was the swab-wetting chemical that yielded the highest DNA quantity in all parameters except for

collecting blood samples from cartridges using cotton swabs. A recent study involving touch DNA samples left on glass surfaces used different wetting chemicals. SDS was found to be the only chemical with significantly higher recovery than water. No significant difference was observed between 2% SDS volumes of 15, 30, 45, and 90 µL for wetting, although foaming occurred at 90 µL (Schulte et al., 2023). Since the risk of DNA precipitation is higher at high SDS concentrations, a 2% SDS solution was used in the study for DNA safety, as recommended by Thomasma and Foran (2013). No precipitation was observed during extraction.

Different cell types were placed on non-porous surfaces and the effectiveness of swab wetting chemicals was tested. While EDTA was found to be the most suitable chemical for blood, water and detergent-based chemicals were found to be more suitable for trace DNA deposits. Detergent-based chemicals were less successful in cellular DNA compared to water. However, no meaningful comparison can be made since no peak was obtained in the collection of cellular samples with cotton swabs in the study (Kuffel et al., 2024). In a 2013 study, traces formed on glass surfaces by touch were sampled first with cotton swabs moistened with 120 µL of SDS or water, followed by a dry swab. SDS produced a higher average DNA yield compared to water. Contrary to Thomasma and Foran's findings, none of the swab samples collected from surfaces by touch using cotton swabs yielded profiles in this study. Since the minifiler kit has STR primers that produce shorter amplicons than the kit used in the study, they were able to obtain a profile by touch (Prinz et al., 2007; Thomasma and Foran, 2013). In a study where the double-swab technique was preferred to collect touch DNA from magazines, 30 µL of 2% SDS was used for cotton swabs, and 60 µL for microfiber swabs (Tasker et al., 2020). The high heat from firing and the absence of a second swab for sampling may explain the insufficient DNA for profiling in contrast to Tasker's study.

In contrast to these studies, swabs moistened with both double-swab techniques using water and SDS were used to sample from various porous and non-porous surfaces. The double swab moistened with water was more successful than SDS for all surfaces (Gilmore and Glynn, 2019). In another study where saliva was deposited on non-porous surfaces, no superiority of water over SDS was observed. Unlike touch DNA, saliva is watery, so the interaction between SDS and saliva is weaker (Grosey, 2011). Additionally, the difference in materials compared to cartridge cases and no exposure high temperatures might explain the variance in results.

Complete profiles were not observed in swabs collected from cartridge cases contaminated with epithelial cells. Microfiber swabs were more successful than cotton swabs as they produced partial DNA profiles. Similarly in two different studies aimed at increasing DNA yield from cells deposited by touch, microfiber swabs were found to be more effective (Templeton et al., 2013; Jansson et al., 2020). The success of obtaining complete profiles in these studies may be due to the use of direct PCR (Templeton et al., 2013) and differences in the isolation method (Jansson et al., 2020).

Te+4 buffer is preferred in many laboratories due to its availability and low cost (Aloraer et al., 2017). Cotton and microfiber swabs moistened with 30 µL of Te+4 buffer were used to collect cells containing touch DNA from various vehicle surfaces. Cotton swabs were more successful than microfiber swabs on all surfaces (Giovanelli et al., 2022). However, contrary to Giovanelli's findings, none of the complete profiles obtained from touch DNA in this study were from swabs moistened with Te+4 buffer. The factors that can negatively impact DNA on vehicle surfaces are fewer compared to those affecting DNA on fired cartridge casings.

In the study, water-moistened swabs were used to collect epithelial cells from cartridge cases and cartridges. However, none of the swabs produced complete DNA profiles, and the collected DNA was degraded. The water showed less degradation for epithelial cells than the Te+4 buffer. In another study conducted in 2024 with buccal cells, Te+4 buffer was more successful than water (Czado et al., 2024). DNA deposited by touch on glass, aluminum, and plastic surfaces was collected using cotton swabs moistened with either buffer (1% n-lauroylsarcosine, 10 mM Tris-HCl, 0.1 mM EDTA, 50 mM NaCl) or water. Afterwards, dry cotton swabs were also used. The buffer yielded a higher DNA concentration in all cases compared to water. When water was used, the quality of the DNA profile degraded over time and with increased temperature, whereas the detergent-based buffer stabilized the DNA for up to 24 hours and at temperatures up to 50°C (Bille et al., 2020). Elwick and colleagues explain this by the oxidation reaction caused when water contacts brass surfaces. The study investigated the DNA recovery of human epidermal keratinocyte cells from nickel and brass cartridges. Samples, including cartridge case, were sampled by rinsing and swabbing or soaking with different chemicals (Elwick et al., 2022). Holland proposes an alternative approach, suggesting that EDTA's chelation plays a role. Brass is an alloy of 70% copper and 30% zinc. Holland proposes that EDTA's chelation may reduce the impact of copper ions on DNA extraction efficiency, thus improving results from brass surfaces (Holland et al., 2019).

At the beginning of the study, it was concluded that cotton swab failed to produce a complete profile compared to microfiber swab in response to the targeted objective. If maximum yield is desired from the cartridge case regardless of the biological sample a microfiber swab moistened with SDS, which shows the highest RFU values, should be preferred.

5. Conclusion

Samples containing trace amounts of cells, such as touch DNA, must undergo maximal extraction. Achieving maximal extraction requires the use of various swab-wetting chemicals. The most commonly used chemical is often water or water-based physiological serum. SDS was chosen due to its ability to interact with the lipid components of cell membranes, and Te+4 buffer was selected to minimize oxidative damage to the DNA template (Farrell, 2010; Holland et al., 2019). The main drawback of using swab-wetting chemicals is that while water does not require prior preparation, chemicals like SDS and Te+4 buffer require preparation in advance, which can be time-consuming (Schulte et al., 2023). However, all three chemicals are commonly used in organic isolation methods and are readily available in laboratories (Semizoğlu, 2013).

SDS was the most successful chemical, irrespective of the swab type or biological material used in terms of average RFU values. In contrast, Te+4 buffer yielded the fewest complete profiles among the tested chemicals. The RFU values of profiles obtained after firing were lower than those of unfired samples. The likelihood of obtaining a complete profile from cartridge cases contaminated with blood was higher than those contaminated with epithelial cells. When situations such as firing can lead to DNA degradation, using SDS as the swab-wetting chemical and microfiber swabs can help obtain higher quality profiles, thus improving forensic analysis outcomes.

Future studies could benefit from expanding the research to include double swab techniques applied to cartridge cases made from various materials, which may yield further insights into DNA recovery efficiency.

Author Contributions

The percentages of the authors' contributions are presented below. The authors reviewed and approved the final version of the manuscript.

	F.E.Y.	E.N.A.	Y.G.
C	30	30	40
D	30	30	40
S	35	30	35
DCP	30	40	30
DAI	45	30	25
L	30	40	30
W	30	40	30
CR	30	30	40
SR	25	25	50
PM	30	30	40
FA	35	30	35

C=Concept, D= design, S= supervision, DCP= data collection and/or processing, DAI= data analysis and/or interpretation, L= literature search, W= writing, CR= critical review, SR= submission and revision, PM= project management, FA= funding acquisition.

Conflict of Interest

The authors declared that there is no conflict of interest.

Ethical Consideration

The study conducted at Kütahya Health Sciences University Application and Research Center was approved by the Non-Interventional Clinical Research Ethics Committee of Kütahya Health Sciences University (approval date: 12 August, 2024, protocol code of 2024/10/07). Also the study was carried out in accordance with the Helsinki criteria.

References

Adamowicz MS, Stasulli DM, Sobestanovich EM, Bille TW. 2014. Evaluation of methods to improve the extraction and recovery of DNA from cotton swabs for forensic analysis. PLoS ONE, 9(12): e116351. https://doi.org/10.1371/journal.pone.0116351

Aditya S, Sharma AK, Bhattacharyya CN, Chaudhuri K. 2011. Generating STR profile from "touch DNA". J Forensic Leg Med, 18(7): 295-298. https://doi.org/10.1016/j.jflm.2011.05.007

Ahyayauch H, Bennouna M, Alonso A, Goñi FM. 2010. Detergent effects on membranes at subsolubilizing concentrations: Transmembrane lipid motion, bilayer permeabilization, and vesicle lysis/reassembly are independent phenomena. Langmuir, 26(10): 7307-7313. https://doi.org/10.1021/la904194a

Aloraer DBN. 2017. Evaluation of collection protocols for the recovery of biological samples from crime scenes. MsC thesis, University of Central Lancashire, Master of Philosophy In Forensic and Applied Sciences, Preston, pp: 12

Aloraer D, Hassan NH, Albarzinji B, Goodwin W. 2017. Improving recovery and stability of touch DNA. Forensic Sci Int Genet Suppl Ser, 6: e390-e392. https://doi.org/10.1016/j.fsigss.2017.09.166

Ambers A, Wiley R, Novroski N, Budowle B. 2018. Direct PCR amplification of DNA from human bloodstains, saliva, and touch samples collected with microFLOQ ® swabs. Forensic Sci Int Genet, 32: 80-87. https://doi.org/10.1016/j.fsigen.2017.10.010

Benschop CCG, Wiebosch DC, Kloosterman AD, Sijen T. 2010. Post-coital vaginal sampling with nylon flocked swabs improves DNA typing. Forensic Sci Int Genet, 4(2): 115-121. https://doi.org/10.1016/j.fsigen.2009.07.003

Bille T, Fahrig G, Peiffer G, Weitz S. 2020. An improved process for the collection and DNA analysis of fired cartridge cases. Forensic Sci Int Genet, 46: 102238. 10.1016/j.fsigen.2020.102238

Bonsu DOM, Higgins D, Austin JJ. 2020. Forensic touch DNA recovery from metal surfaces – A review. Sci Justice, 60(3): 206-215. https://doi.org/10.1016/j.scijus.2020.01.002

Brownlow RJ, Dagnall KE, Ames CE. 2012. A comparison of DNA collection and retrieval from two swab types (Cotton and nylon flocked swab) when processed using three QIAGEN extraction methods. J Forensic Sci, 57(3): 713-717. https://doi.org/10.1111/j.1556-4029.2011.02022.x

Burrill J, Daniel B, Frascione N. 2019. A review of trace "Touch DNA" deposits: Variability factors and an exploration of cellular composition. Forensic Sci Int Genet, 39: 8-18. https://doi.org/10.1016/j.fsigen.2018.11.019

Combs LG, Warren JE, Huynh V, Castaneda J, Golden TD, Roby RK. 2015. The effects of metal ion PCR inhibitors on results

obtained with the Quantifiler ® Human DNA Quantification Kit. Forensic Sci Int Genet, 19: 180-189. https://doi.org/10.1016/j.fsigen.2015.06.013

Czado N, Houston R, Hughes S. 2024. Evaluation of metal ions and DNA recovery from the surface of fired and unfired brass ammunition to improve STR profiling. Int J Leg Med, 38(4):1265-1272. https://doi.org/10.1007/s00414-024-03200-8

Dadhania A, Nelson M, Caves G, Santiago R, Podini D. 2013. Evaluation of Copan 4N6FLOQSwabsTM used for crime scene evidence collection. Forensic Sci Int Genet Suppl Ser, 4(1): e336-e337. https://doi.org/10.1016/j.fsigss.2013.10.171

Elwick K, Gauthier Q, Rink S, Cropper E, Kavlick MF. 2022. Recovery of DNA from fired and unfired cartridge casings: comparison of two DNA collection methods. Forensic Sci Int Genet, 59: 102726. https://doi.org/10.1016/j.fsigen.2022.102726

Eychner AM, Schott KM, Elkins KM. 2016. Assessing DNA recovery from chewing gum. Med Sci Law, 57(1): 7–11. doi:10.1177/0025802416676413.

Farrell RE. 2010. Resilient ribonucleases. In: Farrell RE, editor. RNA methodologies. A Lab. Guid. Isol. Charact., Elsevier, Pennsylvania, USA, 4th ed., pp: 155-172. https://doi.org/10.1016/B978-0-12-374727-3.00007-3

Gilmore RB, Glynn CL. 2019. Recovery of touch DNA: a comparison of four collection methods on various substrates. In: Proceedings of the American Academy of Forensic Sciences Annual Meeting, February, Connecticut, USA, 10.13140/RG.2.2.17925.19688

Giovanelli A, Garrido GR, Rocha A, Hessab T. 2022. Touch DNA recovery from vehicle surfaces using different swabs. J Forensic Sci, 67(2): 707-711. https://doi.org/10.1111/1556-4029.14932

Goray M, Fowler S, Szkuta B, van Oorschot RAH. 2016. Shedder status—An analysis of self and non-self DNA in multiple handprints deposited by the same individuals over time. Forensic Sci Int Genet, 23: 190-196. https://doi.org/10.1016/j.fsigen.2016.05.005

Grosey N. 2011. Effects of different swabbing solutions on DNA recovery. MSc thesis, University of California, Master of Science ın Forensic Science, 1569776

Holland MM, Bonds RM, Holland CA, McElhoe JA. 2019. Recovery of mtDNA from unfired metallic ammunition components with an assessment of sequence profile quality and DNA damage through MPS analysis. Forensic Sci Int Genet, 39: 86-96. https://doi.org/10.1016/j.fsigen.2018.12.008

Horsman-Hall KM, Orihuela Y, Karczynski SL, Davis AL, Ban JD, Greenspoon SA. 2009. Development of STR profiles from firearms and fired cartridge cases. Forensic Sci Int Genet, 3(4): 242-250. https://doi.org/10.1016/j.fsigen.2009.02.007.

Jansson L, Forsberg C, Akel Y, Dufva C, Ansell C, Ansell R, Hedman J. 2020. Factors affecting DNA recovery from cartridge cases. Forensic Sci Int Genet, 48:102343. https://doi.org/10.1016/j.fsigen.2020.102343

Kanokwongnuwut P, Kirkbride P, Linacre A. 2018. Visualising latent DNA on swabs. Forensic Sci Int, 291: 115-123. https://doi.org/10.1016/j.forsciint.2018.08.016

Kedar U, Phutane P, Shidhaye S, Kadam V. 2010. Advances in polymeric micelles for drug delivery and tumor targeting. Nanomed: Nanotechnol Biol Med, 6(6): 714-729

Kuffel A, Gray A, Daeid NN. 2021. Impact of metal ions on PCR inhibition and RT-PCR efficiency. Int J Leg Med, 135(1): 63-72. https://doi.org/10.1007/s00414-020-02363-4

Kuffel A, Daeid NN, Gray A. 2024. Impact of swabbing solutions on the recovery of biological material from non-porous surfaces. Forensic Scı Int Synerg, 9: 100551

Lacerenza D, Aneli S, Omedei M, Gino S, Pasino S, Berchialla P, Robino C. 2016. A molecular exploration of human DNA/RNA co-extracted from the palmar surface of the hands and fingers. Forensic Sci Int Genet, 22: 44-53. https://doi.org/10.1016/j.fsigen.2016.01.012

Lee HC, Ladd C, Scherczinger CA, Bourke MT. 1998. Forensic applications of DNA typing. Am J Forensic Med Pathol, 19(1): 10-18. https://doi.org/10.1097/00000433-199803000-00002

Li R. 2015. Forensic biology. CRC Press, Boca Raton, Florida, USA, 2nd ed., pp: 200.

MacDonald LA, Wan TCR, Perez YS, Bille T, Ammendale MD, Podini DS. 2015. Recovering touch DNA from cartridge casings using a method of tape lifting. In: Proceedings of the 67th Annual Meeting of the American Academy of Forensic Sciences, Washington DC, USA, pp: 401.

Martin NC, Pirie AA, Ford LV, Callaghan CL, McTurk K, Lucy D, Scrimger DG. 2006. The use of phosphate buffered saline for the recovery of cells and spermatozoa from swabs. Sci Justice, 46(3): 179-184. https://doi.org/10.1016/S1355-0306(06)71591-X

Milnthorp HV, McKiernan HE, Danielson P. 2015. The evaluation and optimization of DNA recovery and amplification from bullet cartridge cases. In: Proceedings of the 67th Annual Scientific Meeting, November, Washington DC, ABD, pp: 1-47.

Nandi K, Sen DJ, Mahanti B. 2021. Ballistics: the modern day forensic weapon. World J Pharm Res, 11: 2534-2548.

Prinz M, Carracedo A, Mayr WR, Morling N, Parsons TJ, Sajantila A, Scheithauer R, Schmitter H, Schneider PM. 2007. ISFG: Recommendations regarding the role of forensic genetics for disaster victim identification (DVI). Forensic Sci Int Genet, 1: 3-12.

Prasad E, Hitchcock C, Raymond J, Cole A, Barash M, McNevin D, van Oorschot RAH. 2022. Touch DNA recovery from unfired and fired cartridges: comparison of swabbing, tape lifting and soaking. Forensic Sci Int, 330: 111101. https://doi.org/10.1016/j.forsciint.2021.111101.

Salager JL. 2002. Surfactants types and uses. FIRP booklet, Laboratorio FIRP Escuela de INGENIERIA QUIMICA, UNIVERSIDAD de Los ANDES Mérida 5101 VENEZUELA, pp: 300.

Schulte J, Rittiner N, Seiberle I, Kron S, Schulz I. 2023. Collecting touch DNA from glass surfaces using different sampling solutions and volumes: immediate and storage effects on genetic STR analysis. J Forensic Sci, 68(4): 1133-1147. https://doi.org/10.1111/1556-4029.15305

Semizoğlu İ. 2013. DNA izolasyonu. In: Semizoğlu İ, editor. Adli DNA analizleri. Adalet Yayınevi, Ankara, 1st ed., pp: 125-126.

Sessa F, Salerno M, Bertozzi G, Messina G, Ricci P, Ledda C, Rapisarda V, Cantatore S, Turillazzi E, Pomara C. 2019. Touch DNA: impact of handling time on touch deposit and evaluation of different recovery techniques: an experimental study. Sci Rep, 9(1): 9542. https://doi.org/10.1038/s41598-019-46051-9

Sterling SA. 2017. Range of detection for proteins and DNA from fingerprints on fired and unfired cartridge casings. MSc thesis, City University of New York, Master of Science in Forensic Science, New York, pp: 1-58.

SWGDAM. 2021. Interpretation guidelines for autosomal STR typing by forensic DNA testing laboratories. URL: https://www.swgdam.org/_files/ugd/4344b0_3f94c9a6286048c3924c58e2c230e74e.pdf. (accessed date: August 22,

2024).

Tasker E, Roman MG, Akosile M, Mayes C, Hughes S, LaRue B. 2020. Efficacy of "touch" DNA recovery and room-temperature storage from assault rifle magazines. Leg Med, 43: 101658. https://doi.org/10.1016/j.legalmed.2019.101658

Templeton J, Ottens R, Paradiso V, Handt O, Taylor D, Linacre A. 2013. Genetic profiling from challenging samples: direct PCR of touch DNA. Forensic Sci Int Genet Suppl Ser, 4(1): e224-e225. https://doi.org/10.1016/j.fsigss.2013.10.115

Thanakiatkrai P, Rerkamnuaychoke B. 2019. Direct STR typing from fired and unfired bullet casings. Forensic Sci Int, 301: 182-189. https://doi.org/10.1016/j.forsciint.2019.05.037.

Thomasma SM, Foran DR. 2013. The influence of swabbing solutions on DNA recovery from touch samples. J Forensic Sci, 58(2): 465-469. https://doi.org/10.1111/1556-4029.12036

van Oorschot RAH, Phelan DG, Furlong S, Scarfo GM, Holding NL, Cummins MJ. 2003. Are you collecting all the available DNA from touched objects? Int. Congr Ser, 1239: 803-807. https://doi.org/10.1016/S0531-5131(02)00498-3

van Oorschot RAH, Szkuta B, Meakin GE, Kokshoorn B, Goray M. 2019. DNA transfer in forensic science: a review. Forensic Sci Int Genet, 38: 140-166. https://doi.org/10.1016/j.fsigen.2018.10.014

Wang C, Stanciu CE, Ehrhardt CJ, Yadavalli VK. 2017. Nanoscale characterization of forensically relevant epithelial cells and surface associated extracellular DNA. Forensic Sci Int, 277: 252-258. https://doi.org/10.1016/j.forsciint.2017.06.019

Zoppis S, Muciaccia B, D'Alessio A, Ziparo E, Vecchiotti C, Filippini A. 2014. DNA fingerprinting secondary transfer from different skin areas: morphological and genetic studies. Forensic Sci Int Genet, 11: 137-143. https://doi.org/10.1016/j.fsigen.2014.03.005.

Black Sea Journal of Engineering and Science
doi: 10.34248/bsengineering.1552654

Open Access Journal
e-ISSN: 2619 – 8991

Araştırma Makalesi (Research Article)
Cilt 8 - Sayı 1: 41-53 / Ocak 2025
(Volume 8 - Issue 1: 41-53 / January 2025)

İGNİMBİRİT TAŞ ATIKLARININ DEĞERLENDİRİLMESİNE YÖNELİK EPOKSİ MATRİSLİ KOMPOZİTLERİN MEKANİK VE HİDROFOBİK ÖZELLİKLERİNİN İNCELENMESİ

Ahmet Cihat ARI[1]*

[1]*Yozgat Bozok University, Akdagmadeni Vocational School, Department of Architecture and Urban Planning, 66300, Yozgat, Türkiye*

Özet: Taş ocaklarında blok üretimi ve yapıların inşaatları için taşlar belirli boyutlarda kesilerek kullanılmaktadır. Bu kesim işlemleri neticesinde atık olarak ortaya taş tozu çıkmaktadır. Ancak taş işleme tesislerinde taş atıklarının giderek artması, bu atıkların düzenli olarak depolanmamasına ve doğaya bırakılmasına neden olmaktadır. Bu nedenle, taş atık miktarının azaltılması ve doğaya bırakılmasının önlenmesi için taş atıklarının potansiyel bir hammadde kaynağı olarak değerlendirilmesi gerekmektedir. Bu çalışmada, Nevşehir ilinde taş kesimi sonucunda ortaya çıkan ignimbirit taş atıklarının değerlendirilmesine yönelik epoksi matrisli kompozitler üretilmiştir. Kompozitlerin üretiminde, farklı tane büyüklüğüne (63 µm, 150 µm, 250 µm, 500 µm, 1000 µm) sahip ignimbirit taş tozu (İTT) ve matris olarak ise epoksi reçine (ER) kullanılmıştır. Taş tozlarının tane boyutlarındaki değişimin, kompozitlerin mekanik ve hidrofobik özelliklerine olan etkisi araştırılmıştır. Kompozitin en uygun bileşim oranı, ağırlıkça % 30 epoksi matris ve % 70 oranında <63 µm büyüklüğüne sahip İTT ile hazırlanmıştır. Bu kompozitle, 51 MPa'ya kadar yüksek basınç mukavemeti elde edilmiştir. Ayrıca kompozitin temas açısı 102,9° değeri, orijinal ignimbirit taşının 8,5° değerinden daha yüksek olması, kompozitin ignimbirit taşına göre daha fazla hidrofobik yüzey olduğunu göstermektedir. Sonuç olarak, epoksi matrisli kompozit, yüksek mukavemeti ve hidrofobik özellikleriyle, binalardaki su emme problemini azaltmak üzere çeşitli uygulamalar için büyük bir potansiyel sağlar.

Anahtar kelimeler: İgnimbirit, Taş atıkları, Atıkların değerlendirilmesi, Epoksi kompozit, Hidrofobik

Investigation of Mechanical and Hydrophobic Properties of Epoxy Matrix Composites for Recycling of Ignimbrite Stone Wastes

Abstract: In quarries, stones are cut to certain sizes for block production and construction of structures. As a result of these cutting processes, stone powder is produced as waste. However, the increasing amount of stone waste in stone processing plants causes these wastes not to be stored regularly and to be released into nature. Therefore, stone waste should be recycled as a potential raw material source to reduce the amount of stone waste and prevent it from being released into nature. In this study, epoxy matrix composites were produced for the recycling of ignimbrite stone waste resulting from stone cutting in Nevsehir province. In the production of composites, ignimbrite stone powder (ISP) with different grain sizes (63 µm, 150 µm, 250 µm, 500 µm, 1000 µm) and epoxy resin (ER) were used as the matrix. The effect of the change in the particle size of stone powders on the mechanical and hydrophobic properties of the composites was investigated. The most suitable composition ratio of the composite was prepared with 30% epoxy matrix and 70% ISP with a grain size of <63 µm. High compressive strength up to 51 MPa was obtained with this composite. Moreover, the contact angle of the composite was 102.9°, which was higher than the 8.5° value of the original ignimbrite stone, indicating that the composite has a more hydrophobic surface than the ignimbrite stone. As a result, the epoxy matrix composite provides a great potential for various applications to reduce the water absorption problem in buildings with its high strength and hydrophobic properties.

Keywords: Ignimbrite, Stone waste, Recycling of waste, Epoxy composite, Hydrophobic

***Sorumlu yazar (Corresponding author):** Yozgat Bozok University, Akdagmadeni Vocational School, Department of Architecture and Urban Planning, 66300, Yozgat, Türkiye
E mail: a.cihat.ari@bozok.edu.tr (A. C. ARI)
Ahmet Cihat ARI https://orcid.org/0000-0002-4690-8968

Gönderi: 19 Eylül 2024 **Received:** September 19, 2024
Kabul: 09 Aralık 2024 **Accepted:** December 09, 2024
Yayınlanma: 15 Ocak 2025 **Published:** January 15, 2025

Cite as: Arı AC. 2025. Investigation of mechanical and hydrophobic properties of epoxy matrix composites for recycling of ignimbrite stone wastes. BSJ Eng Sci, 8(1): 41-53.

1. Giriş

Doğal taşlar, tarih öncesi çağlardan günümüze kadar uzanan zaman boyunca çeşitli sektörler için en temel malzemelerden biri olmuştur. Özellikle inşaat sektöründe doğal taşların üretimi ve işleme teknolojisinin gelişmesi, yapıların mimarisinde öne çıkmasını sağlamıştır. Doğal taşların çeşitli renk, doku ve sertliklere sahip olması, yapıların iç ve dış mekânlarında estetik tasarımlarının yapılmasını mümkün kılmaktadır. Taşlar yapıların inşaatlarında kullanırken, standartlara uygun boyut ve şekil için çeşitli cihazlarla işlenmektedir. Bu işlemler sırasında taşlarda kesim atıkları oluşmaktadır. Ayrıca taşların madencilik işlemleri sırasında da atıklar ortaya çıkmaktadır. Örneğin taşların çıkarılmasında geleneksel patlatma tekniklerinin kullanılmasıyla oluşan atıklar % 60-70 arasında iken, taşların çıkarılmasında tel testere tekniği kullanılmasıyla oluşan atıklar ise % 30-40 arasında meydana gelmektedir (Heriyanto vd., 2019).

Türkiye'de 2023 yılında doğal taş üretimi 6,3 milyon ton

olarak gerçekleşmiştir (Anonim, 2023). Ülkenin bulunduğu konum itibariyle Kuzey Anadolu Fay Zonunda yer alması, doğal taşların kırıklı yapı şeklinde oluşmasına neden olmaktadır. Taşların bu kırıklı yapısı, taş üretiminin her aşamasında da atıkları oluşturmaktadır. Bu durum, ülkedeki taş üretim verimini düşürmektedir. Türkiye'de taş üretim verimi ortalama % 0,5 ile % 15 arasında gerçekleşmektedir. Örneğin taş ocak veriminin % 10'da olması, bu ocakta üretilen taşın % 90'nın atık nedeniyle çevreye bırakıldığını göstermektedir (Yurdakul, 2020).

Türkiye'nin İç Anadolu bölgesinde yer alan Nevşehir ili birçok tarihi yapıları, peri bacaları ve eşsiz doğal güzellikleri nedeniyle önemli bir yerdir. Nevşehir ilindeki tarihi yapılarda ve günümüze ait yeni evlerin yapımında ignimbirit taşları kullanılmıştır. Bölgedeki ignimbiritlerin yüksek gözenek oranı, hafifliği, kolay şekillendirebilmesi ve iyi bir ısı yalıtımı gibi özelliklere sahip olması inşaat sektöründe hafif yapı taşı malzemesi olarak kullanılmasını sağlamaktadır. Ancak bu taşların büyük kısmı şekillenme sırasında küçük parçalara ayrılarak rastgele çevreye atılmaktadır (Ertek ve Öner, 2008).

Sanayileşme ve hızlı şehirleşme nedeniyle taşların üretim talebindeki artış, taş işlemeden kaynaklı atıkların da büyük miktarda artışın meydana gelmesine neden olmaktadır. Taş atık miktarlarının büyük hacimlere ulaşması sonucunda uygun bir şekilde ortadan kaldırılmamaktadır. Bu atıklar, taş işleme tesislerinde yeterli depolama alanlarının olmaması nedeniyle atık yönetiminde sorun oluşturmaktadır (Singh vd., 2016). Günümüzde bu atıkların kompozit malzemeye dâhil edilerek değerlendirilmesinin sağlanması, atık yönetimi sorununa bir çözüm önerisi olarak kabul edilmektedir. Literatürde taş atıklarının; seramiklere (Ngayakamo vd., 2022), çimentoya (Savadkoohi ve Reisi, 2020), tuğlaya (Bilgin vd., 2012) ve geopolimer harçlara (Çelikten, 2021) dâhil edildiği görülmektedir. Bu çalışmalarda taş atıkları % 80'e kadar kompozitlerin üretiminde kullanılmıştır. Ayrıca bu kompozitlerde taş atıklarının değerlendirilmesi ve ekonomik katma değeri olan ürünlere dönüştürülmesi bilim adamları tarafından yapılan çalışmalarda odaklanılmıştır. Yapıların inşasında malzemenin tek başına ve doğal haliyle kullanımı istenen özelliği her zaman tam olarak karşılayamadığından kompozit malzemelere olan ihtiyacı giderek arttırmaktadır. Kompozit malzemelerle birden fazla malzemelerin en iyi özelliklerinin bir araya getirilmesiyle istenen özelliklere sahip malzemelerin üretilebilmesini sağlamaktadır. Kompozit malzemeler yapılarda; sıva, kaplama, yalıtım, onarım ve güçlendirme gibi geniş bir uygulama alanına sahiptir (Mathur, 2006). Polimer matris ve doğal taş tozu esaslı olarak üretilen kompozitlerin de üstün özelliklerinin yanı sıra taş atıklarının değerlendirilmesine imkân sağlaması nedeniyle daha fazla avantajlara sahiptir (Carvalho vd., 2018). Örneğin Doan vd. (2018) yaptıkları çalışmada, mermer atıkları ve doymamış polyester reçineyle hazırlanan kompozitlerin taş atık oranının artmasıyla, su emme oranının düştüğünü ve sertliğinde ise % 80 oranında iyileştiğini göstermişlerdir. Sahu vd. (2020) tarafından yapılan araştırmada, epoksi reçine içerisine ağırlıkça % 10, % 20, % 30 ve % 50 oranında atık taş tozlarıyla üretilen kompozitlerin mekanik ve fiziksel özellikleri incelenmiştir. Taş tozu konsantrasyonun artmasıyla, kompozitin mukavemetinin arttığı ve su emme özelliğinin ise düştüğü belirlenmiştir. Silva vd. (2023) tarafından yapılan başka bir araştırmada ise, granit ve cam atıklarının epoksi reçine matrisine dâhil edilmesi yoluyla üretilen kompozitlerin fiziksel, mekanik ve mikroyapı özellikleri incelenmiştir. Kompozitlerin kimyasal saldırılara ve dayanıklılık testlerine karşı dirençli olduğu tespit edilmiştir. Tüm bu çalışmalarda polimer matrisli kompozitlerin; düşük gözenekli yapısı, hafiflikleri, yüksek mukavemeti ve suya dayanıklılığı gibi özellikleri nedeniyle inşaat sektöründe malzeme ihtiyacının karşılanmasında büyük bir potansiyele sahip olduğu bildirilmiştir. Ancak bildiğimiz kadarıyla, ignimbirit taş tozu ile epoksi matris esaslı kompozitlerin üretimi, bu kompozitlerin mekanik ve hidrofobik özellikleriyle ilgili bugüne kadar herhangi bir araştırma yapılmamıştır.

Bu çalışmada ignimbrit taşına ait farklı tane büyüklüğüne (63 µm, 150 µm, 250 µm, 500 µm, 1000 µm) sahip taş tozu ve epoksi reçine kullanılarak kompozitler üretilmiştir. İgnimbirit taş atıklarında değişen ölçüdeki taneciklerin epoksi reçine ile yapışması azalabilir. Bu durum, kompozitlerin morfolojisini ve mekanik özelliklerini etkileyebilir. Bu nedenle reçine ile taş tozu arasındaki yapışmayı arttırmak için taş tozları farklı tane büyüklüklerine ayrılmıştır. Taş tozlarının tane büyüklüklerindeki değişimin, kompozitlerin mekanik ve hidrofobik özelliklerine olan etkisi araştırılmıştır. Bu çalışma kapsamında, üstün mekanik ve fiziksel özelliklerin yanı sıra, su emme problemlerine karşı dayanıklı yeni bir kompozitin geliştirilmesi beklenmektedir. Ayrıca çalışmada hem taş atık miktarının azaltılmasına katkıda bulunmak hem de inşaat sektöründe bina uygulamaları için ekonomik katma değeri olan ürünlere dönüştürülmesi amaçlanmaktadır.

2. Materyal ve Yöntem

2.1. Materyal

Nevşehir ilinden çıkarılan ignimbirit taşları Ürgüp Formasyonu içerisinde yer almaktadır. Ürgüp Formasyonunda her biri ayrı adlarla anılan on bir adet ignimbrit seviyesi bulunmaktadır. Bu seviyelerin en alt kısmında ise Kavak ignimbiriti yer almaktadır (Şekil 1). Bölgedeki yapıların inşaatlarında kullanılan taşlar Kavak ignimbiritinden üretilmektedir (Kazancı ve Gürbüz, 2014). Kavak ignimbiriti sarımsı-bej renkli ve piroklastik kayaç özelliğinde olup, litik, pomza kırıntıları, biyotit, plajiyoklaz, kuvars ve fenokristalleri içermektedir (Aydar vd., 2012). Tablo 1'deki Kavak ignimbiritlerin kimyasal bileşimine göre, çoğunlukla dasit ve trakiandezit, kısmen de riyolit bileşimine sahiptir (Çiflikli, 2020).

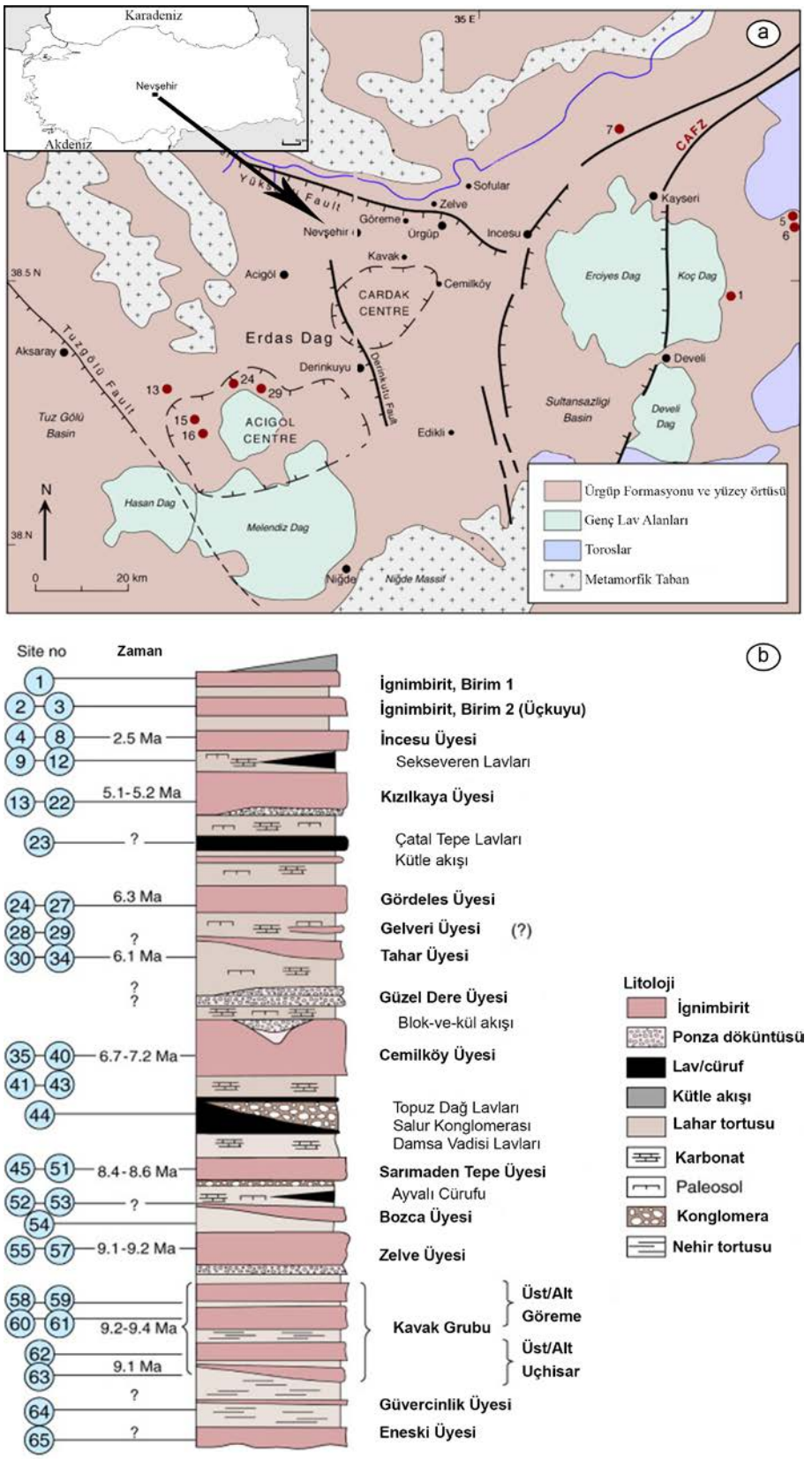

Şekil 1. (a) Nevşehir ilindeki ignimbiritlerin jeolojik haritası, (b) İgnimbiritlerin stratigrafik kesiti (Piper vd., 2013'den değiştirilmiştir).

Tablo 1. Kavak ignimbiritlerin kimyasal bileşimi (Korkanç, 2007)

Oksit	Ağırlık (%)
SiO_2	78,44
Al_2O_3	13,9
Fe_2O_3	0,78
MgO	0,02
CaO	0,05
Na_2O	0,03
K_2O	0,13
TiO_2	0,23
P_2O_5	0,04
MnO	<0,01
Cr_2O_3	<0,001
A.K. (1000°C)	6,4
Toplam	100,05

Bu çalışmada kompozitlerin üretiminde kullanılan epoksi reçine (ER) BRTR Kimya A.Ş. (Türkiye) firmasından satın alınmıştır. Epoksi sistemlerinde reçine ve sertleştirici birbirine karıştırılarak kullanıldığından firmadan alınan epokside, A ve B olarak iki bileşen bulunmaktadır. A bileşeni bisfenol-A tipi kimyasal bileşiği içerirken, B bileşeninde ise cycloalifatik poliamin sertleştirici madde içermektedir. Kompozitlerin üretiminde dolgu olarak ignimbirit taş tozu (İTT) kullanılmıştır. Nevşehir ilinde taş üretimi yapan Özkapadokya Taş firmasından ignimbirit taş kesim atıkları tedarik edilmiştir. Firmadan tedarik edilen taş kesim atıklarında toz ve kırıklı taş parçaları bulunmaktadır. Bu nedenle epoksi reçine ile ignimbirit taş tozu arasındaki yapışmayı arttırmak için taş kesim atıkları farklı boyutlarda (63 µm, 150 µm, 250 µm, 500 µm, 1000 µm) elek set aparatları kullanılarak elenmiştir. Bu eleme işleminde atık taş tozunda tane büyüklüğünün dağılımları (granülometri analizi) yapılmıştır. Elek cihazındaki (Retsch AS 200) elek set aparatların her birine ignimbirit taş kesim atıkları yerleştirilerek 10 dakika boyunca sarsma işlemi uygulanmıştır. Bu işlem sonunda istenilen boyutlara sahip ignimbirit taş tozu elde edilmiştir. Deney çalışmalarında kullanılan materyallerin bazı özellikleri Tablo 2'de verilmiştir.

Tablo 2. Deney çalışma kapsamında kullanılan malzemelerin bazı özellikleri

Kullanılan Malzemeler	Fiziksel Özellikleri	
İgnimbirit Taş Tozu (İTT)	Renk:	Sarı
	Yoğunluk (g.cm^{-3}, 20°C'de):	1,50–1,58
	Su emme (%, 23°C'de):	24,83
Epoksi Reçine (ER)	Renk ve Görünüm:	Şeffaf ve Parlak
	Yoğunluk (g.cm^{-3}):	1,10
	Karışım Oranı (A/B):	5/3
	Viskozite (cps, 20°C'de):	520–550
	Karışım Ömrü (25°C):	30 dakika
	Kuruma Süresi (25°C):	12 saat
	Mekanik Mukavemet:	7 gün

2.2. Epoksi Matrisli Kompozit Numunelerin Hazırlanması

Taş tozu atıklarının birikmesini azaltmak için mümkün olduğu kadar epoksi matrisinin yüksek oranda İTT içermesine özen gösterilmiştir. Ayrıca ticari ürün olan reçinenin üretimi taş tozu atıklarına göre daha maliyetli olduğundan minimum reçine içeriğine sahip kompozitlerin geliştirilmesi için ön çalışmalar yapılmıştır. Yapılan ön çalışmalar neticesinde, kompozitte yapı bütünlüğü sağlayan en yüksek İTT oranının ağırlıkça % 70 olduğu tespit edilmiştir. Ancak İTT oranı % 70'in üzerindeki kompozitlerde matris miktarı, numunelerin yapı bütünlüğünü korumada yetersiz olduğundan, numunelerde parçalanma gözlemlenmiştir. Bu nedenle ER/İTT kompozit numunelerinin hazırlanması için Şekil 2 ve Tablo 3' de görüldüğü gibi ağırlıkça % 30 oranında epoksi matrisi ve % 70 oranında <63 µm büyüklüğüne sahip İTT'ler bir kaba konulduktan sonra üç dakika boyunca elle karıştırılmıştır. Bu karışımda epoksi matrisi, üretici firmanın tavsiye ettiği 5:3 karışım oranına göre hazırlanmıştır. Bileşenleri karıştırmadan önce, 5 kısım reçineye 3 kısım sertleştirici ilave edilmiştir. Daha sonra oluşan karışım üç dakika kadar tekrar karıştırılmış ve 20x20x20 mm boyutlarında polimetil metakrilat (PMMA) kalıbına dökülmüştür. Epoksi malzemeleri üreten firma sertleşme süresini 25°C'de 24 saat belirttiği için, PMMA kalıbındaki karışımlar bu süre boyunca bekletilerek sertleşmesi sağlanmıştır. Bu süre sonunda yeterince kuruyan karışım, kalıptan çıkarılarak EMK63 olarak isimlendirilen kübik şeklinde kompozit numune elde edilmiştir. Aynı işlem süreçleri epoksi matrisine, <150 µm, <250 µm, <500 µm ve <1000 µm tane büyüklüklerine sahip ignimbirit taş tozlarının ilavesi ile tekrarlanarak

sırasıyla EMK150, EMK250, EMK500 ve EMK1000 kompozit numuneler elde edilmiştir. Bu kompozit numunelerin mekanik özelliklerinin ASTM D695 (ASTM-D695-10, 2010) basınç testi standardına göre test edilebilmesi ve kompozit numunelerin ıslanabilirlik derecelerinin temas açısı ölçümüyle belirlenebilmesi için 20x20x20 mm boyutlarında kalıp kullanılmıştır. Polimer kompozitlerin üretim işlemlerine ait süreçler Şekil 2'de kısaca özetlenmiştir. Deney çalışmalarında kullanılan kalıbın ve kompozit numunelerin fotoğrafları Şekil 3'de gösterilmiştir.

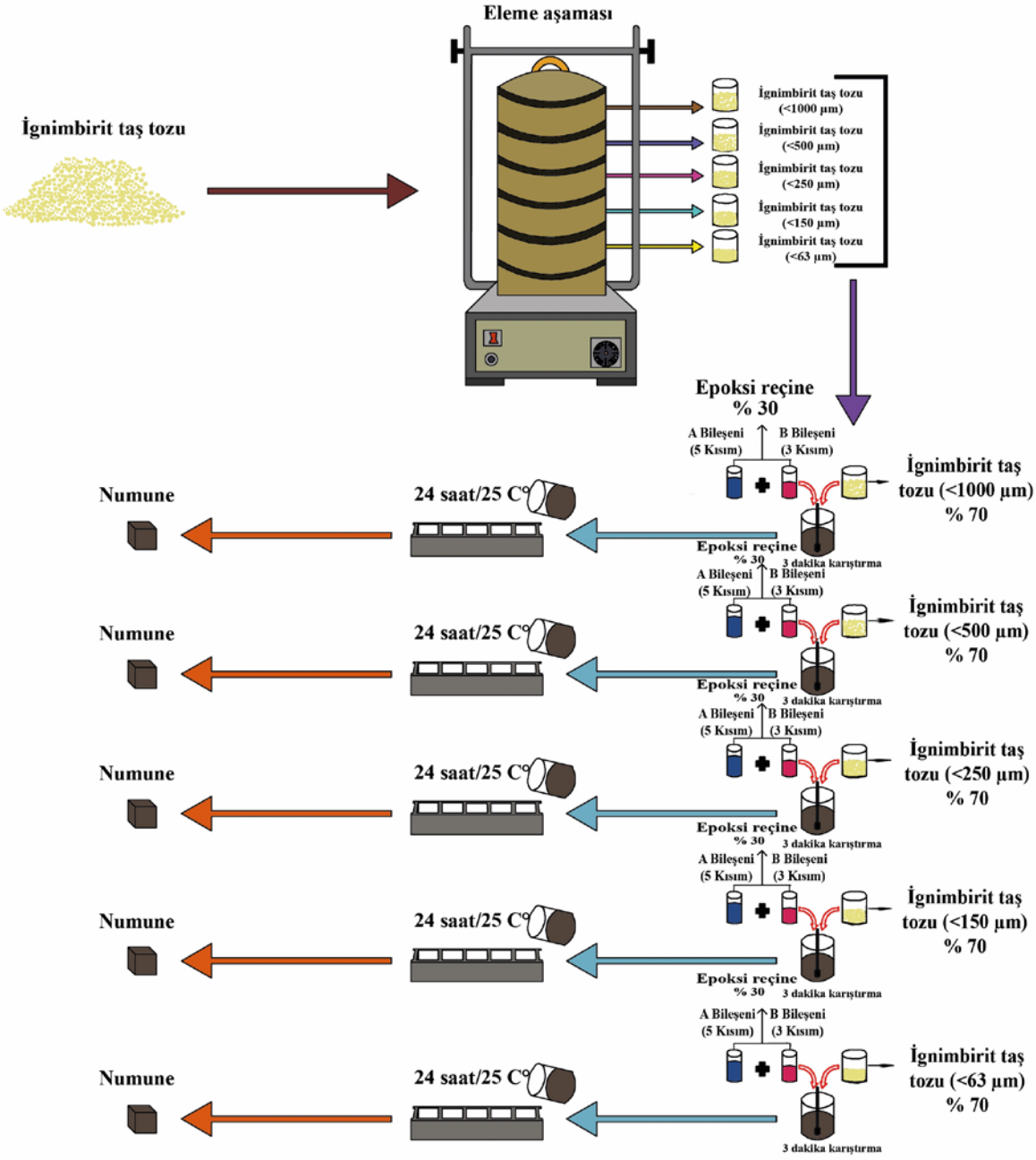

Şekil 2. Polimer kompozit numunelerin üretim aşamaları.

Tablo 3. Deney çalışması kapsamında hazırlanan polimer kompozitlerin kısaltmaları ve içerikleri

Epoksi Matrisli Kompozitlerin (EMK) Kısaltmaları	Reçine/İTT Karışım Oranı	İTT Boyutları (μm)
ER	100/0	—
EMK63	30/70	<63
EMK150	30/70	<150
EMK250	30/70	<250
EMK500	30/70	<500
EMK1000	30/70	<1000

Şekil 3. Deney çalışmalarında kullanılan kalıbın ve kompozit numunelerin fotoğrafları.

2.3. Karakterizasyon ve Deneysel Ölçümler

Kübik şeklinde kompozit numunelerin dayanımını belirlemek için basınç testi yapılmıştır. Kompozit numune türlerinin her birinden 5'er adet hazırlanarak (SHIMADZU AGS-X, Japonya) cihaza yerleştirilmiştir. Daha sonra numuneler 0,5 mm/dk. hızında ASTM D695 (ASTM-D695-10, 2010) standardına göre mekanik özellikleri test edilmiştir. İTT tane boyutunun büyüklüğündeki değişime bağlı olarak, epoksi matrisininin yapışma özellikleri ve kompozitlerin morfolojik yapıları taramalı elektron mikroskobu (SEM) (ZEISS EVO LS10, Almanya) ile incelenmiştir. Kompozitlerin suyla ıslatılmasını nicel olarak belirlemek için temas açısı ölçümleri Attension Theta Lite Optical Tensiometer (Biolin Scientific, İsveç) cihazı ile yapılmıştır. Bu cihaz tarafından her bir numunenin yüzeyine bir damla su damlatılmıştır. Temas eden suyun yüzey gerilimi ile katı yüzeyi arasında belli miktarda açı oluşmaktadır. Bu açının büyüklüğündeki değişimler kompozit numunelerin ıslanabilirlik dereceleri hakkında önemli bilgiler vermektedir.

3. Bulgular ve Tartışma

3.1. İTT Tane Büyüklüğünün Dağılımı

İTT tane büyüklüğünün dağılımı Şekil 4'de gösterilmiştir. Şekil 4'deki verilere göre, taneciklerin yaklaşık % 35'i 63 μm boyutunun altında iken, taneciklerin yaklaşık % 10'dan azının ise 1000 μm boyutundan daha büyük olduğu belirlenmiştir. Literatürde atık taş tozunun granülometrik analizi ile ilgili çeşitli araştırmacılar tarafından çalışmaların yapıldığı görülmektedir. Örneğin Ari vd. (2024) tarafından yapılan araştırmada, atık Sille taş tozu taneciklerinin yaklaşık yarısı 63 μm altı boyutunda iken, taneciklerin % 10'dan azının ise 500 μm boyutundan daha büyük olduğu tespit edilmiştir. Vijayalakshmi vd. (2013) tarafından gerçekleştirilen çalışmada, atık granit tozunun % 55'inin 150 μm altında ve taneciklerin % 31'inin 45 μm'den küçük olduğu belirlenmiştir. Yurt vd. (2024) tarafından yapılan çalışmada, atık bazalt tozunun ortalama tanecik boyutu 50 μm olarak bulunmuştur. Dolayısıyla İTT tane büyüklüğünün dağılımında iri tanecik oranı az, ince tanecik oranının yüksek olması, literatürdeki ilgili çalışmaların sonuçlarıyla uyumlu olduğu görülmektedir.

3.2. Kompozitlerin SEM Analizi Bulguları

ER, EMK63, EMK150, EMK250, EMK500 ve EMK1000 numunelerine ait SEM görüntüleri Şekil 5'de gösterilmiştir. Saf epoksinin, tüm EMK numuneleriyle karşılaştırıldığında, pürüzsüz yüzeye sahip olduğu görülmüştür. Ancak epoksi matrisine İTT eklenmesiyle kompozitlerde pürüzlü yüzeyler meydana gelmiştir. Pürüzlü yüzeylerin oluşması, reçine ile taş tozu parçacıkları arasındaki bağları göstermektedir (Heriyanto vd., 2019). Kompozitlerin yüzeylerinin bazı bölgelerindeki; gözenekler, aglomerasyonlar, boşluklar, küçük oyuklar ve mikro çatlaklar gibi kusurları oluşturması, reçine ve taş tozu arasındaki bağların zayıf olduğunu göstermektedir (Arı, 2024). Ayrıca taş tozunda boyut büyüklüğünün artmasıyla kompozitlerin yüzeylerinde aglomerasyonların sayısı ve büyüklüğü artmıştır (Şekil 5b-f). Kompozitlerde meydana gelen aglomerasyonlar, reçine ile taş tozu arasında ara yüzey yapışmasını zayıflatmaktadır (Arı, 2024; Gonçalves vd., 2014). Bu aglomerasyon EMK'nın mukavemetinin bozulmasına neden olmaktadır.

3.3. Kompozitlerin Basınç Testinin Bulguları

Kompozit numunelerin ve ignimbirit taşının basınç dayanımı Şekil 6'da gösterilmiştir. Şekil 6'da görüldüğü gibi, ER/İTT kompozitlerin ortalama basınç dayanımlarının değerleri 15,55 MPa ile 51,24 MPa arasında değişmektedir. Kompozitler arasında en yüksek ortalama basınç dayanımı 51,24 MPa değeri ile EMK63 numunesinde elde edilmiştir. Bu sonuç, epoksi matrisine <63 μm büyüklüğüne sahip İTT eklendiğinde, matris ile dolgu arasında etkileşimin güçlü olduğunu göstermektedir. Ancak tanecik boyutu her ne olursa olsun tüm kompozitlerin basınç dayanım değerleri

ignimbirit taşının basınç dayanımı değerlerine göre, % 167,64 ile % 781,93 kadar daha yüksek olduğu görülmektedir. İTT'lerin boyutu 63 µm üstüne çıkarıldığında elde edilen kompozitlerin basınç değerlerinin EMK63 kompozitinin basınç dayanım değerlerine göre azaldığı tespit edilmiştir. Örneğin hazırlanan EMK150, EMK250, EMK500 ve EMK1000 kompozitlerinin basınç değerleri, EMK63 numunesinin basınç dayanım değerine göre sırasıyla yaklaşık % 34,31, % 34,97, % 61,14 ve % 69,65 azalış göstermiştir. İTT'lerin boyutu 63 µm üstüne çıkarıldığı zaman matris ile etkileşime girebilen taneciklerin yüzey alanının azalması, kompozilerin basınç dayanım değerlerinin azalma eğilimi göstermesine neden olmuştur. ER/İTT kompozitlerinin basınç dayanım değerleri ile saf ER'nin basınç dayanım değeri karşılaştırıldığında, İTT'lerin boyutu 250 µm kadar elde edilen kompozitlerin basınç değerleri, saf ER'nin basınç dayanım değerine göre % 36,11–% 109,31 artış gösterdiği görülmektedir. Ancak İTT'lerin boyutu 250 µm üstüne çıkarıldığı zaman ise elde edilen EMK500 ve EMK1000 kompozitlerin basınç dayanım değerlerinin, saf ER'nin basınç dayanım değerine göre sırasıyla yaklaşık % 18,67 ve % 36,48 azalış göstermiştir (Şekil 6). Basınç dayanımının azalması, kompozitlerin yüzeyinde büyük miktarda oluşan aglomerasyonlar ve boşluklar ile açıklanabilir (Şekil 5e,f).

Literatürde polimer matrisli üretilen kompozitlerin basınç dayanımlarıyla ilgili çeşitli araştırmacılar tarafından çalışmaların yapıldığı görülmektedir. Örneğin, Nana vd. (2021) tarafından yapılan çalışmada, polimer matris ile 63, 80, 125 ve 200 µm'lik granit ve pegmatit parçacıklarıyla üretilen kompozitlerin mekanik özellikleri incelenmiştir. 125–200 µm arasında tane boyutuna sahip granit ve pegmatit parçacıkları eklendiğinde, kompozitlerin basınç dayanımının arttığı belirlenmiştir. Awad vd. (2020) tarafından yapılan araştırmada, yüksek yoğunluklu polietilen (HDPE) matris ile 75, 440, 701 ve 2300 µm'lik mermer ve granit parçacıklarıyla kompozitler üretilmiş ve bu kompozitlerde tanecik boyutunun artmasıyla, mekanik özelliklerinin azaldığı belirlenmiştir. Cota vd. (2012) tarafından gerçekleştirilen çalışmada, Portland çimentosu ve epoksi reçineyle oluşturulan polimerik faz ile 1,41–0,42 mm ve 0,42–0,15 mm aralığında steatit tanecik boyutlarıyla üretilen kompozitlerin mekanik özellikleri incelenmiştir. Polimer matrise 1,41–0,42 mm büyüklüğüne sahip steatit tanecikler eklendiğinde elde edilen kompozitin basınç değeri, polimer matrise 0,42–0,15 mm aralığına sahip steatit tanecikler eklendiğinde, elde edilen kompozitin basınç değerine göre daha yüksek olduğu tespit edilmiştir. Kompozitlere daha büyük steatit taneciklerinin eklenmesi sonucunda, hacim yoğunluğunun arttığı ve basınç artışına neden olduğu gösterilmiştir.

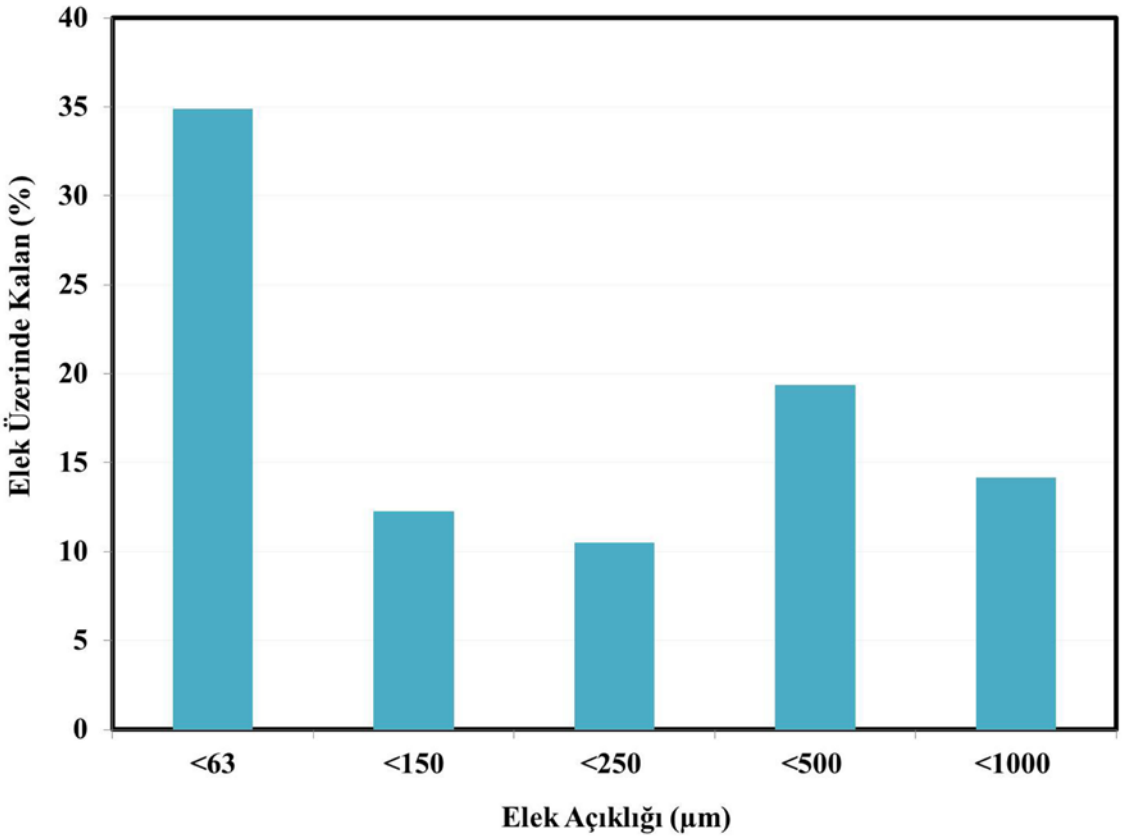

Şekil 4. İTT'nin granülometrik analizi.

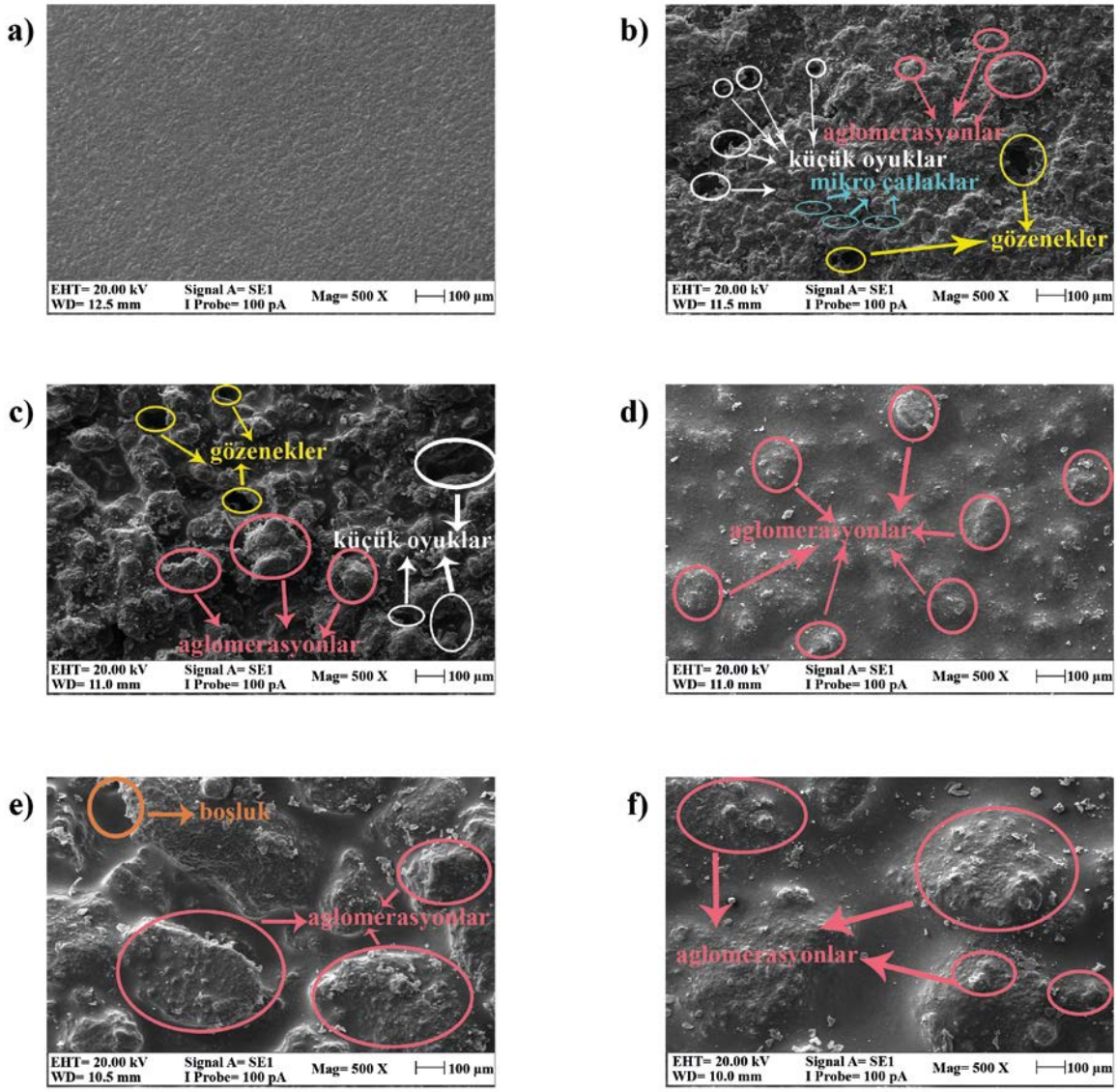

Şekil 5. Kompozit numunelerin SEM görüntüleri (Mag.: 500 X): (a) ER, (b) EMK63, (c) EMK150, (d) EMK250, (e) EMK500, (f) EMK1000.

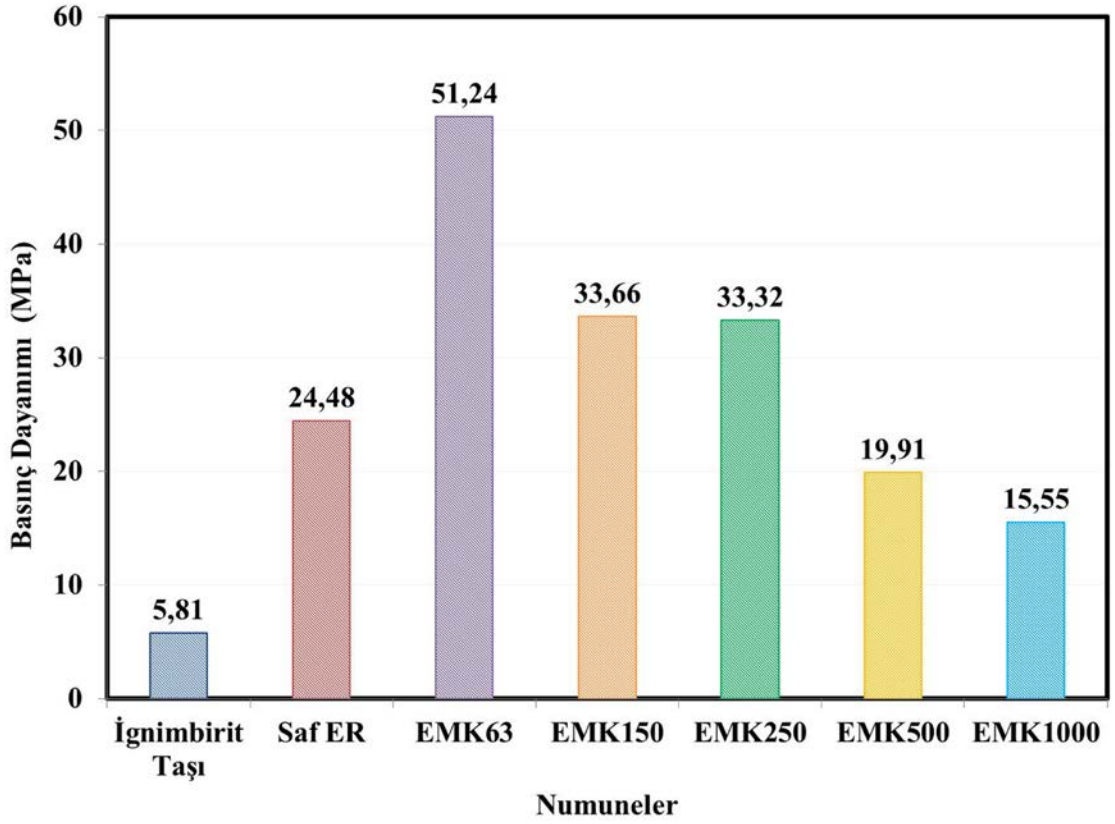

Şekil 6. Kompozit numunelerin ve ignimbirit taşının basınç dayanımı.

3.4. Kompozitlerin Islanabilirlik Derecelerinin Bulguları

İklimsel faktörler veya nem etkisiyle oluşan suyun yapı malzemelerine nüfuz etmesiyle binaların bozulmaları hızlanmaktadır (Dinçer ve Bostancı, 2019; Erguler, 2009; İnce, 2021; Korkanç ve Solak, 2016). Bu nedenle kompozitlerin suya karşı dayanıklılığını araştıran parametrelerden biri yüzey ile su arasındaki temas açısının ölçümünün yapılmasıdır (Wu vd., 2021; Zielecka ve Bujnowska, 2006). Temas açısı ölçümü ile kompozitlerin ıslanabilirlik derecelerinin değerlendirilmesine imkân sağlanmaktadır. Cihaz tarafından incelenen yüzey üzerine bir damla su bırakılır. Suyun yüzey üzerinde yaptığı temas açısının büyüklüğüne göre, incelenen yüzeyler hidrofilik veya hidrofobik olarak sınıflandırılır. Genellikle su temas açısı, 90°'nin altındaki yüzeyler hidrofilik, su temas açısı 90°'nin üzerindeki yüzeyler ise hidrofobik olarak kabul edilir. Şekil 7'de kompozit numunelerin ve ignimbirit taşının temas açılarının ölçümündeki su damlacıklarını göstermektedir. Kompozitlerde su damlacıkları yüzeyde durabilirken, ignimbirit taşının su damlacığını kolayca emdiği görülmektedir. İgnimbirit taşının su temas açısı 8,5° ve saf ER'nin su temas açısı 81,9° olması yüzeylerin hidrofilik olduğunu göstermektedir. Tüm kompozitlerin su temas açılarının 90,2° ile 102,9° arasında olduğu görülmektedir. Bu, kompozitlerin yüzeyinin hidrofobik durum sergilediğini göstermektedir (Şekil 8).

Şekil 8'deki verilere göre, epoksi matrisli kompozitlerin su temas açısı (90,2°–102,9°) değerlerinin saf ER'nin su temas açısı 81,9°'dan daha yüksektir. Bu durum, epoksi matrisine İTT ilavesinin kompozitlerin ıslanabilirliğini azaltabileceğini göstermektedir. Kompozitler arasından en yüksek su temas açısı 102,9° değeri ile EMK63 numunesinin olduğu belirlenmiştir. Bu değer, ignimbirit taşının su temas açısı 8,5°'den çok daha yüksektir. İTT'lerin boyutu 63 µm üstüne çıkarıldığı zaman ise elde edilen kompozitlerin su temas açıları, EMK63 kompozitinin su temas açısına göre azaldığı belirlenmiştir. Örneğin hazırlanan EMK150, EMK250, EMK500 ve EMK1000 kompozitlerinin su temas açı değerleri sırasıyla 96,2°, 93,8°, 91,8° ve 90,2° azalma eğilimi göstermiştir. Ayrıca bu, kompozitlerdeki İTT tanecik boyutunun büyüklüğü 63 µm üstüne çıkarıldığında kompozitlerin hidrofobikliğinin azaldığını göstermektedir. Bunun nedeni, tanecik boyutu büyüklüğünün artması matris ile İTT arasında kimyasal etkileşimin azalmasıyla ilgilidir. Matris ile dolgu arasında yapışma gücündeki azalma, kompozitlerin su moleküllerine karşı dayanımını azaltır.

Literatürde polimer matrisli kompozitlerin ıslanabilirlik dereceleriyle ilgili çalışmaların yapıldığı görülmektedir. Örneğin, Ari vd. (2024) tarafından yapılan araştırmada, Sille taş tozu ve polyester matrisle elde edilen kompozitin temas açısı 62,15° değerinin Sille taşının temas açısı 24,53° değerinden yüksek olduğu tespit edilmiştir. Song vd. (2022) tarafından gerçekleştirilen çalışmada, atık mermer tozu ilaveli polimer kompozitler üretilmiş ve bu kompozitlerde mermer tozunun artmasıyla, kompozitlerin ıslanabilirliğini azalttığını

göstermiştir. Zhang vd. (2021) tarafından yapılan çalışmada, silika mikro tozu (SMP) ile titanat bağlayıcı madde KTTO ve polivinil klorür (PVC) kullanarak üretilen kompozitlerin su temas açısı 134° değerinde olduğu ve SMP numunesine göre daha hidrofobik yüzeyler olduğu tespit edilmiştir. Polimer matris ile SMP arasında kimyasal reaksiyon hidrofobik bir film tabaka oluşturmasına ve kompozitlerin ıslanabilirliğinde önemli azalmaya neden olmuştur. Dolayısıyla epoksi matrisli kompozitlerde hidrofobik bariyer oluşturarak suyun uzaklaştırılması, literatürdeki ilgili çalışmaların sonuçlarıyla uyumlu olduğu görülmektedir. Ayrıca polimer matris içindeki dolgu maddelerinin tanecik boyutunun büyüklüğüne bağlı olarak, kompozitlerin ıslanabilirlik derecelerini ölçen literatürde yeterli sayıda çalışmanın olmadığı görülmektedir. Bundan dolayı bu araştırma kapsamında farklı tane büyüklüğüne sahip ignimbirit taş tozu (63 µm, 150 µm, 250 µm, 500 µm, 1000 µm) ve epoksi matris kullanılarak üretilen kompozitler için ölçülen temas açı değerlerinin literatüre önemli bir katkı sağlayacağı beklenmektedir.

EMK63 kompozitinin diğer kompozitlere göre matris içindeki dolgu maddelerinin tanecik boyutunun büyüklüğünün ve dağılım şeklinin homojen olması hem kompozitin basıncının artmasında hem de kompozitin daha fazla hidrofobik yüzey olmasını sağlamıştır. Epoksi reçine ve İTT arasındaki kimyasal etkileşim, 63 µm tanecik büyüklüğünde yüksek dayanıma sahip kompozit olduğunu göstermektedir. 63 µm'nin üzerindeki tanecik büyüklüğüne sahip EMK150, EMK250, EMK500 ve EMK1000 kompozitlerinde basınç dayanımı ve hidrofobikliğinde sürekli azalma, tanecik boyutunun artmasıyla tanecik yüzeyinin azalmasından kaynaklanmaktadır (Şekil 5-Şekil 8).

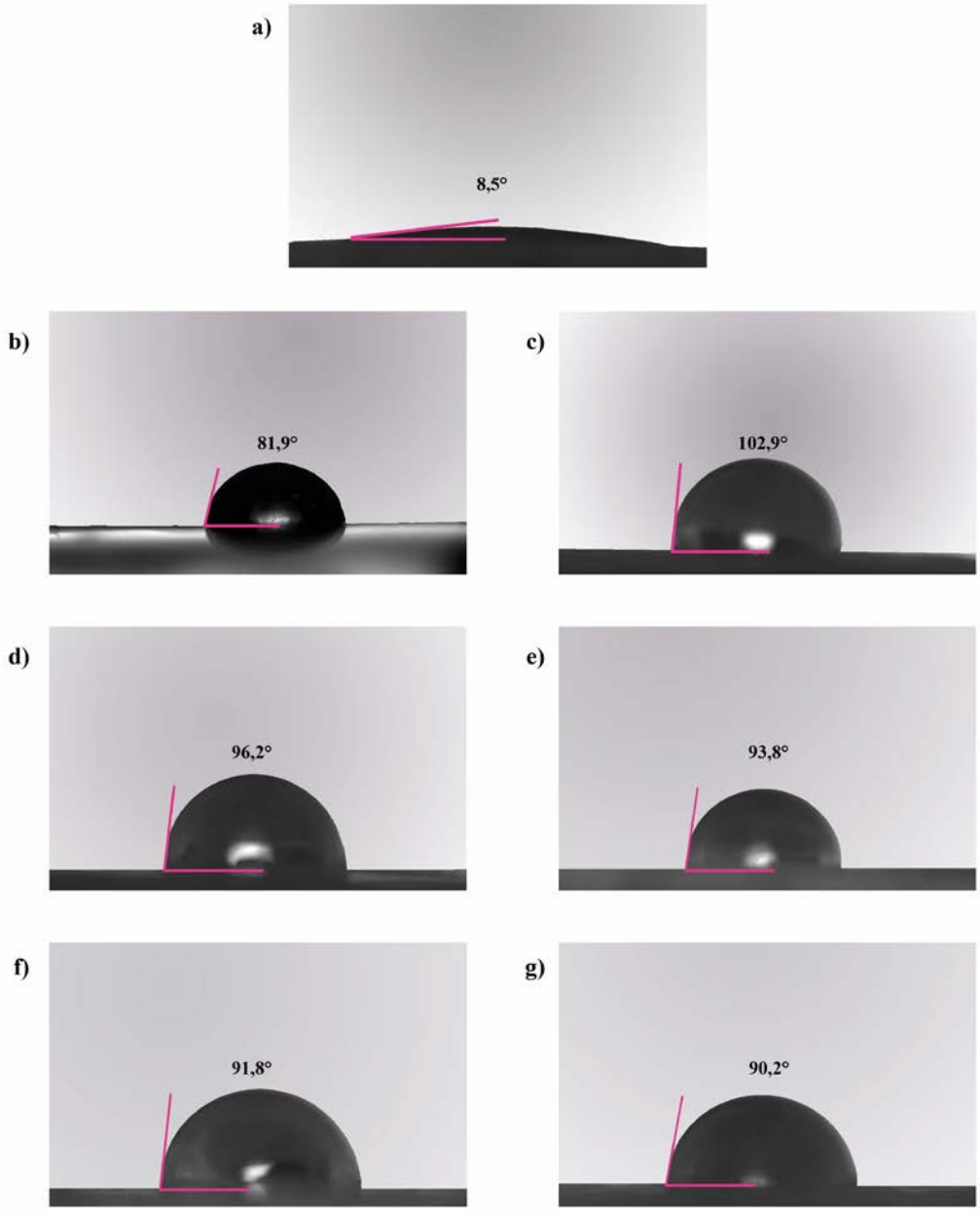

Şekil 7. Kompozit numunelerin ve ignimbirit taşının temas açılarının ölçümündeki su damlacıkları: (a) ignimbirit taşı, (b) saf ER, (c) EMK63, (d) EMK150, (e) EMK250, (f) EMK500, (g) EMK1000.

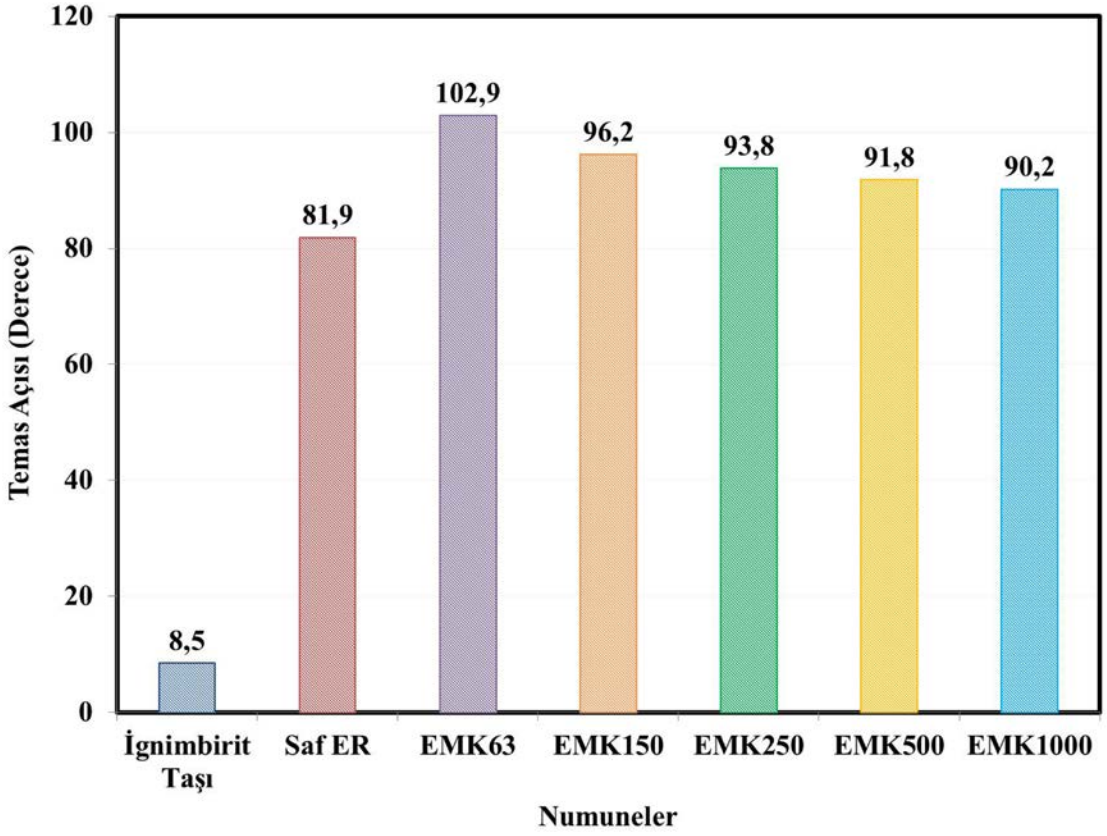

Şekil 8. Kompozit numunelerin ve ignimbirit taşının temas açıları.

4. Sonuç ve Öneriler

Bu çalışmada, farklı tane büyüklüğüne sahip ignimbirit taş tozu (63 µm, 150 µm, 250 µm, 500 µm, 1000 µm) ve epoksi matris kullanılarak kompozitler üretilmiştir. Üretilen kompozitlerde tanecik büyüklüğüne bağlı olarak mekanik ve hidrofobik özelliklerindeki değişimin incelenmesine odaklanılmıştır. İTT'ler epoksi matrisin içerisine ağırlıkça % 70 oranında katılmıştır. Araştırmada <63 µm tanecik büyüklüğüne sahip İTT'lerin kullanılması ile elde edilen kompozitlerin mekanik ve hidrofobik açısından en yüksek dayanıma sahip olduğu tespit edilmiştir. Bu kompozitle 51 MPa'ya kadar yüksek basınç mukavemeti ve 102,9° su temas açısı değeri ile diğer kompozitler arasından teknik özellikleri açısından en iyi kompozit olduğu belirlenmiştir. Taş tozunda tanecik büyüklüğünün artması, taneciğin yüzey alanının azalmasına neden olduğundan kompozitlerde basınç dayanımının ve hidrofobikliğinin sürekli azaldığı tespit edilmiştir. 63 µm üstünde tanecik büyüklüğüne sahip İTT'lerin kullanılması ile hazırlanan kompozitlerin mekanik ve hidrofobik özelliklerinin, ignimbirit taşına göre daha yüksek olmakla beraber meydana gelen aglomerasyonlar ve gözenekler nedeniyle EMK63'e ait mekanik ve hidrofobik özelliklerden daha düşüktür. EMK63 kompozitinin saf ER'ye göre mekanik ve hidrofobik özellikleri açısından daha iyi olmasının yanı sıra, ağırlıkça % 70 oranında İTT kullanılmasından dolayı yapılarda epoksi reçinenin kullanıldığı alanlara göre daha ekonomiktir. Ayrıca atık taş tozunun granülometrik analizinde, <63 µm tanecik büyüklüğü toplam atık malzemenin % 35'ini oluşturması ve bu tanecik büyüklüğüyle üretilen EMK63 kompozitinin diğer tanecik boyutlarıyla üretilen kompozitlere (EMK150, EMK250, EMK500, EMK1000) göre daha ekonomik olmasını sağlamaktadır.

Sonuç olarak, üstün mekanik ve hidrofobik özellikleri olması nedeniyle EMK63 kompozitinin, binalardaki su emme problemini azaltmak üzere çeşitli uygulamalar için önerilmektedir. Ayrıca inşaat sektöründe çeşitli uygulamalarda kullanılmak üzere epoksi matrisi yerine polipropilen, poliüretan ve fenolik gibi farklı polimer matrisler, farklı oranlarda ve tanecik büyüklüğüne sahip ignimbirit taş tozu kullanılarak farklı mekanik ve fiziksel özelliklere sahip yeni kompozitler üretilebilir. Yeni kompozitler; atık ignimbirit taş tozunun değerlendirilmesine, ekonomiye kazandırılmasına ve inşaat sektöründe epoksi reçinenin kullanıldığı alanlara alternatif malzeme olarak katkı sağlayabilir.

Katkı Oranı Beyanı

Yazarın katkı yüzdeleri aşağıda verilmiştir. Yazar makaleyi incelemiş ve onaylamıştır.

	A.C.A.
K	100
T	100
Y	100
VTI	100
VAY	100
KT	100
YZ	100
KI	100
GR	100

K= kavram, T= tasarım, Y= yönetim, VTI= veri toplama ve/veya işleme, VAY= veri analizi ve/veya yorumlama, KT= kaynak tarama, YZ= Yazım, KI= kritik inceleme, GR= gönderim ve revizyon.

Çatışma Beyanı

Yazar bu çalışmada hiçbir çıkar ilişkisi olmadığını beyan etmektedirler.

Etik Onay Beyanı

Bu araştırmada hayvanlar ve insanlar üzerinde herhangi bir çalışma yapılmadığı için etik kurul onayı alınmamıştır.

Kaynaklar

Anonim. 2023. İstanbul madenler ve metaller ihracatçıları ve birliği, maden sektör görünümü. URL: https://imib.org.tr/wp-content/uploads/2023.pdf (erişim tarihi: 9 Haziran 2024).

Arı AC. 2024. Nevşehir taşlarıyla inşa edilen tarihi yapıların restorasyonuna yönelik polyester matris ve taş tozu kullanılarak üretilen kompozit harçlarda tane boyutunun dayanımına etkisinin araştırılması. Online J Art Des, 12(2): 144-157.

Ari AC, Tosun M, Eker YR. 2024. Polymer matrix and stone powder based composite mortar for the restoration of sille stone structures. Stud Conserv, 69(1): 50-57.

ASTM-D695-10. 2010. Standard test method for compressive properties of polymer matrix composite materials. American Society for Testing and Materials, USA, pp: 1-3.

Awad AH, El-Gamasy R, Abd El-Wahab AA, Abdellatif MH. 2020. Assessment of mechanical properties of HDPE composite with addition of marble and granite dust. Ain Shams Eng J, 11(4): 1211-1217.

Aydar E, Schmitt AK, Çubukçu HE, Akin L, Ersoy O, Sen E, Duncan RA, Atici G. 2012. Correlation of ignimbrites in the central Anatolian volcanic province using zircon and plagioclase ages and zircon compositions. J Volcanol Geotherm Res, 213-214: 83-97.

Bilgin N, Yeprem HA, Arslan S, Bilgin A, Günay E, Marşoglu M. 2012. Use of waste marble powder in brick industry. Constr Build Mater, 29: 449-457.

Carvalho EAS, Vilela NdF, Monteiro SN, Vieira CMF, Silva LCd. 2018. Novel artificial ornamental stone developed with quarry waste in epoxy composite. Mater Res, 21: e20171104.

Cota FP, Alves RAA, Panzera TH, Strecker K, Christoforo AL, Borges PHR. 2012. Physical properties and microstructure of ceramic–polymer composites for restoration works. Mater Sci Eng A, 531: 28-34.

Çelikten S. 2021. Mechanical and microstructural properties of waste andesite dust-based geopolymer mortars. Adv Powder Technol, 32(1): 1-9.

Çiflikli M. 2020. Hydrothermal alteration-related kaolinite/dickite occurrences in ignimbrites: an example from Miocene ignimbrite units in Avanos, Central Turkey. Arabian J Geosci, 13: 1044.

Dinçer İ, Bostancı M. 2019. Capillary water absorption characteristics of some Cappadocian ignimbrites and the role of capillarity on their deterioration. Environ Earth Sci, 78: 7.

Doan TTL, Brodowsky HM, Gohs U, Mäder E. 2018. Re-use of marble stone powders in producing unsaturated polyester composites. Adv Eng Mater, 20(7): 1701061.

Erguler ZA. 2009. Field-based experimental determination of the weathering rates of the Cappadocian tuffs. Eng Geol, 105(3-4): 186-199.

Ertek N, Öner F. 2008. Mineralogy, geochemistry of altered tuff from Cappadocia (Central Anatolia) and its use as potential raw material for the manufacturing of white cement. Appl Clay Sci, 42(1-2): 300-309.

Gonçalves JAV, Campos DAT, Oliveira GDJ, Rosa MdLdS, Macêdo, MA. 2014. Mechanical properties of epoxy resin based on granite stone powder from the Sergipe fold-and-thrust belt composites. Mater Res, 17(4): 878-887.

Heriyanto, Pahlevani F, Sahajwalla V. 2019. Effect of different waste filler and silane coupling agent on the mechanical properties of powder-resin composite. J Clean Prod, 224: 940-956.

İnce İ. 2021. Relationship between capillary water absorption value, capillary water absorption speed, and capillary rise height in pyroclastic rocks. Min Metall Explor, 38: 841-853.

Kazancı N, Gürbüz A. 2014. Natural stones qualified as geological heritage in Turkey. Geol Bull Turk, 57(1): 19-44.

Korkanç M, Solak B. 2016. Estimation of engineering properties of selected tuffs by using grain/matrix ratio. J Afr Earth Sci, 120: 160-172.

Korkanç M. 2007. The effect of geomechanical properties of ignimbrites on their usage as building stone: Nevşehir stone. J Geol Eng, 31(1): 49-60.

Mathur VK. 2006. Composite materials from local resources. Constr Build Mater, 20(7): 470-477.

Nana A, Kamseu E, Akono A-T, Ngouné J, Djobo JNY, Tchakoute, HK, Bignozzi MC, Leonelli C. 2021. Particles size and distribution on the improvement of the mechanical performance of high strength solid solution based inorganic polymer composites: a microstructural approach. Mater Chem Phys, 267: 124602.

Ngayakamo B, Bello A, Onwualu AP. 2022. Valorization of granite waste powder as a secondary flux material for sustainable production of ceramic tiles. Clean Mater, 4: 100055.

Piper JDA, Koçbulut F, Gürsoy H, Tatar O, Viereck L, Lepetit P, Roberts AP, Akpınar Z. 2013. Palaeomagnetism of the Cappadocian Volcanic Succession, Central Turkey: Major ignimbrite emplacement during two short (Miocene) episodes and Neogene tectonics of the Anatolian collage. J Volcanol Geotherm Res, 262: 47-67.

Sahu R, Gupta MK, Chaturvedi R, Tripaliya SS, Pappu A. 2020. Moisture resistant stones waste based polymer composites with enhanced dielectric constant and flexural strength. Compos B Eng, 182: 107656.

Savadkoohi MS, Reisi M. 2020. Environmental protection based sustainable development by utilization of granite waste in

Reactive Powder Concrete. J Clean Prod, 266: 121973.

Silva TLDC, Carvalho EAS, Barreto GNS, da Silva TBP, da Cunha Demartini TJ, Vieira CMF. 2023. Characterization of artificial stone developed with granite waste and glass waste in epoxy matrix. J Mater Res Technol, 26: 2528-2538.

Singh S, Nagar R, Agrawal V. 2016. Performance of granite cutting waste concrete under adverse exposure conditions. J Clean Prod, 127: 172-182.

Song W, Wang Q, Qu L, Li X, Xu S. 2022. Study of water absorption and corrosion resistance of the mortar with waste marble powder. Constr Build Mater, 345: 128235.

Vijayalakshmi M, Sekar ASS, Ganesh prabhu G. 2013. Strength and durability properties of concrete made with granite industry waste. Constr Build Mater, 46: 1-7.

Wu X, Yang F, Lu G, Zhao X, Chen Z, Qian S. 2021. A breathable and environmentally friendly superhydrophobic coating for anti-condensation applications. Chem Eng J, 412: 128725.

Yurdakul M. 2020. Natural stone waste generation from the perspective of natural stone processing plants: An industrial-scale case study in the province of Bilecik, Turkey. J Clean Prod, 276: 123339.

Yurt Ü, Çelikten S, Atabey İİ. 2024. Post-fire residual mechanical and microstructural properties of waste basalt and glass powder-based geopolymer mortars. J Build Eng, 94: 109941.

Zhang Y, Ding C, Zhang N, Chen C, Di X, Zhang Y. 2021. Surface modification of silica micro-powder by titanate coupling agent and its utilization in PVC based composite. Constr Build Mater, 307: 124933.

Zielecka M, Bujnowska E. 2006. Silicone-containing polymer matrices as protective coatings: Properties and applications. Prog Org Coat, 55(2): 160-167.

Black Sea Journal of Engineering and Science
doi: 10.34248/bsengineering.1578992

Open Access Journal
e-ISSN: 2619 – 8991

Research Article
Volume 8 - Issue 1: 54-57 / January 2025

HIGHLY UP-REGULATION OF *FAS LIGAND* GENE EXPRESSION AFTER INCREASING IN OXIDIZED LOW-DENSITY LIPOPROTEIN

Burcu BAYYURT[1]*, Serdal ARSLAN[2]

[1]*Sivas Cumhuriyet University, Faculty of Medicine, Department of Medical Biology, 58140, Sivas, Türkiye*
[2]*Mersin University, Faculty of Medicine, Department of Medical Science, 33100, Mersin, Türkiye*

Abstract: Oxidized low-density lipoprotein (ox-LDL) shows many harmful effects such as induction of apoptosis on function of endothelial cell (EC). Fas ligand (FASL) induces apoptosis in divergent pathological conditions. EC apoptosis which induced by ox-LDL is related with FASL. In this study, we aimed to determine how different ox-LDL levels affect *FASL* expression in ECs. We treated human umbilical vein endothelial cells (HUVECs) with two different concentration of ox-LDL. *FASL* gene expression in groups was detected by quantitative polymerase chain reaction (qPCR). We compared *FASL* gene expression level between the groups according to ΔΔCt method. *FASL* gene expression was statistic significantly up-regulated in the group treated higher amounts of ox-LDL ($P<0.001$). We found that treatment with higher amounts of ox-LDL in HUVECs increased *FASL* gene expression dramatically. According to our findings, we concluded that increasing the amount of ox-LDL may be critical in inducing the FASL-dependent apoptotic pathway in ECs.

Keywords: Oxidized low-density lipoprotein, *Fas ligand*, Gene expression, Quantitative polymerase chain reaction, Human umbilical vein endothelial cell

***Corresponding author:** Sivas Cumhuriyet University, Faculty of Medicine, Department of Medical Biology, 58140, Sivas, Türkiye
E mail: ebayyurt@yahoo.com.tr (B. BAYYURT)
Burcu BAYYURT https://orcid.org/0000-0002-5618-457X
Serdal ARSLAN https://orcid.org/0000-0002-3921-8061

Received: September 14, 2024
Accepted: November 17, 2024
Published: January 15, 2025

Cite as: Bayyurt B, Arslan S. 2025. Highly up-regulation of fas ligand gene expression after increasing in oxidized low-density lipoprotein. BSJ Eng Sci, 8(1): 54-57.

1. Introduction

Oxidized low-density lipoprotein (ox-LDL) is composed result from oxidation of low-density lipoprotein (LDL) under oxidative stress (Khatana et al., 2020). Ox-LDL interacts with molecular targets of endothelial cells (ECs) through various mechanisms and play physiological or pathological roles (Poznyak et al., 2021). Fas ligand (FASL) is a membrane-bound protein that recognizes Fas receptor which is transmembrane, death receptor protein (Tian et al., 2017). Death of a cell is occured through contact of soluble FASL to membrane-bound Fas. The functional association of FASL is initiating death signals in the cells (Malarkannan, 2020). FASL binds to death receptor protein at the cell membrane and induces the recruitment of Fas-associated death domain proteins. These proteins interact with other apoptotic proteins to activate the downstream effects of the cell. Then formation of death-inducing signaling complex activates the cell apoptosis (Tian et al., 2017). Ox-LDL binds to ECs and induces apoptosis. Ox-LDL-induced apoptosis activates a death receptor, Fas, when it binds to its ligand FASL. It has been demonstrated that ox-LDL increases expression of the FASL in vascular cells triggering the apoptosis (Munno et al., 2024). Cells expressing FASL bind the Fas receptor on a target cell before apoptotic pathway initiates in target cells (Malarkannan, 2020). It was implicated that FASL-neutralizing antibodies decrease ox-LDL-induced apoptosis (Munno et al., 2024).

It was shown that ox-LDL treatment restrict human umbilical vein endothelial cells (HUVECs) viability, cell proliferation, and accelerate apoptosis of HUVECs (Cao et al., 2024). Studies to date have shown that ox-LDL induces FASL and FASL-mediated apoptosis (Sata and Walsh, 1998; Li et al., 1998; Imanishi et al., 2002, Li et al., 2014; Tian et al., 2017). The hypothesis of this study was created to determine the effect of higher amounts of ox-LDL treatment on FASL gene expression. Within the scope of this hypothesis, it was aimed to compare *FASL* gene expression in HUVECs treated with different amounts of ox-LDL through quantitative polymerase chain reaction (qPCR) method.

2. Materials and Methods

2.1. Materials

HUVECs provided from ATCC were used to cell line experiments. EC growth medium/DMEM (CAPRICORN) supplemented with 10% fetal bovine serum and 1% penicillin-streptomycin was culture medium for HUVECs at 5% CO_2, 37°C, and 95% relative humidity. HUVECs were separated from the EC growth medium/DMEM using 0.25% trypsin. HUVECs obtained from logarithmic growth phase were utilized for experiments (Liu et al., 2020). HUVECs at ~80-90% confluence were used for ox-LDL treatments. HUVECs were divided into two groups. Former group was group 1, in which HUVECs were treated 25 µg/ml ox-LDL (invitrogen LOT2160046, L34357); and

latter group was group 2 in which HUVECs were treated with 40 µg/ml concentration of ox-LDL for 24 hour. Our cell density decreased significantly after the application of 40 µg/ml ox-LDL in HUVECs. Therefore, we determined our experimental group as HUVECs treated with 40 µg/ml ox-LDL. It was determined by reviewing the literature that the ox-LDL concentration level at which cell viability began to be affected was 25 µg/ml, and experiments were carried out with these two ox-LDL concentrations (Ma et al., 2024). Five biological repetitions were made for each ox-LDL concentration.

2.2. Methods

Firstly, total RNA was extracted from HUVECs through RNeasy Mini Kit (QIAGEN, catalog no:74104) for RNA isolation step. Then we synthesized complementary DNA (cDNA) by using reverse transcription kit (A.B.T.™ with RNase Inh. High Capacity, Catalog No:C03-01-20). Finally, amplification of FASL gene expression was detected qPCR utilizing SYBR Green dye (A.B.T.™ 2X qPCR SYBR-Green MasterMix kit, Catalog No:Q03-02-01 ve Q03-02-05), cDNA, RNase free water (nzytech, MB11101) and *FASL* qPCR primers. Spesific human *FASL* gene primer sequences are forward:5'ACAGCATCATCTTTGGAGAAGC3' (A.B.T, ID:20220609/1-117); reverse:5'ACCTTGAGTTGGACTTGCCT3' (A.B.T, ID:20220609/1-118). on qPCR instrument (LightCycler 96 Real-Time PCR Instrument, Roche). *GAPDH* was used as housekeeping control gene in qPCR. Forward and reverse primer sequences of *GAPDH* are forward:5'ACAACTTTGGTATCGTGGAAGG3' and reverse:5'GCCATCACGCCACAGTTTC3', respectively. Three biological repetitions were made for qPCR experiments.

2.3. Statistical Analysis

We used "GeneGlobe Data Analysis Center" (https://geneglobe.qiagen.com/us/analyze QIAGEN, Hilden, Germany) to analyze the gene expression data. qPCR data was uploaded to the analysis system. Threshold cycle (Ct or Cq) values are obtained after qPCR experiments. Analysis system gives to fold change (FC) value obtained from the groups' comparison according to the qPCR results. Gene expression ratios (FC calculations) are calculated performing method of ΔΔCt. FC was calculated as the ratio of the relative gene expression between the group 1 (HUVECs treated 25 µg/ml ox-LDL) and group 2 (HUVECs were treated 40 µg/ml ox-LDL). Numbers higher than 1 show increased gene expression (up-regulation), numbers between 0 and 1 show decreased gene expression (down-regulation), and a FC value of 1 shows no change (Livak and Schmittgen, 2001). P-value was calculated based on a Student's t-test of the replicate $2^{-\Delta Ct}$ values for each gene in each control group (group 1) and experiment group (group 2) comparison (RT2 Profiler PCR Arrays & Assays Data Analysis Handbook, 2019). P-value results less than 0.05 were accepted significant.

3. Results

In this study, we performed qPCR to compare FASL gene expression level between group of HUVEC treated with 25 µg/ml ox-LDL (group 1) and group of HUVECs treated with 40 µg/ml ox-LDL (group 2). Ct values in both group 1 and group 2 were measured to calculate changes in gene expression. FASL expression was up-regulated 179.77 fold ($P<0.001$) in HUVECs treated with 40 µg/ml ox-LDL when compared to HUVEC treated with 25 µg/ml ox-LDL (Table 1).

Table 1. *FASL* gene expression change of in HUVECs after different concentration of ox-LDL treatment

Genes	HUVECs treated with 25 µg/ml ox-LDL	HUVECs treated with 40 µg/ml ox-LDL	FC	FR	P value
FASL					
Mean of Ct	25.34	16.7	179.77	Up-regulation	<0.001*
GAPDH					
Mean of Ct	28.54	27.39	1.00	1.00	Nan

HUVECs= human umbilical vein endothelial cells; ox-LDL= oxidized low-density lipoprotein; FC= fold change; FR= fold regulation; Ct/Cq= threshold cycle; HUVECs+ox-LDL:HUVECs induced with ox-LDL; *GAPDH* (control gene)= g*lyceraldehyde 3-phosphate dehydrogenase*; *:P value<0.001

4. Discussion

Death receptor proteins of apoptotic pathway have critical role in apoptosis. The pathway involving FASL is significant and widely recognized in this process (Tian et al., 2017). In vascular smooth cells, FASL pathway is involved in ox-LDL-induced apoptosis (Li et al., 2021). In HUVECs, FASL-mediated apoptosis is sensitives to ox-LDL. Induction of Fas-related mRNA expression such as FASL expression following ox-LDL treatment in HUVECs were examined previously (Imanishi et al., 2002). Cell death enzyme-linked immunosorbent assay was applied for investingating ox-LDL effect on viability of HUVECs after HUVECs had been treated with 40µg/ml ox-LDL. It was found that treatment of ox-LDL to the HUVECs did not significantly change apoptosis (Imanishi et al., 2002). In our study, we investigated effect of ox-LDL addiction to FASL gene expression in HUVECs. We detected that FASL gene expression was highly up-regulated in HUVECs treated with 40µg/ml ox-LDL. ECs are resilient to Fas-mediated cell death in response to binding of cell surface

Fas with FAS antibody. HUVECs were cultured with combinations of agonistic anti-Fas antibody in the presence or absence of the ox-LDL for evaluating whether ox-LDL induces the Fas death pathway. It was found that incubation with ox-LDL dose dependently triggered apoptosis. Then, Imanishi et al (2002) examined whether influence of the ox-LDL on Fas-induced-apoptosis was related with the change in expression of the death-regulating genes. The amounts of these genes such as FASL mRNA in HUVECs following ox-LDL treatment were evaluated via RT-Multiplex PCR (Imanishi et al., 2002). We used qPCR to assess FASL gene expression in current study. FASL expression did not significantly change incubation of HUVECs with ox-LDL for 6 hours according to the RT-Multiplex PCR analysis results (Imanishi et al., 2002). We found that FASL expression statistic significantly differed after ox-LDL treatment for 24 hours. It had been reported that FASL expression was up-regulated after treatment with ox-LDL and thereby this leads to ox-LDL-induced apoptosis (Sata and Walsh, 1998). But in other study, it was not detected that FASL expression found to be increased after treatment of the ox-LDL (Imanishi et al., 2002). A potential explanation for the difference between these two studies is the ox-LDL concentrations (150 µg/ml vs 40 µg/ml, respectively). Another study had demonstrated that a 20 µg/ml ox-LDL significantly inreased apoptosis of cultured human coronary arterial endothelial cells (Li et al., 1998). In our study, we treated HUVECs with 25 and 40 µg/ml concentrations of ox-LDL. We found that 40 µg/ml concentrations of ox-LDL caused approximately 180 fold in FASL gene expression when we compared to the group which treated 25 µg/ml ox-LDL (Table 1). This up-regulation of *FASL* gene expression may play a significant role in apoptotic process. It was also implicated that overproduction of ox-LDL triggers apoptosis (Wu et al., 2017). Ox-LDL-induced apoptosis of ECs is also related to the FASL (Sata and Walsh, 1998). Vascular ECs have ability to resist Fas-mediated apoptosis. However, high ox-LDL concentration increases Fas-mediated apoptosis of the EC (Imanishi et al., 2002). In addition, ox-LDL effects ox-LDL-induced Treg apoptosis via the FASL pathway (Li et al., 2014). Ox-LDL activated apoptosis, and the up-regulation of death pathway-related proteins, including FASL in RAW264.7 macrophages (Tian et al., 2017). Cells were cultured with 25, 50 and 100 mg/l ox-LDL for 24 hours. The protein levels of Fas/FASL pathway-related molecules were analyzed by western blot protein expression analysis. Ox-LDL considerably raises Fas/FASL pathway-related molecule level, altough pretreatment with an antagonist antibody that blocks Fas/FASL interaction inhibits ox-LDL-induced apoptosis in macrophages (Li et al., 2006). In the other study, it was shown that ox-LDL activated apoptosis and up-regulated the expression of Fas/FASL pathway-related proteins in RAW264.7 cells, although silencing of Fas by FAS siRNA suppressed ox-LDL-induced macrophage apoptosis (Tian et al., 2017). Findings of the current study generally is compatible with results of the previous studies in the literature. The effect of increased ox-LDL levels on *FASL* gene expression in HUVECs was investigated using the qPCR method and the results of this study may guide future comprehensive molecular function studies on ox-LDL-induced FASL-mediated apoptosis in ECs.

5. Conclusion

Our analysis results suggest that highly up-regulation of the *FASL* originated from increased level of the ox-LDL may regulate apoptosis of the ECs.

Author Contributions

The percentages of the authors' contributions are presented below. The authors reviewed and approved the final version of the manuscript.

	B.B.	S.A.
C	70	30
D	70	30
S	40	60
DCP	70	30
DAI	70	30
L	90	10
W	70	30
CR	70	30
SR	70	30
PM	40	60
FA	40	60

C=Concept, D= design, S= supervision, DCP= data collection and/or processing, DAI= data analysis and/or interpretation, L= literature search, W= writing, CR= critical review, SR= submission and revision, PM= project management, FA= funding acquisition.

Conflict of Interest

The authors declared that there is no conflict of interest.

Ethical Consideration

Ethics committee approval was not required for this study because of there was no study on animals or humans.

Acknowledgements

HUVEC and ox-LDL that were used in cell line experiments had been provided from consumables left over from projects by Sivas Cumhuriyet University Scientific Research Unit and Scientific Research and Technological Research Council of Türkiye, respectively.

References

Cao X, Yang J, He L, Liu C. 2024. Circ_0005699 Expedites ox-LDL-Triggered endothelial cell injury via targeting miR-384/ASPH axis. Cardiovasc Toxicol, 24 (10): 1067-1076.

Imanishi T, Hano T, Sawamura T, Takarada S, Nishio I. 2002. Oxidized low density lipoprotein potentiation of Fas-induced apoptosis through lectin-like oxidized-low density lipoprotein receptor-1 in human umbilical vascular endothelial cells. Circ J, 66 (11): 1060-1064.

Khatana C, Saini NK, Chakrabarti S, Saini V, Sharma A, Saini RV, Saini AK. 2020. Mechanistic insights into the oxidized low-density lipoprotein-induced atherosclerosis. Oxid Med Cell Longev, 5245308.

Li D, Yang B, Mehta JL. 1998. Ox-LDL induces apoptosis in human coronary artery endothelial cells: Role of PKC, PTK, bcl-2, and Fas. Am J Physiol, 275: H568-H576.

Li HL, Wang AB, Zhang R, Wei YS, Chen HZ, She ZG, Huang Y, Liu DP, Liang CC. 2006. A20 inhibits oxidized low-density lipoprotein-induced apoptosis through negative Fas/Fas ligand-dependent activation of caspase-8 and mitochondrial pathways in murine RAW264.7 macrophages. Cell Physiol, 208: 307-18.

Li Q, Wang Y, Li H, Shen G, Hu S. 2014. Ox-LDL influences peripheral Th17/Treg balance by modulating Treg apoptosis and Th17 proliferation in atherosclerotic cerebral infarction. Cell Physiol Biochem, 33(6): 1849-1862.

Li X, Yang Y, Wang Z, Jiang S, Meng Y, Song X, Zhao L, Zou L, Li M, Yu T. 2021. Targeting non-coding RNAs in unstable atherosclerotic plaques: Mechanism, regulation, possibilities, and limitations. Int J Biol Sci, 17(13): 3413-3427.

Liu Q, Liu Z, Zhou LJ, Cui YL, Xu JM. 2020. The long noncoding RNA NKILA protects against myocardial ischaemic injury by enhancing myocardin expression via suppressing the NF-κB signalling pathway. Exp Cell Res, 15; 387(2): 111774.

Livak KJ, Schmittgen TD. 2001. Analysis of relative gene expression data using real-time quantitative PCR and the 2(-Delta Delta C(T)) Method. Methods, 25(4): 402-8.

Ma J, Ling J, Tong R, Guo J, Zhu Z. 2024. siLOXL2 inhibits endothelial inflammatory response and EndMT induced by ox-LDL. Cerebrovasc Dis Extra, 14 (1): 165-176.

Malarkannan S. 2020. Molecular mechanisms of FASL-mediated 'reverse-signaling'. Mol Immunol, 127: 31-37.

Munno M, Mallia A, Greco A, Modafferi G, Banfi C, Eligini S. 2024. Radical Oxygen species, oxidized low-density lipoproteins, and lectin-like oxidized low-density lipoprotein receptor 1: a vicious circle in atherosclerotic process. Antioxidants, 13 (5): 583.

Poznyak AV, Nikiforov NG, Markin AM, Kashirskikh DA, Myasoedova VA, Gerasimova EV, Orekhov AN. 2021. Overview of OxLDL and its impact on cardiovascular health: focus on atherosclerosis. Front Pharmacolü 11: 613780.

RT2 Profiler PCR Arrays & Assays Data Analysis Handbook. 2019. https://dataanalysis2.qiagen.com/static/templates/RT2_Profiler_PCR_Data_Analysis_Handbook_190930.pdf (accessed date: November 01, 2024).

Sata M, Walsh K. 1998. Oxidized LDL activates Fas-mediated endothelial cell apoptosis. J Clin Invest, 102: 1682-1689.

Tian H, Yao ST, Yang NN, Ren J, Jiao P, Zhang X, Qin SC. 2017. D4F alleviates macrophage-derived foam cell apoptosis by inhibiting the NF-κB-dependent Fas/FASL pathway. Sci Rep, 7(1): 7333.

Wu MY, Li CJ, Hou MF, and Chu PY. 2017. New insights into the role of inflammation in the pathogenesis of atherosclerosis. Int J Mol Sci, 18 (10): 2034.

Black Sea Journal of Engineering and Science
doi: 10.34248/bsengineering.1567146

Open Access Journal
e-ISSN: 2619 – 8991

Araştırma Makalesi (Research Article)
Cilt 8 - Sayı 1: 58-74 / Ocak 2025
(Volume 8 - Issue 1: 58-74 / January 2025)

ALT PALEOZOYİK YAŞLI SULTANDEDE METASEDİMANTER KAYAÇLARIN JEOKİMYASI, KÖKENİ VE TEKTONİK YERLEŞİMİ (DİNEK, ŞARKİKARAAĞAÇ-ISPARTA, GB TÜRKİYE)

Oya CENGİZ[1], Ahmet Semih DENİZ[2], Didem KIRAY[3]*

[1]*Suleyman Demirel University, Faculty of Engineering and Natural Sciences, Department of Geological Engineering, 32260, Isparta, Türkiye*
[2]*Abide-1 Hurriyet Street Merkez Quarter, 34360, İstanbul, Türkiye*
[3]*Barbaros Quarter Hacı Mustafa Bey Street, 17020, Çanakkale, Türkiye*

Özet: Alt Paleozoyik yaşlı metasedimanter kayaçlar (Sultandede Formasyonu) Türkiye'nin güneyinde bulunan Batı Toroslar'daki Sultandağ Bloğu'nun (Isparta) Dinek (Şarkikaraağaç-Isparta) güneydoğusunda yüzlek vermektedir. Bu çalışmanın amacı, Geyikdağı Birliği içerisindeki düşük dereceli metamorfizma geçiren Alt Paleozoyik yaşlı Sultandede metasedimanter kayaçlarının kökenini, kaynak kayacını ve tektonik ortamlarını petrografik ve jeokimyasal analizler ile ortaya koymaktır. Sultandede Formasyonu sleyt, fillit, metakumtaşı, metakarbonatlar, yumrulu metakireçtaşı, kalkşist, muskovit-serizit-kuvars şist, metakuvarsit ve mermer türü litolojilerden meydana gelmektedir. Petrografik analiz temelinde şist numuneleri muskovit, serizit, kuvars, barit, opak mineral ve demiroksit ayrışma mineralleri, kalkşist numuneleri de kalsit, kuvars, barit, serizit, muskovit ve limonit içermektedir. Kondrite göre normalize edilmiş nadir toprak elementlerinin (NTE) dağılım desenlerinde Sultandede metamorfik kayaçlarında hafif nadir toprak elementlerinden (HNTE) ağır nadir toprak elementlerine (ANTE) doğru bir azalmanın olduğu, HNTE'lerin ANTE'lere göre göreceli olarak zenginleştiği gözlenmektedir. Eu (Eu/Eu*= 0,55-0,98) ve Ce belirgin negatif anomali gösterirken, Gd pozitif anomali gösterir. Metasedimanter kayaçların felsik, tortullaşma sonrası oluştuğu ve kıta kenar rejimini karakterize ettiği tespit edilmiştir. Ana element jeokimyası ve iz-nadir toprak element oranları ile yapılan sınıflama ve kaynak kayaç diyagramlarından (La/Th ve Hf) elde edilen veriler, bu kayaçların mağmatik (felsik ve ortaç) ve geri dönüştürülmüş önceden var olan sedimanter kaynaktan türediğini ve üst kıtasal kabuk eğilimi gösterdiğini belirtmektedir. Şist ve kalkşist numunelerinin ortalama Th/U değeri (6,87) üst kıta kabuk değerinden (3,82) daha yüksektir. Bu sonuç, önceki aşınma eğilimini takip ettiğini ve metasedimanter kayaçların yoğun aşınmaya maruz kaldığının işaretidir. Ni/Co ve V/(V + Ni) jeokimyasal parametreleri, metasedimanter kayaçların oksik ortamı ve disoksik, anoksik ve öksinik koşulları altında biriktiğini göstermektedir.

Anahtar kelimeler: Jeokimya, Sultandede formasyonu, Köken ve tektonik ortam, Şarkikaraağaç-Isparta.

Geochemistry, Origin and Tectonic Setting of Lower Paleozoic Sultandede Metasedimentary Rocks (Dinek, Şarkikaraağaç-Isparta, SW Türkiye)

Abstract: Lower Paleozoic metasedimentary rocks (Sultandede Formation) crop out in the Sultan Mountains in the Western Taurus Belt in the south of Türkiye, southeast of Dinek (Şarkikaraağaç-Isparta). The aim of this study is to reveal the origin, provenance rock and tectonic environments of the Lower Paleozoic Sultandede metasedimentary rocks undergoing low-grade metamorphism within the Geyikdağı Unit by petrographic and geochemical analyses. Sultandede Formation consists of slate, phyllite, metasandstone, metacarbonates, nodular metalimestone, calcschist, muscovite-sericite-quartz schist, metaquartzite and marble type lithologies. Based on petrographic analysis, schist samples contain muscovite, sericite, quartz, barite, opaque minerals and iron oxide weathering minerals, while calc-schist samples contain calcite, quartz, barite, sericite, muscovite and limonite. In the rare earth element (REE) distribution patterns normalised to chondrite, it is observed that there is a decrease from light rare earth elements (LREEs) to heavy rare earth elements (HREEs) in the Sultandede metamorphic rocks, and that HREEs are relatively enriched compared to HREEs. While Eu (Eu/Eu*= 0.55-0.98) and Ce show significant negative anomalies, Gd shows positive anomaly. It was determined that metasedimentary rocks were felsic, formed after sedimentation and characterized the continental margin regime. Classification and source rock diagrams (La/Th and Hf) derived from major element geochemistry and trace-rare earth element ratios indicate that these rocks are derived from magmatic (felsic and intermediate) and recycled pre-existing sedimentary sources and have an upper continental crustal trend. The average Th/U value (6.87) of the schist and calcareous schist samples is higher than that of the upper continental crust (3.82). This result indicates that it follows the previous erosion trend and that the metasedimentary rocks are subject to intense erosion. The Ni/Co and V/(V + Ni) geochemical parameters indicate that the metasedimentary rocks were deposited under oxic, dysoxic, anoxic and euxinic conditions.

Keywords: Geochemistry, Sultandede formation, Origin and tectonic setting, Şarkikaraağaç-Isparta

***Sorumlu yazar (Corresponding author):** Barbaros Quarter Hacı Mustafa Bey Street, 17020, Canakkale, Türkiye
E mail:dkiray17@gmail.com(D. KIRAY)
Oya CENGİZ https://orcid.org/0000-0003-1363-4638
Ahmet Semih DENİZ https://orcid.org/0009-0002-3083-0796
Didem KIRAY https://orcid.org/0000-0002-4187-7285

Gönderi: 14 Ekim 2024 **Received:** October 14, 2024
Kabul: 17 Kasım 2024 **Accepted:** November 17, 2024
Yayınlanma: 15 Ocak 2025 **Published:** January 15, 2025

Cite as: Cengiz O, Deniz AS, Kiray D. 2025. Geochemistry, origin and tectonic setting of lower Paleozoic sultandede metasedimentary rocks (Dinek, Şarkikaraağaç-Isparta, SW Türkiye). BSJ Eng Sci, 8(1): 58-74.

1. Giriş

Belirgin köken özellikleri gösteren farklı tektonik ortamlar tortul süreçlerin fizikokimyasal belirteçleri ile karakterize edilirler. Metasedimanter kayaçların kimyasal bileşimi, kökeni, kaynak kayaçların doğası, kaynak alanının aşınması iklim, taşınma, gömülme, diyajenez ve metamorfizma gibi değişkenler tarafından kontrol edilir (McLennan vd., 1993). Bu değişkenler çeşitli koşullar altında elementlerin hareketliliğine bağlı olarak kaynak kayaçların ve tortulların kimyasal bileşimini değiştirir (McLennan, 1989; Cullers ve Stone, 1991; Nesbitt ve Young, 1996). Çok düşük dereceli metasedimanter kayaçların jeokimyasal verileri kayacın kimyasal bileşimi değişmediği sürece tektonik ortamların ayırımı ve/veya kaynakları hakkında önemli bilgiler vermektedir (Nesbitt ve Young, 1984). Son zamanlarda ana elementlere ve metaklastik tortulların kimyasal bileşimine dayalı tektonik süreçlerin ayrımını ve tektonik ortamlarını sınırlamak ve kaynak kayaçların kökenini belirlemek için jeokimyasal analizler yaygın olarak kullanılmaktadır (Dickinson ve Suczek, 1979; Condie vd., 1992; Nesbitt ve Young, 1996; Marsaglia ve Latter, 2003; Dostal ve Keppie, 2009; Hara vd., 2012; Piñán-Liamas ve Escamilla-Casas, 2013; Tang vd., 2016; Gonzales vd., 2018; Guo vd., 2021; Mendes vd., 2021; Hifzurrahman vd., 2023; Şengün, 2023). La, Ni, Y, Sc, Cr, Th, V, Ti, Hf, Zr ve nadir toprak elementler farklı tektonik ortamların ve/veya kaynakların ayrımında sıklıkla kullanılmaktadır (Bhatia, 1983; Taylor ve McLennan, 1985; McLennan vd., 1993; Roser vd., 1996; Pandey ve Parcha, 2017). Özellikle Zr, Hf, Th, Sc, Nb ve Y göreceli olarak elementler içerisinde düşük hareketliliğe sahip olmaları, bozunma ve sedimanter işlevler sırasında deniz suyunda kısa zamanda kalmaları nedeniyle köken çalışmalarında en uygun iz elementlerdir (Cullers, 2000; Young vd., 2013). Bunun yanında, La veya Th-Co-Sc-Cr oranları kaynak kayaçların bileşimini ortaya koymak için oldukça yararlıdır (Cullers, 2000).

Alt Paleozoik'e ait Sultandede Formasyonu metaklastik kayaçları ve Çaltepe düşük dereceli metakarbonatları Türkiye'nin güneyinde yeralan Batı Toroslar'daki Seydişehir, Hüyük, Şarkikaraağaç ve Yalvaç bölgelerinde yaygın olarak yüzeylenmiştir (Şekil 1). Birkaç araştırmacı, bölgenin jeolojik haritalamasını (Blumenthal, 1947; Dean ve Monod, 1970; Desprairies ve Gutnic, 1972; Özgül ve Gedik, 1973; Öztürk vd., 1977; Öztürk vd., 1981; Demirkol, 1977; Demirkol ve Sipahi, 1979; Cengiz, 1991; Cengiz, 1997), barit, demirli boksit-boksit mineralizasyon alanları çevresinde madencilik jeolojisini (Ayhan ve Karadağ, 1985; Ayhan, 1986; Karadağ, 1987; Cengiz ve Kuşcu, 1993; Cengiz ve Kuşcu, 2002; Karadağ vd., 2009; Elmas vd., 2012), konodontları (Kozlu vd., 2002; Göncüoğlu vd., 2004), Çaltepe ve Fele bölgelerindeki Sultandede (Seydişehir) Formasyonu metasedimanter kayaçları biyostratigrafik veriler ile fasiyes ve dizi stratigrafisinin analizini (Erdoğan vd., 2004) ve jeokimya ile kaynak kaya ve tektonik ortamını (Karadağ, 2014) incelemiştir.

İnceleme alanı Sultandağlarında yer alan Geyikdağı birliği içerisinde KB-GD doğrultulu uzanan Sultandağlarında düşük dereceli metamorfik kayaların yüzeylediği alanları kapsamaktadır. Bu kayaçlar aynı zamanda Türkiye'nin ekonomik öneme sahip barit yataklarının yankayaçları olmaları ve cevher oluşumunda klavuz özelliği göstermesi nedeniyle de önem arzetmektedir. Bu çalışmada Dinek (Şarkikaraağaç-Isparta) ve İlmen (Hüyük-Konya) arasındaki düşük dereceli metamorfik kayaçların kaynak kayaçlarının litolojik özellikleri, petrografik incelemeler ile mineralojik bileşimleri, jeokimyasal analizler (ana, iz ve nadir toprak elementleri) ile tektonik ortamlarının ortaya konulması hedeflenmiştir.

2. Jeolojik Konum

Toroslar'ın Prekambriyen'den Triyas'a kadar Gondwana'nın kuzey kenarının bir parçası olduğu düşünülmektedir (Robertson ve Dixon, 1984; Şengör vd., 1984). Kuzey Gondwana'nın Kambriyen'den Ordovisiyen'e kadar en iyi korunmuş örtü dizilerinden biri (Ghienne vd., 2007) Türkiye'nin kuzeyinden başlayıp Suudi Arabistan'dan güneye doğru 1500 km uzunluğunda bir kuşak olarak uzanmakta ve burada nispeten uzak Alt Paleozoik birimlerini içermektedir (Ghienne vd., 2010). Toros Kuşağı, hem doğu hem de batı Toroslar'da değişken metamorfozlu temel kayaçları içermektedir (Özgül, 1976; Dean ve Özgül, 1994; Göncüoğlu ve Kozlu, 2000; Gürsu, 2002; Gürsu vd., 2004). Toros Kuşağının tabanında Neoproterozoyik-Alt Paleozoik kayaçlar (Özgül, 1976) ve/veya Neoproterozoyik (Gürsu ve Bayhan, 2004) yaşlı bir temel ile bunu uyumsuz örten Geyikdağ biriminde en iyi şekilde ortaya çıkmaktadır. Üst Paleozoyik-Mesozoyik yaşlı platform istifleri içeren örtü birimleri de (Bozkır, Bolkardağı, Aladağ, Antalya ve Alanya birlikleri (Özgül, 1976; 1984) kuşağın üst kesimlerini oluşturmaktadır.

İnceleme alanı, Orta Toroslarda Sultandağlarında yer alan Geyikdağı birliği içerisinde KB-GD doğrultulu metamorfik birimleri kapsamaktadır. İnceleme alanının temel kayaçlarını Alt Paleozoyik yaşlı Sultandede formasyonu (Demirkol, 1977) oluşturmaktadır (Şekil 1). Bu formasyonun tabanını sleyt ve fillit, metakarbonatlar, yumrulu metakireçtaşı ve kalkşist, üst seviyelerini metaklastik kayaçların (kuvars-mikaşist, metasilttaşı, kloritşist) arakatkıları, metakuvarsit ve mermer oluşturmaktadır. Neojen çökelleri, kiltaşı, marn ve kireçtaşı ardalanmalı, yer yer kötü boylanmalı, hematit, götit, limonit, şist ve kuvarsit parçalarından oluşmaktadır. Tüm birimler kötü boylanmalı, çevre kayaçlara ait çakıllar içeren, kumlu-killi ve az tutturulmuş genellikle dere yataklarında ve düzlüklerde yüzeylenen Kuvaterner yaşlı alüvyon tarafından örtülmüştür (Cengiz, 1997) (Şekil 2).

Metakireçtaşı ve dolomit (Çaltepe Formasyonu) biriminin tabanında gri, kızıl kahverengi dolomitik kireçtaşı, üste doğru koyu mavi, açık-koyu gri, beyazımsı metakireçtaşları bulunur (Cengiz, 1997). Birim, çalışma alanının genel morfolojisine uygun olarak KB-GD doğrultusundadır ve yaklaşık 150±250m görünür kalınlığa sahiptir (Dean ve Monod, 1970).

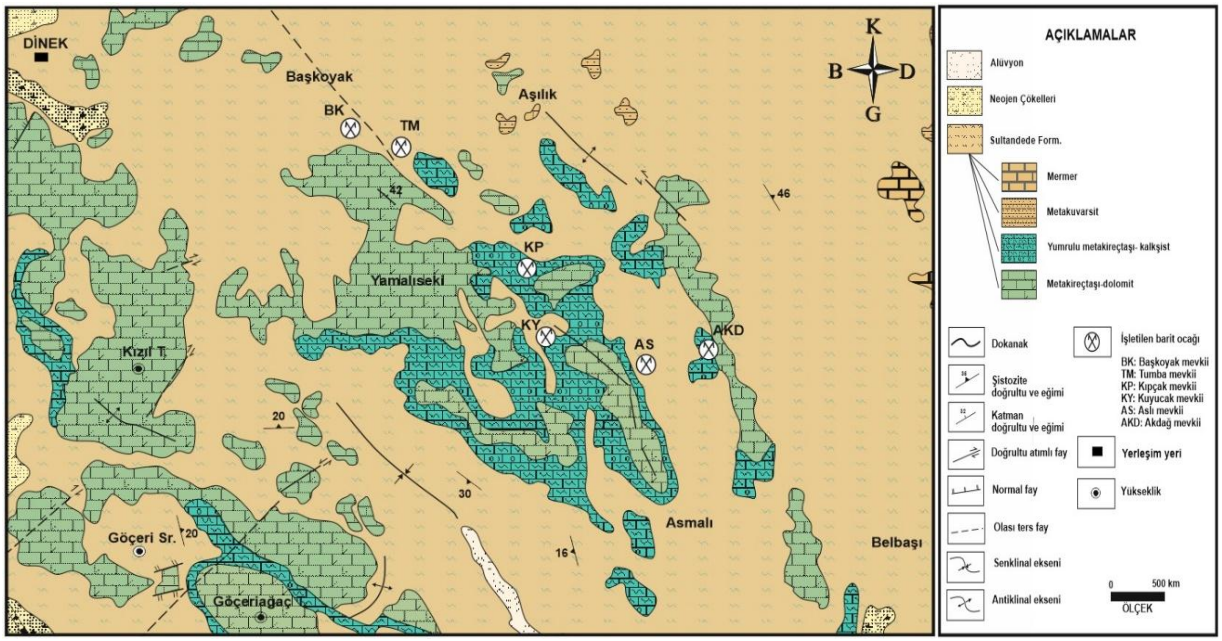

Şekil 1. Dinek (Şarkikaraağaç-Isparta) sahasının jeolojik haritası (Cengiz, 1997)

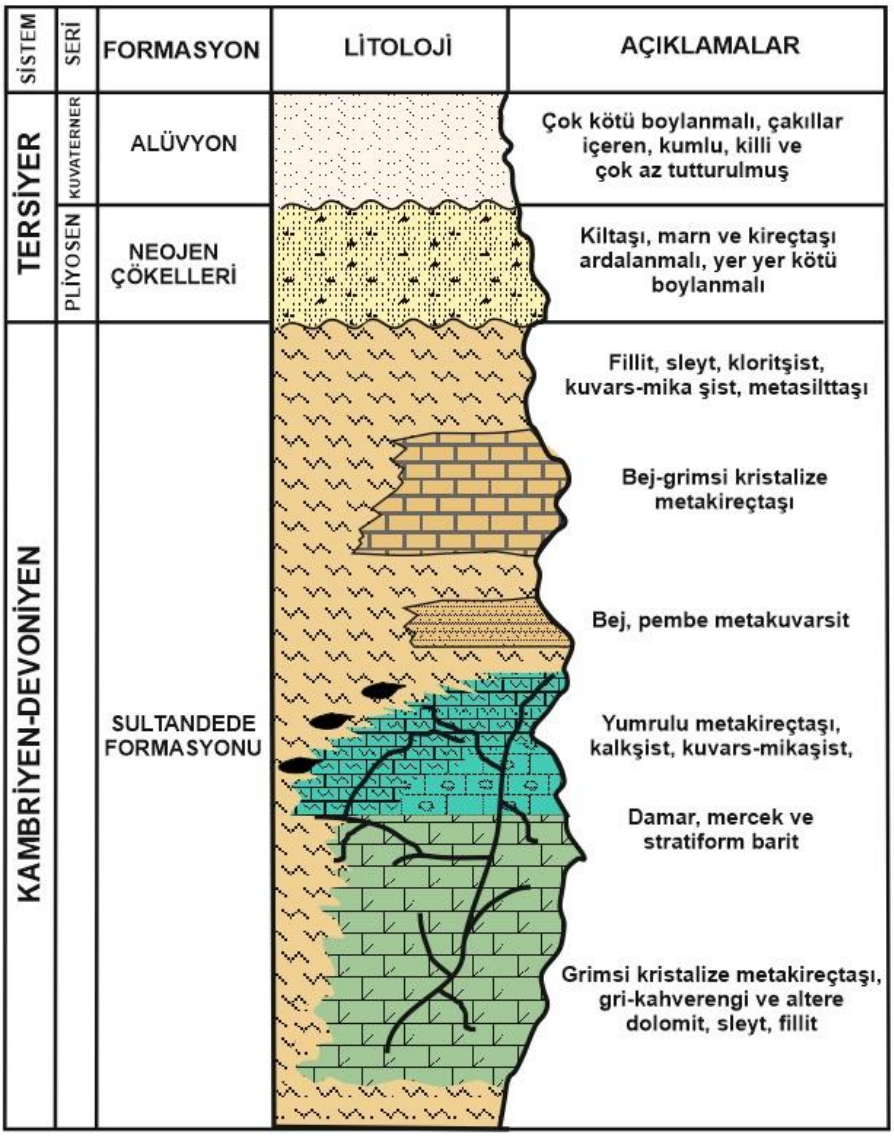

Şekil 2. İnceleme alanına ait stratigrafik sütun kesit (Cengiz, 1997).

Karadağ (2014) dolomitlerin birincil dokularının genellikle yeniden kristalleşme süreçleri nedeniyle korunamadığını, metakireçtaşlarındaki orijinal dokuların ise açıkça gözlendiğini belirtmiştir. Birimin alt dokanağı, Sultandede formasyonu içerisindeki metaklastik kayaçlar ile genellikle uyumlu, üst dokanağı da mor yumrulu metakireçtaşı ve kalkşistler ve/veya metaşeyllerle geçişlidir. Çalışma alanı dışında Özgül (1997) Çaltepe Formasyonu'nun Hamzalar Formasyonu üzerinde uyumlu bir dokanakla yer aldığını belirtmiştir. Birimin yaşı, Dean ve Monod (1970) tarafından Alt (?)-Orta Kambriyen olarak belirlenmiştir. Yumrulu metakireçtaşı alacalı, pembemsi-bejimsi-mor, yer yer ince-orta katmanlı, yer yer de katmansız döküntü şeklindedir. Birim, sert, sıkı dokulu ve kalsit damarlı, üst seviyeleri kil sıvama şeklinde şeyl arakatkılı ve yumru görünümlüdür. Kalınlığı yaklaşık ±50 m dir (Demirkol ve Sipahi, 1979). Karadağ (2014), Çaltepe Formasyonu'nun üst kısmındaki nodüler kireçtaşlarında, neoformalize serisit ve klorit minerallerinden oluşan zayıf gelişmiş bir arduvaz yarılmasının olduğunu belirtmiştir. Kalkşistler sarımsı-bej, grimsi-siyahımsı ve ince şistoziteli bir yapıya sahip olup şistozite yüzeyleri boyunca iyi gelişmiş mangan dendritleriyle tipik bir görünüm sunarlar. Yumrulu metakireçtaşı ve kalkşistler, altta bulunan metakireçtaşları ile yanal/düşey geçişli, üst dokanağındaki şeyller ile geçişlidir. Metakuvarsitler, pembe, beyazımsı-bej renkli, belirgin eklemli ve değişken kalınlığa sahiptir. Genellikle merceksi, ince-orta katmanlı, çok sert dayanımlı, iri kristalli, demir içeriklidir. Kuvarsitlerin çatlaklarında ikincil kuvars damarcıkları izlenmektedir. Demirkol ve Sipahi (1979) inceleme alanı yakınlarında yaptıkları çalışmada metakuvarsitlere (Engili Formasyonu) Orta-Üst Devoniyen yaşını vermişlerdir. Bu metakuvarsitler Sultandede formasyonu içerisindeki şistler ve sleytler ile uyumludur (Cengiz, 1997). Mermerler de Sultandede formasyonunun içerisinde kristalize kireçtaşı ve çok az olarak da kalkşist bantları içermektedir. Birim bej, beyazımsı-gri, sarımsı, ince-orta katmanlı, iri kristalli, az gelişmiş eklemli, demir içerikli ve yer yer dolomitiktir. Bu birim Sultandede formasyonu içerisindeki metaklastik kayaçlarla uyumludur (Cengiz, 1997).

3. Materyal ve Yöntem

İnceleme alanındaki Sultandede Formasyonuna ait metasedimanter kayaçlardan alınan numuneler Başkoyak, Tumba, Kuyucak, Kıpçak, Aslı ve Akdağ barit cevherleşme lokasyonlarından derlenmiştir. Derlenen 6 şist, 4 kalkşist, 3 baritli şist ve 2 baritli kalkşist olmak üzere toplam 15 adet numunenin petrografik ve jeokimyasal analizleri yapılmıştır. Bu numunelerin ince kesitleri Pamukkale Üniversitesi Jeoloji Mühendisliği Bölümü laboratuvarında hazırlanmıştır. İnce kesitlerin mineralojik-petrografik incelemeleri Süleyman Demirel Üniversitesi Jeoloji Mühendisliği Bölümü laboratuvarında 10 Olympus (BH-2) marka polarizan mikroskop altında yapılmıştır. Aynı numunelerin majör oksit, iz ve nadir toprak element içerikleri, Bureau Veritas Mineral (BVM) laboratuvarında (Kanada) Lityum Metaborat/Tetraborat Fusion çözeltisinde Indüktif Couple Plazma-Kütle Spektrometresi (ICP-MS) ve X-ray Floresans (XRF) analiz yöntemleri ile analiz edilmiştir.

4. Bulgular

4.1. Metasedimanter Kayaçların Yayılımı ve Petrografik İncelemeleri

İnceleme alanında Sultandede Formasyonu metakireçtaşı ve dolomit, yumrulu metakireçtaşı, kalkşist, metakumtaşı, metasilttaşı, metakuvarsit ve mermer litolojilerinden oluşmaktadır. Bu litolojiler sahanın topoğrafik yapısına uygun olarak kuzeybatı-güneydoğu doğrultusunda yüzeyler. Bu çalışmada kalkşist ve şist kayaç mostraları barit cevherleşmesinin varolduğu Başkoyak, Kuyucak, Kıpçak, Tumba, Aslı ve Akdağ lokasyonlarında incelenmiştir (Şekil 3). Barit bu kayaçların içerisinde genellikle damar, daha az olarak merceksi ve stratiform şekilde bulunur (Cengiz, 1997).

Şistler Başkoyak mevkiinde killi şistler ve grafit şistler olarak yaygındır. Bu kayaçlar yoğun alterasyona uğradıklarından grimsi, sarımsı-kahverengimsi ve yeşilimsi renklerde gözlenirler (Şekil 3a, b). Kuyucak mevkiinin doğusunda boz sarımsı-kahverengimsi şistler ve grimsi şistler laminalı ve şistoziteli yapıları ile dikkati çekerler. Batıda ise sarımsı-boz renkli kalkşistler ve sarımsı şistler gözlenir. Kıpçak mevkiinde, grimsi–kahverengimsi kalkşist ve şistler yaygındır. Sahada tabandan tavana doğru şist, barit, kahverengi-bordo killi seviye, barit+yankayaç, barit cevheri, grimsi-kahverengimsi kalkşist izlenmektedir (Şekil 3c, d). Tumba mevkiinde, kalkşist içerisinde farklı seviyelerde ve farklı kalınlıklarda katmansı barit bulunur (Şekil 3e). Aslı mevkiinde dayanımsız, yer yer parçalanmış, belirgin şistoziteli, kıvrımlı, genellikle grimsi ve sarımsı şistlerde açılan ocakta barit cevheri işletilmektedir. Ocakta şistler içerisinde ve barit-şist dokanağında iki adet fay mevcuttur (Şekil 3f). Akdağ mevkiinde; grimsi kalkşist ve sarımsı-kahverengimsi şistlerde açılan ocakta barit cevheri merceksi ve damar şeklinde gözlenmektedir (Şekil 3g, h).

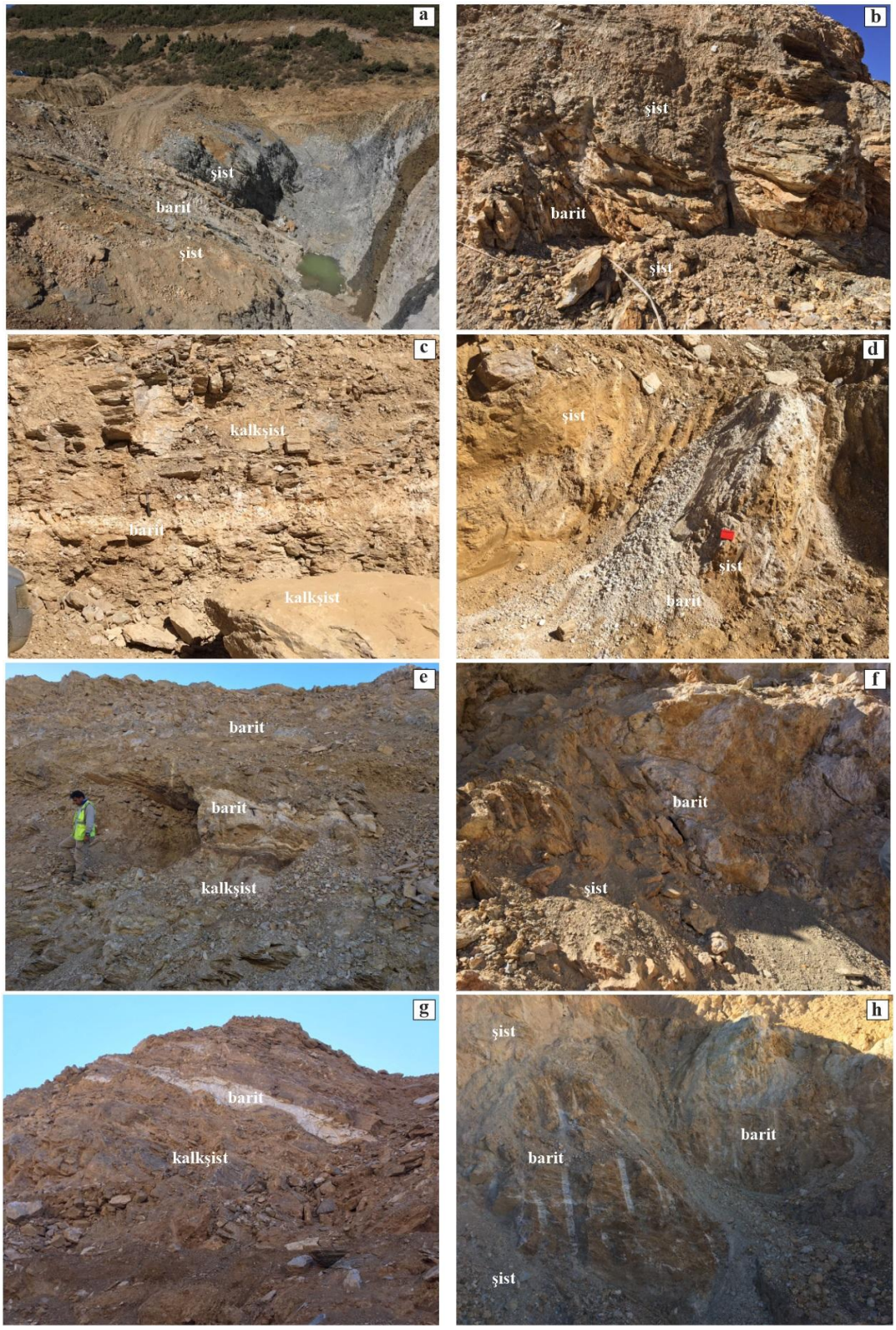

Şekil 3. Sultandede Formasyonu'na ait kalkşist ve şist kayaçları ve barit cevherinin saha görüntüleri (Deniz, 2019). **a)** Haki renkli şistlerde merceksi barit damarı (Başkoyak sahası), **b)** Gri şistler ile haki-sarımsı şistlerde barit cevheri (Başkoyak sahası), **c)** Şistlerdeki kırılmış ve parçalanmış barit (Kuyucak sahası), **d)** Kalkşist ile kahverengi-bordo alterasyon düzeyi arasındaki barit (Kıpçak sahası), **e)** Kalkşistler içerisinde stratiform barit cevheri (Tumba sahası), **f)** Sarımsı-kahverengimsi şistlerde barit (Aslı sahası), **g)** Kalkşist içerisindeki barit damarı (Akdağ sahası), **h)** Sarımsı-kahverengi şistler ve merceksi barit cevheri (Akdağ sahası).

İnceleme sahasındaki şist, kalkşist, baritli kalkşist ve baritli şist incekesit numunelerinin petrografik özellikleri polarizan mikroskopta incelenmiş ve bazılarının mikro-görüntüleri verilmiştir (Şekil 4-5). Sultandede Formasyonu içerisindeki çok düşük dereceli metaklastik kayaç şistin mineralojik bileşimini muskovit, serizit, kuvars, barit, opak mineral ve demiroksit boyamaları oluşturmaktadır. Kayaç muskovit-serizit-kuvars şist olarak tanımlanmıştır. Muskovit-serizit ile sparkalsit arasında değişken kalınlıklı bükülmüş kuvars damarı izlenmektedir (Şekil 4a). Muskovit-serizit arasında breşik yapılı kuvars merceksi damarı vardır (Şekil 4b). Muskovit, serizit ve kuvars minerallerinde şistozite düzeyleri çok belirgindir (Şekil 4c). Şistlerin ve sparkalsitlerin içerisinde breşik kuvars parçaları, merceksi görünümlü silisleşme ve opak mineraller mevcuttur (Şekil 4d). Sparkalsitler ile içerisinde yeralan barit damarının ilişkisi belirgindir (Şekil 4e). Muskovit-serizit şistlerdeki sparlaşmış kalsit damarının içerisinde breşleşmiş kuvars taneleri gelişigüzel dağılmıştır. Muskovit-serizit şistin hemen yanındaki sparkalsit damarının dokanağı boyunca değişen kalınlığa sahip tarak yapılı kuvars izlenir (Şekil 4f). Genellikle silisifiye alanda gelişigüzel dağılmış, daha az da sparkalsitler içerisinde özşekilli, yarı özşekilli ve özşekilsiz opak mineralleri bulunur (Şekil 4g, h). Kayaçta kuvars merceği gözlenir ve yer yer parçalanmış kuvarslar ve demiroksit getirimlerinin varlığı tespit edilmiştir (Şekil 4ı). Ayrıca, sparkalsit içerisinde değişen kalınlığa sahip kırıklara yerleşen breşik barit kristalleri de gözlenmiştir (Deniz, 2019) (Şekil 4i).

İnceleme alanında düşük dereceli metamorfik kayaç kalkşistler kalsit, kuvars, barit, serizit, muskovit ve limonit içerir. Kalkşistlerde merceksi yapıda spar kalsitler ve yer yer siderit zonlanması izlenir (Şekil 5a). Kalkşist kesitinin breş parçalarını kuvars oluşturur ve kayaç içerisinde ince bir kuvars damarının kırılarak atıma uğradığı da dikkati çeker (Şekil 5b). Diğer bir kesitte çoğunluğu sparlaşmış bir kalsit damarı ve içerisinde breşik yapılı kuvars taneleri gözlenir. Bu damarın tavan ve tabanında bükülmüş ve şistoziteli muskovitler ve serizitler bulunur. Ayrıca, breş parçalarını kuvarsın oluşturduğu silisifiye alan da izlenir (Şekil 5c). Belirgin dilinimli spar kalsit içerisinde damar şekilli yarı özşekilli ve özşekilsiz baritler gözlenir ve baritin dilinim düzlemi boyunca kırıklar gelişmiştir (Şekil 5d). Bu kesitte sparkalsitlerin içerisinde gelişen hat boyunca özşekilli, yarıözşekilli opak mineraller ve yer yer özşekilli, özşekilsiz breşik kuvars taneleri gözlenmiştir (Şekil 5e). Kuvars-serizit şist-kalkşist kontağından alınan diğer kesitte kayacın yoğun alterasyona uğradığı gözlenir. Bu kesitte özşekilli opak mineral (olasılıkla pirit), limonitleşme ve yoğun silisleşme egemendir. Limonitleşme genellikle opak mineral kristallerinin kenarları boyunca, daha az olarak da gelişigüzel dağılmıştır. Silisleşme yer yer breşik, daha yoğun olarak da farklı yönlerde gelişen kırık ve çatlakların içerisini dolduran silisifiye olmuş eriyikler şeklindedir (Şekil 5f). Sparkalsitler ile kuvarsların sınırları nettir ve sparkalsitlerin içerisinde kuvars damarları, özşekilli opak mineraller ve demiroksit getirimleri de izlenir (Şekil 5g). Ayrıca, sparkalsitler içerisinde yoğun silisleşme, yer yer bükülmüş tarak yapılı kuvarslar, yer yer de breşik kuvars taneleri ve yarı öz şekilli opak mineral tespit edilmiştir. (Şekil 5h). Bu kalkşist kesitindeki sparkalsitlerin dilinimleri belirgindir. Kalsitlerin içerisindeki kırık ve çatlaklar, farklı yönlerde gelişmiş ve birbirini kesmektedir. Bu kırık ve çatlaklara özşekilli, yarı özşeklli ve özşekilsiz kuvars ve barit yerleşmiştir. Ayrıca, sparkalsitler ile barit ve kuvars dolgulu damarların sınırları çok keskindir (Deniz, 2019) (Şekil 5ı, i).

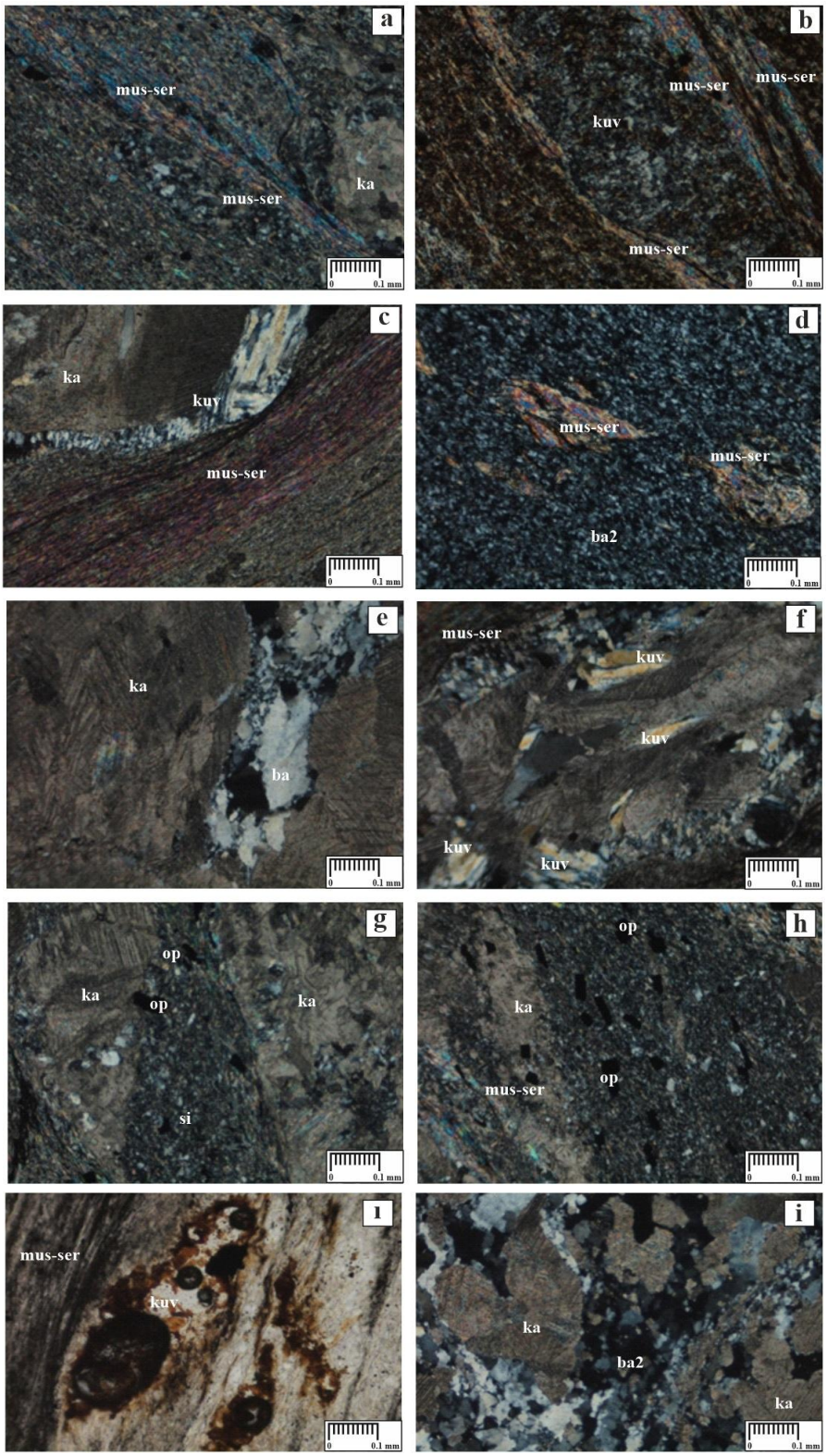

Şekil 4. Muskovit-serizit-kuvars şist ve şist-kalkşist kontağından alınan kayaç numunelerinin mikroskop görüntüleri (Deniz, 2019). a) Muskovit-serizit (mus-ser) şist ile kalsit (ka) ve silisleşme (si) (BK-4), b) Muskovit-serizit (mus-ser) içerisindeki kuvars (q) merceği ve silisleşme (si) (TM-1),c) Muskovit-serizit (mus-ser) şist ile sparkalsit (ka) arasında bükülmüş kuvars (q) damarı (BK-4), d) Kataklastik dokulu mikrokristalli baritler (ba2) içerisindeki merceksi muskovit-serizitler (mus-ser) (BK-2), e) Sparkalsit (ka) içerisindeki barit (ba) damarının ilişkisi (BK-4), f) Muskovit-serizit (mus-ser) şist içinde sparkalsit (ka) damarındaki breşik kuvars (q) parçaları, g) Sparkalsit (ka) içinde breşik kuvars (q) taneleri ve sparkalsitler arasında merceksi görünümlü silisleşme (si) ve opak (op) mineral (BK-4), h) Muskovit-serizit (mus-ser) ile sparkalsit (ka) dokanağı ve sparkalsit içerisindeki silisifiye (si) zon ve opak (op) mineral taneleri (BK-4) ı) Kuvars (q) mercekleri ve demiroksit gelişimi (BK-1), i) Sparkalsitler (ka) içerisinde gelişi güzel kırıklara yerleşen baritler (ba2) ve yer yer breşik barit taneleri (BK-4).

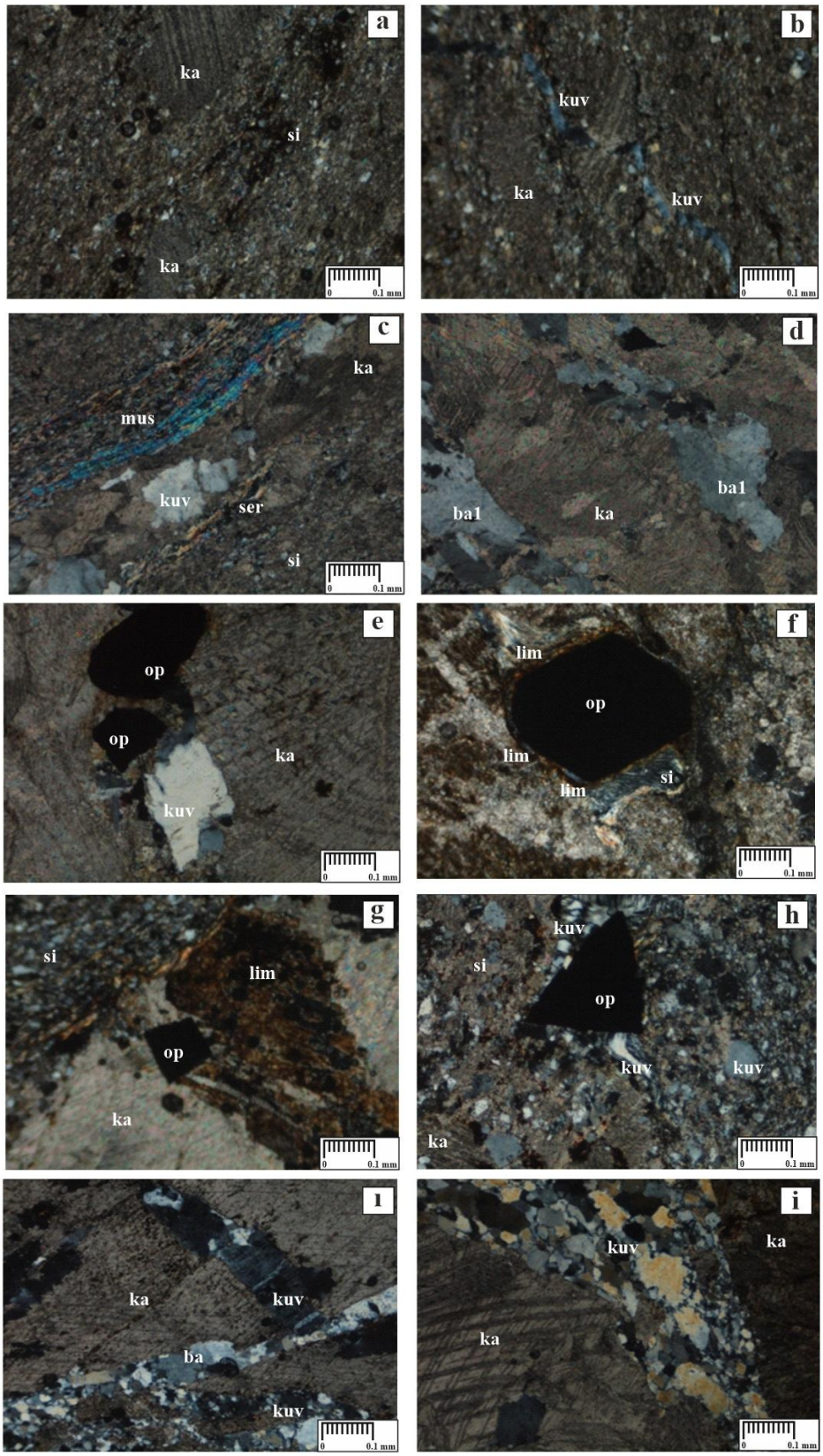

Şekil 5. Kalkşist numunelerinin mikroskop görüntüleri (Deniz, 2019). a) Kalkşist içindeki sparkalsitler (ka) ve silisleşme (si)(KY-3) b) Kalkşist içerisindeki kırılmış ince kuvars (q) damarcığı ve kalsitler (ka), (KY-3) c) Bükülmüş ve muskovit-serizit (mus-ser), sparkalsit (ka) içerisinde breşik kuvars (q) ve silisleşme (si)(BK-6), d) Sparkalsit (ka1) içerisindeki barit (ba1) damarı (BK-6), e) Sparkalsitlerde (ka) kırık içerisinde kuvars (q) breşleri ve opak (op) mineraller (KP-5), f) Zonlanmalı silisleşme (si), özşekilli opak (op) mineral ve limonitleşme (lim) (AS-4), g-h) Sparkalsitler (ka) içerisinde yoğun silisleşme (si), breşik ve tarak yapılı kuvarslar (q) ve yarı özşekilli opak (op) mineral (KP-5), ı-i) Sparkalsitler (ka) içerisinde kırıklara yerleşen barit (ba2) ve kuvars (q) damarları ile breşik yapılı cevherleşme (TM-3).

4.1. Metasedimanter Kayaçların Jeokimyası

4.1.1. Anaoksit ve iz elementler

İnceleme alanındaki Sultandede Formasyonu'na ait düşük dereceli metasedimanter kayaçların kökenini, kaynağını ve tektonik yerleşim alanlarını ortaya koymak için alınan 15 kayaç numunesinin tüm kaya ana oksit, minöroksit ve iz-nadir toprak element analizleri yapılmış ve analiz sonuçları Tablo 1-2'de verilmiştir.

Şist numunelerinin ana element içerikleri %54,00-68,95 SiO_2, %5,05-24,72 Al_2O_3, %0,31-16,95 CaO, %1,30-8,37 Fe_2O_3, %1,15-8,31 K_2O, %0,28-3,67 BaO, %0,15-2,06 MgO, diğer oksitler genellikle %1'in altındadır. Kalkşist numunelerinin ana element içerikleri %33,70-39,32 CaO, %24,30-28,23 SiO_2, %2,11-6,39 Al_2O_3, %0,07-3,14 BaO, %0,44-1,64 Fe_2O_3, %0,85-1,73 Na_2O, %0,23-1,57 K_2O, diğer oksitler %1 in altında değerlere sahiptir. Şist ve kalkşist numunelerinde gözlenen yüksek Al_2O_3 ve K_2O değerleri muskovit ve serizitin bileşiminden, yüksek Fe_2O_3 değerleri opak mineral, limonitleşme ve demiroksitten, yüksek SiO_2 değerleri de kuvars ve silisleşmeden kaynaklanır (Deniz, 2019). Metasedimanter kayaç ve baritli yankayaç örneklerinde Ba (929-34606 ppm), Sr (25,3-6225 ppm), Pb (9,8-600 ppm), Zn (5-116 ppm) ve Cu (1,4-691 ppm) hafif zenginleşmiştir (Tablo 2).

4.1.2. Nadir Toprak Elementleri

İnceleme alanındaki Sultandede Formasyonuna ait metasedimanter kayaç numunelerinin nadir toprak element (NTE) içerikleri Tablo 3'de verilmiştir. Bu numunelerin kondrite göre normalize edilmiş diyagramları Şekil 6'da gösterilmiştir.

Sultandede Formasyonu'nun metasedimanter kayaç numuneleri NTE dağılım diyagramında birbirine benzer eğilimlere sahiptir. Şekil 6 hafif nadir toprak elementlerinden (HNTE) ağır nadir toprak elementlerine (ANTE) doğru bir azalma olduğunu ve HNTE'lerin ANTE'lere kıyasla zenginleştiğini göstermektedir. Bu bulgu, baritin tipik bir özelliğidir, çünkü HNTE iyon boyutlarının (ANTE'ye kıyasla) Ba2+ ile daha fazla benzerliği, HNTE'nin baritte yoğunlaşmasıyla sonuçlanır.

NTE jeokimyasıyla ilgili, kaynak kökenini ve tektonik ortamları belirlemek için çeşitli nadir toprak element oranları kullanılmıştır (Tablo 4). HNTE değerleri 8,7-216,2 ppm, ANTE değerleri de 3,44-21,63 ppm arasındadır. Toplam nadir toprak element değerleri 12,14-234,31 ppm arasında değişmektedir.

HNTE/ANTE 2,53-11,94 arasında ve (La/Yb)N 5,38-17,82 arasında değerlere sahiptir. Belirgin Eu anomalisi (Eu/Eu*= 0,55-0,98), hafif negatif Ce ve pozitif Gd anomalileri mevcuttur. Barit cevherleşmesi yan kayaçlarının ortam koşullarını belirlemek için kullanılan CeN/YbN-YbN ve CeN/SmN-CeN/YbN değerlerinin diyagramları (Şekil 7ab) oluşumunda deniz suyunun egemen olduğunu göstermektedir.

Tablo 1. Sultandede Formasyonu'na ait metasedimanter kayaç numunelerinin ana-minör oksit içerikleri (%) (Deniz, 2019)

		SiO_2	Al_2O_3	Fe_2O_3	CaO	MgO	Na_2O	K_2O	MnO	BaO	TiO_2	P2O5	SrO	SO_3	Ateş Kaybı
BK-1	Şist	54,08	24,72	3,35	0,31	2,06	0,77	8,31	0,03	1,03	1,24	0,19	0,004	0,011	3,72
BK-3		62,73	18,62	5,54	0,31	1,60	0,59	4,68	0,01	0,32	0,97	0,12	0,002	0,071	4,36
BK-8		54,00	13,92	4,74	8,82	1,44	0,45	4,63	0,09	0,46	0,65	0,10	0,026	0,957	8,67
TM-1		61,39	7,57	4,89	11,53	0,62	0,02	2,56	0,20	0,28	0,37	0,18	0,004	0,035	10,65
TM-3		56,44	5,05	1,30	16,95	0,29	0,80	1,15	0,06	2,68	0,31	0,09	0,055	1,553	13,75
AS-3		68,95	7,63	8,37	2,84	0,15	0,20	3,12	0,01	3,67	0,39	1,52	0,030	0,326	2,74
KP-5	Kalkşist	24,45	2,11	1,63	39,32	0,19	0,85	0,23	0,25	0,41	0,10	0,05	0,030	0,196	30,54
BK-6		28,23	3,42	0,44	33,70	0,42	1,31	0,46	0,20	3,14	0,17	0,07	0,580	0,1969	26,31
KY-3		24,30	6,39	1,24	36,61	0,34	1,73	1,07	0,06	0,07	0,39	0,10	0,002	0,002	28,68
AS-4		24,49	6,07	1,64	35,21	0,54	0,99	1,57	0,16	1,04	0,37	0,17	0,040	0,254	28,15
BK-2	Baritli şist	31,97	10,22	2,24	0,11	0,75	1,22	2,91	0,02	29,01	0,48	0,06	0,555	>10	2,40
BK-4		40,50	14,40	3,28	10,90	1,27	0,98	5,19	0,10	7,95	0,66	0,09	0,304	6,280	9,07
AS-1		35,12	7,69	1,50	0,59	0,08	0,18	3,62	0,05	32,18	0,36	0,43	0,186	>10	1,28
KP-2	Baritli kalkşist	1,55	0,06	0,14	15,75	0,08	0,07	0,04	0,05	44,19	0,01	0,03	0,817	>10	11,52
AKD-1		16,07	2,87	0,62	16,05	0,18	0,16	1,03	0,10	31,44	0,12	0,22	0,365	>10	12,14

Tablo 2. Sultandede Formasyonu'na ait metasedimanter kayaç numunelerinin iz element içerikleri (ppm) (Deniz, 2019)

		Ba	Co	Ni	Nb	Rb	Sr	Th	V	Zr	Y	As	Cu	Pb	Zn
BK-1	Şist	10217	10,7	9,1	22,6	317,8	38,9	21,1	139	234,9	23,4	3,2	2,9	247,2	16
BK-3		3246	4,9	9,5	18,2	184,3	25,3	16,6	98	178,6	27,3	3,1	8,8	600,3	32
BK-8		4595	9,7	25,9	11,7	184,2	319,7	13,1	87	110,8	31,6	17,0	3,0	593,4	24
TM-1		2869	23,8	59,1	6,5	85,1	104,9	9,3	40	96,6	16,9	18,2	690,9	44,7	20
TM-3		25123	2,3	6,2	5,0	36,0	593,5	6,3	26	91,8	7,8	6,2	115,8	94,0	13
AS-3		34606	3,4	96,7	6,6	57,1	269,6	10,8	80	144,9	26,6	245,1	11,8	82,4	116
KP-5	Kalkşist	4156	5,3	9,1	1,4	7,3	521,0	2,6	10	23,7	40,6	9,1	3,2	20,1	5
BK-6		29896	0,5	0,2	2,7	15,6	5573,8	3,8	16	46,8	20,1	0,6	1,4	73,8	7
KY-3		929	6,4	3,1	7,0	36,7	73,7	7,8	38	104,5	13,2	1,3	2,5	75,5	8
AS-4		10068	13,6	38,3	6,1	36,7	285,0	8,0	33	116,4	20,0	12,3	2,6	92,0	20
BK-2	Baritli şist	>50000	11,5	11,4	8,9	102,9	4635,5	7,1	73	100,0	5,4	8,6	4,4	191,6	11
BK-4		>50000	29,2	37,1	11,5	136,8	2688,8	11,7	109	110,0	14,6	19,9	11,5	280,0	23
AS-1		>50000	41,9	42,5	6,8	64,7	1417,2	7,2	55	100,2	12,5	17,7	8,1	232,0	47
KP-2	Baritli kalkşist	>50000	<0,2	0,2	<0,1	0,4	6255,1	<0,2	<8	2,3	2,5	0,8	1,4	9,8	4
AKD-1		>50000	1,5	2,6	2,6	24,4	2976,7	3,6	19	41,1	13,2	10,9	80,3	11,6	6

Tablo 3. Sultandede Formasyonu'na ait metasedimanter kayaç numunelerinin nadir toprak element içerikleri (ppm) (Deniz, 2019)

		La	Ce	Pr	Nd	Sm	Eu	Gd	Tb	Dy	Ho	Er	Tm	Yb	Lu
BK-1	Şist	56,9	101,3	11,01	39,1	6,80	1,09	5,48	0,78	4,43	0,89	2,75	0,43	2,90	0,45
BK-3		49,1	94,6	10,80	39,6	6,52	1,08	5,37	0,77	4,67	0,94	2,80	0,41	2,57	0,40
BK-8		40,9	78,9	9,28	34,9	6,65	1,47	5,76	0,89	5,59	1,12	3,26	0,45	2,93	0,44
AS-3		20,4	41,2	6,21	29,1	6,95	1,43	6,90	0,92	4,98	0,87	2,23	0,29	1,57	0,22
TM-1		9,6	17,7	2,51	11,3	2,56	0,52	2,73	0,44	2,78	0,58	1,74	0,27	1,69	0,27
TM-3		6,3	11,1	1,49	6,1	1,29	0,27	1,44	0,19	1,22	0,25	0,80	0,12	0,79	0,13
KY-3	Kalkşist	21,3	36,7	4,17	14,6	2,64	0,46	2,28	0,34	2,17	0,41	1,28	0,20	1,27	0,21
AS-4		20,7	39,1	4,95	18,9	3,64	0,67	3,34	0,48	3,11	0,59	1,72	0,25	1,67	0,25
BK-6		12,6	26,5	3,19	14,2	3,57	1,19	3,84	0,52	3,12	0,60	1,73	0,27	1,58	0,23
KP-5		30,7	52,7	6,54	25,8	5,79	1,85	6,04	0,96	6,30	1,26	3,29	0,50	2,90	0,38
BK-2	Baritli şist	10,2	15,4	1,72	6,5	1,14	0,02	2,89	0,16	0,67	0,18	0,60	0,11	0,82	0,15
BK-4		40,1	60,1	6,70	24,5	4,38	-	4,32	0,49	2,75	0,55	1,67	0,27	1,83	0,28
AS-1		17,6	25,7	2,92	12,0	2,70	-	5,02	0,41	2,23	0,42	1,16	0,17	1,02	0,16
KP-2	Baritli kalkşist	3,7	2,7	0,39	1,5	0,43	-	2,54	0,07	0,50	0,04	0,11	0,02	0,14	0,02
AKD-1		13,3	21,8	3,01	12,9	3,05	-	4,70	0,38	2,20	0,35	1,12	0,15	0,98	0,14

Tablo 4. Sultandede Formasyonu'na ait metasedimanter kayaç numunelerinin nadir toprak element oranları (ppm)

		REE	LREE	HREE	LREE/HREE	Eu/Eu*	Ce/Ce*	CeN/SmN	CeN/YbN	YbN	LaN/YbN
BK-1	Şist	234,31	216,2	18,11	11,94	0,55	0,97	3,60	9,04	13,88	13,23
BK-3		219,63	201,7	17,93	11,25	0,56	0,99	3,50	9,52	12,30	12,88
BK-8		192,54	172,1	20,44	8,42	0,73	0,97	2,86	6,97	14,02	9,41
AS-3		123,28	105,3	17,98	5,86	0,63	0,88	1,43	6,79	7,51	8,76
TM-1		54,70	44,2	10,5	4,21	0,60	0,87	1,67	2,71	8,09	3,83
TM-3		31,54	26,6	4,94	5,38	0,61	0,87	2,08	3,63	3,78	5,38
KY-3	Kalkşist	88,06	79,9	8,16	9,79	0,57	0,94	3,35	7,47	6,08	11,31
AS-4		99,41	88,0	11,41	7,71	0,59	0,93	2,59	6,06	7,99	8,36
BK-6		73,19	61,3	11,89	5,16	0,98	1,01	1,79	4,34	7,56	5,38
KP-5		145,03	123,4	21,63	5,71	0,96	0,90	2,20	4,70	13,88	7,14
BK-2	Baritli şist	40,58	35,0	5,58	6,27	-	0,88	3,26	4,86	3,92	8,39
BK-4		147,96	135,8	12,16	11,17	-	0,88	3,31	8,49	8,76	14,77
AS-1		71,49	60,9	10,59	5,75	-	0,86	2,30	6,52	4,88	11,63
KP-2	Baritli kalkşist	12,14	8,7	3,44	2,53	-	0,54	1,52	4,99	0,67	17,82
AKD-1		64,12	54,1	10,02	5,40	-	0,83	1,72	5,75	4,69	9,15

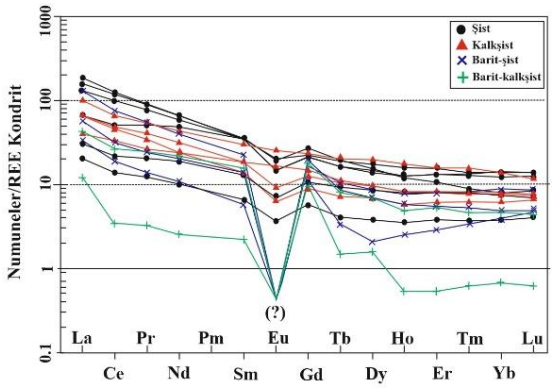

Şekil 6. İncelenen metasedimanter kayaç numunelerinin kondrite göre normalize edilmiş NTE dağılım diyagramı (Boynton, 1984'den değiştirilerek).

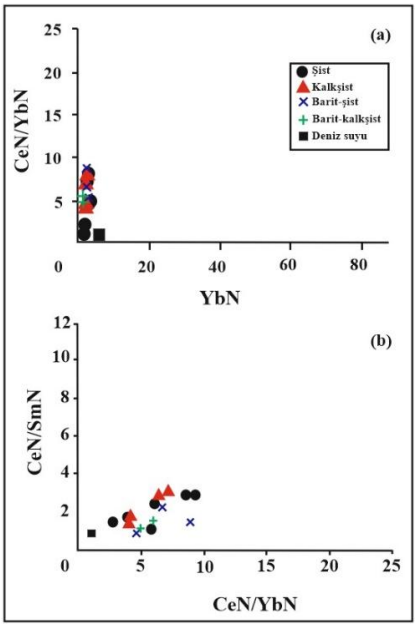

Şekil 7. İncelenen metasedimanter kayaç numunelerinin normalize edilmiş a) CeN/YbN – YbN ve b) CeN/SmN – CeN/YbN diyagramı.

5. Tartışma

Erken Paleozoik yaşlı Çaltepe ve Seydişehir Formasyonları, Türkiye'nin güneyinde Toros Kuşağı boyunca birçok bölgede, Sultandağı-Konya (Eren, 1990), Hadim-Konya, Anamur ve Silifke ilçeleri arasındaki alan (Turan, 2000), Tufanbeyli-Attepe-Adana (Özgül vd., 1973; Küpeli, 2010) ve Amanos Dağı-İskenderun ve Güneydoğu Anadolu'da Pembegül-Tut-Adıyaman ve Derik-Mardin (Ketin, 1966) bölgelerinde varlığı bilinmektedir. Seydişehir Formasyonu metapelitik kayaçların kuvars fillit ve kalkerli metafillit içerdiği, metapsamitlerinde metakumtaşı-metasilttaşı içerdiği, ayrıca bu kayaçların birincil dokusunun orijinal parçaların çözünmesi, taze tanelerin parçalanması ve metamorfizma sırasında basınç çözeltisi ve yeniden kristalleşme süreçleri tarafından yok edildiği belirtilmiştir (Karadağ, 2014). Bu çalışmada metamorfik kayalar sleyt, fillit, metakumtaşı ve kalkşist, muskovit-serizit-kuvars şist bileşimindedir. Ayrıca, metasedimentlerin çok düşük derecede metamorfizmaya uğradığı, metamorfizmadan ve tektonizmadan kaynaklanan basınç ve rekristalize süreçlerinden dolayı kısmen birincil dokuların silindiği ve ayrışmadan dolayı opak mineral oluşumunun varlığı petrografik analizler sonucunda gözlenmiştir. İllit kristalinitesi ve bo değerlerinin sonucuna göre Çelik vd. (1991) Çaltepe bölgesindeki Seydişehir Formasyonu'nun epimetamorfik-ankimetamorfik koşullar altında metamorfize olduğunu, Bozkaya vd. (2006) da Sandıklı-Afyon bölgesinde yüksek ankizonal ile epizonal koşullar altında metamorfize olduğunu ortaya koymuştur.

5.1. Sınıflandırma

Sultandede Fromasyonu metasedimanter kayaç numunelerinin SiO_2/Al_2O_3-Na_2O/K_2O (Pettijohn vd., 1972; Herron, 1988) ve Fe_2O_3/K_2O (Herron, 1988) oranlarının logaritmasının alınarak sınıflama diyagramları oluşturulmuştur (Şekil 8).

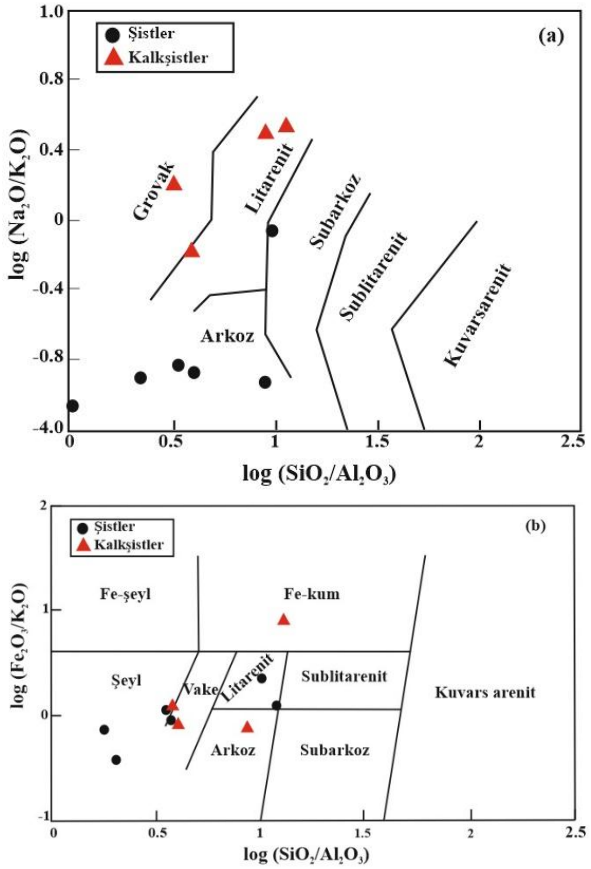

Şekil 8. İncelenen metasedimanter kayaç numunelerinin jeokimyasal sınıflaması a) log(Na_2O/K_2O)-log(SiO_2/Al_2O_3) diyagramı (Pettijohn vd., 1972; Herron, 1988'den değiştirilerek), b) log(Fe_2O_3/K_2O)-log(SiO_2/Al_2O_3) diyagramı (Herron, 1988'den değiştirilerek).

Şekil 8a'daki diyagramlara göre, şistlerin çoğunluğu arkoz, bir tanesi subarkoz alanına düşerken, kalkşistler grovak ve litarenit alanına düşmekte, Şekil 8b'de şistler şeyl ve litarenit, kalkşistler şeyl, vake, arkoz ve Fe-kum alanında görülmektedir.

Şengün (2023) Biga Yarımadasındaki Örenli metasedimanter kayaçlarının logSiO_2/Al_2O_3-logNa_2O/K_2O diyagramında grovak alanında olduğunu belirtmiştir. logSiO_2/Al_2O_3-log Fe_2O_3/K_2O diyagramı kullanılarak Kuzey Çin'de yer alan Lüliang kompleksi içerisindeki Yuanjiacun formasyonu metasedimanter kayaçları arkoz, şeyl, vake ve Fe-şeyl (Wang vd., 2015), Konya-Seydişehir metasedimanter kayaçları da şeyl, vake, arkoz, litarenit, subarkoz, subliteranit, Fe-şeyl ve Fe-kum (Karadağ, 2014) alanlarına düşmektedir.

5.2. Kaynak Kayaç

Sultandede Formasyonu metasedimanter kayaç numunelerinin major element içerikleri kullanılarak yapılan ayırım fonksiyon diyagramında (Roser ve Korsch, 1988), şistler kuvarslı sedimanter, felsik magmatik ve ortaç magmatik kökende, kalkşistler ise ortaç magmatik köken alanındadır. Ayırım diyagramında Şengün (2023), Ören şist örneklerinin ortaç magmatik kaynaktan felsik magmatik kaynağa doğru geçiş gösterdiğini, Wang vd. (2015), metasedimanter kayaçların çoğunlukla magmatik kaynaklardan çok az katkı ile önceden var olan bir tortul mostradan türediğini belirtmiştir.

La/Th ve Hf grafiğinde (Şekil 9), Sultandede Formasyonuna ait şist ve kalkşist kayaç numunelerinden gelen tüm veriler, felsik ve geri dönüştürülmüş eski tortul kaynaklar arasında farklı oranlarda bir karışıma sahip olduğunu ve üst kıtasal kabuk eğilimli olduğunu göstermektedir. Yuanjiacun Formasyonu'na ait metasedimanter kayaçların kaynağı benzerlik gösterse de örnekler alt kıtasal kabuğa doğru eğilimlidir (Wang vd. 2015). Karadağ (2014) La/Th ve Hf diyagramına göre Seydişehir metaklastik kayaçları için felsik ve ortaç kaynak kayaçlarının bir karışımı olduğunu belirtmiştir.

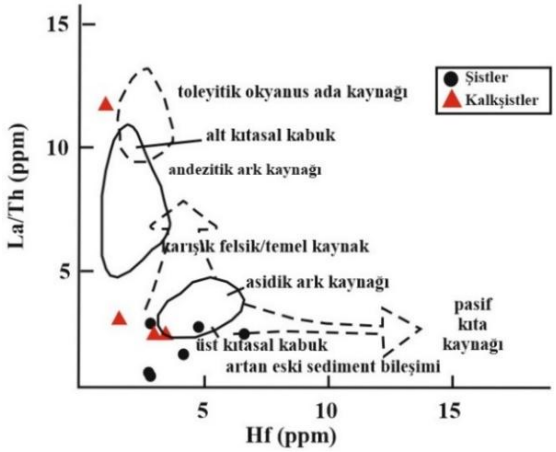

Şekil 9. Metasedimanter kayaçları için kaynak kayaç ayrım diyagramları (La/Th ve Hf) (Floyd ve Leveridge, 1987'den değiştirilerek)

Metasedimanter kayaçların kökenini belirlemek için ayırım fonksiyon diyagramı (Roser ve Korsch, 1988) kullanılmıştır (Şekil 10).

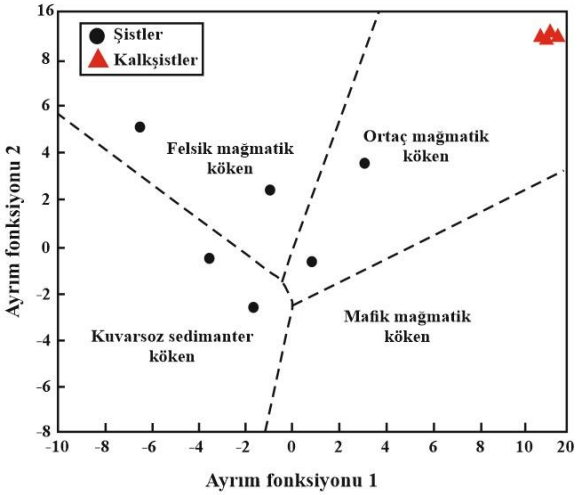

Şekil 10. Sultandede metasedimanter kayaçları için ayrım fonksiyon diyagramı (Roser ve Korsch, 1988'den değiştirilerek).

Şistler kuvarsoz sedimanter, felsik ve ortaç mağmatik kaynakta, kalkşist örnekleri ise ortaç mağmatik kaynak

alanındadır. Bu sonuç metasedimanterlerin çoğunlukla mağmatik kaynaklardan türediği ve bir kısmınında geri dönüştürülmüş önceden var olan sedimanter kaynaktan türediğini gösterir. Şengün (2023), kaynağının felsik ve mafik kaynağın karşımı olduğunu, Wang vd. (2015), ise metasedimanterlerin bazılarının sedimanter alanlardan bazılarının da mağmatik kaynaktan türediğini belirtmiştir.

Sultandede Formasyonu'na ait metasedimanter kayaç numunelerinin NTE içeriklerinden elde edilen Kondrite göre normalize edilmiş NTE dağılım desenlerinde HNTE'in zenginleştiği gözlenmiştir. Bunun yanında, negatif Eu ve Ce anomalileri ve pozitif Gd anomalisi de görülmektedir. Bu durum metasedimanter kayaçların felsik, tortullaşma sonrası oluştuğu ve kıta kenarı rejimini karakterize ettiğini göstermektedir. Barit cevherleşmesinin yan kayacı olması sebebiyle de pozitif Gd anomalisi göstermesi muhtemeldir. Eu anomalilerinin genellikle kaynak kayadan geldiği, Ce anomalilerinin ise tortullaşma sonrası oluştuğu öne sürülmüştür (McLennan, 1989). Belirgin Eu anomalileri, plajiyoklaz zenginleşmesini (Taylor ve McLennan, 1985), üst kıtasal kabuk ortamından gelen bir felsik kaynağı ve şiddetli bir aşınma (ve geri dönüşüm) (Bhai vd., 2015) olduğunu göstermektedir. Düşük Ce anomalileri ile (Ce/Ce* ~0.29), okyanus havzası tabanı ortamından gelenler iyi gelişmiş ancak daha az aşırı Ce anomalileri ile (Ce/Ce* ~0.55) ve kıta kenarı rejimlerinden gelenler hiç veya hafif anomalilerle (Ce/Ce* ~0.90 ila 1.30) karakterize edilir (Murray vd., 1990). Elderfield ve Pagett (1986), oksik diyajenez geçiren derin okyanus sedimanlarının çekirdeklerinde negatif Ce anomalisi tespit etmiştir. Gd anomalilerinin modern okyanus barit oluşumlarında (Griffith ve Paytan, 2012), soğuk sızıntı karbonatlarında (Ge vd., 2010) ve karbonatlarda (Jurković vd., 2010; Zarasvandi vd., 2014) varolabileceği belirtilmiştir. NTE bolluğu ayrıca tortul kayaçların kaynağını çıkarmak için de kullanılmıştır (McLennan vd., 1993). Genellikle, mafik kayaçlar düşük HNTE/ANTE oranları ve Eu anomalileri içermezken, felsik kayaçlar genellikle daha yüksek HNTE/ANTE oranları ve negatif Eu anomalileri içerir (Taylor ve McLennan, 1985; Roddaz vd., 2006).

5.3. Tektonik Yerleşim

Sedimanter ve metasedimanter kayaçların bileşimi farklı tektonik ortamlarda çeşitlilik göstermesi sebebiyle TiO_2 ve (Al_2O_3/SiO_2)-(Fe_2O_3+MgO), $\log(K_2O+Na_2O)$–SiO_2 ve Th–Co–Zr/10 diyagramları tektonik ortamları ayırt etmek için kullanılmaktadır (Şekil 11) (Bhatia ve Crook, 1986; Roser ve Korsch, 1988; Bhatia, 1983; McLennan, 2001). Bu çalışmada numunelerin çoğunluğu pasif kıta kenarı, aktif kıta kenarı ve kıtasal ada yayında (Şekil 11a-c), geneli de yay alanında (Şekil 11d) gözlenmiştir. Metasedimanter kayaçların tektonik ortamı için kullanılan diyagramlarda Şengün (2023) pasif kıta kenarı ve okyanusal ada yayı, Wang vd. (2015) pasif kıta kenarı ve kıtasal ada yayı, kıtasal ada yayı, pasif ve aktif kıta kenarı, Karadağ (2014) ve Augustsson ve Bahlburg (2008) kıtasal ada yayı, pasif ve aktif kıta kenarı tektonik ortamı olduğunu ileri sürmüşlerdir.

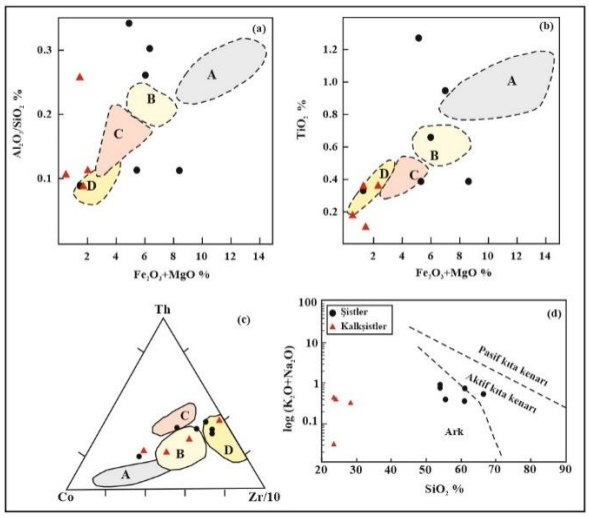

Şekil 11. Sultandede Formasyonuna ait metasedimanter kayaç numunelerinin major ve iz element içeriklerine göre tektonik ortam ayrım diyagramları, **a-b)** Bhatia (1983'den değiştirilerek); **c)** Bhatia and Crook (1986'dan değiştirilerek)**; d)** Roser and Korsch, (1988'den değiştirilerek). (A- Okyanus ada yayı, B-Kıtasal ada yayı, C-Aktif kıta kenarı, D-Pasif kıta kenarı).

Şist ve kalkşistlerin Th/U değerleri 1,48 ile 11,14 arasında ve ortalama değeri 6,87'dir. Örnekler üst kabuk değerinden daha yüksek Th/U oranlarına sahip olduğunu ve önceki aşınma eğilimini takip ettiğini ortaya koymaktadır (Şekil 12), bu da metasedimanter kayaçların yoğun aşınmaya uğradığını göstermektedir. Bu veriler Wang vd. (2015)'in inceledikleri Yuanjiacun formasyonu metasedimanterleri ile benzer sonuçlar göstermektedir.

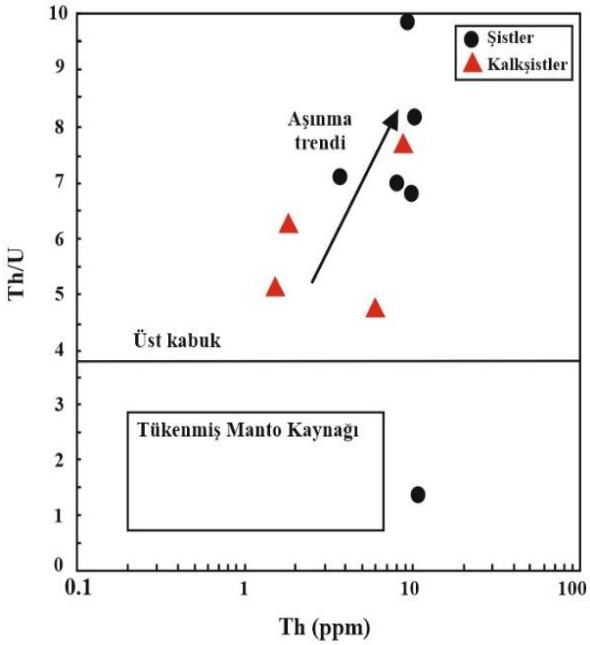

Şekil 12. Metasedimanterlerin Th/U ve Th tektonik ortam diyagramı (McLennan vd., 1993'den değiştirilerek)

Çoğu üst kabuk kayası için Th/U genellikle yaklaşık 3,5 ile 4,0'dır. Genellikle, oksitleyici koşullar altında aşınma ve tortul geri dönüşümü genellikle U^{4+}'nin U^{6+}'ye oksidasyonuyla sonuçlanır ve U^{6+} daha çözünürdür. Çökelme sırasında çözünme ve kayıp birbirini takip eder, böylece Th/U oranı yükselir (McLennan vd., 1980; McLennan vd., 1993).

Şist ve kalkşistlerin Ni/Co değerleri 0,40 ile 2,82 arasında, şistlerin bir numunesi de 28.47 değerindedir. Metasedimanter kayaç örneklerinin Ni/Co ve V/(V + Ni) diyagramına göre Ni/Co oranları oksik ortamları, V/(V + Ni) oranları da şistler için disoksik, anoksik ve öksinik, kalkşistler için ise disoksik ve öksinik koşulları göstermektedir (Şekil 13).

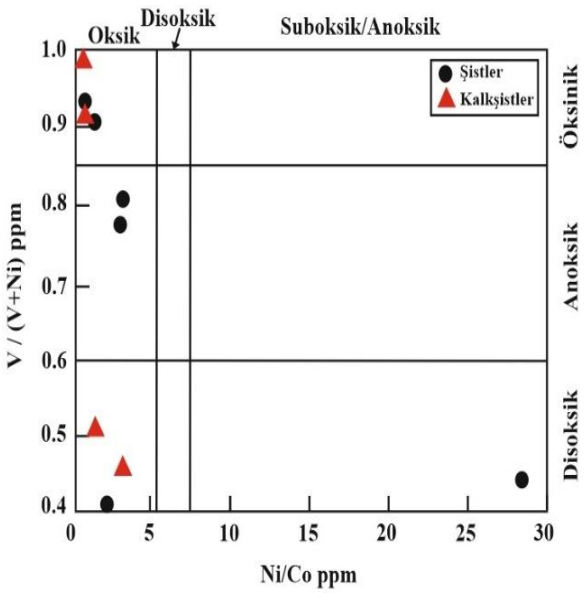

Şekil 13. Sultandede metasedimanter kayaç numunelerinin Ni/Co ve V/(V + Ni) ikili diyagramı (Rimmer, 2004'den değiştirilerek). (V/(V + Ni) aralıkları Hatch ve Leventhal (1992)'dan alınmıştır)

Jones ve Manning (1994), 5'in altındaki Ni/Co oranlarının oksik ortamları, 5'in üzerindeki oranların ise suboksik ve anoksik ortamları, V/(V + Ni) oranlarının da 0,84'ten büyük öksinik koşulları, 0,54-0,82 anoksik koşulları ve 0,46-0,60 disoksik koşulları gösterdiğini öne sürmüşlerdir. Mir (2015), Doğu Hindistan, Singhbhum mobil kuşağındaki Neo-Arkeyen sonrası şistlerin Ni/Co ve V/ (V+Ni) oranladığında anoksik ile öksinik redoks koşullarını yansıttığını, Xu vd. (2012) ise Güney Çin'deki Alt Kambriyen siyah şeyllerinin çoğunluğunun öksinik koşullara ait olduğunu ve bu durumunda yüksek Ni/Co oranlarına yansıdığını belirtmişlerdir.

5. Sonuç

Orta Toroslar'da Geyikdağı Birliği içerisindeki çok düşük dereceli metamorfizma geçiren Sultandede Formasyonu metamorfik kayaçlarının kökenini, kaynak kayasını ve tektonik ortam koşullarına göre yerleşimini ortaya koymak amacıyla petrografik ve ana oksit, iz element ve nadir toprak elementi analizleri yapılmıştır. Bu analizler sonucunda elde edilen sonuçlar aşağıda verilmiştir:

- Arazi gözlemlerine ve petrografik incelemelerin sonucuna göre metamorfik kayaların sleyt, fillit, metakumtaşı, metakarbonatlar, yumrulu metakireçtaşı ve kalkşist, muskovit-serizit-kuvars şist, metakuvarsit ve mermer bileşiminde olduğu saptanmıştır. Şist numunelerinin petrografik incelemesi sonucu bu kayaların genel olarak muskovit, serizit, kuvars, barit, opak mineral ve demiroksit ayrışma mineralleri içerdiği, kalkşist kayacının da kalsit, kuvars, barit, serizit, muskovit ve limonit kapsadığı tespit edilmiştir.
- Sultandede Formasyonu metasedimanter kayaçların jeokimyasal sınıflamalarının sonucunda; şistlerin arkoz-subarkoz, şeyl ve litarenit bileşiminde, kalkşistlerin grovak, litarenit, şeyl, vake, arkoz ve Fe-kum bileşiminde olduğu belirlenmiştir.
- Kondrite göre normalize edilmiş NTE dağılım desenlerinde Sultandede metamorfik kayaçlarında hafif nadir toprak elementlerinden (HNTE) ağır nadir toprak elementlerine (ANTE) doğru bir azalma ve HNTE'ler ANTE'lere göre göreceli olarak zenginleşme göstermektedir. Eu (Eu/Eu*= 0,55-0,98) ve Ce da belirgin negatif anomali ve pozitif Gd anomalisi gözlenmiştir. Metasedimanter kayaçların felsik, tortullaşma sonrası oluştuğu ve kıta kenar rejimini karakterize ettiği tespit edilmiştir.
- Kaynak kayaç diyagramlarına göre (La/Th ve Hf) şist ve kalkşistlerden gelen tüm veriler, felsik ve ortaç magmatik kaynakların geri dönüştürülmüş yaşlı tortul kaynaklar arasında farklı oranlarda bir karışıma işaret ettiğini ve üst kıtasal kabuk eğilimi gösterdiğini belirtmektedir.
- Sultandede Formasyonundan alınan şist ve kalkşist numunelerinin ortalama Th/U değeri 6,87 olup, üst kabuk değerinden (3,82) daha yüksektir. Bu değer, önceki aşınma eğilimini takip ettiğini ve metasedimanterlerin yoğun aşınmaya maruz kaldığına işaret etmektedir. Ni/Co oranlarına göre incelenen metasedimanter kayaçların oksik ortamda ve V/(V + Ni) oranlarına göre de disoksik, anoksik ve öksinik koşullarına göre çökeldiği düşünülmektedir.

Katkı Oranı Beyanı

Yazarların katkı yüzdeleri aşağıda verilmiştir. Yazarlar makaleyi incelemiş ve onaylamıştır.

	O.C	A.S.D	D.K
K	50	25	25
T	40	20	40
Y	40	20	40
VTI	35	30	35
VAY	40	20	40
KT	40	30	30
YZ	35	30	35
KI	30	30	40
GR	40	20	40
PY	40	30	30
FA	40	40	20

K= kavram, T= tasarım, Y= yönetim, VTI= veri toplama ve/veya işleme, VAY= veri analizi ve/veya yorumlama, KT= kaynak tarama, YZ= Yazım, KI= kritik inceleme, GR= gönderim ve revizyon, PY= proje yönetimi, FA= fon alımı.

Çatışma Beyanı

Yazarlar bu çalışmada hiçbir çıkar ilişkisi olmadığını beyan etmektedirler.

Etik Onay Beyanı

Bu araştırmada hayvanlar ve insanlar üzerinde herhangi bir çalışma yapılmadığı için etik kurul onayı alınmamıştır.

Destek ve Teşekkür Beyanı

Bu çalışma, ikinci yazarın yüksek lisans tezinin bir kısmına ait verilerden yararlanılarak üretilmiştir. Yazarlar bu çalışmayı 4495-YL2-15 No'lu proje ile maddi olarak destekleyen Süleyman Demirel Üniversitesi Bilimsel Araştırma Projeleri Yönetim Birimi Başkanlığı'na teşekkürlerini sunarlar. Ayrıca, saha çalışmaları sırasında maddi ve manevi desteklerinden dolayı ADO Madencilik A.Ş. personellerine teşekkür ederler.

Kaynaklar

Augustsson C, Bahlburg H. 2008. Provenance of late Palaeozoic metasediments of the Patagonian proto-Pacific margin (southernmost Chile and Argentina). Inter J Earth Sci, 97: 71-88.

Ayhan A, Karadağ MM. 1985. Geology and origin of bauxitic iron and ferruginous bauxite deposits in the south of Şarkikaraağaç, (Isparta). Geol Bull Turk, 28: 137–146.

Ayhan A. 1986. Hüyük (Beyşehir) Yöresinin Alt-Orta Kambriyen Yaşlı Birimlerde Bulunan Barit Zuhurlarının Özellikleri. Selçuk Üni Müh-Mim Fak Derg, 1: 1-17.

Bhai Y, Liu Z, Sun P, Liu R, Hu X, Zhao H, Xu Y. 2015. Rare earth and major element geochemistry of Eocene fine-grained sediments in oil shale-and coal-bearing layers of the Meihe Basin, Northeast China. J Asian Earth Sci, 97: 89-101.

Bhatia MR, Crook KA. 1986. Trace element characteristics of graywackes and tectonic setting discrimination of sedimentary basins. Contributions to Miner and Petrol, 92(2): 181-193.

Bhatia MR. 1983. Plate tectonics and geochemical composition of sandstones. The J Geol, 91(6): 611-627.

Blumenthal MM. 1947. Beyşehir-Seydişehir hinterlandındaki Toros dağlarının jeolojisi. Miner Resource and Explor Pub, Series D, 2: 1-242.

Boynton WV. 1984. Cosmochemistry of the rare earth elements: Meteorite studies. Chapter 3. Dev. Geochem 2: 63–114.

Bozkaya O, Gürsu S, Göcüoglu MC. 2006. Textural and mineralogical evidence for a Cadomian tectonothermal event in the eastern Mediterranean (Sandıklı–Afyon area, western Taurides, Türkiye). Gondwana Res, 1: 301–315.

Cengiz O, Kuşcu M. 1993. Çarıksaraylar (Şarkikaraağaç-Isparta) Kuzeyinin Jeolojisi ve Kurşunlu Barit Yatakları. TJK Bült, 36: 63-74.

Cengiz O, Kuşcu M. 2002. Şarkikaraağaç (Isparta) ile Hüyük (Konya) Arasındaki Barit Yataklarının Jeokimyasal Özellikleri ve Kökeni. MTA Derg, 123-124: 67-89.

Cengiz O. 1991. Çarıksaraylar (Şarkikaraağaç-Isparta) Kuzeyinin Jeolojisi ve Kurşunlu Barit Yatakları.Yüksek Lisans Tezi, Akdeniz Üni, Fen Bil Enst, Isparta, ss:75.

Cengiz O. 1997. Şarkikaraağaç (Isparta) ile Hüyük-Doğanhisar (Konya) Arasındaki Barit Yatakları ve Oluşumu. Doktora Tezi, Süleyman Demirel Üni, Fen Bil Enst, Isparta, ss: 317.

Condie KC, Noll Jr, PD, Conway CM. 1992. Geochemical and detrital mode evidence for two sources of Early Proterozoic sedimentary rocks from the Tonto Basin Supergroup, Central Arizona. Sed Geol, 77(1-2): 51-76.

Cullers RL, Stone J. 1991. Chemical and mineralogical comparison of the Pennsylvanian Fountain Formation, Colorado, USA (an uplifted continental block) to sedimentary rocks from other tectonic environments. Lith, 27(2): 115-131.

Cullers RL. 2000. The geochemistry of shales, siltstones and sandstones of Pennsylvanian–Permian age, Colorado, USA: implications for provenance and metamorphic studies. Lith, 51(3): 181-203.

Çelik M, Karakaya N, Turan A. 1991. Metamorphism and mineralogic characteristics of Paleozoic aged clays: south and southwest of Konya. In: Zor, M. (Ed.), Fourth National Clay Symposium, Proceedings 62–73 (in Turkish with English abstract).

Dean VT, Monod O. 1970. The Lower Paleozoic Stratigraphy and Faunas of the Taurus Mountains Near Beyşehir, Türkiye. I. Stratigraph Bull Brit Mus Nat Hist Geol. 19(8): 411-426.

Dean WT, Özgül N. 1979. Orta Toroslar'da Çaltepe Formasyonunun Bağbaşı (Hadım-Konya) Yöresindeki Yüzeylemesinde Bulunan Orta Kambriyen Trilobitleri. MTA Derg, 92:1-7.

Dean WT, Özgül N. 1994. Cambrian rocks and faunas, Hüdai area, Tauride Mountains, southwestern Türkiye. Bulletin dei 'Institut Royal Des Scienes Naturelles de Beigique, Sci de la Terra, 64: 5–20.

Demirkol C, Sipahi H. 1979. Bağkonak–Çimendere-Muratdağı (Isparta) Yöresinin Jeolojisi. Jeo Müh, 7: 29-36.

Demirkol C. 1977. Yalvaç-Akşehir Dolayının Jeolojisi. S.Ü. Jeoloji Bölümü, Doçentlik Tezi, Konya Selçuk Üniversitesi, Yerbilimleri Bölümü (Yayınlanmamış).

Deniz AS. 2019. Dinek (Şarkikaraağaç-Isparta) Bölgesindeki Barit Cevherinin ve Yan Kayaçlarının Mineralojik ve Jeokimyasal Özellikleri. Yüksek Lisans Tezi, Süleyman Demirel Üni, Fen Bil Enst, Isparta, ss: 81.

Desprairies A, Gutnic M. 1972. Les Gresrouges au Sommet du Paleozoique du Masif du Sultan Dağ et Les Niveaux (North-East du Taururs Occiedentale, Turquie) Aanalyses Chimi Gues

et Mineraloqie Ques Signification Paleogeographie. Bull de La Soc Geol de France Ser (7) tem XII., 3: 505-514.

Dickinson WR, Suczek CA. 1979. Plate tectonics and sandstone compositions. AAPG Bull, 63(12): 2164-2182.

Dostal J, Keppie JD. 2009. Geochemistry of low-grade clastic rocks in the Acatlán Complex of southern Mexico: Evidence for local provenance in felsic–intermediate igneous rocks. Sed Geol, 222(3-4): 241-253.

Elderfield H, Pagett R. 1986. Rare earth elements in ichthyoliths: variations with redox conditions and depositional environment. Sci the Tot Envir, 49: 175-197.

Elmas N, Kumral M, Süner F, Taşdelen S. 2012. Stratiform barite deposits hosted in metamorphic assemblages of Dinek and surrounding regions, Isparta, Türkiye. J Asian Earth Sci, 48: 150-159.

Erdoğan B, Uchman A, Güngör T, Özgül N. 2004. Lithostratigraphy of the Lower Cambrian metaclastics and their age based on trace fossils in the Sandıklı region, southwestern Türkiye. Geob, 37: 346–360.

Eren Y. 1990. Tectonic features of the Sultandagları Massif between Engili(Aksehir) and Bagkonak villages. Geol Bull Turk, 1: 39–51.

Floyd PA, Leveridge BE. 1987. Tectonic environment of the Devonian Gramscatho basin, south Cornwall: framework mode and geochemical evidence from turbiditic sandstones. J Geol Soc, 144(4): 531-542.

Ge C, Shi L, Yang H, Tang S. 2010. Nonisothermal melt crystallization kinetics of poly (ethylene terephthalate)/barite nanocomposites. Polymer Comp, 31(9): 1504-1514.

Ghienne JF, Le Heron DP, Moreau J, Denis M, Deynoux M. 2007. The Late Ordovician glacial sedimentary system of the North Gondwana platform. Glacial Sed Proc Prod, 295-319.

Ghienne JF, Monod O, Kozlu H, Dean WT. 2010. Cambrian–Ordovician depositional sequences in the Middle East: a perspective from Türkiye. Earth-Sci Rev, 101(3-4): 101-146.

Göncüoğlu MC, Göncüoğlu Y, Kozlu H, Kozur H. 2004. Geological evolution of the Taurides during the infra-Cambrian to Carboniferous period: a Gondwana perspective based on new biostratigraphic findings. Geol Carp, 55: 433–447.

Göncüoğlu MC, Kozlu, H. 2000. Early Paleozoic evolution of the NW Gondwanaland: data from southern Türkiye and surrounding regions. Gondwana Res, 3(3): 315-324.

Gonzales-Inca C, Valkama, Lill, JO, Slotte J, Hietaharju E, Uusitalo R. 2018. Spatial modeling of sediment transfers and identification of sediment sources during snowmelt in an agricultural watershed in boreal climate. Sci the Tot Envir, 612: 303-312.

Griffith EM, Paytan A. 2012. Barite in the ocean–occurrence, geochemistry and palae oceanographic applications. Sed, 59 (6): 1817-1835.

Guo Y, Li C, Wang C, Xu J, Jin C, Yang S. 2021. Sediment routing and anthropogenic impact in the Huanghe River catchment, China: An investigation using Nd isotopes of river sediments. Water Resources Res, 57(9): e2020WR028444.

Gürsu S, Göncüoğlu MC, Bayhan H. 2004. Geology and petrology of the Pre-Middle Cambrian rocks in Sandıklı area: implications for the Pan-African evolution in NW Gondvanaland. Gondwana Res, 7(4): 923-935.

Gürsu S. 2002. İç Batı Anadolu (GB Afyon) bölgesindeki Pre-Paleozoyik magmatik kayaçların jeolojisi ve petrojenezi. Doktora Tezi, Hacettepe Üni, 1–204

Hara H. Kunii M, Hisada KI, Ueno K, Kamata Y, Srichan W, Charusiri P, Charoentitirat T, Watarai M, Adachi Y, Kurihara T. 2012. Petrography and geochemistry of clastic rocks within the Inthanon zone, northern Thailand: implications for Paleo-Tethys subduction and convergence. J Asian Earth Sci, 61: 2-15.

Hatch JR, Leventhal JS. 1992. Relationship between inferred redox potential of the depositional environment and geochemistry of the Upper Pennsylvanian (Missourian) Stark Shale Member of the Dennis Limestone, Wabaunsee County, Kansas, USA. Chem Geol, 99(1-3), 65-82.

Herron MM. 1988. Geochemical classification of terrigenous sands and shales from core or log data. J Sed Res, 58(5): 820-829.

Hifzurrahman Nasipuri P, Joshi KB. 2023. Geochemistry of Jutogh Metasediments, Lesser Himachal Himalaya, India, and their implications in source area weathering, provenance, and tectonic setting during Paleoproterozoic Nuna Assembly. J Geol Soc India, 99(7): 897-905.

Jones B, Manning DA. 1994. Comparison of geochemical indices used for the interpretation of palaeoredox conditions in ancient mudstones. Chem Geol, 111(1-4): 111-129.

Jurković I, Garašić V, Hrvatović H. 2010. Geochemical characteristics of the barite occurrences in the Paleozoic complex of the Southeastern Bosnia and their relationship to the barite deposits of the Mid-Bosnian Schist Mountains. Geol Croatica, 63(2): 241-258.

Karadağ MM, Küpeli S, Arık F, Ayhan A, Zedef, V, Döyen A. 2009. Rare earth element (REE) geochemistry and genetic implications of the Mortas-bauxite deposit (Seydişehir/Konya-Southern Türkiye). Chem der Erde, 69: 143–159.

Karadağ MM. 1987. Geological, petrographical and geochemical investigations of Seydişehir region bauxites. Institute of the Naturel and Applied Sciences. Ph.D. Dissertation Thesis, Konya, Türkiye, p. 265 (unpublished).

Karadağ MM. 2014. Geochemistry, provenance and tectonic setting of the Late Cambrian–Early Ordovician Seydişehir Formation in the Çaltepe and Fele areas, SE Türkiye. Geochem, 74(2): 205-224.

Ketin I. 1966. Cambrian outcrops in southeastern Türkiye and their comparison with the Cambrian of east Iran. Bull. Miner Resource and Explor Institute, 66: 77–89.

Kozlu H, Göncüoğlu MC, Sarmiento G, Gül MA. 2002. Mid-Ordovician (Late Darriwilian) conodonts from the southern-central Taurides, Türkiye: geological implications. Turk J Earth Sci., 11: 113–126.

Küpeli S. 2010. Trace and rare-earth element behaviors during alteration and mineralization in the Attepe iron deposits (Feke–Adana, southern Türkiye). J Geochem Explor, 105: 51–74.

Marsaglia KM. Latter KK. 2003. The recycled orogenic sand provenance from an uplifted thrust belt, Betic Cordillera, Southern Spain. J Sed Res, 73 (1): 72-81.

McLennan SM, Hemming S, McDaniel DK, Hanson GN. 1993. Geochemical approaches to sedimentation, provenance, and tectonics. In: Johnsson, M.J., Basu, A, editors. Processes controlling the composition of clastic sediment. Geol Soc America, USA, pp 284.

McLennan SM, Nance WB, Taylor SR. 1980. Rare earth element-thorium correlations in sedimentary rocks, and the composition of the continental crust. Geochim et Cosmochim Acta, 44(11): 1833-1839.

McLennan SM. 1989. Rare earth elements in sedimentary rocks: influence of provenance and sedimentary processes. Rev Miner 21: 170–199

McLennan SM. 2001. Relationships between the trace element composition of sedimentary rocks and upper continental crust. Geochem, Geophy, Geosys, 2(4).

Mendes AM, Golden N, Bermejo R, Morrison L. 2021.

Distribution and abundance of microplastics in coastal sediments depends on grain size and distance from sources. Marine Poll Bull, 172: 112802.

Mir AR. 2015. Rare earth element geochemistry of Post-to Neo-archean shales from Singhbhum mobile belt, Eastern India: implications for tectonic setting and paleo-oxidation conditions. Chinese J Geochem, 34: 401-409.

Murray RW, Buchholtz ten Brink MR, Jones DL, Gerlach DC, Russ III GP. 1990. Rare earth elements as indicators of different marine depositional environments in chert and shale. Geol, 18(3): 268-271.

Nesbitt HW, Young GM. 1984. Prediction of some weathering trends of plutonic and volcanic rocks based on thermodynamic and kinetic considerations. Geochim et Cosmochim Acta, 48(7):1523-1534.

Nesbitt HW, Young GM. 1996. Petrogenesis of sediments in the absence of chemical weathering: effects of abrasion and sorting on bulk composition and mineralogy. Sed, 43: 341–358.

Özgül N, Gedik İ. 1973. Orta Toroslarda Alt Paleozoyik Yaşta Çaltepe Kireçtaşı ve Seydişehir Formasyonunun Stratigrafisi ve Konodont Faunası Hakkında Yeni Bilgiler. TJK Bült, 16(2): 39-52.

Özgül N, Metin S, Erdogan B, Göger E, Bingöl I, Baydar O. 1973. Cambrian-Tertiary rocks of the Tufanbeyli region, eastern Taurus, Türkiye. Bull the Geol Soc Turk., 1:82–100.

Özgül N. 1976. Toroslar'ın Bazı Temel Jeoloji Özellikleri. TJK Bült 19: 65-78.

Özgül N. 1984. Alanya Tektonik Penceresi ve Batı Kesiminin Jeolojisi, Ketin Sempozyumu. Türk Jeol Kur, 97-120.

Özgül N. 1997. Bozkır-Hadim-Taşkent (Orta Torosların Kuzey Kesimi) Dolayında Yeralan Tektono-Stratigrafik Birliklerin Stratigrafisi, MTA Derg, 119: 113-174.

Öztürk EM, Dalkılıç H, Ergin A, Avşar ÖP. 1981. Sultandağı Güneydoğusu ile Anamasdağı Dolayının Jeolojisi. MTA Raporu, No: 8191.

Öztürk EM, Öztürk Z, Acar, Ayaroğlu, A. 1977. Şarkikaraağaç (Isparta) ve Dolayının Jeolojisi. MTA Raporu, No: 7045: 190 s.

Pandey S, Parcha SK. 2017. Provenance, tectonic setting and source-area weathering of the lower Cambrian sediments of the Parahio valley in the Spiti basin, India. J Earth System Sci, 126: 1-16.

Pettijohn FJ, Potter PE, Siever R. 1972. Sand and sandstones. Springer-Verlag, New York, USA, pp 583.

Piñán-Liamas A, Escamilla-Casas JC. 2013. Provenance and tectonic setting of Neoproterozoic to Early Cambrian metasedimentary rocks from the Cordillera Oriental and Eastern Sierras Pampeanas, NW Argentina. Bol de la Soc Geol Mexicana, 65(2): 373-395.

Rimmer SM. 2004. Geochemical paleoredox indicators in Devonian–Mississippian black shales, central Appalachian Basin (USA). Chem Geol, 206(3-4): 373-391.

Robertson AHF, Dixon JE. 1984. Introduction: aspects of the geological evolution of the Eastern Mediterranean. Geological Society, London, Special Pub, 17(1): 1-74.

Roddaz M, Viers J, Brusset S, Baby P, Boucayrand C, Hérail G. 2006. Controls on weathering and provenance in the Amazonian foreland basin: Insights from major and trace element geochemistry of Neogene Amazonian sediments. Chem Geol, 226(1-2): 31-65.

Roser BP, Cooper RA, Nathan S, Tulloch AJ, 1996. Reconnaissance sandstone geochemistry, provenance and tectonic setting of the lower Paleozoic terranes of the West Coast and Nelson, New Zealand. New Zealand J Geol and Geophy, 39: 1–16.

Roser BP, Korsch RJ. 1988. Provenance signatures of sandstone-mudstone suites determined using discriminant function analysis of major-element data. Chem Geol, 67(1-2): 119-139.

Şengör AMC, Yılmaz Y, Sungurlu O. 1984. Tectonics of the Mediterranean Cimmerides: nature and evolution of the western termination of Palaeo-Tethys. Geological Society, London, Special Pub, 17(1): 77-112.

Şengün F. 2023. Örenli metamorfitlerinin jeokimyası, kökeni ve tektonik yerleşimi (Çanakkale, Biga Yarımadası, KB Türkiye). Dokuz Eylül Üni Müh Fak Fen Müh Derg, 25(73): 131-147.

Tang Q, Bao Y, He X, Fu B, Collins AL, Zhang X. 2016. Flow regulation manipulates contemporary seasonal sedimentary dynamics in the reservoir fluctuation zone of the Three Gorges Reservoir, China. Sci the Tot Envir, 548: 410-420.

Taylor SR, McLennan SM. 1985. The geochemical evolution of the continental crust. Rev Geophy, 33(2): 241-265.

Turan A. 2000. Structural characteristic of the area between Korualan and Bağbaşı, Hadim–Konya. J Engin Sci Dokuz Eylül Uni, 3: 51–65.

Wang C, Zhang L, Dai Y, Lan C. 2015. Geochronological and geochemical constraints on the origin of clastic meta-sedimentary rocks associated with the Yuanjiacun BIF from the Lüliang Complex, North China. Lith, 212: 231-246.

Xu L, Lehmann B, Mao J, Nägler TF, Neubert N, Böttcher ME, Escher P. 2012. Mo isotope and trace element patterns of Lower Cambrian black shales in South China: Multi-proxy constraints on the paleoenvironment. Chem Geol, 318: 45-59.

Young SM, Pitawala A, Ishiga H. 2013. Geochemical characteristics of stream sediments, sediment fractions, soils, and basement rocks from the Mahaweli River and its catchment, Sri Lanka. Geochem, 73(3): 357-371.

Zarasvandi A, Zaheri N, Pourkaseb H, Chrachi A, Bagheri H. 2014. Geochemistry and fuid-inclusion microthermometry of the Farsesh barite deposit, Iran. Geol, 20(3): 201-214.

Black Sea Journal of Engineering and Science
doi: 10.34248/bsengineering.1542181

Open Access Journal
e-ISSN: 2619 – 8991

Research Article
Volume 8 - Issue 1: 75-93 / January 2025

GENOTOXIC AND CYTOTOXIC EFFECTS OF NANOPARTICLE AND BULK FORMS OF MOLYBDENUM TRIOXIDE AND MOLYBDENUM DISULFIDE

Nur KORKMAZ[1]*, Fatma ÜNAL[2], Ece AKBAŞ[2], Gökçe ÇALIŞ İSMETOĞLU[3], Deniz YÜZBAŞIOĞLU[2]

[1]*Gazi University, Graduate School of Natural and Applied Sciences, Teknikokullar, 06500, Ankara, Türkiye*
[2]*Gazi University, Faculty of Science, Department of Biology, Teknikokullar, 06500, Ankara, Türkiye*
[3]*Gazi University, Faculty of Science, Department of Chemistry, Teknikokullar, 06500, Ankara, Türkiye*

Abstract: Nanoparticles (NPs) and bulk forms of MoO_3 and MoS_2 (0.1, 1, 10, 100 µg/mL) were investigated by chromosome aberrations, CBMN-Cyt and comet assay in human lymphocytes for the first time. This study compared both MoO_3 and MoS_2 and their NPs and bulk forms. Both NP and bulk forms of MoO_3 and MoS_2 did not cause an increase in the frequency of abnormal cell and CA/Cell compared to the control. While both NPs and bulk forms of MoS_2 significantly increased the micronucleus frequency, MoO_3 did not cause an increase. This increase was slightly higher in MoS_2 NPs than in their bulk form. According to our comet assay results, both NPs and bulk forms of the MoO_3 and MoS_2 significantly increased the DNA damage at all concentrations. Both MoO_3 and MoS_2 significantly decreased MI. Neither MoO_3 nor MoS_2 caused a significant variation in NDI, CBPI, % cytostasis, NPB, and NBUD frequency compared to the negative control. Both particles were also characterized physicochemically. Our results revealed that MoO_3 and MoS_2 may have weak genotoxic and cytotoxic effects. Therefore, the toxicity potential of these particles and their underlying mechanisms for safer usage need to be investigated in more detail by other *in vivo* and *in vitro* genotoxicity and cytotoxicity tests.

Keywords: MoO_3, MoS_2, Genotoxicity, Cytotoxicity

***Corresponding author:** Gazi University, Graduate School of Natural and Applied Sciences, Teknikokullar, 06500, Ankara, Türkiye
E mail: nur.korkmaz1@gazi.edu.tr (N. KORKMAZ)
Nur KORKMAZ https://orcid.org/0000-0003-4969-2872
Fatma ÜNAL https://orcid.org/0000-0002-7468-6186
Ece AKBAŞ https://orcid.org/0000-0002-4978-3638
Gökçe ÇALIŞ İSMETOĞLU https://orcid.org/0000-0002-3369-6193
Deniz YÜZBAŞIOĞLU https://orcid.org/0000-0003-2756-7712

Received: September 03, 2024
Accepted: November 22, 2024
Published: January 15, 2025

Cite as: Korkmaz N, Ünal F, Akbaş E, Çalış İsmetoğlu G, Yüzbaşıoğlu D. 2025. Genotoxic and cytotoxic effects of nanoparticle and bulk forms of molybdenum trioxide and molybdenum disulfide used in bioimaging and cancer therapy. BSJ Eng Sci, 8(1): 75-93.

1. Introduction

Cancer continues to be a significant cause of morbidity and mortality despite basic and clinical research and the testing of promising new treatments. Treatments such as chemotherapy, radiation therapy, immunotherapy, and targeted therapy used in cancer may induce oxidative stress through numerous free radicals that can attack cellular targets, leading to various side effects in biological systems. A lack of good selectivity, cytotoxicity, and multiple drug resistance also obstruct these therapies. Therefore, in recent years, non-traditional cancer treatments using nanotechnology and nanomedicine, a multidisciplinary field, have been applied for detection, diagnosis, and therapy (Indrakumar and Korrapati, 2020). Nanotechnology, thanks to its applications in diverse fields of medical science, has revolutionized the healthcare industry for bioimaging, diagnosis, and treatment of many fatal diseases, including cancer, by overcoming biological barriers in the body with nanosized drug carrier systems. One of the most promising candidates for developing more effective drugs is nanoparticles, the most effective strategies for earlydiagnosis and treatment of tumors and for controlling cancer development and progression (Verma et al., 2023). In particular, two-dimensional (2D) nanomaterials (NMs), including metal chalcogenides and oxides, have been increasingly used in sensors, catalysis, and biomedicine with their attractive physicochemical properties such as high surface-to-volume ratio and free surface energy levels (Li et al., 2021). Smaller than human cells, NPs are 1-100 nm in size, which allows them to enter live cells easily. Therefore, NPs can interact and/or rivalry with biological system cells and molecular components (Verma et al., 2023). Bulk forms (microparticles (MPs)) are substances between 1-1000 µm in properties compared to NPs. Both the designed NPs and MPs have many applications as next-generation biomedical agents in various biomedical fields such as bioimaging, treatment of cancer and other diseases, biosensor, and drug and gene delivery (Kothaplamoottil Sivan et al., 2019; Indrakumar and Korrapati, 2020; Li et al., 2021; Wang et al., 2021; Sobańska et al., 2023).

Molybdenum is one of the essential trace elements, similar to boron, cobalt, copper, iron, and zinc, for humans', animals', and plants' lives. These elements are structural constituents (co-factors) of enzymes that carry out diverse functions such as regulating gene expression, antioxidant defense, and reproductive system, achieving immune functions, and preventing chronic diseases. Therefore, it is added to mineral supplements and fertilizers (Wang et al., 2021). In addition, the distinctive features of Mo-based nanomaterials, such as their relatively low toxicity, suitable catalytic activities (Kailasa et al., 2024), unique physicochemical properties, high surface-to-volume ratios, and their ability to serve as drug delivery platforms for loading different types of chemotherapeutic drugs to achieve improved chemotherapy, made their use in various biomedical investigations (Zhou et al., 2022). Semiconductor MoO_3 in the transition metal oxide group is one of the materials used in bioimaging and cancer treatment studies as a series of rising optothermal materials due to its ease of excretion, photoacoustic imaging capabilities, and surface plasmonic absorption properties. The presence of inherent van der Waals voids in layered materials allows the easy incorporation of MoO_3 with varying guest species, presenting a strategy to optimize their physicochemical features and practice performance (Xing et al., 2020; Zhou et al., 2022). Considered all together, understanding the role of MoO_3 NPs in cancer and angiogenesis opens new avenues for nano-biological interference of selective cancer cell targeting with minimal damage to normal cells using natural trace elements being generally known to affect several metabolic enzymes (Indrakumar and Korrapati, 2020). It can efficiently kill cancer cells by generating reactive oxygen species (ROS) (Zhou et al., 2022). As a Mo-based compound, MoS_2 nanomaterials have recently attracted more attention in drug transport systems studies due to their unique physical and chemical properties. MoS_2 can adsorb various biomolecules and drug molecules through covalent or non-covalent interactions and is easy to be modified (Wang et al., 2021; Santos et al., 2023). MoS_2 NPs as a transition metal are preferred due to their large surface/volume ratio, distinct electronic characteristics, tunable band gap, high carrier mobility, friction, and catalytic and optical physio- chemical properties in various studies. MoS_2-nanocomposite can respond specifically to the tumor microenvironment, increasing drug accumulation at the tumor site, reducing side effects on non-cancerous tissues, and increasing the therapeutic effect. MoS_2 NPs are typically representative of 2D structures in the form of discs, plates, platelets, films, or sheets, similar to graphene, which is the most known 2D nanomaterial (Wang et al., 2021; Singh et al., 2024).

Since NPs and MPs are widely used in many areas, living beings are constantly exposed to these particles, and it is crucial to assess the toxicological effects of NPs and MPs comparatively to clarify the impact of different forms of the same material since the physicochemical and biological characteristics of NPs are different from those of the MPs, in general (Sobańska et al., 2023). For this reason, the genotoxic effects of NPs and MPs have been investigated with various *in vitro* and *in vivo* test systems using different cell lines, primary cells, or organisms (Sobańska et al., 2023; Singh et al., 2024). The results of these studies revealed that while some particles have genotoxic potential, others do not. In the case of NPs and MPs of molybdenum trioxide and molybdenum disulfide, both positive and negative genotoxic results have been reported following both *in vitro* and in vivo studies (Asadi et al., 2019; Sobańska et al., 2020a; Kumari and Mangala, 2022; García-Carpintero et al., 2023; Santos et al., 2023). Due to insufficient and contradictory data in the literature, the toxic, especially genotoxic, effects of NPs and MPs of molybdenum trioxide and molybdenum disulfide need more detailed investigation with numerous test systems using various cell types. Chromosome aberrations (CAs), cytokinesis-block micronucleus cytome (CBMN-Cyt), and comet (single-cell gel electrophoresis-SCGE) assays are valuable biomarkers in determining the genotoxicity/cytotoxicity potential of various agents (Bakhoum and Cantley, 2018; Fenech et al., 2020; Mamur et al., 2022; Collins et al., 2023). Therefore, we aimed to investigate, for the first time, the genotoxic and cytotoxic potential of NPs and MPs of molybdenum trioxide and molybdenum disulfide on human lymphocytes *in vitro* using CAs, CBMN-Cyt, and comet assays. To our knowledge, no data have yet been published on these two NPs and MPs by assays as mentioned earlier in human lymphocytes as genotoxicity and cytotoxicity biomarkers.

2. Materials and Methods

2.1. Materials

In this research, the peripheral blood was obtained from three healthy volunteers, two women and one man (<30 years old), who had no health problems, did not smoke, did not consume alcohol, and had not taken any medication in the last three months.

2.1.1. Test materials

All NPs and MPs were obtained from Nanografi (Türkiye). The information given by the company is as follows: the size of MoO_3 NPs is 10-80 nanometers (99% purity) (Cas No: 1313-27-5), the particle size of MoO_3 MPs is 325 mesh (Cas No: 1313-27-5) and their shapes are nearly spherical. The mean size of MoS_2 NPs is 100 nanometers, its shape is spherical, and its purity is 99.95% (Cas No: 1313-33-5); the particle size of MoS_2 MPs is 325 mesh. Its shape is flaky and 99.9% pure (Cas No: 1313-33-5).

2.1.2. Chemicals

Methyl alcohol (CAS No: 67-56-1), glacial acetic acid (CAS No: 64-19-7), Giemsa (CAS No: HX947066), NaOH (Catalog No: 1310-73-2), Buffer tablets pH 6.8 (CAS No: 111374) and Entellan (CAS No: 1079610500) were obtained from

Merck. Mitomycin-C (CAS No: 200-008-6), colchicine (CAS No: 64-86-8), and cytochalasin-B (CAS No: 14930-96-2) were obtained from Sigma. DMSO (CAS. No: 67-68-5), EDTA (CAS. No: 6381-92-6), triton X-100 (CAS. No: 9002-93-1), tris (CAS. No: 77-86-1), agarose low EEO (CAS. No: 9012-36-6), H_2O_2 (CAS. No: 7722-84-1), ethidium bromide (CAS No: 1239-48-8), Tris (CAS No: 77-86-1), Triton X-100 (CAS No: 9002-93-1) and formaldehyde (CAS No: 50-00-0) were supplied from Applichem. LymphoPlus (Catalog No: CY100-100), Dulbecco's PBS (Catalog No: PBSH0500- 540), and Lymphocyte separation medium (Catalog No: J0100-840) were obtained from Cegrogen Biotech. Trypan Blue (CAT No: L 6323) was supplied from Biochrom.

2.2. Characterization of NPs and MPs of MoO_3 and MoS_2

The shape and particle size of both NPs and MPs of MoO_3 and MoS_2 were examined by transmission electron microscopy (TEM) (JEOL JEM-2100PLUS) at 200 kV and scanning electron microscopy (SEM) (ZEISS EVO40) at 5.00-10.00 kV at Yeditepe University SEM/TEM Imaging Laboratory. All particles were suspended in double distilled water (DDW), homogenized in an ultrasonic bath for 10 minutes, and transferred to a carbon-coated copper grid with a pipette for TEM. For SEM, particles were coated with gold after transfer to double-sided tape on the stubs. The particles were photographed, and 50 were randomly measured with the Image J program to determine the average diameter. The zeta potential (mV) (as a measure of surface charge) was determined by dynamic light scattering (DLS). Hydrodynamic diameter (HD) and polydispersity index (PDI) of MoO_3 NPs and MoS_2 NPs were obtained using a Zeta-sizer Nano-ZS instrument (Malvern, Worcestershire, UK) equipped with a 4-mW He-Ne laser operating at λ=633 nm and a noninvasive backscatter system (NIBSTM) which measures the light scattered at a backscatter angle of 173°. Before measurement, all samples were suspended in DDW (HD- 0.5 g/L, ζ-potential-0.1 g/L) and homogenized in an ultrasonic bath at 10 min. All analyses were measured using the Malvern Zeta-sizer Nano-ZS (Worcestershire, UK) by photon correlation spectroscopy for HD (10^{-3} M NaCl (aq) (0.1 g/L) at 25°C) and by laser Doppler electrophoresis technique for zeta potential. All samples were transferred to zeta cells and placed in the chamber at about 1 mL for measurement (Kizilkaya et al., 2023).

2.3. Preparation of Test Suspensions

Application concentrations (0.1, 1, 10, and 100 µg/mL) of NPs and MPs of molybdenum trioxide and molybdenum disulfide were diluted in distilled water from their stock suspensions that were sonicated for 30 minutes. Following serial dilutions, all suspensions were sonicated for another 10 minutes. Before addition to the cell culture medium, all concentrations of NPs and MPs were homogenized using a vortex for 1 minute.

2.4. Selection of Test Concentrations

Literature searches were carried out and considered as the first reference to determine the concentrations to be used in this study. LD_{50} of MoO_3 was 1831.25 ppm in the HepG2 cell line, 193.91 ppm in the HEK 293 cell line (Kothaplamoottil Sivan et al., 2019), 2.689 mg/kg in rat oral intake, 106±73.79 mg/kg in the rat heart, 136±99.42 mg/kg in rat liver, 143±44 mg/kg in rat kidney and 107±595 mg/kg in rat stomach (Akhondipour et al., 2018). Additionally, the LD50 dose was reported as 242 mg/kg in the rat oral toxicity data program PROTOX (Sharma et al., 2020). It has been observed that toxicity studies in the literature range between 0.25 and 5000 µg/mL (Kothaplamoottil Sivan et al., 2019; Sharma et al., 2020). Toxicity values determined for MoS_2 in the literature were between 0.1 and 1000 µg/mL (Appel et al., 2016; Desai et al., 2020). MoS_2 caused toxic effects in 10 and 100 µg/mL in *Eisenia fetida* (Sun et al., 2023), 5-20 µg/mL on human lung epithelial cells (Sahoo et al., 2022), 0-100 µg/mL in Kupffer cells (Li et al., 2021). In another study, the LD_{50} value was reported as 1 mg/kg (intraperitoneal) in Swiss albino rats (Yadav et al., 2021). Depending on these data, a preliminary dose range finder test was carried out with the concentrations of 0.1, 1, 5, 10, 20, 25, 50, 75, 100, 150, 200, 250, 300, 350, 400, 450 and 500 µg/mL in human lymphocytes using mitotic index test. In the preliminary trial, toxic effects were observed at concentrations above 300 µg/mL, which differed from some of the data in the literature. The cytotoxic effects of concentrations between 100 and 300 µg/mL were not significantly different. Therefore, we decided to apply 0.1, 1, 10, and 100 µg/mL for both MoO_3 and MoS_2.

2.5. Chromosome Aberration Test

The chromosome aberration assay was applied using Evans's method (1984) with some modifications (Yüzbaşioğlu et al., 2006). In this assay, 200 µL of 1/10 heparinized peripheral blood was added to a 2.5 mL chromosome medium. The incubation was carried out at 37ºC for 72 h. The cells were treated with four concentrations (0.1, 1, 10, and 100 µg/mL) of either NPs or MPs of molybdenum trioxide and molybdenum disulfide for 24 and 48 hours. A negative (distilled water) and a positive control (Mitomycin-C, MMC, 0.20 µg/mL) were also included. 0.06 µg/mL colchicine was added into each culture 2 hours before cell harvesting. The cell suspension was centrifuged for 10 min, treated with hypotonic solution (KCl, 0.075M) for 20 min at 37°C, and then fixed in cold and fresh fixative (methanol: glacial acetic acid, 3:1, v/v). Finally, metaphase spreads were prepared by dropping the cell suspension onto slides. Slides prepared for CAs were stained with 5% Giemsa (pH 6.8) for 20-25 min, dried at room temperature, and mounted with entellan.

2.6. Cytokinesis-Block Micronucleus Cytome Test

The cytokinesis-block micronucleus cytome (CBMN-Cyt) test was applied with some modifications in the method of Fenech (2000; 2007) and Kirsch-Volders et al. (2011). 200 µL of 1/10 heparinized peripheral blood samples were added into a 2.5 mL chromosome medium and incubated for 72 h at 37°C. The cells were treated with

four concentrations (0.1, 1, 10, and 100 µg/mL) of NPs and MPs of molybdenum trioxide and molybdenum disulfide for 48 hours. Cytochalasin-B (5.2 µg/mL) was added to arrest the cytokinesis at the 44th hour of incubation (Fenech, 2007). A negative (distilled water) and a positive control (Mitomycin-C, MMC, 0.20 µg/mL) were also maintained. Following incubation, the cultures were treated with hypotonic solution (0.075M KCl for 5 min at +4 °C) and then fixed in cold and fresh fixative (methanol: glacial acetic acid, 3:1, v/v) supplemented with formaldehyde according to the method of Palus et al. (2003). The slides were then stained with 5% Giemsa at room temperature.

2.7. Comet Assay

To determine the DNA-damaging effect of NPs and MPs of MoO_3 and MoS_2 on human lymphocytes, the comet assay was applied using Singh et al. (1988) protocol with some modifications (Akbas et al., 2022). Isolated lymphocytes by suspending blood specimens in PBS were then treated with four different concentrations (0.1, 1, 10, and 100 µg/mL) of the NPs and MPs of MoO_3 and MoS_2 for 1 and 3 hours at 37°C. A negative (sterile distilled water) and a positive (100 µM H_2O_2) controls were also maintained. A trypan blue test was conducted for cell viability, which was >75% for all treatment groups. Lymphocytes in suspension were centrifuged and then resuspended in PBS. The mixture of cell and low melting point agarose (1:1) was gently layered onto the slides precoated with normal melting agarose (%1). Slides were covered with a cover slip and kept in a cold lysing solution (2.5M NaCl, 100 mM EDTA, 10 mM Tris pH=10, comprising %10 DMSO and %1 Triton X-100) for at least 1 h. Slides were electrophoresed for DNA unwinding at 25V, 300 mA for 20 min in electrophoresis buffer (10M NaOH+ 0.2M EDTA+ distilled water). At the end, slides were neutralized in 0.4 M Tris (pH 7.5) for 15 mins and then stained with ethidium bromide.

2.8. Cell Scoring

In the CAs test, 100 well-spread metaphases from each donor (a total of 300 metaphases) were analyzed to determine the frequency of CAs and CAs/cell for each treatment. To determine the mitotic index (MI=the frequency of cells undergoing mitosis among the total number of cells examined), 1000 cells from each donor (total 3000 cells) were evaluated. In the CBMN-Cyt assay, a total of 3000 binucleated cells (1000 cells per donor) were analyzed for each treatment to determine the frequency of micronucleus, nucleoplasmic bridge (NPB), and nuclear bud (NBUD). To evaluate the nuclear division index (NDI), a total of 1500 cells (500 cells per donor) were scored, and the following formula was used: NDI=[1xM1+2xM2+3xM3+4xM4]/N, where M1-M4 represent the number of cells with 1-4 nuclei, respectively, and N is the total number of cells examined (Michalová et al., 2020). Cytokinesis block proliferation index (CBPI) was evaluated from a total of 1500 cells (500 cells for each donor) by the following formula: [(1xnumber of mononuclear cells) + (2x number of binuclear cells) + (3x number of multinuclear (3 and more) cells)/ n(total number of cells) (Lorge et al., 2008). The percentage of cytostasis was also determined using the following formula: % cytostasis: 100-100 [(CBPIT-1): (CBPIC-1)]; where T stands for test substance, and C stands for control (Lorge et al., 2008). In comet assay, a total of 300 cells (50 cells x² slides)/donor were analyzed for each treatment and control group under a fluorescence microscope (Olympus BX51, Japan) equipped with an excitation filter (546 nm) and a barrier filter (590 nm) using a specialized image analysis system (Comet Assay IV, Perceptive Instruments Ltd., Haverhill, UK).

2.9. Statistical Analyses

To determine the statistical difference between treated and untreated cells, the z-test was used for the frequency of abnormal cells, CAs/Cell, MI, frequency of MN, NPB, NBUD, NDI, CBPI, and % cytostasis. T-test was applied for comet scores. The regression analysis was performed to determine concentration-response relationships by using the SPSS 22.0 program.

3. Results

3.1. Characterization of NPs and MPs of MoO_3 and MoS_2

The results of electron microscopy and DLS measurements (HD, PDI and zeta potential) were given in Table 1. Size of NPs appears as two dimensions (2D) in the images obtained by electron microscopy. TEM/SEM images of the particles supplied by the company revealed that while the shape of the MoO_3 NPs is formed from a mixture of spherical and ellipsoid, MoO_3 MPs are lamellar in structure, (Cas No: 1313-27-5). The shape of the MoS_2 NPs is mainly lamellar in structure, and MoS_2 MPs are mainly formed from lamellar structure, but some particles are also present and distributed homogeneously (Cas No: 1313-33-5). In this research we also determined the shape of these NPs and MPs. SEM and TEM images in Figure 1 revealed that the(shape of the MoO_3 NPs is formed from a mixture of spherical, ellipsoid, and rod-like particles, while MoO_3 MPs are formed from a mixture of lamellar, ellipsoid, and rod-like particles. On the other hand, the shape of MoS_2 NPs consists of a mixture of lamellar, ellipsoidal, and spherical particles. MoS_2 MPs consist of rod, lamellar, and ellipsoidal structures.

3.2. Cytotoxicity

The present study showed that MoO_3 NPs significantly and dose-dependently decreased the mitotic index in all concentrations (except 1 µg/mL) at 24-h treatment (r= -0.87) (Figure 3). At 48-h treatment, these NPs also significantly decreased the mitotic index at all concentrations (except 100 µg/mL) (r=-0.15) (Figure 4). MoO_3 MPs also reduced the mitotic index significantly and dose-dependently at all concentrations at both 24 h (r=-0.78) and 48 h (r=-0.88) treatments (Figure 3 and Figure 4). Similarly, MoS_2 NPs declined the mitotic index at all

concentrations at both 24- (except 1 µg/mL) (r= -0.70) and 48-h (r=-0.47) treatments. MoS_2 MPs reduced the mitotic index in a slightly dose-dependent manner at 1 and 100 µg/mL concentrations at both 24- (r=-0.49) and 48-h (r=-0.75) treatments (Figure 5 and Figure 6). In the present study, none of the test materials significantly altered NDI, CBPI, and % cytostasis and did not affect cell proliferation.

Table 1. Electron microscopy and DLS characterization of test chemicals

	Average length (nm)	Average diameter (nm)	The smallest size (nm)	The largest size (nm)	Zeta potential (mV)	Hydrodynamic diameter (HD) (nm)	HD Intensity (%)	Polydispersity index
MoO_3 NPs	697.46	631.64	40	2486	-34.5±9.91	423.2±75.54	100.0	0.704
MoO_3 MPs	32030	24745.52	3162	70228	-16.1±4.32	-	-	-
MoS_2 NPs	928	644.12	74	6036	-27.9±7.18	484.9±39.33	100.0	0.958
MoS_2 MPs	14858.98	10086.10	1967	46920	-14.2±5.94	-	-	-

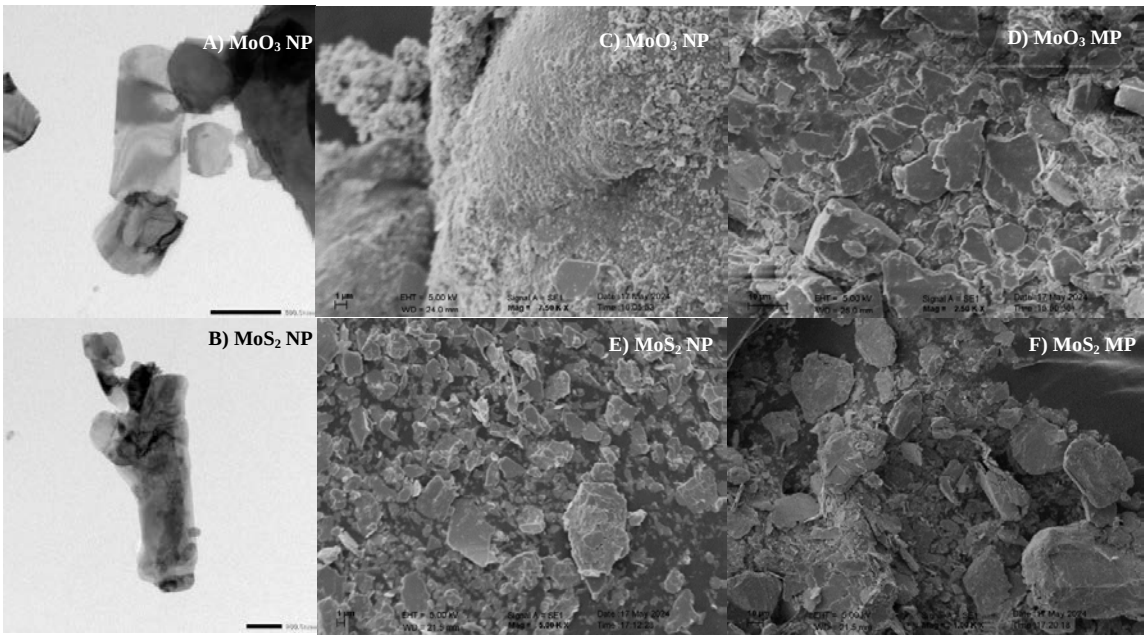

Figure 1. TEM images of MoO_3 and MoS_2 NPs (A and B) and SEM images of MoO_3 and MoS_2 MPs (C, D, E and F).

3.3. Chromosome Aberration Test Results of NPs and MPs of MoO_3 and MoS_2

In this study, the genotoxic effect of MoO_3 and MoS_2 NPs and MPs were evaluated using the CA test in human lymphocytes *in vitro*, and the results were given in Tables 2 and 3. While a few concentrations of both NPs and MPs slightly increased the frequency of abnormal cells and CAs/Cell in human lymphocytes at both 24 h and 48 h treatments, none was significant compared to the negative control. A few concentrations revealed the same frequency as the respective negative control. While 10 µg/mL concentration of MoO_3 NPs at 48 h application did not induce any structural aberration, other concentrations induced only one, two, or scarcely three structural aberrations in lymphocytes. Interestingly, all the concentrations of both MoO_3 NPs and MPs at 24 h treatment and MoS_2 NPs at 48 h treatment generated polyploidy.

The most common type of abnormality in MoO_3-treated cells was polyploidy, followed by chromatid break, fragment, and endoreduplication. In the MoS_2 treatment, polyploidy was the most common abnormality, followed by chromatid break, chromosome break, and chromatid exchange = endoreduplication.

a)

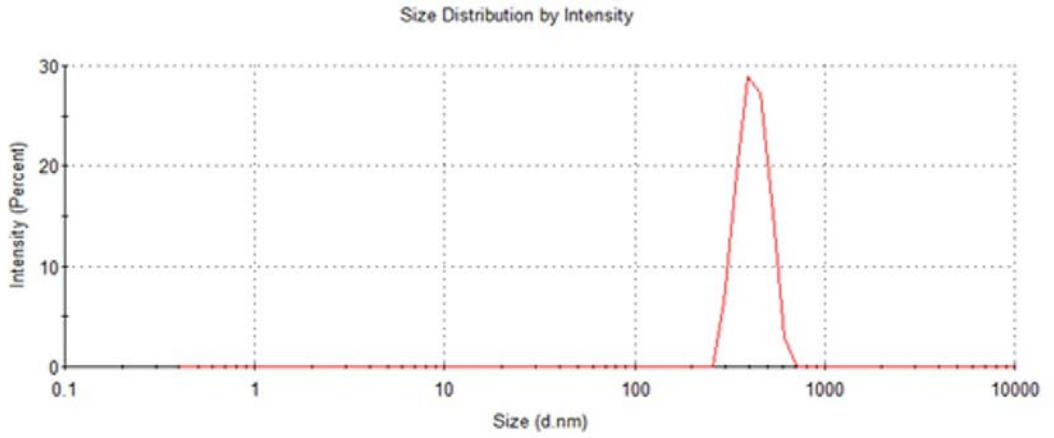

b)

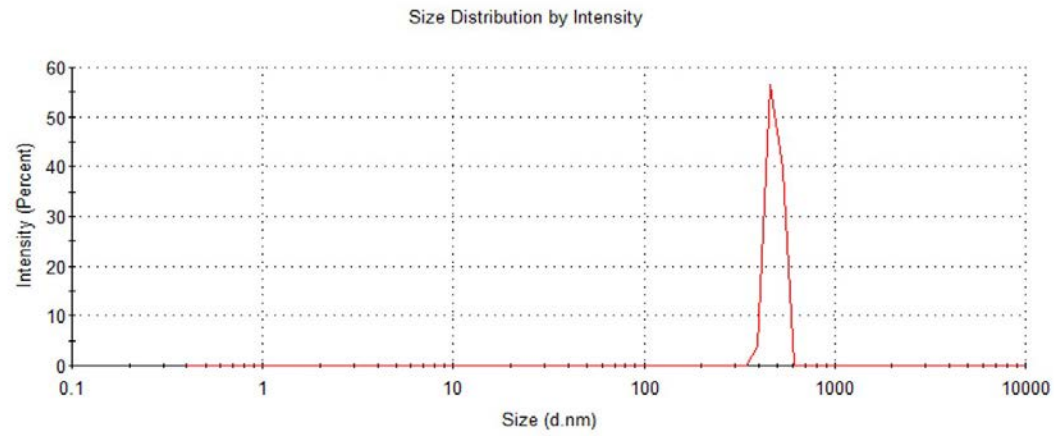

Figure 2. Frequency curve of (a) hydrodynamic diameter of MoO_3 NPs and (b) hydrodynamic diameter of MoS_2 NPs.

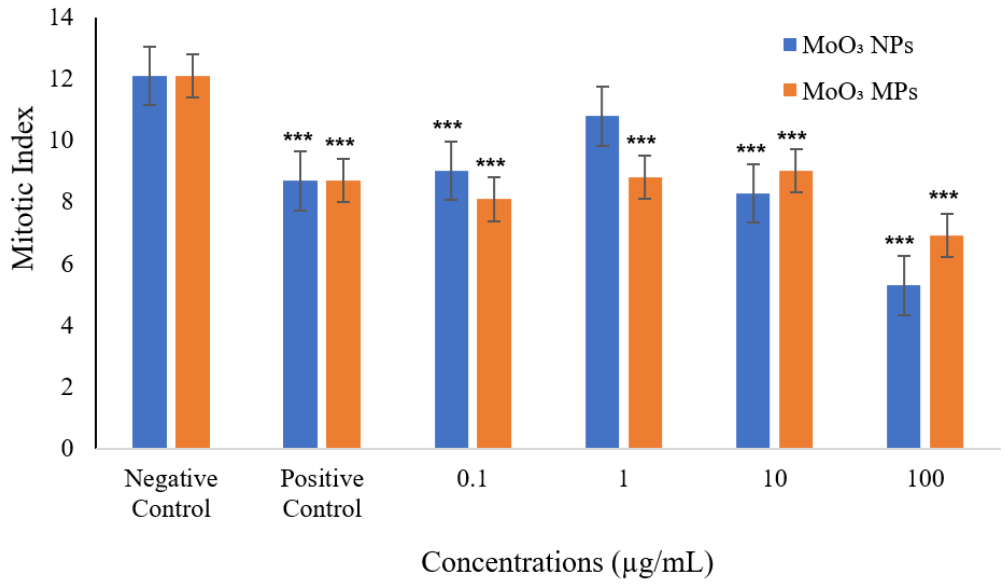

Figure 3. The frequency of MI in human lymphocytes exposed to MoO_3 NPs and MPs for 24 h. ***Significantly different from the control $p<0.001$(z test).

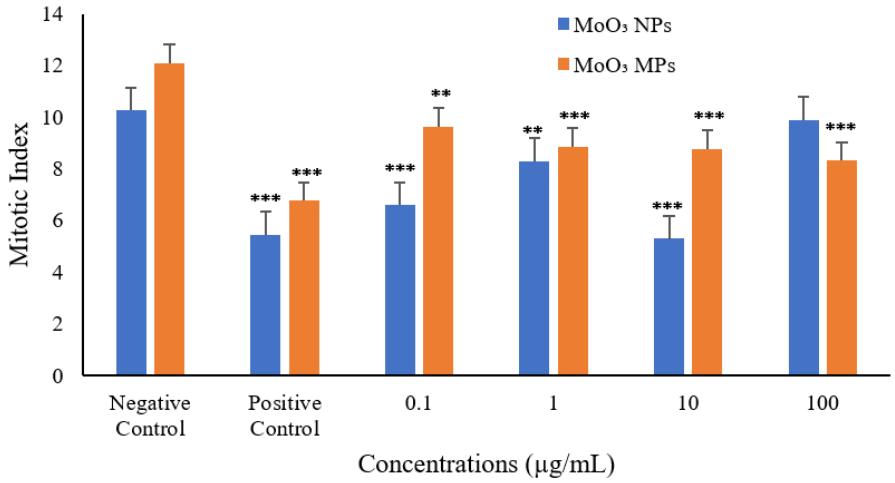

Figure 4. The frequency of MI in human lymphocytes exposed to MoO_3 NPs and MPs for 48 h.**Significantly different from the control p<0.01 (z test). ***Significantly different from the control p<0.001(z test).

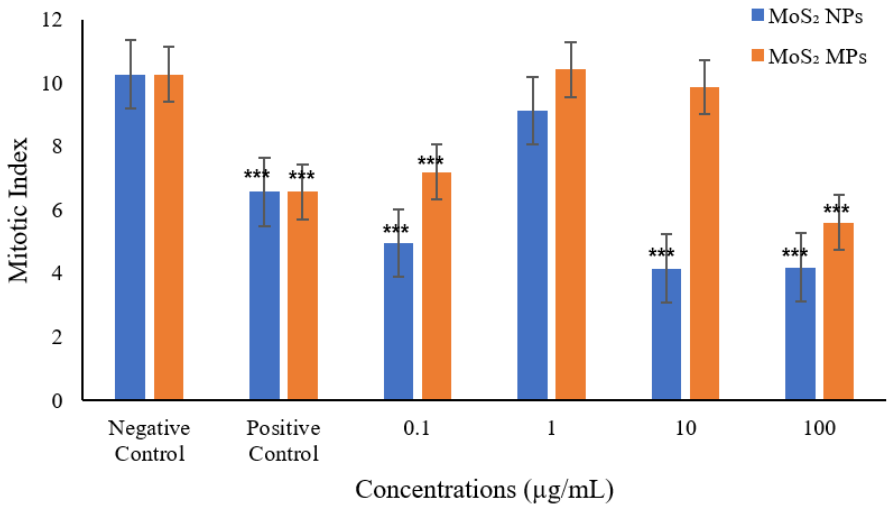

Figure 5. The frequency of MI in human lymphocytes exposed to MoS_2 NPs and MPs for 24 h. ***Significantly different from the control p<0.001(z test).

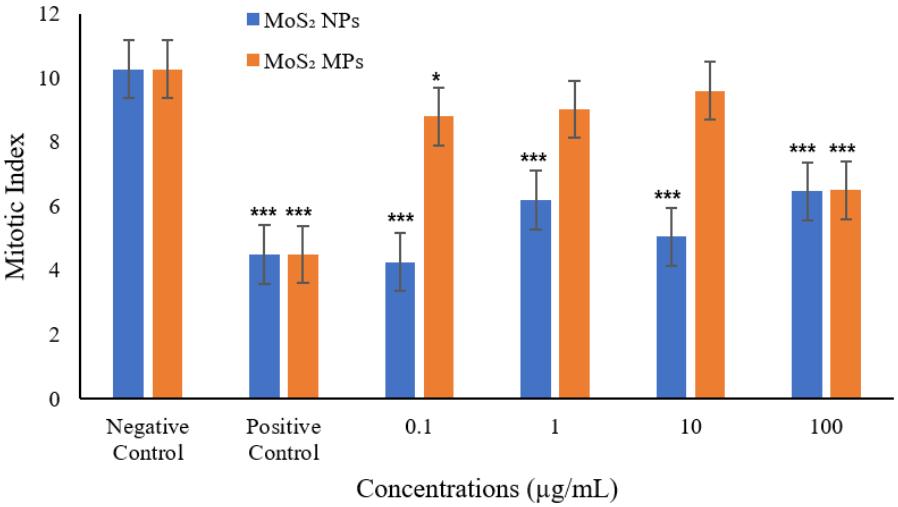

Figure 6. The frequency of MI in human lymphocytes exposed to MoS_2 NPs and MPs for 48-h. *Significantly different from the control p<0.05 (z test). ***Significantly different from the control p<0.001(z test).

Table 2. Effects of NP_S and MPs of MoO_3 on CAs frequency in cultured human lymphocytes

Test substance	Treatment		Aberrations								Abnormal cell ± SE (%)	CAs/Cell ± SE
	Time (h)	Concentration (µg/mL)	ctb	csb	f	dic	scu	ex	p	en		
NC	24	0.00	1	-	-	-	-	-	-	-	0.33±0.11	0.003±0.003
PC (MMC)	24	0.20	11	1	-	-	4	1	8	-	8.33±1.60***	0.080±0.016***
MoO_3 NP_S	24	0.1	2	-	-	-	-	-	1	-	1.00±0.57	0.010±0.005
		1	-	-	-	-	-	-	1	-	0.33±0.33	0.003±0.010
		10	-	-	-	-	-	-	2	-	0.67±0.47	0.007±0.004
		100	-	-	-	-	-	-	2	-	0.67±0.47	0.007±0.004
MoO_3 MP_S	24	0.1	-	-	-	-	-	-	3	-	1.00±0.57	0.010±0.005
		1	-	-	-	-	-	-	2	-	0.67±0.47	0.007±0.004
		10	-	-	-	-	-	-	1	-	0.33±0.33	0.003±0.010
		100	2	-	-	-	-	-	1	-	1.00±0.57	0.010±0.005
NC	48	0.00	1	-	-	-	-	-	-	-	0.33±0.11	0.003±0.003
PC (MMC)	48	0.20	12	3	1	-	1	4	9	3	11,00±1,81***	0.110±0.017***
MoO_3 NP_S	48	0.1	1	-	1	-	-	-	1	-	1.00±0.57	0.010±0.005
		1	-	-	1	-	-	-	-	-	0.33±0.33	0.003±0.010
		10	-	-	-	-	-	-	-	-	0.00±0.00	0.000±0.000
		100	1	-	1	-	-	-	-	-	0.67±0.47	0.007±0.004
NC	48	0.00	1	-	-	-	-	-	-	-	0.33±0.11	0.003±0.003
PC (MMC)	48	0.20	11	5	-	1	3	1	7	-	9,33±0,55***	0,090±0,020***
MoO_3 MP_S	48	0.1	-	-	-	-	-	-	1	-	0.33±0.33	0.003±0.010
		1	2	-	-	-	-	-	-	-	0.67±0.47	0.007±0.004
		10	-	-	-	-	-	-	-	1	0.33±0.33	0.003±0.010
		100	-	-	-	-	-	-	-	1	0.33±0.33	0.003±0.010

ctb= chromatid break, csb= chromosome break, f= fragment, dic= dicentric chromosome, scu= sister chromatid union, ex= chromatid exchange, p= polyploidy, en= endoreduplication, SE= standard error, PC (MMC)= positive control- mitomycin C, NC= Negative control, ***Significantly different from the negative control P<0.001 (z test)

Table 3. Effects of NP_S and MPs of MoS_2 on CAs frequency in cultured human lymphocytes

Test substance	Treatment		Aberrations								Abnormal cell ± SE (%)	CAs/Cell ± SE
	Time (h)	Concentration (µg/mL)	ctb	csb	f	dic	scu	ex	p	en		
NC	24	0.00	-	-	-	-	-	-	-	-	0.00±0.00	0.000±0.000
PC (MMC)	24	0.20	10	7	3	-	2	5	3	-	10.00±1.73***	0.100±0.017***
MoS_2 NP_S	24	0.1	1	-	-	-	-	-	1	1	1.00±0.57	0.010±0.005
		1	2	-	-	-	-	-	1	-	1.00±0.57	0.010±0.005
		10	1	-	-	-	-	-	-	-	0.33±0.33	0.003±0.010
		100	-	-	-	-	-	-	-	-	0.00±0.00	0.000±0.000
MoS_2 MP_S	24	0.1	2	-	-	-	-	1	2	-	1.67±0.73	0.020±0.008
		1	-	-	-	-	-	-	-	-	0.00±0.00	0.000±0.000
		10	-	-	-	-	-	-	1	-	0.33±0.33	0.003±0.003
		100	1	-	-	-	-	-	-	-	0.33±0.33	0.003±0.003
NC	48	0.00	2	-	-	-	-	-	-	-	0.67±0.47	0.006±0.004
PC (MMC)	48	0.20	12	10	1	3	4	2	2	-	11.33±1.83***	0.120±0.019***
MoS_2 NP_S	48	0.1	1	-	-	-	-	-	2	-	1.00±0.57	0.010±0.005
		1	1	-	-	-	-	-	5	-	2.00±0.65	0.020±0.008
		10	-	-	-	-	-	-	2	-	0.67±0.47	0.007±0.004
		100	-	1	-	-	-	-	1	-	0.67±0.47	0.007±0.004
MoS_2 MP_S	48	0.1	1	1	-	-	-	-	-	-	0.67±0.47	0.007±0.004
		1	3	-	-	-	-	-	-	-	1.00±0.57	0.010±0.005
		10	-	-	-	-	-	-	1	-	0.33±0.33	0.003±0.003
		100	1	-	-	-	-	-	-	-	0.33±0.33	0.003±0.003

ctb= chromatid break, csb= chromosome break, f= fragment, dic= dicentric chromosome, scu= sister chromatid union, ex= chromatid exchange, p= polyploidy, en= endoreduplication, SE= standard error, PC (MMC)= positive control- mitomycin C, NC= Negative control, ***Significantly different from the negative control P<0.001 (z test).

3.4. CBMN-Cyt Assay Results of NPs and MPs of MoO_3 and MoS_2

In this study, while the NPs and MPs of MoO_3 slightly increased micronucleus frequency in human lymphocytes, none was significant compared to the negative control (Figure 7). On the contrary, all the concentrations of MoS_2 NPs (except 0.1 µg/mL) significantly increased the micronucleus frequency over the control value (Figure 8). This increase was strongly concentration-dependent(r=0.84). MoS_2 MPs also increased the frequency of micronucleus, but only two of them (1 and 10 µg/mL) were significant and weakly concentration-dependent (r=0.53) compared to the negative control. Regarding nuclear bud, neither MoO_3 NPs and MPs nor MoS_2 NPs and MPs increased the frequency. None of these particles generated nucleoplasmic bridge (except MoS_2 NPs at 100 µg/mL, 48 h; was not significant) either. In our study, the nuclear division index and CBPI were not significantly affected by MoO_3 NPs and MPs or MoS_2 NPs and MPs. Either of these particles did not significantly change the frequency of cytostasis.

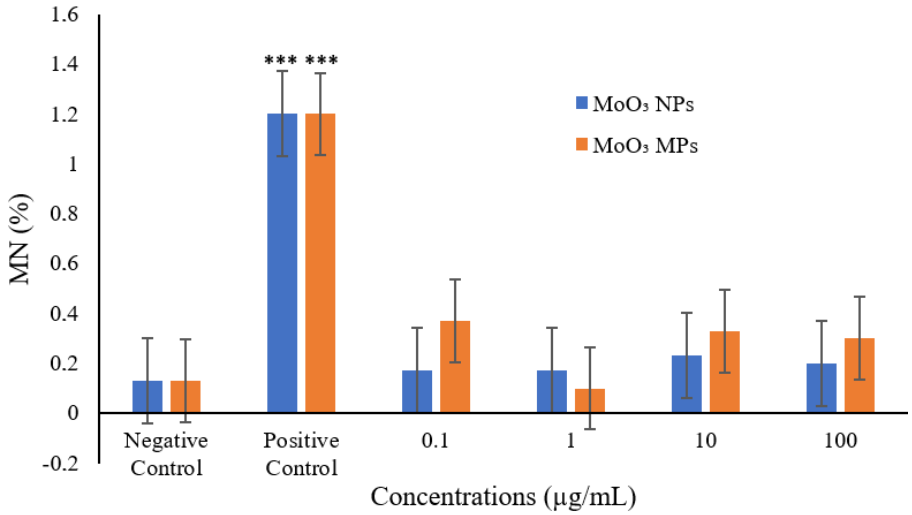

Figure 7. The frequency of MN in human lymphocytes exposed to MoO_3 NPs and MPs for 48 h.

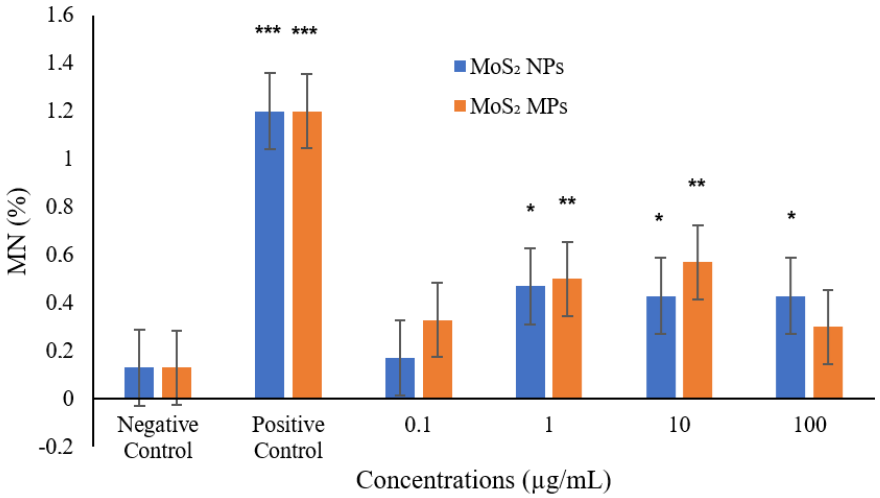

Figure 8. The frequecny of MN in human lymphocytes exposed to MoS_2 NPs and MPs for 48-h. *Significantly different from the control p<0.05 (z test). **Significantly different from the control p<0.01 (z test). ***Significantly different from the control p<0.001(z test).

3.5. Comet Assay Results of NPs and MPs of MoO_3 and MoS_2

In this investigation, both NPs and MPs of MoO_3 and MoS_2 significantly increased the tail length, tail intensity, and tail moment at all concentrations in isolated human lymphocytes compared to the negative control at both 1 and 3 h treatments (except the tail intensity at 0.1 µg/mL for MoS_2 MPs at 3 h treatment) (Tables 4 and 5). These increases were observed in tail length, tail density and tail moment for MoO_3 NPs (r=0.75, r=0.68 and r=0.68, respectively), MoO_3 MPs (r=0.21, r=0.50 and r=0.22, respectively), MoS_2 NPs (r=0.24, r=0.44 and r=0.27, respectively) and MoS_2 MPs (r=0.42, r=0.43 and r=0.49, respectively) during 1 h of treatment. At 3-h treatments, all the particles increased DNA damage in terms of tail length, tail intensity, and tail moment as follows; r=0.93, r=0.77 and r=0.77, respectively, for MoO_3 NP, r=0.69, r=0.55 and r=0.58, respectively, for MoO_3 MPs, r=0.58,

r=0.52 and r=0.39, respectively, for MoS_2 NPs and r=0.70, r=0.43 and r=0.57, respectively, for MoS_2 MPs. Cell viability at 1- and 3-h treatments in isolated lymphocytes was determined as ≥ 80% and 87% for MoO_3 NPs, ≥ 75% and 89% for MoO_3MPs, ≥ 75% and 80% for MoS_2 NPs, and ≥ 76% and 75% for MoS_2 MPs by trypan blue exclusion test, respectively.

Table 4. Effects of NPs and MPs of MoO_3 on DNA damage in human lymphocytes

Test substance	Treatment		Tail Length (μm)	Tail Intensity (%)	Tail Moment
	Time (h)	Concentration (μg/mL)			
NC	1	0.00	45.10±0.56	5.27±0.61	1.23±0.18
PC (H_2O_2)	1	100 μM	154.36±5.53*	30.24±1.38*	17.02±1.30*
MoO_3 NPs	1	0.1	83.02±2.99*	19.00±1.55*	7.34±0.84*
		1	86.55±2.68*	13.55±1.10*	4.33±0.52*
		10	105.32±4.40*	17.26±1.49*	7.96±0.96*
		100	86.42±3.42*	18.36±1.31*	6.87±0.94*
MoO_3 MPs	1	0.1	94.96±4.32*	21.71±1.48*	9.84±0.99*
		1	100.79±4.59*	19.04±1.26*	8.33±0.76*
		10	71.73±2.96*	19.50±1.21*	6.50±0.79*
		100	72.07±2.56*	16.71±1.07*	5.16±0.52*
NC	3	0.00	55.20±0.90	9.25±0.86	2.11±0.22
PC (H_2O_2)	3	100 μM	126.63±4.80*	23.56±1.29*	9.67±0.66*
MoO_3 NPS	3	0.1	55.20±0.90*	15.09±1.26*	5.88±0.93*
		1	68.11±2.44*	13.97±1.15*	4.51±0.53*
		10	70.73±2.88*	14.35±1.36*	6.26±1.00*
		100	139.06±6.13*	47.84±1.95*	32.64±2.27*
MoO_3 MPS	3	0.1	78.96±3.71*	14.38±1.13*	5.53±0.82*
		1	72.71±3.56*	13.81±1.18*	5.91±0.92*
		10	79.13±3.47*	13.90±1.20*	5.62±0.87*
		100	75.26±2.61*	13.13±1.11*	4.92±0.72*

NC= negative control, PC (H_2O_2)= positive control- H_2O_2, *significantly different from the negative control P<0.05 (t-test)

Table 5. Effects of NPS and MPs of MoS_2 on DNA damage in human lymphocytes

Test substance	Treatment		Tail Length (μm)	Tail Intensity (%)	Tail Moment
	Time (h)	Concentration (μg/mL)			
NC	1	0.00	45.10±0.56	5.27±0.61	1.23±0.18
PC (H_2O_2)	1	100 μM	154.36±5.53*	30.24±1.38*	17.02±1.30*
MoS_2 NPS	1	0.1	128.58±6.68*	25.15±1.62*	13.22±1.08*
		1	129.12±6.29*	22.51±1.37*	12.55±1.04*
		10	116.57±5.59*	23.66±1.62*	11.97±1.19*
		100	79.42±3.23*	18.37±1.24*	6.25±0.68*
MoS_2 MPS	1	0.1	65.85±2.24*	11.61±1.04*	3.55±0.48*
		1	128,87±5.72*	23.18±1.53*	11.32±1.04*
		10	100.61±5.82*	19.77±1.46*	12.29±1.74*
		100	70.68±3.47*	11.09±1.06*	4.48±0.75*
NC	3	0.00	55.20±0.90	9.25±0.86	2.11±0.22
PC (H_2O_2)	3	100 μM	126.63±4.80*	23.56±1.29*	9.67±0.66*
MoS_2 NPS	3	0.1	77.62±3.10*	13.43±1.13*	4.80±0.66*
		1	74.52±2.54*	14.39±1.07*	4.67±0.60*
		10	67.20±2.11*	12.23±1.15*	4.34±0.62*
		100	66.28±1.66*	13.09±1.08*	3.70±0.44*
MoS_2 MPS	3	0.1	72.83±3.22*	9.51±1.03	3.34±0.55*
		1	68.86±2.72*	15.72±1.36*	5.89±0.79*
		10	66.13±2.31*	11.88±0.94*	3.46±0.48*
		100	73.95±3.71*	11.57±0.96*	4.61±0.91*

NC= negative control, PC (H_2O_2)= positive control-H_2O_2, *significantly different from the negative control P<0.05 (t-test).

4. Discussion

The most critical features influencing nanomaterials

interaction with cells and cellular components are morphology, size, size distribution, hydrodynamic diameter, polydispersity index, and surface chemistry (Murdock et al., 2008). Therefore, TEM, SEM, and DLS measurements were made in the present study. These sizes assessed by electron microscopy, exceeded the manufacturer's specification of 10-80 nm for MoO3 NPs and 100 nm for MoS2 NPs, resulting in larger particle sizes, may be due to the presence of extended 2D structures (Figures 1A-1F and Table 1) (Santos et al., 2023). Likewise, the average length/diameter measured for MoO_3 and MoS_2 MPs was deviated from the manufacturer's stated average size of 44 µm (325 mesh) (Table 1). There is a difference in shape and structure between the manufacturer and our results.

Regarding toxicity, various results were obtained in studies depending on size/shape. Disk-shaped MoS_2 NP (size 97 ± 32 nm and thickness equal to 8.5 nm ± 1.5 nm) and hexagonal-shaped micro-MoS_2 (size 1.92 ± 0.64 µm and thickness equal to 0.27 ± 0.15 µm) did not cause toxic effects in human hepatoma HepG2 cell line. After treating cells with MoS_2, the diameter of cells with particle clusters reached 300-400 µm on day 4. It was suggested that the lack of toxic effect was due to the lack of cell membrane disruption (Sobańska et al., 2020a). In a study, while bulk MoS_2 (> 2 µm) induced DNA damage in soil organisms, 2D MoS_2 NPs (90 nm) induced less damage to the DNA integrity, and it was observed that toxicity decreased as the size decreased. It has been suggested that these results are probably due to 2D MoS_2 NPs remaining particulate and retard ion leakage. This hypothesis suggests that 2D MoS_2 NP genotoxicity is primarily due to ion leaching rather than the particles themselves (Santos et al., 2023). MoS_2 showed more toxic effects in our study than MoO_3. Therefore, it can be argued that size indirectly affects toxicity.

DLS is an important technique widely used to determine particle size, size distribution, polydispersity index, and surface charge of small particles in suspension as simple, easy, and reproducible technique (Bhattacharjee, 2016). In our study, the electron microscopy measurement values of MoO_3 NPs and MoS_2 NPs were larger than the observed HD measurement (Table 1 and Figure 2). The hydrodynamic diameter, which is determined using the DLS approach, is related to the particle's movement in the plate's thickness, width, and length in all three directions. Consequently, the hydrodynamic diameter is ultimately determined by the thickness of a single particle. This situation may be resulted in a decrease in comparison with the size determined by electron microscope observations (Sobańska et al., 2020b). This study showed that the polydispersity index for both MoO_3 NPs (0.704) and MoS_2 NPs (0.958) had a wide particle size distribution, confirming the presence of agglomerates. The study by Singh et al. (2024) yielded considerable variation in both the effective diameter (HD) and polydispersity index (PI) of MoS_2 nanosheets (trigonal prismatic) depending on the dispersion medium employed. In RPMI medium, HD was 549.08 ± 41.15 nm to 6959.12 ± 7185.11 nm and PDI was 0.17 ± 0.07 to 1.77 ± 2.49, while in FBS (20 % v/v) + RPMI medium HD was 197.30 ±31.43 nm to 262.94 ± 5.92 nm and PDI 0.17 ± 0.03 to 0.37 ± 0.07. After 48 and 72 hours, the abrupt decrease observed in these values indicates that MoS_2 nanosheets precipitated in the medium. The addition of 500 mg/L of MoS_2 to a culture containing RPMI resulted in a reduction in cell viability in both HepG2 and HL-60 cells over 48 h. These situations may be due to the aggregation of nanosheets in RPMI medium. It has been reported that the significant change in the effective diameter and polydispersity index of MoS_2 dispersed in RPMI can be attributed to the high ionic strength of the medium and may be affected by interactions with biomolecules in environmental matrices, serum, etc (Singh et al. (2024).

Zeta potential is another chemical property that exhibits the electrochemical equilibrium at the particle-liquid interface and provides information about the particle's surface charge (Lunardi et al., 2021). The electrostatic stability of a suspension is typically regarded as adequate when the absolute value of the ζ-potential is 30 mV or greater. Particles having zeta potentials between ±10 and ±30 mV reveal incipient instability, while between ±0 and ±10 mV show rapid coagulation or flocculation (Clogston et al., 2011; Kaur et al., 2021; Lunardi et al., 2021). We applied ultrasonication to all suspensions to prevent agglomeration and disperse particles into single nanoparticles. However, the NPs tend to agglomerate over time because of interparticle adhesion forces. Positively charged NPs have been reported to provide higher interaction strength with cells than negatively charged particles and cationic particles generally exhibit more significant toxicity associated with the disruption of cell walls (Clogston et al., 2011; Shao et al., 2015). DLS measurements the negative zeta potential was 34.5 ± 9.91 mV for MoO_3 NPs, 16.1± 4.32 mV for MoO_3 MPs, 27.9± 7.18 mV for MoS_2 NPs and 14.2± 5.94 mV for MoS_2 MPs (Table 2). Zeta potential between -30 and +30 mV may cause agglomeration and affect cell membrane interaction (Clogston et al., 2011; Kaur et al., 2021; Lunardi et al., 2021).

MI, NDI, CPBI, and % cytostasis were assessed in human lymphocytes to investigate the cytotoxic effects of both MoO_3 and MoS_2. MI measures the proportion of cells undergoing mitosis (Akbas et al., 2022). The present study demonstrated that most concentrations of MoO_3 NPs, MoO_3 MPs, and MoS_2 NPs exhibited cytotoxic effects. Conversely, only the lowest and highest concentrations of MoS_2 MPs showed such effects. Although there are slight differences between the cytotoxic effects of particles, the order of toxic effect is as follows: MoO_3 MPs> MoS_2 NPs> MoO_3 NP> MoS_2 MPs. This reveals that NPs are not always more cytotoxic compared to MPs. In this investigation, none of the NPs and MPs significantly affected NDI, CBPI, and % cytostasis compared to the negative control. Kumari and Mangala (2022) determined that the MoO_3

NPs (30-47 nm) (78.64 µg/mL) and MPs (190.23 µg/mL) decreased cell viability by 50% in MCF7-human breast adenocarcinoma cells at 24-h application. MoO_3 NPs, at 0.4 mg/mL concentration, were also found to have cytotoxic effects on invasive breast cancer cell line iMCF-7, induced apoptosis, and generated reactive oxygen species (Anh Tran et al. 2014). Sahoo et al. (2022) demonstrated that MoS_2 NPs (hexagonal; 2-10 nm; 5, 10, and 20 µg/mL; 24 h) elicited a dose-dependent increase in ROS formation and a concomitant decrease in cell viability, ultimately resulting in a cytotoxic effect at high concentrations. Our results revealed that the test substances investigated decreased the mitotic index, which was in accordance with some of the previous studies. The decrease in the mitotic index may be due to the cell cycle inhibition, induction of mitochondria-dependent apoptosis, and ROS production or zeta potential value and agglomeration behavior of MoO_3 and MoS_2 (Terpilowska and Siwicki, 2018; Li et al., 2021; Libalova et al., 2024). On the other hand, increasing the mitotic index might be due to the increasing effect of test substances on cell viability by scavenging ROS and reducing inflammation at different concentrations and application periods (Decker et al., 2021; Duan et al., 2022). For example, Chen et al. (2018) developed a nanozymatic antioxidant system with few-layer MoS_2 nanotubes that scavenged ROS in Escherichia coli, Staphylococcus aureus, and A549 cells in vivo. Moreover, MoS_2 nanosheets showed superior protection against H_2O_2-induced oxidative damage with peroxidase-like activity by transferring electrons instead of ROS production with its enzyme feature. This can be attributed to Mo^{4+}/Mo^{6+} oxidation on the surface of MoS_2 nanosheets.

The genotoxicity of a chemical can be determined from variations in cellular behavior and examination of damage generated to DNA and chromosomes. No single genotoxicity assay can compare, rank, and evaluate the genotoxic potential for all ENMs currently available and used for various purposes. Therefore, in this study, we applied three genotoxicity tests to obtain whether MoO_3 and MoS_2 NPs and MPs generate damage in human lymphocyte cells: chromosome aberration, cytokinesis block micronucleus, and comet tests. One of them, the chromosome aberration test, is used to determine agents that produce structural and numerical chromosomal abnormalities resulting from the treatment with genotoxic chemicals (Mamur et al., 2022; Santibáñez-Andrade et al., 2022). CAs comprise structural and numerical abnormalities, resulting in genomic instability. Structural aberrations, either chromatid or chromosome, may result from chemicals' clastogenic effects (DNA damage). Deletions are the most common, followed by amplification and then unbalanced translocations. Numerical abnormalities primarily comprise aneuploidy and chromosome instability (CIN), represented by chromosome gain or loss. Both types of CAs are reported to be the reason for various genetic and non-communicable diseases. There is also considerable evidence that chromosomal aberrations and associated events triggering modifications in oncogenes and tumor suppressor genes of somatic cells are connected to cancer production in humans and experimental animals (Rossner et al., 2005; Santovito et al., 2014; Vodenkova et al., 2015;Raj et al., 2023).

While NPs and MPs did not cause significant chromosome abnormalities, some structural and numerical chromosome abnormalities were observed. These damages may originate from non-repair or misrepair of DNA double-strand breaks, mismatches between two breaks along the length of the chromosome, and insufficient activation of the G2 checkpoint in cells with a markedly reduced G2 arrest (Helleday et al., 2007; Zeng et al., 2023). Polyploidy may result from increased genome DNA content (Frawley and Orr-Weaver, 2015). Endoreduplication arises if DNA replication occurs without mitosis (Jiang et al., 2022). When DNA damage occurs, the cell cycle checkpoints detect this damage and arrest G1, DNA synthesis, and G2/M transition until various repair mechanisms repair the damage. The activation of the checkpoint prevents mitotic entry of the damaged cells. If damages cannot be repaired or are defectively repaired, this may lead to p53-dependent apoptosis (Zeng et al., 2023; Libalova et al., 2024). Defective DNA damage repair or defects of DNA damage checkpoints generate genomic instability and rapid aging and predispose the organism to neurological disorders, immunodeficiency, and cancer progression (Santovito et al., 2014; Vodenkova et al., 2015; Raj et al., 2023).

In the literature, both negative and positive findings of molybdenum and molybdenum species have been reported for mutations in bacterial and mammalian cells. For example, Burzlaff et al. (2017) reported that sodium molybdate dihydrate (1.6-5000 mg/mL) did not induce reverse mutations in five Salmonella typhimurium strains (TA98, TA100, TA1535, TA1537 and TA102) and mutagenic or clastogenic effects in the tk locus of L5178Y mouse lymphoma cells (1000-2060 mg/mL). It did not generate clastogenic or aneugenic effects in micronucleus test in human lymphocytes. Due to their negative results and all species release the molybdate ion $(MoO_4)_2$ under morphological conditions, authors suggested that their results can be read across to other molybdenum species; no evidence of genotoxicity of molybdenum species (Burzlaff et al. 2017). The absence of mutagenic potential was also demonstrated in TA98 and TA100 strains of Salmonella typhimurium for sodium (Burzlaff et al., 2017) and potassium molybdate (Nishioka, 1975). Calcium molybdate ($CaMoO_4$) NPs (spherical; 50-250 nm, forming some agglomerates of mesostructures with size ~6 µm) synthesized by Nobre et al. (2020) did not affect the survival rate between 1.5625 and 100 mM and did not induce a genotoxic effect at the investigated concentrations (6.25, 25.0, and 100.0 mM) in Drosophila melanogaster. Authors suggested that calcium molybdate nanocrystals could not interact with the DNA and did not induce point mutations, breaks, deletions, or mitotic

recombination (Nobre et al., 2020). In Daphnia magna, a microcrustacean sensitive enough to evaluate the toxicity of the various compounds, sodium molybdate (LC50 value at 48 h was 2847.5 mg/L) did not reveal toxic or genotoxic effects either (Diamantino et al., 2000). Moreover, Duan et al. (2022) reported excellent scavenging properties of Mo against H_2O_2, $\cdot O_2$- and ·OH ROS species by catalyzing redox and oxygen-transfer reactions (Chen et al., 2018; Duan et al., 2022).

Contrary to the previous observations, Ladon et al. (2004) determined in patients who underwent metal hip arthroplasty that high molybdenum concentration had a higher rate of chromosomal translocations than patients with low molybdenum concentration at 6th, 12th, and 24th months after surgery. Daley et al. (2004) have revealed that the molybdenum concentration in wear debris removed from the body was associated with the total micronucleus index, both centromere-positive and centromere-negative (indicating chromosomal breakage and aneuploidy, respectively) in tissue culture. Increased frequencies of chromosomal aberrations in peripheral blood lymphocytes have been reported to occur when workers are exposed to molybdenum, molybdenite and molybdenum trioxide (Babayan et al., 1980). Terpilowska and Siwicki (2018) showed that MoO_3 stimulated significant chromosome abnormalities in BALB/3T3 and HepG2 cells between 100 and 1400 µM. Furthermore, an increase in the number of reverse mutations with or without metabolic activation was detected. Cui et al. (2023) reported that excessive molybdenum (5, 10, 20, and 50 mg/kg BW/day) induced apoptosis-related DNA damage in splenocytes and thymocytes and caused apoptosis of lymphocytes in sheep. The toxic effects of two-dimensional molybdenum disulfide nanomaterials on *Eisenia fetida* were reported by Sun and colleagues (2023). While surface perfect MoS_2 (1.79±0.07 nm) produced an increase in the level of reactiveoxygen species (ROS) and a decrease in the activity of the mitochondrial respiratory electron transport chain III complex, surface-defective MoS_2 (1.91±0.27 nm) triggered a more severe ROS increase and apoptosis with depolarization of the mitochondrial membrane potential. Therefore, researchers have reported that the role of surface defects resulting from synthesis or accumulated from environmental effects should be considered when evaluating the toxicity of 2D materials (Sun et al., 2023). Wang et al. (2016) evaluated acute toxicity of various salts from Mo to *D. magna* following 48 h of treatment and observed that toxicity elevated in the following order: sodium molybdate ($Na_2MoO_4 \cdot 2H_2O$) < molybdenum trioxide (MoO_3)< ammonium molybdate (NH4)6Mo7O24.4H2O), in solution. The authors report that the toxic effect of molybdenum in the aquatic system depends largely on the form of molybdenum salts used. However, they concluded that the toxicity of molybdenum is also linked to the influence of background water quality. High concentrations of molybdenum have been reported to be toxic effective to many organisms, including mammals and freshwater invertebrates (Khangarot, 1991). In addition, the toxic effect of molybdenum has been also reported to depend on the contribution of associated conjugate cations (Wang et al., 2016).

While our study's result coincided with some of the experiments in the literature, it was not coincident with others. Our results indicated that while MoO_3 and MoS_2 did not significantly increase the frequency of aberrant cells and CAs/Cell, they caused a significant decrease in the mitotic index. The significant reductions in the mitotic index might be due to the toxic or genotoxic effects of these NPs, therefore, a decrease in the proportion of cells, cells undergoing mitosis, or an increase in the number of cells encountering apoptosis due to unrepairable damages in DNA, chromosome or cell cycle checkpoints (Nobre et al., 2020; Li et al., 2021; Santibáñez-Andrade et al., 2022; Libalova et al., 2024; Singh et al., 2024). The lack of a significant increase in CAs frequency may be due to the scavenging of ROS by Mo showing nanozyme properties; DNA repair mechanisms repaired the damages in cells that were not directed apoptosis, controlled cell death. In our study, MoO_3 and MoS_2 have negative zeta potential and have shown agglomeration potential. These physicochemical properties may have caused the test substances not to interact strongly with DNA (Nobre et al., 2020). As a result, variations in toxicity of Mo species may be due to the size, shape, and other physicochemical properties, different compounds in that substance, the difference in the synthesis protocol, the difference in the cell types treated, and behavior in culture media of particles (Uboldi et al., 2016; Sikder et al., 2020; Vazquez-Muñoz et al., 2020; Sun et al., 2023).

CBMN-Cyt is an extensively used test to assess cytotoxic, clastogenic (DNA and chromosome damage), aneugenic (principally affects non-DNA targets like spindle fibers and kinetochore and disturbs the cell division cycle), and cytostatic effects generated by genotoxic agents (Fenech et al., 2020; Farabaugh et al., 2023; Raj et al., 2023). It is a comprehensive, accurate, and well-established method that is especially used with comet assay to evaluate the genotoxic effects of nanomaterials. Genomic instability, such as micronuclei (MNi), nucleoplasmic bridges (NPBs), and nuclear buds (NBUDs), can be evaluated by this assay. MNi are formed from whole chromosomes or chromosome fragments that do not correctly segregate to the poles of the cell in mitosis. NPBs are produced from dicentric chromosomes triggered by telomere end-fusions, mis-repaired DNA breaks, or failure of complete chromatid separation. Nuclear bud represent the procedure of exclusion of amplified DNA, DNA repair complexes, and probably extra chromosomes from aneuploid cells (Fenech et al., 2020; Mamur et al., 2022; Struys et al., 2023). In this study, while the NPs (except 0.1 µg/mL) and MPs (1 and 10 µg/mL) of MoS_2 significantly increased micronucleus frequency in human lymphocytes, none the NPs and MPs of MoO_3 was increased significant compared to the negative control. NDI, NPB, NBUD, CBPI and CBPI showed that the results were not significantly affected by MoO_3 NPs and MPs or MoS_2 NPs and MPs. NDI is an index of cellular mitotic

division that oddly elevates or decreases in line with the proliferative capability of the cell. CBPI displays the cytotoxic effects resulting from the exposure of chemical agents. Cytostasis is used for chemicals that inhibit cellular growth and division (Lorge et al., 2008; Nefic and Handzic, 2013; Rodrigues et al., 2018). Investigations unveiled both positive and negative results for MoO_3 and MoS_2 particles. Gibson et al. (1997) reported that molybdenum trioxide (250, 500, and 750 mg/mL) revealed a positive effect in Syrian Hamster Embryo (SHE) cells in micronucleus and cell transformation assay when applied for 24 h. Titenko-Holland et al. (1998) evaluated ammonium molybdate [(NH4)6 Mo7O24r4H2O] and sodium molybdate [(Na2MoO4rH2O)] (0.1, 0.5, 1 and 5 mM) using three genotoxicity assays; micronucleus in human lymphocytes *in vitro* and in mouse *in vivo* and dominant lethal assay in mice. All three tests revealed positive evidence of modest genotoxicity for molybdenum salts, especially at relatively high concentrations, both *in vitro* and *in vivo*. Ammonium molybdate was more effective than sodium molybdate, induced a dose-dependent decrease in cell viability and replicative index, as well as an increase in micronucleus formation in binucleated lymphocytes. Significant dose effect was determined for both chemicals for centromere positive MN and negative MN. Therefore, the authors suggested that the most probable mechanism of molybdenum genotoxicity involves chromosome lagging, resulting in aneuploidy and chromosome breakage (Titenko-Holland et al., 1998). In contrast, using the MN test, Burzlaff et al. (2017) did not determine clastogenic or aneugenic effects following sodium molybdate dihydrate exposure of cultured lymphocytes. In CHO-K1 cells, MoS_2 NPs (138±52 nm; 0, 0.05, 0.5, 5, 20, and 50 µg/mL) have no toxic effect at low doses (0.5 and 5 µg/mL), but the number of cells per field decreased at the highest concentration tested (50 µg/mL). While shaking the culture medium contributed to agglomerate reduction in size and number, these NPs did not affect the MN formation. Therefore, sodium molybdate dihydrate was reported to have non-genotoxic effects (García-Carpintero et al., 2023). Moreover, MoO_{3-X} nanodots were reported to have excellent ROS scavenging capacity (Duan et al., 2022). In Chinese hamster ovary (CHO) cells exposed to molybdenum trioxide, there was no increase in either chromosome aberrations or SCEs with or without metabolic activation [NTP, 1997; NTP (National Toxicology Program) (1997). Such discrepancies might result from the shape, size, size distribution, hydrodynamic diameter, zeta potential, agglomeration, concentrations, and treatment periods. Interspecies variations in sensitivity to molybdenum and variations in sensitivity of short-term human lymphocytes in culture versus other tests might be other explanations (Titenko- Holland et al., 1998).

The comet assay, together with the CBMN-Cyt, is the most frequently applied test to determine the genotoxicity of NMs. The types of damage detected include DNA strand breaks, alkali labile regions, alkylated and oxidized nucleobases, DNA-DNA and DNA-protein cross-links, and DNA adducts. It also determines the repair of all the damages mentioned above at the individual cell level (Collins et al., 2023). The tail length, intensity (% tail DNA), and moment (the product of the tail length and the fraction of total DNA in the tail) are the most common parameters used as indicators of DNA damage caused by chemicals. Though some researchers select the tail moment as a common descriptor, % tail DNA is the most common parameter and reveals a linear correlation with DNA damage induced by chemicals, either by direct or indirect attacks on the DNA (Collins, 2004).

In this study, both NPs and MPs of MoO_3 and MoS_2 caused a significant increase in DNA damage in both 1 and 3 h treatment. In general, DNA damaging parameters were higher for both NPs and MPs at 1 h treatment compared to 3 h treatments, except for the highest concentration of MoO_3 NPs at 3 h treatment. The increase in tail length, tail intensity, and tail moment might have resulted from DNA damage that was not repaired. Decreasing DNA damage after 3 h treatment, on the other hand, may indicate the repairing process of damages or the death or apoptosis of heavily damaged cells (Duijf et al., 2019; Bankoglu et al., 2021; Tung and Gandhi, 2023).

While our results coincide with some of the previous studies, they differ from others. For example, Terpilowska and Siwicki (2018) reported that 100-1400 µM MoO_3 (microelements-24 h) caused DNA damage in BALB/3T3 and HepG2 cells. In another experiment, Siddiqui et al. (2015) showed molybdenum NPs (40 nm) to induce significant induction of DNA damage in L929 mouse fibroblast cells in a concentration-dependent manner using the standard alkaline comet assay. The cells exposed to 10, 25, 50, and 100 µg/mL of Mo-NPs for 24 h revealed a 9.9-, 15-, 23.2-, and 27.7-fold increase in % tail DNA, respectively. In addition, significant production of oxidative stress verified by the increase in lipid peroxidation (LPO) and ROS generation, as well as the reduction in the antioxidant enzyme GSH and catalase levels, were determined. In the cell cycle analysis, NPs generated a significant G2/M arrest and an increase in apoptotic G2/M peak. Therefore, the authors proposed that oxidative stress may be the primary mechanism of toxicity, and ROS may be a crucial mediator of cell death induced by Mo-NPs.

Sobańska et al. (2020b) evaluated nanosized (97± 32 nm-disc-shaped) and micron-sized (1.92± 0.64 µm-lamellar shape and a layered structure) MoS_2 (dose of 1.5 or 5 mg/kg body weight) after single intratracheal instillation in rats. After exposure to both forms for 24 hours or 7 days, numerous macrophages containing particles were detected in the BALF cells isolated from animals; macrophages are much more for the microform of MoS_2. Inflammatory changes in the respiratory system were observed, which were slightly powerful for the micron-sized form. However, the hematological and biochemical

parameters revealed no statistically significant differences. In the comet assay, MoS_2 nano- and microparticles showed no increase in DNA damage over the control values (Sobańska et al., 2020b). In mice, Wang et al. (2015b) compared 2D MoS_2 NPs with the aggregated MoS_2 and observed that the nanoform generated a lower inflammatory response than the microsized aggregated MoS_2. As a photothermal therapy agent, MoS_2 nanosheets and nanoplates coated with poly(ethylene glycol) (PEG) were found nontoxic for Balb/c mice, but they revealed anti-tumor abilities when combined with infrared irradiation (Wang et al., 2015a). MoO_3 NPs at prolonged exposure caused an increase in the level of release of interleukin 6, DNA damage, and cell death (Božinović et al., 2020). MoS_2 has been observed to cause increased genotoxicity in mouse lungs at moderate and high exposures (Sørli et al., 2023).

In *Oryza sativa* seedlings, molybdenum trioxide (MoO_3) exposure at 100, 500, and 1000 ppm doses induced a gradual reduction in root and shoot lengths (Sharma et al., 2021). In *Allium cepa*, sodium molybdate dihydrate (1000, 2000, and 4000 mg/L; 72 h) induced a significant and dose-dependent decrease in physiological (germination percent, root length, and weight gain) parameters, while a significant increase was observed in biochemical (free proline content, MDA, SOD, and CAT enzyme activity) features. In addition, it caused a significant increase in MN frequency, chromosomal aberrations, and anatomical damage dose-dependently. In the comet assay, increasing DNA damage was correlated with increasing molybdenum dose. This molybdenum compound caused a significant and dose-dependent decrease in mitotic index. The decline determined in physiological parameters as a result of excessive molybdenum treatment was clarified by the fact that molybdenum inhibits micro and macro element uptake by *A. cepa* roots, generates damage to the anatomical construction of the roots, and decreases the mitotic division of root cells (Özkan et al., 2024). In the literature, investigations revealed that high quantities of trace elements, such as copper, create physiological toxicity and prevent the uptake of water and nutrients (Kalefetoğlu Macar et al., 2020), damage the physiological structure of plants by causing a decrease in starch, sugar, protein, and nitrogen contents (Gopal et al., 2016). As a result, it hinders cell division in plant root tips and decreases root elongation (Macar et al., 2020). In our study, we observed a significantly reduced mitotic index for both molybdenum NPs and MPs following 24- and 48- hour exposure in human lymphocytes. Decreasing was more prominent, especially at higher concentrations. Although there was a significant increase in DNA damage in comet assay following 1- and 3-h treatments, these particles did not increase the frequency of chromosome aberrations. While MoO_3 particles induced no MN formation, some concentrations of MoS_2 particles generated significant MN formation. To investigate some discrepancies and the timewise variations of induction and reduction of DNA damage, TK6 cells were treated with one concentration (60 μM) of the oxidizing and highly reactive substance hydrogen peroxide (H_2O_2). The alkaline comet assay was applied with the treated cells and the solvent controls after 0.5, 1, 2, 3, 4, 5, 6, and 20 h. H_2O_2 exposure drives its maximum damage after 0.5 h; the damage decreased to about half within an hour, and the DNA strand breaks decreased progressively over time, reaching the control level after 20 h (Bankoglu et al. (2021). In HeLa cells, Duthie and Collins (1997) measured the DNA repair activity up to an hour following 30 min H_2O_2 treatment on ice. They reported a quick repair of H_2O_2-induced damage, which almost completely reduced within an hour after the treatment. In HepG2 cells treated with H_2O_2 for 5 min, 30 min, 40 min, 1 h, and 24 h, a significant increase in DNA damage after 5 min, which reached its maximum at 1 h was determined. However, there was no significant difference in DNA damage after 24 hours compared to control (Benhusein et al., 2010). Ngo et al. (2021) reported that halftime for the repair of H_2O_2-induced DNA damage in the comet assay was 24 min for TK6 cells and 39 min for a human lymphocyte. DNA damages we observed might be interpreted in such a way that MoO_3 and MoS_2 NPs and MPs can interact with DNA and induce damage following 1- and 3-h of exposure, but most or some of these damages might be repaired after 24-h of exposure because we did not observe any significant increase in CAs following 24- and 48-h treatment. Similarly, DNA damage was not significant in long-term treatment (24 h and 7 days), possibly due to the repair of DNA damage or death of damaged cells during long-term treatment, compared to control (Sobańska et al., 2020b). On the other hand, the reduction in the mitotic index may show an inhibitory effect of molybdenum in terms of micro and macro element uptake by human cells and then a decrease in the mitotic division. This may also result from the activation of the DNA repair process with an obvious cell cycle arrest in the G2/M phase in damaged cells or cell death/apoptosis of heavily damaged cells induced by these particles (Siddiqui et al., 2015; Bankoglu et al., 2021; Singh et al., 2024).

The genotoxic mechanisms of NPs are still not fully understood. However, based on the data obtained, it is stated that exposure to NPs can be genotoxic in living things and cells in two critical ways: primary and/or secondary (Magdolenova et al., 2014). Primary genotoxicity refers to ROS-mediated DNA damage without inflammation and direct physical interaction between particles and genomic DNA (Schins and Knaapen, 2007; Saber et al., 2015). Secondary genotoxicity implies that DNA damage results from the effects of reactive oxygen species and reactive nitrogen species (RNT), particle-induced inflammation, and other secondary mediators (cytokines, chemokines) that occur during the acute response. NPs entering the cell induce microglia activation, ROS production, and activation of signaling

pathways in inflammation, affecting the central nervous system and immune cells through proinflammatory response and genotoxicity (Joo and Zhao, 2017).

4. Conclusion

Our results demonstrated that neither MoO_3 nor MoS_2 increased the frequency of CAs and CAs/Cell. Only MoS_2 caused a significant increase in MN frequency. Both MoO_3 and MoS_2 displayed a significant decrease in the mitotic index. Comet assay results showed that both NPs and MPs of MoO_3 and MoS_2 increased the DNA damage. The reduction in mitotic index may be due to DNA damage causing apoptosis or mitotic inhibition. Decreased mitotic index, increased MN frequency, and DNA damage may be caused by oxidative stress. The decrease in the mitotic index may be caused by DNA damage or oxidative stress- inducing mitotic inhibition or apoptosis. Apoptosis may also be why no significant abnormalities were observed in the CAs assay (Sun et al., 2023). With comet assay, we evaluated the effects of short-term exposure in isolated lymphocytes. CAs and CBMN-Cyt assay determined the effects of long-term exposure in cultured lymphocytes. While DNA damage was observed in the comet test, the abnormality frequency did not increase in the CAs test. These results may be due to the repair of DNA damage or the death of damaged cells in the CAs test. While MoO_3 NPs and MPs did not cause significant abnormalities in the CAs and MN tests, MoS_2 NPs and MPs caused significant abnormalities in MN. No abnormality in treatment with MoO_3 NPs and MPs may have been observed due to DNA damage repair or scavenging ROS through catalyzing redox and oxygen-transfer reactions of Mo or apoptosis (Duan et al., 2022; Singh et al., 2024). We observed that the size of both NPs and MPs of MoO_3 and MoS_2 had no direct effect on toxicity. Negative zeta potential value and agglomeration potential may have played a role in the toxicity of both NPs and MPs of MoO_3 and MoS_2 (Nobre et al., 2020). In this study, potential genotoxic and cytotoxic effects of NPs and MPs of MoO_3 and MoS_2 were investigated for the first time on human lymphocytes *in vitro*. MoS_2 showed more toxic effects than MoO_3. Our results suggest that MoO_3 and MoS_2 may have weak genotoxic and cytotoxic effects. There are conflicting data in the literature regarding the genotoxic/cytotoxic effects of NPs and MPs (Decker et al., 2021; Kumari and Mangala, 2022; García-Carpintero et al., 2023; Sun et al., 2023). The contradictory results of MoO_3 and MoS_2 NPs on living organisms may be due to nanomaterials' different physical and chemical properties, concentrations, treatment periods, varying test species, and test systems. The differences in results available can be due to changes in the properties of NPs by the synthesis protocol used, coating, zeta potential, agglomeration, the presence of natural organic matter, behavior in culture media, and size and the difference in cell types (Uboldi et al., 2016; Sikder et al., 2020; Vazquez-Muñoz et al., 2020; Sun. et al., 2023; Singh et al., 2024). Therefore, these particles' toxicity potential and underlying mechanisms should be investigated in more detail.

Author Contributions

The percentages of the authors' contributions are presented below. The authors reviewed and approved the final version of the manuscript.

	N.K.	F.U.	E.A.	G.Ç.İ.	D.Y.
C	60	40	-	-	-
D	40	30	10	10	10
S	-	100	-	-	-
DCP	40	30	10	20	-
DAI	40	30	10	10	10
L	40	20	20	10	10
W	40	20	20	10	10
CR	30	40	10	10	10
SR	40	30	10	10	10

C=Concept, D= design, S= supervision, DCP= data collection and/or processing, DAI= data analysis and/or interpretation, L= literature search, W= writing, CR= critical review, SR= submission and revision.

Conflict of Interest

The authors declared that there is no conflict of interest.

Ethical Consideration

This research was approved by the Clinical Research Ethics Committee of the Faculty of Medicine at Gazi University (Approved Date: 18/10/2021; protocol no: 07; modified format 27/12/2021; No: 240).

Acknowledgements

This study is based on Nur Korkmaz's doctoral thesis. The supervisor of this thesis is Fatma Ünal.

References

Akbas E, Unal F, Yuzbasioglu D. 2022. Genotoxic effects of gadobutrol and gadoversetamide active substances used in magnetic resonance imaging in human peripheral lymphocytes in vitro. Drug Chem Toxicol, 45(6): 2471-2482.

Akhondipour M, Faghihi Zarandi A, Amirri A, Gommnami N, Vazirinejad R. 2018. Studying the toxicity of molybdenum trioxide nanoparticles in male Wister rats. J Occup Health Epidemiol, 7(4): 233-239.

Anh Tran T, Krishnamoorthy K, Song, YW, Cho SK, Kim SJ. 2014. Toxicity of nano molybdenum trioxide toward invasive breast cancer cells. ACS Appl Mater Interfaces, 6(4): 2980-2986.

Appel JH, Li DO, Podlevsky JD, Debnath A, Green AA, Wang QH, Chae J. 2016. Low cytotoxicity and genotoxicity of two-dimensional MoS2 and WS2. ACS Biomater Sci Eng, 2(3): 361-367.

Asadi F, Sadeghzadeh M, Jalilvand A, Nedaei K, Asadi Y, Heidari A. 2019. Effect of molybdenum trioxide nanoparticles on ovary function in female rats. J Adv Med Biomed Res, 27(121): 48-53.

Babayan EA, Bagramyan SB, Pogosyan AS. 1980. Effect of some chemical hazards involved in molybdenum production on the

chromosome apparatus of experimental animals and humans. Gig T Prof Zabol, 33-36.

Bakhoum SF, Cantley LC. 2018. The multifaceted role of chromosomal instability in cancer and its microenvironment. Cell, 174(6): 1347-1360.

Bankoglu EE, Schuele C, Stopper H. 2021. Cell survival after DNA damage in the comet assay. Arch Toxicol, 95(12): 3803-3813.

Benhusein G, Mutch E, Aburawi S, Williams F. 2010. Genotoxic effect induced by hydrogen peroxide in human hepatoma cells using comet assay. Libyan J Med, 5(1): 4637.

Bhattacharjee S. 2016. DLS and zeta potential–what they are and what they are not?. J Cont Release, 235: 337-351.

Božinović K, Nestić D, Centa UG, Ambriović-Ristov A, Dekanić A, de Bisschop L, Majhen D. 2020. In-vitro toxicity of molybdenum trioxide nanoparticles on human keratinocytes. Toxicology, 444: 152564.

Burzlaff A, Beevers C, Pearce H, Lloyd, Klipsch K. 2017. New studies on the in vitro genotoxicity of sodium molybdate and their impact on the overall assessment of the genotoxicity of molybdenum substances. Regul Toxicol Pharmacol, 86: 279-291.

Chen T, Zou H. Wu X, Liu C, Situ B, Zheng L, Yang G. 2018. Nanozymatic antioxidant system based on MoS2 nanosheets. ACS Appl Mater Interfaces, 10(15): 12453-12462.

Clogston JD, Patri AK. 2011. Zeta potential measurement. In: McNeil S, editors. Characterization of nanoparticles intended for drug delivery: Methods in molecular biology. Humana Press, Totowa, New Jersey, USA, pp: 63-70.

Collins A, Møller P, Gajski G, Vodenková S, Abdulwahed A, Anderson D, Azqueta A. 2023. Measuring DNA modifications with the comet assay: A compendium of protocols. Nat Protoc, 18(3): 929-989.

Collins AR. 2004. The comet assay for DNA damage and repair: principles, applications, and limitations. Mol Biotechnol, 26(3): 249-261.

Cui SG, Zhang YL, Guo HW, Zhou BH, Tian EJ, Zhao J, Wang HW. 2023. Molybdenum-induced apoptosis of splenocytes and thymocytes and changes of peripheral blood in sheep. Biol Trace Elem Res, 201: 1-11.

Daley B, Doherty AT, Fairman B, Case CP. 2004. Wear debris from hip or knee replacements causes chromosomal damage in human cells in tissue culture. J Bone Joint Surg Br, 86(4): 598-606.

Decker S, Kunisch E, Moghaddam A, Renkawitz T, Westhauser F. 2021. Molybdenum trioxide enhances viability, osteogenic differentiation and extracellular matrix formation of human bone marrow-derived mesenchymal stromal cells. J Trace Elem Med Biol, 68: 126827.

Desai ML, Jha S, Basu H, Saha S, Singhal RK, Kailasa SK. 2020. Simple hydrothermal approach for synthesis of fluorescent molybdenum disulfide quantum dots: Sensing of Cr^{3+} ion and cellular imaging. Mater Sci Eng C, 111: 110778.

Diamantino TC, Guilhermino L, Almeida E, Soares AM. 2000. Toxicity of sodium molybdate and sodium dichromate to Daphnia magna Straus evaluated in acute, chronic, and acetylcholinesterase inhibition tests. Ecotoxicol Environ Saf, 45(3): 253-259.

Duan G, Wen L, Sun X, Wei Z, Duan R, Zeng J, Gao M. 2022. Healing diabetic ulcers with MoO3− X nanodots possessing intrinsic ROS-scavenging and bacteria-killing capacities. Small, 18(10): 2107137.

Duijf PH, Nanayakkara D, Nones K, Srihari S, Kalimutho M, Khanna KK. 2019. Mechanisms of genomic instability in breast cancer. Trends Mol Med, 25(7): 595-611.

Duthie SJ, Collins AR. 1997. The influence of cell growth, detoxifying enzymes and DNA repair on hydrogen peroxide-mediated DNA damage (measured using the comet assay) in human cells. Free Radic Biol Med, 22(4): 717-724.

Evans HJ. 1984. Human peripheral blood lymphocytes for the analysis of chromosome aberrations in mutagen tests. In: Kilbey B J, Legator M, Nichols W, Ramel C editors, Handbook of mutagenicity test procedures, Elsevier Sciences, Amsterdam, the Netherlands, pp: 405-424.

Farabaugh CS, Doak S, Roy S, Elespuru R. 2023. In vitro micronucleus assay: Method for assessment of nanomaterials using cytochalasin B. Front Toxicol, 5:1171960.

Fenech M. 2000. The in vitro micronucleus technique. Mutat Res, 455(1): 81-95.

Fenech M. 2007. Cytokinesis-block micronucleus cytome assay. Nat Protoc, 2(5): 1084-1104.

Fenech M. 2020. Cytokinesis-block micronucleus cytome assay evolution into a more comprehensive method to measure chromosomal instability. Genes, 11(10): 1203.

Frawley LE, Orr-Weaver TL. 2015. Polyploidy. Curr Biol, 25(9): R353-R358.

García-Carpintero S, González VJ, Frontiñán-Rubio J, Esteban-Arranz A, Vázquez E, Durán-Prado M. 2023. Screening the micronucleus assay for reliable estimation of the genotoxicity of graphene and other 2D materials. Carbon, 215: 118426.

Gibson DP, Brauninger R, Shaffi HS, Kerckaert GA, LeBoeuf RA, Isfort RJ, Aardema MJ. 1997. Induction of micronuclei in Syrian hamster embryo cells: comparison to results in the SHE cell transformation assay for National Toxicology Program test chemicals. Mutat Res Genet Toxicol Environ Mutagen, 392(1-2): 61-70.

Gopal R, Sharma YK, Shukla AK. 2016. Effect of molybdenum stress on growth, yield and seed quality in black gram. J Plant Nutr, 39(4): 463-469.

Helleday T, Lo J, van Gent DC, Engelward BP. 2007. DNA double-strand break repair: from mechanistic understanding to cancer treatment. DNA Repair, 6(7): 923-935.

Indrakumar J, Korrapati PS. 2020. Steering efficacy of nano molybdenum towards cancer: mechanism of action. Biol Trace Elem Res, 194: 121-134.

Jiang S, Wei J, Li N, Wang Z, Zhang Y, Xu R, Li Y. 2022. The UBP14-CDKB1; 1-CDKG2 cascade controls endoreduplication and cell growth in Arabidopsis. Plant Cell, 34(4): 1308-1325.

Joo SH, Zhao D. 2017. Environmental dynamics of metal oxide nanoparticles in heterogeneous systems: A review. J Hazard Mater, 322: 29-47.

Kailasa SK, Patel MR, Koduru JR, Park TJ. 2024. Recent advances of molybdenum-based nanostructures for molecular and ionic species sensing and separation applications. Coord Chem Rev, 501, 215595.

Kalefetoğlu Macar T, Macar O, Yalçın E, Çavuşoğlu K. 2020. Resveratrol ameliorates the physiological, biochemical, cytogenetic, and anatomical toxicities induced by copper (II) chloride exposure in Allium cepa L. Environ Sci Pollut Res, 27: 657-667.

Kaur J, Kaur K, Pervaiz N, Mehta SK. 2021. Spherical MoO_3 Nanoparticles for Photocatalytic Removal of Eriochrome Black T. ACS Appl Nano Mater, 4(11): 12766-12778.

Khangarot BS. 1991. Toxicity of metals to a freshwater tubificid worm Tubifex tubifex (Muller). Bull Environ Contam Toxicol, 46(6).

Kirsch-Volders M, Plas G, Elhajouji A, Lukamowicz M, Gonzalez L, Loock KV, Decordier I. 2011. The in vitro MN assay in 2011: origin and fate, biological significance, protocols, high throughput methodologies and toxicological relevance. Arch Toxicol, 85(8): 873-899.

Kizilkaya D, Unal F, Beyzi E, Kulahci MB, Calis Ismetoglu G, Yuzbasioglu D, Suludere Z. 2023. Comparative investigation of iron oxide nanoparticles and microparticles using the in vitro bacterial reverse mutation and in vivo Allium chromosome aberration and comet assays. J Nanopart Res, 25(9): 173.

Kothaplamoottil Sivan S, Padinjareveetil AK, Padil VV, Pilankatta R, George B, Senan C, Varma RS. 2019. Greener assembling of MoO3 nanoparticles supported on gum arabic: cytotoxic effects and catalytic efficacy towards reduction of p-nitrophenol. Clean Technol Environ Policy, 21(8): 1549-1561.

Kumari J, Mangala P. 2022. Fabrication and characterization of molybdenum trioxide nanoparticles and their anticancer, antibacterial and antifungal activities. MJChem, 24(1): 36-53.

Ladon D, Doherty A, Newson R, Turner J, Bhamra M, Case C.P. 2004. Changes in metal levels and chromosome aberrations in the peripheral blood of patients after metal-on-metal hip arthroplasty. J Arthroplasty, 19(8): 78-83.

Li J, Guiney LM, Downing JR, Wang X, Chang CH, Jiang J, Xia T. 2021. Dissolution of 2D molybdenum disulfide generates differential toxicity among liver cell types compared to non-toxic 2D boron nitride effects. Small, 17(25): 2101084.

Libalova H, Zavodna T, Margaryan H, Elzeinova F, Milcova A, Vrbova K, Rössner P. 2024. Differential DNA damage response and cell fate in human lung cells after exposure to genotoxic compounds. In Vitro Toxicol, 94: 105710.

Lorge E, Hayashi M, Albertini S, Kirkland D. 2008. Comparison of different methods for an accurate assessment of cytotoxicity in the in vitro micronucleus test: I. Theoretical aspects. Mutat Res Genet Toxicol Environ Mutagen, 655(1-2): 1–3.

Lunardi CN, Gomes AJ, Rocha FS, De Tommaso J, Patience GS. 2021. Experimental methods in chemical engineering: Zeta potential. The Can J Chem Eng, 99(3): 627-639.

Macar O, Kalefetoğlu Macar T, Çavuşoğlu K, Yalçın E. 2020. Protective effects of anthocyanin-rich bilberry (Vaccinium myrtillus L.) extract against copper (II) chloride toxicity. Environ Sci Pollut Res, 27: 1428-1435.

Magdolenova Z, Collins A, Kumar A, Dhawan A, Stone V, Dusinska M. 2014. Mechanisms of genotoxicity. A review of in vitro and in vivo studies with engineered nanoparticles. Nanotoxicology, 8(3): 233-278.

Mamur S, Yüzbaşıoğlu D, Bülbül SN, Ünal F. 2022. Investigation of cyto-genotoxic effects of a food sweetener Acesulfame potassium. Food and Health, 8(4): 273-283.

Michalová V, Galdíková M, Holečková B, Koleničová S, Schwarzbacherová V. 2020. Micronucleus assay in environmental biomonitoring. Folia Vet, 64(2): 20-28.

Murdock RC, Braydich-Stolle L, Schrand AM, Schlager JJ, Hussain SM. 2008. Characterization of nanomaterial dispersion in solution prior to in vitro exposure using dynamic light scattering technique. Toxicol Sci, 101(2): 239-253.

Nefic H, Handzic I. 2013. The effect of age, sex, and lifestyle factors on micronucleus frequency in peripheral blood lymphocytes of the Bosnian population. Mutat Res Genet Toxicol Environ Mutagen, 753(1): 1-11.

Ngo LP, Kaushal S, Chaim IA, Mazzucato P, Ricciardi C, Samson LD, Engelward BP. 2021. CometChip analysis of human primary lymphocytes enables quantification of inter-individual differences in the kinetics of repair of oxidative DNA damage. Free Radic Biol Med, 174, 89-99.

Nishioka H. (1975). Mutagenic activities of metal compounds in bacteria. Mutat Res, 31(3):185-189.

Nobre FX, Muniz R, Martins F, Silva BO, de Matos JME, da Silva ER, Leyet Y. 2020. Calcium molybdate: Toxicity and genotoxicity assay in Drosophila melanogaster by SMART test. J Mol Struct, 1200: 127096.

NTP. 1997. National Toxicology Program: Molybdenum trioxide. NTP TR 462, NIH Pub. No. 95–3378.

Özkan B, Çavuşoğlu K, Yalçin E, Acar A. 2024. Investigation of multidirectional toxicity induced by high-dose molybdenum exposure with Allium test. Sci Rep, 14(1): 8651.

Palus J, Rydzynski K, Dziubaltowska E, Wyszynska K, Natarajan AT, Nilsson R. 2003. Genotoxic effects of occupational exposure to lead and cadmium. Mutat Res Genet Toxicol Environ Mutagen, 540(1): 19-28.

Raj SG, Rajitha V. 2023. Assessment of genotoxic instability markers in peripheral blood lymphocytes of breast cancer patients: a case control study. Mutat Res Genet Toxicol Environ Mutagen, 42: 1559-1563.

Rodrigues MA, Beaton-Green LA, Wilkins RC, Fenech MF. 2018. The potential for complete automated scoring of the cytokinesis block micronucleus cytome assay using imaging flow cytometry. Mutat Res Genet Toxicol Environ Mutagen, 836: 53-64.

Rossner P, Boffetta P, Ceppi M, Bonassi S, Smerhovsky Z, Landa K, Šrám RJ. 2005. Chromosomal aberrations in lymphocytes of healthy subjects and risk of cancer. Environmental Health Perspectives, 113(5): 517-520.

Saber AT, Mortensen A, Szarek J, Koponen IK, Levin M, Jacobsen NR, Atluri R. 2015. Epoxy composite dusts with and without carbon nanotubes cause similar pulmonary responses, but differences in liver histology in mice following pulmonary deposition. Part Fibre Toxicol, 13(1): 37-57.

Sahoo D, Behera SP, Shakya J, Kaviraj B. 2022. Cost-effective synthesis of 2D molybdenum disulfide (MoS_2) nanocrystals: An exploration of the influence on cellular uptake, cytotoxicity, and bio-imaging. Plos One, 17(1): e0260955.

Santibáñez-Andrade M, Sánchez-Pérez Y, Chirino YI, Morales-Bárcenas R, Quintana-Belmares R, García-Cuellar CM. 2022. Particulate matter (PM10) destabilizes mitotic spindle through downregulation of SETD2 in A549 lung cancer cells. Chemosphere, 295: 133900.

Santos J, Barreto A, Fernandes C, Silva ARR, Cardoso DN, Pinto E, Maria VL. 2023. A comprehensive ecotoxicity study of molybdenum disulfide nanosheets versus bulk form in soil organisms. Nanomaterials, 13(24): 3163.

Santovito A, Cervella P, Delpero M. 2014. Chromosomal damage in peripheral blood lymphocytes from nurses occupationally exposed to chemicals. Hum Exp Toxicol, 33(9): 897-903.

Schins RP, Knaapen AM. 2007. Genotoxicity of poorly soluble particles. Inhal Toxicol, 19: 189-198.

Shao XR, Wei XQ, Song X, Hao L Y, Cai XX, Zhang ZR, Lin YF. 2015. Independent effect of polymeric nanoparticle zeta potential/surface charge, on their cytotoxicity and affinity to cells. Cell Prolif, 48(4): 465-474.

Sharma PK, Raghubanshi AS, Shah K. 2020. Examining dye degradation and antibacterial properties of organically induced α-MoO3 nanoparticles, their uptake and phytotoxicity in rice seedlings. Environ Nanotechnol Monit Manag, 14: 100315.

Sharma PK, Raghubanshi AS, Shah K. 2021. Examining the uptake and bioaccumulation of molybdenum nanoparticles and their effect on antioxidant activities in growing rice seedlings. Environ Sci Pollut Res, 28: 13439-13453.

Siddiqui MA, Saquib Q, Ahamed M, Farshori NN, Ahmad J, Wahab R, Pant AB. 2015. Molybdenum nanoparticles-induced cytotoxicity, oxidative stress, G2/M arrest, and DNA damage in mouse skin fibroblast cells (L929). Colloids Surf B Biointerfaces, 125: 73-81.

Sikder M, Wang J, Poulin BA, Tfaily MM, Baalousha M. 2020. Nanoparticle size and natural organic matter composition

determine aggregation behavior of polyvinylpyrrolidone coated platinum nanoparticles. Environ Sci Nano, 7(11): 3318-3332.

Singh AV, Panchal D, Sharma A, Nandanwar C, Kumar MS, Pal S, Naoghare PK. 2024. Dispersion behaviour of molybdenum disulfide (MoS_2) nanosheets in different exposure media and determination of its toxicity using *in-vitro* and in-silico approaches. Appl Mater Today, 36: 102023.

Singh NP, McCoy MT, Tice RR, Schneider EL. 1988. A simple technique for quantitation of low levels of DNA damage in individual cells. Exp Cell Res, 175(1): 184-191.

Sobańska Z, Domeradzka-Gajda K, Szparaga M, Grobelny J, Tomaszewska E, Ranoszek-Soliwoda K, Stępnik M. 2020a. Comparative analysis of biological effects of molybdenum (IV) sulfide in the form of nano-and microparticles on human hepatoma HepG2 cells grown in 2D and 3D models. In Vitro Toxicol, 68: 104931.

Sobańska Z, Sitarek K, Gromadzińska J, Świercz R, Szparaga M, Domeradzka-Gajda K, Stępnik M. 2020b. Assessment of acute toxicological effects of molybdenum (IV) disulfide nano-and microparticles after single intratracheal administration in rats. Sci Total Environ, 742: 140545.

Sobańska Z, Sitarek K, Gromadzińska J, Świercz R, Szparaga M, Domeradzka-Gajda K, Stępnik M. 2023. Biological effects of molybdenum (IV) sulfide nanoparticles and microparticles in the rat after repeated intratracheal administration. J Appl Toxicol. 44: 595-608.

Sørli, J.B., Jensen, A.C., Mortensen, A., Szarek, J., Gutierrez, C.A., Givelet, L., Hadrup, N. 2023. Pulmonary toxicity of molybdenum disulphide after inhalation in mice. Toxicology, 447: 153428. https://doi.org/10.1016/j.tox.2023.153428

Struys I, Verscheure E, Lenaerts L, Amant F, Godderis L, Ghosh M. 2023. Characterization of the genotoxic profile of antineoplastic drugs using the cytokinesis-block micronucleus cytome assay. Environ Toxicol Pharmacol, 97: 104036.

Sun K, White JC, He E, Van Gestel CA, Qiu H. 2023. Surface defects regulate the in Vivo bioenergetic response of earthworm Eisenia fetida coelomocytes to molybdenum disulfide nanosheets. ACS Nano, 17(3): 2639-2652.

Terpilowska S, Siwicki AK. 2018. Interactions between chromium (III) and iron (III), molybdenum (III) or nickel (II): Cytotoxicity, genotoxicity and mutagenicity studies. Chemosphere, 201: 780-789.

Titenko-Holland N, Shao J, Zhang L, Xi L, Ngo H, Shang N, Smith MT. 1998. Studies on the genotoxicity of molybdenum salts in human cells in vitro and in mice in vivo. Environ Mol Mutagen, 32(3): 251-259.

Tung GK, Gandhi G. 2023. Baseline and oxidatively damaged DNA in end-stage renal disease patients on varied hemodialysis regimens: a comet assay assessment. Mol Cell Biochem, 479: 199-201.

Uboldi C, Urbán P, Gilliland D, Bajak E, Valsami-Jones E, Ponti J, Rossi F. 2016. Role of the crystalline form of titanium dioxide nanoparticles: Rutile, and not anatase, induces toxic effects in Balb/3T3 mouse fibroblasts. Toxicol in Vitro, 31: 137-145.

Vazquez-Muñoz R, Bogdanchikova N, Huerta-Saquero A. 2020. Beyond the nanomaterials approach: Influence of culture conditions on the stability and antimicrobial activity of silver nanoparticles. ACS Omega, 5(44): 28441-28451.

Verma J, Warsame C, Seenivasagam RK, Katiyar NK, Aleem E, Goel S. 2023. Nanoparticle-mediated cancer cell therapy: Basic science to clinical applications. Cancer Metastasis Rev, 42(3): 601-627.

Vodenkova S, Polivkova Z, Musak L, Smerhovsky Z, Zoubkova H, Sytarova S, Svoboda M. 2015. Structural chromosomal aberrations as potential risk markers in incident cancer patients. Mutagenesis, 30(4): 557-563.

Wang CW, Liang C, Yeh HJ. 2016. Aquatic acute toxicity assessments of molybdenum (+ VI) to Daphnia magna. Chemosphere, 147: 82-87.

Wang J, Sui L, Huang J, Miao L, Nie Y, Wang K, AK. 2021. MoS_2-based nanocomposites for cancer diagnosis and therapy. Bioact Mater, 6(11): 4209-4242.

Wang S, Li K, Chen Y, Chen H, Ma M, Feng J, Shi J. 2015a. Biocompatible PEGylated MoS_2 nanosheets: controllable bottom-up synthesis and highly efficient photothermal regression of tumor. Biomaterials, 39: 206-217.

Wang X, Mansukhani ND, Guiney LM, Ji Z, Chang CH, Wang M, Nel AE. 2015b. Differences in the toxicological potential of 2D versus aggregated molybdenum disulfide in the lung. Small, 11(38): 5079-5087.

Xing Y, Cai, Cheng J, Xu X. 2020. Applications of molybdenum oxide nanomaterials in the synergistic diagnosis and treatment of tumor. Appl Nanosci, 10(7): 2069-2083.

Yadav U, Singh V, Mishra H, Saxena PS, Srivastava A. 2021. Evaluation of in vitro and in vivo toxicity of pristine molybdenum disulphide nanosheets in Swiss albino mice. BioRxiv, 2021: 05.

Yüzbaşıoğlu D, Çelik M, Yılmaz S, Ünal F, Aksoy H. 2006. Clastogenicity of the fungicide afugan in cultured human lymphocytes. Mutat Res Genet Toxicol Environ Mutagen, 604(1): 53-59.

Zeng J, Hills SA, Ozono E, Diffley JF. 2023. Cyclin E-induced replicative stress drives p53-dependent whole-genome duplication. Cell, 186(3): 528-542.

Zhou Z, Wang Y, Peng F, Meng F, Zha J, Ma L, Tan C. 2022. Intercalation-Activated Layered MoO3 Nanobelts as Biodegradable Nanozymes for Tumor-Specific Photo-Enhanced Catalytic Therapy. Angewandte Chemi, 134(16): e202115939.

Black Sea Journal of Engineering and Science
doi: 10.34248/bsengineering.1528581

Open Access Journal
e-ISSN: 2619 – 8991

Research Article
Volume 8 - Issue 1: 94-101 / January 2025

ORAL CANCER CLASSIFICATION WITH CNN BASED STATE-OF-THE-ART TRANSFER LEARNING METHODS

Kaan GÜMELE[1], Muhammet Sinan BAŞARSLAN[1*]

[1]*İstanbul Medeniyet University, Faculty of Science, Department of Computer Engineering, 34700, İstanbul, Türkiye*

Abstract: The importance of oral and dental health closely affects other vital organs. In this study, CNN-based transfer learning models are built on histopathologic and intraoral images with benign and malignant lesions. Histopathologic and intraoral images from two different sources have benign or malignant classes of lesions in the mouth. EfficientNetB7, ResNet50, VGG16, and VGG19, Xception, ConvNextBase, and MobileNetV2 were used as transfer learning methods. Model training was performed with 80%-20% train test separation and 20% validation separation on the train set. Accuracy (Acc), Precision (Prec), Recall (Rec), and F1-score (F1) metrics were used to evaluate the model. In histopathologocial images, ResNet50 was ahead with 0.8125 Acc and 0.8525 F1. In intraoral images, ConvNextBase with 0.84 Acc, and 0.80 F1 was found to be more accurate.

Keywords: Oral cancer, Image processing, Convolutional neural network, Transfer learning

Corresponding author: İstanbul Medeniyet University, Faculty of Science, Department of Computer Engineering, 34700, İstanbul, Türkiye
E mail: msinanbasarslan@gmail.com (M. S. BAŞARSLAN)
Kaan GÜMELE https://orcid.org/0009-0002-4262-0585
Muhammet Sinan BAŞARSLAN https://orcid.org/0000-0002-7996-9169

Received: August 05, 2024
Accepted: November 25, 2024
Published: January 15, 2025

Cite as: Gümele K, Başarslan MS. 2025. Oral cancer classification with CNN based state-of-the-art transfer learning methods. BSJ Eng Sci, 8(1): 94-101.

1. Introduction

Early detection of oral cancer is crucial for successful treatment and patient outcomes. Oral cancer, which includes cancers of the lips, tongue, gums, floor of the mouth and other sites in the oral cavity, can often be asymptomatic in its early stages, leading to late diagnosis and poor prognosis. Therefore, effective and accurate diagnostic methods are essential in the fight against this disease Goswami et al. (2024).

Histopathologic examination, which involves taking tissue samples from the oral cavity for analysis in a laboratory setting, is the primary method for diagnosing oral cancer. However, this process is time-consuming as it requires meticulous examination of tissue samples under a microscope at different magnifications, typically 40x, 100x, and 200x. Moreover, the Acc of the diagnosis relies heavily on the expertise of the pathologists, leading to potential discrepancies and delays in initiating treatment. On the other hand, obtaining intraoral images offers a non-invasive and relatively quick way to screen for oral abnormalities. Unlike histopathologic examination, intraoral imaging can be performed by individuals without specialized training, making it accessible for routine screening and self-assessment. This accessibility not only enables individuals to monitor their oral health, but also facilitates early detection of suspicious lesions, thereby increasing the chances of successful treatment outcomes. Intraoral images are obtained from digital images acquired during routine examinations, while histopathologic images are obtained by examining tissue samples under a microscope (de Lima et al., 2023).

It has become very important for health that imaging devices produce well-defined visual outputs. With artificial intelligence (AI) technologies, especially images on health will be highly efficient for human health.

In this study, transfer learning methods were used to build models to identify oral cancer and potentially malignant lesions on an open-source dataset with two different sources and data types (histopathologic, intraoral).

The dataset used in the study is an important resource for training and testing deep learning algorithms, while also providing a guide for researchers to improve oral cancer diagnosis. However, the collection, processing and evaluation of these images require more expertise and time than the detection of a photograph taken with a camera. This process involves the careful work of one or more pathologists and the accurate analysis of each image. Therefore, the collection and processing of histopathologic images usually takes longer and requires more expertise.

The contribution of this study is listed below:

- Open source Two different types of images (intraoral, histopathologic) of oral cancer patients will be analyzed to see which state-of-the-art Transfer learning method gives the best results in the ImageNet competition.
- The performance of transfer learning models with different parameters will be investigated in the

classification of images that can be taken with all kinds of cameras that can be accessed as well as images that require expertise to determine whether the lesion in the mouth is benign or malignant.

The block diagram of the study is given in Figure 1.

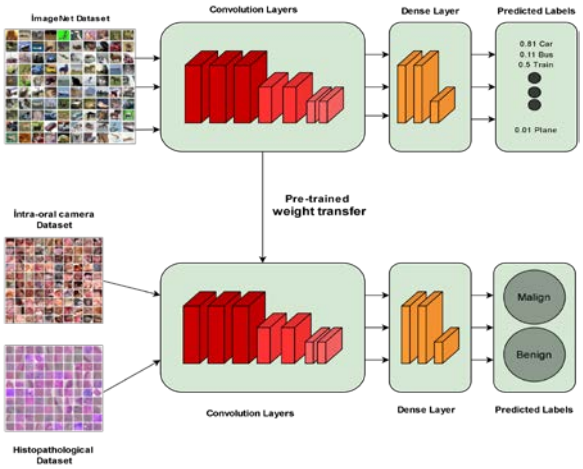

Figure 1. Block diagram of study.

The remainder of this paper is structured as follows: Section 2 reviews the literature. Section 3 details the data sources and discusses the deep learning techniques, transfer learning methods, and CNN-based approaches utilized in this study. Section 4 outlines the experimental settings and presents the results. Section 5 provides an evaluation and discussion of the study's overall findings.

2. Literature Review

In this section, we review the studies on the detection of good or bad lesions in the human mouth. Babu et al. proposed a CNN-based transfer learning method for early detection and diagnosis of oral cancer after various preprocessing and categorizing images by clustering with Fuzzy C means. They used UTI medical data sets in the study. Image categorization was developed using various Artificial Neural Network (ANN) topologies. VGG16, VGG19, DenseNet121, and DenseNet169 were used, as well as EfficientNetB0, EfficientNetB1, and EfficientNetB2, InceptionV3, and ResNet101. These include ResNetV3, MobileNet, Exception and ANN. Prominent trends in the field of oral cancer detection include the use of Inception-V3 and MobileNet architectures Babu et al. In the models they created on intraoral images; they obtained results of 0.7059 Acc with Support Vector Machine (SVM) (Chu et al., 2020) and 0.856 Acc with VG19 (Song et al., 2021).

In this work, we propose a method that can effectively distinguish between benign and malignant oral lesions and also classify their precancerous stages. After preprocessing the color spaces, they created a classifier model with Light Gradient Boosting Machine. The overall performance is promising with 0.9925 Acc, 0.9918 Prec, 0.9931 Rec, 0.9924 F1, and 0.9931 specificity for binary classification and 0.9888 tests Acc, 0.9886 Prec, 0.9792 Rec, 0.9838 F1, and 0.9903 specificity for multiclass classification, outperforming the latest methods for the task of oral cancer classification Goswami et al. (2024). Welikala et al. (2020) proposed architecture for detecting malignant or benign lesions that may lead to oral cancer in the form of image classification with ResNet-101 after Faster R-CNN object Rec. The classification achieved an F1 of 0.8707 for the identification of images containing lesions. Jeyaraj and Samuel (2019) proposed CNN architecture for segmentation and classification of multidimensional hyperspectral images in a regression-based segmented deep learning method. They obtained 0.914 Acc on facial cancer images and 0.945 Acc on 500 images. After extracting features such as energy and entropy from the color components of histopathological images of 1224 people with suspected oral cancer, models were created with SVM and K-Nearest Neighbor to classify them as normal and abnormal. They obtained better results from these images with 0.98 Acc with SVM (Bakare and Kumarasamy, 2021). Warin et al. created models with DenseNet121 and Faster R-CNN on images of 350 oral carcinoma and 350 normal oral mucosa images from retrospective images. In the study, they obtained 0.99 Acc and 0.99 F1 with DenseNet121. In the Faster R-CNN model, they obtained an F1 of 0.7931 (Warin et al., 2021).

3. Material and Methods

This section describes the dataset, the classification algorithm (CNN) used in the study and the VGG16, VGG19, EfficientNetB7, MobileNetV2, ResNet50, Xception, ConvNextBase transfer learning architectures developed based on this algorithm.

3.1. Data Source

The intraoral dataset used in the study includes color images of oral lesions captured using mobile cameras and intraoral cameras. These images can be used to identify potential oral malignancies through image analysis. The dataset was collected through consultations with doctors from various hospitals and colleges in the Indian state of Karnataka. This dataset contains images of 165 benign lesions and 158 malignant lesions. This dataset is an important resource for training and testing deep learning algorithms and can be used for early detection and diagnosis of oral cancer (Chandrashekar et al., 2021).

Intraoral images consist of digital photographs that can be easily obtained during routine examinations. Considering that almost everyone nowadays has a mobile device, the collection of such images is an extremely easy and accessible process. The creation of this data set requires only a camera and no special medical training. Therefore, the collection of intraoral images is much less time-consuming and requires less expertise compared to the examination of histopathologic images under a microscope. A benign and malign sample of the intraoral images in the study is given in Figure 2.

a) Bening b) Malign

Figure 2. An example of intraoral images from the dataset.

Microscopic analysis is conducted by two or three oral pathologists who reach a consensus on the histopathological diagnosis, considering sociodemographic, clinical, and imaging data in conjunction with histopathological findings. The dataset comprises a total of 237 samples (images and metadata) from 77 lesions in 69 patients. The primary objective of this dataset is to provide open access to histopathologic images and metadata of oral potentially malignant disorders and oral cancer, facilitating the testing of machine learning and deep learning models. It also serves educational purposes, such as training dental students and standardizing the diagnostic criteria for oral epithelial dysplasia and squamous cell carcinoma among specialists at the same center. This dataset complements (Ribeiro-de-Assis et al., 2023) which demonstrates that curated demographic and clinical data enhance the performance of AI models in the automated classification of oral cancer.

The histopathologic dataset contains images obtained by examining tissues under a microscope. The images were acquired using high-resolution microscopes to enable precise assessment of oral lesions. These images are labeled to include diseased and healthy tissues. Of particular note, histopathologic images are obtained during the examination of tissue samples under a microscope. This process is performed by a specialized pathologist and is often time-consuming and specialized. Meticulous work is required to correctly assess and label each image. Therefore, these images show in detail the cellular structures and morphologic features of oral lesions (Ribeiro-de-Assis et al., 2023). A benign and malign sample of the histopathologic images in the study is given in Figure 3.

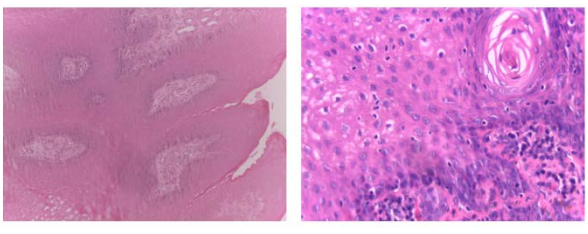

a) Bening b) Malign

Figure 3. An example of histopathologic images from the dataset.

In this study, models for benign and malignant image classification were developed using transfer learning methods. When building the models with the images belonging to the two datasets, 80-20% training and 20% test separation was made. In addition, 20% validation set separation was made in the training set.

3.2. Convolution Neural Network

Deep learning is a multi-layered method that performs traditional processes like feature extraction during the learning phase without requiring additional cost and yields better results, especially with large datasets. Deep learning networks consist of interconnected nodes (neurons) that process and transform data. Each layer extracts increasingly abstract features from the input, enabling the learning of complex patterns (Zavrak and Yilmaz, 2023). Deep neural networks, often referred to as deep architectures, contain multiple hidden layers through which forward and backpropagation occurs to perform the learning process (Başarslan and Kayaalp, 2023).

CNN is a specialized type of neural network designed to process data with a grid-like structure. Convolution is a specific type of linear operation. In simpler terms, CNNs are neural networks that apply convolution instead of a general matrix multiplication in at least one of their layers. A typical CNN architecture consists of five main layers: the input layer, convolutional layer, pooling layer, fully connected layer, and output layer. Figure 4 illustrates a CNN architecture.

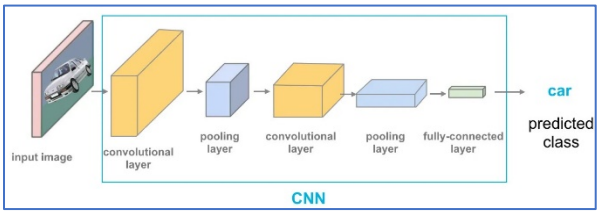

Figure 4. CNN architecture (Bal and Kayaalp, 2023).

In this study, a CNN-based transfer learning method was utilized. Transfer learning reduces the need for labeled data by leveraging pre-trained models that have already learned robust features from large datasets. This is particularly important for medical image analysis, where labeled data can be scarce, especially for rare conditions.

3.3. Transfer Learning

Transfer learning is the process of taking the knowledge gained from training a deep learning model, such as a CNN, and applying it to a different or similar domain. It involves taking a pre-trained model, usually large in size and trained with different datasets, and fine-tuning it to a new dataset or task (Dawud et al., 2019).

Transfer learning can be performed in various ways. A common approach is to freeze some layers in the pre-trained model and fine-tune only the upper layers for the new task. This helps to preserve the general features learned by the model and adapt them to the specific nuances of the new task. Another approach is to use the

pre-trained model as a feature extractor, extracting its upper layers and using the activations in the lower layers as input to a new model specifically designed for the new task (Kabakus and Erdogmus, 2022). The following image illustrates transfer learning (Gilik et al, 2022).

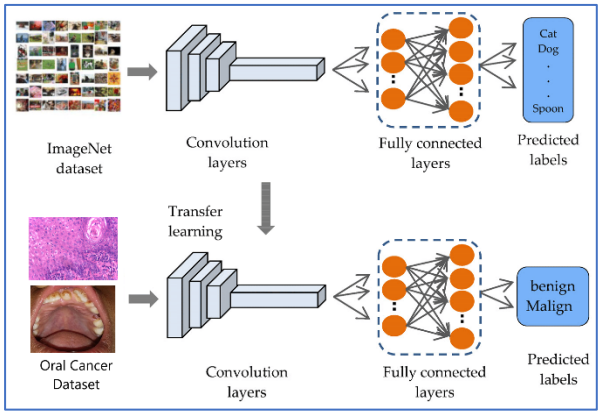

Figure 5: Transfer learning (Gilik et.al., 2022)

The study applied architectures such as VGG16, EfficientNetB7, and ResNet50 to identify the model that performs best in distinguishing between benign and malignant lesions.

3.3.1. EfficientNet

EfficientNet is a family of models developed by Google that offers an innovative approach to scaling CNN. EfficientNet uses Compound Scaling, a simple but effective method to solve the model scaling problem. This method optimizes the trade-off between the width, depth and resolution of the model. EfficientNet-B7 is one of the largest and most powerful models in the EfficientNet family, and the EfficientNet-B7 model consists of 66 layers in total (Koonce, 2021a). EfficientNetB7 was used in this study.

3.3.2. MobileNet

MobileNet is a family of CNN developed by Google that provides high Acc rates in resource-limited environments such as mobile and embedded devices. MobileNet uses depthwise separable convolutions to reduce the number of parameters and computational cost. MobileNetV2 is an improved version of MobileNet and further improves its performance by adding some innovative components. While MobileNet consists of 28 layers, MobileNetV2 consists of 58 layers. MobileNetV2 is used in this study (Dong et al., 2020).

3.3.3. ResNet

ResNet is a CNN architecture developed by He et al. (2016) facilitates the training of deep ANN. ResNet50 is a popular variation of the ResNet family and is a 50-layer deep ANN. ResNet50 is used in this study.

3.3.4. VGGNet

VGG refers to a set of CNN models developed by the Visual Geometry Group from Oxford University in 2014. VGG models build deep layered networks using predominantly small 3x3 convolution filters. This approach increases the depth of the model while at the same time ensuring computational efficiency. VGG19 is a CNN model with a total of 19 layers, while VGG16 has 16 layers (Koonce, 2021b). VGG16 and VGG19 were used in this study.

3.3.5. Xception

Xception is a CNN architecture used in deep learning and image recognition. It was developed by Chollet (2017) and introduced in 2017. Xception is a model based on and extending the Inception architecture. Its name is derived from the phrase "Extreme Inception".

3.3.6. ConvNextBase

ConvNextBase is a CNN architecture developed to improve the performance and efficiency of existing convolutional networks. ConvNextBase has deeper and wider layers and is equipped with advanced data processing capabilities. This model is optimized to achieve high Acc rates, especially on large datasets. The ConvNextBase model is usually characterized by a 12-layer structure. These layers can include convolutional filters of different sizes and types, pooling layers and normalization layers. Through these layers, ConvNextBase can learn deeper and more complex data representations. ConvNextBase was used in this study (Woo et al., 2023).

3.4. Performance metric

Performance evaluation methods such as Acc, Pre, Rec, and F1 are used to assess models developed for classification tasks, including image processing. These metrics are derived from the confusion matrix. The confusion matrix is presented in Table 1 (Öztürk et al., 2022).

Table 1. Confusion Matrix

		Actual Value	
Estimate Value	Positive	Positive	Negative
		TP	FP
	Negative	FN	TN

The Acc of a model is determined by the ratio of correctly classified samples to the total number of samples. A high Acc indicates that the model performs well in making accurate predictions, whereas a low Acc implies that there is room for improvement in the model's performance. The method for computing the Acc value is provided in equation 1 (Öztürk et al., 2022).

$$Acc = \frac{TP + TN}{TP + FP + FN + TN} \quad (1)$$

The Acc performance metric is calculated as in equation 5). Prec refers to the proportion of true positive predictions out of all the samples that the model predicts as positive. A high precision indicates that the number of false positive predictions is low, meaning most of the samples classified as positive are actually positive. Prec is calculated as shown in equation 2 (Kayaalp et al., 2018).

$$Prec = \frac{TP}{TP + FP} \quad (2)$$

Rec is a performance measure used in classification problems. It refers to the rate at which all true positive examples are correctly predicted as positive. Sensitivity, another term for Rec, is crucial for reducing the number of false negatives and minimizing the omission of true positive examples. Rec is calculated as shown in equation 3 (Öztürk et al., 2022).

$$Rec = \frac{TP}{TP + FN} \quad (3)$$

F1 is a measure often used in classification tasks such as information retrieval and machine learning. It provides a balance for evaluating the performance of a model, taking into account both Prec and Rec. Mathematically, F1 is defined as the harmonic mean of Prec and Rec. The F1 is given in equation 4 (Kayaalp et al., 2018).

$$F1 = 2 * \frac{Prec * Rec}{Prec + Rec} \quad (4)$$

Prec measures the ratio of correct positive predictions to total predicted positives. It aims to quantify how accurate positive predictions are. Prec, also known as sensitivity or true positive rate. It measures the ratio of correct positive predictions to total true positives. It shows how well the model is able to detect all positive samples.

The F1 balances these two metrics, considering Prec and Rec, and provides a single value. It is particularly useful when the class distribution is unbalanced or when false positives and false negatives lead to different results. The F1 is especially important when both Prec and Rec are important when evaluating tasks such as medical diagnostics or information retrieval systems (Kayaalp et al., 2018).

4. Results and Discussions

In this study, models were created separately on histopathologic and intaoral images using transfer learning methods. The models were run on Google Colab Pro with Python language and Tensorflow. During the model building phase for the two separate datasets, 80%-20% training and 20% test separation was made. In addition, 20% validation set separation was made in the train set. Callbacks such as early stopping and reduceonLr were used to ensure that all models were not over fit. In Table 2, detailed parameters of all models are given in the order of model creation.

The Acc, F1, Rec, Prec, AUC results of the performance of the models created on histopathological images are shown in Table 3. According to Table 3, in terms of Acc, the model created with ResNet50 is well ahead of the other models. ResNet50 is followed by EfficientNetB7, VGG19, Xception, ConvNextBase, MobilNetV2 and VGG16. While F1 and AUC also yielded similar results, EfficientNetB7 came first in terms of Prec. Similarly, ResNet50 is ahead in the Rec metric.

Table 2. Detailed Model's Parameters

Parameters	Values
Input Shape	64x64
Transfer Learning layer	EfficientNetB7, ResNet50, VGG16, VGG19, Xception, ConvNExtBase, MobileNetV2
Pooling Layer	Global Averege Pooling 2D
Dense Layer 1 Unit	256
Dense Layer 1 Activaton	ReLU
Dense Layer 2 Unit	2

Table 3. Histopatalogical Dataset Results

Models	Acc	F1	Rec	Prec	AUC
ConvNextBase	0.7083	0.7742	0.7742	0.7742	0.80
EfficientNetB7	0.7500	0.8333	0.7317	0.9677	0.84
MobileNetV2	0.6875	0.7761	0.7222	0.8387	0.73
ResNet50	0.8125	0.8525	0.8667	0.8387	0.85
VGG16	0.6875	0.7826	0.7105	0.8710	0.71
VGG19	0.7500	0.8182	0.7714	0.8710	0.71
Xception	0.7083	0.7742	0.7742	0.7742	0.71

Figure 6 shows the relative ROC of the ResNet50 transfer learning model that performs best on histopathological images. When evaluated with the ROC curve and the AUC value (0.85) shown in Figure 6, it can be seen that the classification success is quite good. The fact that the AUC is close to 1 indicates that the model successfully discriminates between positive and negative classes. However, considering the F1 value and the accuracy metrics, we can say that the overall performance of the model is balanced and satisfactory.

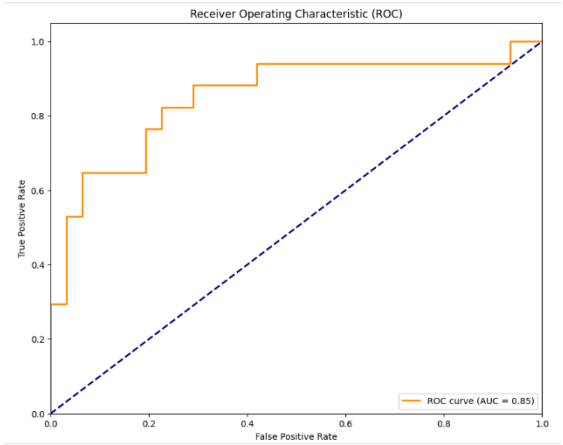

Figure 6. ROC of the ResNet50, which gives the best result in the histopathologic images.

The values of the confusion matrices of the models created with histopathological data are tabulated in Table 4. Acc, F1, Rec, Prec, AUC results of the performance of the models created on intraoral images are shown in Table 5. According to Table 5, in terms of Acc, the model created with ConvNextBase is well ahead of the other models. The next order is VGG16, ResNet50,

VGG-19, Xception, MobilNetV2. Similarly, ConvNextBase is ahead in F1 and AUC, while ResNet50 is ahead in Prec and VGG-16 is ahead in Rec. Figure 7 shows the relative ROC of the ConvNextBase transfer learning model that performs best on intraoral images.

Table 4. Confusion Matrix Values of Histopathological images

	TN	FP	FN	TP
ConvNextBase	24	7	7	10
MobileNetV2	26	5	10	7
EfficientNetB7	30	1	11	6
XCEPTION	24	7	7	10
ResNet50	28	3	4	15
VGG19	24	7	8	9
VGG16	27	4	11	8

Table 5. Intraoral Dataset Results

Models	Acc	F1	Rec	Prec	AUC
ConvNextBase	0.84	0.80	0.80	0.8387	0.7647
EfficientNetB7	0.82	0.7077	0.7246	0.7143	0.7353
MobileNetV2	0.68	0.6308	0.6364	0.6563	0.6176
ResNet50	0.80	0.7538	0.7778	0.7368	0.8235
VGG16	0.80	0.7937	0.8621	0.7353	0.82
VGG19	0.6769	0.6866	0.6970	0.6765	0.70
Xception	0.6769	0.6441	0.7600	0.5588	0.65

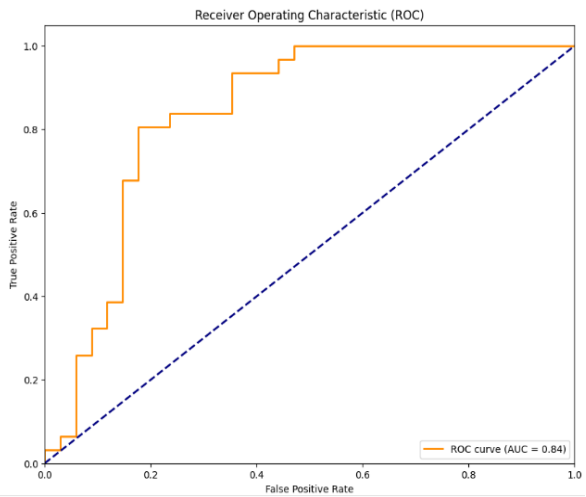

Figure 7. ROC of the ConvNextBase, which gives the best result in the histopathologic images.

In Figure 7, the ROC curve and the AUC value of the model are shown as 0.84. An AUC close to 1 indicates that the classification performance of the model is good. An AUC value of 0.84 indicates that the model is successful in balancing the true positive and false positive rates. In terms of F1 value and accuracy, it can be said that the model successfully discriminates between both positive and negative classes and misclassifications are kept to a minimum. These results indicate that the overall performance of the model is balanced and its ability to correctly identify positive classes is satisfactory.

The values of the confusion matrices of the models created with intraoral data are tabulated in Table 6.

Table 6. Confusion Matrix Values of Intraoral Images

	TN	FP	FN	TP
ConvNextBase	26	8	5	26
MobileNetV2	14	16	10	25
EfficientNetB7	26	5	5	25
XCEPTION	19	15	6	25
ResNet50	25	9	10	21
VGG19	25	9	4	27
VGG16	23	11	10	21

The performance of the models based on intraoral and histopathological image data was calculated using the TN, FP, FN, TP values shown in Table 5. Detailed information about the calculations is described under the title Performance Metrics.

This study demonstrated that CNN-based transfer learning models can be effectively applied to both histopathological and intraoral images for disease detection, even without the involvement of a pathologist. This finding highlights the potential of AI-based decision support systems to assist medical professionals in diagnosing diseases with high accuracy. By utilizing CNN-based transfer learning methods, clinicians and physicians can gain reliable insights from diverse image sources, highlighting the adaptability and scalability of AI in medical imaging. Furthermore, this study highlights the importance of selecting appropriate transfer learning models for different image types and sources. The differences in performance between histopathological and intraoral images indicate that there is no one-size-fits-all solution when it comes to applying AI in healthcare. Instead, the choice of model should be carefully tailored to the specific characteristics of the data.

Comparison of the models that gave the best results in the study with similar data sets of histopathologic and intraoral data of oral cancer is given in Table 7 and Table 8, respectively.

According to Table 7, the best model in our experiments on histopathologic image data competes with the literature with similar content. Bayesian and quadratic discriminant analysis gave better results than our model. According to Table 8, our model built on the intraoral dataset competes with the literature with similar content. The Roboflow model differs from our work as it performs object detection.

Table 7. Compare to Similar Histopathologic Oral Cancer Data Set

References	Model	Acc	F1
(Welikala et al., 2020).	ResNet101	0.7500	0.7830
(Muthu et al., 2012)	Bayesian	0.9075	None
(Chang S.W. et al.2013)	SVM	0.75	None
(Lu et al. 2017)	quadratic discriminant analysis	0.88	None
The present	ResNet50	0.8125	0.8525

Table 8. Compare to Similar Intraoral Oral Cancer Data Set

References	Model	Acc	F1
(Chu et al., 2020).	SVM	0.7059	None
(Dinesh, et.al.,2023)	Roboflow	0.8947	None
(Song, et.al, 2021)	VGG19	0.856	None
The present	ConvNextBase	0.84	0.80

Looking ahead, the potential for developing hybrid models that integrate different transfer learning techniques offers exciting opportunities. By combining methods designed for different image types or sources, it may be possible to achieve even more robust and accurate diagnostic support systems. These hybrid models could increase the flexibility of AI applications, making them more adaptable to a variety of medical scenarios. With further work, this approach could help refine the role of AI in healthcare, providing more comprehensive tools for early diagnosis and treatment, particularly in settings with limited access to specialist expertise.

Author Contributions

The percentages of the authors' contributions are presented below. The authors reviewed and approved the final version of the manuscript.

	K.G.	M.S.B.
C	50	50
D	50	50
S	50	50
DCP	50	50
DAI	50	50
L	50	50
W	50	50
CR	50	50
SR	50	50

C=Concept, D= design, S= supervision, DCP= data collection and/or processing, DAI= data analysis and/or interpretation, L= literature search, W= writing, CR= critical review, SR= submission and revision.

Conflict of Interest

The authors declared that there is no conflict of interest.

Ethical Consideration

Ethics committee approval was not required for this study because of there was no study on animals or humans.

References

Babu PA, Rai AK, Ramesh JVN, Nithyasri A, Sangeetha S, Kshirsagar PR, Rajendran A, Rajaram A, Dilipkumar S. 2024. An explainable deep learning approach for oral cancer detection. J Electr Eng Technol., 19: 1837–1848.

Bakare YB, Kumarasamy M, 2021. Histopathologıcal image analysis for oral cancer classification by support vector machine. Int J Adv Signal Image Sci, 7: 1–10.

Bal F, Kayaalp F, 2023. A novel deep learning-based hybrid method for the determination of productivity of agricultural products: apple case study. IEEE access, 11:7808–7821.

Başarslan MS, Kayaalp F, 2023. MBi-GRUMCONV: A novel Multi Bi-GRU and Multi CNN-Based deep learning model for social media sentiment analysis. J Cloud Comput, 12: 1-16.

Chandrashekar HS. Geetha A, Kiran S, Murali MS, Dinesh BR, Nanditha, 2021. Oral images dataset, URL: https://data.mendeley.com/datasets/mhjyrn35p4/2 (accessed date 13 April, 2024)

Chang SW, Abdul-Kareem S, Merican AF, Zain RB. 2013. Oral cancer prognosis based on clinicopathologic and genomic markers using a hybrid of feature selection and machine learning methods. BMC Bioinform, 14: 1-15.

Chollet F. 2017. Xception: Deep Learning with depthwise separable convolutions. IEEE Conference on Computer Vision and Pattern Recognition (CVPR), Honolulu, HI, USA, pp: 1800–1807.

Chu CS, Lee NP, Adeoye J, Thomson P, Choi SW. 2020. Machine learning and treatment outcome prediction for oral cancer. J Oral Pathol Med, 49: 977-985.

Dawud AM, Yurtkan K, Oztoprak H, 2019. Application of deep learning in neuroradiology: brain haemorrhage classification using transfer learning. Comput Intell Neurosci, 2019:

4629859

de Lima LM, de Assis MCFR, Soares JP, Grão-Velloso TR, de Barros LAP, Camisasca DR, Krohling RA, 2023. Importance of complementary data to histopathological image analysis of oral leukoplakia and carcinoma using deep neural networks. Intell Med 3: 258–266.

Dinesh Y, Ramalingam K, Ramani P, Deepak RM, 2023. Machine learning in the detection of oral lesions with clinical intraoral images. Cureus 15:e44018

Dong K, Zhou C, Ruan Y, Li Y, 2020. MobileNetV2 model for image classification. 2nd International Conference on Information Technology and Computer Application (ITCA), December 18-20, Guangzhou, China, pp: 476–480.

Gilik A, Ogrenci AS, Ozmen A. Air quality prediction using CNN+LSTM-based hybrid deep learning architecture. Environ Sci Pollut Res 29: 11920–11938 2022.

Goswami B, Bhuyan MK, Alfarhood S, Safran M, 2024. Classification of oral cancer into pre-cancerous stages from white light images using LightGBM algorithm. IEEE Access, 12: 31626–31639.

He K, Zhang X, Ren S, Sun J. 2016. Deep residual learning for image recognition. Proceedings of the IEEE Conference on Computer Vision and Pattern Recognition (CVPR), Las Vegas, 17-20 March, NV, USA, pp: 770-778.

Jeyaraj PR, Samuel N, 2019. Computer-assisted medical image classification for early diagnosis of oral cancer employing deep learning algorithm. J Cancer Res Clin Oncol, 145: 829–837.

Kabakus AT, Erdogmus P, 2022. An experimental comparison of the widely used pre-trained deep neural networks for image classification tasks towards revealing the promise of transfer-learning. Concurr Comput Pract Ex, 34: e7216.

Kayaalp F, Basarslan MS, Polat K, 2018. TSCBAS: A novel correlation based attribute selection method and application on telecommunications churn analysis. International Conference on Artificial Intelligence and Data Processing (IDAP), 28-30 September, Malatya, Tükiye, pp: 1–5.

Koonce B. 2021a EfficientNet. In convolutional neural networks with swift for tensorflow. Apress Berkeley, CA, USA, 1st ed., pp: 109–123

Koonce B. 2021b. VGG Network. convolutional neural networks with swift for tensorflow. Apress Berkeley, CA, USA, 1st ed., pp: 35-50

Lu C, Lewis Jr, JS, Dupont WD, Plummer Jr, WD, Janowczyk A, Madabhushi, A. 2017. An oral cavity squamous cell carcinoma quantitative histomorphometric-based image classifier of nuclear morphology can risk stratify patients for disease-specific survival. Mod Pathol, 30: 1655-1665.

Muthu Rama Krishnan M, Shah P, Chakraborty C. 2012 Statistical analysis of textural features for improved classification of oral histopathological images. J Med Syst 36: 865–881.

Öztürk T, Turgut Z, Akgün G, Köse C. 2022. Machine learning-based intrusion detection for SCADA systems in healthcare. Netw Model Anal Health Inform Bioinform, 11: 47.

Ribeiro-de-Assis MCF, Soares JP, de Lima LM, de Barros LAP, Grão-Velloso TR, Krohling RA, Camisasca DR. 2023 NDB-UFES: An oral cancer and leukoplakia dataset composed of histopathological images and patient data. Data Brief, 48: 109128.

Song B, Sunny S, Li S, Gurushanth K., Mendonca P, Mukhia N, Liang R, 2021. Bayesian deep learning for reliable oral cancer image classification. Biomed Opt Express, 12: 6422-6430.

Warin K, Limprasert W, Suebnukarn S, Jinaporntham S, Jantana P, 2021. Automatic classification and detection of oral cancer in photographic images using deep learning algorithms. J Oral Pathol Med, 50: 911–918.

Welikala, RA, Remagnino P, Lim JH, Chan CS, Rajendran S, Kallarakkal TG, Zain RB, Jayasinghe RD, Rimal J, Kerr AR, Amtha R, Patil K, Tilakaratne WM, Gibson J, Cheong SC, Barman SA. 2020. Automated detection and classification of oral lesions using deep learning for early detection of oral cancer. IEEE Access, 8: 132677–132693.

Woo S, Debnath S, Hu R, Chen X, Liu Z, Kweon IS, Xie, S. 2023. ConvNeXt V2: Co-Designing and scaling convnets with masked autoencoders. Proceedings of the IEEE/CVF Conference on Computer Vision and Pattern Recognition (CVPR), June 11-15 Vancouver, BC, Canada, pp: 16133–16142.

Zavrak S, Yilmaz S, 2023. Email spam detection using hierarchical attention hybrid deep learning method. Expert Syst Appl, 233: 120977.

Black Sea Journal of Engineering and Science
doi: 10.34248/bsengineering.1502427

Open Access Journal
e-ISSN: 2619 – 8991

Araştırma Makalesi (Research Article)
Cilt 8 - Sayı 1: 102-114 / Ocak 2025
(Volume 8 - Issue 1: 102-114 / January 2025)

DOĞAL GAZ FİYATININ ELMAN SİNİR AĞLARI VE YUSUFÇUK OPTİMİZASYON ALGORİTMASINA DAYALI HİBRİT MODEL İLE TAHMİNİ

Seçkin KARASU*[1]

[1]Zonguldak Bülent Ecevit University, Faculty of Engineering, Department of Electrical and Electronics Engineering, 67100, Zonguldak, Türkiye

Özet: Dünya nüfusunun artışı ile çeşitli fosil ve yenilenebilir enerji kaynaklarının kullanımı giderek artmaktadır. Doğal gaz, fosil enerji kaynakları arasında yer alan kömür ve petrolle karşılaştırıldığında, daha düşük karbondioksit emisyonu, yüksek verimlilik, kolay erişim ve düşük depolama maliyeti gibi özellikleri nedeniyle bireysel ve kurumsal düzeyde kullanım alanı bulmuştur. Doğal gaz fiyatı ekonomik açıdan önemli olduğu kadar stratejik öneme de sahiptir. Özellikle doğal gaz fiyatının gelecekte alacağı değerin tahmini, enerji üreticilerine ve tüketicilerine, yatırımcılara ve hükümetlere stratejik kararlar alırken yol gösterici olmaktadır. Bu çalışmada, Elman Sinir Ağları (ENN) ve Yusufçuk Optimizasyon Algoritması (DOA) yaklaşımları kullanılarak bir adım sonraki doğal gaz kapanış fiyatının tahmini yapılmıştır. Çalışma 01,06,2009-31,05,2024 tarihleri arasında 3986 adet kapanış fiyatı içeren veri seti kullanılarak yapılmıştır. Bir adım sonraki kapanış fiyatının tahmini için yapay zekâ yaklaşımlarından ENN yöntemi kullanılmıştır. Geri beslemeli sinir ağları arasında yer alan ENN, geçmiş verileri dikkate alarak gelecekteki değerleri tahmin etme yeteneğine sahiptir ve özellikle zaman serisi tahmininde kullanılmaktadır. Model eğitim aşamasında yusufçukların avlanma ve göç etme davranışlarından ilham alınarak geliştirilmiş bir sezgisel optimizasyon algoritması olan DOA yöntemiyle ENN'nin ağırlık ve bias değerleri bulunmuştur. Modelin değerlendirilme aşamasında veri setinin eğitim, doğrulama ve test setlerine bölünmesiyle modelin genelleme kapasitesi daha güvenilir bir şekilde ölçülmektedir. Model başarımı, çeşitli istatistiksel hata kriterleri kullanılarak değerlendirilmiş ve elde edilen sonuçlar tatminkâr bulunmuştur. Yapay zekâ yaklaşımlarının kullanımı, enerji piyasaları gibi dinamik ve karmaşık sistemlerde tahmin doğruluğunu artırmak için kritik önem taşımaktadır. ENN ve DOA'nın birleşimi, bu tür problemler için güçlü ve esnek bir çözüm sunmaktadır. Bu çalışma, doğal gaz fiyatlarının tahmininde yapay zekâ yöntemlerinin etkinliğini göstermekte ve bu yaklaşımların pratik uygulamalarda kullanılabilirliğini ortaya koymaktadır.

Anahtar kelimeler: Doğal gaz tahmini, Elman sinir ağları, Yusufçuk optimizasyon algoritması, Zaman serisi, Tahmin

Prediction of Natural Gas Price with Hybrid Model Based on Elman Neural Networks and Dragonfly Optimization Algorithm

Abstract: With the increasing in the world population, the use of various fossil and renewable energy resources is increasing. Compared to coal and oil, which are among the fossil energy sources, natural gas has found use at individual and institutional levels due to its features such as lower carbon dioxide emissions, high efficiency, easy access and low storage costs. The price of natural gas is not only economically important but also strategically important. In particular, the prediction of the future value of natural gas prices provides guidance for energy producers, consumers, investors and governments when making strategic decisions. In this study, the one step ahead natural gas close price is predicted by using Elman Neural Networks (ENN) and Dragonfly Optimization Algorithm (DOA) approaches. The analysis utilized a dataset spanning from June 01, 2009, to May 31, 2024, encompassing 3986 close prices. ENN, one of the artificial intelligence approaches, is used to predict the next closing price. ENN, which is among the feedback neural networks, has the ability to predict future values by taking into account past data and is especially used in time series forecasting. During the model training phase, the weight and bias values of the ENN are found with the DOA method, which is a heuristic optimization algorithm developed inspired by the hunting and migration behavior of dragon flies. In the evaluations of the model, the generalization capacity of the model is measured more reliably by dividing the data set into training, validation and test sets. Model performance is evaluated using various statistical error criteria and the results are found to be satisfactory. The use of artificial intelligence approaches is critical to increase forecast accuracy in dynamic and complex systems such as energy markets. The combination of ENN and DOA provides a powerful and flexible solution for such problems. This study demonstrates the effectiveness of artificial intelligence methods in predicting natural gas prices and reveals the usability of these approaches in practical applications.

Keywords: Natural gas prediction, Elman neural networks, Dragonfly optimization algorithm, Time series, Forecasting

***Sorumlu yazar (Corresponding author):** Zonguldak Bülent Ecevit University, Faculty of Engineering, Department of Electrical and Electronics Engineering, 67100, Zonguldak, Türkiye
E mail: seckin.karasu@beun.edu.tr (S. KARASU)
Seçkin KARASU https://orcid.org/0000-0001-5277-5252

Gönderi: 18 Haziran 2024 **Received:** June 18, 2024
Kabul: 25 Kasım 2024 **Accepted:** November 25, 2024
Yayınlanma: 15 Ocak 2025 **Published:** January 15, 2025

Cite as: Karasu S. 2025. Prediction of natural gas price with hybrid model based on elman neural networks and dragonfly optimization algorithm. BSJ Eng Sci, 8(1): 102-114.

1. Giriş

Doğal gaz, modern dünyanın enerji ihtiyaçlarını karşılayan temel bir kaynaktır. Endüstriyel üretimden evlerimizin ısıtılmasına kadar geniş bir yelpazede hayati bir rol üstlenmektedir (Afgan vd., 2007). Aynı zamanda elektrik üretimi (Kong vd., 2023), ulaşım (Khan vd., 2015) ve kimyasal sanayi (Szklo vd., 2004) gibi kritik sektörlerde kullanılarak yaşamımızın her yönünü etkilemektedir. Bu çok yönlü kaynağın öne çıkan avantajlarından biri, yakıldığında daha az kirletici salınımı sağlayan fosil yakıtlar içerisinde nispeten temiz bir enerji olmasıdır (Rizvi vd., 2022). Doğal gazın bu çevre dostu yanma özelliği, çevresel sürdürülebilirlik hedeflerine katkıda bulunmasını sağlamaktadır. Bunun yanı sıra, enerji güvenliği ve uluslararası ilişkiler açısından da büyük bir stratejik öneme sahiptir. Enerji sektöründeki değişen dinamikler ve çevre bilincinin artmasıyla, doğal gazın rolü giderek daha fazla önem kazanmaktadır (Gillessen vd., 2019). Ekonomik büyüme ve gelişim için gerekli enerji arzının sağlanmasında, doğal gazın esnek ve temiz özellikleri ön plana çıkmaktadır. Bu durum, enerji piyasalarında tedarik güvenliğini artırarak istikrarı desteklemekte ve alternatif enerji kaynaklarının geliştirilmesi yönündeki çabaları teşvik etmektedir (Gillessen vd., 2019). Ancak, doğal gazın yaygın kullanımı beraberinde bazı zorlukları da getirmektedir. Özellikle kaynak dağılımı, enerji arzı ve talebi dengesi gibi konularda stratejik planlama gerekmektedir (Villicaña-García ve Ponce-Ortega, 2019; Goodell vd., 2023). Doğal gaz fiyatının zaman serisi tahmini enerji sektörü ve ekonomi açısından büyük önem taşımaktadır. Doğal gaz fiyatı zaman serisi tahminleri, enerji sektöründe stratejik kararların alınmasında ve işletme süreçlerinin yönetilmesinde hayati bir rol oynamaktadır (Khan, 2018). Bu tahminler, enerji şirketlerinin risk yönetimi, tedarik zinciri planlaması ve maliyet kontrolü gibi alanlarda etkili olmasını sağlamaktadır. Ayrıca yatırım kararlarının yapılması, temiz enerji geçişi sürecinin yönetimi, politika oluşturulması ve rekabetçilik analizleri gibi alanlarda da kritik bir öneme sahiptir (Farrokhifar vd., 2020; Gürsan ve Gooyert, 2021). Ancak, doğal gaz fiyatlarındaki dalgalanmaların etkisi, güvenilir tahminlerin sağlanması için ileri düzeyde makine öğrenmesi, yapay zekâ ve optimizasyon tekniklerinin kullanımını ön plana çıkartmaktadır.

Literatür incelendiğinde doğal gaz fiyatının tahmini için makine öğrenimi algoritmalarının kullanımının giderek popüler hale geldiği görülmektedir. Yapılan bir çalışmada Yapay Sinir Ağları (ANN), Destek Vektör Makineleri (SVM), Gradyan Artırma Makineleri (GBM) ve Gaussian Süreç Regresyonu (GPR) gibi yaygın makine öğrenimi araçlarına dayalı tahmin modelleri kıyaslanmıştır (Su vd., 2019). Model eğitimi için çapraz doğrulama yöntemi kullanılmış ve Ocak 2001'den Ekim 2018'e kadar olan aylık Henry Hub doğal gaz spot fiyat verileri değerlendirilmiştir. Sonuçlar, bu dört makine öğrenimi yönteminin doğal gaz fiyatlarını tahmin etmede farklı performans sergilediğini göstermektedir. Ancak genel olarak, ANN'in SVM, GBM ve GPR'ye kıyasla daha iyi bir tahmin performansı ortaya koyduğu görülmüştür (Su vd., 2019). Bir başka çalışmada doğal gaz fiyatlarının daha güvenilir bir şekilde tahmin edilmesi amacıyla Varyasyonel Kip Ayrıştırma (VMD) ve Topluluk Ampirik Kip Ayrıştırma (EEMD) yöntemlerini birleştirerek, VMD'den sonra kalan artık terimi (Res) EEMD ile ayrıştırmaktadır (Zhan ve Tang, 2022). Daha sonra, bu ayrıştırılmış veriler Uzun-Kısa Süreli Bellek (LSTM) tahmin modeli ile birleştirilerek VMD-EEMD-Res-LSTM adı verilen yeni bir hibrit model oluşturulmuştur (Zhan ve Tang, 2022). Bu modelde mevcut ayrıştırma teknolojileri ile LSTM modelini birleştirildiği ve VMD'den sonra kalan artık terimdeki önemli bilgilerin göz ardı edilmediği için diğer ayrıştırma yaklaşımlarından farklı olduğu belirtilmiştir. Modelin tahmin performansını doğrulamak için, ABD'deki doğal gaz spot fiyat verileri kullanılarak çok adımlı bir ampirik karşılaştırma analizi yapılmıştır. Sonuçlar, önerilen yeni hibrit modelin önemli tahmin avantajlarına sahip olduğunu göstermektedir (Zhan ve Tang, 2022). Li vd. (2021) tarafından aylık Henry Hub doğal gaz fiyatının tahmin edilmesi için VMD, Parçacık Sürü Optimizasyonu (PSO) ve Derin İnanç Ağları (DBN) ile entegre edilmiş hibrid bir model önerilmiştir. Bunun yanında doğal gaz fiyatını uzun vadeli olarak etkileyen faktörler incelenerek bu faktörlerin tahmin performansına katkı sağladığı belirtilmiştir. Yapılan deneysel sonuçlar, önerilen hibrid modelin geleneksel yöntemlere göre daha yüksek tahmin doğruluğuna sahip olduğunu ortaya çıkartmıştır. Özellikle, doğal gaz tüketimi, Amerikan Batı Texas (WTI) ham petrol spot fiyatları, aşırı sıcak ve soğuk hava durumlarının doğal gaz fiyat tahminlerinde belirgin etkileri olduğu belirtilmektedir. Mittakola vd. (2024) tarafından doğal gaz tahmini için veri odaklı modellerden Destek Vektör Regresyonu (SVR), LSTM ve modifiye edilmiş veri odaklı model olan Geliştirilmiş Desen Dizisi Benzerlik Araması (IPSS) yaklaşımı olmak üzere üç yaygın model tanıtılmaktadır. Bu üç model temel alınarak ağırlıklı hibrit veri odaklı model önerilmektedir. Modelin eğitimi için, Haziran 2018 öncesinde ABD'deki günlük doğal gaz spot fiyatlarıyla ilgili veriler kullanılmakta ve modelin tahmin yeteneği Haziran 2018'den Mayıs 2019'a kadar olan verilerle test edilmektedir. Önerilen yeni IPSS modelinin günlük doğal gaz fiyatlarını doğru bir şekilde tahmin edebildiği gösterilmektedir. Duan vd. (2023) tarafından doğal gaz fiyatlarının tahminine katkıda bulunan yeni bir hibrit model önerilmektedir. Uyarlanabilir Gürültü ile Komple Topluluk Ampirik Kip Ayrıştırması (CEEMDAN), Birlikte Çalışma Torbalama (Bagging) yaklaşımı ile entegre edilen Harris Hawks Optimizasyonu (HHO) ve SVR gibi yöntemleri birleştiren yeni bir hibrit model geliştirilmektedir. Aylık Henry Hub doğal gazı tahmini için önerilen yöntemin zaman serisini tahmin etmede daha etkili olduğu gösterilmektedir. Saghi ve Rezaee (2021) tarafından doğal gaz fiyatlarının tahminine yönelik girdi ve hedef vektörleri arasındaki Öklid Mesafesi'ne dayalı yeni bir yaklaşım kullanılarak

optimal zaman gecikmeleri belirlenmektedir. Daha sonra veri setindeki gürültüyü azaltmak amacıyla dalgacık ayrıştırması yöntemi uygulanmaktadır. Ayrıca, zaman serisindeki belirsizliği modellemek için farklı üyelik fonksiyonlarına sahip bulanık dönüşüm yöntemi kullanılmaktadır. Dalgacık ayrıştırması ve bulanık dönüşüm yöntemleri, verinin ön işleme aşamasında birleştirilmektedir. Çeşitli sinir ağlarının çıktılarını entegre etmek için birlikte çalışma yöntemi kullanılmakta ve elde edilen sonuçlar önerilen ön işleme yöntemlerinin doğal gaz fiyat tahminindeki doğruluğu artırdığını göstermektedir.

Bu çalışmada, Elman Sinir Ağları (ENN) ile tahmin modeli oluşturularak doğal gaz fiyatının bir gün sonra alacağı değerin tahmini yapılmıştır. ENN'de gizli katman nöron sayısı ve bias değerlerinin eğitim aşamasında bulunması için optimizasyon yöntemleri kullanılmıştır. Yusufçuk Optimizasyon Algoritması (DOA) yaklaşımı, Genetik Algoritma (GA) ile kıyaslandığında olası modeller içerisinde hata değeri düşük, tahmin başarımı yüksek olan modelin bulunması sağlanmıştır. Oluşturulan hibrit modelin performansını ölçmek için istatistiksel ölçütlerden Ortalama Kare Hatası (MSE), Ortalama Karekök Sapma Hatası (RMSE) ve Pearson korelasyon katsayısı kullanılmıştır. Devam eden kısımlarda oluşturulan model ve alınan sonuçlar hakkında detaylı bilgi verilmiştir.

2. Materyal ve Yöntem

Bu bölümde, doğalgaz fiyatının tahmini için kullanılan veri seti, yapay zekâ yöntemlerinden ENN ve optimizasyon yaklaşımı olarak DOA yaklaşımı detaylı bir şekilde açıklanmıştır.

2.1. Veri Seti

Bu çalışmada 01,06,2009-31,05,2024 tarihleri arasında 3986 adet kapanış fiyatı içeren doğal gaz zaman serisi kullanılmıştır (Anonymous, 2024). Şekil 1'de doğalgaz zaman serisinin her yılın başlangıcına dikine çizgiler eklenmiş ve farklı renkte renklendirilmiş şekilde çizdirilmiştir.

Şekil 1. Doğalgaz kapanış fiyatının zamana göre değişimi.

Tablo 1'de doğalgaz zaman serisi için yıllara göre hesaplanan en düşük, en yüksek, ortalama değer, standart sapma, çarpıklık ve basıklık gibi istatistiksel değerler verilmiştir.

Yıllara göre doğalgaz kapanış fiyatının dağılım grafiği ise Şekil 2'deki gibi verilmiştir. Devam eden kısımlarda hibrit modelin kısımları daha detaylı açıklanmıştır.

2.2. Elman Sinir Ağları

Elman Sinir Ağları (ENN) Jeffrey L. Elman tarafından önerilmiş bir tür tekrarlayan sinir ağıdır (Elman, 1990). ENN'ler zaman içinde sıralı verilerle çalışabilen ve veri kalıplarındaki zaman bağımlılığını öğrenebilen ağlar olarak tanımlanmıştır. Geleneksel ileri beslemeli sinir ağındaki gibi giriş katmanı, gizli katman ve çıkış katmanından oluşmaktadır. Farklı olarak gizli katmanın çıkışından bir geri besleme mekanizmasına sahiptir. Bu kısım bağlam katmanı (context layer) ile kurulmaktadır. Bu mekanizma ile ağın önceki zaman adımlarındaki bilgiyi hatırlamasına ve bu bilgiyi mevcut zaman adımındaki hesaplamalarda kullanmasına olanak tanınmaktadır. Bağlam katmanı gizli katmanın çıkışını bir sonraki zaman adımına girdi olarak taşımakta ve bir bellek elemanı rolü oynamaktadır. Bu bağlantı yöntemi ile ağ tarihsel verilere duyarlı hale gelmektedir (Elman, 1990; Liu vd., 2023). Şekil 3'te ENN'nin genel topolojisi gösterilmektedir. ENN modeli eşitlik 1'deki gibi tanımlanmaktadır.

$$y(k) = g(\omega_3 x(k) + b_2) \quad (1)$$

Burada y çıkış katmanının düğüm vektörü, x gizli katmanın düğüm vektörünü, ω_3 gizli katman ve çıkış katmanı arasındaki ağırlık katsayılarını, b_2 gizli katman eşik değerlerini, g aktivasyon fonksiyonunu ifade etmektedir. Gizli katman düğüm vektörü x ise eşitlik 2'deki gibi tanımlanmaktadır.

$$x(k) = f(\omega_1 x_c(k) + \omega_2(u(k-1)) + b_1) \quad (2)$$

Burada x_c geribesleme durum vektörünü, u giriş vektörünü, ω_1 bağlam katmanı ve gizli katman arasındaki ağırlık katsayılarını, ω_2 giriş katmanı ve gizli katman arasındaki ağırlık katsayılarını, b_1 giriş katmanı eşik değerlerini, f aktivasyon fonksiyonunu ifade etmektedir. Geribesleme durum vektörü ise gizli katman düğüm vektörünün önceki değerleri olacak şekilde eşitlik 3'teki gibi ifade edilmektedir.

$$x_c(k) = x(k-1) \quad (3)$$

Tablo 1. Doğalgaz zaman serisi için yıllara göre hesaplanan istatistiksel değerler

Yıllar	En Düşük	En Yüksek	Ortalama	Standart Sapma	Çarpıklık	Basıklık
2009	2,51	5,99	4,1643	0,8195	0,1804	-0,7766
2010	3,33	6,01	4,3931	0,5600	0,8071	0,1379
2011	2,96	5,01	4,1061	0,4693	-0,2940	-0,6023
2012	1,90	3,91	2,8401	0,5037	0,3236	-0,8672
2013	3,13	4,53	3,7420	0,3285	0,3741	-0,6076
2014	2,91	5,47	4,2515	0,4331	-0,2117	0,0437
2015	1,74	3,31	2,6285	0,2679	-0,9924	0,8974
2016	1,63	3,87	2,5628	0,5365	0,2886	-0,7725
2017	2,61	3,72	3,0267	0,1805	0,2998	0,1587
2018	2,56	4,68	3,0604	0,4852	1,8846	2,8091
2019	2,08	3,56	2,5263	0,2742	0,8226	0,9597
2020	1,52	3,38	2,1595	0,4611	0,6543	-0,8084
2021	2,45	6,32	3,7298	1,0358	0,6534	-0,7830
2022	3,75	9,73	6,5483	1,5743	0,0170	-1,0304
2023	2,01	4,14	2,7020	0,4046	0,9508	0,6708
2024	1,59	3,32	2,1187	0,4261	0,9432	-0,1938

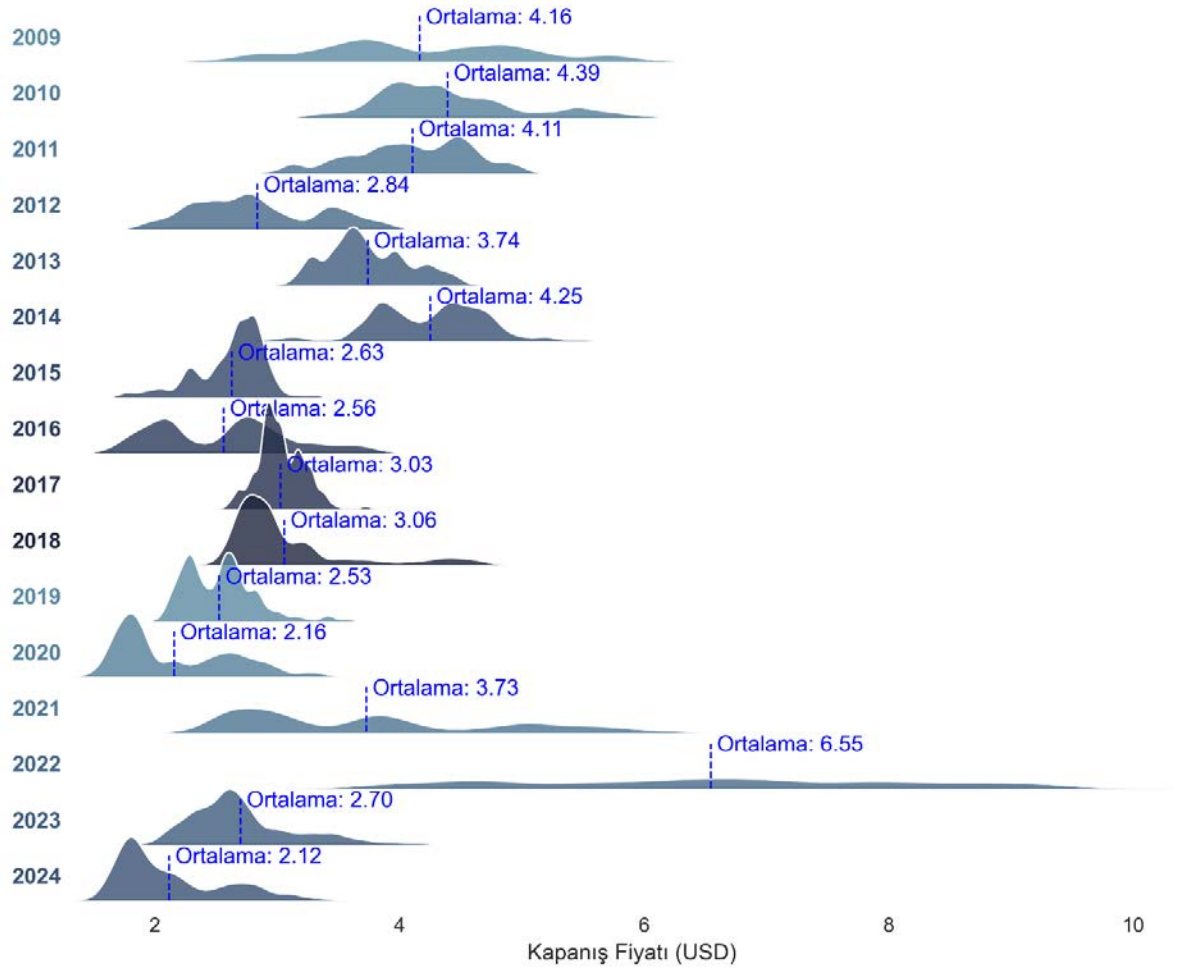

Şekil 2. Yıllara göre doğalgaz kapanış fiyatının dolar bazlı dağılım grafiği.

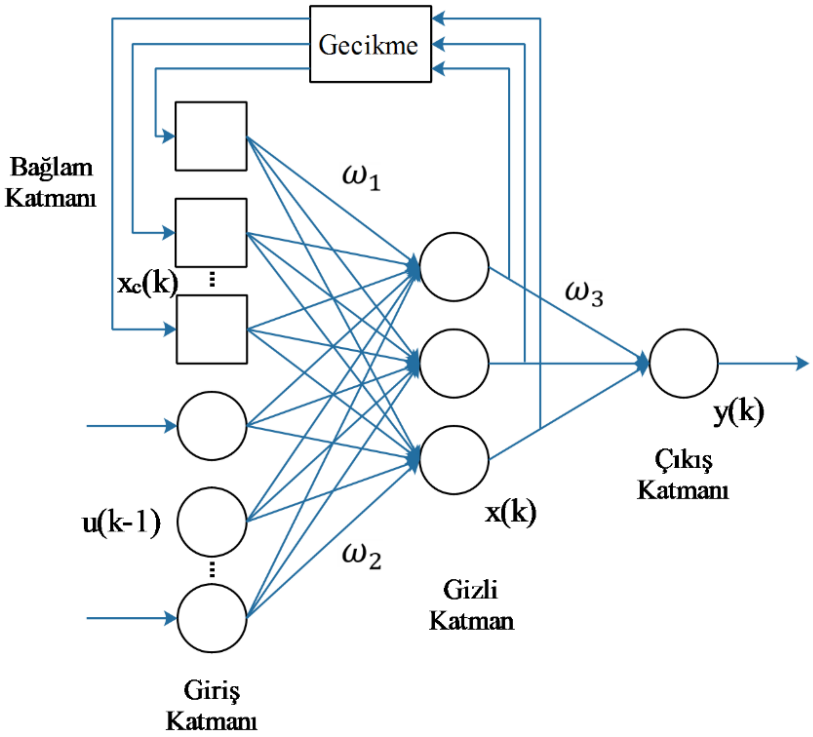

Şekil 3. Elman Sinir Ağlarının genel topolojisi (Elman, 1990; Zhou vd., 2023).

2.3. Yusufçuk Optimizasyon Algoritması

Yusufçuk sineği, büyük birleşik gözleri, güçlü saydam kanatları, göz alıcı renkleri ve uzun vücutlarıyla tanınan bir böcek türüdür. Dünya genelinde çok farklı türleri bulunmaktadır. Yaşam döngüsü larva ve yetişkin olmak üzere iki evreden oluşmaktadır. Avlanma sırasında zeki ve nadir davranışlar sergilemektedirler. Statik sürülerde küçük gruplar halinde uçup avlanmak için ileri geri hareket etmektedirler. Dinamik sürülerde ise çok sayıda yusufçuk, büyük gruplar halinde göç için uzun yolculuklar yapmaktadırlar (Mirjalili, 2016).

Reynolds'a göre, sürülerin davranışları ayrılma, hizalanma ve birliktelik olmak üzere üç temel ilkeyi takip etmektedir (Reynolds, 1987; Mirjalili, 2016). Sürülerin ana hedefi hayatta kalmak olduğundan, bireyler genellikle yiyecek kaynaklarına çekilirken dışarıdaki tehditlerden kaçınmaya yönelmektedirler. Bu iki temel davranış göz önüne alındığında, Şekil 4'teki gibi bireylerin hayatta kalma ve etkili iş birliği için bir yiyecek kaynağına doğru çekim ve düşmanın dikkatini dağıtma gibi faktörlerde göz önüne alındığında beş ana davranış söz konusudur.

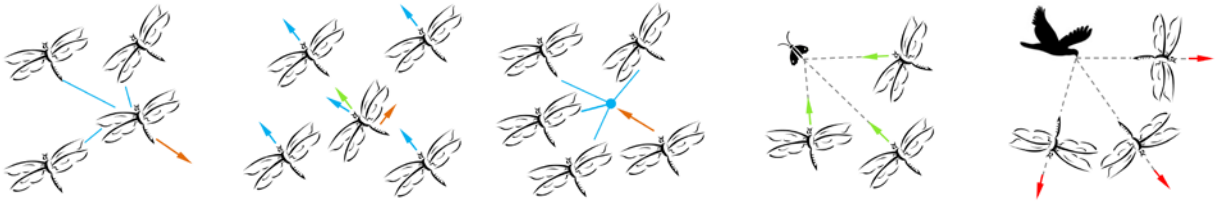

a b c d e

Şekil 4. Sürülerdeki bireylerin konum güncellemelerinde beş davranış kalıbı. a. ayrılma b. hizalanma c. birliktelik d. bir yiyecek kaynağına doğru çekim e. düşmanın dikkatini dağıtma (Mirjalili, 2016).

Her bir davranış matematiksel olarak eşitlik 4-8'deki gibi modellenmektedir (Reynolds, 1987; Mirjalili, 2016). Ayrılma, sürü içindeki bireylerin komşuluklarındaki diğer bireylerden statik olarak çarpışmayı önlemeye çalışmalarını ifade etmektedir. Başka bir ifadeyle, bireylerin birbirlerine yakın olmaktan kaçınarak aralarında güvenli bir mesafe korumalarını sağlayan bir davranıştır. Böylece sürü içindeki her bir birey, çevresindeki diğer bireylerle etkileşime girerken çarpışma riskini minimize etmekte dolayısıyla sürünün genel güvenliğini ve düzenini sağlamaya yardımcı olmaktadır. Ayrılma matematiksel olarak eşitlik 4'teki gibi ifade edilmektedir.

$$S_i = -\sum_{j=1}^{N} X - X_j \quad (4)$$

Burada X mevcut bireyin konumunu, X_j ise j. komşu bireyin konumunu ve N komşu bireylerin sayısını göstermektedir. Hizalanma, sürü içindeki her bireyin, çevresindeki diğer bireylerin hareket yönü ve hızına yakın bir şekilde hareket etmesi olarak ifade

edilmektedir. Bu davranış, bireyler arasında birliği ve koordinasyonu sağlayarak sürünün etkili bir şekilde hareket etmesini ve grup hedeflerine ulaşmasını kolaylaştırmaktadır. Hizalanma eşitlik 5'teki gibi ifade edilmektedir.

$$A_i = \frac{\sum_{j=1}^{N} V_j}{N} \quad (5)$$

Bu denklemde V_j komşu bireylerin hızını göstermektedir. Birliktelik, sürü içindeki bireylerin komşuluklarındaki diğer bireylerin ağırlık merkezi yönünde eğilim gösterme durumunu ifade etmektedir. Bir başka ifadeyle, bir bireyin bulunduğu çevredeki diğer bireylerin bulunduğu alanın merkezine doğru çekilme eğilimi olarak bu davranış tanımlanmaktadır. Böylece sürü içindeki her bir birey, sürünün bütünlüğünü korumak ve grup içinde birliği sağlamak için yakınlaşma ve bir araya gelme eğilimindedir. Birliktelik ise matematiksel olarak eşitlik 6'daki gibi ifade edilmektedir.

$$C_i = \frac{\sum_{j=1}^{N} X_j}{N} - X \quad (6)$$

Bir besin kaynağına doğru çekim ise eşitlik 7'deki gibi ifade edilmektedir.

$$F_i = X^+ - X \quad (7)$$

Burada X^+ yiyecek kaynağının konumunu göstermektedir. Düşmanın dikkatini dağıtma ise matematiksel olarak eşitlik 8'deki gibi verilmektedir.

$$E_i = X^- + X \quad (8)$$

Burada X^- düşmanın konumunu göstermektedir.

Yapay yusufçukların bir arama alanındaki konumlarını güncellemek ve hareketlerini simüle etmek için iki vektör dikkate alınmaktadır. Bunlar adım (ΔX) ve konum (X) olarak tanımlanmaktadır. Adım vektöründe, PSO algoritmasındaki hız vektörü temel alınmıştır. PSO'daki hız vektörüne benzer şekilde eşitlik 9'daki gibi yusufçukların hareket yönü beş temel ilkenin kombinasyonu olarak ifade edilmektedir.

$$\Delta X_{t+1} = (sS_i + aA_i + cC_i + fF_i + eE_i) + w\Delta X_t \quad (9)$$

Burada s, ayrılma ağırlığını, S_i, i. bireyin ayrılmasını, a hizalanma ağırlığını, A_i, i. bireyin hizalanmasını, c, birliktelik ağırlığını, C_i, i. bireyin birlikteliğini, f, yiyecek faktörünü, F_i, i. bireyin yiyecek kaynağını e, düşman faktörünü, E_i, i. bireyin düşmanının konumunu ifade etmektedir. Pozisyon vektörü ise eşitlik 10'daki gibi hesaplanmaktadır.

$$X_{t+1} = X_t + \Delta X_{t+1} \quad (10)$$

Rastgeleliği, stokastik davranışı ve yapay yusufçukların keşif özelliklerini geliştirmek amacıyla, komşu çözümler olmadığında arama alanında rastgele yürüyüş (*Lévy* uçuşu) kullanarak dolaşmaları gerekmektedir. Bu yöntem, yusufçukların daha geniş bir arama alanını keşfetmelerine ve daha etkili çözümler bulmalarına olanak tanımaktadır. Bu durumda, yusufçukların pozisyonları eşitlik 11'deki gibi güncellenmektedir.

$$X_{t+1} = X_t + Lévy(d) \times X_t \quad (11)$$

Lévy uçuşu ise eşitlik 12'deki gibidir.

$$Lévy(x) = 0{,}01 \times \frac{r_1 \times \sigma}{|r_2|^{\frac{1}{\beta}}} \quad (12)$$

Burada $r_1$ve r_2 [0, 1] aralığında iki rastgele sayı, β ise bir sabit olmak üzere σ eşitlik 13'teki gibi hesaplanmaktadır.

$$\sigma = \left(\frac{\Gamma(1+\beta) \times \sin\left(\frac{\pi\beta}{2}\right)}{\Gamma\left(\frac{1+\beta}{2}\right) \times \beta \times 2^{\left(\frac{\beta-1}{2}\right)}} \right)^{(1/\beta)} \quad (13)$$

Yusufçuk Optimizasyon Algoritması (DOA'nda verilen, optimizasyon problemi için hesaplamaya rastgele çözümler seti oluşturularak başlanmaktadır. Bu süreçte, yusufçukların konum ve adım vektörleri, değişkenlerin alt ve üst sınırları içinde rastgele değerlerle başlatılmaktadır. Her yinelemede, her yusufçuğun konumu ve adımı eşitlik 10, 11 ve 12 kullanılarak güncellenmektedir. X ve ΔX vektörlerini güncellemek için, her yusufçuğun komşuluğu, tüm yusufçuklar arasındaki Öklid mesafesi hesaplanarak ve N tanesi seçilerek belirlenmektedir. Konum güncelleme süreci, bitiş kriteri karşılanana kadar devam etmektedir. DOA'nın sözde kodu Şekil 5'te verilmiştir.

Algoritma: DOA'nin sözde kodu.

1. **Initialization:** Yusufçuk popülasyonunu başlat $Xi(i = 1,\ldots,N)$
2. Adım vektörlerini başlat
3. **while** Bitirme koşulu sağlanana kadar devam et
   - Tüm yusufçukların amaç değerlerini hesapla
   - Yiyecek kaynağını ve düşmanı güncelle
   - w, s, a, c, f ve e değerlerini güncelle
   - Denklem 4 ile 8 kullanılarak S, A, C, F ve E değerlerini hesapla
   - Komşuluk yarıçapını güncelle
   - **if** Bir yusufçuğun en az bir komşu yusufçuğu varsa
     i. Denklem 9 kullanılarak hız vektörünü güncelle
     ii. Denklem 10 kullanılarak konum vektörünü güncelle
   - **else**
     i. Denklem 11 kullanılarak konum vektörünü güncelle
   - Eğer yeni konumlar sınırların dışındaysa, yeni konumları kontrol et ve düzelt
   - **end if**
4. **end while**

Şekil 5. DOA'nın sözde kod gösterimi (Mirjalili, 2016).

2.4. Genetik Algoritma

Genetik Algoritma (GA), biyolojik evrim süreçlerinden ilham alınarak optimizasyon problemlerini çözmek için kullanılan bir yöntemdir (Holland, 1992). GA, bir popülasyon içindeki bireylerin evrimleşerek daha iyi çözümler üretmesini sağlamaktadır. Bu süreçte, her bir birey genetik bir yapı ile temsil edilmekte ve doğal seçilim, çaprazlama ve mutasyon gibi genetik operatörler kullanılarak yeni nesiller oluşturulmaktadır. Doğal seçilim, en iyi uyum sağlayan bireylerin bir sonraki jenerasyona seçilmesini sağlarken, çaprazlama ve mutasyon, genetik çeşitliliği artırarak çözüm uzayını daha etkili bir şekilde taramaktadır (Holland, 1992). Çalışmada DOA yaklaşımı ile kıyaslamak amacıyla GA yöntemi kullanılmaktadır.

2.5. Performans Metrikleri

Bu çalışmada MSE, RMSE ve Pearson korelasyon katsayısı performans metrikleri olarak kullanılmıştır. MSE, her bir tahminin gerçek değerden olan farkının karesi alınarak bu karelerin ortalamasını hesaplayan bir ölçüm yöntemidir. MSE formülü eşitlik 14'te verilmiştir.

$$MSE = \frac{1}{n}\sum_{i=1}^{n}(x_i - y_i)^2 \quad (14)$$

RMSE ise gerçek değerlerle tahmin edilen değerler arasındaki farkların karelerinin ortalamasının karekökü alınarak hesaplanmaktadır. eşitlik 15'teki gibi hesaplanmaktadır.

$$RMSE = \sqrt{\frac{1}{n}\sum_{i=1}^{n}(x_i - y_i)^2} \quad (15)$$

Pearson korelasyon katsayısı iki değişken arasındaki ilişkinin gücünü ve yönünü ölçen istatistiksel bir ölçüdür. eşitlik 16'daki gibi hesaplanmaktadır. Burada $\hat{x}_i$ ve $\hat{y}_i$ sırasıyla gerçek ve tahmin edilen zaman serisinin ortalama değeri olarak hesaplanmaktadır.

$$R = \frac{\sum_{i=1}^{n}(x_i-\hat{x}_i)(y_i-\hat{y}_i)}{\sqrt{\sum_{i=1}^{n}(x_i-\hat{x}_i)^2}\sqrt{\sum_{i=1}^{n}(y_i-\hat{y}_i)^2}} \quad (16)$$

3. Bulgular ve Tartışma

Benzetim çalışması MATLAB ortamında gerçekleştirilmiştir. Öncelikle Şekil 6'daki gibi ENN modeli oluşturulmuştur.

Burada örnek olarak gecikme sayısı 1, gizli katman nöron sayısı 30 olan bir ENN modelinin MATLAB ortamında temsili çizimi verilmiştir. Benzetim çalışmasında gizli katman nöron sayısı 3 ile 30 arasında değiştirilmiştir. Veri seti %70 eğitim, %15 doğrulama ve %15 test olmak üzere ayrılmıştır. Benzetim çalışması 20 kez tekrar edilmiştir. ENN modelinin eğitimi aşamasında model ağırlık ve bias değerleri kıyaslama yöntemi olarak Genetik Algoritma (GA) ile bulunmuştur. Tablo 2'deki ağırlık ve bias değerleri dikkate alındığında gizli katman nöron sayısı (M) değerine bağlı olarak bireyler M^2+3M+1 adet değerden oluşmaktadır. DOA yaklaşımı içinde aynı değerler optimize edilmektedir.

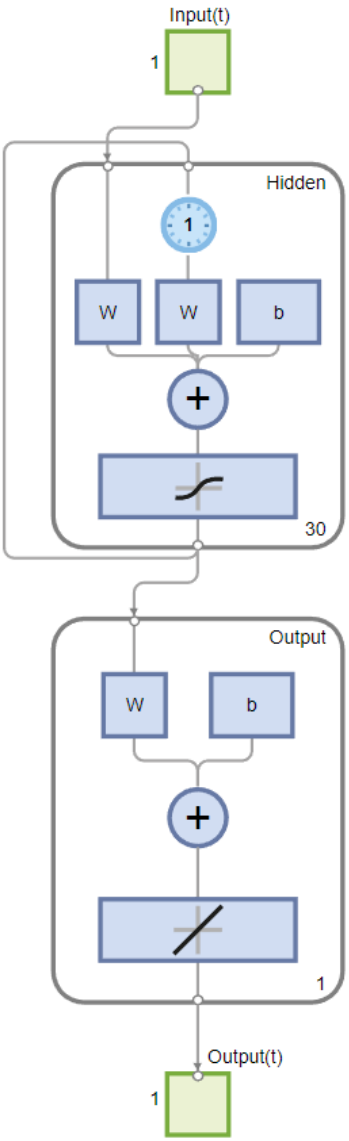

Şekil 6. Oluşturulan ENN'nin MATLAB programında görüntüsü.

Tablo 2. GA ve DOA için gizli katman nöron sayısına bağlı olarak popülasyondaki bireylerin ağırlık ve bias değerleri

M^2 Adet	M Adet	M Adet	M Adet	1 Adet
ω_1	ω_2	ω_3	b_1	b_2

ENN+GA yöntemi için jenerasyon sayısı 200 popülasyon büyüklüğü 100 olacak şekilde çalıştırılmıştır. GA'da çaprazlama oranı 0,80, mutasyon oranı 0,20 olarak seçilmiştir. GA'da Rulet tekerleği seçme yaklaşımı kullanılmıştır. Bunun dışında çalışmada önerilen hibrit tahmin sisteminin bir parçası olan DOA yaklaşımı ile farklı parametreler araştırılarak en iyi modelin bulunması için parametre optimizasyonu sağlanmıştır. Popülasyonda yusufçukların konumları rastgele olarak belirlenmektedir. Başlangıçta belirlenen yusufçukların temel alındığı her jenerasyonda yarıçaplar dinamik olarak güncellenmektedir. Maksimum ve minimum aralık arasındaki farkın dörtte biri alınarak başlamakta ve jenerasyon ilerledikçe bu değer artmaktadır. PSO'dan

esinlenilen atalet ağırlığı w ise başlangıç değeri olarak 0,90 değeri kullanılmakta ve jenerasyon ilerledikçe bu değeri 0,40 olmaktadır. Bir adet kontrol parametresi c ve atalet ağırlığı w'ye bağlı olarak beş ana davranışın ağırlığı hesaplanmaktadır. Bu dinamik parametrelerin dışında yusufçuk popülasyonu GA'daki popülasyon sayısı ile benzer şekilde 100 olmakta ve jenerasyon 200 olana kadar benzetim devam etmektedir. ENN+GA ve ENN+DOA hibrit yöntemlerin uygunluk fonksiyonu ise RMSE'nin minimizasyonunu ifade edecek şekilde eşitlik 17'deki gibi verilmiştir.

$$Uygunluk\ değeri = \min(\sqrt{\frac{1}{n}\sum_{i=1}^{n}(x_i - y_i)^2}) \quad (17)$$

ENN için Şekil 7'de gizli katman nöron sayısının değişimine ve tekrar edilen eğitim sayısına göre hata değerinin değişiminin üç boyutlu grafiği çizdirilmiştir. Tekrarlama sonucunda beklenildiği gibi çok farklı aralıklarda hata değerleri ile karşılaşılmıştır. Bu görüntüyü daha sade bir biçimde ifade etmek amacıyla Şekil 8'deki gibi kutu bıyık grafiği ile tekrarlama sonucunda her bir gizli katman nöron sayısı için oluşturulan modelin RMSE dağılımı gösterilmektedir. Bu dağılım incelendiğinde nöron sayısının artışı ile hata değerinin değişimi arasında genel bir trend eğilimi görülmemektedir. En düşük hata değerleri 11, 14, 16, 23, 27 ve 30 gizli katman nöron sayısı için elde edilmiştir. Nöron sayısı arttıkça aykırı değerlerin arttığı söylenebilir. Buda, Momentuma Sahip ve Adaptif Öğrenme Hızlı Gradyan İnişi (GMALR) eğitim yaklaşımının kullanıldığı modelin eğitim sürecinde beklenmedik şekilde yüksek hatalar üretebileceğini göstermektedir.

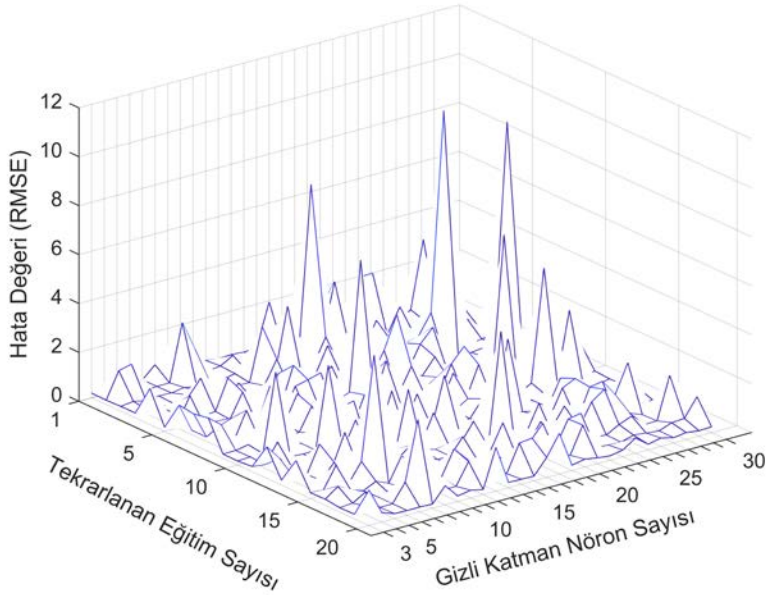

Şekil 7. ENN yöntemi için gizli katman nöron sayısının değişimine göre tekrar edilen eğitim sayısı için RMSE değişimi.

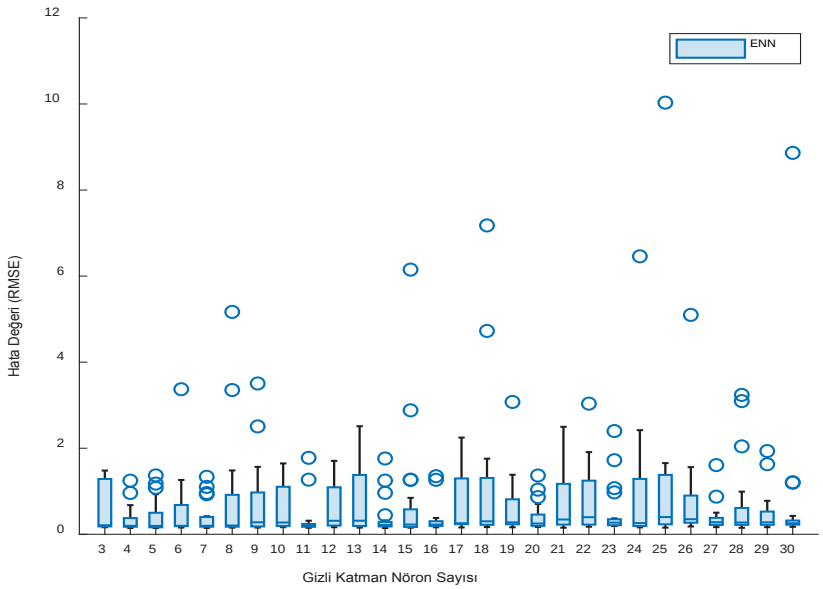

Şekil 8. ENN yöntemi için gizli katman nöron sayısının değişimine göre tekrar edilen eğitim sayısı için RMSE değişiminin kutu bıyık grafiği ile gösterimi.

ENN+GA ve ENN+DOA yöntemleri için gizli katman nöron sayısının değişimine göre jenerasyon boyunca RMSE değişimi Şekil 9 ve Şekil 10'daki üç boyutlu yüzey grafik ile çizdirilmiştir. Üç boyutlu yüzey grafiklerinde gizli katman nöron sayısı, jenerasyon sayısı ve uygunluk değeri sırasıyla x, y ve z eksenlerinde temsil edilmektedir. Şekil 9'daki ENN+GA için yüzey grafiği incelendiğinde x ekseninde gizli katman nöron sayısı 3'ten 30'a kadar artırıldığında belirli bir noktaya kadar RMSE değerlerinde bir azalma trendi gözlemlenebilmektedir. Ancak, nöron sayısı arttıkça RMSE değerleri arasındaki dalgalanmalar da artmaktadır. Özellikle jenerasyonun ilk başlangıcında RMSE değerleri nispeten artış gösterdiği görülmektedir. y ekseninde jenerasyon sayısı 1'den 200'e kadar arttıkça yani GA ile ENN daha fazla evrim geçirdikçe genel olarak RMSE değerlerinde bir azalma görülmektedir. Burada z eksenindeki RMSE değerleri optimizasyonda minimizasyonu amaçlayan uygunluk değerini temsil etmektedir. Daha düşük RMSE değerleri, modelin tahmin performansının daha iyi olduğunu göstermektedir. Grafikte, RMSE değerlerinin genel olarak düşük seviyelerde seyrettiği ve zamanla azaldığı gözlemlenmektedir. Ancak bazı bölgelerde ani yükselmeler ve dalgalanmalar da dikkat çekmektedir. Genel eğilimlerden bahsedilecek olursa ilk 1-50 jenerasyonda başlangıçta RMSE değerleri genellikle daha yüksektir ve daha fazla dalgalanma görülmektedir. Jenerasyon sayısı arttıkça genel olarak 50'den sonra, RMSE değerlerinde belirgin bir azalma eğilimi gözlemlenmektedir. Gizli katman nöron sayısı arttıkça, özellikle 15-30 aralığında, RMSE değerlerinde dalgalanmalar artmakta, ancak genel olarak düşük RMSE değerleri jenerasyon sayısı arttıkça elde edilmektedir. ENN'de gizli katman nöron sayısı arttıkça model karmaşıklığı artmakta ve bununla birlikte düşük nöron sayısına göre hata değerinin arttığı görülmektedir. Şekil 10'daki ENN+DOA yöntemi için gizli katman nöron sayısının değişimine göre jenerasyon boyunca RMSE değişimi incelendiğinde ENN+GA yöntemine kıyasla başlangıçta RMSE değerleri düşük modellerin elde edildiği görülmektedir. 1-50 jenerasyon aralığında dalgalanma miktarı yüksek olmakla birlikte tüm gizli katman nöron sayısı boyunca 50'den sonraki jenerasyonlarda düşük seviyelerde seyrettiği görülmüştür. ENN+GA'ya göre ENN+DOA yönteminde dalgalanma miktarının düşük kaldığı söylenebilir.

ENN+GA yaklaşımı ile elde edilen RMSE değerlerinin ENN ile benzer olduğunu ve aykırı değerlerin çokça görüldüğü, gizli katman nöron sayısının değişimine göre jenerasyon boyunca uygunluk değeri olan RMSE değişiminin kutu bıyık grafiği Şekil 11'de incelenmesi ile ortaya çıkmaktadır. Buna paralel bir inceleme olarak ENN+DOA yaklaşımında ise aykırı değerler elde edilmekle birlikte diğer yöntemlere oranla daha düşük kaldığı görülmüştür.

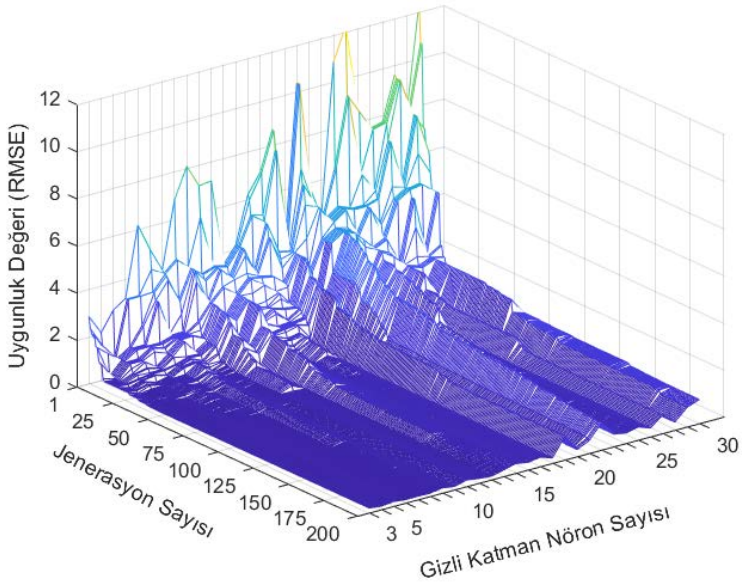

Şekil 9. ENN+GA yöntemi için gizli katman nöron sayısının değişimine göre jenerasyon boyunca RMSE değişimi.

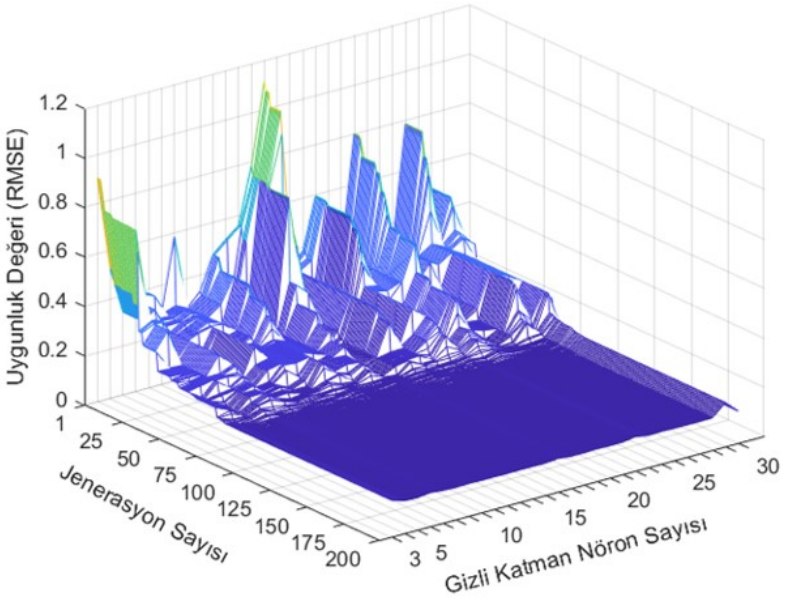

Şekil 10. ENN+DOA yöntemi için gizli katman nöron sayısının değişimine göre jenerasyon boyunca RMSE değişimi.

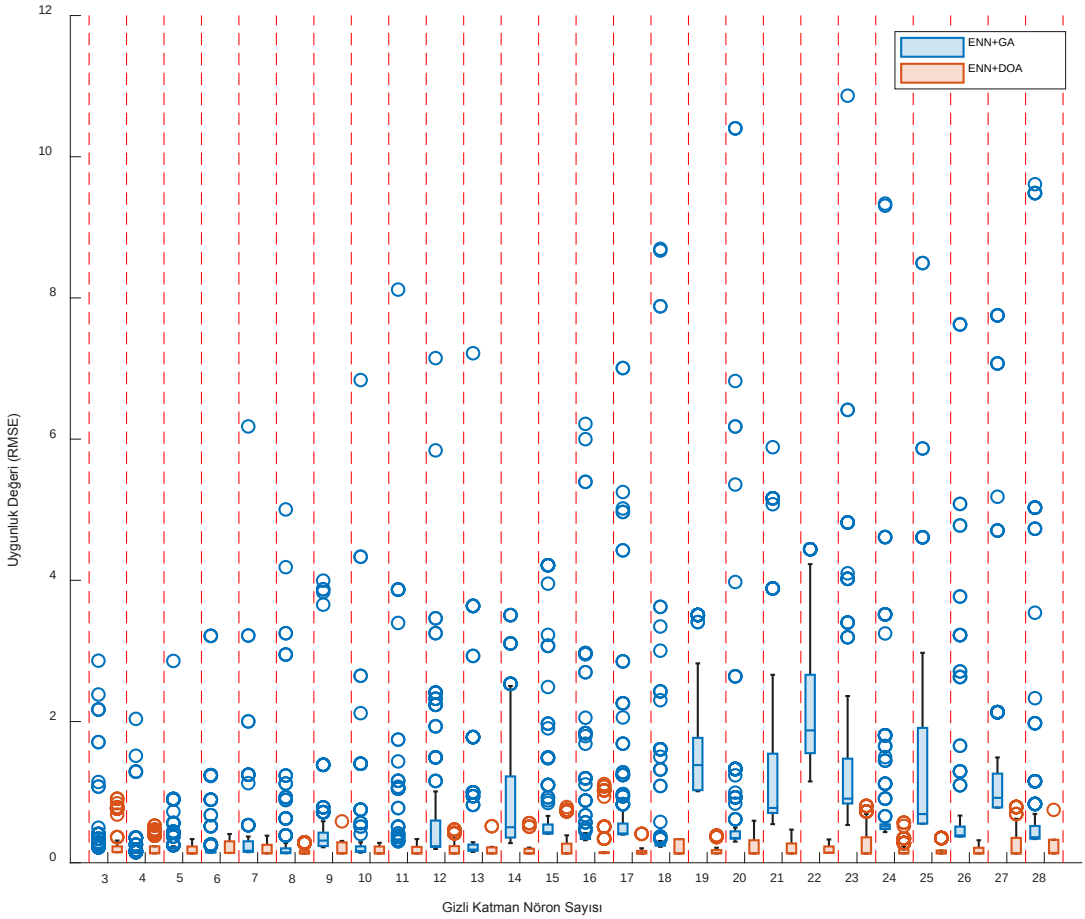

Şekil 11. ENN+GA ve ENN+DOA yöntemlerinin gizli katman nöron sayısının değişimine göre jenerasyon boyunca uygunluk değeri olan RMSE değişiminin kutu bıyık grafiği.

20 kere tekrar eden benzetim çalışması sonucunda Tablo 3'teki gibi ENN, ENN+GA ve ENN+DOA yaklaşımlarının MSE, RMSE ve R değerleri birlikte verilmiştir. Tablodaki değerler incelendiğinde ENN modeli için istatistiksel hata ölçütleri uygulandığında MSE, RMSE ve R ortalama değerleri 0,0782, 0,2549 ve 0,9518 olarak standart sapma değerleri ise 0,0939, 0,1193 ve 0,0577 olarak bulunmuştur. ENN+GA modeli için ise MSE, RMSE ve R ortalama değerleri 0,0425, 0,1928 ve 0,9739 olarak standart sapma değerleri ise 0,0372, 0,0748 ve 0,0229

olarak bulunmuştur. Son olarak ENN+DOA modeli için MSE, RMSE ve R ortalama değerleri 0,0176, 0,1328 ve 0,9891 olarak standart sapma değerleri ise 0,0013, 0,0046 ve 0,0008 olarak bulunmuştur. Sonuçlar incelendiğinde ENN+DOA yöntemi, MSE, RMSE ve R değerleri açısından ENN ve ENN+GA yöntemlerinden daha iyi performans gösterdiği görülmektedir. Daha düşük hata oranı ve daha yüksek korelasyon katsayısı ile daha doğru doğal gaz kapanış fiyatı tahmini yapıldığı söylenebilir. ENN+GA yöntemi, genellikle ENN yönteminden daha iyi performans göstermektedir, ancak ENN+DOA yöntemi ile kıyaslandığında daha yüksek hata oranı ve daha düşük korelasyon katsayısı görülmektedir. ENN yöntemi için diğer iki yöntemden daha düşük performans göstermektedir, yüksek MSE ve RMSE değerleri ile daha az doğru tahminler yapıldığı gözlemlenmektedir. ENN+GA, ENN'ye göre R hata metriği için %2,32'lik iyileşme sağlamaktadır. ENN+DOA, ENN+GA'ya göre R hata metriği için %1,56'lık iyileşme sağlamaktadır.

Benzetim sonucunda elde edilen ENN+DOA hibrit modeli için gerçek doğal gaz zaman serisine karşılık tahmin edilen zaman serisi çizimi Şekil 12'deki gibi olmaktadır.

Tablo 3. ENN, ENN+GA ve ENN+DOA yaklaşımlarının MSE, RMSE ve R değerleri ile kıyaslanması

Yöntemler	MSE	RMSE	R
ENN	0,0782±0,0939	0,2549±0,1193	0,9518±0,0577
ENN+GA	0,0425±0,0372	0,1928±0,0748	0,9739±0,0229
ENN+DOA	0,0176±0,0013	0,1328±0,0046	0,9891±0,0008

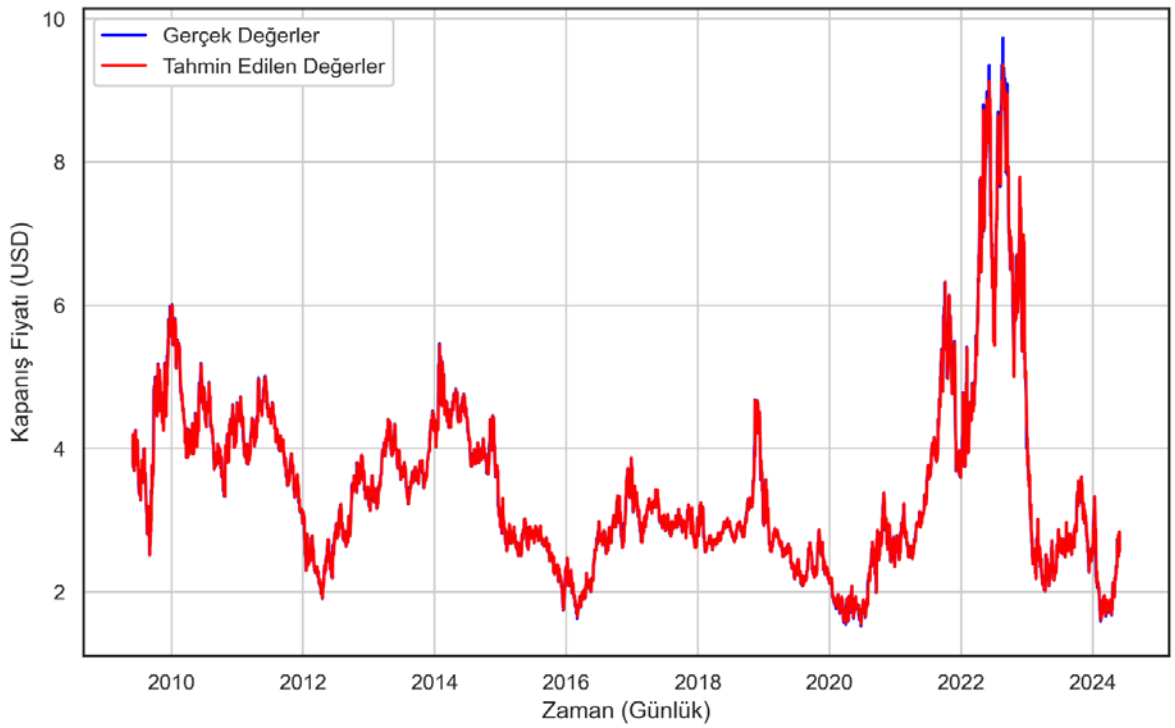

Şekil 12. ENN+DOA yaklaşımı ile elde edilen en iyi model için gerçek ve tahmin edilen doğal gaz zaman serisinin çizdirilmesi.

4. Sonuç

Doğal gaz zaman serisi tahmini çalışması ENN ve DOA hibrit modeli ile gerçekleştirilmiştir. Genel olarak belirli bir model yapısının farklı parametre değerleri ile elde edilen sonuçlarına ve bu sonuçların DOA yaklaşımı ile elde edilmesine ve GA ile kıyaslanmasına odaklanılmıştır. Gecikme sayısı 1 ve nöron sayısı 3-30 aralığı için yapılan hesaplamalar sonucunda elde edilen RMSE değeri en düşük ENN+DOA ile elde edilmiştir. Adil olması açısından optimizasyon yöntemleri 200 iterasyon boyunca çalıştırılmıştır. 20 tekrar sonucunda ortalama ve standart sapma cinsinden performans metrikleri hesaplanmıştır. ENN, ENN +GA ve ENN +DOA modellerinin MSE, RMSE ve R değerleri birbiri ile kıyaslandığında en düşük hata değeri ve en yüsek başarım değeri ENN+DOA ile elde edilmiştir. ENN+DOA modeli ile ENN+GA'ya göre R değerinde %1,56'lık iyileşme sağlanmıştır. ENN'ye göre ise ENN+DOA modeli ile R değerine göre %3,91'lik bir iyileşme sağlanmıştır. DOA yaklaşımının kullanılmasıyla en iyi model parametrelerinin belirlenmesi optimizasyon sürecinde başarılı sonuçlar elde etmek için önemli olmaktadır. DOA diğer sezgisel yöntemlerin özelliklerini kullanarak model yapılandırmasını en iyi şekilde

ayarlamayı amaçlamaktadır. Sonuç olarak bu çalışma ile ENN modelinin parametrelerini optimize etmek için DOA'nın etkili bir yöntem olduğunu ve daha iyi performans sağladığını göstermiştir. İlerleyen çalışmalarda, model performansını artırmak için hiper-parametre optimizasyonu üzerine daha derinlemesine odaklanılabilir. Örneğin, yapay sinir ağları modellerinde öğrenme oranı, momentum katsayısı gibi parametrelerin dikkatli bir şekilde optimize edilmesi, modelin eğitim sürecindeki doğruluk ve genelleme kapasitesini artırabilir. Genetik algoritmalar gibi sezgisel yöntemlerde ise çaprazlama ve mutasyon oranları vb. optimize ederek başarıma etkisi incelenebilir. Bunların yanı sıra, farklı zaman dilimlerinde ve mevsimsel etkileri kapsayan daha geniş veri setleriyle çalışmalar yapılarak modelin tahmin gücü artırılabilir. Böylece, modelin yalnızca bir dönem veya sınırlı bir zaman dilimi için değil, çeşitli dönemler için de genellenebilir hale gelmesi sağlanabilir. Bu şekilde, çalışmanın doğruluğu ve güvenilirliği dahada artırılarak kapsamlı katkılar sağlanabilir.

Katkı Oranı Beyanı

Yazarın katkı yüzdeleri aşağıda verilmiştir. Yazar makaleyi incelemiş ve onaylamıştır.

	S.K.
K	100
T	100
Y	100
VTI	100
VAY	100
KT	100
YZ	100
KI	100
GR	100
PY	100
FA	100

K= kavram, T= tasarım, Y= yönetim, VTI= veri toplama ve/veya işleme, VAY= veri analizi ve/veya yorumlama, KT= kaynak tarama, YZ= Yazım, KI= kritik inceleme, GR= gönderim ve revizyon, PY= proje yönetimi, FA= fon alımı.

Çatışma Beyanı

Yazar bu çalışmada hiçbir çıkar ilişkisi olmadığını beyan etmektedirler.

Etik Onay Beyanı

Bu araştırmada hayvanlar ve insanlar üzerinde herhangi bir çalışma yapılmadığı için etik kurul onayı alınmamıştır.

Kaynaklar

Afgan NH, Pilavachi PA, Carvalho MG. 2007. Multi-criteria evaluation of natural gas resources. Energy Policy, 35(1): 704-713.

Anonymous. 2024. Natural Gas Price. URL: https://www.investing.com/commodities/natural-gas (accessed date: 31 May 2024).

Duan Y, Zhang J, Wang X. 2023. Henry Hub monthly natural gas price forecasting using CEEMDAN–Bagging–HHO–SVR. Front Energy Res, 11: 1323073.

Elman JL. 1990. Finding structure in time. Cogn Sci, 14(2): 179-211.

Farrokhifar M, Nie Y, Pozo D. 2020. Energy systems planning: A survey on models for integrated power and natural gas networks coordination. Appl Energy, 262: 114567.

Gillessen B, Heinrichs H, Hake JF, Allelein HJ. 2019. Natural gas as a bridge to sustainability: Infrastructure expansion regarding energy security and system transition. Appl Energy, 251: 113377.

Goodell JW, Gurdgiev C, Paltrinieri A, Piserà S. 2023. Global energy supply risk: Evidence from the reactions of European natural gas futures to Nord Stream announcements. Energy Econ, 125: 106838.

Gürsan C, de Gooyert V. 2021. The systemic impact of a transition fuel: Does natural gas help or hinder the energy transition?. Renew Sustain Energy Rev, 138: 110552.

Holland JH. 1992. Genetic algorithms. Sci Am, 267(1): 66-73.

Khan MI. 2018. Evaluating the strategies of compressed natural gas industry using an integrated SWOT and MCDM approach. J Clean Prod, 172: 1035-1052.

Khan MI, Yasmin T, Shakoor A. 2015. Technical overview of compressed natural gas (CNG) as a transportation fuel. Renew Sustain Energy Rev, 51: 785-797.

Kong F, Liu Y, Tong L, Guo W, Jin Y, Wang L, Ding Y. 2023. A novel optimization for liquefied natural gas power plants based on the renewable energy. Appl Therm Eng, 233: 121172.

Li J, Wu Q, Tian Y, Fan L. 2021. Monthly Henry Hub natural gas spot prices forecasting using variational mode decomposition and deep belief network. Energy. 227: 120478.

Liu W, Sun J, Liu G, Fu S, Liu M, Zhu Y, Gao Q. 2023. Improved GWO and its application in parameter optimization of Elman neural network. PLoS One, 18(7): e0288071.

Mirjalili S. 2016. Dragonfly algorithm: a new meta-heuristic optimization technique for solving single-objective, discrete, and multi-objective problems. Neural Comput Appl, 27: 1053-1073.

Mittakola RT, Ciais P, Zhou C. 2024. Short-to-medium range forecast of natural gas use in the United States residential buildings. J Clean Prod, 437: 140687.

Reynolds CW. 1987. Flocks, herds and schools: A distributed behavioral model. In: Proceedings of the 14th annual conference on Computer graphics and interactive techniques, August 01, Volume 21 ACM, ABD, pp: 25-34.

Rizvi SKA, Naqvi B, Boubaker S, Mirza N. 2022. The power play of natural gas and crude oil in the move towards the financialization of the energy market. Energy Econ, 112: 106131.

Saghi F, Rezaee MJ. 2021. An ensemble approach based on transformation functions for natural gas price forecasting considering optimal time delays. PeerJ Comput Sci, 7: e409.

Su M, Zhang Z, Zhu Y, Zha D, Wen W. 2019. Data driven natural gas spot price prediction models using machine learning methods. Energies, 12(9): 1680.

Szklo AS, Soares JB, Tolmasquim MT. 2004. Economic potential

of natural gas-fired cogeneration—analysis of Brazil's chemical industry. Energy Policy, 32(12): 1415-1428.

Villicaña-García E, Ponce-Ortega JM. 2019. Sustainable strategic planning for a national natural gas energy system accounting for unconventional sources. Energy Convers Manag, 181: 382-397.

Zhan L, Tang Z. 2022. Natural gas price forecasting by a new hybrid model combining quadratic decomposition technology and LSTM model. Math Probl Eng, 2022(1): 5488053.

Zhou L, Fan Q, Huang X, Liu Y. 2023. Weak and strong convergence analysis of Elman neural networks via weight decay regularization. Optim, 72(9): 2287-2309.

Black Sea Journal of Engineering and Science
doi: 10.34248/bsengineering.1549965

Open Access Journal
e-ISSN: 2619 – 8991

Research Article
Volume 8 - Issue 1: 115-118 / January 2025

BISECTOR CURVES OF COMFORMABLE CURVES IN $\mathbb{R}^2$

Şeyda ÖZEL[1]*, Mehmet BEKTAŞ[1]

[1]*Fırat University, Faculty of Science, Department of Mathematics, 23100, Elazığ, Türkiye*

Abstract: In this study, initially, information about the derivative of fractional order was given. Subsequently, one of the fractional derivative types, namely the comformable derivative was discussed in detail. Additionally, the studies conducted on this comformable derivative type were also included. The importance of the bisector structure on the theory of curves was mentioned. In the second part of the study, the materials and methods were demonstrated using the comformable derivative. Finally, in this work, the bisector curves of two regular comformable curves from C^1-regular parametric category is inspected in $\mathbb{R}^2$. Then, multivariable functions which are corresponded to bisector curves of regular comformable curves are calculated. The bisector curves are procured by two similar paths. The methods of finding this function were demonstrated in detail using comformable derivatives. Then, the equations which are corresponded to bisector curves are obtained in $\mathbb{R}^2$.

Keywords: Bisector curve, Comformable derivative, Frenet frame

***Corresponding author:** Fırat University, Faculty of Science, Department of Mathematics, 23100, Elazığ, Türkiye
E mail: s_demir2323@outlook.com (Ş. ÖZEL)
Şeyda ÖZEL https://orcid.org/0000-0002-1519-2418
Mehmet BEKTAŞ https://orcid.org/0000-0002-5797-4944

Received: September 14, 2024
Accepted: November 26, 2024
Published: January 15, 2025

Cite as: Özel Ş, Bektaş M, 2025. Bisector curves of comformable curves in $\mathbb{R}^2$. BSJ Eng Sci, 8(1): 115-118.

1. Introduction

The fractional analysis phrase first appears in a letter written by L' Hospital to Leibniz. In this letter, L-Hospital asked Leibniz about a special structure he used in his work for $\frac{d^n y}{dx^n}$, which is the nth order derivative of the linear function $f(x) = x$. L-Hospital wanted to get the number derivative and didn't know how to do, for example if the derivative's order come out to be rational number what would the consequence happen (Nishimoto, 1991). This question created the first glint of fractional analysis. Lately, Khalil at al. defined an unprecedented of the fractional derivative denominated comformable fractional derivative (Khalil et.al., 2014).

Similarly, Gözütok, Çoban and Sağıroğlu (2019) have study the Frenet frame with respect to comformable fractional derivative. Then, the comformable derivative and its properties have been denoted by geometers (Atangana et al., 2015). In addition, a more precise definition of a comformable derivative is introduced (Anderson and Ulness, 2015). The bisector for two objects is defined as a series of points equality from the two objects. The structure of bisectors plays an important role in many geometric calculation. Curves are one of the areas frequently studied by geometricians. By constructing various frames on a curve, the differential properties of the curve can be obtained. The theory of curves is a very comprehensive subject that finds application in many disciplines such as architecture, engineering, computer technologies, as well as mathematics. Some studies on any regular curve and also some studies on especially conformable and bisector curves are as follows. According to Farouki and Johnstone (1994) the bisector of two geometrical elements (such as points, curves, surfaces ets.) is the path traced by a variable point that remains equidistant from this elements. Elber and Kim (1998) demonstrated that bisector surfaces are rational ruled surfaces. In 3-dimensional Euclidean space, the relationships between N-Bishop and Frenet frames for any regular curve, as well as the relationships between type-1 Bishop and N-Bishop frames, are given (Gür Mazlum, 2024). Additionally, pole vectors associated with these frames are calculated by Gür Mazlum. In addition, Gür Mazlum and Bektaş (2023) studied the involute curves of any non-lightlike curve in 3-dimensional Euclidean space. Many special curves and the Frenet frame, initially defined using classical derivatives, have been redefined through the use of comformable fractional derivatives (Has et al., 2022). Bektaş and Gür Mazlum (2022) examined the modified frames with both the non-zero curvature and the torsion of the non-unit speed curves in Euclidean 3-space.

In this study, the bisector curves of two regular plane curves from C^1-regular parametric category is inspected in $\mathbb{R}^2$. Then, multivariable function which is corresponded to bisector curves of regular plane curves is calculated (Dede and Ünlütürk, 2013). The bisector curves are procured by two different paths. As a result, the equations which are corresponded to bisector curves are obtained in $\mathbb{R}^2$.

2. Materials and Methods

Let us consider a smooth curve $\gamma(t) = (x(t), y(t))$, γ from a subset $I \subset \mathbb{R}$ to a two-dimensional space $\mathbb{R}^2$,

where t is an arbitrary parameter. Then, the ordinary definition of the length $\tilde{s}$ of a curve γ starting at $t = 0$ is given by equation 1

$$\tilde{s} = \int_0^t \left\| \frac{d\gamma}{du} \right\| du = \int_0^t \sqrt{\left(\frac{dx}{dt}\right)^2 + \left(\frac{dy}{dt}\right)^2}\, dt \quad (1)$$

for $t \in I$. Then, it is well-known that equation 1 is an arc length of curve for the tangent vector:

$$E_1(\tilde{s}) = \left(\frac{dx}{d\tilde{s}}, \frac{dy}{d\tilde{s}}\right)$$

Now, let us consider the comformable derivative on the curvature of the curve. Basically, since the curvature is given by the change of the tangent vector of the curve, we can define a comformable tangent vector (equation 2):

$$E_1^{(\alpha)}(\tilde{s}) = (T_\alpha x(\tilde{s}), T_\alpha y(\tilde{s})) = \left(\frac{d^{(\alpha)}x(\tilde{s})}{d\tilde{s}^{(\alpha)}}, \frac{d^{(\alpha)}y(\tilde{s})}{d\tilde{s}^{(\alpha)}}\right) \quad (2)$$

For equation 2, $\left\| E_1^{(\alpha)}(\tilde{s}) \neq 1 \right\|$. Then, we have

$$\frac{d^{(\alpha)}\gamma(t(s))}{ds^{(\alpha)}} = s^{\mathbf{1-\alpha}} \frac{d\gamma(s)}{dt}\frac{dt}{ds} \quad (3)$$

Considering equation 3, let us define the transformation $\tilde{s} \to s$ as follows (equation 4):

$$s = (\alpha\tilde{s})^{\frac{1}{\alpha}} \quad (4)$$

where α is the degree of the comformable derivative and $0 < \alpha \leq 1$. For this parameter s, if the derivative of both sides with respect to t is taken, we can write as follows (equation 5).

$$\frac{ds}{dt} = s^{1-\alpha}\frac{d\tilde{s}}{dt}. \quad (5)$$

Then, let us describe the tangent vector of the curve using the parameter s and comformable derivative. In other words (equation 6),

$$e_1{}^{(\alpha)}(s) = T_\alpha\gamma(s) = \left(T_\alpha(x(s)), T_\alpha(y(s))\right) = \left(\frac{d^\alpha x(s)}{ds^\alpha}, \frac{d^\alpha y(s)}{ds^\alpha}\right) \quad (6)$$

The norm of the tangent vector from equation 3 is (equation 7)

$$\left\| e_1{}^{(\alpha)}(s) \right\| = \|T_\alpha\gamma(s)\| = \left\| s^{1-\alpha}\frac{d\gamma}{dt}\frac{dt}{ds} \right\| = s^{1-\alpha}\left\|\frac{d\gamma}{dt}\right\|\frac{dt}{ds} = s^{1-\alpha}\frac{d\tilde{s}}{dt}s^{\alpha-1}\frac{dt}{d\tilde{s}} = 1\,. \quad (7)$$

Moreover, the unit vector of the curve orthonormal to $e_1^{(\alpha)}(s)$ is defined by using equation 3 as follows (equation 8):

$$e_2^{(\alpha)}(s) = (-T_\alpha y(s), T_\alpha x(s)). \quad (8)$$

For the γ curve with parameter s, $e_1^{(\alpha)}(s)$ and $e_2^{(\alpha)}(s)$ are, respectively, the unit tangent vector and the normal vector of this curve. Also, the parameter s is the arc length. As a result of this, we have the following definition: Definition 1; Let's take a function $f: [0,\infty] \to \mathbb{R}$. The comformable derivative of the function f of order α is indicated by:

$$T_\alpha f(x) = \lim_{h\to 0}\frac{f(x + hx^{1-\alpha}) - f(x)}{h} = x^{1-\alpha}f'(x)$$

for all $x > 0, \alpha \in (0,1)$ (Dede, 2013; Ekici, 2013, Ünlütürk, 2013).

3. Results

At $\mathbb{R}^2$, we suppose that there is regular comformable curves from C^1-regular parametric category. Furthermore, these curves are parameterized by (equation 9)

$m_1(\varrho) = (v_1(\varrho), w_1(\varrho))$
and
$m_2(\varsigma) = (v_2(\varsigma), w_2(\varsigma))$. (9)

Now, multivariable function $F(\varrho, \varsigma) = 0$ which correspond to the bisector curves of $m_1(\varrho)$ and $m_2(\varsigma)$ is being calculated for $i = 1,2$.

3.1. $F_1(\varrho, \varsigma)$ Function

Tangent vector of curves $m_1(\varrho)$ and $m_2(\varsigma)$ are defined by
$t_1(\varrho) = (T_\alpha v_1(\varrho), T_\alpha w_1(\varrho))$
and (equation 10)

$t_2(\varsigma) = (T_\alpha v_2(\varsigma), T_\alpha w_2(\varsigma))$, respectively. (10)

Moreover, the normal vectors of curves are written by
$n_1(\varrho) = (-T_\alpha w_1(\varrho), T_\alpha v_1(\varrho))$
and (equation 11)

$n_2(\varsigma) = (-T_\alpha w_2(\varsigma), T_\alpha v_2(\varsigma))$, respectively. (11)

On the other and, for multivariable functions, which are $\lambda = \lambda(\varrho, \varsigma)$ and $\beta = \beta(\varrho, \varsigma)$, crossing points in accordance with the normals of curves $m_1(\varrho)$ and $m_2(\varsigma)$ denoted by

$$m_1(\varrho) + n_1(\varrho)\lambda = m_2(\varsigma) + n_2(\varsigma)\beta. \quad (12)$$

Later, by use of equation 9, equation 11 in equation (12), we get (equation 13)

$$\left(v_1(\varrho), w_1(\varrho)\right) + \left(-T_\alpha w_1(\varrho), T_\alpha v_1(\varrho)\right)\lambda = \left(v_2(\varsigma), w_2(\varsigma)\right) + \left(-T_\alpha w_2(\varsigma), T_\alpha v_2(\varsigma)\right)\lambda$$

or

$$\left[v_1(\varrho) - \left(T_\alpha w_1(\varrho)\right)\lambda + \left(T_\alpha v_1(\varrho)\right)\lambda\right] = [v_2(\varsigma) - (T_\alpha(w_2(\varsigma))\beta, w_2(\varsigma) + (T_\alpha(v_2(\varsigma))\beta]$$

or

$$v_1(\varrho) - \left(T_\alpha w_1(\varrho)\right)\lambda = v_2(\varsigma) - \left(T_\alpha w_2(\varsigma)\right)\beta,$$
$$w_1(\varrho) + (T_\alpha v_1(\varrho))\lambda = w_2(\varsigma) + (T_\alpha v_2(\varsigma))\beta$$

or

$$(-T_\alpha w_1(\varrho))\lambda + (T_\alpha w_2(\varsigma))\beta = v_2(\varsigma) - v_1(\varrho),$$
$$T_\alpha v_1(\varrho)\lambda - T_\alpha v_2(\varsigma)\beta = w_2(\varsigma) - w_1(\varrho). \quad (13)$$

We accept it so (equation 14)

$$\Delta = \begin{vmatrix} (-T_\alpha w_1(\varrho)) & (T_\alpha w_2(\varsigma)) \\ T_\alpha v_1(\varrho) & -T_\alpha v_2(\varsigma) \end{vmatrix} \neq 0,$$
$$\Delta_1 = \begin{vmatrix} v_2(\varsigma) - v_1(\varrho) & (T_\alpha w_2(\varsigma)) \\ w_2(\varsigma) - w_1(\varrho) & -T_\alpha v_2(\varsigma) \end{vmatrix} \quad (14)$$

and

$$\Delta_2 = \begin{vmatrix} (-T_\alpha w_1(\varrho)) & v_2(\varsigma) - v_1(\varrho) \\ T_\alpha v_1(\varrho) & w_2(\varsigma) - w_1(\varrho) \end{vmatrix}$$

in order that equation 13 solution to be calculated Cramer's rule.

Thus, from the expression $\lambda = \lambda(\varrho,\varsigma) = \frac{\Delta_1}{\Delta}$, we obtain

$$\lambda = \lambda(\varrho,\varsigma) = \frac{\begin{vmatrix} v_2(\varsigma) - v_1(\varrho) & (T_\alpha w_2(\varsigma)) \\ w_2(\varsigma) - w_1(\varrho) & -T_\alpha v_2(\varsigma) \end{vmatrix}}{\begin{vmatrix} (-T_\alpha w_1(\varrho)) & (T_\alpha w_2(\varsigma)) \\ T_\alpha v_1(\varrho) & -T_\alpha v_2(\varsigma) \end{vmatrix}}.$$

Similarly, from the expression $\beta = \beta(\varrho,\varsigma) = \frac{\Delta_2}{\Delta}$, we obtain

$$\beta = \beta(\varrho,\varsigma) = \frac{\begin{vmatrix} (-T_\alpha w_1(\varrho)) & v_2(\varsigma) - v_1(\varrho) \\ T_\alpha v_1(\varrho) & w_2(\varsigma) - w_1(\varrho) \end{vmatrix}}{\begin{vmatrix} (-T_\alpha w_1(\varrho)) & (T_\alpha w_2(\varsigma)) \\ T_\alpha v_1(\varrho) & -T_\alpha v_2(\varsigma) \end{vmatrix}}.$$

Functions of two variables $\lambda(\varrho,\varsigma)$ and $\beta(\varrho,\varsigma)$ can write with function of two variables at vertex point. In other words, we can express the formula as following (equation 15):

$$P(\varrho,\varsigma) = c_1(\varrho) + n_1(\varrho)\lambda(\varrho,\varsigma) = c_2(\varsigma) + n_2(\varsigma)\beta(\varrho,\varsigma). \quad (15)$$

Also, function of two variables $P(\varrho,\varsigma)$ has to be equal distance from $m_1(\varrho)$ and $m_2(\varsigma)$ $\|P(\varrho,\varsigma) - m_1(\varrho)\| = \|P(\varrho,\varsigma) - m_2(\varsigma)\|$ can be written like this. Then, by use of (15), in the last equation, we get (equation 16)

$$n_1^2(\varrho,\varsigma)\big(\lambda(\varrho,\varsigma)\big)^2 = n_2^2(\varrho,\varsigma)\big(\beta(\varrho,\varsigma)\big)^2. \quad (16)$$

Later, by use of $\lambda = \lambda(\varrho,\varsigma)$ and $\beta = \beta(\varrho,\varsigma)$ in equation 16, we get (equation 17)

$$n_1^2(\varrho)\left(\frac{\begin{vmatrix} v_2(\varsigma)-v_1(\varrho) & (T_\alpha w_2(\varsigma)) \\ w_2(\varsigma)-w_1(\varrho) & -T_\alpha v_2(\varsigma) \end{vmatrix}}{\begin{vmatrix} (-T_\alpha w_1(\varrho)) & (T_\alpha w_2(\varsigma)) \\ T_\alpha v_1(\varrho) & -T_\alpha v_2(\varsigma) \end{vmatrix}}\right)^2 -$$
$$n_2^2(\varsigma)\left(\frac{\begin{vmatrix} (-T_\alpha w_1(\varrho)) & v_2(\varsigma)-v_1(\varrho) \\ T_\alpha v_1(\varrho) & w_2(\varsigma)-w_1(\varrho) \end{vmatrix}}{\begin{vmatrix} (-T_\alpha w_1(\varrho)) & (T_\alpha w_2(\varsigma)) \\ T_\alpha v_1(\varrho) & -T_\alpha v_2(\varsigma) \end{vmatrix}}\right)^2 = 0 \quad (17)$$

or (equation 18)

$$n_1^2(\varrho)\big[-\big(v_2(\varsigma) - v_1(\varrho)\big)T_\alpha v_2(\varsigma) - (w_2(\varsigma) - w_1(\varrho))T_\alpha w_2(\varsigma)\big]^2 - n_2^2(\varsigma)\big[-\big(w_2(\varsigma) - w_1(\varrho)\big)T_\alpha w_1(\varrho) - (v_2(\varsigma) - v_1(\varrho))T_\alpha v_1(\varrho)\big]^2 = 0. \quad (18)$$

Here, by use of equations 11, we obtain (equation 19)

$$P(\varrho,\varsigma) = \big(T_\alpha^2 w_1(\varrho) + T_\alpha^2 v_1(\varrho)\big)\big[\big(v_2(\varsigma) - v_1(\varrho)\big)T_\alpha v_2(\varsigma) + \big(w_2(\varsigma) - w_1(\varrho)\big)T_\alpha w_2(\varsigma)\big]^2 - \big(T_\alpha^2 w_2(\varsigma) + T_\alpha^2 v_2(\varsigma)\big)\big[\big(w_2(\varsigma) - w_1(\varrho)\big)T_\alpha w_1(\varrho) + \big(v_2(\varsigma) - v_1(\varrho)\big)T_\alpha v_1(\varrho)\big]^2 = 0. \quad (19)$$

The equation 11 is bisector curve of $m_1(\varrho)$ and $m_2(\varsigma)$.

3.2. $F_2(\varrho,\varsigma)$ Function

In this method, we obtained bisector point of $P(\varrho,\varsigma)$. When the bisector of the curves $m_1(\varrho)$ and $m_2(\varsigma)$ are at one point of $P(\varrho,\varsigma)$, the curves $m_1(\varrho)$ and $m_2(\varsigma)$ have two points such as $m_1(\varrho)$ and $m_2(\varsigma)$, which contain P. As a result, the point P provides linear equations as follows (equation 20):

$$L_1(\varrho): \langle P - m_1(\varrho), T_1(\varrho)\rangle = 0,$$
$$L_2(\varsigma): \langle P - m_2(\varsigma), T_2(\varsigma)\rangle = 0. \quad (20)$$

Hence, with direct calculation, we get (equation 21 and 22)

$$\langle P - T_1(\varrho)\rangle = \langle c_1(\varrho), T_1(\varrho)\rangle, \quad (21)$$

$$\langle P - T_2(\varsigma)\rangle = \langle c_2(\varsigma), T_2(\varsigma)\rangle. \quad (22)$$

If we take $P(\varrho,\varsigma) = (v(\varrho,\varsigma), w(\varrho,\varsigma))$ and by use of equation 9 and 10 in equation 21, we get (equation 23)

$$\begin{aligned}\langle\big(v(\varrho,\varsigma), w(\varrho,\varsigma)\big), \big(T_\alpha v_1(\varrho), T_\alpha w_1(\varrho)\big)\rangle &= \langle\big(v_1(\varrho), w_1(\varrho)\big), \big(T_\alpha v_1(\varrho), T_\alpha w_1(\varrho)\big)\rangle \\ &= v(\varrho,\varsigma)T_\alpha v_1(\varrho) + w(\varrho,\varsigma)T_\alpha w_1(\varrho) \\ &= v_1(\varrho)T_\alpha v_1(\varrho) + w_1(\varrho)T_\alpha w_1(\varrho). \quad (23)\end{aligned}$$

Similarly, by use of equation 9 and 10 in equation 22, we get

$$\begin{aligned}\langle\big(v(\varrho,\varsigma), w(\varrho,\varsigma)\big), \big(T_\alpha v_2(\varsigma), T_\alpha w_2(\varsigma)\big)\rangle &= \langle\big(v_2(\varsigma), w_2(\varsigma)\big), \big(T_\alpha v_2(\varsigma), T_\alpha w_2(\varsigma)\big)\rangle \\ &= v(\varrho,\varsigma)T_\alpha v_2(\varsigma) + w(\varrho,\varsigma)T_\alpha w_2(\varsigma) \\ &= v_2(\varsigma)T_\alpha v_2(\varsigma) + w_2(\varsigma)T_\alpha w_2(\varsigma). \quad (24)\end{aligned}$$

Thus, from expression equation 23 and equation 24, we get system of equations

$$v(\varrho,\varsigma)T_\alpha v_1(\varrho) + w(\varrho,\varsigma)T_\alpha w_1(\varrho) = v_1(\varrho)T_\alpha v_1(\varrho) + w_1(\varrho)T_\alpha w_1(\varrho)$$

and

$$v(\varrho,\varsigma)T_\alpha v_2(\varsigma) + w(\varrho,\varsigma)T_\alpha w_2(\varsigma) = v_2(\varsigma)T_\alpha v_2(\varsigma) + w_2(\varsigma)T_\alpha w_2(\varsigma). \quad (25)$$

In equation 25, let's take it as

$$\widetilde{\Delta} = \begin{vmatrix} T_\alpha v_1(\varrho) & T_\alpha w_1(\varrho) \\ T_\alpha v_2(\varsigma) & T_\alpha w_2(\varsigma) \end{vmatrix} \neq 0.$$

If this equation 25 tried to be solve according to Cramer's rule, we get

$$\widetilde{\Delta}_1 = \begin{vmatrix} v_1(\varrho)T_\alpha v_1(\varrho) + w_1(\varrho)T_\alpha w_1(\varrho) & T_\alpha w_1(\varrho) \\ v_2(\varsigma)T_\alpha v_2(\varsigma) + w_2(\varsigma)T_\alpha w_2(\varsigma) & T_\alpha w_2(\varsigma) \end{vmatrix}$$

and

$$\widetilde{\Delta}_2 = \begin{vmatrix} T_\alpha v_1(\varrho) & v_1(\varrho)T_\alpha v_1(\varrho) + w_1(\varrho)T_\alpha w_1(\varrho) \\ T_\alpha v_2(\varsigma) & v_2(\varsigma)T_\alpha v_2(\varsigma) + w_2(\varsigma)T_\alpha w_2(\varsigma) \end{vmatrix}.$$

Thereby, from expression $v(\varrho,\varsigma) = \frac{\widetilde{\Delta}_1}{\widetilde{\Delta}}$, we get

$$v(\varrho,\varsigma)=\frac{\begin{vmatrix} v_1(\varrho)T_\alpha v_1(\varrho)+w_1(\varrho)T_\alpha w_1(\varrho) & T_\alpha w_1(\varrho) \\ v_2(\varsigma)T_\alpha v_2(\varsigma)+w_2(\varsigma)T_\alpha w_2(\varsigma) & T_\alpha w_2(\varsigma)\end{vmatrix}}{\begin{vmatrix} T_\alpha v_1(\varrho) & T_\alpha w_1(\varrho) \\ T_\alpha v_2(\varsigma) & T_\alpha w_2(\varsigma)\end{vmatrix}}.$$

Similarly, from expression $w(\varrho,\varsigma)=\frac{\bar{\Delta}_2}{\bar{\Delta}}$, we get

$$w(\varrho,\varsigma)=\frac{\begin{vmatrix} T_\alpha v_1(\varrho) & v_1(\varrho)T_\alpha v_1(\varrho)+w_1(\varrho)T_\alpha w_1(\varrho) \\ T_\alpha v_2(\varsigma) & v_2(\varsigma)T_\alpha v_2(\varsigma)+w_2(\varsigma)T_\alpha w_2(\varsigma)\end{vmatrix}}{\begin{vmatrix} T_\alpha v_1(\varrho) & T_\alpha w_1(\varrho) \\ T_\alpha v_2(\varsigma) & T_\alpha w_2(\varsigma)\end{vmatrix}}.$$

That is to say, from expression $P(\varrho,\varsigma)=(v(\varrho,\varsigma),w(\varrho,\varsigma))$ we get

$$\begin{aligned}P(\varrho,\varsigma)=(&T_\alpha^2 w_1(\varrho)\\&+T_\alpha^2 v_1(\varrho)\big[\big(v_2(\varsigma)-v_1(\varrho)\big)T_\alpha v_2(\varsigma)\\&+\big(w_2(\varsigma)-w_1(\varrho)\big)T_\alpha w_2(\varsigma)\big]^2\\&-\big(T_\alpha^2 w_2(\varsigma)\\&+T_\alpha^2 v_2(\varsigma)\big)\big[\big(w_2(\varsigma)-w_1(\varrho)\big)T_\alpha w_1(\varrho)\\&+\big(v_2(\varsigma)-v_1(\varrho)\big)T_\alpha v_1(\varrho)\big]^2=0.\end{aligned}$$

Furthermore, $P(\varrho,\varsigma)$ provides equation as follow

$\|P(\varrho,\varsigma)-c_1(\varrho)\|=\|P(\varrho,\varsigma)-c_2(\varsigma)\|$.

Therefore, provides equation as follow

$$\begin{aligned}&\langle P(\varrho,\varsigma)-m_1(\varrho),P(\varrho,\varsigma)-m_1(\varrho)\rangle\\&\quad=\langle P(\varrho,\varsigma)-m_2(\varsigma),P(\varrho,\varsigma)-m_2(\varsigma)\rangle\end{aligned}$$

or

$$\begin{aligned}&\langle P(\varrho,\varsigma),P(\varrho,\varsigma)\rangle-2\langle P(\varrho,\varsigma),m_1(\varrho)\rangle+\\&\langle m_1(\varrho),m_1(\varrho)\rangle=\langle P(\varrho,\varsigma),P(\varrho,\varsigma)\rangle-2\langle P(\varrho,\varsigma),m_2(\varsigma)\rangle+\\&\langle m_2(\varsigma),m_2(\varsigma)\rangle\end{aligned}$$

or

$$\begin{aligned}&2(\langle P(\varrho,\varsigma),m_1(\varrho)\rangle-\langle P(\varrho,\varsigma),m_2(\varsigma)\rangle)\\&\quad=\langle m_2(\varsigma),m_2(\varsigma)\rangle-\langle m_1(\varrho),m_1(\varrho)\rangle\end{aligned}$$

or

$$\begin{aligned}&\langle P(\varrho,\varsigma),m_1(\varrho)-m_2(\varsigma)\rangle\\&\quad=\frac{\langle m_2(\varsigma),m_2(\varsigma)\rangle-\langle m_1(\varrho),m_1(\varrho)\rangle}{2}.\end{aligned}$$

4. Conclusion

In differential geometry, the theory of curves has become a widely studied field. However, recently, using the comformable derivative has provided many scientists different perspectives. In this study, methods for finding functions corresponding to angle bisector curvatures of two plane curves in $\mathbb{R}^2$ are provided using comformable derivatives. We present a geometric interpretation of the multivariable function corresponding to the angle bisector curvatures by using different derivatives. For example; Caputo, Rieman-Liouville and non-local derivative and so.

Author Contributions

The percentages of the authors' contributions are presented below. All authors reviewed and approved the final version of the manuscript.

	Ş.Ö.	M.B.
C	40	60
D	40	60
S	40	60
DCP	40	60
DAI	30	70
L	40	60
W	40	60
CR	40	60
SR	40	60
PM	30	70
FA	40	60

C=Concept, D= design, S= supervision, DCP= data collection and/or processing, DAI= data analysis and/or interpretation, L= literature search, W= writing, CR= critical review, SR= submission and revision, PM= project management, FA= funding acquisition.

Conflict of Interest

The authors declared that there is no conflict of interest.

References

Anderson DR, Ulness DJ. 2015. Newly defined conformable derivatives. Adv Dyn Syst Appl, 10(2): 109-137.

Atangana A, Baleanu D, Alsaedi A. 2015. New properties of conformable derivative. Open Math, 13(1): 889-898.

Dede M, Ünlütürk Ekici C. 2013. Bisector curves of planar rational curves in Lorentzian plane. Inter J Geo, 2(1): 47-53.

Elber G, Kim MS. 1998. The bisector surface of rational space curves. ACM Transact Graph, 17(1): 32-49.

Farouki RT, Johnstone JK. 1994. The bisector of a point and a plane parametric curve. Comput Aided Geom Desig, 11(2): 117-151.

Gözütok U, Çoban H, Sağıroğlu Y. 2019. Frenet frame with respect to conformable derivative. Filomat, 33(6): 1541-1550.

Gür Mazlum S, Bektaş M. 2022. On the modified orthogonal frames of the non-unit speed curves in Euclidean 3-space E^3. Turkish J Sci, 7(2): 58-74.

Gür Mazlum S, Bektaş M. 2023. Involüte curves of any non-unit speed curve in Euclidean 3-space E^3. In: Akgül H, Baba H, İyit N, editors. In international studies in Science and Mathematics. Serüve Publishing, Ankara, Türkiye, pp: 177-195.

Gür Mazlum S. 2024. On Bishop frames of any regular curve in Euclidean 3- space E^3. Afyon Kocatepe Univ J Sci Engin, 24(1): 23-33.

Has A, Yılmaz B, Akkurt A, Yıldırım H. 2022. Comformable special curves in Euclidean 3-space E^3. Filomat, 36(14): 4687-4698.

Khalil R, Al Horani M, Yousef A, Sababheh M. 2014. A new definition of fractional derivative. J Comput Appl Math, 264: 65-70.

Nishimoto K. 1991. Essence of Nishimoto's fractional calculus (Calculus of the 21st Century). Integrals and Differentiations of Arbitrary order, Descartes Press, Koriyama, Japan, pp: 208.

Black Sea Journal of Engineering and Science
doi: 10.34248/bsengineering.1569765

Open Access Journal
e-ISSN: 2619 – 8991

Research Article
Volume 8 - Issue 1: 119-127 / January 2025

TECHNO-ECONOMIC ANALYSIS OF ZINC BORATE PRODUCTION FROM ZINC OXIDE AND BORIC ACID

Selin DİNÇER FİL[1]*, Fatma Burcu ALP[1], Mehmet GÖNEN[1]

[1]*Süleyman Demirel University, Department of Chemical Engineering, 32260, Isparta, Türkiye*

Abstract: The synthesis of zinc borate, $2ZnO{\cdot}3B_2O_3{\cdot}3.5H_2O$, was investigated via reaction of solid zinc oxide with boric acid aqueous phase in the existence on seed crystals. Commercially important type of zinc borate was synthesized using the 4.7 M boric acid concentration and B_2O_3 to ZnO molar ratio of 2 at 90°C, at 900 rpm and for 4 hours reaction time in a stainless-steel reactor. The amount of seed crystals was 1.5% of the boric acid initially used. At the end of each experiment, X-ray diffraction (XRD) instrument as well as Fourier-Transform infrared spectroscopy (FTIR) instrument were carried out for identifying final products. A continuous process was developed with SuperPro Designer software. The design was derived from experimental and literature data. A techno-economic analysis of the zinc borate synthesis process was carried out for different annual plant capacities (6,000-12,000t). Unit prices of raw materials and final product were obtained from the literature and the market as US$600/ton boric acid, US$2,200/ton zinc oxide and US$4,500/ton zinc borate. The fixed investment cost of the zinc borate production plant with capacity of 10,000 ton/year was found to be US$22,780,000 and the operating cost was found to be US$26,273,000/yr. The payback time was determined as 1.93 years from the economic analysis of the process.

Keywords: Zinc borate, Economic analysis, SuperPro designer, Process development, Production cost

***Corresponding author:** Süleyman Demirel University, Department of Chemical Engineering, 32260, Isparta, Türkiye
E mail: dincer_selin_@hotmail.com (S. DİNÇER FİL)
Selin DİNÇER FİL https://orcid.org/0009-0004-6327-8314
Fatma Burcu ALP https://orcid.org/0000-0002-0380-2020
Mehmet GÖNEN https://orcid.org/0000-0001-5780-4622

Received: October 18, 2024
Accepted: November 28, 2024
Published: January 15, 2025

Cite as: Dinçer Fil S, Alp FB, Gönen M. 2025. Techno-economic analysis of zinc borate production from zinc oxide and boric acid. BSJ Eng Sci, 8(1): 119-127.

1. Introduction

Zinc borates are important borate salts that can be produced from the reaction of boron compounds e.g., borax, boric acid and zinc compounds e.g. zinc oxide and zinc sulfate (Cui et al., 2012). Although there have been a number of zinc borates synthesized in the literature, $2ZnO{\cdot}3B_2O_3{\cdot}3.5H_2O$ is commercially important borate compound produced in large quantities in the world (Roskill, 2010). Although the zinc borates of $2ZnO{\cdot}3B_2O_3{\cdot}3H_2O$ and $2ZnO{\cdot}3B_2O_3{\cdot}3.5H_2O$ are same compounds, there has been a controversial case in naming of those compounds in commerce until the appearance of Schubert's article which has proven that zinc borate has oxide chemical formula and closed formula as following $2ZnO{\cdot}3B_2O_3{\cdot}3H_2O$, $Zn[B_3O_4(OH)_3$, respectively (Schubert et al., 2003). Zinc borate of $2ZnO{\cdot}3B_2O_3{\cdot}3.5H_2O$ is going to be called as just zinc borate hereafter in this manuscript. It is widely used in the production of fire-resistant products e.g., cables, fabrics, electronic parts, paints in an automobiles and aircrafts (Mergen et al., 2012). Those products are mainly manufactured using polymers, such as nylon, PVC, polyester, and ABS (Engin, 2009; Ting et al., 2008). A fire-retardant additive should be thermally stable during the processing of the polymers in the extruder. Zinc borate of $2ZnO{\cdot}3B_2O_3{\cdot}3.5H_2O$ is most frequently used as a polymer additive due to its comparatively higher dehydration start at 290°C (Çakal et al., 2020). The ability of zinc borate to retain dehydration water up to 290°C enables its use in a high temperature polymer processing (Schubert, 2003). Since it does not have toxic properties during thermal processing, special methods are not required during its addition to polymers. The extrusion temperature varies depending on the percent of zinc borate used, the type of polymer and other additives (Baltacı, 2010). Since zinc borate is used as a flame retardant, it reduces the flammability properties of the polymer and increases its decomposition resistance (Bardakçı, 2009). Therefore, polymers containing zinc borate could be processed at higher extrusion temperatures up to 290°C.

Zinc borate is produced by arranging the molar ratio of ZnO to B_2O_3 and reaction conditions e.g., reaction temperature and time, boric acid concentration and stirring rate (Eltepe et al., 2007). The boric acid mixture reacts with solid zinc oxides at 90°C and atmospheric pressure. Sawada and his colleagues produced zinc borate in a two-step process: in the first stage, solid boric acid and zinc oxide were added into an aqueous boric acid solution at 60°C and were mixed during 1.5 hours. Then, that mixture was then agitated for a further 4 hours at 90°C. In their experiment, Sawada and his coworkers used zinc borate as seed crystals. The amount

of the seed crystals is 1.5 wt. % of the boric acid initially used. The characterization study of the produced materials was carried out by XRD. It was determined that $2ZnO{\cdot}3B_2O_3{\cdot}3H_2O$ zinc borates were obtained in the experiments using seed crystal (Sawada et al., 2004). An 85L reactor was utilized to examine the large scale at which zinc borate can be manufactured through the reacting zinc oxide with a boric acid solution at 85°C (Kılınç et al., 2010). Particle size is one of the most important properties of materials used as additives. Therefore, Shete et al. investigated the particle size of the final product and the conversion parameters of zinc oxide affecting the formation of zinc borate in the synthesis of zinc borate using zinc oxide and boric acid starting materials. In the experiments; agitation speed, impeller type, particle size of zinc oxide, temperature, initial boric acid concentration were studied to determine the effects of mixing. From the experimental results, it was seen that the mixing parameters influenced the particle size of zinc borate. It was determined that with the increase in the average initial size of zinc oxide, the time taken for the conversion of zinc oxide to zinc borate increased. The increase in reaction time with the increase in particle size proved that the reaction is a surface controlled reaction. (Shete et al., 2004).

The widespread use of zinc borate as a flame retardant in recent years is one of the factors encouraging the increase in the production capacity of zinc borate. Due to the increasing demand for zinc borate use and changing market conditions, it is necessary to increase the number of zinc borate production facilities and the capacity of existing production facilities. There are several companies which produce zinc borate in thousands of metric tons for more than four decades in the world. Although Türkiye has the highest boron minerals, the most of the boron products, such as zinc borates were not produced commercially until the announcement of Akdeniz-Chemson Inc. which launched its zinc borate plant with the capacity of 3,000 t/y in 2021 (Rais, 2021). Process modelling, using data from laboratory experiments and from the markets, can usually improve performance of the process, purity of the product and identify effective inputs for the process (Kwan et al., 2018). A sustainable synthesis of boric acid by reacting the solid colemanite with sulphuric acid was examined using the SuperPro Designer program, taking into account the cost of treating the waste and processing the raw material. The evaluation of zinc borate ($2ZnO{\cdot}3B_2O_3{\cdot}3.5H_2O$) synthesis from zinc oxide reaction with boric acid was not examined considering raw material availability and transport advantages in Türkiye (Gönen et al., 2022).

A continuous process was selected for zinc borate production and its flowsheet having reactor and other unit operations (filtration, drying and milling) was designed in this program. Reactions taking place in the reactor, parameters of separation units, raw material and product properties obtained from laboratory experiment and from the literature (Eltepe et al., 2007; Sawada et al., 2004; Gönen, 2009) were used in the SuperPro Designer program. The objective of this investigation in this study was to develop a process for zinc borate ($2ZnO{\cdot}3B_2O_3{\cdot}3.5H_2O$) reaction which was based upon between zinc oxide with boric acid. SuperPro Designer Program (version 9.0) was applied to conduct the technical and economic analysis of this process.

2. Materials and Methods

2.1. Materials Used in the Experiments

Zinc oxide (99.0%, wt.) obtained from Merck Inc. and boric acid (99.92%, wt.) obtained from Eti Mine Inc. were used in zinc borate production. Commercial zinc borate ($2ZnO{\cdot}3B_2O_3{\cdot}3.5H_2O$) obtained from Eti Mine Inc. was utilized as seed crystals in reaction. EDTA, NaOH, NH_4Cl, Phenolphthalein, Methyl Orange, HCl (37%, Merck) and Mannitol from Sigma-Aldrich were used in the titration of the final product. Deionized water was used in all experiments and analyses.

2.2. Zinc Borate ($2ZnO{\cdot}3B_2O_3{\cdot}3.5H_2O$) Production

In this study, zinc borate was synthesised through a reacting zinc oxide with boric acid as described in Equation 1 in a stainless steel reactor with an electromagnetic mixer at the laboratory scala.

$$2ZnO_{(s)} + 6H_3BO_{3(aq)} \rightarrow 2ZnO{\cdot}3B_2O_3{\cdot}3.5H_2O_{(s)} + 5.5H_2O_{(l)} \quad (1)$$

Design of the experiment consisted of a stainless steel reactor with a magnetic drive unit, surrounding aluminum heater unit, a split-ring valve, thermostate, manometer, needle valve and rupture disc mounted on the reactor cover. A four bladed, turbo impeller was fitted to the reactor.

The experiments were carried out in a stainless steel reactor which was run at 90 °C during 4 hours and molar ratio of B_2O_3 to ZnO equal to is 2.0, a boric acid concentration that is 4.7 M (Gönen, 2009) and a stirring rate of 900 rpm. Initially, 50 ml of H_2O, a stoichiometric amount that is boric acid (H_3BO_3) as well as zinc oxide (ZnO) were added to reactor. After closing the reactor lid, the mechanical stirrer was started and a temperature controller was adjusted to the desired reaction temperature 90 °C. A second experiment was done with same condition but zinc borate amount of 1.5% boric acid used was added as seed crystal.

Boric acid was used in excess to consume all the zinc oxide used in the reaction. Zinc oxide is not soluble in an aqueous phase. Therefore, it was difficult to separate the unreacted zinc oxide from the solid product (zinc borate). The precipitated solid products were separated by vacuum filtration. Then, it was washed deionized water to free the unreacted boric acid from the final reaction solution when the reaction was completed. The boric acid content of the maternal solution and the Zn, B_2O_3 content of the synthesized solid samples were evaluated by analytical titration at the end of each experiment. An

oven at 105 °C was used to dry the wet cake obtained from the filtration for five hours. X-ray diffractometer (Bruker D8 Advance Twin-Twin) was used to analyze the crystal structures of the formed powders with CuKα radiation at 45 kV and 40 mA. The absorption spectra of KBr pellets prepared by mixing 2.0 mg of sample and 100 mg of KBr in an agate mortar and pressing the mixture under certain pressure were obtained using Fourier transform infrared (FTIR) spectrophotometer (Jasco FT/IR 4700).

3. Results

3.1. Product Characterization

An overconcentration of boric acid was utilised to synthesise zinc borate, because boric acid is soluble in an aqueous phase (Gönen et al., 2011). In these experiments, the boric acid concentration was first adjusted to 4.7 M. Then, the quantity of zinc oxide which corresponds to a molar ratio of B_2O_3 to ZnO equal to 2.0 was added into the reactor. Experiments were carried out in the absence and in the presence of a seed crystals to synthesise zinc borate. Under these experimental conditions, FTIR spectra of final solid powders are shown in Figure 1 and XRD patterns are shown in Figure 2.

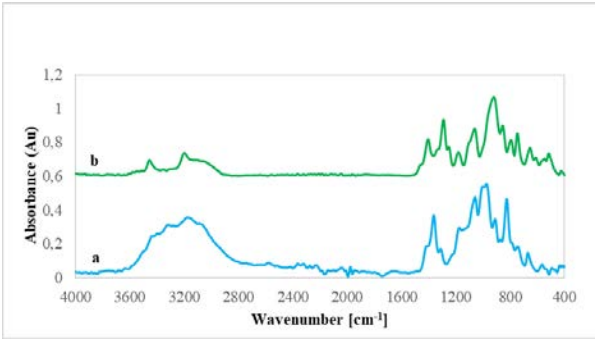

Figure 1. FTIR spectrum of (a) zinc borate sample synthesized at 90°C for 4 h without seed crystals (b) zinc borate sample synthesized at 90°C for 4 h including seed crystals.

The characterization study of the synthesised zinc borate powders was performed via Fourier Transform Infrared (FTIR) spectroscopy. Both spectra in Figure 1 were obtained in the 4000-400 cm^{-1} wavenumbers and are completely different each other. The "O-H" groups present in the structural of zinc borate with the formulae $2ZnO{\cdot}3B_2O_3{\cdot}7H_2O$ are represented by the broadening peak at 3600 cm^{-1} to 2800 cm^{-1} in the Figure 1.a. The spectrum peak placed into 1370 cm^{-1} indicates asymmetric stretching vibrations of the BO3 structure. Both peaks at 1053 and 997 cm^{-1} wavenumbers indicate the asymmetric stretching vibration of BO_4 bonding (Gönen, 2009). The symmetrical stretch motions of the BO_3 and BO_4 units were differentiated from the peak at 907 and 822 cm^{-1} wavenumbers respectively (Jun et al., 1995). It was concluded that reaction boric acid with zinc oxide in the absense of a seeding crystals produced zinc borate of $2ZnO{\cdot}3B_2O_3{\cdot}7H_2O$ at 90°C over a reaction time 4 hours. FTIR spectrum of zinc borate sample synthesized using seed crystals is shown in Figure 1.b. Both strong peaks at wavenumbers 3438 and 3187 cm^{-1} belong to the vibration of O-H groups, which is the fingerprint associated with zinc borate having formula $2ZnO{\cdot}3B_2O_3{\cdot}3.5H_2O$ (Eltepe et al, 2007). The peaks at these wavelengths can be seen in Figure 1.b. In addition, of these peaks in Fig.1.b, the one at 3200 cm wavelength is the characteristic peak belonging to the $ZnO{\cdot}B_2O_3$ group (Eltepe, 2004; Gönen, 2009). The peaks at wavenumbers of 1363 cm^{-1} and 1312 cm^{-1} represent asymmetric stretching vibration of BO_3 groups, and the peaks at wavenumbers of 1175 and 1059 cm^{-1} represent asymmetric stretching vibration of BO_4 groups. Others at 974 and 745 cm^{-1} correspond to symmetrical BO_3 and BO_4 (Jun et al., 1995). When FTIR spectra shown in Fig. 1.a and Fig.1.b are compared it is seen that they have different chemical structures. The desired zinc borate has the chemical structure $2ZnO{\cdot}3B_2O_3{\cdot}3.5H_2O$ and was synthesized at 90°C and 4h reaction time using seed crystals.

Figure 2.a and Figure 2.b show XRD patterns obtained from zinc borate samples prepared in the absence and presence of seed crystals at 90°C and 4h reaction time, respectfully. The principal peaks in the X-ray diffraction diagram for the powdered zinc borate sample shown in Figure 2.a. are at 10.59°, 12.95°, 20.83°, 21.20°, 28.10°, 30.10°, 31.0° and 33.25° 2θ. On the basis of the correspondence of these main peaks, the solid product obtained in the absence of seed crystals could be zinc borate whose chemical formula is $2ZnO{\cdot}3B_2O_3{\cdot}2H_2O$ (Gönen, 2009). However, the main signals in the XRD pattern from the zinc borate sample shown in Fig. 2.a. has peaks at 18.0°, 20.60°, 21.7°, 22.5°, 23.7°, 24.1°, 27.5° and 28.7° 2θ values By looking at the XRD pattern in Fig. 2.a., it can be said that the synthesized zinc borate 4h reaction time without seed crystals has a different chemical structure from the zinc borate composed by $2ZnO{\cdot}3B_2O_3{\cdot}3.5H_2O$. Referring to the XRD diagram of zinc borate recorded by Sawada and co-workers and JCPDS 32-1464 database, the zinc borate which was gained in 4.7 molar boric acid concentration in the absence of seed crystals is zinc borate with a type $2ZnO{\cdot}3B_2O_3{\cdot}3.5H_2O$ (Sawada et al., 2004).

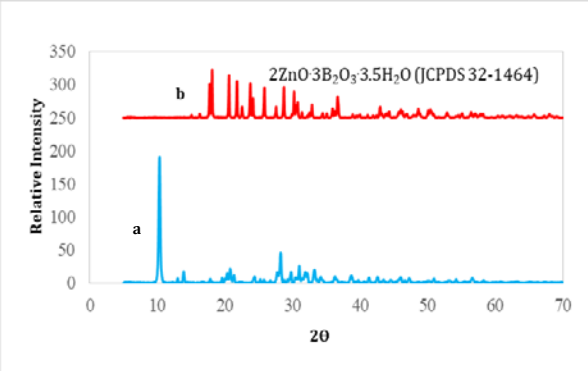

Figure 2. XRD patterns acquired from (a) zinc borate sample synthesised at 90°C for 4 hours without seed crystals (b) zinc borate sample synthesised at 90°C for 4 hours with seed crystals.

3.2. Techno-Economic Analysis of Zinc Borate Production Process

3.2.1. Process Description

The zinc borate production process was designed in SuperPro Designer program (Version 9.0) as shown in Fig. 3. The process consists of blending tank, reactor, filtration unit, washing unit, drying unit, milling and powder storage tank. The process starts with the preparation of a boric acid solution in the blending tank, where raw boric acid and water are mixed together with a recycle stream from the filtration unit. To obtain the desired zinc borate, $2ZnO{\cdot}3B_2O_3{\cdot}3.5H_2O$, the boric acid concentration was then precisely adjusted to the specific one required. Filtrate from washing unit was directly recycled to the reactor. Zinc borate cake from the belt filter is fed to the fluidized bed dryer where hot air at 105°C is used to remove the water from the zinc borate less than 0.5% by wt. Finally, dried zinc borate is stored in a silo for being packed.

The chemicals used in the zinc borate production plant, the reactions in the reactor and the conversion value were entered into the SuperPro Designer program as data. The units used in the process were determined and the units were connected to each other with pipe connections. The parameters of the units (temperature, reaction time, solid/liquid ratio) were defined in the program. In addition, labour costs, costs of raw materials, unit prices of the final products produced and the utilities used were defined to the program by making use of market conditions. Here, the values in the database of the program were used for the prices of some utilities (such as air price, waste treatment cost, steam cost and operator price).

The properties and unit prices of the chemicals and final products used in the production process are shown in Table 1. These data were obtained from the market. In the SuperPro Designer program all prices were entered in US$. For this reason, all costs and outputs in the project are given in US$.

Table 1. Market values of raw materials and products

Chemicals	Purity	Price ($/t)
Boric Acid	99.92%	600
Process Water	Industrial	0.12
Zinc Oxide	99.0%	2,200
Zinc Borate	99.0%	4,500

Since the process is designed in a continuous mode, two reactors were operated in staggered mode to achieve the required reaction time of four hours. The 2023 data was used to calculate the economic assessment variables for the whole project. The building of the facility starts in 2023 and lasts for 15 months. The commissioning period was set at 4 months and the project lifetime was set at 15 years. An inflation rate of 4% and an annual interest rate of 7 % were used in the economic analyses.

The economic The total capital investment was determined by summing total direct cost (TDC), total indirect cost (TIC), contractor's fee & contingency (CFC), working performance of the zinc borate production process was investigated through evaluation of total capital investment, operating expenses and income generation. The total capital investment was determined by summing total direct cost (TDC), total indirect cost (TIC), contractor's fee & contingency (CFC), working capital and startup costs cost as presented in Table 2. To calculate the total capital investment and operating costs, the factors determined by SuperPro Designer were multiplied by the purchase cost (PC) of the main equipment in the plant. The total direct cost (TDC) includes the construction of the facility, comprising the purchase of equipment (PC), installation of equipment, process piping and other related costs. Total indirect cost (TIC) comprises engineering and supervising and constructing costs.

Equipment size and the number of equipment needed for each capacity have been computed from mass and energy balances for the zinc borate synthesis reaction. The increase in the capacity of the zinc borate plant has a significant effect on the number of equipment used in the process. As a function of capacity, the purchase price of the required process equipment has been on the rise. The costs of these items are estimated by multiplying the equipment purchase cost by the coefficients indicated in Table 2. e.g. process piping is seen as 0.35 times the cost of the equipment.

Annual operating costs are computed by summing total variant production costs, fixed costs, factory overheads and general expenses, and details of the production cost parameters are given in Table 3. As the plant is assumed to be very close as far as raw materials and markets are concerned, logistics costs have not been included in the operating cost calculations. Data from the integrated module in SuperPro Designer Program and from the literature were used for the mass and energy balance calculations (Peters et al., 2003). The annual operating cost for the zinc borate production process was calculated based on raw materials, labor, facilities, laboratory and utilities.

Table 2. Total capital investment (US$M) required for a zinc borate plant

		Plant Capacity ($t.yr^{-1}$)			
Items	Estimation Assumption	6,000	8,000	10,000	12,000
Total Direct Cost (TDC)		10.42	10.50	12.38	12.70
Equipment purchase cost (PC)	Listed Equipment Cost	3.19	3.21	3.77	3.87
Installation	Equipment Specific	1.23	1.24	1.51	1.54
Process piping	0.35 x PC	1.11	1.12	1.31	1.35
Instrumentation	0.40 x PC	1.27	1.28	1.51	1.55
Isolation	0.03 x PC	0.09	0.1	0.11	0.12
Electricals	0.1 x PC	0.31	0.32	0.37	0.38
Buildings	0.45 x PC	1.43	1.44	1.69	1.74
Yard improvement	0.15 x PC	0.47	0.48	0.56	0.58
Service facilities	0.55 x PC	1.27	1.28	1.51	1.55
Total Indirect Cost	TIC	6.25	6.30	7.43	7.62
Engineering and supervision	0.25 x TDC	2.60	2.62	3.09	3.17
Construction expenses	0.35 x TDC	3.64	3.67	4.33	4.44
Total Plant Cost (TPC)	TPC=TDC+TIC	16.67	16.80	19.81	20.32
Contractor's Fee & Contingency (CFC)	CFC	2.50	2.52	2.97	3.04
Contractor's fee	0.05 x (TDC+TIC)	0.83	0.84	0.99	1.01
Contingency	0.1 x (TDC+TIC)	1.66	1.68	1.98	2.03
Direct Fixed Cost (DFC)	DFC=TPC+CFC	19.17	19.32	22.78	23.36
Working Capital		1.33	1.63	1.93	2.23
Startup Cost		0.95	0.96	1.14	1.16
Total Capital Invesment (TCI)	(TCI= TDC + TIC + CFC)	21.4	21.92	25.86	26.77

Table 3. Parameters for annual operating cost

Items	Estimation Assumption
Total variant production costs	
Raw materials	From mass balance
Labour-dependent	Monthly Salary: US$ 418
	Supervision factor: 0.15
Utility Cost	Electricity: US$ 0.10 kWh^{-1}
	Steam: US$ 12 MT^{-1}
	Steam(High pressure): US$ 20 MT^{-1}
	Process water: US$ 0.12 m^{-3}
	Cooling water: US$ 0.05 m^{-3}
	Chilled water: US$ 0.4 m^{-3}
Waste water treatment	US$ 102.6 MT^{-1}
Solid waste disposal	US$ 12.8 MT^{-1}
Maintaining and repairing of equipment	7% of the FCI
Laboratory cost for QC and QA	15% of the total labour cost
Operating supplies	15% of the equipment maintenance and repair cost
Royalties	4% of the capital cost
Fixed Cost	
Depreciation (15 year straight line)	Depreciated 5% of the FCI
Assurance	1% of the FCI
Factory overhead costs	50% of labour, equipment maintenance and repair costs
Administration costs	15% of operating labour cost
Distribution and marketing costs	No less than 2% of the total operating cost

3.2.2. Techno-Economic Analysis (TEA)

Zinc borate production flowsheet was designed in SuperPro Designer program as shown in Figure 3. The operating mode was set to be 7,920 operating hours per year for production of zinc borate. The data obtained from experimental study (reaction time, solid liquid ratio, boric acid concentration, solubility and etc.) and from the literature (molecular weights, heat of reactions, heat capacities and etc.) were entered into the program. As the boric acid was used in excess to reach higher conversion values, the amount of boric acid separated from the product was recycled to the reactor.

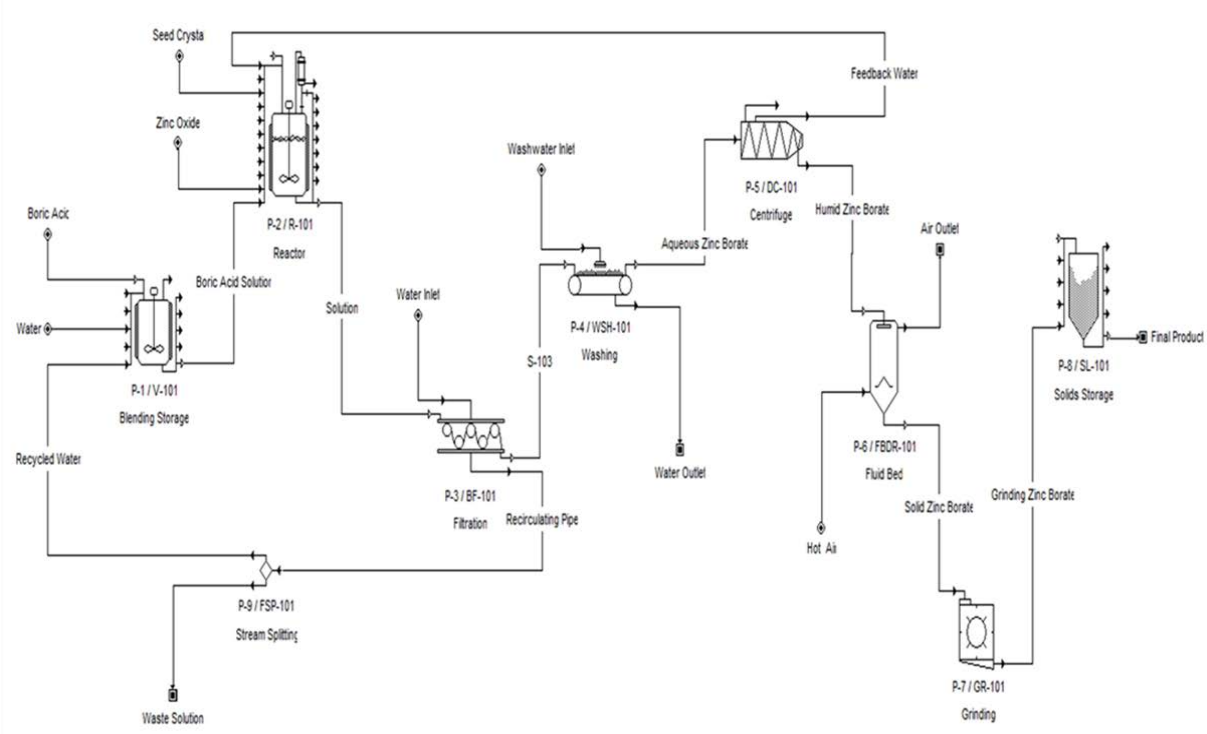

Figure 3. Flowsheet of Zinc Borate Production Process

A percentage of the recycle stream is purified to prevent the accumulated boric acid and to remove the water formed in the reaction and that used in the filtration unit. SuperPro Designer 9.0 software was used for mass and energy balance calculations.

The economic performance for the zinc borate plant was investigated by determining the total capital cost, operating cost and revenue generation for different production capacities ranging from 6,000 t/y to 12,000 t/y. Table 2 summarizes the total investment for a zinc borate process calculated by SuperPro Designer program. As shown in Figure 4, the total capital investment of the zinc borate production process varies between US$21.4 and US$26.77 M depending on the capacity of the production plant (6,000-12,000 t/yr). It can be seen from Figure 4, total capital investment increases as production capacity rises. On the other hand, the production cost per ton decreases as the production capacity increases.

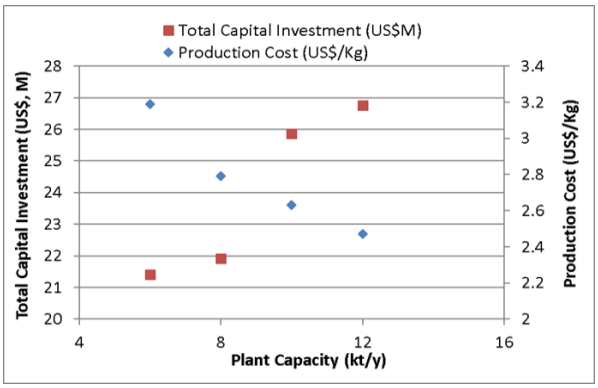

Figure 4. The Impact of Plant Capacity on Total Capital Investment and Production Costs.

Table 4. Payback time and revenues for different plant capacities

Plant capacity (t/y)	Revenues (US$M/yr)	Payback time (yr)
6,000	27	3.24
8,000	36	2.18
10,000	45	1.93
12,000	54	1.89

The payback time (PBT) and net present value (NPV) equations were used to assess the financial viability of the process (Peters et al., 2003). The payback time is described in equation 2. The payback time has been computed using the revenues for each capacity and presented in Table 4.

$$\text{Payback time (years)} = \frac{\text{Total Invesment}}{\text{Net Profit}} \quad (2)$$

The payback time was found out to be 3.24 years for the 6,000 t/yr capacity and when the factory capacity is upgraded to 10,000 t/yr, the payback time decreases to 1.93 years. As the capacity of the zinc borate production facility increases, there is no significant change in the payback time. Therefore, a production capacity of 10,000 t/yr was selected to investigate the other parameters listed in the TEA. For an annual production capacity of 10,000 ton zinc borate, the total capital investment was found to be US$25.86 M. The operating cost was calculated as US$26.4 M.

The net present value is a measurement of economic viability used to determine whether an investment project is profitable or not. It can be used to make comparisons between the economic viability of different investments. It can be estimated by means of equation 3. In this formula, i is the rate of interest, NCF is the cash-flow for year k and N is the lifetime of the project in years.

$$NPV = \sum_{k=1}^{N} \frac{\text{NCF}}{(1+i)^{\text{k}}} \quad (3)$$

The total direct plant cost for a 10,000 t/yr capacity is approximately US$12,380,000. The total cost of the plant is US$19,810,000 when the indirect engineering and construction costs (US$7,430,000) are added to the direct plant costs. The total of the contractors' fees and the contingency costs is US$2,970,000. The direct fixed capital cost for this zinc borate production process was calculated to be US$22,780,000 and is given as Table 1. The SuperPro Designer program database and literature data are used to determine the percentage cost contribution of each equipment for the FCI (Rais, 2021).

Annual operating cost of zinc borate production that was calculated by using SuperPro Designer program is presented in Figure 5. The plant producing 10,000 ton of zinc borate has the total annual operating cost of US$26,273,000. Raw materials, especially zinc oxide, have the largest contribution in the operating cost. Consumables, waste water treatment, transportation, advertising, running royalties, disposal of failed product were excluded in the estimation of annual operating cost as pointed out in Figure 5.

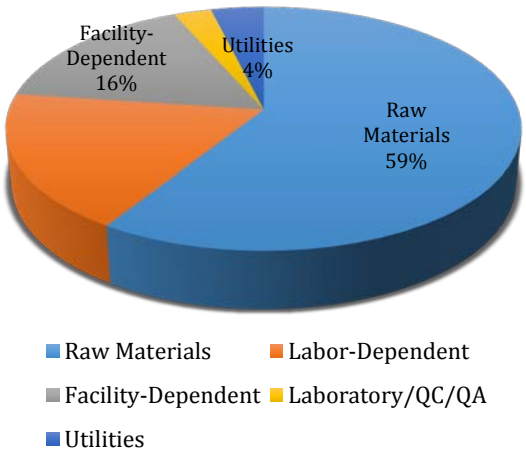

Figure 5. Annual operating cost.

Raw materials are the most important contributor to the cost of producing of zinc borate, accounting for 59%. The cost of zinc borate production for a 10,000 t/yr capacity was calculated as US$2.63/kg using Superpro Designer 9.0 software and a purchase cost of US$600/ton of boric acid. The purchase cost of boric acid was identified as an important component of the raw material cost as it is consumed three times more based on stoichiometry. To evaluate the impact of boric acid price on zinc borate manufacturing costs, boric acid prices ranging from US$600 to US$3,000 per ton were entered into Superpro Designer 9.0 for a 10,000 t/yr zinc borate production capacity.

Figure 6 shows the impact of boric acid purchase price on zinc borate production cost. As can be seen in Figure 6, as the price of the boric acid mineral used in the zinc borate production process rises, the cost of producing zinc borate also goes up. According to the information obtained from market research, the price of zinc borate varies between US$2,000 and US$4,700/ton. If boric acid mineral is purchased at a price of $2,400/ton and above, the zinc borate production plant cannot make a profit. In order to keep zinc borate production cost between market values, the cost of boric acid mineral should be kept below US$2,400/ton. The net present value of the project considering 7% interest rate was calculated as US$68,180,000. Gross profit was calculated as US$18,747,000/yr deducting annual operating costs from annual revenues. 40% income tax rate was used in the calculation of net profit.

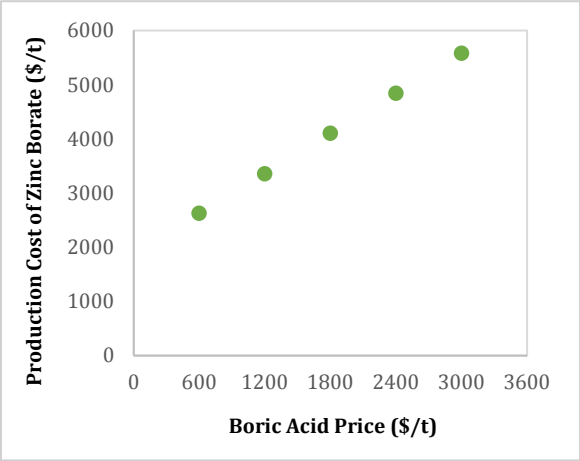

Figure 6. Zinc borate production costs as a function of boric acid price.

4. Conclusion

Using zinc oxide, boric acid and seed crystals, zinc borate was synthesized in this work. XRD as well as FTIR analyses were carried out on the final product obtained at the end of the experiment. The results show that it is possible to produce the desired product zinc borate using seed crystals amount of 1.5 % boric acid initially used and for the reaction time of 4 hours. Zinc borate in the desired form $2ZnO{\cdot}3B_2O_3{\cdot}3.5H_2O$ could not be synthesised without using the seed crystals. Production process of zinc borate ($2ZnO{\cdot}3B_2O_3{\cdot}3.5H_2O$) was designed using SuperPro Designer program. The total capital investment (TCI) of the zinc borate production plant was estimated to be in the range of US$21.4 M and US$26.77 M depending on the production capacity from 6,000 to 12,000 t/yr. Raw material costs (59%) are the most important factor contributing to Total Capital Investment (TCI). The detailed techno-economic analysis of zinc borate production process was performed for 10,000t annual zinc borate capacity. The unit production cost of zinc borate was calculated as US$2.63/kg by using SuperPro Designer 9.0. Purchase price of raw materials zinc oxide and boric acid were obtained from market as US$2.2/kg and US$0.60/kg, respectively. Selling price of zinc borate was used as US$4.5/kg in the process. The fixed and operating costs of designed zinc borate process are calculated as US$22,780,000 and US$26,273,000/yr. The payback time was determined as 1.93 years from the economic analysis of the process. This is a preliminary study for the zinc borate production. In future, the process will be re-analyzed for different scenarios considering waste water treatment, consumables, transportation, and different price of raw materials.

Author Contributions

The percentages of the authors' contributions are presented below. All authors reviewed and approved the final version of the manuscript.

	S.D.F	F.B.A	M.G.
C	40	20	40
D	45	10	45
S	40	30	30
DCP	50	20	30
DAI	40	30	30
L	50	10	40
W	50	10	40
CR	40	30	30
SR	40	20	40
PM	40	20	40
FA	40	30	30

C=Concept, D= design, S= supervision, DCP= data collection and/or processing, DAI= data analysis and/or interpretation, L= literature search, W= writing, CR= critical review, SR= submission and revision, PM= project management, FA= funding acquisition.

Conflict of Interest

The authors declared that there is no conflict of interest.

Ethical Consideration

Ethics committee approval was not required for this study because of there was no study on animals or humans.

Acknowledgements

Authors would like to thank Eti Mine Inc. for their support in providing boric acid used as raw material and zinc borate used as seed in the experimental study.

References

Baltacı B. 2010. Synthesis and characterization of nano zinc borate and its usage as a flame retardant for polymers. MSc thesis, Middle East Technical University, Department of Chemical Engineering, Ankara, Türkiye, pp: 2.

Bardakçı, M. 2009. Determination of zinc borate production methods and investigation of kinetics. MSc thesis, Yıldız Technical University, Institute of Science and Technology, İstanbul, Türkiye, pp: 63.

Cui Y, Liu X, Tian Y, Ding N. 2012. Controllable synthesis of three kinds of zinc borates and flame retardant properties in polyurethane foam. Colloids Surf. A Physicochem Eng Asp, 414: 274-280.

Çakal G. Ö, Baltacı B, Bayram G, Özkar S, Eroğlu I. 2020. Synthesis of zinc borate using water soluble additives: kinetics and product characterization. J Cryst Growth, 533: 125461.

Eltepe HE, Balköse D, and Ülkü S. 2007. Effect of temperature and time on zinc borate species formed from zinc oxide and boric acid in aqueous medium. Ind Eng Chem Res, 46(8): 2367-2371.

Engin B, 2009. Çinko borat üretimi optimizasyonu. MSc thesis,

Atatürk University, Institute of Science and Technology, Erzurum, Türkiye, pp: 20.

Gönen M, Rodone D, Panda S. 2022. Techno-economic analysis of boric acid production from colemanite mineral and sulfuric acid. Miner. Process. Extr Metall Rev, 43: 402-410.

Gönen M. 2009. Nanosized zinc borate production. PhD thesis, İzmir Institute of Technology, Engineering and Science, İzmir, Türkiye, pp: 74-81.

Gönen M, Balköse D, Ülkü S. 2011. Supercritical ethanol drying of zinc borates of $2ZnO{\cdot}3B_2O_3{\cdot}3H_2O$ and $ZnO{\cdot}B_2O_3{\cdot}2H_2O$. J Supercrit Fluids, 59(0): 43-52.

Jun L, Shuping X, Shiyang G. 1995. FT-IR and Raman spectroscopic study of hydrated borates. Spectrochim Acta-A:Mol Biomoll Spectrosc, 51A(4): 519-532.

Kılınç M, Çakal GÖ, Yeşil S, Bayram G, Eroğlu İ, Özkar S. 2010. Scale-up synthesis of zinc borate from the reaction of zinc oxide and boric acid in aqueous medium. J Cryst Growth, 312(22): 3361-3366.

Kwan TH, Hu Y, Lin CSK. 2018. Techno-economic analysis of a food waste valorisation process for lactic acid, lactide and poly(lactic acid) production. J Clean Prod, 181: 72-87.

Mergen A, Ipek Y, Bolek H, Oksuz M. 2012. Production of nano zinc borate and its effect on pvc. J Eur Ceram, 32(9): 2001-2005.

Peters M, Timmerhaus K, West, R. 2003. Plant Design and Economics for Chemical Engineers. Boston: McGraw-Hill, Inc.

Rais A. 2021. Akdeniz Chemson increases zinc borate capacity. Addit Polym, 3: 1-10.

Roskill IS. 2010. Boron: global industry markets and outlook. London: Roskill Information Services Limited, London, UK, 12th ed., pp: 223-224.

Schubert DM, Alam F, Visi MZ, Knobler CB. 2003. Structural characterization and chemistry of the industrially important zinc Borate, $Zn[B_3O_4(OH)_3]$. Chem Mater, 15(4): 866-871.

Shete AV, Sawant SB, Pangarkar VG. 2004. Kinetics of fluid–solid reaction with an insoluble product: zinc borate by the reaction of boric acid and zinc oxide. J Chem Technol Biotechnol, 79(5): 526-532.

Sawada H, Tatebe A, Sakao K. 2004. Zinc borate and production method and use thereof. US Patent No:6780913 B2, New York, USA.

Ting C, Jian-Cheng D, Long-Shou, W. Fan, Y. Gang, F. 2008. Synthesis of a new net like nano zinc borate. Mater Lett, 62: 2057-2059.

Black Sea Journal of Engineering and Science
doi: 10.34248/bsengineering.1569433

Open Access Journal
e-ISSN: 2619 – 8991

Araştırma Makalesi (Research Article)
Cilt 8 - Sayı 1: 128-131 / Ocak 2025
(Volume 8 - Issue 1: 128-131 / January 2025)

OYUN TEORİSİNDE DENETİM AMAÇLI BİR DEĞERİN AKSİYOMATİK KARAKTERİZASYONU

Mahmut Sami ÖZTÜRK[1]*

[1]*Süleyman Demirel University, Faculty of Economics and Administrative Sciences, Department of Business Administration, 32200, Isparta, Türkiye*

Özet: Bu çalışmanın amacı adalet aksiyomunun kullanılması neticesinde işbirlikçi oyun teorisindeki etkili çözümlerden biri olan Shapley değerinin yeni bir karakterizasyonun elde edilmesidir. Adalet aksiyomu, iki oyuncunun kazançlarının aynı oranda değişmesini gerektirmektedir. Adalet aksiyomu kaynakların dağıtılması konusunda ve karar alma aşamalarında eşitlik, hakkaniyet ve adalet prensiplerini dikkate aldığı için denetim açısından önem taşımaktadır. Oyun teorisi bünyesinde denetim ise oyun teorisinin kontrol mekanizmasını oluşturmakta ve sistemlerin etkinliğini artırılmasında önemli bir rol oynamaktadır. Çalışmada adalet aksiyomlarının yanı sıra kazanç-kayıp aksiyomu ve null oyuncu özelliği ile Shapley değeri yeniden tanımlanmaktadır. Shapley değerini aksiyomatik karakterize etmek için çeşitli önermeler kullanılmakta ve ana teorem ispatları yapılarak aksiyomatik karakterizasyon neticelendirilmektedir.

Anahtar kelimeler: Shapley değeri, İşbirlikçi oyunlar, Aksiyomatik karakterizasyon, Adalet aksiyomu, Kazanç-kayıp aksiyomu, Denetim

The Axiomatic Characterization of a Value for Audit Purpose in Game Theory

Abstract: The aim of this study is to obtain a new characterization of the Shapley value, one of the effective solutions in cooperative game theory, using the fairness axiom. The axiom of fairness requires that the payoffs of two players change at the same rate. The axiom of justice is important in terms of auditing as it considers the principles of equality, fairness and justice in the distribution of resources and decision-making stages. Audit within game theory constitutes the control mechanism of game theory and plays an important role in increasing the effectiveness of systems. In the study, in addition to the justice axioms, the gain-loss axiom and the Shapley value with the null player property are redefined. Various propositions are used to axiomatically characterize the Shapley value, and the axiomatic characterization is concluded by proving the main theorem.

Keywords: Shapley value, Cooperative games, Axiomatic characterization, Fairness axiom, Gain-loss axiom, Audit

***Sorumlu yazar (Corresponding author):** Süleyman Demirel University, Faculty of Economics and Administrative Sciences, Department of Business Administration, 32200, Isparta, Türkiye
E mail: samiozturk@sdu.edu.tr (M.S. ÖZTÜRK)
Mahmut Sami ÖZTÜRK https://orcid.org/0000-0002-7657-3150

Gönderi: 17 Ekim 2024 **Received:** October 17, 2024
Kabul: 28 Kasım 2024 **Accepted:** November 28, 2024
Yayınlanma: 15 Ocak 2025 **Published:** January 15, 2025
Cite as: Öztürk MS. 2025. The axiomatic characterization of a value for audit purpose in game theory. BSJ Eng Sci, 8(1): 128-131.

1. Giriş

Oyun teorisi, iş birliği ve çatışma modelleriyle ilgilenen matematiksel bir teori olarak tanımlanır (Ergüneş Berkin vd., 2022). Bilindiği üzere matematik biliminin mühendislik, ekonomi, işletme, muhasebe, denetim ve sosyal bilimler başta olmak üzere birçok alanda uygulaması bulunmaktadır. Oyun teorisi başlıca işbirlikçi olmayan ve işbirlikçi olmak üzere iki kısma ayrılmaktadır. Bu çalışmada işbirlikçi oyun teorisi ele alınmaktadır.

İşbirlikçi oyunlar oyuncuların oluşturdukları koalisyonlarla ilgilenmektedir. İşbirlikçi oyun teorisi koalisyonlar oluşturulduğunda, kazanç ve kaybın oyuncular arasında paylaştırılması problemini çözmeye çalışmaktadır. Bu sorunun cevabı işbirlikçi oyun teorisindeki çözüm kavramları ile yanıtlanmıştır. İşbirlikçi oyun teorisindeki çözüm kavramlarından bazıları tek nokta çözümleri olup bunların en kullanışlı olanı Shapley değeridir (Shapley, 1953).

Shapley değeri, işbirlikçi oyun teorisinin en önemli tek nokta çözümlerinden biridir. Bu değeri, (Shapley, 1953) verimlilik, toplamsallık, simetri ve null oyuncu aksiyomlarını kullanılarak karakterize etmiştir. Aksiyomatik karakterizasyon, bir çözümü farklı aksiyomlar kullanarak yeniden tanımlamak anlamına gelmektedir.

Literatürde konu ile ilgili aksiyomatik karakterizasyon üzerine çeşitli çalışmalar bulunmaktadır (Ekici vd., 2018; Palancı vd., 2021; Ekici, 2023, Ekici, 2024).

Young (1985), verimlilik, simetri ve güçlü monotonluk özelliğini kullanarak; Chun (1991), stratejik denklik adını verdiği farklı bir aksiyom kullanarak; van den Brink (2001), adalet özelliğini kullanarak; Casajus (2011), diferansiyel marjinaliti özelliğini kullanarak; Casajus (2014), verimlilik ve toplamsallık şartını kullanmadan Shapley değerini karakterize etmişlerdir.

Verimlilik aksiyomu, oyuncuların ödemelerinin toplamının büyük koalisyonun ödemesine eşit olması

olarak tanımlanmaktadır. Null oyuncu aksiyomu, null oyuncunun girdiği oyunda oyuna herhangi bir katkı vermediği anlamına gelmektedir. Diferansiyel marjinaliti aksiyomu, iki oyuncunun ödeme farkının yalnızca onların marjinal katkılarının farkı ile belirlendiğini göstermektedir. Bu makalede, oyun teorisinde denetimin uygulanması amacıyla bu aksiyomları kullanarak Shapley değerini aksiyomatik olarak karakterize edilmiştir.

Bu çalışmada, Kısım 2'de işbirlikçi oyun teorisindeki önemli kavramlar ve Shapley değerini aksiyomatik olarak karakterize etmek için kullanılan aksiyomlar verilmiştir. Kısım 3'te Shapley değerini aksiyomatik karakterize etmek için kullanılan önermeler ve ana teorem ispatları yer almaktadır. Son kısımda, makalenin sonuçları yeniden hatırlatılmış ve gelecek çalışmalarda ne yapılacağına yer verilmiştir.

2. Materyal ve Yöntem

Bu bölümde işbirlikçi oyun teorisindeki bazı önemli kavramlarından bahsedeceğiz (Tijs, 2003).

$N = \{1, 2, \dots, n$ oyuncuların kümesi ve $w: 2^N \to \mathbb{R}$ karakteristik fonksiyon olmak üzere, işbirlikçi bir oyun $\langle N, w \rangle$ ifadesi ile gösterilmektedir. N nin alt kümelerin oluşan 2^N kümesi her alt kümesi koalisyon olarak isimlendirilmektedir. Tüm işbirlikçi oyuncuların kümesi G^N ile gösterilmektedir. Bu çalışmada, S koalisyonunun eleman sayısı $|S|$ yerine $|s|$ ifadesi kullanılacaktır.

Şimdi, tek nokta çözümlerinden biri olan Shapley değerinin tanımı yeniden hatırlatılacaktır. İşbirlikçi oyun teorisinde tek nokta çözümleri $g : G^N \to \mathbb{R}^N$ dönüşümü ile gösterilmektedir.

Tanım: $v \in G^N$ oyununun Shapley değeri,

$$\Phi : G^N \to \mathbb{R}^N$$

olmak üzere (eşitlik 1)

$$\Phi_i(w) = \sum_{i \in S} \frac{\Delta_w(S)}{s} \qquad (1)$$

şeklinde tanımlanmaktadır. Burada, $S \subset N$ için

$$\Delta_w(S) = \sum_{T \subset S} (-1)^{s-t} w(T)$$

kar payı olarak isimlendirilir ve (Harsanyi, 1959) tarafından bulunmuştur.

G^N kümesi bilinen toplama ve skalerle çarpma işlemlerine göre bir vektör uzayı olup bu vektör uzayının bir tabanı olan $T \subset N$ için u_T oybirliği oyunu

$$u_T(S) = \begin{cases} 1 & , \quad T \subset S \; ise \\ 0 & , \quad aksi \; halde \end{cases}$$

biçiminde tanımlanmaktadır. $\forall w \in G^N$ oyunu

$$w = \sum_{\emptyset \neq T \subset N} \Delta_w(S) u_T$$

şeklinde yazılabilir.

Şimdi, tek nokta çözümleri için bilinen bazı temel aksiyomlardan bahsedilecektir.

Aksiyom 1 (Verimlilik): Her $w \in G^N$ için

$$\sum_{i \in N} g_i(w) = w(N)$$

dir.

Her $S \subset N$ için

$$w(S) = w(S \backslash \{i\})$$

ise $i \in N$ oyuncusuna $w \in G^N$ oyununda bir null oyuncu denir.

Aksiyom 2 (Kazanç-kayıp)

$$w(N) = v(N)$$

ve

$$g_i(w) > g_i(v)$$

olacak şekilde, her $w, v \in G^N$ için

$$g_j(w) < g_j(v)$$

olmasını sağlayan en az bir $j \in N$ vardır.

Aksiyom 3 (Toplamsallık): $\forall w, v \in G^N$ için,

$$g_i(w + v) = g_i(w) + g_i(v)$$

dur.

Aksiyom 4 (Null oyuncu özelliği): Eğer $i \in N$, $w \in G^N$ oyununda bir null oyuncu ise

$$g_i(w) = 0$$

dır.

Her $S \subset N \backslash \{i, j\}$ için

$$w(S \cup \{i\}) = w(S \cup \{i\})$$

ise $i, j \in N$ oyuncularına simetrik oyuncular denir.

Aksiyom 5 (Simetri): Eğer, $i, j \in N, w \in G^N$ oyununda simetrik oyuncular ise

$$g_i(w) = g_j(w)$$

Aksiyom 6 (Adalet): Eğer, $i, j \in N$, $v \in G^N$ oyununda simetrik oyuncular ise

$$g_i(w + v) - g_i(w) = g_j(w + v) - g_j(w)$$

dir (van den Brink, 2001).

3. Bulgular

Bu bölümde, ilk olarak Shapley değerinin aksiyomatik karakterizasyonunda kullanılacak olan önermeler ispatları ile birlikte verilmiştir.

Önerme 1: $g : G^N \to \mathbb{R}^N$ çözümü simetri ve toplamsallık aksiyomlarını sağlarsa, adalet aksiyomunu da sağlar.

İspat: $g : G^N \to \mathbb{R}^N$ çözümü simetri ve toplamsallık aksiyomlarını sağlasın.

Eğer $i, j \in N$ oyuncuları $v \in G^N$ de simetrik oyuncular ise, $\forall w \in G^N$ için (eşitlik 2)

$$\begin{aligned} & g_i(w + v) - g_i(w) = g_i(w) + g_i(v) - g_i(w) \\ & = g_i(v) = g_j(v) \\ & = g_j(v) + g_j(w) - g_j(w) \\ & = g_i(w + v) - g_j(w) \end{aligned} \qquad (2)$$

olup adalet aksiyomu sağlanır.

Önerme 2: $g:G^N\to\mathbb{R}^N$ çözümü null oyuncu özelliği ve adalet aksiyomunu sağlarsa, simetri aksiyomunu da sağlar.

İspat: $g:G^N\to\mathbb{R}^N$ çözümü null oyuncu özelliği ve adalet aksiyomunu sağlasın. Her $S\subset N$ olmak üzere $w_0(S)=0$ olarak verilen $w_0\in G^N$ null oyunu için, null oyuncu özelliği her $i\in N$ için $g_i(v_0)=0$ olmasını gerektirir. Eğer $i,j\in N$ oyuncuları $w\in G^N$ de simetrik oyuncular ise adalet aksiyomu ve w_0 durumu dikkate alındığında,

$$g_i(w)=g_i(w_0+w)-g_i(w_0)=g_j(w_0+w)-g_j(w_0)\\=g_j(w)$$

olup g çözümü simetri özelliğini sağlar.

Adalet aksiyomu ile diferansiyel marjinaliti aksiyomunun eşit olduğu ve birbiri yerine kullanılabildiğini (Casajus, 2011) göstermiştir. Bundan dolayı, Shapley değeri için aksiyomatik karakterizasyonda diferansiyel marjinaliti aksiyomu yerine adalet aksiyomu kullanılacaktır. Şimdi, bu çalışmanın ana teoremini ifade edelim.

Teorem: $g:G^N\to\mathbb{R}^N$ çözümünün kazanç-kayıp aksiyomu, null oyuncu özelliği ve adalet aksiyomunu sağlaması için gerek ve yeter şart g çözümünün Shapley değerine eşit olmasıdır.

İspat: Shapley değerinin kazanç-kayıp aksiyomu ve null oyuncu özelliğini sağladığı iyi bilinmektedir. Önerme 1'den, Shapley değeri simetri ve toplamsallık aksiyomlarını sağladığı için adalet aksiyomunu da sağlar.

Şimdi $g:G^N\to\mathbb{R}^N$ çözümünün kazanç-kayıp aksiyomu, null oyuncu özelliği ve adalet aksiyomunu sağladığını varsayalım.

Eğer $|N|=1$ ise, null oyuncu özelliğinden $g=\Phi$ dir.

Şimdi $|N|>1$ olsun. $v\in G^N$ için

$$S_1(v):=\left\{S\subseteq N\middle||S|>1\ ve\ \Delta_v(T)\neq 0\right\} \quad (3)$$

kümesini tanımlayalım.

Her $v\in G^N$ ve $S\in S_1(v)$ için,

$$v^S=v-\Delta_v(T)\cdot\left(u_S-|S|^{-1}\cdot\sum_{i\in S}u_{\{i\}}\right) \quad (4)$$

biçiminde veriliyor.

Bu denklem, her $i,j\in S$ ve her $i,j\in N\backslash S$ için adalet aksiyomunun sağlandığını yani

$$g_i(v+v^S)-g_i(v)=g_j(v+v^S)-g_j(w) \quad (5)$$

olmasını gerektirir.

Şimdi $|S_1(v)|$ üzerinden tümevarım yaparak $g=\Phi$ olduğunu göstereceğiz.

Tümevarım Esası: Eğer $|S_1(v)|=0$ ise null oyuncu özelliğinden $g=\Phi$ dir.

$|S_1(v)|=1$ yani $|S_1(v)|=\{S\}$ olması $\lambda\in\mathbb{R}\backslash\{0\}$ ve $\lambda_k\in\mathbb{R}, k\in N$ için

$$v=\lambda\cdot u_S+\sum_{k\in N}\lambda_k\cdot u_{\{k\}}$$

olmasını sağlar. Böylece null oyuncu özelliği ve (2) den her $i\in N\backslash S$ için

$$g_i(v)=g_i(v^S)=\Phi_i(v) \quad (6)$$

olur.

Bazı $i\in S$ için $g_i(v)>\Phi_i(v)$ olsun. Böylece null oyuncu özelliği ve (2) den

$$g_i(v)>\Phi_i(v)=\Phi_i(v^S)=\mathrm{g}_i(v^S)$$

olur. $v^S(N)=v(N)$, kazanç-kayıp aksiyomu ve (6) dan bazı $j\in S$ için

$$g_j(v)<g_j(v^S)$$

olup (5) nolu eşitlik ile çelişir. Benzer şekilde $i\in S$ için $g_i(v)<\Phi_i(v)$ olması da (5) nolu eşitlik ile çelişir. Böylece her $i\in S$ için $g_i(v)=\Phi_i(v)$ olup (6) dan $g(v)=\Phi(v)$ olur.

Tümevarım Hipotezi: $|S_1(v)|=k+1>1$ olacak şekilde $v\in G^N$ için $g(v)=\Phi(v)$ olduğunu göstermektedir.

Tümevarım Adımı: $|S_1(v)|=k+1>1$ olacak şekilde $v\in G^N$ olsun. (3) ve (4) den, $|S_1(v^S)|=|S_1(v)|-1$ olur. Tümevarım hipotezi ve (2) den her $S\in S_1(v)$ için

$$g(v^S)=\Phi(v^S)=\Phi(v) \quad (7)$$

elde edilir.

(5) ve (7) den, $i,j\in S$ veya $i,j\in N\backslash S$ olmak üzere herhangi bir $S\in S_1(v)$ olacak şekilde her $i,j\in N$ için

$$g_i(v)-\Phi_i(v)=g_j(v)-\Phi_j(v) \quad (8)$$

olur. Şimdi, $S\in S_1(v)$ nin olmadığı $i,j\in N$ oyuncuları ile ilgilenilecektir.

Durum 1: Her $S\subseteq N$, $S\neq\emptyset$, $N\backslash S\neq\emptyset$ için $S_1(v)\neq\{S,N\backslash S\}$ olsun. Aşağıda verilen durumlardan biri sağlanır.

(i) $S\cap T=\emptyset$ olacak şekilde birbirine eşit olmayan $S,T\in S_1(v)$ vardır.

(ii) $S\cup T\neq N$ olacak şekilde birbirine eşit olmayan $S,T\in S_1(v)$ vardır.

Durum 1 (i): $S\neq T$ olduğu için $S\backslash T\neq\emptyset$ dir. $i\in S\cap T$, $j\in T\backslash S$, $k\in T$ ve $l\in N\backslash(S\cup T)$ olsun. (8) den,

$$g_i(v)-\Phi_i(v)=g_j(v)-\Phi_j(v)=g_i(v)-\Phi_i(v)=g_k(v)-\Phi_k(v) \quad (9)$$

olur.

Durum 1 (ii): $S\neq T$ olduğu için $S\backslash T\neq\emptyset$ dir. $l\in S\cap T$, $j\in T\backslash S$, $k\in S\backslash T$ ve $i\in N\backslash(S\cup T)$ olsun. (8) den,

$$g_i(v)-\Phi_l(v)=g_j(v)-\Phi_j(v)=g_i(v)-\Phi_i(v)=g_k(v)-\Phi_k(v) \quad (10)$$

olur.

Durum 2: $S\subseteq N$, $S\neq\emptyset$, $N\backslash S\neq\emptyset$ için $S_1(v)=\{S,N\backslash S\}$ olsun. $i\in S$ ve $j\in N\backslash S$ yi sabitleyelim. λ_S, $\lambda_{N\backslash S}\in\mathbb{R}\backslash\{0\}$, $\lambda_k\in\mathbb{R}, k\in N$ için

$$v=\lambda_S\cdot u_S+\lambda_{N\backslash S}\cdot u_{N\backslash S}+\sum_{k\in N}\lambda_k\cdot u_{\{k\}}$$

$$w=\lambda_S\cdot u_S-\lambda_{N\backslash S}\cdot u_{N\backslash S}+\sum_{k\in N}\lambda_k\cdot u_{\{k\}}$$

olacak şekilde $w\in G^N$ oyunu verilsin.

$$S_1(w)=\left\{S,\left((N\backslash S)\backslash\{j\}\right)\cup\{i\}\right\}$$

ve

$T \cap \big((N\backslash T)\backslash\{j\}\big) \cup \{i\} = \{i\}$

olduğuna dikkat edelim.

Adalet aksiyomunu kullanarak

$$\begin{aligned} g_i(v) - g_j(v) &= g_i(w) - g_j(w) \\ &= \Phi_i(w) - \Phi_j(w) \\ &= \Phi_i(v) \\ &\quad - \Phi_j(v) \end{aligned} \tag{11}$$

olduğunu elde ederiz.

(8), (9), (10) ve (11) den her $i, j \in N$ için

$$g_i(v) - \Phi_i(v) = g_j(v) - \Phi_j(v) \tag{12}$$

olur.

$i \in N$ için $g_i(v) > \Phi_i(v)$ olduğunu varsayalım. Buradan,

$g_i(v) > \Phi_i(v) = g_i(v^S)$

olur. $v^S(N) = v(N)$ ve kazanç-kayıp aksiyomundan,

$g_j(v) < g_i(v^S) = \Phi_j(v)$

olması (12) ile çelişir. Benzer şekilde $i \in N$ için $g_i(v) < \Phi_i(v)$ olup (12) ile çelişir. Sonuç olarak, $g(v) = \Phi(v)$ olur.

Böylece ispat tamamlanmış olur.

4. Sonuç

Bu makalede işbirlikçi oyun teorisinin en etkili çözümlerinden bir olan Shapley değeri, bazı aksiyomlar kullanılarak karakterize edilmiştir. Bu aksiyomlar; kazanç-kayıp aksiyomu, null oyuncu özelliği ve adalet aksiyomudur. Bu aksiyomlar ile kaynakların dağıtımında ve karar alma aşamalarında eşitlik, hakkaniyet ve adalet prensipleri dikkate alınmakta ve denetimin amacına ulaşması sağlanmaktadır. Oyun teorisi kapsamındaki etkin bir denetim sayesinde ise oyun teorisinin kontrol mekanizması oluşturulmakta ve sistemlerin etkinliği artmaktadır. Gelecekteki çalışmalarda ise, işbirlikçi oyun teorisindeki diğer çözüm kavramları da aksiyomatik olarak karakterize edilebilir.

Katkı Oranı Beyanı

Yazarın katkı yüzdesi aşağıda verilmiştir. Yazar makaleyi incelemiş ve onaylamıştır.

	M.S.Ö.
K	100
T	100
Y	100
VTI	100
VAY	100
KT	100
YZ	100
KI	100
GR	100

K= kavram, T= tasarım, Y= yönetim, VTI= veri toplama ve/veya işleme, VAY= veri analizi ve/veya yorumlama, KT= kaynak tarama, YZ= Yazım, KI= kritik inceleme, GR= gönderim ve revizyon.

Çatışma Beyanı

Yazar bu çalışmada hiçbir çıkar ilişkisi olmadığını beyan etmektedir.

Etik Onay Beyanı

Bu araştırmada hayvanlar ve insanlar üzerinde herhangi bir çalışma yapılmadığı için etik kurul onayı alınmamıştır.

Kaynaklar

Casajus A. 2011. Differential marginality, van den Brink fairness, and the Shapley value. Theory Decis, 71(2): 163-174.

Casajus A. 2014. The Shapley value without efficiency and additivity. Math Soc Sci, 68: 1-4.

Chun Y. 1991. On the symmetric and weighted Shapley values. Int J Game Theory, 20: 183-190.

Ekici M, Palanci O, Gök SZA. 2018. The grey Shapley value: an axiomatization. In IOP Conference Series: Materials Science and Engineering, August 21-23, Medan, Indonesia, 300: 012082. https://doi.org/10.1088/1757-899X/300/1/012082

Ekici M. 2023. On an axiomatization of the grey Banzhaf value. AIMS Math, 8(12): 30405-30418.

Ekici M. 2024. An alternative approach to the axiomatic characterization of the ınterval shapley value. J New Theory, 46: 1-10.

Ergüneş Berkin E, Önder H, Aydoğmu ÖH. 2022. A game theoretic approach to design mating programs for livestock. Turkish J Vet Anim Sci, 46: 124-129.

Harsanyi JC. 1959. A Bargaining model for cooperative n-person games. In Contributions to the Theory of Games IV, vol. 40, Tucker AW, Luce RD (editors). Princeton University Press, Princeton, US, pp: 325-355.

Palanci O, Ekici M, Gök SZA. 2021. On the equal surplus sharing interval solutions and an application. J Dynam Games, 8(2): 139-150.

Shapley LS. 1953. A value for n-person games. Annals Math Stud, 28: 307-317.

Tijs S. 2003. Introduction to game theory. Springer, Hindustan Book Agency, India.

van den Brink R. 2001. An axiomatization of the Shapley value using a fairness property. Int J Game Theory, 30: 309-319.

Young HP. 1985. Monotonic solutions of cooperative games. Int J Game Theory, 14(2): 65-72.

Black Sea Journal of Engineering and Science
doi: 10.34248/bsengineering.1569645

Open Access Journal
e-ISSN: 2619 – 8991

Araştırma Makalesi (Research Article)
Cilt 8 - Sayı 1: 132-141 / Ocak 2025
(Volume 8 - Issue 1: 132-141 / January 2025)

DİŞ SEGMENTASYONUNDA SEGFORMER YÖNTEMİNİN MODEL PARAMETRELERİ ÜZERİNDEKİ ETKİSİNİN ARAŞTIRILMASI

Egemen BELGE[1], Seçkin KARASU[1]*

[1]*Zonguldak Bülent Ecevit University, Faculty of Engineering, Department of Electrical and Electronics Engineering, 67100, Zonguldak, Türkiye*

Özet: Son yıllarda bilgisayar destekli tedavilerde yapay zekâ temelli uygulamalar diş hekimleri için hastalık teşhisinde kullanımı giderek artmaktadır. Diş hastalığın belirlenmesi sürecinde doğru bir şekilde bölütleme işlemi oldukça önemlidir. Diş bölütlenmesinin manuel olarak yapılması diş hekimleri tarafından yapılan teşhis için geçen süreyi ve işlem yükünü önemli ölçüde arttırmaktadır. Bu aşamada, makine öğrenmesi ve yapay zekâ yöntemleriyle otomatik olarak diş bölgesinin bölütlenmesi araştırmacıların ilgi duyduğu güncel bir konu olmaktadır. Çalışmada 12 diş stajyeri tarafından 15318 poligonlu 598 hastadan alınan X-Ray diş görüntüleri kullanılmaktadır. Kullanılan veri seti eğitim, doğrulama ve test olarak %70, %15, %15 olarak bölünmüştür. Bu veri seti otomatik olarak diş bölütlemeyi amaçlayan derin öğrenme ağının eğitim sürecinde kullanılmaktadır. SegFormer eğitim bloğu hiper parametrelerinin değişimine bağlı oluşturulan mimarilerinin performansları incelenmektedir. Burada MiT BO-B5 mimarilerine göre oluşturulan modellerin Dice benzerlik katsayılarına göre test verisi için performansları sırasıyla %92,61, %92,82, %93,25, %93,13, %93,17 ve %93,09 olarak elde edilmektedir. Elde edilen test sonuçlarına göre geliştirilen yapay zekâ tabanlı SegFormer ağı diş bölütlemeyi yüksek doğrulukla gerçekleştirmektedir. Geliştirilen derin öğrenme ağı özellikle diş hastalıklarının teşhisinde girdi olarak verimli bir şekilde kullanılabilecektir. Yüksek Dice benzerlik katsayıları, çalışmada sunulan SegFormer ağının diş bölgesini doğru bir şekilde tespit edebildiğini ifade etmektedir.

Anahtar kelimeler: Yapay zekâ, Diş bölütlenmesi, SegFormer, X-Ray görüntüleme, Dice benzerlik katsayısı

Investigation of the Effect on Model Parameters in SegFormer Method for Tooth Segmentation

Abstract: In recent years, AI-based applications in computer-aided treatments have been increasingly used by dentists for disease diagnosis. Accurate segmentation is crucial in the process of identifying dental diseases. Manual segmentation of teeth significantly increases the time and workload for dentists when making diagnoses. At this stage, the automatic segmentation of the dental region using machine learning and artificial intelligence methods has become a topic of great interest for researchers. In the study, X-Ray tooth ratios taken from 598 patients with 15318 polygons by 12 dental interns are used. The dataset is split into 70% for training, 15% for validation, and 15% for testing. This dataset is used in the training process of a deep learning network for automatic tooth segmentation. The performances of architectures generated based on changes in the hyperparameters of the SegFormer training block are examined. Here, according to the Dice similarity coefficients of the models according to the Mix BO-B5 architectures, the performances for the test data are obtained as 92.61%, 92.82%, 93.25%, 93.13%, 93.17% and 93.09%, respectively. According to the test results obtained, the developed artificial intelligence-based SegFormer network performs tooth segmentation with high accuracy. The developed deep learning network can be efficiently used especially in the diagnosis of dental diseases. High Dice similarity coefficients indicate that the SegFormer network presented in this study can accurately detect the tooth region.

Keywords: Artificial intelligence, Tooth segmentation, SegFormer, X-Ray imaging, Dice similarity coefficient

***Sorumlu yazar (Corresponding author):** Zonguldak Bülent Ecevit University, Faculty of Engineering, Department of Electrical and Electronics Engineering, 67100, Zonguldak, Türkiye
E mail: seckin.karasu@beun.edu.tr (S. KARASU)
Egemen BELGE https://orcid.org/0000-0001-5852-1085
Seçkin KARASU https://orcid.org/0000-0001-5277-5252

Gönderi: 18 Ekim 2024 **Received:** October 18, 2024
Kabul: 28 Kasım 2024 **Accepted:** November 28, 2024
Yayınlanma: 15 Ocak 2025 **Published:** January 15, 2025

Cite as: Belge E, Karasu S. 2025. Investigation of the effect on model parameters in SegFormer method for tooth segmentation. BSJ Eng Sci, 8(1): 132-141.

1. Giriş

Yapay zekanın ortaya çıkışıyla birlikte son on yıl içerisinde önemli teknolojik gelişmeler meydana gelmektedir. Her sektörde olduğu gibi yapay zekanın diş bilimi alanında da kullanımı artmaktadır. Yapay zekâ, diş ve tıp biliminde hastaların tıbbi verilerinin toplanmasında, makine öğrenmesi kullanılarak diş çürüklerinin tahmininde ve hastaların verilerini işleyerek hastalık tanısının belirlenmesi gibi farklı uygulama alanlarında tercih edilmektedir (Lee vd., 2022). Günümüzde yapay zekâ yöntemleri kullanılarak diş segmentasyonu gerçekleştirilmektedir. Diş segmentasyonu bilgisayar destekli işlemlerde ve klinik tanılamada önemli bir rol oynamaktadır. Diş bölgesinin ve diğer dokuların arasındaki özelliklerin ayrımı segmentasyon tekniğiyle mümkün olmaktadır. Uygun tanının belirlenmesi ve gerekli cerrahi işlemlerin anında yapılabilmesi aşamalarında dişin doğru bir şekilde segmentasyonu gereklidir. Ortodonti alanında diş hekimleri, hastaların diş hareketi ve diş kökü emilimi hakkında bilgilere ihtiyaç duymaktadır. Elde edilen bu bilgiler kullanılarak ortodonti tedavi aşamaları önemli

ölçüde kısaltılmaktadır. Dişlerin panoramik X-ışını görüntülerinden segmentasyon işlemi gerçekleştirilmektedir. Bunun yanı sıra, diş segmentasyonunun doğru yapılması, hastaların diş yaşının tahmin edilmesi, kişinin adli olarak biyometrik özelliklerinin tanımlanması ve gizli diş yapılarının ortaya çıkarılmasında kullanılabilmektedir (Zhao vd., 2020). Tüm bu sebepler birlikte değerlendirildiğinde diş segmentasyonu hem araştırma hem de klinik uygulamalarda kritik rol oynamaktadır.

Bununla birlikte diş segmentasyonu diş hekimleri tarafından manuel ya da yarı otomatik etkileşimli yöntemlerle gerçekleştirilmektedir (Kang vd., 2015; Wang vd., 2016; Li ve Wang, 2016). Bu durum diş hekimlerinin bilgisine doğrudan bağlı olup, oldukça zaman alıcı bir işlemdir. Düşük kaliteli diş görüntülerinden dolayı diş hekimleri diş bölgesini belirleme işleminde zorlanmaktadır. Görüntü kalitesinin düşük olması, diş bölgesinin belirleme işlemini olumsuz etkilemektedir. Tüm sebeplerden dolayı diş segmentasyonu için daha iyi bir görüntüleme ve analiz yöntemine ihtiyaç duyulmaktadır.

Son yıllarda diş segmentasyonunun zorluklarına karşı bilim insanları yenilikçi çözümler üretmektedir. Geliştirilen segmentasyon metotları geleneksel ve derin öğrenme tabanlı olarak iki ana alanda açıklanmaktadır (Zhao vd., 2020). Geleneksel teknikler çoğu zaman görüntünün gradyanları ve bölge tabanlı benzerlik ölçümü gibi ön bilgilere ve görüntü özelliklerine dayanmaktadır (Gao vd., 2013; Indraswari vd., 2015; Gao vd., 2018). Bazı panoramik X-ışını görüntülerinde dişlerin segmentasyonu işleminde lokal adaptif eşik yöntemi kullanılmaktadır (Indraswari vd., 2015). Bu yöntem görüntünün istatistiksel özelliklerini çıkarmaktadır. Başka bir çalışmada ise Otsu eşiği ve Mahalanobis mesafesinin birlikte değerlendirildiği şablon eşleştirme yöntemi kullanılmaktadır (Poonsri vd., 2016). Eşikleme stratejisine dayanan bu modelin diş köklerini tanımlaması oldukça zordur. Piksel yoğunluk seviyesindeki süreksizliğe göre görüntüyü bölgelere ayırarak segmentasyon işlemi gerçekleştirilmektedir (Modi ve Desai, 2011). Matematiksel morfolojiyi kullanan Watershed dönüşümü gri tonda verilen görüntünün segmentasyonunda kullanılmaktadır (Li vd., 2012). Diş görüntüsünün segmentasyonunda morfolojik metot kullanılmaktadır. Çalışmada metodun yüksek doğruluklu ve düşük zaman karmaşıklığı vurgulanmaktadır (Said vd., 2006). Aktif kontur metodu ve diş segmentasyonu için şekil analizi birleştirilmektedir (Lira vd., 2009). Şekil modelleri dişin algılanmasında kullanılmaktadır (Lira vd., 2009). Geleneksel görüntü segmentasyonu teknikleri, önceden belirlenmiş bilgiler ve görüntü özelliklerinin eşleştirilmesine doğrudan bağlıdır (Zhao vd., 2020). Özel uzmanlık bilgisi gerektiren geleneksel segmentasyon tekniğinin uygulama alanını önemli ölçüde kısıtlamaktadır. Derin öğrenme tabanlı diş segmentasyonu uygulamaları son yıllarda önemli ölçüde artmaktadır. Son yıllarda küresel ve yerel özelliklerin kodlanmasının özellik gösterimi ve görsel özellik öğrenimini güçlendirdiği vurgulanmaktadır (Wu vd., 2019; Zhu ve Yang, 2020). Görüntü içerisindeki arka planı çıkarma ve kendi kendine öğrenme alanında çalışmalar yer almaktadır (Yong vd., 2017; Meng vd., 2017). Panoramik X ışını görüntüsünden diş segmentasyonu probleminin çözümü için birkaç yaklaşım geliştirilmektedir (Yang vd., 2018; Chen vd., 2019; Wirtz vd., 2018). Yang vd. (2018) 196 vakanın yer aldığı veri setinden diş görüntü analizi sunulmaktadır. Çalışmada, diş hastalıklarının teşhisi ve sınıflandırılması için Convolutional Neural Networks (CNN) kullanılmaktadır. Chen vd. (2019) diş alanının segmentasyonu için Mask R-CNN yapısında (He vd., 2017) derin öğrenme ağı geliştirmektedir. Geliştirdikleri bu yöntem ile örnek segmentasyon yöntemlerinin diş segmentasyonunda kullanılabileceğini gösterilmektedir. Yağılan bir çalışmada yeni bir ölçüm yaklaşımının önerildiği ve diş segmentasyonu için önerilen modelin performansının değerlendirilebilmesi için kompakt bir fonksiyon önerildiği belirtilmiştir (Kato ve Hotta, 2024). Dice kaybı yeniden ele alınarak kosinüs benzerliği yerine t-vMF benzerliğiyle daha kompakt bir kayıp fonksiyonu olan t-vMF Dice kaybı önerilmiştir Ayrıca, sınıf zorluğuna göre adaptif eğitim sağlayan ve parametre □'yı otomatik belirleyen "Adaptive t-vMF Dice loss" algoritması geliştirilmiştir. CVC-ClinicDB, Kvasir-SEG, Automated Cardiac Diagnosis Challenge ve Synapse veri setleri üzerinde yapılan deneylerde, önerilen yöntemle Dice skorunun orijinal Dice kaybına göre iyileştirildiği gösterilmiştir. Alveolar yarıklı hastalarda diş şekil varyasyonu, interdental benzerlik ve bitişik dişlerin örtüşmesi gibi zorlukları aşmak için yeni bir "diş tanımlayıcı" (tooth descriptor) göstergesi önerilmiştir (Gong vd., 2024). İki aşamalı bir ağ kullanarak önce diş tanımlayıcılarını ve merkez noktalarını tahmin eder, ardından bu bilgilerle diş küpleri oluşturmakta ve segmentasyon ağı bu küplerden tam diş yapısını çıkartmaktadır. Yapılan deneylerde, önerilen yöntem %94,4 Dice doğruluğu ile mevcut diş segmentasyon yöntemlerinden daha üstün performans gösterilmiştir. Panoramik radyografilerde dişlerin otomatik segmentasyonu için derin öğrenmeye dayalı çok ölçekli mekânsal havuzlama (ms-SP) tekniği test edilmiştir (Nagaraju ve Sudha, 2024). Dişler, bir oral radyolog tarafından etiketlenmiş ve aşırı öğrenmeyi önlemek için veri artırma stratejisi kullanılmıştır. Sonuçlar, ortalama IoU %87, F1 skoru %98,9 ve doğruluk %98,5 olarak elde edilmiştir. Görsel analiz, elde edilen sonuçların gerçek verilere benzer olduğunu göstermiştir. Önerilen teknik panoramik diş fotoğraflarında segmentasyonu otomatikleştirmenin yanı sıra adli kimlik tespiti ve tanı otomasyonu gibi alanlarda da faydalı olabileceği bildirilmiştir (Nagaraju ve Sudha, 2024). Panoramik radyografilarda süt, karma ve kalıcı dişlerin otomatik olarak sınıflara ayrılması ve numaralandırılması için derin öğrenme tabanlı bir yöntem geliştirilerek model doğrulaması yapılmıştır (Xu vd., 2023). Çalışmada kullanılan derin öğrenme ağı, U-Net tabanlı ilgilenilen bölgenin çıkarılması ve Hibrit Görev Kaskatı tabanlı bir

diş segmentasyonu ve numaralandırma modelinden oluşmaktadır. Derin öğrenme ağı, 4232 diş görüntü üzerinde eğitilmiş olup, 605 diş görüntüsü doğrulamada ve 1209 görüntü ise test aşamasında kullanılmıştır. Panoramik radyografi bölütlemesini gerçekleştirmek için atlama bağlantılarının yer aldığı transformatör tabanlı Ushaped kodlayıcı-kod çözücü mimarisi olan SWinUnet tanıtılmaktadır (Sheng vd., 2023). SWin-Unet'in diş segmentasyon performansını analiz edebilmek için, çalışmada PLAGH-BH veri seti tanıtılmıştır. Bu veri seti üzerinde çalışmada önerilen derin öğrenme ağının model doğruluğu %88,52 olarak elde edilmektedir. Önerilen diş bölütleme yöntemin doğruluğu U-Net, Link-Net ve FPN ağlarıyla kıyaslanmaktadır. Performans sonuçlarına göre maksimum doğruluğun önerilen SWinUnet ağında elde edildiği vurgulanmaktadır. Diş tanıma modülü tasarlamak için R-CNN ağı kullanılmakta ve VGG-16 konvolüsyon mimarisine dayanan diş numaralandırma sistemi çalışmada geliştirilmektedir (Alam vd., 2023). Çalışmada, panoramik diş görüntüleri içeren veri seti eğitim ve doğrulama olarak bölümlere ayrılarak önerilen derin öğrenme ağı eğitilmiştir. Bu çalışmada önerilen ağın model doğruluğu %89,8 olarak elde edilmiştir. Üç boyutlu olarak diş bölütlenme ve sınıflandırma amacıyla evrişimsel sinir ağlarına dayanan yeni bir yaklaşım önerilmiştir (Tian vd., 2019). Burada geliştirilen evrişimsel sinir ağının diş bölütleme doğruluğu %89.81 olarak elde edilmiştir.

Bu çalışmada diş segmentasyonu için derin öğrenme tabanlı SegFormer yöntemi sunulmaktadır. SegFormer yönteminin içerisindeki hiyerarşik transformatör kodlayıcısının model büyüklüğü değiştirilerek diş segmentasyonunun başarımı incelenmektedir. Burada, 12 diş stajyeri tarafından toplanan 15318 poligonlu 598 X-ray diş görüntüleri üzerinde derin öğrenme ağı eğitilmiştir. Çalışmada kullanılan veri seti %70 eğitim, %15 doğrulama ve %15 test olarak ayrılmaktadır. SegFormer segmentasyon tekniğinin içerisinde yer alan MiT-BO ile MiT-B5 aralığındaki kodlayıcı parametrelerinin model büyüklükleri değiştirilerek derin öğrenme ağının performansı incelenmektedir.

Bu çalışmanın geri kalan kısmı şu şekilde organize edilmektedir. Çalışmada kullanılan veri seti, performans değerlendirme kriteri ve SegFormer segmentasyon modeli Bölüm 2'de sunulmaktadır. Çalışmada kullanılan SegFormer derin öğrenme ağının performansı Bölüm 3'de açıklanmaktadır. Derin öğrenme ağının performans sonuçları Bölüm 4'de tartışılmaktadır.

2. Materyal ve Yöntem

2.1. Veri Seti

Segmentasyon işlemi, Kongo Demokratik Cumhuriyeti'ndeki 12 Humans in Loop stajyeri tarafından, Lopez ve arkadaşları tarafından yayınlanan Panoramik radyografi veri tabanını kullanarak eğitimlerinin bir parçası olarak manuel olarak gerçekleştirilmektedir (Human In The Loop, 2023). Çalışmada kullanılan veri seti, her dişin farklı bir sınıfa göre bölütlendiği toplam 15318 poligona sahip 598 görüntüden oluşmaktadır. Veri setinin içerisinde 32 farklı diş sınıfı yer almaktadır. Dişlerin numaralandırılması üst sol dişlerden başlar ve saat yönünde alt dişlere doğru devam etmektedir. Her dişin pozisyonuna göre benzersiz bir numarası bulunmaktadır.

2.2 SegFormer Segmentasyon Modeli

SegFormer görüntü segmentasyonu amacıyla tasarlanmış bir derin öğrenme modelidir. Anlamsal segmentasyon işleminde yüksek performans elde etmek için hem dönüşüm bloklarının (Şekil1) hem de evrişimsel sinir ağlarının (CNN) güçlü yanlarını birleştirmektedir (Xie vd., 2021). SegFormer derin öğrenme modeli iki farklı modülün bir arada kullanıldığı bir yapıdan oluşmaktadır. Burada kullanılan dönüşüm kodlayıcı blokları yüksek çözünürlüklü özelliklerin çıkarılmasında kullanılmaktadır. Bunun yanı sıra kod çözücü kısmında kullanılan derin öğrenme ağları, anlamsal segmentasyon maskesini üretmek için çok seviyeli özellikleri birleştirmektedir. SegFormer modelinin genel şeması Şekil 2'de sunulmaktadır. Burada kodlayıcı ve kod çözücü katmanlarının sıralı yapısı yer almaktadır. Kodlayıcı bloğu 4 farklı birimden oluşmaktadır. Kod çözücü bloğunda ise, iki farklı derin öğrenme ağı bulunmaktadır. SegFormer modelinde verilen bir $H \times W \times 3$ boyutundaki görüntü ilk olarak 4×4 boyutundaki parçalara bölünmektedir. Burada H görüntünün yüksekliği, W görüntünün genişliğini ifade etmektedir. İkinci olarak orijinal görüntünün $\{\frac{1}{4}, \frac{1}{8}, \frac{1}{16}, \frac{1}{32}\}$ çok seviyeli çözünürlüklerini çıkarmak için hiyerarşik dönüşüm bloğu kullanılmaktadır. $\frac{H}{4} \times \frac{W}{4} \times N_{cls}$ çözünürlüğün de segmentasyon maskesini tahmin etmek için MPL kod çözücüsü kullanılmaktadır. Burada N_{cls} kategori sayısını ifade etmektedir. C_i ise özellik haritasını elde etmek için kullanılan vektördür. Hiyerarşik dönüşüm kodlayıcılarının sadece boyutları değiştirilerek MiT-BO ile MiT-B5 arasındaki yapılar segmentasyon işlemlerinde kullanılmaktadır. Tablo 1'de bu model yapılarının parametre büyüklükleri gösterilmektedir. Şekil 2(a)' da görüldüğü gibi SegFormer dönüşüm bloğu; verimli öz dikkat, karma ileri beslemeli sinir ağı (FFN) ve örtüşen yama birleştirme olmak üzere üç farklı yapıdan oluşmaktadır. Verimli öz dikkat bloğunda, giriş özelliklerindeki dikkat puanları hesaplanarak, modelin pikseller arasındaki ilişkileri yakalaması sağlanmaktadır. Karma FFN bloğu, doğrusal olmayan bir aktivasyon fonksiyonuna sahip iki doğrusal katmandan oluşmaktadır. Örtüşen yama birleştirmeleri, görüntü üzerindeki üst üste binen bölgelerin özelliklerini birleştirmek için kullanılan bir katmandır. Bu katman, modelin karmaşık bölgeleri anlama yeteneğini geliştirmektedir. Şekil 2(b)' de MLP katmanın içyapısı gösterilmektedir. Burada kanal boyutunu birleştirebilmek amacıyla kodlayıcıdan gelen çok seviyeli özellikler MLP katmanından geçmektedir. Daha sonrasında bu özellikler $\frac{1}{4}$ kadar yukarı örneklenmekte ve birleştirilmektedir.

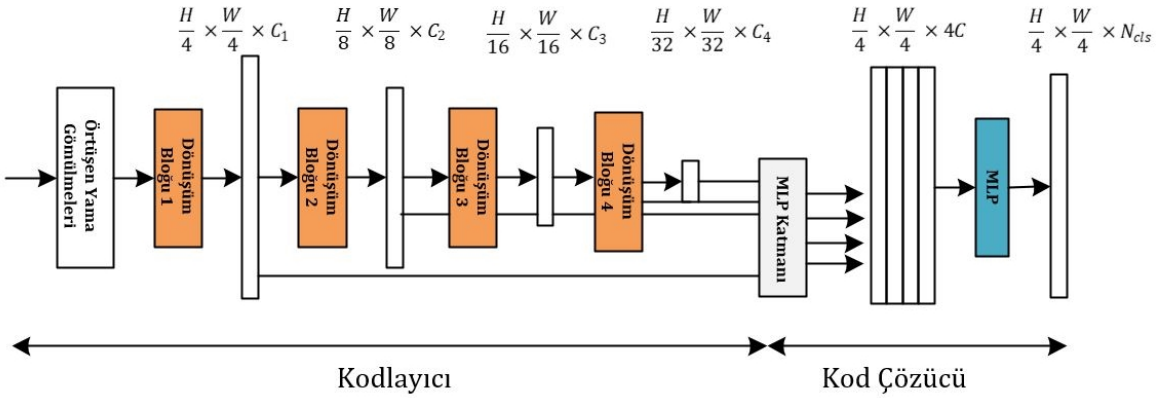

Şekil 1. SegFormer modelinin blok şema gösterimi.

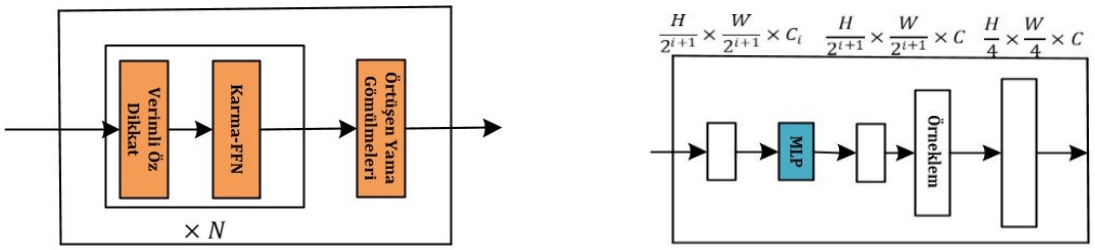

(a) (b)

Şekil 2. Dönüşüm (a) ve MLP katmanının (b) içyapısı.

Çalışmada SegFormer modelinin içerisinde yer alan AdamW optimizasyonuyla eğitilmiş olan hiper parametreler kullanılmaktadır. Bu hiper parametreler, DE20K ve Cityscapes üzerinde 160K ve COCO-Stuff üzerinde ise 80K iterasyon boyunca eğitilerek belirlenmektedir (Xie vd., 2021).

Tablo 1. SegFormer modelinin Enkoder ve Kod çözücü parametreleri

Enkoder Model Boyutu	Enkoder Parametresi	Dekoder Parametresi
MiT-BO	3,4	0,4
MiT-B1	13,1	0,6
MiT-B2	24,2	3,3
MiT-B3	44	3,3
MiT-B4	60,8	3,3
MiT-B5	81,4	3,3

Bu çalışmada SegFormer modeli içerisinde yer alan MiT-BO ile MiT-B5 yapılarının diş bölütleme başarımına olan etkisi incelenmektedir. Aynı zamanda model büyüklüğündeki değişimine bağlı performans kıyaslaması da çalışmada yer almaktadır.

2.3 Dice Değerlendirme Kriteri

Dice, görüntü segmentasyonunun model performansını değerlendirmek amacıyla geliştirilen bir katsayısıdır. Bu katsayı eşitlik 1'de verildiği şekilde tanımlanmaktadır (Yan, 2018).

$$Dice = \frac{2|A \cap B|}{|A| + |B|} \quad (1)$$

Burada A ve B sırasıyla tahmin edilen diş segmentasyonu bölgesini, gerçek diş bölgesini ifade etmektedir. Dice katsayısının maksimum değeri 1'e eşittir. Bu durum segmentasyon işleminin doğruluk oranının en yüksek olduğu belirtmektedir. Segmentasyon başarımının en düşük olduğunu durumda ise Dice değeri 0 değerini almaktadır. Çalışmada kullanılan Dice benzerlik katsayısı SegFormer ağının eğitim aşamasında diş bölütlemesinin başarımını ölçen bir değerlendirme kriteridir. Modelin eğitimi sırasında her bir iterasyonda Dice benzerlik katsayısı hesaplanarak diş segmentasyon başarımı elde edilmekte ve bu değerlendirme kriterine göre SegFormer ağı her iterasyonda güncellenmektedir.

3. Bulgular

Şekil 3'de SegFormer modelinin B0-B5 versiyonları için eğitim adım sayısına karşılık hata değerinin değişimi gösterilmektedir. Yatay eksen, eğitim adım sayısını, dikey eksen ise hata değerini temsil etmektedir. Grafikte her bir model (B0-B5) farklı renkte gösterilmiştir. Grafikte ilk aşamada hata değerinin hızla düştüğü, ardından belirli bir adım sayısından sonra stabil hale geldiği gözlemlenmiştir. Eğitim aşamasının ilk adımlarında özellikle 100-200 eğitim adımından sonra hata değerlerinde yaklaşık %80 üzerinde bir azalma yaşanmaktadır. Bu noktadan sonra hatalar kısmen düşük seviyelerde, sabit bir şekilde ilerlemektedir. Farklı modeller arasında (B0'dan B5'e) belirgin bir performans farkı görünmemekle birlikte, bazı modellerin daha hızlı yakınsadığı, ancak genel hata seviyelerinin birbirine yakın olduğu söylenebilir. Bu durum, SegFormer modelinin tüm versiyonlarının benzer eğitim performansı gösterdiğini ve eğitim sürecinde hataların hızla azaldığını, ancak belirli bir noktadan sonra daha az iyileşme olduğunu ortaya koymaktadır.

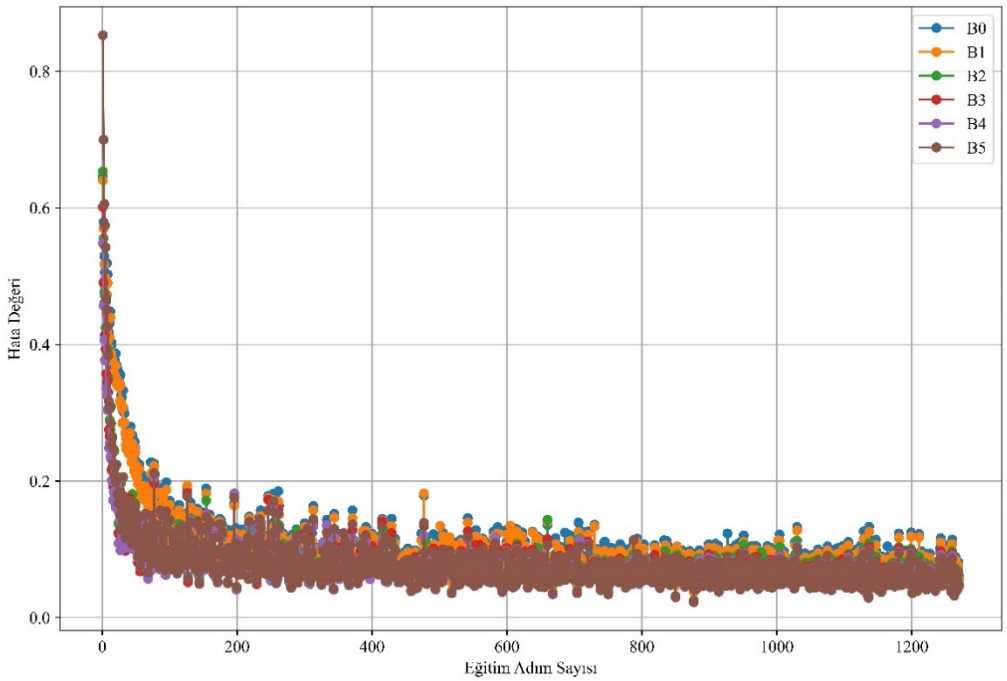

Şekil 3. SegFormer B0-B5 için eğitim adım sayısına karşılık hata değerinin değişimi.

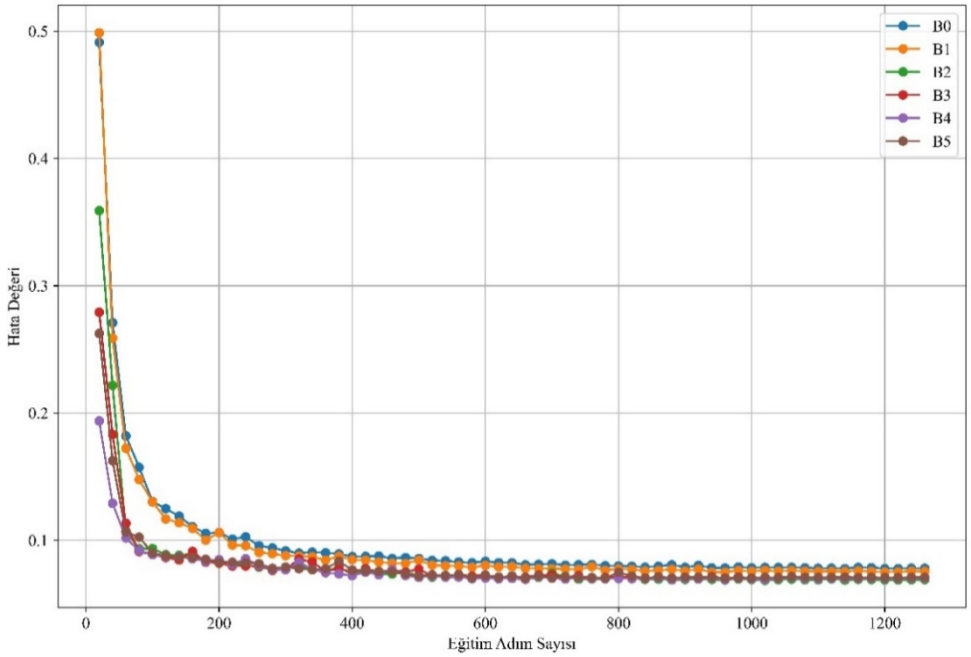

Şekil 4. SegFormer B0-B5 için doğrulama adım sayısına karşılık hata değerinin değişimi.

Şekil 4'te, Grafikte, B0, B1, B2, B3, B4 ve B5 olmak üzere altı farklı model mimarisinin eğitim adımları boyunca doğrulama hatası (validation loss) değerlerindeki değişim gözlemlenmektedir. Grafikte, x ekseni eğitim adımlarını, y ekseni ise hata değerini (loss) temsil etmektedir. Grafik incelendiğinde, tüm modellerin başlangıç aşamasında özellikle 0-100 adımları arasında hızlı bir hata azalması yaşadığı görülmektedir. Bu, modelin veriden temel özellikleri öğrenmeye başladığı ve eğitim sürecine hızla adapte olduğu anlamına geldiği belirtilebilir. Bu aşamada hata değeri yaklaşık olarak 0,5 seviyesinden 0,1 seviyesine kadar hızlı bir düşüş göstermektedir. Eğitim süreci ilerledikçe, özellikle 100. adımdan sonra hata azalmasında bir yavaşlama meydana gelmektedir. Tüm modeller bu noktada daha detaylı örüntüleri öğrenmeye başlamakta ve bu da daha yavaş bir hata azalması ile sonuçlanmaktadır. Yaklaşık 400. adıma kadar, tüm modellerin hata değeri 0,05 ile 0,1 aralığına düşmekte ve bu noktada modellerin öğrenme sürecinde bir dengeye ulaşmaya başladıkları gözlemlenmektedir. 400. adımdan itibaren, modellerin hata değerlerinde önemli bir değişiklik olmadığı, hatanın belirli bir seviyeye oturduğu ve artık kayda değer bir öğrenmenin gerçekleşmediği görülmektedir. Bu durum, modellerin veriden öğrenebileceği özellikleri büyük ölçüde öğrendiğini ve daha fazla eğitimle yalnızca

minimal iyileşmeler elde edilebileceğini göstermektedir.
B0 modeli, başlangıç aşamasında (ilk 100 adım) diğer modellere göre daha hızlı bir düşüş sergilemekte ve erken aşamada daha düşük hata değerlerine Şekil 3'teki grafik incelendiğinde ulaşılmaktadır. Bu, B0 modelinin başlangıçta daha hızlı öğrenme gösterdiğini düşündürmektedir. Ancak eğitim sürecinin ilerleyen aşamalarında (100 adımdan sonra) tüm modellerin performanslarının birbirine yaklaştığı görülmektedir. B1, B2, B3, B4 ve B5 modelleri arasında hata değerleri açısından çok az fark vardır ve genellikle benzer bir hata seviyesinde stabil hale gelmektedirler. Son aşamada B5 modeli, diğer modellere kıyasla biraz daha düşük hata değeriyle (yaklaşık 0,05) en iyi performansı sergilediği söylenebilir. Ancak bu fark oldukça azdır.
Genel olarak tüm modeller başlangıçta hızla öğrenip hatalarını azaltmakta ve yaklaşık 400. adımdan sonra stabilize olmaktadır. Farklı mimariler (B0-B5) arasında erken aşamalarda bazı farklılıklar görülse de özellikle ilerleyen adımlarda bu farklar oldukça azalmaktadır. B5 modeli, diğerlerine göre biraz daha iyi sonuç verse de tüm modellerin genel performanslarının birbirine oldukça yakın olduğu söylenebilir.
Şekil 5'te, çeşitli modellerin eğitim süreçlerindeki segmentasyon başarımları (y-ekseni) ve eğitim adım sayıları (x-ekseni) karşılaştırılmaktadır. Eğitim adımları arttıkça tüm modellerin segmentasyon başarımları önemli ölçüde artmakta ve belirli bir noktadan sonra sabitlenmektedir. İlk 100 adımda, başarımlar hızla artarak yaklaşık %90 seviyesine ulaşmakta, ardından artış daha yavaş bir tempoda devam etmektedir. B0, B1, B2, B3 ve B5 modelleri benzer bir başarı eğrisi izlerken, B4 modeli diğerlerinden ayrışmakta ve daha dalgalı bir performans sergilemektedir. Bu segmentasyon modelinin diğerlerine göre ayrışmasının sebebi veri çeşitliliğinin eksikliğinden kaynaklandığı düşünülmektedir. Bütün modeller, yaklaşık 300 adım sonrasında segmentasyon başarımlarını büyük ölçüde sabitlemekte ve %90 ile %95 bandında stabil bir başarı oranına ulaşmaktadır. Özetle, çoğu model belirli bir eğitim sürecinden sonra yüksek segmentasyon başarımına ulaşırken, B4 modelinin performansı diğerlerine kıyasla daha düşük kalmaktadır.

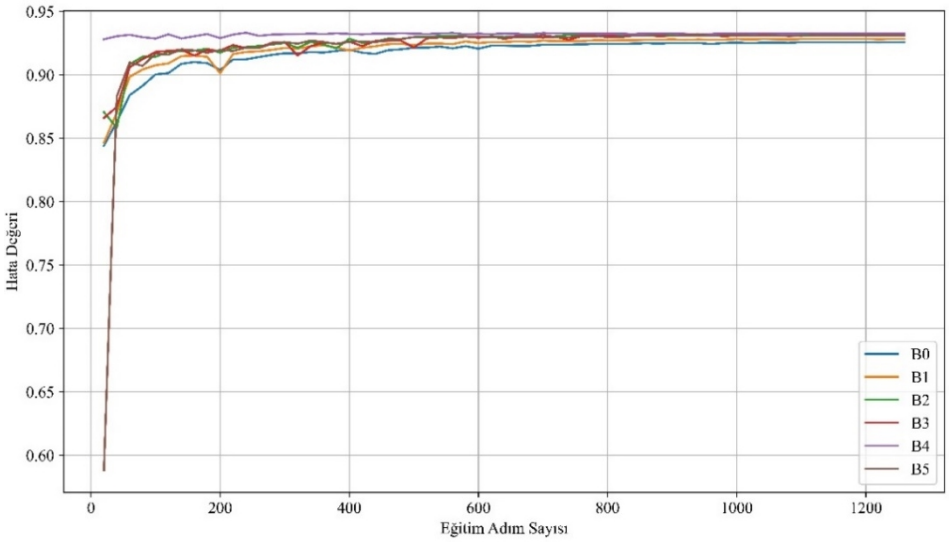

Şekil 5. SegFormer B0-B5 için eğitim verisine karşılık segmentasyon doğruluk değeri değişimi.

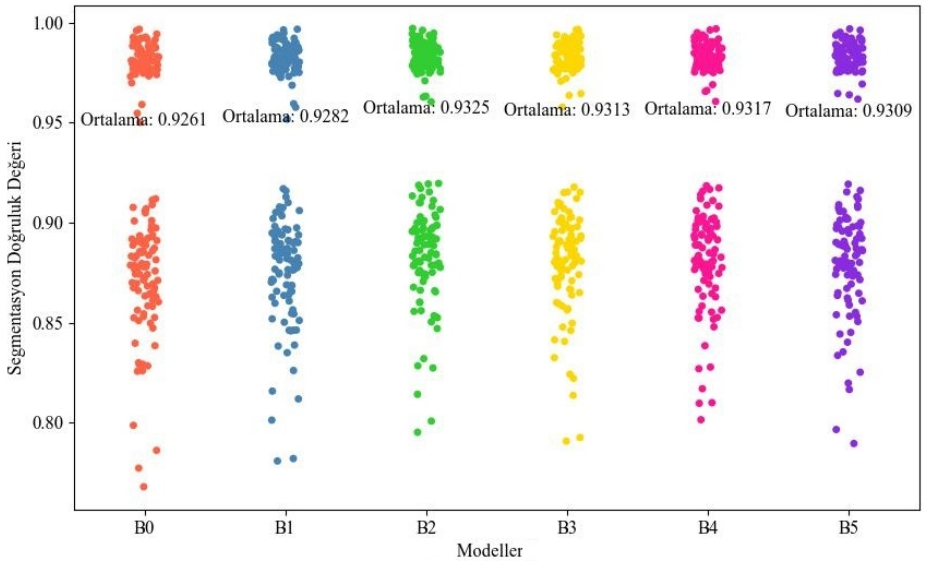

Şekil 6. SegFormer B0-B5 için test verisine karşılık segmentasyon doğruluk değeri değişimi.

Şekil 6'da modellerin test verisi için genel performanslarının karşılaştırılması verilmiştir. B0 modelinin ortalama doğruluk değeri %92.61 olarak belirlenmiştir. Bu, diğer modellere kıyasla en düşük doğruluk oranını temsil etmektedir. B0 modelinin doğruluk dağılımında, doğruluk değerlerinin genel olarak daha düşük bir aralıkta seyrettiği ve birkaç düşük performanslı noktanın olduğu gözlemlenmektedir. B1 modeli, ortalama doğruluk açısından B0'dan daha iyi bir performans sergileyerek %92,82 ortalama doğruluk değeri elde etmiştir. B1 modelindeki dağılım, daha dar bir aralık göstermekte ve bu durum daha tutarlı bir performansı işaret etmektedir. B2 modeli ise ortalama %93,25 doğruluk değeriyle tüm modeller arasında en yüksek ortalama doğruluğa sahiptir. Doğruluk dağılımı da oldukça yoğun ve sıkı bir şekilde yüksek değerlerde toplanmıştır; bu da modelin yüksek bir performansa sahip olduğunu göstermektedir. B3, B4 ve B5 modellerinin ortalama doğruluk değerleri sırasıyla %93,13, %93,17 ve %93,09'dur. Bu üç modelin doğruluk sonuçları birbirine oldukça yakındır ve aralarındaki farklar çok azdır. Grafik üzerinde, B2 ile B5 modelleri arasındaki performans farkı oldukça azdır ve bu modeller genel olarak yüksek doğruluk oranlarına sahiptir.

B0 ve B1 modellerinin doğruluk dağılımları, diğer modellere göre daha geniş bir aralığa yayılmıştır. Özellikle B0 modeli, doğruluk açısından bazı uç (outlier) noktalara sahiptir; yani bazı denemelerde çok düşük doğruluk değerleri elde edilmiştir. Bu durum, B0 modelinin bazı veri örneklerinde zayıf performans gösterdiğini işaret etmektedir. Diğer taraftan, B2, B3, B4 ve B5 modellerinin doğruluk dağılımı daha yoğun ve belirli bir aralığa sıkışmış durumdadır. Bu ise bu modellerin daha tutarlı bir performans gösterdiğini ve doğruluk değerlerinin daha homojen dağıldığını göstermektedir. Özellikle B2 modeli hem yüksek ortalama doğruluk değeri hem de dar bir dağılım ile diğer modellerden daha başarılı görünmektedir.

Farklı modeller arasındaki doğruluk değerlerinde büyük sapmalar olmamakla birlikte, küçük farklar gözlemlenmektedir. B2 modeli, en yüksek ortalama doğrulukla diğer modellerden biraz daha önde görünmektedir. Ancak B3, B4 ve B5 modellerinin ortalamaları da B2 modeline çok yakındır. Bu modeller, neredeyse aynı doğruluk seviyelerinde performans sergilemektedir. B0 modeli ise doğruluk açısından en düşük performansı göstermekte olup, dağılımın geniş olması, bu modelin daha değişken bir performansa sahip olduğunu düşündürmektedir.

Şekil 7'de, beş farklı durum için X-ray giriş görüntüsü, referans (ground truth) görüntü ve model segmentasyon görüntüsü içeren üç farklı görüntü verilmiştir. Burada X-ray giriş görüntüsü modelin segmentasyon işlemi için temel aldığı ham veriyi temsil etmektedir. İkinci görüntü, ground truth yani referans görüntü olup, X-ray verisinde beklenen doğru segmentasyonu veya bölütlemeyi göstermektedir. Bu, modelin ne kadar doğru sonuçlar ürettiğini değerlendirmek için kullanılmaktadır. Son olarak, model segmentasyon görüntüsü, modelin giriş verisi üzerinden gerçekleştirdiği tahmini sonuçları göstermektedir. Bu üç görüntü yan yana incelendiğinde, modelin segmentasyon doğruluğu referans görüntü ile karşılaştırılarak başarı seviyesi değerlendirilebilir. Bu tür bir görsel analiz, modelin hatalarını ve iyileştirme alanlarını tespit etmek açısından önemli olmaktadır.

4. Tartışma ve Sonuç

Çalışmada SegFormer modelinin farklı versiyonlarının (B0-B5) eğitim sürecinde benzer performans sergilediği, başlangıçta hızlı bir öğrenme ve hata azaltma sağladıkları, ancak belirli bir adım sayısından sonra bu iyileşmenin yavaşladığı ve hataların stabilize olduğu görülmektedir. B2 modeli, doğruluk açısından diğer modellerden hafif bir üstünlük gösterdiği bulunmuştur. Modellerin segmentasyon başarımları ve doğruluk sonuçları, eğitim adımlarının artmasıyla büyük ölçüde sabitlenmiş ve %90 ile %95 arasında yüksek bir performansa ulaşmıştır. Ancak, B0 modeli diğer modellere kıyasla daha düşük doğruluk ve daha geniş bir dağılım sergileyerek daha değişken bir performans göstermiştir. Özellikle B2 modeli hem doğruluk hem de tutarlılık açısından en başarılı model olarak öne çıkmıştır. Sonuçlar, SegFormer modelinin çeşitli versiyonlarının diş segmentasyonu gibi karmaşık görevlerde oldukça etkili olduğunu göstermektedir. Başlangıç aşamasında hızlı öğrenme yetenekleri olsa da modellerin eğitim sürecinin ileri aşamalarında küçük iyileştirmeler dışında daha fazla gelişim sağlamadığı gözlemlenmiştir. Test veri setinde farklı modeller için segmentasyon performansları arasında bazı farklar olsa da genelde ortalamaların birbirine oldukça yakın olduğu görülmüştür. Ancak Şekil 5'te, her modelde ağırlıklı olarak %95 ve üzeri başarı sergileyen bir küme ile %80-92 aralığında bir başka küme olmak üzere iki farklı dağılım gözlemlenmektedir. Bu durum, test verisinde hangi model kullanılırsa kullanılsın belirli bir grubun sürekli daha iyi veya az da olsa daha düşük performans sergilediğini göstermektedir. Test veri setinde farklı çözünürlükte görüntülerin bulunması ya da belirli diş tiplerini segmente ederken modelin doğruluğunu olumsuz etkileyen yapısal farklılıklar olabileceğini düşündürmektedir. Ayrıca dişlerin şekli, büyüklüğü ve yapısı gibi faktörler ışığında, bazı diş tiplerinde modelin yüksek doğruluk gösterdiği, diğerlerinde ise ince detayların kaybolarak modelin performansının düştüğü düşünülmektedir. Sonuç olarak, bu bulgular, SegFormer modelinin dental segmentasyon gibi tıbbi görüntüleme alanlarında etkili bir şekilde kullanılabileceğini göstermektedir. Özellikle B2 versiyonu, en iyi genel performansı sunmaktadır. Ancak modellerin test verisinde iki farklı küme oluşturması, veri setindeki heterojenlikten kaynaklanabilecek olası sorunlara da işaret etmektedir.

Literatürdeki çalışmalarla kıyaslandığında, R-CNN ağı ve VGG-16 konvolüsyon mimarisine dayanan diş segmentasyonu modelinin model doğruluk oranı %89.8 olarak elde edilmiştir (Alam vd., 2023).

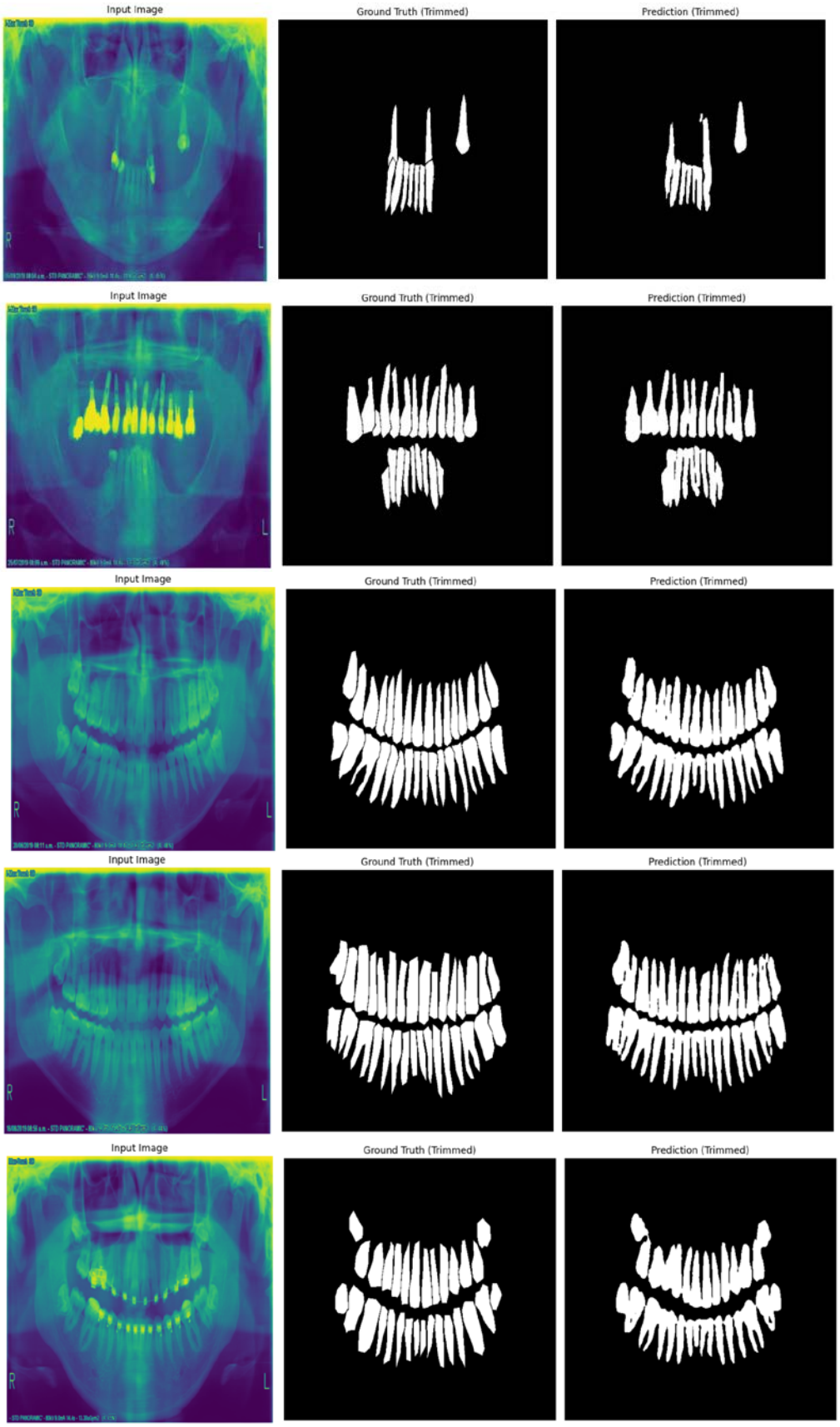

Şekil 7. X-ray giriş görüntüsü, referans (ground truth) görüntü ve model segmentasyon görüntüsü.

SWin-Unet'in diş segmentasyon performansını analiz edebilmek için, çalışmada PLAGH-BH veri seti için geliştirilen derin öğrenme ağının model doğruluğu %88.52 olarak elde edilmiştir (Sheng vd., 2023). Bir başka çalışmada ise U-Net tabanlı ilgilenilen bölgenin çıkarılması ve Hibrit Görev Kaskatı tabanlı bir diş segmentasyonu ve numaralandırma modeline dayanan diş segmentasyonu için model başarımı %92,00 olarak

elde edilmiştir (Xu vd., 2023). Bu çalışmada önerdiğimiz diş segmentasyonu için elde edilen modelin başarımı %93,25 olarak elde edilmiştir.

Gelecek çalışmalarda, SegFormer modelinin performansını daha da iyileştirmek amacıyla farklı veri setleri üzerinde detaylı incelemeler yapılacaktır. Özellikle farklı çözünürlüklerdeki dental görüntüler ve çeşitli diş tiplerine ait veriler kullanılarak modelin genelleme yeteneği test edilecektir. Diş sınıfı veya çürük gibi daha özel verilerin test ve doğrulama aşamalarında daha belirgin bir şekilde ele alınması, modelin doğruluğunu ve pratik uygulanabilirliğini artırabilir. Bu yöndeki katkılar, özellikle klinik uygulamalarda segmentasyonun daha ayrıntılı bir şekilde değerlendirilmesine olanak tanıyacaktır. Gelecekteki çalışmalarda bu tür detaylı analizlere yer verilmesi planlanmaktadır. Ayrıca, veri setindeki çeşitliliğin artırılması, modelin segmentasyon doğruluğunu nasıl etkilediğini değerlendirmek açısından önemli bir adım olacaktır. Hibrit yaklaşımlar ile modelin daha geniş bir yelpazede test edilmesi ve genelleme kabiliyetinin artırılması için çeşitli stratejiler (örneğin, veri artırma teknikleri, transfer öğrenme) planlanmaktadır.

Katkı Oranı Beyanı

Yazarların katkı yüzdesi aşağıda verilmiştir. Tüm yazarlar makaleyi incelemiş ve onaylamıştır.

	E.B.	S.K.
K	50	50
T	50	50
Y	50	50
VTI	50	50
VAY	50	50
KT	50	50
YZ	50	50
KI	50	50
GR	50	50
PY	50	50
FA	50	50

K= kavram, T= tasarım, Y= yönetim, VTI= veri toplama ve/veya işleme, VAY= veri analizi ve/veya yorumlama, KT= kaynak tarama, YZ= Yazım, KI= kritik inceleme, GR= gönderim ve revizyon, PY= proje yönetimi, FA= fon alımı.

Çatışma Beyanı

Yazarlar bu çalışmada hiçbir çıkar ilişkisi olmadığını beyan etmektedir.

Etik Onay Beyanı

Bu araştırmada hayvanlar ve insanlar üzerinde herhangi bir çalışma yapılmadığı için etik kurul onayı alınmamıştır.

Kaynaklar

Alam MK, Haque T, Akhte, F, Albagieh HN, Nabhan AB, Alsenani MA, Islam S. 2023. Teeth segmentation by optical radiographic images using VGG-16 deep learning convolution architecture with R-CNN network approach for biomedical sensing applications. Optic Quant Electron, 55(9): 808.

Chen H, Zhang K, Lyu P, Li H, Zhang L, Wu J, Lee CH. 2019. A deep learning approach to automatic teeth detection and numbering based on object detection in dental periapical films. Sci Rep, 9(1): 3840.

Gao C, Meng D, Yang Y, Wang Y, Zhou X, Hauptmann AG. 2013. Infrared patch-image model for small target detection in a single image. IEEE Transact Image Proces, 22(12): 4996-5009.

Gong Y, Zhang J, Cheng J, Yuan W, He L. 2024. Automatic tooth segmentation for patients with alveolar clefts guided by tooth descriptors. Biomed Signal Proces Cont, 90: 105821.

He K, Gkioxari G, Dollár P, Girshick R. 2017. Mask R-CNN. In Proc IEEE Int Conf Comput Vision, 2017: 2961-2969.

Humans In The Loop. 2023. Teeth Segmentation on dental X-ray images [Data set]. Kaggle.

Indraswari R, Arifin AZ, Navastara DA, Jawas N. 2015. Teeth segmentation on dental panoramic radiographs using decimation-free directional filter bank thresholding and multistage adaptive thresholding. International Conference on Information & Communication Technology and Systems (ICTS), September 16, Surabaya, Indonesia, pp: 49-54.

Kang HC, Choi C, Shin J, Lee J, Shin YG. 2015. Fast and accurate semiautomatic segmentation of individual teeth from dental CT images. Computat Math Meth Medic, 2015(1): 810796.

Kato S, Hotta K. 2024. Adaptive t-vMF dice loss: An effective expansion of dice loss for medical image segmentation. Comput Biol Medic, 168: 107695.

Lee SJ, Chung D, Asano A, Sasaki D, Maeno M, Ishida Y, Kobayashi T, Kuwajima Y, Silva JDD, Nagai S. 2022. Diagnosis of tooth prognosis using artificial intelligence. Diagnostics, 12(6): 1422.

Li H, Sun G, Sun H, Liu W. 2012. Watershed algorithm based on morphology for dental x-ray images segmentation. International Conference on Signal Processing, August 12-15, Hong Kong, China, pp: 877-880.

Li Z, Wang H. 2016. Interactive tooth separation from dental model using segmentation field. PloS One, 11(8): e0161159.

Lira PHM, Giraldi GA, Neves LA. 2009. An automatic morphometrics data extraction method in dental x-ray image. International Conference on Biodental Enginnering, June 26-27, Porto, Portugal, pp: 77-82.

Meng D, Zhao Q, Jiang L. 2017. A theoretical understanding of self-paced learning. Info Sci, 414: 319-328.

Modi CK, Desai NP. 2011. A simple and novel algorithm for automatic selection of ROI for dental radiograph segmentation. Canadian Conference on Electrical and Computer Engineering, May 08-11, Niagara Falls, Canada, pp: 000504-000507. https://doi.org/10.1109/CCECE.2011.6030501.

Nagaraju P, Sudha SV. 2024. Design of a novel panoptic segmentation using multi-scale pooling model for tooth segmentation. Soft Comput, 28(5): 4185-4196.

Poonsri A, Aimjirakul N, Charoenpong T, Sukjamsri C. 2016. Teeth segmentation from dental x-ray image by template matching. 9th Biomedical Engineering International Conference, December 7-9, Laung Prabang, Laos, pp: 1-4.

Said EH, Nassar DEM, Fahmy G, Ammar HH. 2006. Teeth segmentation in digitized dental X-ray films using mathematical morphology. IEEE Transact Info Forens Secur, 1(2): 178-189.

Sheng C, Wang L, Huang Z, Wang T, Guo Y, Hou W, Yan X. 2023. Transformer-based deep learning network for tooth segmentation on panoramic radiographs. J Syst Sci Compl, 36(1): 257-272.

Tian S, Dai N, Zhang B, Yuan F, Yu Q, Cheng X. 2019. Automatic classification and segmentation of teeth on 3D dental model

using hierarchical deep learning networks. IEEE Access, 7: 84817-84828.

Wang CW, Huang CT, Lee JH, Li CH, Chang SW, Siao MJ, Lai TM, Ibragimov B, Vrtovec T, Ronneberger O, Fischer P, Cootes TF, Lindner C. 2016. A benchmark for comparison of dental radiography analysis algorithms. Medic Image Analy, 31: 63-76.

Wirtz A, Mirashi SG, Wesarg S. 2018. Automatic teeth segmentation in panoramic X-ray images using a coupled shape model in combination with a neural network. In Medical Image Computing and Computer Assisted Intervention–MICCAI 2018: 21st International Conference, September 16-20, Granada, Spain, Part IV(11): 712-719.

Wu A, Zhu L, Han Y, Yang Y. 2019. Connective cognition network for directional visual commonsense reasoning. Adv Neural Info Proces Syst, 32.

Xie E, Wang W, Yu Z, Anandkumar A, Alvarez JM, Luo P. 2021. SegFormer: Simple and efficient design for semantic segmentation with transformers. Adv Neural Info Proces Syst, 34: 12077-12090.

Xu M, Wu Y, Xu Z, Ding P, Bai H, Deng, X. 2023. Robust automated teeth identification from dental radiographs using deep learning. J Dentistry, 136: 104607.

Yan M, Guo J, Tian W, Yi Z. 2018. Symmetric convolutional neural network for mandible segmentation. Know Based Syst, 159: 63-71.

Yang J, Xie Y, Liu L, Xia B, Cao Z, Guo C. 2018. Automated dental image analysis by deep learning on small dataset. 42nd Annual Computer Software and Applications Conference (COMPSAC), July 23-27, Tokyo, Japan, pp: 492-497.

Yong H, Meng D, Zuo W, Zhang L. 2017. Robust online matrix factorization for dynamic background subtraction. IEEE Transact Pattern Analy Machine Intel, 40(7): 1726-1740.

Zhao Y, Li P, Gao C, Liu Y, Chen Q, Yang F, Meng D. 2020. TSASNet: Tooth segmentation on dental panoramic X-ray images by Two-Stage Attention Segmentation Network. Know Based Syst, 206: 106338

Zhu L, Yang Y. 2020. Actbert: Learning global-local video-text representations. IEEE/CVF Conference on Computer Vision and Pattern Recognition, June 13-19, Seattle, US, pp: 8746-8755.

Black Sea Journal of Engineering and Science
doi: 10.34248/bsengineering.1566359

Open Access Journal
e-ISSN: 2619 – 8991

Araştırma Makalesi (Research Article)
Cilt 8 - Sayı 1: 142-148 / Ocak 2025
(Volume 8 - Issue 1: 142-148 / January 2025)

SAKARYA BÖLGESİNDE YETİŞTİRİLEN KESTANE KABAĞINDA SEL BASKINI STRESİ ŞARTLARINDA FİZYOLOJİK VE BİYOKİMYASAL DEĞİŞİMLER

Necibe KAYAK*[1], Ömer BEYHAN[1], Ecenur SARI[1]

[1]*Sakarya University of Applied Sciences, Faculty of Agriculture, Department of Horticulture, 54580, Sakarya, Türkiye*

Özet: İklim değişikliği kaynaklı sel (su) baskınları, bitki büyümesi ve gelişimi üzerinde önemli bir etkiye sahip olup verimi büyük ölçüde etkileyen abiyotik stres faktörlerindendir. Sel baskını stresinin olumsuz etkisinden korunmak için tolerant tür veya çeşitlerin kullanılması en önemli stratejilerden birisidir. Bu amaçla yapılan çalışmada, kestane kabağında oluşturulan on günlük sel baskını stresinin, Sakarya bölgesinde yoğun olarak yetiştiriciliği yapılan Arıcan 97 ve Balkız çeşitlerinin, agronomik, fizyolojik ve biyokimyasal değişimleri üzerine etkileri belirlenmeye çalışılmıştır. Tesadüf parselleri deneme deseni kullanılarak yürütülen çalışmada, tam sulama ve yapay sel baskını stres konularını içeren iki sulama uygulaması yapılmış; her uygulama, üç tekrarlı ve her tekrarda üç saksı olacak şekilde düzenlenmiştir. Çalışma sonucunda, sel baskını stresi kabak çeşitlerinin fide döneminde agromorfolojik özelliklerinde önemli kayıplara neden olmuştur. Kestane kabağında sel stresinde farklı hasat dönemlerinde elde edilen sonuçlar temel bileşenler analizine (PCA) tabi tutulmuştur. Bileşenler göz önüne alındığında ilk beş bileşen çalışmanın % 87,060'ını açıklamıştır. Dolayısıyla ilk beş bileşenin çalışmayı yüksek oranda açıkladığı görülmüştür. Sonuç olarak, özellikle Sakarya bölgesinde kabak yetiştiriciliği için sel baskını riski taşıyan ve suyun doğal akışının yavaş olduğu, akarsu ve nehir yataklarına yakın taban arazilerinin tercih edilmemesi büyük önem taşımaktadır. Bu tür arazilerde, verim ve kalite kayıplarını önlemek amacıyla tolerant çeşitlerin kullanılması önerilmektedir.

Anahtar kelimeler: Abiyotik stres, Antioksidant aktivite, kestane kabağı, PCA

Physiological and Biochemical Changes in Cucurbita maxima Grown in the Sakarya Region under Flooding Stress Conditions

Abstract: Floods caused by climate change are a significant abiotic stress factor that has a profound impact on plant growth and development, substantially affecting crop yield. One of the most important strategies today to mitigate the adverse effects of flood stress is the cultivation of tolerant species or varieties. In this study, the effects of artificially induced ten-day flood stress on the agronomic, physiological, and biochemical changes of commercially grown Arıcan 97 and Balkız pumpkin varieties were investigated. The study was conducted using a randomized complete block design, with two irrigation treatments: full irrigation and artificially induced flood stress. Each treatment was organized with three replicates, and each replicate included three pots. At the end of the stress period, all treatments were harvested on the same day, and agronomic, physiological, and biochemical measurements were conducted to determine the effects of flood stress on the pumpkin varieties. The results indicated that flood stress caused significant losses in the agronomic characteristics of the pumpkin varieties at the seedling stage. The results obtained from different harvest periods under flood stress in pumpkins were subjected to Principal Component Analysis (PCA). The first five components explained 87.060% of the variation in the study, showing that these components captured a high proportion of the variability. As a result, for pumpkin cultivation in the Sakarya region, it is crucial to avoid lowland areas where the natural flow of water is slow, and which are located near riverbeds, as they pose a high risk of flooding.

Keywords: Abiotic stress, Antioxidant activity, Pumpkin, Principal Component Analysis (PCA)

***Sorumlu yazar (Corresponding author):** Sakarya University of Applied Sciences, Faculty of Agriculture, Department of Horticulture, 54580, Sakarya, Türkiye
E mail: necibekayak@subu.edu.tr (N. KAYAK)
Necibe KAYAK https://orcid.org/0000-0001-7104-8544
Ömer BEYHAN https://orcid.org/0000-0001-6047-5727
Ecenur SARI https://orcid.org/0009-0003-6188-8349

Gönderi: 14 Ekim 2024 **Received:** October 14, 2024
Kabul: 29 Kasım 2024 **Accepted:** November 29, 2024
Yayınlanma: 15 Ocak 2025 **Published:** January 15, 2025
Cite as: Kayak N, Beyhan Ö, Sarı E. 2025. Physiological and biochemical changes in cucurbita maxima grown in the Sakarya region under flooding stress conditions. BSJ Eng Sci, 8(1):142-148.

1. Giriş

Sanayi devrimi ile birlikte karbondioksit (CO_2), metan gazı (CH_4) gibi sera gazlarının seviyesindeki artışlar, yağış düzeninin değişmesi küresel ısınmaya neden olan faktörler arasında yer almaktadır (Soltekin, 2019; Hao vd., 2010). Bu değişken çevresel koşullar tuzluluk, kuraklık, soğuk hava, sıcaklık (yüksek/düşük), ve sel stresi gibi olumsuz çevresel faktörlerin meydana gelmesine sebep olmuştur. Bu çevresel stres faktörleri bitkilerde ürün miktarını ve kalitesini azaltarak tarımsal verimliliği düşürmekte, tarımsal faaliyetler için kullanılan arazilerinin alanını daraltmakta ve doğal ekosistemin dengesini bozmaktadır. İklim değişiklikleri, su mevcudiyetinde bazı bölgelerde şiddetli kuraklığa neden

olurken, aşırı yağış olaylarından kaynaklanan taşkınlar diğer coğrafi alanları etkilemektedir (Bailey-Serres, 2012). Dünyada ki toplam arazi varlığının yaklaşık %13'ü ve tarım arazilerinin yaklaşık %10'u sel sorunu nedeniyle olumsuz etkilenmektedir (Cramer vd., 2011). Bitki türüne, toprak yapısına ve stresin boyutuna bağlı olarak sel baskınına maruz kalan farklı ürünlerdeki verim kaybı %15 ila %80 arasında değişmektedir (Patel vd., 2014). Sel baskınları, ürün miktarı ve kalitesi üzerinde önemli bir etkiye sahip olan ve sonuçta bitkilerin veriminin ve üretiminin azalmasına yol açan önemli stres faktörlerinden birisi olarak karşımıza çıkmaktadır (Tewari ve Mishra 2018).

Sel baskını koşulları, su altında kalma, anoksi, hipoksi veya toprak doygunluğu olarak da bilinir ve şiddetli ürün kayıplarına (Drew ve Lynch, 1980; Nishiuchi vd., 2012) hatta bitki ölümlerine yol açabilmektedir.

Anoksi, toprakta tam oksijen yoksunluğunun ortaya çıkması ve suyun birkaç saat içinde birikmesi durumunu ifade ederken; hipoksi koşulları, köklerde kısmi oksijen yoksunluğuna yol açmaktadır. Sel baskını birkaç saat içinde toprakta anoksi koşullar meydana getirmekte, turgor basıncının kaybına, mikrobiyal ortamdaki potansiyel değişiklikler nedeniyle su içeriği de aynı şekilde azalmakta ve kök gelişimini sınırlayarak sonuç olarak bitki büyümesini ve gelişmesini etkilemektedir (Irfan vd., 2010; Nguyen vd., 2018). Bitki rizosferindeki hipoksi nedeniyle, sel baskını sebzelerin morfolojik ve fizyolojik tepkilerini ciddi şekilde etkilemektedir.

Bitkiler su stresine maruz kaldığında meydana gelen biyokimyasal değişikliklerden biri ROS (reaktif oksijen türleri) birikimidir (Tewari ve Mishra, 2018). Reaktif oksijen türleri savunma mekanizmalarını aktive etmeye ve metabolik süreçte üretilen temel ikincil habercilerdir. ROS, hücre içi/hücreler arası sinyalleşme için gereklidir, ancak ROS konsantrasyonu membran lipitlerinin, pigmentlerin, proteinlerin ve nükleik asitlerin oksidasyonu yoluyla bitki metabolizmasını bozmaktadır. Bitkide ölümcül zararlanmalarda bulunan reaktif oksijen türleri arasında süperoksit (O_2^-), hidrojen peroksit (H_2O_2) ve hidroksil radikali (OH) bulunmaktadır. Bununla birlikte, bitkiler sel basması stresi gibi bazı çevresel streslerle karşı karşıya kaldıklarında, ROS konsantrasyonu, fotosentez, PS II' nin etkinliği gibi bitkilerin çeşitli hücresel metabolik reaksiyonlarına zarar verecek bir seviyeye yükselir (Ashraf, 2009). Bitkiler ROS'ların olumsuz etkilerini azaltmak için farklı antioksidan tiplerini üretmektedirler. Enzimatik antioksidanlar arasında askorbat peroksidaz (APX), süperoksit dismutaz (SOD), peroksidaz (POD), katalaz (CAT), glutatyon redüktaz (GR) yer almaktadır (Gupta vd., 2005).

Kabaklar, ülkemizde irilik, şekil ve değerlendirme biçimlerine göre yazlık, kışlık ve süs kabakları olarak üç grupta sınıflandırılmaktadır (Düzeltir, 2004). *Cucurbita pepo* L. türüne ait yazlık kabaklar genellikle olgunlaşmamış genç meyveleri ile tüketilirken, *Cucurbita moschata* Poir ve *Cucurbita maxima* Duch. türleri kışlık kabaklar olarak kabul edilmekte ve olgun meyveleri çorba, tatlı ve börek yapımında kullanılmaktadır (İnan, 2008). Kabaklar dünyada ekonomik olarak çok önemli sebze türleri arasında yer almakta olup değişik ekolojik koşullarda yetiştirilebilmektedir.

Türkiye'de Sakarya ilinde 2021 yılında 11217 ton balkabağı üretimi gerçekleştirilmiştir (Anonim, 2022). Kabak üretiminin erken dönemlerinde Sakarya ilinde meydana gelen yoğun yağışlar bitki gelişimini olumsuz etkilemektedir. Özellikle su birikintisi ve göllenme, bitkilere çimlenme, çıkış ve fide döneminde zarar verirken, sıcaklıkların artmasıyla bitki gelişiminin hızlandığı dönemlerde de önemli kayıplara neden olmaktadır. Yıllık ortalama 887 mm yağış alan Sakarya'da, yüzeysel su birikimi ve göllenmenin yoğun olduğu bölgelerde üretim verimliliği düşmektedir. Bu durum, her yıl 400 mm'den fazla yağış alan bölgelerde bitki performansını ciddi şekilde sınırlandırmaktadır (İkiel, 2018).

Bölgede tarımsal verimi kısıtlayan birçok faktör bulunmakta olup, en önemlisi, hem bölgeye uyum sağlayabilecek hem de yeterli verim ve kalite sunabilecek çeşitlere duyulan ihtiyaçtır. Özellikle sel baskını riski yüksek olan arazilerde, üreticilerin taleplerine cevap verebilecek tolerant çeşitlerin geliştirilmesi büyük önem taşımaktadır. Bu bağlamda, kestane kabağında sel stresine dayanıklı genotiplerin belirlenmesi ve geliştirilmesi gereklidir.

Bitkinin sel baskısına karşı dayanıklılığını artırmak için, stres faktörlerinin bitki üzerinde yarattığı etkilerin ve bu etkilerin arkasındaki fizyolojik ve biyokimyasal mekanizmaların anlaşılması önemlidir. Ancak, Sakarya'da özellikle yağışlı yaz aylarında, kestane kabağında meydana gelen ürün kayıplarını azaltmaya yönelik kapsamlı bir araştırma henüz yapılmamıştır.

Sel stresi üzerine yapılan bazı çalışmalarda, kabakgiller ailesindeki türlerin farklı günlerde (1, 3, 7 ve 13. gün) fizyolojik parametreleri incelenmiştir (Lin vd., 2020). Ayrıca, başka bir çalışmada *Cucumis sativus* bitkisine hipoksi koşullarında kalsiyum uygulanmış ve bitkinin verdiği tepkiler değerlendirilmiştir (He vd., 2018).

Son zamanlarda küresel iklim değişikliğinin etkisiyle yaşanan şiddetli yağışlar, kabak yetiştirme alanlarını olumsuz yönde etkilemektedir. Bu durum, sel baskını stresinin bitkilerdeki verim ve kalite üzerindeki etkilerinin yanı sıra, fizyolojik ve biyokimyasal değişikliklerin de tam olarak anlaşılmasını gerektiren önemli bir konu haline gelmiştir. Sel baskını stresinin olumsuz etkilerini azaltmaya yönelik stratejilerin geliştirilmesi ise giderek daha fazla önem kazanmaktadır. Çalışmanın ana amacı, ülkemiz de dahil olmak üzere dünya genelinde günümüzdeki en önemli abiyotik stres faktörü olan sel stresine tolerans gösteren tarım ürünlerinin fizyolojik ve biyokimyasal değişimlerini incelemek olmuştur.

2. Materyal ve Yöntem

Araştırma, Haziran 2024 ile Ağustos 2024 zaman aralığında (yaklaşık 3 ay), Sakarya Uygulamalı Bilimler Üniversitesi Ziraat Fakültesi Bahçe Bitkileri Bölümü'ne ait plastik serada saksı denemesi olarak yürütülmüştür.

Araştırmada, bitki materyali olarak; Sakarya Mısır Araştırma Enstitüsünün geliştirdiği Arıcan-97 ve Balkız kestane kabağı çeşitleri kullanılmıştır. Araştırmada üst çapı 17 cm, alt çapı 14 cm ve yüksekliği 15 cm olan plastik saksılar kullanılmıştır. Saksılarda daha sonra sel baskını stresi oluşturmak için saksı içine deliksiz poşet yerleştirilmiştir. Denemede kullanılan saksıların her birine 2,1 kg ağırlığında hava kurusu toprak konulmuştur. Saksılara konulan toprakların eşit ağırlıkta olması için 1gr hassasiyetli dijital tartı kullanılmıştır. Saksılara toprak konulduktan sonra saksı üst yüzeyinden yaklaşık 3 cm boşluk kalmıştır.

Daha sonra her saksıya 2 tohum ekimi (27 Mayıs 2024) yapılmış ve can suyu olarak 500 mL sulama suyu verilmiştir. Tohumlar çimlendikten sonra her saksıda 1 bitki kalacak şekilde seyreltme yapılmıştır.

Çalışma, tesadüf parselleri deneme desenine göre, bir tam sulama ve sel baskını stresi olmak üzere iki sulama konusundan oluşturulmuştur. Toplamda 2x2=4 farklı çalışma konusu yer almakta olup, her bir denemede 3 tekrarlı olarak toplam 9 saksı kullanılmıştır. Tohum ekiminden hemen sonra tüm saksılara eşit miktarda sulama suyu uygulanmış ve toprak nemi faydalı su kapasitesine (FC) çıkarılmıştır. Saksılara uygulanan sulama suyu miktarları, gravimetrik toprak nemi ölçme yöntemine göre belirlenmiştir. Bu amaçla, tanık konu olarak seçilen kontrol %100 konusundaki faydalı su kapasitesi %40-45'e düştüğünde sulama yapılmış ve her defasında toprak nemi tarla kapasitesine ulaştırılmıştır.

Sel baskını stresi konuları ve tam sulama konularının hepsine, stres oluşana kadar eşit sulama yapılmıştır. Sel baskını uygulaması 1.07.2024 tarihinde başlamış ve hasat sonuna kadar her gün buharlaşan suyun yerine bitkilere su eklenerek su tabakasının toprak yüzeyinde tutulması sağlanmıştır. İlk hasat 5.07.2024 tarihinde gerçekleştirilmiş, ardından bitkiler taşkın stresine maruz bırakıldıktan sonra 10 ve 15 Temmuz tarihlerinde toplam üç kez hasat edilmiştir. Kontrol saksılarında toprak su tutma kapasitesinin yaklaşık %40-45 oranında azalması üzerine tüm saksılara tarla kapasitesine ulaşacak şekilde sulama suyu verilmiştir. Deneme süresince, toprağı düzenli olarak hafifçe odun parçasıyla karıştırmak ve yabancı ot temizliği el ile zamanında ve düzenli olarak yapılmıştır. Deneme toprağında yapılan analiz sonucunda pH 7,17 ve saturasyon % 63,8 olarak bulunmuştur.

2.1. Büyüme Parametresi

Çalışmada büyüme parametreleri olarak toprak üstü taze ve kuru ağırlığı, toprak altı taze ve yaş ağırlığı, bitki boyu ve yaprak sayısı ölçülmüştür. Toprak yüzeyinden hasat edilen her tekerrürden üç bitki hassas terazi yardımı ile tartılmıştır. Bitkiler hasat edildikten sonra her tekerrürden saksıdan sökülen üç adet kök temizlenip yıkandıktan sonra kurutma kâğıdı ile nemi alınmış, örnekler hassas terazi yardımı ile tartılmıştır. Toprak üstü ve altı kuru ağırlığı için bitkiler etüvde 65℃ bekletilmiş bitki kısımları kuruduktan sonra hassas terazide ölçülmüştür. Bütün bitkilerin boyları toprak yüzeyinden en uç yaprak yüksekliğine kadar cetvel yardımı ile ölçülmüştür. Her tekerrürden hasat edilen beş bitkinin toprak altı ve toprak üstü aksamlarının yaş ağırlıkları ayrı ayrı hassas terazi yardımı ile tartılarak belirlenmiştir. Daha sonra tartımları belli olan örnekler 65°C sıcaklıkta 72 saat etüvde kurutulduktan sonra toprak altı kuru ağırlığı (g) ve toprak üstü kuru ağırlığı (g) belirlenmiştir (Seymen, 2021).

2.2. Yaprak Örneklerinin Oransal Su İçeriği (RWC)

Her hasad sonunda yaprak örneklerinden alınmış 3 adet yaprak diski hassas terazide tartılıp yaş ağırlıkları belirlenmiş ardından yaprak örneklerinin oransal su içeriklerinin belirlenmesi için, 4 saat süre ile saf su içerisinde bekletilmiş ve bu süre sonunda turgor ağırlıkları saptanmıştır. Sonra yaprak diskleri 80℃'de etüvde 48 saat tutularak kuru ağırlığı tartılmış ve aşağıdaki formüle göre nispi su içeriği hesaplanmıştır.

YOSİ%= [(YA-KA)/(TA-KA)]*100

(YNSİ= Yaprak Nispi Su İçeriği, YA= Yaş Ağırlık, KA= Kuru Ağırlık, TA= Turgor Durumundaki Ağırlık)

2.3. Yaprak Örneklerinin Klorofil İçeriğinin Belirlenmesi

Her saksıda üç bitkinin yaprağından klorofil içeriği SPAD 502 cihazı kullanılarak ölçülmüştür.

2.4. Biyokimyasal Parametreler (Malondialdehyde, Hidrojen Peroksit, Protein ve Prolin Tayini)

Bitkilerde lipid peroksidasyonunun bir göstergesi olarak, malondialdehit (MDA) içeriği belirlenmektedir. MDA tayini Heath ve Packer, (1968)'ın belirlediği yönteme göre 2- thiobarbiturik asit (TBAA) ve lipid peroksidasyonun ölçülmesi ile belirlenmiştir. Ölçümler spektrofotometre cihazında 532 ve 600 nm dalga boyunda yapılmıştır. Aynı karışımdan kullanılan yüzeysel kalıntı ile Hidrojen peroksit konsantrasyonu belirlenmiş ve oluşturulan standart grafikten hesaplanmıştır (Velikova vd., 2000). Prolin tayini asit ninhidrin metodu kullanılarak, yine spektrofotometrik olarak yapılmıştır (Bates vd., 1973). Alınan kabak yaprak örneklerinden protein tayini için 0,5 g'lık örnekler kullanılmış ve protein tayini "Bradford" (Bradford, 1976) metoduna göre yapılmıştır.

2.5. Antioxidant Enzim Aktivtesi Tayini

Hasat işlemleri bittikten sonra kabak yapraklarından yapılan örneklemeler Angelini ve Federico, (1989)'nın yöntemine göre numuneler hazırlanmıştır. Hazırlanan numunelerden Agarwal ve Pveey (2004)'in yöntemine göre 560 nm dalga boyunda okunmuş ve inhibisyona neden olan enzimlerin içerikleri belirlenerek SOD aktivitesi hesaplanmıştır. CAT aktivite tayini Havir ve McHale (1987)'in uyguladığı metot kullanılmış ve meydana gelen absorbans değişimi 240 nm dalga boyunda okunmuştur. POD aktivitesi tayini için Chance (1955) tarafından belirlenen yönteme göre 470 nm dalga

boyunda yapılan ölçümlerde alınan değerler kullanılmıştır.

2.6. İstatistik Analiz

Elde edilen veriler temel bileşenler analizi (PCA) ve kümeleme (cluster) analizleri JUMP Bilgisayar programı kullanılarak PCA ve kümeleme analizi ile değerlendirilmiştir**.**

3. Bulgular ve Tartışma

Kestane kabağında sel stresinde farklı hasat dönemlerinde elde edilen sonuçlar temel bileşenler analizine (PCA) tabi tutulmuştur. Bileşenler göz önüne alındığında ilk beş bileşen çalışmanın % 87,060'ını açıklamıştır. Dolayısıyla ilk beş bileşenin çalışmayı yüksek oranda açıkladığı görülmüştür. Analiz sonucunda, ilk bileşen çalışmanın %33,404'ünü açıklamış olup, bitki boyu, yaprak sayısı, toprak üstü yaş ağırlığı, toprak altı yaş ağırlığı, toprak üstü kuru ağırlığı, toprak altı kuru ağırlığı, toplam klorofil, yosi, prolin, protein, SOD parametreleri pozitif yönde açıklanırken, MDA, H_2O_2, CAT, POD parametreleri negatif yönde açıklanmıştır (Tablo 1). İkinci bileşen çalışmanın %24.288'sini açıklamış olup toprak üstü kuru ağırlığı, toprak altı kuru ağırlığı, prolin, yosi, MDA, CAT, POD, SOD parametreleri pozitif yönde açıklanırken bitki boyu, yaprak sayısı, toprak üstü yaş ağırlığı, toprak altı yaş ağırlığı, toplam klorofil, H_2O_2, protein negatif yönde açıklanmıştır (Tablo 1). Üçüncü bileşen çalışmanın %12,336'sını açıklamış olup bitki boyu, yaprak sayısı, toprak altı yaş ağırlığı, toprak üstü kuru ağırlığı, toprak altı kuru ağırlığı, toplam klorofil, yosi, , MDA, H_2O_2, protein, CAT, POD, SOD parametreleri pozitif yönde açıklanırken toprak üstü yaş ağırlığı, prolin parametreleri negatif yönde açıklanmıştır. Temel Bileşen Analizi (PCA) sonucunda elde edilen temel bileşen (PC) eksenleri, eigen değerleri, varyasyon ve kümülatif varyasyon oranları ile özellik bazında ortaya çıkan temel bileşenlerdeki ağırlık TBA analizinde özelliklerin temel bileşenlerdeki ağırlık değerleri 0,3'ün üzerinde olduğu takdirde önemli ağırlığa sahip oldukları kabul edilmiştir (Brown, 1991). İlk 4 temel bileşeninin eigen değerleri ise 5,06-1,71 arasında bulunmuştur. Eigen değerlerinin 1'den büyük olması ele alınan temel bileşen ağırlık değerlerinin güvenilir olduğunu göstermektedir (Mohammadi ve Prasanna, 2003).

Farklı kavun çeşitlerinde uygulanan sel stresinde morfolojik, fizyolojik ve biyokimyasal parametreler PCA ile değerlendirilmiş ve varyansın %82,47'si ilk beş bileşenle açıklamıştır. Bu da kavun çeşitlerinin bu koşullardaki farklılıklarının büyük ölçüde bu bileşenlerle ifade edilebildiğini göstermektedir (Kıratlı vd., 2024). Benzer şekilde, Seymen (2021) çalışmasında ıspanağın morfo-fizyolojik ve biyokimyasal parametreleri kontrol ve sel stresi koşullarında incelenmiş, PCA analizi sonucunda varyasyonun stres olmayan koşullarda %71,59'u, su baskını stresinde ise %73,50'si ilk iki bileşenle açıklanmıştır. Ayrıca, farklı hasat dönemlerinde lahana ve karnabaharın morfo-fizyolojik ve biyokimyasal parametreleri kontrol ve su baskını koşullarında incelenmiş ve toplam varyasyonun %67,83'ü lahana, %63,89'u ise karnabahar uygulamalarında ilk iki bileşen tarafından açıklanmıştır (Kayak, 2024). Bu çalışmalar PCA'nın bitkilerin çevresel streslere verdiği tepkileri anlamada ne kadar etkili olduğunu ve bitkisel parametrelerdeki varyasyonları açıklamada güçlü bir yöntem olduğunu ortaya koymaktadır.

Tablo 1. Sel baskını ve tam sulama koşulları altında kabak çeşitlerinin büyüme, fizyolojik, biyokimyasal içerikleri üzerine Temel Bileşenler Analizi (PCA)

Öz değer	5,06	3,64	1,85
Yüzde varyans	33,404	24,288	12,336
Toplam varyans	33,404	57,692	70,028
Öz vektörler	PC1	PC2	PC3
Bitki Boyu	0,415	-0,00	0,022
Yaprak Sayısı	0,415	-0,008	0,022
Toprak Üstü Yaş Ağırlığı	0,342	-0,114	-0,026
Toprak Altı Yaş Ağırlığı	0,300	-0,192	0,24
Toprak Üstü Kuru Ağırlığı	0,272	0,388	0,110
Toprak Altı Kuru Ağırlığı	0,346	0,005	0,334
Toplam Klorofil	0,167	-0,395	0,122
Yosi (%)	0,005	0,456	0,012
MDA	-0,188	0,175	0,309
H_2O_2	-0,269	-0,129	0,266
Prolin	0,19	0,152	-0,422
Protein	0,123	-0,170	0,359
SOD	0,201	0,361	0,026
CAT	-0,154	0,153	0,556
POD	-0,000	0,422	0,124

PC1 ve PC2 bileşenleri kullanılarak kuraklık ve uygulama dozları arasındaki karşılıklı ilişkiyi incelemek için bir loading plot grafiği oluşturulmuştur. Özellikler arasındaki interaksiyonu gösteren grafikte % PC1 (%33,4) (the first Principal Component - 1. Ana Bileşen) % PC2 (the second Principal Component- 2. Ana Bileşen) (%24,3) değerleri toplamı %57,7 olarak hesaplandığı görülmektedir. Biplot grafiklerinde % PC1 ve % PC2 değerlerinin mümkün olduğunca yüksek olması istenir. Çünkü bu toplam yüzde değerinin yüksek olması ele alınan konularda interaksiyonun önem derecesinin yüksek olduğunu göstermektedir (Fırıncıoğlu vd., 2012). Bu nedenle PC1 ve PC2 yüzde değerleri toplamının en az % 50 olması istenmektedir. Çalışmada PC1 ve PC2 yüzde değerleri toplamı %57,7 olarak bulunmuş ve grafiğin güvenilir bir şekilde yorumlanmasına olanak sağlamıştır. Grafik incelendiğinde, yaprak sayısı ve bitki boyu arasında güçlü bir pozitif ilişki olduğu görülmektedir (Şekil 1). Diğer taraftan MDA, CAT arasında negatif yönde güçlü bir ilişki sergilenmiş ve bu vektörler kendi aralarında pozitif ilişki sergilemiştir. Korelasyon

tablosunda POD ve Yosi (%) arasında güçlü bir pozitif ilişkinin olduğu görülmektedir.

Kıratlı vd. (2024), oluşturdukları loading plot grafiğinde POD ile protein arasında güçlü pozitif ilişkiler ve bitki büyüme parametreleri ile de güçlü pozitif ilişkiler bulmuşlardır. Ayrıca, yaprak oransal su içeriği, membran zararlanması, protein, CAT ve MDA arasında güçlü pozitif ilişkiler bulunmuş, ancak bu parametrelerin bitki büyüme parametreleriyle güçlü negatif ilişkiler gösterdiği belirtilmiştir. Seymen (2021) loading plot grafiğinde, su baskını stresine maruz kalan ıspanakta toprak üstü yaş ağırlığı, toprak üstü kuru ağırlığı, toprak altı yaş ağırlığı, toprak altı kuru ağırlığı ve POD'nun önemli parametreler olduğunu ortaya koymuştur. Kayak (2024) çalışmasında H_2O_2, MDA, POD, SOD, prolin, CAT parametreleri pozitif bir şekilde korelasyon gösterdiğini gözlemlemiştir. Bu bulgular, bitki stresine karşı yanıt olarak belirli fizyolojik ve biyokimyasal parametrelerin ilişkisini ve önemini vurgulamaktadır.

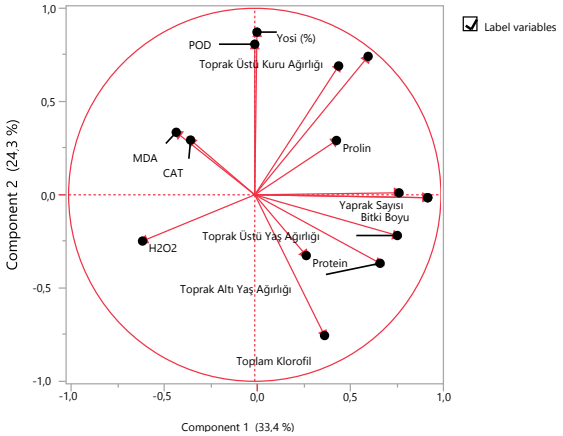

Şekil1. Sel stresi koşulları altında kabağın fizyolojik ve biyokimyasal özelliklerini kullanarak PCA'dan elde edilen PC 1 ve 2'ye dayalı Loading plot grafiği.

Aynı şekilde PC1 ve PC2 bileşenleri kullanılarak yapılan uygulamalar arasındaki ilişkiyi incelemek için score plot grafiği oluşturulmuştur. Grafik incelendiğinde ikinci eksende Arıcan 97 flooding 15. Gün, Arıcan 97 flooding 10. Gün, Balkız flooding 15. Gün ve Balkız flooding 10. Gün'ün aynı eksende olduğu görülmektedir (Şekil 2).

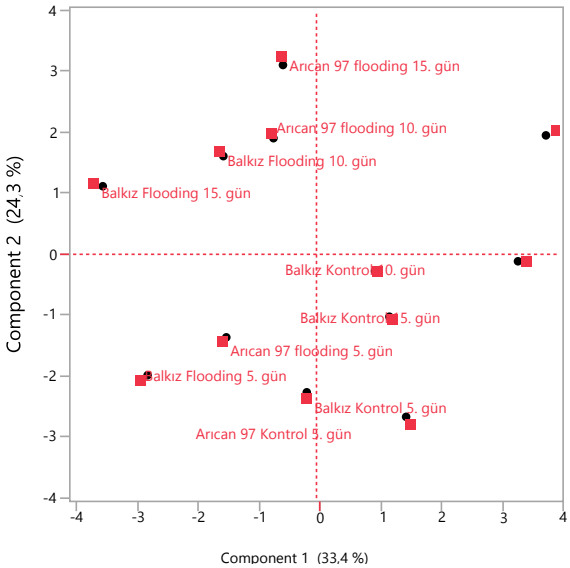

Şekil 2. Sel stresi koşulları altında kabağın fizyolojik ve biyokimyasal özelliklerini kullanarak PCA'dan elde edilen PC 1 ve 2'ye dayalı Score plot grafiği.

4. Sonuç

Bu çalışmada, farklı hasat zamanlarında, sel stresinin kestane kabağı'nın fizyolojik ve biyokimyasal parametreleri üzerinde önemli etkileri olmuştur. Uygulanan sel baskını stresi kabak çeşitlerinin agronomik özelliklerinde önemli azalışlar meydana getirmiştir. Sonuç olarak, kestane kabağında sel stresinde farklı hasat dönemlerinde yapılan temel bileşenler analizi (PCA), ilk beş bileşenin çalışmanın %87,060'ını açıklayarak, bitki boyu, yaprak sayısı, toprak üstü ve altı yaş ve kuru ağırlıkları, toplam klorofil, yosi, prolin, protein ve SOD parametrelerinin pozitif yönde etkili olduğunu, MDA, H_2O_2, CAT ve POD parametrelerinin ise negatif yönde etkili olduğunu ortaya koymuştur. Balkız ve Arıcan 97'de farklı hasat zamanı taşkın stresi önemli kayıplara neden olmuş olup, Balkız ve Arıcan 97'nin taşkın stresine duyarlı olduğunu göstermektedir. Bu nedenle Balkız ve Arıcan 97 yetiştirilen tarlalarda yükselen su seviyesine dikkat edilmesi ve çukur arazilerde kabak yetiştirilmemesi verim ve kalite kayıplarının önlenmesinde önemli rol oynayacaktır.

Katkı Oranı Beyanı

Yazarların katkı yüzdeleri aşağıda verilmiştir. Yazarlar makaleyi incelemiş ve onaylamıştır.

%	N.K.	Ö.B.	E.S.
K	100		
T	100		50
Y	100	100	
VTI	50		50
VAY	100		
KT	20		70
YZ	20		70
GR	100		
PM	70	70	20

K= kavram, T= tasarım, Y= yönetim, VTI= veri toplama ve/veya işleme, VAY= veri analizi ve/veya yorumlama, KT= kaynak tarama, YZ= Yazım, GR= gönderim ve revizyon, PY= proje yönetimi.

Çatışma Beyanı

Yazarlar bu çalışmada hiçbir çıkar ilişkisi olmadığını beyan etmektedirler.

Etik Onay Beyanı

Bu araştırmada hayvanlar ve insanlar üzerinde herhangi bir çalışma yapılmadığı için etik kurul onayı alınmamıştır.

Destek ve Teşekkür Beyanı

Bu çalışmanın gerçekleştirilmesi, Sakarya Uygulamalı Bilimler Üniversitesi BAP birimi tarafından 194-2024 numaralı proje kapsamında mümkün olmuştur.

Kaynaklar

Agarwal S, Pveey V. 2004. Antioxidant enzyme responses to NaCl stress in Cassia angustifolia. Biol Plantarum, 48(4): 555-560.

Angelini R, Federico R. 1989. Histochemical evidence of poly amine oxidation and generation of hydrogen peroxide in the cell wall. J Plant Physiol 135(2): 212–217. https://doi.org/10.1016/S0176-1617(89)80179-8

Anonim. 2022. T.C. Tarım ve Orman Bakanlığı Strateji Geliştirme Başkanlığı Tarımsal Yatırımcı Danışma Ofisi. Tarım ve Orman Bakanlığı, Ankara, Türkiye, ss: 23.

Ashraf MJBA. 2009. Biotechnological approach of improving plant salt tolerance using antioxidants as markers. Biotechnol Adv, 27(1): 84-93.

Bailey-Serres J, Lee SC, Brinton E. 2012. Waterproofing crops: effective flooding survival strategies. Plant Physiol, 160(4): 1698-1709.

Bates L, Waldren RPA, Teare ID. 1973. Rapid determination of free proline for water-stress studies. Plant Soil, 39(1): 205-207.

Bradford MM. 1976. A rapid and sensitive method for the quantitation of microgram quantities of protein utilizing the principle of protein-dye binding. Anal Biochem, 72(1-2): 248-254.

Brown JS. 1991. Principal component and cluster analysis of cotton cultivar variability a cross the U.S. cotton belt. Crop Sci, 31: 915-922.

Chance B. 1955. Assay of catalase and peroxidase. Methods Enzymol, 2: 765-775.

Cramer G, Urano K, Delrot S, Pezzotti M, Shinozaki K. 2011. Effects of abiotic stress on plants: a systems biology perspective. BMC Plant Biol, 11(1): 163.

Drew M, Lynch JM. 1980. Soil anaerobiosis, microorganisms, and root function. Annual Rev Phytopathol, 18 (1): 37-66.

Düzeltir B. 2004. Çekirdek kabağı (Cucurbita pepo L.) hatlarında morfolojik özelliklere göre tanımlama ve seleksiyon çalışmaları. Yüksek Lisans Tezi, Ankara Üniversitesi, Fen Bilimleri Enstitüsü, Ankara, Türkiye, ss: 76.

Fırıncıoğlu HK, Ünal S, Pank Z, Beniwal SPS. 2012. Growth and development of narbon vetch (Vicia narbonensis L.) genotypes in the semi-arid central Turkey. Spanish J Agri Res, 10(2): 430-442.

Gupta KJ, Stoimenova M, Kaiser WM. 2005. In higher plants, only root mitochondria, but not leaf mitochondria reduce nitrite to NO, in vitro and in situ. J Exp Bot, 56(420): 2601-9.

Hao X-y, Han X, Ju H, Lin E. 2010. Impact of climatic change on soybean production; A review. J Appl Ecol, 21(10): 2697-706.

Havir EA, McHale NA. 1987. Biochemical and developmental characterization of multiple forms of catalase in tobacco leaves. Plant Physiol, 84(2): 450-455.

He L, Yu L, Li BDN, Guo S. 2018. The effect of exogenous calcium on cucumber fruit quality, photosynthesis, chlorophyll fluorescence, and fast chlorophyll fluorescence during the fruiting period under hypoxic stress. BMC Plant Biol, 18: 1-10.

Heath RL, Packer L. 1968. Photoperoxidation in isolated chloroplasts: I. Kinetics and stoichiometry of fatty acid peroxidation. Arch Biochem Biophys, 125(1): 189-198.

Irfan M, Hayat S, Hayat Q, Afroz S, Ahmad A. 2010. Physiological and biochemical changes in plants under waterlogging. Protoplasma, 241(1-4): 3-17.

İkiel C. 2018. Sakarya'nın fiziki, beşeri ve iktisadi coğrafya özellikleri. Yüksek Lisans Tezi, Sakarya Üniversitesi, Fen Bilimleri Enstitüsü, Sakarya, Türkiye, ss: 76.

İnan N. 2008. Çekirdek kabaklarında morfolojik ve moleküler karakterizasyon. Yüksek Lisans Tezi. Çukurova Üniversitesi, Fen Bilimleri Enstitüsü, Tarımsal Biyoteknoloji Bölümü, Adana, Türkiye, ss: 83.

Kayak N. 2024. The effect on morpho-physiological and biochemical characteristics of cauliflower and cabbage harvested at different times under flooding stress conditions. J Crop Health, 76(1): 145-159.

Kıratlı H, Seymen M, Kıymacı G. 2024. Determination of tolerance to flooding stress in melon cultivars by agronomic and physio-biochemical responses. Genet Resour Crop Evol, 71(4): 1643-1657.

Lin HH, Lin KH, Huang MY, Su YR. 2020. Use of non-destructive measurements to identify Cucurbit species (Cucurbita maxima and Cucurbita moschata) tolerant to waterlogged conditions. Plants, 9(9): 214586.

Mohammadi SA, Prasanna BM. (2003.) Analysis of genetic diversity in crop plants-salient statistical tools and considerations. Crop Sci, 43: 1235–1248

Nguyen LTT, Osanai Y, Anderson Ian C, Bange MP, Tissue DT, Singh BK. 2018. Flooding and prolonged drought have differential legacy impacts on soil nitrogen cycling, microbial communities and plant productivity. Plant Soil, 431(1): 371–387

Nishiuchi S, Yamauchi T, Takahashi H, Kotula L, ve Nakazono M. 2012. Mechanisms for coping with submergence and waterlogging in rice. Rice, 5, 1-14.

Patel PK, Singh A, Tripathi N, Yadav D, Hemantaranjan A. 2014. Flooding: abiotic constraint limiting vegetable pro ductivity.

Adv Plants Agricult Res 1(3): 00016. https://doi.org/10.15406/apar.2014.01.00016

Seymen M. 2021. How does the flooding stress occurring in different harvest times affect the morpho-physiological and biochemical characteristics of spinach. Sci Hortic, 275: 109713.

Soltekin RO. 2019. Bazı sofralık üzüm çeşitlerinde su stresinin omca gelişimi, verimi ve üzüm kalitesi üzerine etkileri. Yüksek Lisans Tezi, Ege Üniversitesii Fen Bilimleri Enstitüsü Bahçe Bitkileri Bölümü, İzmir, Türkiye, ss: 79.

Tewari S, Mishra A. 2018. Flooding Stress in Plants and Approaches to Overcome. Academic Press, 2018: 355-366.

Velikova V, Yordanov I, Edreva A. 2000. Oxidative stress and some antioxidant systems in acid rain-treated bean plants: Protective role of exogenous polyamines. Plant Sci, 151(1): 59-66.

Black Sea Journal of Engineering and Science
doi: 10.34248/bsengineering.1516593

Open Access Journal
e-ISSN: 2619 – 8991

Research Article
Volume 8 - Issue 1: 149-160 / January 2025

BIBLIOMETRIC ANALYSIS OF MATH AND ARTIFICIAL INTELLIGENCE RESEARCH

Şeyma BOZKURT UZAN[1*], Nesibe MANAV MUTLU[2], İrem Deniz ARBERK[3]

[1]*Istanbul Beykent University, Faculty of Engineering - Architecture, Department of Software Engineering, 34396, Istanbul, Turkiye*
[2]*Istanbul Nisantasi University, Faculty of Economics, Administrative And Social Sciences, Department of Management Information Systems, 34481, Istanbul, Turkiye*
[3]*Bogazici University, Faculty of Arts and Science, , Department of Mathematics, 34342, Istanbul, Turkiye*

Abstract: This study conducts a comprehensive bibliometric analysis to explore the landscape of research in mathematics and artificial intelligence (AI). Using Scopus as the primary data source, we identify key publications and trends in these fields. Through VOSviewer, we visualize networks of keywords and collaborations among researchers and institutions. The analysis reveals the prominence of topics such as AI and mathematics in academic discourse, as well as the central role played by countries like the United States, the United Kingdom, and China in research collaboration. Limitations include potential biases in data sources and the reliance on keywords for analysis. Future research could integrate alternative metrics and qualitative analyses to provide a more nuanced understanding of research trends and impact.

Keywords: Bibliometric analysis, Mathematics, Artificial intelligence, Research trends, Collaboration

Corresponding author: Istanbul Beykent University, Faculty of Engineering - Architecture, Department of Software Engineering, 34396, Istanbul, Turkiye
E mail: seymauzan@beykent.edu.tr (S. BOZKURT UZAN)
Şeyma BOZKURT UZAN https://orcid.org/0000-0003-3527-3730
Nesibe MANAV MUTLU https://orcid.org/0000-0002-7853-6337
İrem Deniz ARBERK https://orcid.org/0009-0001-5192-6781

Received: July 15, 2024
Accepted: December 02, 2024
Published: January 15, 2025

Cite as: Bozkurt Uzan Ş, Manav Mutlu N, Arberk İD. 2025. Bibliometric analysis of math and artificial intelligence. BSJ Eng Sci, 8(1): 149-160.

1. Introduction

1.1. Overview of Artificial Intelligence

Artificial Intelligence (AI) has emerged as a transformative technology with the potential to revolutionize various aspects of human life. It encompasses a wide array of techniques that enable machines to simulate human intelligence and perform tasks that typically require human cognition. From automating mundane tasks to making complex decisions, AI has become an indispensable tool across numerous industries and fields.

1.2. Significance of AI

The significance of AI lies in its ability to augment human capabilities and streamline processes, leading to enhanced efficiency and innovation. By leveraging AI, organizations can analyze vast amounts of data to gain valuable insights, make data-driven decisions, and predict future trends. Moreover, AI has the potential to revolutionize sectors such as healthcare, finance, manufacturing, and transportation, offering solutions to complex problems and improving overall quality of life.

1.3. Applications of AI

AI finds applications in various domains, including natural language processing, computer vision, robotics, and data analysis. In natural language processing, AI enables machines to understand and respond to human language, facilitating the development of virtual assistants and language translation tools. In computer vision, AI algorithms enable machines to interpret and analyze visual data, leading to advancements in facial recognition, object detection, and autonomous vehicles. Furthermore, AI-driven robotics has revolutionized industries by enabling the development of autonomous machines capable of performing intricate tasks with precision and efficiency.

1.4. Fundamentals of Machine Learning and its Mathematical Basis

Machine Learning (ML), a subset of AI, forms the backbone of many intelligent systems. It involves the development of algorithms that enable machines to learn from data and make data-driven predictions or decisions. At its core, machine learning heavily relies on mathematical concepts such as linear algebra, calculus, and probability theory (Tyagi and Chahal, 2022).

Linear algebra facilitates the representation and manipulation of data in the form of vectors and matrices, allowing ML algorithms to process and transform data efficiently. Calculus plays a crucial role in optimizing ML models by enabling the calculation of gradients and minimizing error functions during the training process. Moreover, probability theory helps in modeling uncertainties and making probabilistic predictions, which is essential in various machine learning applications such as recommendation systems and predictive analytics (Aggarwal, 2020). By harnessing these mathematical foundations, machine learning algorithms can extract patterns and insights from complex data sets, enabling the development of

sophisticated AI systems capable of performing intricate tasks with high accuracy and reliability. In the subsequent sections, we delve deeper into the specific mathematical principles that underpin the functioning of AI, exploring their role in various AI applications and the challenges associated with their implementation.

1.5. Role of Linear Algebra in AI

Linear algebra serves as a fundamental pillar for the development and functioning of various artificial intelligence (AI) applications. Its applications range from data representation and transformation to the optimization of AI models. The use of vectors, matrices, and linear transformations enables AI systems to process and manipulate complex data efficiently, facilitating the extraction of meaningful insights and patterns (Dydak, 2023).

1.6. Data Representation and Transformation

In AI, data is often represented and manipulated in the form of vectors and matrices. Vectors serve as a means to represent individual data points, such as features of an input, while matrices provide a structured way to organize and process data sets. Through vector and matrix operations, AI algorithms can perform tasks such as data preprocessing, feature scaling, and dimensionality reduction, which are essential for enhancing the performance and efficiency of machine learning models (Senaratne and Seneviratne, 2023).

1.7. Model Representation and Transformation

Linear algebra plays a pivotal role in the representation and transformation of AI models. Neural networks, a popular class of AI models, heavily rely on linear algebra operations for their architecture and functioning. Matrices of weights and biases are manipulated during the feedforward and backpropagation phases of neural network training, enabling the model to learn complex patterns and relationships within the data. Through matrix multiplications and activations functions, neural networks can make sophisticated decisions and predictions based on the input data (Wylie and Kamel, 1997).

1.8. Optimization of AI Models

Linear algebra techniques are also instrumental in the optimization of AI models. During the training process, AI algorithms aim to minimize a defined cost or error function. Gradient descent, a widely used optimization algorithm, involves calculating gradients using linear algebra operations to iteratively update the model parameters. By adjusting the weights and biases based on the computed gradients, AI models can converge towards optimal solutions, thereby improving their predictive accuracy and generalization capability (Torres Tello, 2022).

1.9. Eigenvalues and Eigenvectors in AI

Eigenvalues and eigenvectors, another key concept in linear algebra, find applications in various AI tasks, such as dimensionality reduction and principal component analysis (PCA). By computing eigenvalues and eigenvectors of covariance matrices, AI systems can identify the most significant patterns and features within high-dimensional data, facilitating the reduction of data complexity without significant information loss. This process aids in enhancing the interpretability and performance of AI models, particularly in tasks involving large and intricate data sets. By leveraging the principles of linear algebra, AI systems can efficiently process, represent, and optimize complex data, thereby facilitating the development of robust and effective AI applications across diverse domains (Nawaz, 2019).

1.10. Significance of Probabilistic and Statistical Approaches in AI

In the realm of Artificial Intelligence (AI), probabilistic and statistical approaches play a critical role in enabling machines to make informed decisions, predictions, and inferences based on data. By leveraging these approaches, AI systems can handle uncertainties, model complex relationships within data, and make rational decisions in various real-world scenarios.

1.11. Bayesian Inference and Decision Making

Bayesian inference forms a cornerstone of probabilistic AI, allowing systems to update their beliefs based on new evidence or data. By incorporating prior knowledge and incorporating observed data, AI models can compute posterior probabilities, enabling the assessment of the likelihood of various outcomes. This process is instrumental in decision-making tasks, as it allows AI systems to make rational decisions by considering both prior knowledge and new information (Golchi and Willard, 2023).

Probability Distributions in Modeling Uncertainties

Probability distributions serve as powerful tools in AI for modeling uncertainties and capturing the variability of data. By fitting probability distributions to observed data, AI models can quantify the likelihood of different outcomes, enabling the assessment of risks and uncertainties associated with decision-making processes. Common distributions such as the Gaussian (normal) distribution, Bernoulli distribution, and Poisson distribution find widespread applications in tasks such as risk assessment, anomaly detection, and predictive modeling (Ismail and Wediawati, 2023).

1.12. Statistical Analysis and Pattern Recognition

Statistical analysis forms the backbone of pattern recognition and data-driven decision-making in AI. By employing statistical techniques such as hypothesis testing, regression analysis, and analysis of variance (ANOVA), AI systems can identify meaningful patterns and relationships within complex data sets. These statistical methods facilitate the extraction of actionable insights from data, enabling AI models to make accurate predictions and classifications in tasks such as image recognition, natural language processing, and predictive analytics (Wang et al., 2018).

1.13. Probabilistic Graphical Models for Complex Inferences

Probabilistic graphical models provide a powerful framework for representing and reasoning under

uncertainty in AI systems. By utilizing graphical models such as Bayesian networks and Markov random fields, AI models can capture complex dependencies and relationships among variables, facilitating the representation of causal relationships and making sophisticated inferences about the underlying data. These models enable AI systems to handle complex decision-making tasks and perform probabilistic reasoning in scenarios involving interconnected variables and uncertain relationships (Pitkow and Angelaki, 2017).

1.14. Importance of Statistical Learning Theory

Statistical learning theory forms the theoretical basis for understanding the behavior and performance of AI algorithms. By leveraging concepts such as bias-variance trade-off, model complexity, and generalization error, AI practitioners can develop robust and reliable AI models with optimal predictive performance. This theoretical framework guides the selection of appropriate learning algorithms, model architectures, and regularization techniques, ensuring the development of AI systems that can generalize well to unseen data and adapt to changing environments. By integrating probabilistic and statistical approaches into AI systems, researchers and practitioners can build robust, adaptive, and reliable AI models capable of handling uncertainties and making informed decisions in dynamic and complex environments (Tsiamis et al., 2023).

1.15. Unraveling the Calculus of AI: The Subtle Dynamics at Play

Amid the burgeoning realm of artificial intelligence (AI), the intricate application of calculus stands as the bedrock of numerous cutting-edge algorithms and models. From optimization techniques to gradient-based learning, calculus serves as the fundamental framework that empowers AI systems to adapt, learn, and evolve within complex and dynamic environments (Zhenpeng, 2024).

1.16. The Power of Derivatives in Gradient Descent

At the heart of AI lies the omnipotent concept of derivatives, enabling the optimization of various AI models through gradient descent algorithms. By calculating derivatives with respect to model parameters, AI systems can iteratively adjust their internal configurations to minimize errors and enhance predictive accuracy. This iterative process, guided by the principles of calculus, enables AI models to traverse the multidimensional landscape of loss functions, steering them towards the global or local optima that signify the convergence of optimal solutions (Lin et al., 2024).

1.17. Chain Rule and Backpropagation in Neural Networks

The intricate dynamics of neural networks are governed by the calculus-based technique of backpropagation, which relies on the fundamental principle of the chain rule. Through the systematic propagation of errors backward across the network, the chain rule facilitates the computation of gradients with respect to each layer's parameters, enabling the network to refine its weights and biases based on the calculated error gradients. This recursive application of the chain rule empowers neural networks to learn complex representations and discern intricate patterns within vast and multidimensional datasets (Liu, 2024).

1.18. Integral Calculus for Probability Distributions

In the realm of probabilistic modeling and inference, the integration of calculus through probability density functions enables AI systems to effectively quantify uncertainties and make informed decisions. By leveraging integral calculus to compute the cumulative distribution functions and probabilities associated with various events, AI models can assess the likelihood of specific outcomes and make probabilistic inferences that drive robust decision-making processes (Pap, 2021).

1.19. Partial Derivatives and Multivariable Optimization

The seamless integration of partial derivatives in the optimization of multivariable functions facilitates the fine-tuning of AI models to perform efficiently in high-dimensional spaces. By computing partial derivatives with respect to multiple variables, AI systems can navigate complex landscapes of objective functions, allowing for the identification of optimal parameter configurations that maximize performance and minimize error rates. This multidimensional approach to optimization, rooted in the principles of calculus, empowers AI models to exhibit adaptability and resilience in addressing diverse and dynamic real-world challenges.

In essence, the profound influence of calculus on the evolution and advancement of AI underscores the indispensability of mathematical rigor in shaping the trajectory of intelligent systems. By delving deeper into the intricate interplay between calculus and AI, researchers and practitioners can unlock transformative insights that transcend conventional boundaries, propelling the landscape of AI-driven innovations into uncharted realms of possibility (Pal and Kaushik, 2023).

2. Materials and Methods

2.1. Data Analysis

This article employs bibliometric analysis to examine publications related to mathematics and artificial intelligence (AI). Bibliometrics refers to the mathematical and statistical analysis of specific data in scientific communication, focusing on the examination of data such as authors, topics, cited authors, and cited sources in a statistical manner. This approach enables us to understand the general structure of a particular discipline through the statistical outcomes of such data.

In this context, our study investigates bibliometric variables including the total number of publications concerning mathematics and AI, the languages of these publications, types of documents, author affiliations, institutions of authors, journals cited, active countries, citation counts, types of sources cited in articles, and keyword analysis. A keyword network map was created

using the Vosviewer software, a computer program designed for generating and visualizing bibliometric maps. Through this process, the study examines the literature in the fields of mathematics and AI, identifying significant topics and trends within these areas, and supports these findings with bibliometric analyses.

2.1. Methodology

This research aimed to explore the topic of "Mathematics and artificial intelligence" by utilizing the Scopus Index. To conduct the study, the keywords "mathematics, artificial intelligence" were searched across the database within the fields “Abstract title, Abstract, Keywords”,. The research was conducted in a chronological order, ranging from the most recent to the oldest studies.

No modifications were made during the research, and the current situation was examined as is. Therefore, a Scanning Model was employed due to its ability to handle large datasets, and the research was carried out using the General Scanning Model. Bibliometric methods were utilized to perform the analyses. Within the scope of the research, the keywords "mathematics, artificial intelligence" were employed in the SCOPUS Index. These keywords generated a dataset of 6,298 records in Scopus, which constituted the universe of this scientific study.

All the studies from Scopus were examined based on bibliometric data such as authors, publications, citations, keywords, and publication dates. These 6298 studies were downloaded in CSV file format and network maps were created using the Vosviewer software for further analysis.

2.1. Collecting Data

This research initially focused on mathematics but then shifted its focus upon finding 78,607 publications under the 'math' keyword in Scopus. To refine the investigation, a detailed query was conducted using keywords such as "mathematics and artificial intelligence." This resulted in the selection of 6286 publications from Scopus, which were subsequently exported in CSV format for analysis. The exported data was prepared for analysis using the Vosviewer software and was stored in both Excel and RIS formats for further examination.

3. Results and Discussion

3.1. Scopus Database and Analysis of Obtained Values

Scopus is a multidisciplinary database provided by Elsevier, offering access to a wide range of scientific literature; it equips researchers with intelligent tools for analyzing journals, monitoring research outcomes, and visualization. This platform boasts a rich content base that includes peer-reviewed journals, books, and conference publications, continuously updated and expanded to meet the extensive information needs of researchers.

3.2. Scopus Data

A search was conducted in Scopus using the keywords "mathematics, artificial intelligence" within the fields “Abstract title, Abstract, Keywords”, resulting in a total of 6298 documents. The research was carried out on November 21, 2024, and the findings from these search results were analyzed accordingly. Table of documents per year is presented in Table 1.

Table 1. Table of documents per year

Year	Documents
2025	2
2024	266
2023	241
2022	218
2021	284
2020	307
2019	328
2018	435
2017	370

For the year 2025, a total of 2 documents have been cataloged, indicating the data may be partial as the year is ongoing. In 2024, there were 266 documents, which show a substantial increase and possibly reflect a growing interest or advancements in the fields of mathematics and artificial intelligence.

The year 2023 had 241 documents, a solid number that could signify sustained research activity within the respective areas. In 2022, the count was at 218 documents, which may suggest a steady engagement with the topics, albeit with a slight decrease from the previous year. The year 2021 saw 284 documents published, which might indicate a dip in research output, possibly due to global events affecting academic productivity. For 2020, the document count was 307, representing what may be a normal fluctuation in research publications year over year.

The year 2019 had 328 documents, a figure that aligns with the general output trends of the previous years. In 2018, there were 435 documents, showing an increase that might point to changes in research focus or funding landscapes. The year 2017 had 370 documents, which was lower compared to the subsequent years, suggesting a period of less activity or emerging interest in the topics. Finally, in 2016, there were 450 documents, which might reflect the early stages of growing academic attention in the fields of math and artificial intelligence for that decade. Table of documents per year by source is presented in Table 2. The table provides a breakdown of the number of documents per source in a given dataset.

•Lecture Notes in Computer Science (Including Subseries Lecture Notes in Artificial Intelligence and Lecture Notes in Bioinformatics): This source, which includes various subseries, is the most prolific, contributing 920 documents. It suggests a strong emphasis on computer science and its subfields, especially artificial intelligence and bioinformatics, indicating an interdisciplinary approach within the realm of computational research.

•Lecture Notes In Artificial Intelligence Subseries of Lecture Notes In Computer Science: With 117 documents,

this source is a significant contributor to the field of artificial intelligence, showcasing a specialized focus on AI research.

•Advances in Intelligent Systems and Computing: The presence of 103 documents from this prestigious interdisciplinary journal indicates the high relevance and impact of research at the intersection of computing and intelligent systems.

•International Joint Conferences on Artificial Intelligence (IJCAI): The inclusion of 96 documents from IJCAI highlights its critical role in the academic and professional development of Artificial Intelligence (AI). These conferences serve as essential platforms for researchers and practitioners to engage in networking, foster collaboration, and disseminate knowledge. The outcomes of these events are widely shared through high-quality proceedings, books, and other educational materials.

•Proceedings of The National Conference on Artificial Intelligence: This outlet has 91 documents, are one of the most prestigious venues in the field. These proceedings document significant advancements in AI research, spanning diverse topics such as machine learning, robotics, natural language processing, and reasoning.

Serving as an essential resource for academics, professionals, and students, the proceedings enable the dissemination of innovative methodologies, theoretical breakthroughs, and practical applications. They not only reflect the state-of-the-art in artificial intelligence but also foster dialogue and collaboration within the global AI research community

•ACM International Conference Proceeding Series: The 74 documents from this series reflect the contribution of conference proceedings, which typically include cutting-edge research presented at ACM conferences, emphasizing innovation and current trends in computer science and related areas.

•CEUR Workshop Proceedings: This outlet has 73 documents, pointing towards a significant number of research works being disseminated through workshops, which are often more focused on recent developments and community engagement in research.

•Communications in Computer and Information Science: This source, with 68 documents, indicates its role in providing a platform for disseminating research related to computer science and the processing of information, which likely includes intersections with mathematical algorithms and AI methodologies.

Table 2. Table of documents per year by source

Source	Documents
Lecture Notes in Computer Science Including Subseries Lecture Notes In Artificial Intelligence And Lecture Notes In Bioinformatics	920
Lecture Notes In Artificial Intelligence Subseries Of Lecture Notes In Computer Science	117
Advances In Intelligent Systems And Computing	103
Ijcai International Joint Conference On Artificial Intelligence	96
Proceedings Of The National Conference On Artificial Intelligence	91
ACM International Conference	74

The data implies a vibrant and diverse landscape of research outputs across various platforms, ranging from academic journals to conference proceedings, indicating a robust and interdisciplinary research community. Table of documents by subject area is presented in Table 3.

The table categorizes documents by their respective subject areas, illustrating the interdisciplinary reach of the research fields of computer science, mathematics, and related domains:

•Computer Science: With 4,771 documents, this subject area tops the list, underscoring computer science as a central field of study, possibly due to its broad applicability and integration with artificial intelligence.

•Mathematics: The 1,927 documents in this area highlight mathematics as a foundational discipline that supports and intersects significantly with fields like AI and engineering.

•Engineering: Featuring 1,592 documents, engineering showcases the practical applications and design aspects that often incorporate mathematical and computational methods.

•Environmental Science: The 387 documents reflect the use of computational and mathematical tools in addressing environmental challenges and studying ecological phenomena.

•Social Sciences: With 387 documents, this field illustrates the impact and relevance of computational methods and mathematical modeling in areas like psychology, sociology, and economics.

•Decision Sciences: This area, with 301 documents, emphasizes the role of quantitative methods and AI in making informed decisions within various sectors, such as business and policy-making.

•Medicine: The 257 documents suggest an intersection of computational methods with medical research, such as in biostatistics or health informatics.

•Energy: With 217 documents, this category highlights the application of computational methods and artificial intelligence in addressing challenges in energy

production, distribution, and sustainability.

•Physics and Astronomy: Accounting for 217 documents, these sciences employ mathematical models and computational simulations to understand the physical universe.

• Earth and Planetary Sciences: This category contains 193 documents demonstrating the use of computer tools and artificial intelligence to investigate complex geological and planetary phenomena. This field's research includes advances in climate modeling, remote sensing, seismic analysis, and planetary exploration. These contributions improve our ability to investigate Earth's systems, predict natural disasters, and explore other celestial bodies, encouraging a more in-depth understanding of both our planet and the larger cosmos through data-driven insights and novel approaches.

•Biochemistry, Genetics and Molecular: This field, with 162 documents, indicates the use of computational biology and bioinformatics in studying complex biological systems and genetic materials.

This distribution showcases the pervasive nature of mathematical and computational techniques across various disciplines, indicating their essential role in advancing research and contributing to diverse fields of knowledge.

Table 3. Table of documents by subject area

Subject Area	Documents
Computer Science	4771
Mathematics	1927
Engineering	1592
Environmental Science	387
Social Sciences	387
Decision Sciences	301
Medicine	257
Energy	217
Physics and Astronomy	217

Table of documents by type is presented in Table 4. The table categorizes documents by type, which reflects the various formats of scholarly communication in the dataset:

•Conference Paper: There are 4,000 conference papers, this is the most common type, signifying a significant contribution from conference proceedings. These papers often present preliminary findings, innovative ideas, or work-in-progress research and are essential for scholarly exchange in academic conferences.

•Article: With 2,039 documents, indicating that full-fledged, peer-reviewed articles constitute the bulk of the research output. Articles are typically detailed studies reporting original research, comprehensive studies, or theoretical discussions.

•Review: There are 94 review documents, which are likely comprehensive analyses of literature in a particular field. Reviews synthesize existing research, identify trends, and often highlight areas for future exploration.

•Note: With 39 documents, notes are generally short descriptions or announcements of preliminary research findings, corrections, or updates to previous work.

•Book Chapter: The presence of 31 book chapters suggests that compilations of research works in the form of book sections also form a substantial part of the academic discourse. Book chapters allow authors to delve into specific topics in detail within a broader thematic collection.

•Conference Review: There are 26 conference reviews, which may provide overviews or critiques of conference themes, organization, or individual presentations, offering insights into the conference's contribution to the field.

•Editorial: The table shows 22 editorials, which are typically written by the editors of journals or books and may discuss the direction of the research field, comment on current trends, or provide context for the collection of works.

•Book: With 15 documents, books are authored or edited volumes that cover extensive research topics or present comprehensive knowledge in a field. They are valuable for in-depth understanding and often serve as key resources for academics and practitioners.

•Short Survey: With 7 documents, short surveys provide concise overviews of specific research areas, highlighting key developments, challenges, and future directions. These documents are instrumental for readers seeking a quick yet insightful understanding of a topic, serving as valuable references for both newcomers and experienced researchers aiming to stay updated in their fields.

•Letter: Also with 6 documents, letters are brief written communications that may discuss recent research, comment on previously published works, or present small-scale studies.

The distribution of these document types highlights the diversity of research outputs and the various means through which scholars communicate their findings and contribute to their respective fields.

Table 4. Table of documents by type

Document Type	Documents
Conference Paper	4000
Article	2039
Review	94
Note	39
Book Chapter	31
Conference Review	26
Editorial	22
Book	15
Short Survey	7

3.3. Bibliometric Analysis and Visualization of Results Obtained from VOSviewer

Bibliometric analysis is a methodological approach that applies quantitative analysis and statistics to written communication such as publications. It is used to map and evaluate academic literature, tracking the influence and spread of research through citations and revealing patterns of collaboration among authors and institutions. This analysis can identify key trends, prolific authors, and geographic distributions within a field. The technique has evolved to include complex network analyses, exploring relationships between various academic outputs, and has spread beyond library science to multiple disciplines. It is instrumental in understanding the landscape of scholarly communication and the impact of research within and across fields (Mejia et al., 2021).

3.4. VOSViewer

VOSviewer is a tool developed specifically for constructing and visualizing bibliometric networks, which include citation, co-citation, bibliographic coupling, keyword co-occurrence, and co-authorship networks. This software is particularly noted for its graphical representation capabilities, which are essential for displaying large bibliometric maps in an easy-to-understand manner. Its use in exploratory research is quite significant, as it enables researchers to identify and display the relationships between various scientific outputs like publications, researchers, or concepts within a particular field.

The significance of VOSviewer in academia stems from its ability to facilitate preliminary studies that can guide subsequent, more formal research. By visualizing data from sources such as Scopus, researchers can examine co-occurrence data among publications and uncover patterns that may not be immediately apparent through traditional analysis. This not only opens new avenues of inquiry but also enhances the understanding of a field's landscape, showcasing the main actors, networks, and thematic concentrations.

Moreover, VOSviewer has been integrated into various research methodologies and has found a place in research evaluation and management contexts, helping to map out the scholarly activities and collaborations within and across disciplines. Its application extends to various academic domains, making it a versatile tool for those interested in exploring scientific data visually. The developers of VOSviewer, affiliated with Leiden University's Centre for Science and Technology Studies (CWTS), offer courses that provide in-depth training in science mapping techniques, highlighting the tool's importance and application in the broader research management and evaluation sphere (Kirby, 2023).

3.5. VOS Viewer- co-occurrence of keywords

In the intricate world of research, bibliometric analysis stands as a powerful tool, providing insights through the quantitative evaluation of academic literature. The visual representations of such analyses can uncover the depth and spread of knowledge across various fields, making complex data more comprehensible. The upcoming images and their subsequent explanations aim to delve into this process, showcasing the capabilities of VOSviewer, software instrumental in mapping and visualizing scientific landscapes through its analysis of keyword occurrences and co-occurrences. This process is described below (Figure 1).

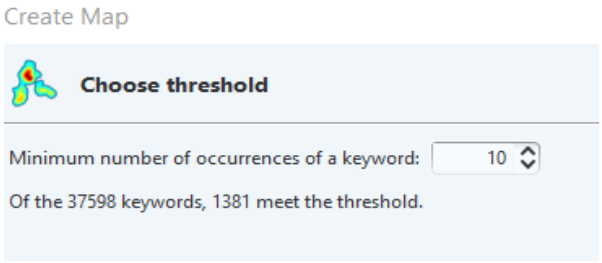

Figure 1. Choose threshold screen.

This image from VOSviewer is displaying the interface where a threshold is set for keyword occurrences in a bibliometric analysis. The user has selected a minimum number of 10 occurrences for a keyword to be included in the analysis. Out of 37,598 keywords, 1,381 meet this threshold, indicating that they appear at least 10 times in the dataset under examination. This thresholding step is crucial in bibliometric analysis as it helps to focus on the most relevant and frequently occurring terms, ensuring that the resulting visualization represents the most significant data points.

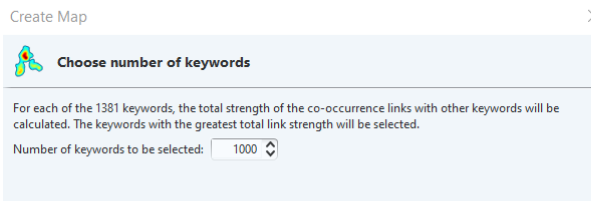

Figure 2. Choose number of keywords screen.

Choose number of keywords screen is presented in Figure 2. In this image from VOSviewer, it's explained that for the set of keywords that passed the previously determined threshold, the software will calculate the total strength of the co-occurrence links between them. Keywords with the highest total link strength will be selected for further analysis. The number to be selected has been set to 270, which is presumably the total number of keywords that met the initial threshold. This selection process is key in identifying the most significant and interconnected terms within a dataset, which are crucial for in-depth bibliometric analysis and visualization.

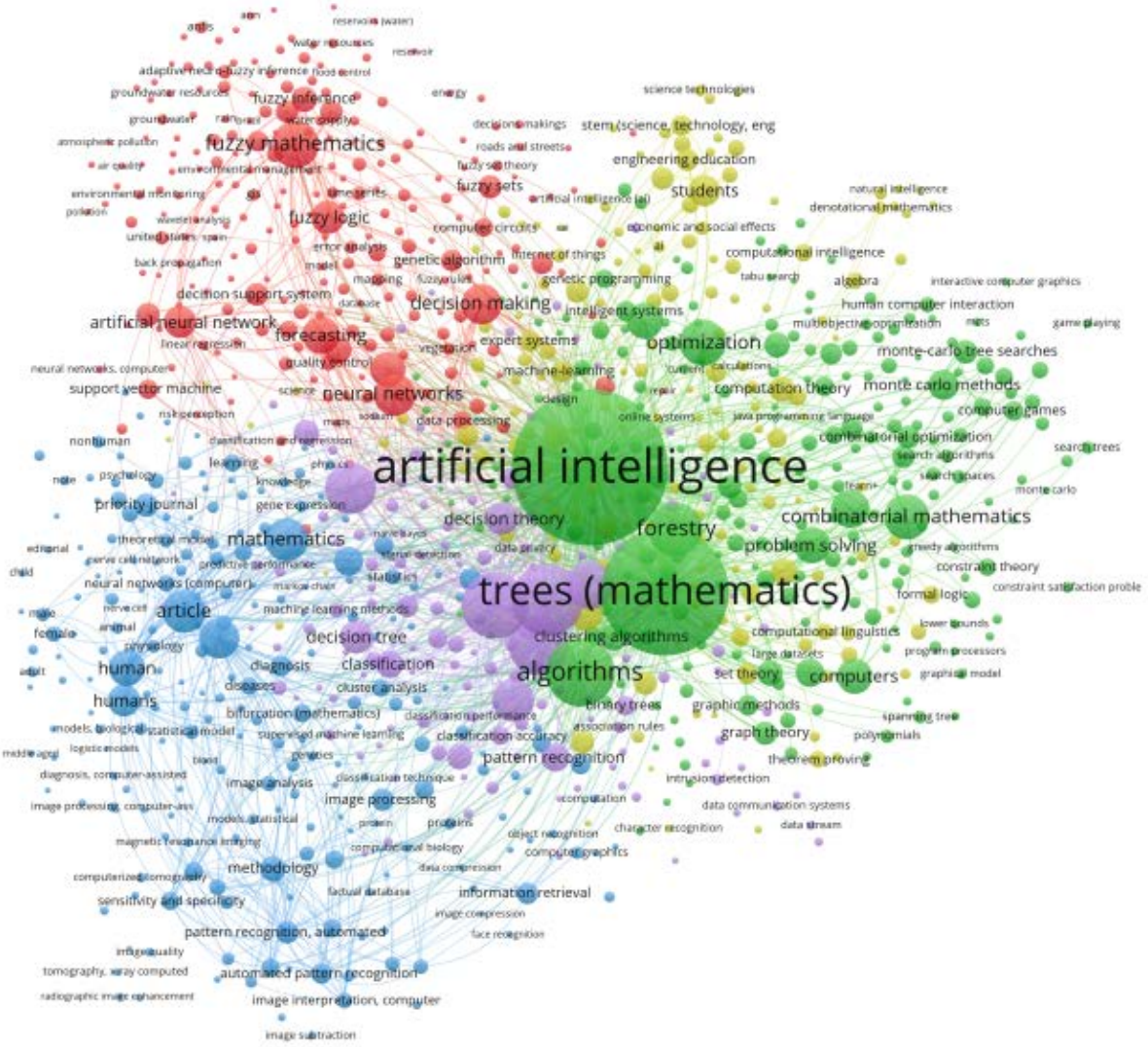

Figure 3. Network visualization.

This is a network visualization map (Figure 3) from VOSviewer, showing the relationships between different keywords in a bibliometric dataset. The largest, most central nodes, such as "artificial intelligence" and "mathematics," represent the most frequently occurring and therefore most significant keywords within the research field being analyzed. The lines connecting the nodes are indicative of the keywords' co-occurrence within the same papers, suggesting thematic linkages. The closer the nodes are to each other, the stronger their relatedness in the literature, suggesting sub-fields or areas of concentrated study within the broader topics.

Overlay visualization is presented in Figure 4. The image depicts a bibliometric network visualization, specifically an overlay visualization, where each node represents a keyword. The size of a node indicates the frequency of the keyword in the dataset, while the lines between nodes represent co-occurrence relationships. Colors likely correspond to different years or time intervals, showing the evolution of topics over time. For instance, larger nodes like "artificial intelligence," "mathematics," and "learning systems" suggest these are central themes within the field, and their connections to other keywords reveal interrelated research areas. The overlay of colors across the network could indicate the historical progression of research emphasis from one year to another.

Density visualization is presented in Figure 5. This image appears to be a density visualization map from bibliometric analysis software such as VOSviewer. It represents a density distribution of keywords within a specific academic field, where areas of higher keyword concentration are depicted with a brighter or more intense color. Such visualizations help identify the most researched areas or hot topics within a field. Keywords like "artificial intelligence," "learning systems," and "trees (mathematics)" are prominently placed and likely represent key research focuses due to their size and central location in the visualization.

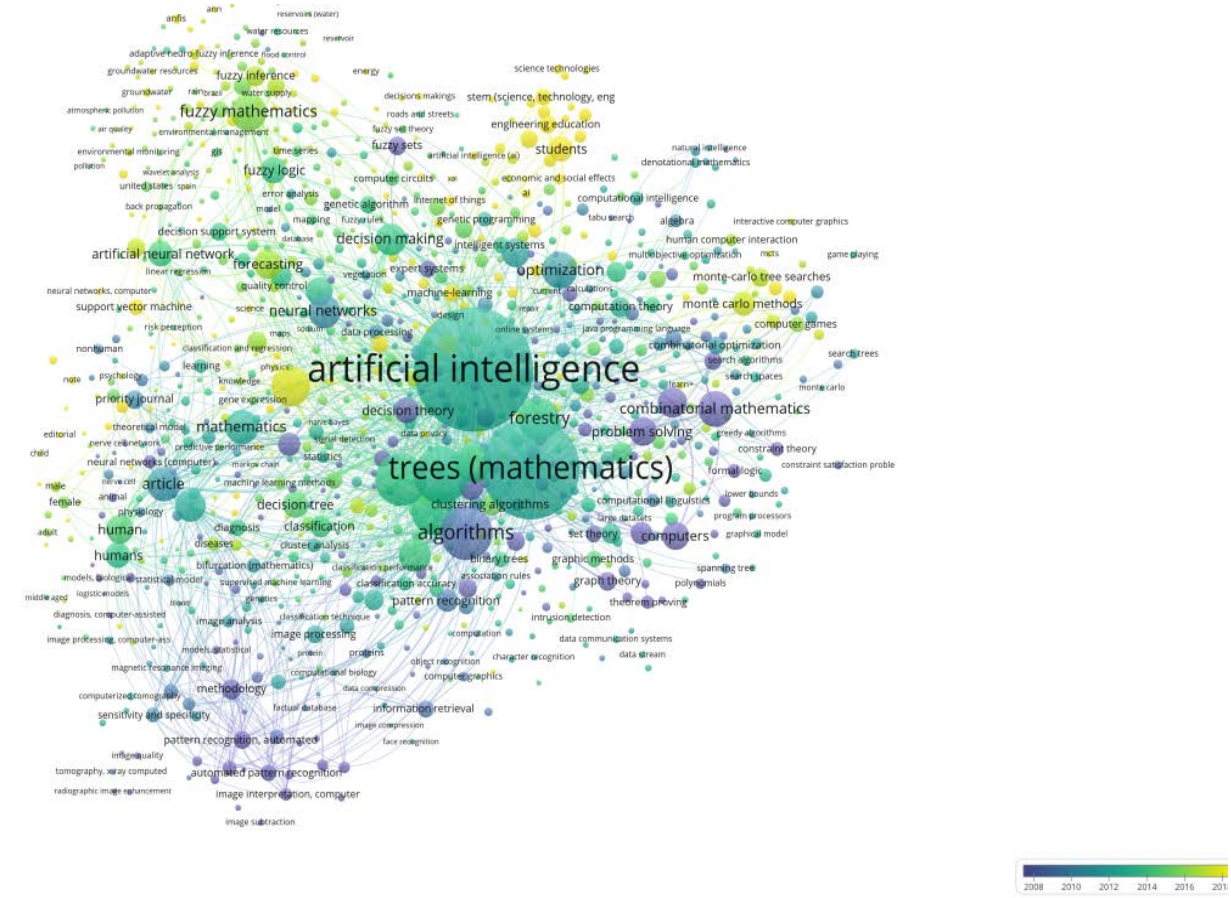

Figure 4. Overlay visualization.

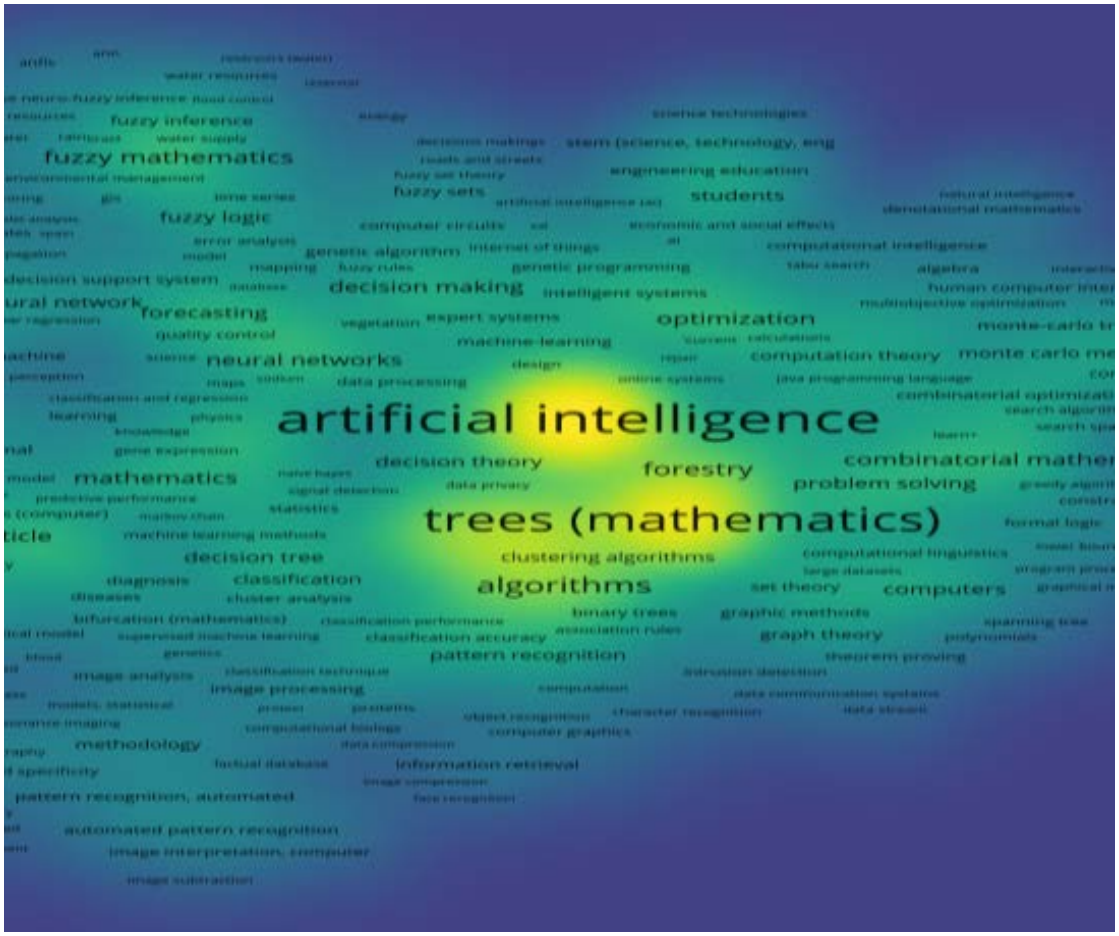

Figure 5. Density visualization.

Each node represents a country, with the node size likely corresponding to the volume of publications or level of activity. The lines indicate collaboration or relationship strength; the thicker and more numerous the lines, the stronger the connections. Central nodes like the United States, China, India, and United Kingdom suggest these countries are major hubs in the network, indicating they may have higher levels of international collaboration or output.

The image shows a network visualization typically used to illustrate international collaboration based on academic publications or similar data. The various nodes represent different countries, and the size of each node may signify the volume of research output or the level of collaborative activity of that country. The lines connecting the nodes denote collaborations between countries, with thicker lines indicating stronger or more numerous collaborations. The colors along the lines and nodes may represent different years, illustrating the evolution of collaboration over time, with newer years possibly represented by cooler colors and older years by warmer colors. Countries with a central position and larger nodes, like the United States, China, India, Germany and United Kingdom are often key players with extensive international collaborations.

Figure 6 and 7 are network visualizations that depict connections, but they differ in their focus and perhaps in the data they represent. The first image seems to be a keyword co-occurrence visualization, showing the relationships between different research topics. The second image looks like it visualizes the collaboration between countries, possibly in research or academic publishing. The color coding could also indicate changes over time or the intensity of activity in both images, but the specific application of the color gradient may vary between them.

Figure 6. Distribution of connections between countries- network visualization.

Figure 7. Distribution of Connections Between Countries- Overlay visualization

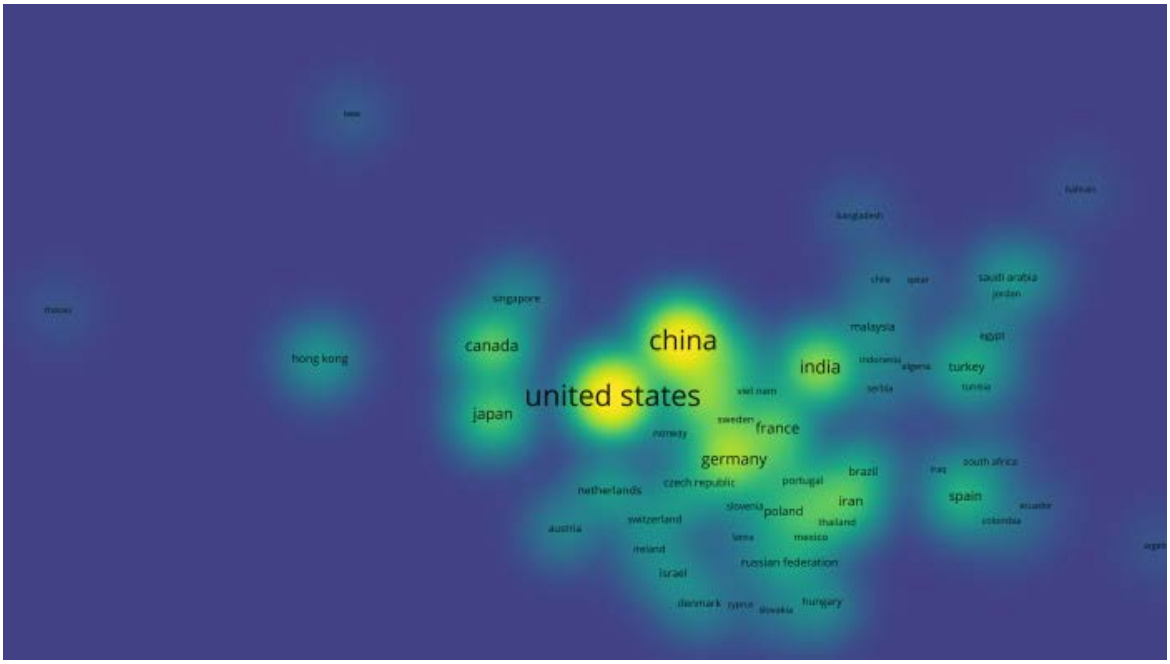

Figure 8. Density visualization

This image (Figure 8) is a density visualization map, which is used to represent the intensity and concentration of connections between entities—in this case, countries. It highlights areas of high activity or interaction by the brightness or density of color. In such visualizations, commonly seen in bibliometric analyses, the areas where the color is most intense typically indicate higher levels of collaboration or publication output. The map does not show the individual lines between countries, focusing instead on the overall pattern of activity. This type of visualization is useful for identifying which countries are most central or active in a given context, such as scientific research, based on the dataset analyzed.

4. Conclusion

Throughout this investigation, we have engaged in a meticulous examination of the interconnected landscape that underpins research in mathematics and artificial intelligence (AI). Initiating the inquiry with a bibliometric approach, we delved into Scopus, a comprehensive repository of scientific output, to extract data using specific keywords that embody our research focus. The deployment of VOSviewer software facilitated the exploration of this data, bringing to light the complex networks of keywords and the international collaborations they entail.

In analyzing the visualizations generated by VOSviewer, we observed the dominance of certain keywords, such as "artificial intelligence" and "mathematics," highlighting their centrality within the academic discourse. The country collaboration network revealed the strategic importance of the United States, China, India, and United Kingdom underscoring the geographical nodes of prolific scientific production and exchange. The shift from individual connections to a density visualization further illuminated the broader patterns of international research engagement.

From these insights, one can extrapolate the trajectory of future research directions and international collaboration trends. This analysis underscores the value of bibliometric methods in gauging the pulse of academic progress. Recommendations stemming from this study could advocate for a strengthened focus on emerging areas where AI intersects with other disciplines, the fostering of collaborative networks, and the promotion of research initiatives that address gaps identified in the less connected regions. The dynamism depicted in these visual representations is a testament to the ever-evolving nature of the scientific endeavor, where cross-disciplinary synergy and global cooperation are not only beneficial but necessary for impactful advancements.

Research limitations and further research

Research limitations in bibliometric studies often stem from the data sources themselves—databases may not be comprehensive, leading to potential bias. Another limitation is the reliance on keywords, which can miss nuances in research themes or fail to capture emerging trends not yet solidified in the lexicon. Future research could expand by integrating alternative metrics such as altmetrics, which consider the impact of research in online and social media platforms, to provide a more holistic view of research influence. Moreover, qualitative analyses could complement the quantitative focus of bibliometric methods, capturing the substance behind the statistics.

Author Contributions

The percentages of the authors' contributions are presented below. All authors reviewed and approved the final version of the manuscript.

	Ş.B.U.	N.M.M.	İ.D.A.
C	40	30	30
D	40	30	30
S	40	30	30
DCP	40	30	30
DAI	40	30	30
L	40	30	30
W	40	30	30
CR	40	30	30
SR	40	30	30
PM	40	30	30
FA	40	30	30

C=Concept, D= design, S= supervision, DCP= data collection and/or processing, DAI= data analysis and/or interpretation, L= literature search, W= writing, CR= critical review, SR= submission and revision, PM= project management, FA= funding acquisition.

Conflict of Interest

The authors declared that there is no conflict of interest.

Ethical Consideration

This study is a bibliometric analysis that includes a systematic review of the existing literature and does not involve human or animal subjects.

References

Aggarwal CC. 2020. Linear algebra and optimization for machine learning. Springer International Publishing, New York, USA, pp: 97-120.

Dydak J. 2023. Artificial intelligence and teaching of linear algebra. PhD thesis, University of Tennessee, Knoxville, USA, pp: 2-42.

Golchi S, Willard J. 2023. Estimating the sampling distribution of test-statistics in bayesian clinical trials. Biomet J, 66: e70002.

Ismail A, Wediawati B. 2023. Understanding the fundamentals of machine learning and AI for digital business. Asadel Publisher, New York, USA, pp: 20-35.

Kirby A. 2023. Exploratory bibliometrics: using vosviewer as a preliminary research tool. Publicat, 11(1): 1-14.

Lin WC, Hsiao CH, Huang WT, Yao KC, Lee YD, Jian JL, Hsieh Y. 2024. Network reconfiguration framework for CO_2 emission reduction and line loss minimization in distribution networks using swarm optimization algorithms. Sustainability, 16(4): 1493.

Liu FLF. 2024. Financial statement analysis based on RNN-RBM Model. J Electrical Systems, 20(1), 106-123.

Mejia C, Wu M, Zhang Y, Kajikawa Y. 2021. Exploring topics in bibliometric research through citation networks and semantic analysis. Front Res Metrics Analytics, 6: 742311.

Nawaz N. 2019. Artificial Intelligence Face Recognition for applicant tracking system. Inter J Emerg Trends Engin Res, 7(12): 895 – 901.

Pal T, Kaushik M. 2023. Aircraft parameter estimation using a novel hybrid Luus–Jaakola/Hooke–Jeeves neural-network based optimization technique. Proceed Instit Mechan Engin Part G: J Aerospace Engin, 237(9): 2196-2208.

Pap E. 2021. Mathematical foundation of artificial intelligence. Artificial intelligence: Theory Applicat, 2021: 3-30.

Pitkow X, Angelaki DE. 2017. Inference in the brain: statistics flowing in redundant population codes. Neuron, 94(5): 943-953.

Senaratne A, Seneviratne L. 2023. Embedded to interpretive: A paradigm shift in knowledge discovery to represent dynamic knowledge. AAAI Spring Symposium on Challenges Requiring the Combination of Machine Learning and Knowledge Engineering, March 27-29, San Francisco, USA, pp: 102.

Wang Q, Zhou D, Guan Q, Li Y, Yang J. 2018. A privacy-preserving classifier in statistic pattern recognition. Springer International Publishing, Haikou, China, 4: 496-507.

Torres Tello JW. 2022. Optimization of AI models as the main component in prospective edge intelligence applications. PhD thesis, University of Saskatchewan, Faculty of Engineering, Saskatchewan, Canada, pp: 50-65.

Tsiamis A, Ziemann I, Matni N, Pappas GJ. 2023. Statistical learning theory for control: A finite-sample perspective. IEEE Control Systems Magaz, 43(6): 67-97.

Tyagi AK, Chahal P. 2022. Artificial intelligence and machine learning algorithms. In Research anthology on machine learning techniques, methods, and applications. IGI Global, 2022: 421-446.

Wylie R, Kamel MS. 1997. Model transformations in simulation and planning: behavior preserving model simplifications. IEEE Transacti Systems Man Cybernetics-Part A: System Humans, 27(4): 424-435.

Zhenpeng Y. 2024. Application of artificial intelligence in computer network technology in the age of big data. J Artificial Intel Pract, 7(1): 11-16.

Black Sea Journal of Engineering and Science
doi: 10.34248/bsengineering.1581168

Open Access Journal
e-ISSN: 2619 – 8991

Araştırma Makalesi (Research Article)
Cilt 8 - Sayı 1: 161-171 / Ocak 2025
(Volume 8 - Issue 1: 161-171 / January 2025)

ÜLKELERİN İNSANİ GELİŞMİŞLİK ÖLÇÜSÜNE GÖRE SEVİYELERİNİN BELİRLENMESİNDE KÜMELEME ALGORİTMALARININ KULLANILMASINA İLİŞKİN BİR UYGULAMA

Latife Sinem SARUL[1]*

[1]*İstanbul University, School of Business, Department of Quantitative Techniques, 34322, İstanbul, Türkiye*

Özet: Temel yaşam standartlarına erişim, eğitim ve sağlıklı yaşama süresi gibi üç temel gösterge dikkate alınarak oluşturulan İnsani Gelişme İndeksi (Human Development Index) ilk olarak 1990 yılında Birleşmiş Milletler Kalkınma Programı tarafından ortaya konulmuştur. Belirtilen temel göstergeler dikkate alınarak tüm dünya ülkelerinin İnsani Gelişme İndeksi hesaplanmakta, oluşturulmuş olduğu ilk yıldan itibaren her yıl düzenli olarak Birleşmiş Milletler tarafından kamuoyu bilgisine sunulmaktadır. Bu çalışmada veri madenciliği kapsamında kümeleme analizi teknikleri detaylı olarak incelenmiş ve bu teknikler kullanılarak İnsani Gelişme İndeksine göre ülkelerin gruplaması yapılmıştır. Elde edilen sonuçlar Birleşmiş Milletler Kalkınma Programı tarafından açıklanan listeye göre karşılaştırılarak yapılan analizlerin bu alanda uygulanabilirliği tartışılmıştır.

Anahtar kelimeler: Veri madenciliği, Kümeleme algoritmaları, İnsani Gelişme İndeksi

An Application on the Use of Clustering Algorithms in Determining the Levels of Countries According to their Human Development Index

Abstract: The Human Development Index, which is created by considering three basic indicators such as access to basic living standards, education and healthy life expectancy, was first created by the United Nations Development Program in 1990. The Human Development Index of all countries in the world is calculated by taking into account the specified basic indicators and is regularly presented to the public by the United Nations every year since its creation. In this study, cluster analysis techniques within the scope of data mining are examined in detail and countries are grouped according to the Human Development Index using these techniques. The results obtained are compared according to the list announced by the United Nations Development Program and the applicability of the analyses in this field was discussed.

Keywords: Data mining, Clustering algorithms, Human Development Index

Sorumlu yazar (Corresponding author): *İstanbul University, School of Business, Department of Quantitative Techniques, 34322, İstanbul, Türkiye*
E mail: lasinem@istanbul.edu.tr (L. S. SARUL)
Latife Sinem SARUL https://orcid.org/0000-0001-7013-3755

Gönderi: 07 Kasım 2024 **Received:** November 07, 2024
Kabul: 10 Aralık 2024 **Accepted:** December 10, 2024
Yayınlanma: 15 Ocak 2025 **Published:** January 15, 2025

Cite as: Sarul LS. 2025. An application on the use of clustering algorithms in determining the levels of countries according to their Human Development Index. BSJ Eng Sci, 8(1): 161-171.

1. Giriş

İnsani Gelişme İndeksi, Sağlıklı Yaşam İndeksi, Eğitime Ulaşılabilirlik İndeksi, Temel Yaşam Düzeyine Erişebilirlik İndeksinden oluşan üç temel faktörün normalleştirilmiş değerlerinin geometrik ortalaması alınarak elde edilen bir ölçüdür. İnsani Gelişme İndeksini oluşturan üç temel faktörden Sağlıklı Yaşam İndeksi, sağlıklı doğan bir bireyin beklenen yaşam süresi ile ölçülmektedir. İkinci temel faktör olan Eğitim İndeksi, 25 yaş ve üzeri bireylerin ortalama eğitim süresi ve okula başlama yaşındaki çocuklar için beklenen eğitim alma süresi ile ölçülmektedir. Son olarak Temel Düzeyde Yaşam Standartlarına Erişme İndeksi ise kişi başına düşen gayri safi milli gelir değeri ile ölçülmektedir (HDI Reports, 2024). Birleşmiş Milletler Kalkınma Programı tarafından açıklanan rapora göre ülkeler insani gelişmişlik düzeylerine göre dört gruba ayrılmaktadır. Birleşmiş Milletler Kalkınma Programı tarafından açıklanan 2023-2024 yılı raporuna göre en yüksek İnsani Gelişmişlik düzeyine sahip ilk beş ülke sırasıyla İsviçre, Norveç, İzlanda, Hong Kong- Çin (SAR), Danimarka olarak açıklanmıştır. Açıklanan 191 ülke içerisinde Türkiye 45. sırada yer almaktadır. Bu noktada ülkelerin gelişmişlik düzeylerine göre gruplanmasında sınır değerlerinin belirlenmesi ile ilgili literatürde yapılan pek çok çalışma bulunmaktadır. Bu alanda yapılan en son çalışmalardan biri olan Wang vd. (2023) tarafından yapılmış çalışmada sınır değerlerinin belirlenmesinde denetimsiz makine öğrenmesi tekniklerinden K-Means ve K-Medoids algoritmaları kullanılmıştır. Bu çalışmada ülkelerin insani gelişmişlik düzeylerine göre düşük, orta ve yüksek olarak üç düzeyde gruplanması önerilmiştir.

Bu çalışmada ise hiyerarşik olmayan yöntemlerden K-Means Algoritması ve K-Medoids Algoritması, hiyerarşik

yöntemlerden En Yakın Komşuluk Algoritması (Single Linkage), En Uzak Komşu Algoritması (Complete Linkage), Ortalama Bağlantı Yöntemi(Average Linkage), Ward Yöntemi ve yoğunluk bazlı yöntemlerden DBSCAN (Density based Spatial Clustering of Applications with Noise) Algoritmasının kullanıldığı 39 farklı model oluşturulmuştur. Elde edilen sonuçlar, Birleşmiş Milletler Kalkınma Programı tarafından yapılmış gerçek sınıflamalarla karşılaştırılmıştır. Hiyerarşik ve Hiyerarşik Olmayan Yöntemlerin birarada incelenmiş olması bakımından bu çalışmanın literatüre önemli katkı sağlayacağı düşünülmektedir.

2. Literatür

Literatürde Kümeleme Algoritmaları ve İnsani Gelişim İndeksi üzerine yapılmış pek çok çalışma yer almaktadır. Bu kısımda kümeleme algoritmaları ile yapılan çalışmalar ve ayrıca kümeleme algoritmaları ile İnsani Gelişim İndeksinin birlikte incelendiği çalışmalardan bazılarına yer verilmiştir. Bu anlamda Ezugwu vd. (2022) veri madenciliği çerçevesinde kümeleme algoritmaları kullanımına ilişkin kapsamlı bir çalışma yapmışlardır. Bu çalışmada pek çok farklı alanda kullanılmakta olan kümeleme algoritmaları ve ileri düzey teknikler açıklanmış ayrıca detaylı bir literatür taraması yapılmıştır. Buna göre Ezugwu vd. (2022) küme sayısının önceden belirlenmesinin gerekliliğinin kümeleme algoritmalarının uygulanmasında önemli bir sorun olduğunu tespit etmişler bu nedenle de küme sayısının önceden belirlenmesini gerektirmeyen algoritmaların diğer algoritmalara göre daha çok tercih edildiğini ifade etmişlerdir. Literatürde yapılan çalışmalara bakıldığında diğer algoritmalara kıyasla K-Means algoritmasının önemli ölçüde fazla kullanılmakta olduğu yapılan grafik analizlerle de gösterilmiştir.

Veri Madenciliği çerçevesinde Kümeleme Algoritmalarının kullanımına ilişkin bir diğer çalışma Neha ve Vidyavathi (2015) tarafından yapılmıştır. Bu çalışmada kümeleme algoritmaları, Hiyerarşik, Hiyerarşik Olmayan, Yoğunluk Bazlı ve Izgara Bazlı Yöntemler olarak dört başlık altında incelenmiştir. Bu çalışmada da K-Means algoritmasının daha iyi sonuçlar üretmesi ve daha hızlı uygulanabilir olması nedeniyle diğer algoritmalara kıyasla daha fazla kullanılmakta olduğu ifade edilmiştir. Ayrıca kümeleme algoritmalarının suç tespiti, eğitim gibi alanlarda kullanımının önemine dikkat çekmişlerdir.

Shah ve Nair (2015) yine veri madenciliği çerçevesinde kümeleme algoritmalarını inceledikleri bir çalışma yapmışlardır. Bu çalışmada Kümeleme Algoritmaları Hiyerarşik, Hiyerarşik Olmayan, Yoğunluk Bazlı ve Izgara Bazlı olarak dört başlıkta incelenmiştir. Hiyerarşik kümeleme teknikleri başlığı altında K-Means ve K-Medoids (PAM ve CLARA) Algoritmaları, Hiyerarşik Teknikler başlığı altında Birleştirici (BIRCH ve CHAMELEON) ve Ayrıştırıcı Yöntemler incelenmiştir. Yoğunluk Bazlı Yöntemler başlığı altında literatürde en çok kullanılan algoritmalar DBSCAN ve DENCLUE Algoritmaları, Izgara Bazlı Yöntemler başlığı altında ise STING ve CLIQUE Algoritmalarından bahsedilmiş bu yöntemlerin birbirlerine göre üstün ve üstün olmayan yönleri vurgulanmıştır. Buna göre K-Means Algoritmasının büyük veri setlerinde kullanıma uygun olduğu, gürültü ve aykırı değerlere karşı duyarlı olduğu belirtilmiştir. Bununla birlikte hiyerarşik tekniklerden biri olan BIRCH Algoritmasının da büyük veri setleri için en uygun seçimlerden biri olabileceği belirtilmiştir. DBSCAN ve DENCLUE Algoritmalarının ise büyük veri setleri için çok uygun olmamakla birlikte veri seti içindeki kümelenmelerin konveks olmaması halinde iyi sonuçlar verdiğini belirtmişlerdir.

Kameshwaran ve Malarvizhi (2014) çalışmalarında veri madenciliği çerçevesinde kümeleme tekniklerini incelemişlerdir. Bu çalışmada kümeleme tekniklerinin Dağılım Modelleri, Merkez Modelleri, Yoğunluk Modelleri, Alt Uzay Modelleri, Grup Modelleri ve Grafik Bazlı Modeller olarak sınıflanabileceği gibi bir başka yaklaşım olarak da Hiyerarşik, Hiyerarşik Olmayan, Izgara Bazlı, Yoğunluk Bazlı ve Grafik Bazlı olarak da gruplanabileceğini belirtmişler ve bu yöntemlere ilişkin açıklamalara yer vermişlerdir.

Rocha vd. (2021) çalışmasında Kümeleme ve K-Means Algoritmalarını kullanarak İnsani Gelişim İndeksine göre Peru'da bir uygulama yapmışlardır. Buna göre, yaşam beklentisi, eğitime erişebilirlik ve gelir düzeyi açısından insani gelişmişliklerine göre Peru dört bölgeye ayrılmıştır. Optimal bölge sayısının belirlenmesinde Elbow Yöntemi ve Temel Bileşenler Analizi kullanılmıştır. Çalışmada, K-Means ve diğer kümeleme algoritmalarının tutarlı sonuç verdiği sonucuna varılmıştır.

Nurhasanah vd. (2021) çalışmasında K-Means Algoritmasını kullanarak İnsani Gelişim İndeksine bağlı olarak Endonezya'nın şehirlerini düşük, orta, yüksek ve çok yüksek gelişim düzeyinde dört bölgeye ayırmışlardır. K-Means Algoritması çok değişkenli istatistik tekniklerden biri olarak ele alınmış, değişkenler arasında çoklu doğrusal bağlantı olup olmaması durumu VIF (Variance Inflation Factor) değerlerine bakılarak incelenmiştir.

Muttaqin (2022) çalışmasında Endonezya'nın Sumatra adasının ilçe ve şehirlerini çok değişkenli istatistik analizi tekniklerinden biri olan kümeleme analizini kullanarak İnsani Gelişmişlik İndeksine göre yüksek, orta ve düşük olarak üç kategoriye ayırmışlardır. Bu çalışmada oluşturulan üç kümenin birbirlerinden anlamlı bir şekilde farklı olup olmadığını test etmek için Anova Analizi yapılmıştır.

3. Kümeleme Algoritmaları

Kümeleme Algoritmaları Çok Değişkenli İstatistik Teknikler başlığı altında ve Veri Madenciliği Teknikleri başlığı altında incelenen pek çok çalışmada kullanılmış ve kullanılmakta olan oldukça temel bir konudur. Bu çalışmada Veri Madenciliği Teknikleri başlığı altında kümeleme algoritmalarının incelenmesi hedeflenmiştir. Kümeleme algoritmaları temel olarak Hiyerarşik (Hierarchical Methods) ve Hiyerarşik Olmayan

Yöntemler (Partitioning Methods) olarak iki ana başlık altında incelenebilmektedir (Pujari, 2001; Kurnaz vd, 2022). Bununla birlikte daha ileri düzey gelişmiş tekniklerle birlikte, Hiyerarşik Olmayan Yöntemler/ Bölümleme Yöntemleri (Partitioning Methods), Hiyerarşik Yöntemler (Hierarchical Methods), Yoğunluk Bazlı Yöntemler (Density Based Methods) ve Izgara Bazlı Yöntemler (Grid Based Methods) olarak dört başlıkta da incelenebilmektedir (Han vd., 2023). Bu ayrımı ileri düzey tekniklerin eklenmesiyle artırmak mümkündür (Ezugwu vd., 2022).

3.1. Hiyerarşik Olmayan Yöntemler (Partitioning Techniques)

Bölümlemeli Yöntemler veya diğer adıyla Hiyerarşik Olmayan Yöntemler öncelikle "k" parametresinin araştırmacı tarafından önceden belirlenmesini gerektirmektedir. Bu yöntemler içerisinde literatürde en çok karşımıza çıkan algoritma K-Means Algoritması olmakla birlikte K-Medoids ve K-Modes Algoritmaları da bu bölüm altında incelenmektedir (Pujari vd., 2001; Han, 2023).

3.1.1. K-Means Algoritması

K-Means Algoritması, MacQueen tarafından 1967 yılında geliştirilmiş olup daha sonra farklı algoritmalar da üretilmiştir (MacQueen, 1967; Morissette and Chartier 2013). K-means Algoritması kavramsal olarak sezgisel ve uygulanabilirliği kolay bir yöntem olarak literatürde çok sayıda uygulamada karşımıza çıkmaktadır. Ezugwu vd. (2022)'de yapılan çalışmaya göre, K-Means Algoritması diğer kümeleme algoritmalarına kıyasla literatürde en çok kullanılan algoritma olarak tespit edilmiştir.

Merkez bazlı algoritmalar olarak da ifade edilen K-Means Algoritması, veri setini oluşturan gözlemleri, birbirleriyle ortak bir eleman içermeyen k sayıda kümeye ayırmaktadır. Burada "k" parametresinin belirlenmesi veri setinin özelliklerine göre araştırmacının öngörüsüne dayanmaktadır. "k" parametresinin belirlenmesiyle ilgili olarak Calinski-Harabasz index, Gap Statistic gibi yöntemler de literatürde kullanılan bazı yöntemlerdir (Han, 2023). K-Means Algoritması sadece nümerik değerler olduğunda ve veri seti içindeki kümelerin konveks yapıda olması durumunda kullanılabilmektedir (Kameshwaran ve Malarvizhi K, 2014). Bu algoritmada, her bir kümenin merkezi, kümeyi oluşturan gözlemlerin aritmetik ortalaması alınarak hesaplanmaktadır. Her bir kümeyi temsil eden küme merkezi ile gözlemler arasındaki uzaklıklar genellikle Öklid Algoritması ile hesaplanmaktadır. Ancak uzaklık ölçüsü olarak Öklid Algoritmasının dışında, Manhattan Mesafesi, Minkowski Mesafesi gibi diğer uzaklık ölçüleri de kullanılabilmektedir (Han, 2023). K-Means Algoritmasında, her bir kümeyi oluşturan gözlemlerin ait oldukları küme merkezlerine olan mesafelerinin toplamını bir diğer ifadeyle küme içi varyanslarını en küçük yapacak gözlemlerin biraraya getirilmesi hedeflenmektedir.

K-Means Algoritması İterasyonlar

1. Küme sayısının (k) belirlenmesi
2. Verisetindeki tüm gözlemlerin her birinin kendisine en yakın uzaklıktaki kümeye atanması
3. Küme merkezlerinin hesaplanması

$$M_k = \frac{1}{n_k}\sum_{i=1}^{n_k} x_{ik}$$

4. Her bir gözlemin küme merkezlerine uzaklıklarının hesaplanması
5. Küme içi varyanslarının hesaplanması

$$e_i^2 = \sum_{i=1}^{n_k}(x_{ik} - M_k)^2$$

Bu iterasyonlar ikinci aşamadan başlayarak küme içi varyasyon en küçük kalacak biçimde gözlemlerin yer değiştirmesi ile devam etmektedir. Küme içi varyasyonu en küçük olduğunda iterasyon sonlandırılmaktadır. Burada k, küme sayısını, n, veri seti içindeki gözlem sayısını, x_{ik}, k. kümeye ait i. gözlemi, M_k, k. kümenin merkezini, e_i^2, hata karelerini ifade etmektedir.

Gözlem sayısının büyüklüğü, küme sayısının fazla olması gibi değişkenliklere bağlı olarak algoritmanın sonuca ulaşma süresi de değişmektedir. Bu anlamda büyük veri setlerine de uygulanabilir bir yöntemdir. Ancak veri seti içerisinde aykırı gözlemlerin olması küme merkezlerini etkileyeceğinden iterasyon süresi de buna bağlı olarak değişmektedir (Han, 2023). Bununla birlikte, veri setini oluşturan gözlemlerin konveks olarak gruplanabildiği ve lineer olarak ayrılabildiği durumlarda oldukça kullanışlı bir yöntem olmakla birlikte, belirtilen durumların dışında kullanıldığında etkinliğini yitirmektedir (Han, 2023).

3.1.2. K-Medoids Algoritması

K-Medoids Algoritması veya bir diğer adı ile PAM (Partitioning Around Medoids) Algoritması, 1990 yılında Kaufman ve Rousseeuw (1990) tarafından geliştirilmiştir. K-Medoids Algoritması merkez bazlı yöntemlerden biri olup aslında, K-Means Algoritmasının aykırı değerler ve gürültü içeren veri setleri için daha iyileştirilmiş bir hali olarak literatürde kullanılmakta olan bir yöntemdir. K-Medoids Algoritmasının K-Means Algoritmasından farkı oluşturulan kümelerin merkezi olarak, kümeyi oluşturan gözlemlerin aritmetik ortalamasından oluşan bir merkez seçmek yerine, kümenin içinden bir gözlem noktasının merkez olarak belirlenmesidir. Algoritma, seçilen merkez nokta ile diğer gözlemler arasındaki mesafelerin toplamı minimum olana kadar devam etmektedir (Han, 2023).

PAM Algoritması İterasyonlar

1. Küme sayısının (k) belirlenmesi
2. Verisetindeki tüm gözlemlerin her birinin kendisine en yakın uzaklıktaki kümeye atanması
3. Oluşturulan her bir küme için küme merkezi olabilecek bir gözlemin belirlenmesi
4. Her bir gözlemin küme merkezlerine uzaklıklarının hesaplanması
5. Küme içi varyanslarının hesaplanması

$$e_i^2 = \sum_{i=1}^{n_k}(x_{ik} - M_k)^2$$

Bu iterasyonlar üçüncü aşamadan başlayarak küme içi varyasyon en küçük kalacak biçimde gözlemlerin yer değiştirmesi ile devam etmektedir. Küme içi varyasyonu en küçük olduğunda iterasyon sonlandırılmaktadır. PAM Algoritması çok büyük veri setlerinde iterasyon sayısı artacağından çok elverişli bir yöntem olmayabilir. Bu durumda bu soruna çözüm olarak geliştirilen CLARA Algoritması kullanılabilir (Kassambara, 2017).

K-Medoids Algoritması başlığı altında incelenen bir diğer Algoritma ise PAM Algoritmasının büyük veri setleri için geliştirilmiş hali olan CLARA (Clustering Large Applications) algoritmasıdır (Kassambara, 2017).

3.1.3. CLARA Algoritması (Clustering Large Applications)

CLARA Algoritması, Kaufman ve Rousseeuw tarafından 1990 yılında geliştirilen PAM algoritmasının büyük veri setleri için geliştirilmiş bir halidir (Kaufman ve Rousseeuw, 1990). CLARA Algoritmasında PAM Algoritmasından farklı olarak bütün veri seti içinde k farklı küme oluşturmak yerine veri seti tesadüfi olarak belirlenmiş belirli sayıdaki gözlem kümelerine ayrılarak küme merkezleri belirlenir.

CLARA Algoritması İterasyonlar

1. Veri setini oluşturan gözlemler belirli sayıdaki birimden oluşan alt kümelere tesadüfi olarak ayrılır.
2. Bundan sonraki aşamada oluşturulan her bir alt kümeye yukarıda ifade edilen PAM Algoritmasının aşamaları uygulanır.
3. Her bir küme içi hata kareleri toplamı(varyansların)nın hesaplanması

$$e_i^2 = \sum_{i=1}^{n_k} (x_{ik} - M_k)^2$$

3.2. Hiyerarşik Yöntemler (Hierarchical Techniques)

Hiyerarşik yöntemler genel olarak birleştirici (aşağıdan yukarıya) ve ayrıştırıcı/bölücü (yukarıdan aşağıya) yöntemler olarak iki başlık altında incelenmektedir. Birleştirici yöntemler veri setindeki tek bir gözlem biriminden başlayarak benzer özellikteki ikinci gözlemin eklenmesiyle aşağıdan yukarıya doğru ilerleyen bir yapıdır. Ayrıştırıcı/ Bölücü Yöntemler ise bütün veri setini oluşturan gözlemleri tek bir veri seti olarak kabul ederek başlayan ve benzer özellikteki gözlemleri bir araya getirmek için en uygun küme sayısına göre gözlemleri gruplara ayıran bir yapıdır (Berkhin, 2002). Hiyerarşik Yöntemlerde bir gözlem herhangi bir kümeye atandıktan sonra başka bir kümeye geçirilmesi durumu söz konusu olmamaktadır (Han, 2023). Bununla birlikte hiyerarşik olmayan yöntemlerden farklı olarak küme sayısının önceden araştırmacı tarafından belirlenmesi gerekmemektedir. Bu durum araştırmacılar açısından bir kolaylık gibi görünse de verisetinin hiyerarşik bir yapıya sahip olmaması durumunda hiyerarşik yöntemlerin seçilmesi konusunda dikkatli olunması gerekmektedir (Everitt, 2011). Hiyerarşik Yöntemlerde küme sayısının belirlenmesinde Dendrogram adı verilen ağaç diyagramından yararlanılmaktadır (James vd., 2013).

3.2.1. Birleştirici (Agglomerative) Yöntemler

Birleştirici Yöntemler, Hiyerarşik Yöntemler içerisinde literatürde en çok kullanılan yöntemler olarak görülmektedir. En Yakın Komşuluk Algoritması (Single Linkage), En Uzak Komşu Algoritması (Complete Linkage), Ortalama Bağlantı Yöntemi (Group Average Linkage), Ward Yöntemi (Ward's Method) ise en fazla bilinen birleştirici algoritmalardır. Bu algoritmaların dışında literatürde var olan diğer Birleştirici Algoritmalar ise, Merkezi Bağlantı Yöntemi (Centroid Linkage), Ağırlıklı Ortalama Bağlantı Yöntemi (Weighted Average Linkage), Median Bağlantı Yöntemi (Median Linkage) olarak sıralanabilir (Everit, 2011). Hiyerarşik Yöntemler mesafeye dayalı yöntemler olup gözlemler arasındaki mesafenin hesaplanmasında sıklıkla Öklid Mesafesi kullanılmaktadir. Bunun dışında Manhattan Mesafesi, Minkowski Mesafesi, City Block Mesafesi gibi diğer mesafe ölçüleri de kullanılabilmektedir (Everit, 2011; Bramer, 2016).

En Yakın Komşuluk Algoritması (Single Linkage)

En Yakın Komşuluk Algoritmasında temel yaklaşım gözlemler arasındaki mesafenin en küçük olması şeklindedir. Başlangıçta her bir gözlem tek başına bir küme olarak kabul edilir. İkinci aşamada ise bütün gözlemler arasındaki mesafeler yukarıda bahsedilen mesafe ölçüleri kullanılarak hesaplanır. Aralarındaki mesafenin en küçük olduğu iki gözlem birleştirilerek yeni bir küme olarak kabul edilir bundan sonraki aşamada yine var olan kümeler arasındaki mesafeler hesaplanarak kümeler birleştirilir. Bu işlem bütün gözlemler tek bir kümede birleşene kadar devam ettirilir (Bramer, 2016).

En Yakın Komşuluk Algoritması İterasyonlar

1. Öncelikle gözlemler arasındaki uzaklıklar hesaplanır.
2. Birbirine en benzer özellikteki gözlemleri birleştirebilmek için $min\, d(i,j)$ belirlenir.
3. Minimum uzaklığa sahip gözlemler birleştirilerek yeni bir küme elde edilir. Bu duruma göre uzaklıklar yeniden hesaplanır.
4. Birden fazla gözlem değerine sahip iki küme söz konusu olduğunda, iki farklı küme içinden alınan gözlemler arasında birbirine en yakın olanların uzaklığı iki kümenin birbirine olan uzaklığı olarak kabul edilir.

$$d_{A\to B} = \min_{\substack{\forall i\in A \\ j\in B}} d_{i,j}$$

5. Bütün gözlem birimleri tek bir kümede birleşene kadar iterasyonlar devam ettirilir.

Burada $d(i,j)$; i. ve j. gözlemler arasındaki mesafeyi ifade etmektedir (Özkan, 2013).

En Uzak Komşu Algoritması (Complete Linkage)

En Uzak Komşu Algoritması, En Yakın Komşu Algoritmasından farklı olarak küme içindeki farklılığın maksimum olması esasına dayanır (James, 2013). Burada da algoritmanın işleyişi En Yakın Komşu Algoritmasında ifade edildiği gibi birbirlerine en yakın olan gözlemlerin birleştirilmesi şeklindedir (Bramer, 2016).

En Uzak Komşuluk Algoritması İterasyonlar

1. Öncelikle gözlemler arasındaki uzaklıklar belirlenir.
2. Daha sonra uzaklıklar dikkate alınarak $min\, d(i,j)$ belirlenir. (En Yakın Komşu Algoritmasında olduğu gibi)
3. Minimum uzaklığa sahip gözlemler birleştirilerek yeni bir küme elde edilir. Bu duruma göre uzaklıklar yeniden hesaplanır.
4. Birden fazla gözlem değerine sahip iki küme söz konusu olduğunda, iki farklı küme içinden alınan gözlemler arasında birbirine en uzak gözlemler arasındaki mesafe iki kümenin birbirine olan uzaklığı olarak kabul edilir.
   $d_{A\to B} = \max_{\substack{\forall i\in A \\ j\in B}} d_{i,j}$
5. Bütün gözlem birimleri tek bir kümede birleşene kadar iterasyonlar devam ettirilir.

Burada $d(i,j)$; i. ve j. gözlemler arasındaki mesafeyi ifade etmektedir (Özkan, 2013).

Ortalama Bağlantı Yöntemi (Average Linkage)

En Yakın Komşu Algoritması (Single Linkage) ve En Uzak Komşu Algoritmalarında (Complete Linkage) mesafelerin hesaplanmasında minimum ve maksimum değerlerin kullanılmasından dolayı aykırı değerlere daha duyarlıdır. Ortalama Bağlantı Yönteminde gözlemler arasındaki mesafeler hesaplanırken gözlem değerlerinin ortalaması hesaplanır. Bu durum aykırı değerlerin var olduğu veri setlerinde daha iyi sonuç alınmasına olanak sağlamaktadır (Han, 2023).

Ortalama Bağlantı Algoritması İterasyonlar

1. Öncelikle gözlemler arasındaki uzaklıklar belirlenir.
2. Daha sonra uzaklıklar dikkate alınarak $min\, d(i,j)$ belirlenir. (En Yakın Komşu Algoritmasında olduğu gibi)
3. Minimum uzaklığa sahip gözlemlerden oluşan yeni bir küme elde edilir. Bu duruma göre uzaklıklar yeniden hesaplanır.
4. Birden fazla gözlem değerine sahip iki küme söz konusu olduğunda iki kümenin birbirine olan uzaklığı hesaplanırken kümeyi oluşturan gözlem mesafelerinin ortalaması alınır (Everitt, 2011).
   $d_{A\to B} = \operatorname{ort}_{\substack{\forall i\in A \\ j\in B}} d_{i,j}$
5. Bütün gözlem birimleri tek bir kümede birleşene kadar iterasyonlar devam ettirilir.

Burada $d(i,j)$; i. ve j. gözlemler arasındaki mesafeyi ifade etmektedir.

Ward Yöntemi (Ward's Method)

Ward Yöntemi 1963 yılında Ward tarafından geliştirilmiştir (Ward, 1963). Daha önce bahsettiğimiz hiyerarşik algoritmalarda gözlemler arası mesafeye dayanan bir yaklaşım mevcut iken Ward Algoritması K-Means yöntemine benzer şekilde grup içi varyanslarını en küçük yapacak gözlemleri biraraya getirmeyi hedeflemektedir. Bu nedenle bu yöntemde elde edilen küme büyüklüklerinin yaklaşık olarak eşit olma eğiliminde olduğu görülmektedir (Hair vd., 2014).

3.2.2. Ayrıştırıcı (Divisive) Yöntemler

Hiyerarşik Kümeleme Yöntemleri başlığı altnda incelenen bir diğer grup kümeleme algoritması ise Ayrıştırıcı Yöntemler olarak incelenmektedir. Ayrıştırıcı Yöntemler, Birleştirici Yöntemlerden farklı olarak başlangıçta incelenen veri setini tek bir küme olarak kabul ederek daha sonra birbirinden farklı özelliklerine göre veri setini gruplara ayırmaktadır. Ancak bu yöntem Ayrıştırıcı Yöntemlere göre uygulanabilirliği daha zor olduğundan daha az tercih edilmektedir.

3.3. Yoğunluk Bazlı Yöntemler (Density Based Methods)

Yoğunluk Bazlı Yöntemler, veri seti içindeki gruplanmaların konveks yapıda olmadığı durumlarda kümeleri ayrıştırmada oldukça başarılıdır. DBSCAN Algoritması Yoğunluk Bazlı Yöntemler içerisinde en çok literatürde karşımıza çıkan algoritmalardan birisidir. Yoğunluk Bazlı Yöntemlerin en önemli avantajı, analiz öncesinde küme sayının belirlenmesinin gerekmemesi, gürültü içeren veri setlerinde kullanılabiliyor olması ve aykırı değerlerin belirlenmesinde başarılı olmasıdır (Kameshwaran, 2014). Ancak boyut nedeniyle çok büyük boyutlu veri setlerinde kullanımı elverişli değildir (Ezugwu, 2022).

3.4. Izgara Bazlı Yöntemler (Grid Based Methods)

Çok büyük boyutlu veri setlerinde Yoğunluk Bazlı Yöntemlerin etkili bir çözüm sunamamasına karşılık, Izgara Bazlı Yöntemler veri setini küçük parçalara ayırarak incelemekte bu nedenle de daha hızlı bir çözüm sunabilmektedir (Han, vd., 2023). Izgara bazlı yöntemlerde veri seti ızgara yapısına benzer şekilde küçük parçalara ayrılmakta ve her bir parçanın yoğunluğu hesaplanmaktadır. Daha önceden belirlenen bir eşik değere göre her bir parçanın yoğunluğuna karar verilmektedir.

3. Bulgular

Bu çalışmada hiyerarşik olmayan yöntemlerden K-Means Algoritması ve K-Medoids Algoritması, hiyerarşik yöntemlerden En Yakın Komşuluk Algoritması (Single Linkage), En Uzak Komşu Algoritması (Complete Linkage), Ortalama Bağlantı Yöntemi (Average Linkage), Ward Yöntemi ve Yoğunluk Bazlı Yöntemlerden DBSCAN Algoritmasının kullanıldığı 55 farklı model oluşturulmuştur. Ancak Silhouette Skoruna göre anlamlı 39 model çalışmada sunulmuştur. Ayrıca metodoloji kısmında açıklanan CLARA Algoritması ve Izgara Bazlı Yöntemler verisetinin boyutu nedeniyle analize dahil edilmemiştir. Elde edilen sonuçlar bu veri seti üzerinden Birleşmiş Milletler Kalkınma Programı tarafından yapılmış gerçek sınıflamalarla karşılaştırılmıştır. Çalışma Birleşmiş Milletler Kalkınma Programı tarafından açıklanan en güncel veri seti üzerinde yapılmıştır. Verisetindeki değerler normalize edildikten sonra sırasıyla En Yakın Komşu Algoritması (Single Linkage), Average Linkage, En Uzak Komşu Algoritması (Complete Linkage) ve Ward Yöntemleri için dendrogramlar elde

edilmiştir. Elde edilen diyagram sonuçlarına göre 4 veya 5 kümelemenin uygun olacağı tespit edilmiştir.

Tablo 1. Silhouette skoruna göre model sıralaması

No	Model	Standardizasyon	k değeri	Silhouette Skoru
1	Ward(k=6)	MinMax	6	0.79
2	Completelink(k=6)	MinMax	6	0.78
3	Averagelink(k=6)	MinMax	6	0.77
4	Ward(k=4)	MinMax	4	0.77
5	Ward(k=5)	MinMax	5	0.77
6	Completelink(k=5)	MinMax	5	0.76
7	Averagelink(k=4)	MinMax	4	0.74
8	Averagelink(k=5)	MinMax	5	0.74
9	Completelink(k=4)	MinMax	4	0.74
10	Kmedoids(k=4)	MinMax	4	0.71
11	Completelink(k=4)	StdScaler	4	0.6
12	Completelink(k=5)	StdScaler	5	0.6
13	Singlelink(k=4)	MinMax	4	0.54
14	Singlelink(k=4)	StdScaler	4	0.54
15	Singlelink(k=5)	MinMax	5	0.53
16	Singlelink(k=6)	MinMax	6	0.53
17	Averagelink(k=4)	StdScaler	4	0.5
18	Averagelink(k=5)	StdScaler	5	0.5
19	Ward(k=4)	StdScaler	4	0.5
20	Averagelink(k=6)	StdScaler	6	0.49
21	Kmedoids(k=4)	StdScaler	4	0.48
22	Completelink(k=6)	StdScaler	6	0.48
23	Ward(k=6)	StdScaler	6	0.46
24	Ward(k=5)	StdScaler	5	0.38
25	Kmeans(k=4)	MinMax	4	0.33
26	Kmedoids(k=5)	MinMax	5	0.32
27	Kmeans(k=4)	StdScaler	4	0.31
28	Kmeans(k=8)	MinMax	8	0.31
29	Kmeans(k=5)	StdScaler	5	0.3
30	Kmeans(k=7)	StdScaler	7	0.29
31	Kmeans(k=5)	MinMax	5	0.28
32	Kmeans(k=6)	MinMax	6	0.28
33	Kmeans(k=8)	StdScaler	8	0.28
34	Dbscan(k=6)	StdScaler	6	0.28
35	Singlelink(k=6)	StdScaler	6	0.27
36	Kmeans(k=7)	MinMax	7	0.26
37	Kmedoids(k=5)	StdScaler	5	0.24
38	Kmeans(k=6)	StdScaler	6	0.23
39	Singlelink(k=5)	StdScaler	5	0.17

K-Means ve K-Medoids Algoritmalarını uygulamadan önce küme sayısının belirlenmesinde Elbow Yöntemi kullanılmış ancak yapılan farklı denemelere göre k değerinin 10 ve üzerinde olması gerektiği sonucu elde edilmiştir. Şekil 1' de Hiyerarşik Kümeleme Algoritmaları için yapılan dendrogram sonucu görülmektedir. Buna göre 4 veya 5 kümelenmenin uygun olacağı görülmektedir. Şekil 2' de ise Hiyerarşik Olmayan Kümeleme Algoritmaları için küme sayısının belirlenmesinde kullanılan Elbow Grafiği görülmektedir.
Küme sayısı Birleşmiş Milletlerin öngördüğü şekilde 4 küme olacak şekilde ve bununla birlikte Dendrogram ve Elbow Yöntemlerinin sonuçları dikkate alınarak 4 ile 10 arasında farklı küme sayıları için de belirtilen tüm yöntemler uygulanmıştır. Oluşturulan kümelerin uygunluğu için Silhouette Skoru değerleri elde edilmiştir. Silhouette Skoru değerine göre modeller en yüksek skoru veren modelden en düşük skoru veren modele doğru Tablo 1' de verilmiştir.

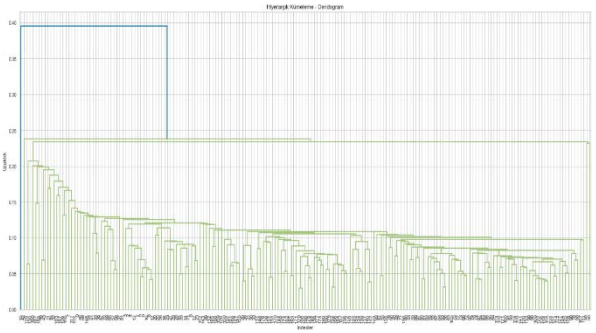

Şekil1. Hiyerarşik kümeleme için dendrogram grafiği.

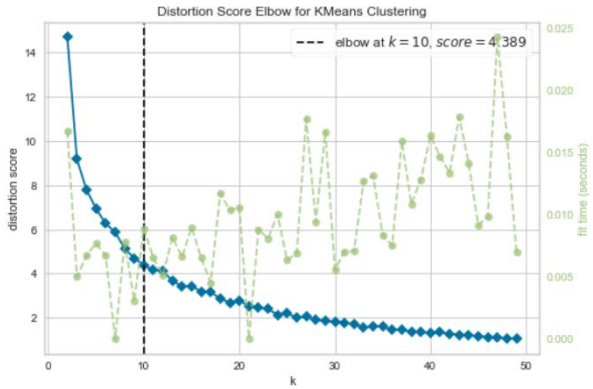

Şekil2. Hiyerarşik olmayan kümeleme için Elbow grafiği

Elde edilen sonuçlara göre en iyi kümelenme Ward tekniği ile k küme sayısının 6 olması durumunda elde edilmiştir. Ancak Birleşmiş Milletlerin öngördüğü şekilde 4 küme olmaya zorladığımızda da yine en iyi sonuç Ward Tekniği ile elde edilmiştir. Tablo 2' de Ward Tekniği 6 küme için yapıldığında elde edilen kümeleme sonucu verilmiştir.
Tablo 2, Tablo3, Tablo4, Tablo5, Tablo6 ve Tablo7' de Ward Tekniği 6 küme için yapıldığında elde edilen kümeleme sonuçları her küme için ayrı ayrı tablolar ile verilmiştir. Bu tablolar Ward Tekniği 6 küme için yapıldığında elde edilen sonuçları ve Birleşmiş Milletler tarafından yapılan sıralamayı da içerecek biçimde düzenlenmiştir.
Tablo 8, Tablo 9, Tablo 10 ve Tablo 11 ise Birleşmiş Milletlerin öngördüğü biçimde 4 küme oluşturulduğunda elde edilen sonuçları her bir küme ayrı bir tablo olacak şekilde göstermektedir. 4 küme için de en iyi sonuç Ward Tekniği ile elde edilmiştir.

Tablo2. Ward Tekniğine göre oluşturulan k=6 küme için Küme 1 Sonuçları

Küme No	Ülke No	BMI Sıralaması
1	İsviçre	1
1	Norveç	2
1	İzlanda	3
1	Hong Kong, Çin (SAR)	4
1	Danimarka	5
1	İsveç	5
1	İrlanda	7
1	Almanya	7
1	Singapur	9
1	Avustralya	10
1	Hollanda	10
1	Finlandiya	12
1	Belçika	12
1	Lihtenştayn	12
1	Birleşik Krallık	15
1	Yeni Zelanda	16
1	Birleşik Arap Emirlikleri	17
1	Kanada	18
1	Kore (Cumhuriyeti)	19
1	Lüksemburg	20
1	Amerika Birleşik Devletleri	20
1	Slovenya	22
1	Avusturya	22
1	Japonya	24
1	İsrail	25
1	Malta	25
1	İspanya	27
1	Fransa	28
1	Kıbrıs	29
1	İtalya	30
1	Estonya	31
1	Çekya	32
1	Yunanistan	33
1	Bahreyn	34
1	Andorra	35
1	Polonya	36
1	Litvanya	37
1	Letonya	37
1	Hırvatistan	39
1	Suudi Arabistan	40
1	Katar	40
1	Portekiz	42
1	San Marino	43
1	Şili	44
1	Slovakya	45
1	Macaristan	47
1	Arjantin	48
1	Kuveyt	49
1	Karadağ	50
1	Brunei Darussalam	55

Tablolar incelendiğinde, Ward Tekniği ile elde edilen sonuçların Birleşmiş Milletler tarafından açıklanan listeyle uyumlu olduğu görülmektedir. Bu durum uygulanan kümeleme algoritmalarının kullanılmasının pratikte önemli bir katkı sağlayacağını göstermektedir.

Tablo 3. Ward Tekniğine göre oluşturulan k=6 küme için Küme 2 Sonuçları

Küme No	Ülke No	BMI Sıralaması
2	Fas	120
2	Butan	125
2	Hindistan	134
2	Guatemala	136
2	Lao Demokratik Halk Cumhuriyeti	139
2	Sao Tome ve Principe	141
2	Namibya	142
2	Esvatini (Krallık)	142
2	Myanmar	144
2	Nepal	146
2	Kenya	146
2	Kamboçya	148
2	Kongo	149
2	Kongo (Demokratik Cumhuriyeti)	149
2	Angola	150
2	Kamerun	151
2	Komorlar	152
2	Zambiya	153
2	Doğu Timor	155
2	Solomon Adaları	156
2	Suriye Arap Cumhuriyeti	157
2	Zimbabve	159
2	Nijerya	161
2	Togo	163
2	Tanzanya (Birleşik Cumhuriyeti)	167
2	Lesoto	168
2	Malawi	172

Tablo 4. Ward Tekniğine göre oluşturulan k=6 küme için Küme 3 Sonuçları

Küme No	Ülke No	BMI Sıralaması
3	Ekvator Ginesi	133
3	Papua Yeni Gine	157
3	Haiti	158
3	Uganda	159
3	Ruanda	161
3	Moritanya	164
3	Pakistan	164
3	Fildişi Sahili	166
3	Senegal	169
3	Sudan	170
3	Cibuti	171
3	Benin	173
3	Gambiya	174
3	Eritre	175
3	Etiyopya	176
3	Madagaskar	177
3	Liberya	177
3	Gine-Bissau	179
3	Gine	181
3	Afganistan	182
3	Mozambik	183
3	Sierra Leone	184
3	Burkina Faso	185
3	Yemen	186
3	Burundi	187
3	Mali	188
3	Nijer	189
3	Çad	189
3	Orta Afrika Cumhuriyeti	191
3	Güney Sudan	192

Tablo 5. Ward Tekniğine göre oluşturulan k=6 küme için Küme 4 Sonuçları

Küme No	Ülke No	BMI Sıralaması
4	Romanya	53
4	Rusya Federasyonu	56
4	Bahamalar	57
4	Panama	57
4	Umman	59
4	Trinidad ve Tobago	60
4	Gürcistan	60
4	Malezya	63
4	Sırbistan	65
4	Kazakistan	67
4	Seyşeller	67
4	Belarus	69
4	Bulgaristan	70
4	Palau	71
4	Mauritius	72
4	Arnavutluk	74
4	Ermenistan	76
4	Sri Lanka	78
4	İran (İslam Cumhuriyeti)	78
4	Bosna Hersek	80
4	Saint Vincent ve Grenadinler	81
4	Kuzey Makedonya	83
4	Küba	85
4	Moldova (Cumhuriyeti)	86
4	Azerbaycan	89
4	Türkmenistan	94
4	Tonga	98
4	Ürdün	99
4	Ukrayna	100
4	Fiji	104
4	Özbekistan	106
4	Lübnan	109
4	Filistin Devleti	111
4	Samoa	116
4	Kırgızistan	117
4	Venezuela (Bolivar Cumhuriyeti)	119
4	Tacikistan	126

Tablo 6. Ward Tekniğine göre oluşturulan k=6 küme için Küme 5 Sonuçları

Küme No	Ülke No	BMI Sıralaması
5	Libya	92
5	Guyana	95
5	Dominika	97
5	Paraguay	102
5	Marshall Adaları	102
5	Mısır	105
5	Vietnam	107
5	Aziz Lucia	108
5	Güney Afrika	110
5	Endonezya	112
5	Filipinler	113
5	Botsvana	114
5	Jamaika	115
5	Belize	118
5	Bolivya (Çokuluslu Devlet)	120
5	Gabon	123
5	Surinam	124
5	El Salvador	127
5	Irak	128
5	Bangladeş	129
5	Nikaragua	130
5	Yeşil Burun Adaları	131
5	Tuvalu	132
5	Mikronezya (Federal Devletleri)	135
5	Kiribati	137
5	Honduras	138
5	Vanuatu	140
5	Gana	145

Tablo 7. Ward Tekniğine göre oluşturulan k=6 küme için Küme 6 Sonuçları

Küme No	Ülke No	BMI Sıralaması
6	Türkiye	45
6	Saint Kitts ve Nevis	51
6	Uruguay	52
6	Antigua ve Barbuda	54
6	Barbados	62
6	Kosta Rika	64
6	Tayland	66
6	Grenada	73
6	Çin	75
6	Meksika	77
6	Dominik Cumhuriyeti	82
6	Ekvador	83
6	Peru	87
6	Maldivler	87
6	Brezilya	89
6	Kolombiya	91
6	Cezayir	93
6	Moğolistan	96
6	Tunus	101

Tablo 8. Ward Tekniğine göre oluşturulan k=4 küme için Küme 1 Sonuçları

Küme No	Ülke No	BMI Sıralaması
1	Fas	120
1	Butan	125
1	Ekvator Ginesi	133
1	Hindistan	134
1	Guatemala	136
1	Lao Demokratik Halk Cumhuriyeti	139
1	Sao Tome ve Principe	141
1	Namibya	142
1	Esvatini (Krallık)	142
1	Myanmar	144
1	Nepal	146
1	Kenya	146
1	Kamboçya	148
1	Kongo	149
1	Kongo (Demokratik Cumhuriyeti)	149
1	Angola	150
1	Kamerun	151
1	Komorlar	152
1	Zambiya	153
1	Doğu Timor	155
1	Solomon Adaları	156
1	Suriye Arap Cumhuriyeti	157
1	Papua Yeni Gine	157

1	Haiti	158
1	Zimbabve	159
1	Uganda	159
1	Nijerya	161
1	Ruanda	161
1	Togo	163
1	Moritanya	164
1	Pakistan	164
1	Fildişi Sahili	166
1	Tanzanya (Birleşik Cumhuriyeti)	167
1	Lesoto	168
1	Senegal	169
1	Sudan	170
1	Cibuti	171
1	Malawi	172
1	Benin	173
1	Gambiya	174
1	Eritre	175
1	Etiyopya	176
1	Madagaskar	177
1	Liberya	177
1	Gine-Bissau	179
1	Gine	181
1	Afganistan	182
1	Mozambik	183
1	Sierra Leone	184
1	Burkina Faso	185
1	Yemen	186
1	Burundi	187
1	Mali	188
1	Nijer	189
1	Çad	189
1	Orta Afrika Cumhuriyeti	191
1	Güney Sudan	192

Tablo 9. Ward Tekniğine göre oluşturulan k=4 küme için Küme 2 Sonuçları

Küme No	Ülke	BMI Sıralaması
2	Türkiye	45
2	Saint Kitts ve Nevis	51
2	Uruguay	52
2	Romanya	53
2	Antigua ve Barbuda	54
2	Rusya Federasyonu	56
2	Bahamalar	57
2	Panama	57
2	Umman	59
2	Trinidad ve Tobago	60
2	Gürcistan	60
2	Barbados	62
2	Malezya	63
2	Kosta Rika	64
2	Sırbistan	65
2	Tayland	66
2	Kazakistan	67
2	Seyşeller	67
2	Belarus	69
2	Bulgaristan	70
2	Palau	71
2	Mauritius	72
2	Grenada	73
2	Arnavutluk	74
2	Çin	75
2	Ermenistan	76
2	Meksika	77
2	Sri Lanka	78
2	İran (İslam Cumhuriyeti)	78
2	Bosna Hersek	80
2	Saint Vincent ve Grenadinler	81
2	Dominik Cumhuriyeti	82
2	Kuzey Makedonya	83
2	Ekvador	83
2	Küba	85
2	Moldova (Cumhuriyeti of)	86
2	Peru	87
2	Maldivler	87
2	Brezilya	89
2	Azerbaycan	89
2	Kolombiya	91
2	Cezayir	93
2	Türkmenistan	94
2	Moğolistan	96
2	Tonga	98
2	Ürdün	99
2	Ukrayna	100
2	Tunus	101
2	Fiji	104
2	Özbekistan	106
2	Lübnan	109
2	Filistin, Devlet	111
2	Samoa	116
2	Kırgızistan	117
2	Venezuela (Bolivar Cumhuriyeti)	119
2	Tacikistan	126

Tablo 10. Ward Tekniğine göre oluşturulan k=4 küme için Küme 3 Sonuçları

Küme No	Ülke	BMI Sıralaması
3	İsviçre	1
3	Norveç	2
3	İzlanda	3
3	Hong Kong, Çin (SAR)	4
3	Danimarka	5
3	İsveç	5
3	İrlanda	7
3	Almanya	7
3	Singapur	9
3	Avustralya	10
3	Hollanda	10
3	Finlandiya	12
3	Belçika	12
3	Lihtenştayn	12
3	Birleşik Krallık	15
3	Yeni Zelanda	16
3	Birleşik Arap Emirlikleri	17
3	Kanada	18
3	Kore (Cumhuriyeti)	19
3	Lüksemburg	20
3	Amerika Birleşik Devletleri	20
3	Slovenya	22
3	Avusturya	22
3	Japonya	24
3	İsrail	25
3	Malta	25
3	İspanya	27
3	Fransa	28

3	Kıbrıs	29
3	İtalya	30
3	Estonya	31
3	Çekya	32
3	Yunanistan	33
3	Bahreyn	34
3	Andorra	35
3	Polonya	36
3	Litvanya	37
3	Letonya	37
3	Hırvatistan	39
3	Suudi Arabistan	40
3	Katar	40
3	Portekiz	42
3	San Marino	43
3	Şili	44
3	Slovakya	45
3	Macaristan	47
3	Arjantin	48
3	Kuveyt	49
3	Karadağ	50
3	Brunei Darussalam	55

Tablo 11. Ward Tekniğine göre oluşturulan k=4 küme için Küme 4 Sonuçları

Küme No	Ülke	BMI Sıralaması
4	Libya	92
4	Guyana	95
4	Dominika	97
4	Paraguay	102
4	Marshall Adaları	102
4	Mısır	105
4	Vietnam	107
4	Saint Lucia	108
4	Güney Afrika	110
4	Endonezya	112
4	Filipinler	113
4	Botsvana	114
4	Jamaika	115
4	Belize	118
4	Bolivya (Çokuluslu Devlet)	120
4	Gabon	123
4	Surinam	124
4	El Salvador	127
4	Irak	128
4	Bangladeş	129
4	Nikaragua	130
4	Yeşil Burun Adaları	131
4	Tuvalu	132
4	Mikronezya (Federal Devletleri)	135
4	Kiribati	137
4	Honduras	138
4	Vanuatu	140
4	Gana	145

4. Sonuçlar ve Tartışma

Birleşmiş Milletler Kalkınma Programı tarafından ilk olarak 1990 yılında oluşturulmuş ve bu yıldan itibaren her yıl düzenli olarak sunulmakta olan İnsani Gelişim İndeksi sağlıklı yaşam, eğitim ve temel yaşam standartlarına erişim gibi üç temel göstergeye dayanmaktadır.

Bu çalışmada denetimsiz makine öğrenmesi tekniklerinden kümeleme algoritmaları başlığı altında incelenen Hiyerarşik ve Hiyerarşik Olmayan Yöntemler açıklanmış uygulamada Hiyerarşik Olmayan Yöntemlerden K-Means Algoritması ve K-Medoids Algoritması, Hiyerarşik Yöntemlerden En Yakın Komşuluk Algoritması (Single Linkage), En Uzak Komşu Algoritması (Complete Linkage), Ortalama Bağlantı Yöntemi (Average Linkage), Ward Yöntemi ve Yoğunluk Bazlı Yöntemlerden DBSCAN Algoritması kullanılmıştır. Uygulanan bu yöntemlerde k sayısının belirlenmesinde Hiyerarşik Yöntemler için Dendrogram Grafikleri ve Hiyerarşik Olmayan Yöntemler için Elbow Grafiklerinden yararlanılmıştır. Bu analizler dikkate alınarak k sayısının 4 ile 10 arasında değiştiği farklı durumlar için 39 farklı model oluşturulmuştur. Oluştulan modeller elde edilen kümelerin uygunluğunun değerlendirilmesinde kullanılan Silhoutte İndeksi değerlerine göre en yüksekten en düşük Silhoutte değerine sahip modele göre sıralanmıştır. Buna göre Hiyerarşik Tekniklerden Ward Tekniğine göre 6 küme şeklinde yapılan gruplamalar en yüksek Silhoutte skor değerini vermiştir. Ancak model Birlemiş Milletler Kalkınma programının öngördüğü biçimde 4 küme olarak yapıldığında elde edilen kümelenmeler de tablo halinde verilmiştir. Elde edilen sonuçlar, Birleşmiş Milletler Kalkınma programı tarafından yapılmış gerçek sınıflamalarla karşılaştırıldığında sonuçların tutarlı olduğu gözlenmektedir. Bu durum uygulanan kümeleme algoritmalarının pratikte de kullanılabileceğini göstermekte, uzman kişiler için yol gösterici olabileceğine de işaret etmektedir. Bu çalışmada pek çok algoritmanın bir arada incelenerek araştırmacılar için detaylı bir analiz sunması hedeflenmiştir. Bu kapsamda, yapılan çalışmanın, kullanılan yöntemlerin avantajları ve dezavantajları konusunda derinlemesine incelemeler yapması bakımından literatüre önemli bir katkı sağlayacağı düşünülmektedir. Bununla birlikte bu çalışmada ülkelerin gelişmişlik düzeylerine göre ayrımlarının kesin sınırlarla belirlenmesi yerine, makine öğrenmesi tekniklerinden kümeleme algoritmaları kullanılarak değişen koşullara göre gruplamaların yapılabileceği yönünde bir öneri sunulmaktadır.

Katkı Oranı Beyanı

Yazarın katkı yüzdeleri aşağıda verilmiştir. Yazar makaleyi incelemiş ve onaylamıştır.

	L.S.S.
K	100
T	100
Y	100
VTI	100
VAY	100
KT	100
YZ	100
KI	100
GR	100
PY	100
FA	100

K= kavram, T= tasarım, Y= yönetim, VTI= veri toplama ve/veya işleme, VAY= veri analizi ve/veya yorumlama, KT= kaynak tarama, YZ= Yazım, KI= kritik inceleme, GR= gönderim ve revizyon, PY= proje yönetimi, FA= fon alımı.

Çatışma Beyanı

Yazar bu çalışmada hiçbir çıkar ilişkisi olmadığını beyan etmektedir.

Etik Onay Beyanı

Bu araştırmada hayvanlar ve insanlar üzerinde herhangi bir çalışma yapılmadığı için etik kurul onayı alınmamıştır.

Kaynaklar

Berkhin P. 2002. A survey of clustering data mining techniques, In Grouping multidimensional data: Recent advances in clustering. Springer, Berlin, Germany, pp: 25-71.

Bramer M. 2016, Principles of data mining, 3rd. ed. Springer, London,UK, pp: 221-238.

Everitt BS. 2011. Cluster Analysis. Wiley, Londok, UK, ss: 15-110.

Ezugwu AE, Ikotun AM, Oyelade OO, Abualigah L, Agushaka JO, Eke CI, Akinyelu AA. 2022. A comprehensive survey of clustering algorithms: State-of-the-art machine learning applications, taxonomy, challenges, and future research prospects. Eng Appl Artif Intel, 110: 104743.

Hair JF, Black WC, Babin BJ, Anderson RE. 2014. Multivariate statistical analysis. Pearson, New York, US, pp: 415-474.

Han J, Kamber M, Pei J. 2023. Data mining concepts and techniques. Morgan Kaufmann Publications, San Francisco, US, pp: 379-425.

HDI Reports. 2024. Human development index. URL: https://hdr.undp.org/data-center/human-development-index#/indicies/HDI (accesed date: March 11, 2024).

James G, Witten D, Hastie T, Tibshirani R. 2013. An Introduction to Statistical Learning with Applications in R. Springer, New York, US, pp: 516-542.

Kameshwaran K, Malarvizhi K. 2014. Survey on clustering techniques in data mining. Int J Comput Sci Info Technol, 5(2): 2272-2276.

Kassambara A. 2017. Practical guide to clustering analysis in R, unsupervised machine learning. STHDA, Marseille, France, pp: 17-185.

Kaufman L, Rousseeuw P. 1990. Finding groups in data: an introduction to cluster analysis. John Wiley& Sons, New York, USA, pp: 163.

Kurnaz B, Yüksel HM, Önder H, Tırınk C. 2022. 3-D Classification of agricultural areas of Turkey using mammalian livestock existence. BSJ Agri, 5(3): 311-313.

MacQueen J. 1967. Some methods for classification and analysis of multivariate observations. Fifth Berkeley Symposium on Mathematical Statistics and Probability, December 27, Berkeley, US, pp: 281-297.

Morissette L, Chartier S. 2013. The k-means clustering technique: General considerations and implementation in Mathematica. Tutor Quantit Meth Psychol, 9(1): 15-24.

Muttaqin MFJ. 2022. Cluster analysis using k-means method to classify sumatera regency and city based on human development ındex ındicator. Nas Offic Stat, 2022: 967-976.

Neha D, Vidyavathi BM. 2015. A survey on applications of data mining using clustering techniques. Int J Comput Appl, 126(2): 7-12.

Nurhasanah N, Salwa N, Ornila L, Hasan A, Mardhani M. 2021. Classifying regencies and cities on human development index dimensions: Application of K-Means cluster analysis. J Sains Sosio Humaniora, 5(2): 759-765.

Özkan Y. 2013. Veri madenciliği yöntemleri. Papatya Yayınclık, İstanbul, Türkiye, ss: 131-156.

Pujari AK. 2001. Clustering techniques in data mining- A survey. JETE J Res, 47(1&2): 19-28.

Rocha JLM, Zela MAC, Torres NIV, Medina GS. 2021. Analogy of the application of clustering and K-means techniques for the approximation of values of human development indicators. Int J Adv Comput Sci Appl, 12(9): 526-532.

Shah M, Nair S. 2015. A survey of data mining clustering algorithms. Int J Comput Appl, 128(1): 1-5.

Wang H, Feil JH, Yu X. 2023. Let the data speak about the cut-off values for multidimensional index: Classification of human development index with machine learning, Socio-Econ Plan Sci, 87:101523.

Ward JH. 1963. Hierarchical grouping to optimize an objective function. J Amer Stat Assoc, 5(301): 236-244.

Black Sea Journal of Engineering and Science
doi: 10.34248/bsengineering.1581822

Open Access Journal
e-ISSN: 2619 – 8991

Research Article
Volume 8 - Issue 1: 172-178 / January 2025

LATTICE STRUCTURES OF MULTI-FUZZY SOFT SETS

Rabia İŞÇİ[1], Şerife YILMAZ[2]*

[1]*Karadeniz Technical University, Graduate School of Natural and Applied Science, Department of Mathematics, 61080, Trabzon, Türkiye*
[2]*Karadeniz Technical University, Faculty of Science, Department of Mathematics, 61080, Trabzon, Türkiye*

Abstract: The multi-fuzzy soft set theory has recently been introduced and it has started to be applied in some fields such as decision making and medical diagnosis. In this paper, algebraic structure of multi-fuzzy soft sets is studied. Several related properties of some operations on multi-fuzzy soft sets are investigated. Two lattice structures of multi-fuzzy soft sets are constructed. It is shown that these lattices are distributive and whence modular. Additionally, the ordering relations on the lattices of multi-fuzzy soft sets are presented. Moreover, by giving an example, it is indicated that some pairs of operations on multi-fuzzy soft sets do not satisfy the absorption rule which is necessary to form a lattice. So it is proved that a lattice structure cannot be constructed by using these operations.

Keywords: Lattice, Multi-fuzzy set, Multi-fuzzy soft set

***Corresponding author:** Karadeniz Technical University, Faculty of Science, Department of Mathematics, 61080, Trabzon, Türkiye
E mail: serifeyilmaz@ktu.edu.tr (Ş. YILMAZ)
Rabia İŞÇİ https://orcid.org/0000-0003-2426-1873
Şerife YILMAZ https://orcid.org/0000-0002-0282-9483

Received: November 08, 2024
Accepted: December 12, 2024
Published: January 15, 2025

Cite as: İşçi R, Yılmaz Ş. 2025. Lattice structure of multi-fuzzy soft sets. BSJ Eng Sci, 8(1): 172-178.

1. Introduction

A big part of our lives is full of uncertainty and vagueness. Uncertainties are problems waiting to be solved for us. Traditional tools are not always successful to solve these problems. While probability theory, fuzzy set theory (Zadeh, 1965), rough set theory (Pawlak, 1982) and other mathematical tools are well-known and often useful approaches to describe uncertainty, each of these theories has its inherent difficulties as pointed out in Molodtsov (1999)'s paper that introduced the notion of soft set to deal with uncertainty. From then on, the soft set model has been combined with other mathematical models. Sun et al. (2008) proposed the notion of soft modules and studied their basic properties. Jun (2008) introduced the concept of soft BCK/BCI-algebras. Feng et al. (2008) initiated the study of soft semirings, soft ideals on soft semirings and idealistic soft semirings. Kazancı et al. (2010) introduced the concepts of soft BCH-algebra and soft BCH-subalgebra. They discussed some of their properties and structural characteristics. Qin and Hong (2010) gave the lattice structures of soft sets and introduced the concept of soft equality.

Fuzzy set theory was initiated by Zadeh (1965). Maji et al. (2001) presented the definition of fuzzy soft set, which is a combination of fuzzy set and soft set, and they studied its properties. Further, Aygünoğlu and Aygün (2009) introduced the concept of fuzzy soft group and discussed some of their properties. Majumdar and Samanta (2010) generalized the notion of fuzzy soft sets as introduced by Maji et al. (2001). The definition of generalized fuzzy soft set is more practical than the definition of fuzzy soft set as it adds one more degree to the parametrization of the fuzzy set. Yang (2011) presented the notions of fuzzy soft semigroup and fuzzy soft ideal.

Birkhoff's work in 1930s started the general development of lattice theory (Birkhoff, 1984). Because of the lattices are one of the algebraic structures widely used and discussed in mathematics and its applications, many authors focused on studying lattice structures of algebraic systems. For example, Shao and Qin (2012) applied the notion of fuzzy soft set to lattice theory and they investigated the algebraic structure of fuzzy soft lattices.

The concept of multi-fuzzy sets presents a new method that contributes to explaining some problems that are difficult to represent with fuzzy set theory. Sebastian and Ramakrishnan (2011a) proposed the concept of multi-fuzzy set which is a more general fuzzy set using ordinary fuzzy sets. Yang et al. (2013) combined the multi-fuzzy set and soft set models. They introduced the concept of multi-fuzzy soft sets and defined some operations on multi-fuzzy soft sets. Akın (2021) applied the multi-fuzzy soft sets to the theory of groups and form a new algebraic structure which is called a multi-fuzzy soft group as an extension of multi-fuzzy sets. Kazancı et al. (2022) combined the multi-fuzzy soft set and polygroup structure, from which they obtain a new soft structure called the multi-fuzzy soft polygroup. The organization of this paper is as follows: In Section 2, some basic definitions and theorems of the lattice theory, soft set

theory, fuzzy soft sets, multi-fuzzy sets and multi-fuzzy soft sets are introduced. In Section 3, the lattice structure of multi-fuzzy soft sets is studied. Some algebraic structures of multi-fuzzy soft sets are presented. In Section 4, the results obtained in this work are summarized.

2. Preliminaries

In this section, we present some basic definitions and facts related to lattices, soft sets, fuzzy soft sets, multi-fuzzy sets and multi-fuzzy soft sets; see the references (Birkhoff, 1984; Molodtsov, 1999; Skornjakov, 1977; Gratzer, 1978; Zadeh, 1965; Maji et al., 2001; Sebastian and Ramakrishnan, 2011 a; Sebastian and Ramakrishnan, 2011 b; Yang et al., 2013; Kazancı et al., 2022).

By a partly ordered set is meant a system X in which a binary relation " $\leq$ " is reflexive, antisymmetric and transitive. An upper bound of a subset X of a partially ordered set P is an element $a \in P$ which is greater than every $x \in X$. A least upper bound (l.u.b.) is an upper bound lesser than every other upper bound of X. The notions of a lower bound and greatest lower bound *(g.l.b.)* are defined dually (Birkhoff, 1984).

Definition 2.1. A *lattice* is a partly ordered set in which any pair of elements a, b have a g.l.b. or "meet" $a \wedge b$ and a l.u.b. or "join" $a \vee b$ (Birkhoff, 1984).

Theorem 2.2. For a lattice L, the following identities are satisfied, for all $a, b, c \in L$ (Skornjakov, 1977):

(i) $a \vee a = a, a \wedge a = a$,
(ii) $a \vee b = b \vee a, a \wedge b = b \wedge a$,
(iii) $a \vee (b \vee c) = (a \vee b) \vee c$, $a \wedge (b \wedge c) = (a \wedge b) \wedge c$,
(iv) $a = a \vee (a \wedge b), a = a \wedge (a \vee b)$

Let L be the set of propositions, $\vee$ denote the connective "or" and $\wedge$ denote the connective "and". Then (i) to (iv) are well-known properties from propositional logic.

Let L be a set endowed with two binary operations $'' \wedge ''$ and $'' \vee ''$ which satisfy the identities given in Theorem 2.2. Then if we set

$a \leq b \Leftrightarrow a \wedge b = a$ (or $a \leq b \Leftrightarrow a \vee b = b$),

then L is a lattice with the ordering relation $'' \leq ''$ (Gratzer, 1978).

Definition 2.3. The algebra $(L, \circ)$ is a *semilattice* iff " $\circ$ " is idempotent, commutative and associative (Gratzer, 1978).

Definition 2.4. Let L be a lattice and L' be a subset of L such that for every pair of elements a, b in L' both $a \vee b$ and $a \wedge b$ are in L', then we say that L' with the same operations is a *sublattice e* of L (Birkhoff, 1984).

For a lattice L, $\emptyset$ is considered as a sublattice of L.

Definition 2.5. Let L be a partially ordered set. L is a *complete lattice* in which every subset had a least upper bound and a greatest upper bound (Birkhoff, 1984).

Theorem 2.6. Let L be a partly ordered set with 1 and every non-void subset of L have a g.l.b., then L is a complete lattice (Birkhoff, 1984).

Definition 2.7. A *distributive lattice* is a lattice which satisfies either of the distributive laws, for all $a, b, c \in L$,

(i) $a \wedge (b \vee c) = (a \wedge b) \vee (a \wedge c)$,
(ii) $a \vee (b \wedge c) = (a \vee b) \wedge (a \vee c)$.

One can see a lattice L satisfies (i) if and only if satisfies (ii) (Birkhoff, 1984).

Definition 2.8. A lattice is called a *modular lattice* if and only if its elements satisfy the condition,

if $x \leq z$, then $x \vee (y \wedge z) = (x \vee y) \wedge z$.

Any distributive lattice is modular (Birkhoff, 1984).

Definition 2.9. Let U be an initial universe set and E be a set of parameters. $P(U)$ denotes the power set of U and $A \subseteq E$. A pair (F, A) is called a *soft set* over U, where F is a set-valued function $F: A \to P(U)$ can be defined as

$F(x) = \{y \in P(U): (x, y) \in R\}$, for all $x \in A$

and R will refer to an arbitrary binary relation between an element of A and an element of U, that is, R is a subset of $A \times U$. In fact, a soft set over U is a parameterized family of subsets of universe U (Molodtsov,1999).

Definition 2.10. Let X be a non-empty set. A *fuzzy subset* μ of X is a function $\mu: X \to [0,1]$ (Zadeh, 1965).

Definition 2.11. Let $\tilde{P}(U)$ be the set of all fuzzy subsets of U. A pair (F, A) is called *fuzzy soft set* over U, where F is a mapping given by $F: A \to \tilde{P}(U)$. That is, for each $a \in A$,

$F(a) = F_a: U \to [0,1]$ is a fuzzy set on U (Maji et al., 2001).

Definition 2.12. Let k be a positive integer. A *multi-fuzzy set* $\tilde{A}$ in U is a set of ordered sequences

$\tilde{A} = \{u/(\mu_1(u), \mu_2(u), \dots, \mu_k(u)): u \in U\}$,

where $\mu_i \in \tilde{P}(U)$, $i = 1,2, \dots, k$. The function $\mu_{\tilde{A}} = (\mu_1, \dots, \mu_k)$ is called the multi membership function of multi-fuzzy set $\tilde{A}$ denoted by $MM_{\tilde{A}}$, k is called a dimension of $\tilde{A}$. The set of all multi-fuzzy sets of dimension k in U is denoted by $M^k F^S(U)$ (Sebastian and Ramakrishnan, 2011a).

Definition 2.13. Let $\tilde{A} \in M^k F^S(U)$. If $\tilde{A} = \{u/(0, 0, \dots, 0): u \in U\}$, then $\tilde{A}$ is called the *null multi-fuzzy* set of dimension k, denoted by $\tilde{\emptyset}_k$. If $\tilde{A} = \{u/(1, 1, \dots, 1): u \in U\}$, then $\tilde{A}$ is called the *absolute multi-fuzzy* set of dimension k, denoted by $\tilde{1}_k$ (Sebastian and Ramakrishnan, 2011a).

Definition 2.14. Let

$\tilde{A} = \{u/(\mu_1(u), \mu_2(u), \dots, \mu_k(u)): u \in U\}$,
$\tilde{B} = \{u/(\gamma_1(u), \gamma_2(u), \dots, \gamma_k(u)): u \in U\} \in M^k F^s(U)$.

We define the following relations and operations.

(i) $\tilde{A} \sqsubseteq \tilde{B}$ if and only if $MM_{\tilde{A}} \leq MM_{\tilde{B}}$, i.e $\mu_i(u) \leq \gamma_i(u), \forall u \in U$ and $1 \leq i \leq k$.
(ii) $\tilde{A} = \tilde{B}$ if and only if $MM_{\tilde{A}} = MM_{\tilde{B}}$, i.e $\mu_i(u) = \gamma_i(u), \forall u \in U$ and $1 \leq i \leq k$.
(iii) $\tilde{A} \sqcup \tilde{B} = \{u / (\mu_1(u) \vee \gamma_1(u), \dots, \mu_k(u) \vee \gamma_k(u)): u \in U\}$. That is $MM_{\tilde{A} \sqcup \tilde{B}} = MM_{\tilde{A}} \vee MM_{\tilde{B}}$.

(iv) $\tilde{A} \sqcap \tilde{B} = \{u / (\mu_1(u) \wedge \gamma_1(u), \dots, \mu_k(u) \wedge \gamma_k(u)) : u \in U\}$. That is $MM_{\tilde{A}\sqcap\tilde{B}} = MM_{\tilde{A}} \wedge MM_{\tilde{B}}$.

(v) $\tilde{A}^c = \{u/(\mu_1{}^c, \mu_2{}^c, \dots, \mu_k{}^c) : u \in U\}$

(Sebastian and Ramakrishnan, 2011 a).

Theorem 2.15. Let $\tilde{A}, \tilde{B}, \tilde{C} \in M^k F^s(U)$. Then

(i) $\tilde{A} \sqcup \tilde{A} = \tilde{A}, \tilde{A} \sqcap \tilde{A} = \tilde{A}$,

(ii) $\tilde{A} \sqsubseteq \tilde{A} \sqcup \tilde{B}, \tilde{B} \sqsubseteq \tilde{A} \sqcup \tilde{B}$,

$\tilde{A} \sqcap \tilde{B} \sqsubseteq \tilde{A}, \tilde{A} \sqcap \tilde{B} \sqsubseteq \tilde{B}$.

(iii) $\tilde{A} \sqsubseteq \tilde{B}$ if and only if $\tilde{A} \sqcup \tilde{B} = \tilde{B}$ and $\tilde{A} \sqcap \tilde{B} = \tilde{A}$

(Sebastian and Ramakrishnan, 2011b).

Theorem 2.16. Let $\tilde{A}, \tilde{B}, \tilde{C} \in M^k F^s(U)$. Then

(i) $\tilde{A} \sqcup \tilde{B} = \tilde{B} \sqcup \tilde{A}, \tilde{A} \sqcap \tilde{B} = \tilde{B} \sqcap \tilde{A}$,

(ii) $\tilde{A} \sqcup (\tilde{B} \sqcup \tilde{C}) = (\tilde{A} \sqcup \tilde{B}) \sqcup \tilde{C}$,

$\tilde{A} \sqcap (\tilde{B} \sqcap \tilde{C}) = (\tilde{A} \sqcap \tilde{B}) \sqcap \tilde{C}$,

(iii) $\tilde{B} \sqsubseteq \tilde{C}$ implies

$\tilde{A} \sqcup \tilde{B} \sqsubseteq \tilde{A} \sqcup \tilde{C}$ and $\tilde{A} \sqcap \tilde{B} \sqsubseteq \tilde{A} \sqcap \tilde{C}$

(Sebastian and Ramakrishnan, 2011a).

Proposition 2.17. $\tilde{A}, \tilde{B} \in M^k F^s(U)$. Then

(i) $(\tilde{A} \sqcup \tilde{B}) \sqcap \tilde{A} = \tilde{A}$,

(ii) $(\tilde{A} \sqcap \tilde{B}) \sqcup \tilde{A} = \tilde{A}$.

Proof. (i) Let $\tilde{A} = \{u/(\mu_1(u), \mu_2(u), \dots, \mu_k(u)) : u \in U\}$, $\tilde{B} = \{u/(\gamma_1(u), \gamma_2(u), \dots, \gamma_k(u)) : u \in U\}$. Then

$(\tilde{A} \sqcup \tilde{B}) \sqcap \tilde{A}$

$= \{u/(\mu_1(u) \vee \gamma_1(u), \dots, \mu_k(u) \vee \gamma_k(u)) : u \in U\}$

$\sqcap \{u/(\mu_1(u), \mu_2(u), \dots, \mu_k(u)) : u \in U\}$

$= \{u/((\mu_1(u) \vee \gamma_1(u)) \wedge \mu_1(u), \dots, (\mu_k(u) \vee \gamma_k(u)) \wedge \mu_k(u)) : u \in U\}$

$= \{u/(\mu_1(u), \mu_2(u), \dots, \mu_k(u)) : u \in U\} = \tilde{A}$.

(ii) The proof is similar to (i).

Proposition 2.18. Let $\tilde{A}, \tilde{B}, \tilde{C} \in M^k F^s(U)$. Then,

(i) $\tilde{A} \sqcup (\tilde{B} \sqcap \tilde{C}) = (\tilde{A} \sqcup \tilde{B}) \sqcap (\tilde{A} \sqcup \tilde{C})$,

(ii) $\tilde{A} \sqcap (\tilde{B} \sqcup \tilde{C}) = (\tilde{A} \sqcap \tilde{B}) \sqcup (\tilde{A} \sqcap \tilde{C})$.

Proof. (i) Let $\tilde{A} = \{u/(\mu_1(u), \mu_2(u), \dots, \mu_k(u)) : u \in U\}$, $\tilde{B} = \{u/(\gamma_1(u), \gamma_2(u), \dots, \gamma_k(u)) : u \in U\}$ and $\tilde{C} = \{u/(\theta_1(u), \theta_2(u), \dots, \theta_k(u)) : u \in U\}$. Then

$\tilde{A} \sqcup (\tilde{B} \sqcap \tilde{C})$

$= \{u/(\mu_1(u), \mu_2(u), \dots, \mu_k(u)) : u \in U\} \sqcup$

$\{u/(\gamma_1(u) \wedge \theta_1(u), \dots, \gamma_k(u) \wedge \theta_k(u)) : u \in U\}$

$= \{u/(\mu_1(u) \vee (\gamma_1(u) \wedge \theta_1(u)), \dots, \mu_k(u) \vee (\gamma_k(u) \wedge \theta_k(u))) : u \in U\}$

$= \{u/((\mu_1(u) \vee \gamma_1(u)) \wedge (\mu_1(u) \vee \theta_1(u))), \dots, ((\mu_k(u) \vee \gamma_k(u)) \wedge (\mu_k(u) \vee \theta_k(u))) : u \in U\}$

$= \{u/(\mu_1(u) \vee \gamma_1(u), \dots, \mu_k(u) \vee \gamma_k(u)) : u \in U\} \sqcap$

$= \{u/(\mu_1(u) \vee \theta_1(u), \dots, \mu_k(u) \vee \theta_k(u)) : u \in U\}$

$= (\tilde{A} \sqcup \tilde{B}) \sqcap (\tilde{A} \sqcup \tilde{C})$.

(ii) The proof is similar to (i).

Definition 2.19. A pair $(\tilde{F}, A)$ is called a *multi-fuzzy soft set* of dimension k over U, where $\tilde{F}$ mapping given by $\tilde{F}: A \to M^k F^S(U)$. That is, for each $a \in A$, $\tilde{F}(a) = MM_{\tilde{F}(a)} \in M^k F^S(U)$. For $a \in A$, $\tilde{F}(a)$ may be considered a set of a-approximate elements of the multi-fuzzy soft set $(\tilde{F}, A)$. Let $A \subseteq E$, denote the set of all multi-fuzzy soft sets of dimension k over U by $M^k F_S^S(U)$ (Yang et al., 2013).

Definition 2.20. Let $A, B \in E$, $(\tilde{F}, A)$ and $(\tilde{G}, B)$ be two multi-fuzzy soft sets of dimension k over U. $(\tilde{F}, A)$ is said to be a *multi-fuzzy soft subset* of $(\tilde{G}, B)$ if, $A \subseteq B$ and for each $a \in A$, $\tilde{F}(a) \sqsubseteq \tilde{G}(a)$. In this case, we write $(\tilde{F}, A) \tilde{\subseteq} (\tilde{G}, B)$ (Yang et al., 2013).

Definition 2.21. A multi-fuzzy soft set $(\tilde{F}, A)$ of dimension k over U is said to be *null multi-fuzzy soft set*, denoted by $\widetilde{\emptyset_A}^k$ if $\tilde{F}(a) = \widetilde{\emptyset_A}^k$ for all $a \in A$. A multi-fuzzy soft set $(\tilde{F}, A)$ of dimension k over U is said to be *absolute multi-fuzzy soft set*, denoted by $\widetilde{U_A}^k$ if $\tilde{F}(a) = \widetilde{U_A}^k$ for all $a \in A$ (Yang et al., 2013).

Definition 2.22. The *extended union* of two multi-fuzzy soft sets sets $(\tilde{F}, A)$ and $(\tilde{G}, B)$ of dimension k over U is the multi-fuzzy soft set $(\tilde{H}, C)$, where $C = A \cup B$ and for all $x \in C$, $\tilde{H}(x) = \tilde{F}(x)$ if $x \in A - B$, $\tilde{H}(x) = \tilde{G}(x)$ if $c \in B - A$ and $\tilde{H}(x) = \tilde{F}(x) \sqcup \tilde{G}(x)$ if $x \in A \cap B$. We write $(\tilde{F}, A) \tilde{\sqcup}_\varepsilon (\tilde{G}, B) = (\tilde{H}, C)$ (Yang et al., 2013).

Definition 2.23. The *restricted union* of two multi-fuzzy soft sets $(\tilde{F}, A)$ and $(\tilde{G}, B)$ of dimension k over U is the multi-fuzzy soft set $(\tilde{H}, C)$, where $C = A \cap B$ and for all $x \in C, \tilde{H}(x) = \tilde{F}(x) \sqcup \tilde{G}(x)$. We write $(\tilde{F}, A) \tilde{\sqcup}_R (\tilde{G}, B) = (\tilde{H}, C)$.

Definition 2.24. The *extended intersection* of two multi-fuzzy soft sets sets $(\tilde{F}, A)$ and $(\tilde{G}, B)$ of dimension k over U is the multi-fuzzy soft set $(\tilde{H}, C)$, where $C = A \cup B$ and for all $x \in C$, $\tilde{H}(x) = \tilde{F}(x)$ if $x \in A - B$, $\tilde{H}(x) = \tilde{G}(x)$ if $x \in B - A$ and $\tilde{H}(x) = \tilde{F}(x) \sqcap \tilde{G}(x)$ if $x \in A \cap B$. We write $(\tilde{F}, A) \tilde{\sqcap}_\varepsilon (\tilde{G}, B) = (\tilde{H}, C)$ (Kazancı et al., 2022).

We define the restricted intersection of two multi-fuzzy soft sets as follows. Note that our definition is different from the definition given by Yang at al. (Yang et al., 2013). Because even if $A \cap B = \emptyset$ we can still define $(\tilde{F}, A) \tilde{\sqcap}_R (\tilde{G}, B) = (\tilde{H}, \emptyset)$, where $\tilde{H} = \emptyset: \emptyset \to M^k F^S(U)$.

Definition 2.25. The *restricted intersection* of two multi-fuzzy soft sets $(\tilde{F}, A)$ and $(\tilde{G}, B)$ of dimension k over U is the multi-fuzzy soft set $(\tilde{H}, C)$, where $C = A \cap B$ for all $x \in C, \tilde{H}(x) = \tilde{F}(x) \sqcap \tilde{G}(x)$. We write $(\tilde{F}, A) \tilde{\sqcap}_R (\tilde{G}, B) = (\tilde{H}, C)$.

3. Lattice Structure of Multi-Fuzzy Soft Sets

In this section, we investigate some properties of the operations given on multi-fuzzy soft sets. Then we give the lattice structure of multi-fuzzy soft sets.

Proposition 3.1. $(M^k F_S^S(U), \tilde{\sqcup}_\varepsilon)$ is a semilattice.

Proof. (i) Let $(\tilde{F}, A) \tilde{\sqcup}_\varepsilon (\tilde{F}, A) = (\tilde{H}, C)$, where $C = A \cup A = A$ and for all $c \in A$, $\tilde{H}(c) = \tilde{F}(c)$. Therefore,

$(\tilde{F},A)\,\tilde{\sqcup}_{\varepsilon}\,(\tilde{F},A)=(\tilde{F},A)$.

(ii) Let $(\tilde{F},A)\,\tilde{\sqcup}_{\varepsilon}\,(\tilde{G},B)=(\tilde{K},C)$ and $(\tilde{G},B)\,\tilde{\sqcup}_{\varepsilon}\,(\tilde{F},A)=(\tilde{L},D)$. Then, $C=A\cup B$ and $D=B\cup A$.

Since $A\cup B=B\cup A$, then $C=D$. If $x\in A-B$, $\tilde{K}(x)=\tilde{F}(x)$ and $\tilde{L}(x)=\tilde{F}(x)$. If, $x\in B-A$, $\tilde{K}(x)=\tilde{G}(x)$ and $\tilde{L}(x)=\tilde{G}(x)$. If, $x\in A\cap B$, $\tilde{K}(x)=\tilde{F}(x)\sqcup\tilde{G}(x)$ and $\tilde{L}(x)=\tilde{G}(x)\sqcup\tilde{F}(x)$. Therefore, $(\tilde{F},A)\,\tilde{\sqcup}_{\varepsilon}\,(\tilde{G},B)=(\tilde{G},B)\,\tilde{\sqcup}_{\varepsilon}\,(\tilde{F},A)$.

(iii) Let $(\tilde{F},A)\,\tilde{\sqcup}_{\varepsilon}\,(\tilde{G},B)=(\tilde{K},A\cup B)$ and $(\tilde{K},A\cup B)\,\tilde{\sqcup}_{\varepsilon}\,(\tilde{H},C)=(\tilde{L},(A\cup B)\cup C)$. Similarly, $(\tilde{G},B)\,\tilde{\sqcup}_{\varepsilon}\,(\tilde{H},C)=(\tilde{M},B\cup C)$ and $(\tilde{F},A)\,\tilde{\sqcup}_{\varepsilon}\,(\tilde{M},B\cup C)=\left(\tilde{N},A\cup(B\cup C)\right)$.

It is clear that $(A\cup B)\cup C=A\cup(B\cup C)=A\cup B\cup C$. Let $x\in A\cup B\cup C$. Then $x\in A$ or $x\in B$ or $x\in C$. Without loss of generality, we can assume that $x\in C$. Then,

a) If, $x\notin A$ and $x\notin B$, $\tilde{L}(x)=\tilde{H}(x)=\tilde{N}(x)$.
b) If, $x\in A$ and $x\notin B$, $\tilde{L}(x)=\tilde{F}(x)\sqcup\tilde{H}(x)=\tilde{N}(x)$.
c) If, $x\notin A$ and $x\in B$, $\tilde{L}(x)=\tilde{G}(x)\sqcup\tilde{H}(x)=\tilde{N}(x)$.
d) If, $x\in A$ and $x\in B$,

$$\tilde{L}(x)=\left(\tilde{F}(x)\sqcup\tilde{G}(x)\right)\sqcup\tilde{H}(x)=\tilde{F}(x)\sqcup\left(\tilde{G}(x)\sqcup\tilde{H}(x)\right)=\tilde{N}(x).$$

Therefore,

$$\left((\tilde{F},A)\,\tilde{\sqcup}_{\varepsilon}\,(\tilde{G},B)\right)\tilde{\sqcup}_{\varepsilon}\,(\tilde{H},C)=(\tilde{F},A)\,\tilde{\sqcup}_{\varepsilon}\left((\tilde{G},B)\,\tilde{\sqcup}_{\varepsilon}\,(\tilde{H},C)\right).$$

Proposition 3.2. $(M^kF_S^S(U),\tilde{\sqcup}_R)$ is a semilattice.

Proof. (i) Let $(\tilde{F},A)\,\tilde{\sqcup}_R\,(\tilde{F},A)=(\tilde{H},C)$, where $C=A\cap A=A$ and for all $x\in A$, $\tilde{H}(x)=\tilde{F}(x)$. Therefore, $(\tilde{F},A)\,\tilde{\sqcup}_R\,(\tilde{F},A)=(\tilde{F},A)$.

(ii) Let $(\tilde{F},A)\,\tilde{\sqcup}_R\,(\tilde{G},B)=(\tilde{K},C)$ and $(\tilde{G},B)\,\tilde{\sqcup}_R\,(\tilde{F},A)=(\tilde{L},D)$. Then, $C=A\cap B=B\cap A=D$. For any $x\in A\cap B$, $\tilde{K}(x)=\tilde{F}(x)\sqcup\tilde{G}(x)=\tilde{G}(x)\sqcup\tilde{F}(x)=\tilde{L}(x)$. Therefore, $(\tilde{F},A)\,\tilde{\sqcup}_R\,(\tilde{G},B)=(\tilde{G},B)\,\tilde{\sqcup}_R\,(\tilde{F},A)$.

(iii) Let $(\tilde{F},A)\,\tilde{\sqcup}_R\,(\tilde{G},B)=(\tilde{K},A\cap B)$ and $(\tilde{K},A\cap B)\,\tilde{\sqcup}_R\,(\tilde{H},C)=(\tilde{L},(A\cap B)\cap C)$. Similarly, $(\tilde{G},B)\,\tilde{\sqcup}_R\,(\tilde{H},C)=(\tilde{M},B\cap C)$ and $(\tilde{F},A)\,\tilde{\sqcup}_R\,(\tilde{M},B\cap C)=\left(\tilde{N},A\cap(B\cap C)\right)$. It is clear that $(A\cap B)\cap C=A\cap(B\cap C)=A\cap B\cap C$.

Let $x\in A\cap B\cap C$, we have $x\in A$ and $x\in B$ and $x\in C$.

$$\tilde{L}(x)=\left(\tilde{F}(x)\sqcup\tilde{G}(x)\right)\sqcup\tilde{H}(x)=\tilde{F}(x)\sqcup\left(\tilde{G}(x)\sqcup\tilde{H}(x)\right)=\tilde{N}(x).$$

Therefore,

$$\left((\tilde{F},A)\,\tilde{\sqcup}_R\,(\tilde{G},B)\right)\tilde{\sqcup}_R\,(\tilde{H},C)=(\tilde{F},A)\,\tilde{\sqcup}_R\left((\tilde{G},B)\,\tilde{\sqcup}_R\,(\tilde{H},C)\right).$$

Proposition 3.3 $(M^kF_S^S(U),\tilde{\sqcap}_{\varepsilon})$ is a semilattice.

Proof. (i) Let $(\tilde{F},A)\,\tilde{\sqcap}_{\varepsilon}\,(\tilde{F},A)=(\tilde{H},C)$, where $C=A\cup A=A$ and for all $x\in A$, $\tilde{H}(x)=\tilde{F}(x)$. Therefore, $(\tilde{F},A)\,\tilde{\sqcap}_{\varepsilon}\,(\tilde{F},A)=(\tilde{F},A)$.

(ii) Let $(\tilde{F},A)\,\tilde{\sqcap}_{\varepsilon}\,(\tilde{G},B)=(\tilde{K},C)$ and $(\tilde{G},B)\,\tilde{\sqcap}_{\varepsilon}\,(\tilde{F},A)=(\tilde{L},D)$. Therefore, $C=A\cup B$ and $D=B\cup A$. Since $A\cup B=B\cup A$, then $C=D$. If $x\in A-B$, $\tilde{K}(x)=\tilde{F}(x)$ and $\tilde{L}(x)=\tilde{F}(x)$. If $x\in B-A$, $\tilde{K}(x)=\tilde{G}(x)$ and $\tilde{L}(x)=\tilde{G}(x)$. If $x\in A\cap B$, $\tilde{K}(x)=\tilde{F}(x)\sqcap\tilde{G}(x)$ and $\tilde{L}(x)=\tilde{G}(x)\sqcap\tilde{F}(x)$. Therefore, $(\tilde{F},A)\,\tilde{\sqcap}_{\varepsilon}\,(\tilde{G},B)=(\tilde{G},B)\,\tilde{\sqcap}_{\varepsilon}\,(\tilde{F},A)$.

(iii). Let $\left((\tilde{F},A)\,\tilde{\sqcap}_{\varepsilon}\,(\tilde{G},B)\right)\tilde{\sqcap}_{\varepsilon}\,(\tilde{H},C)=(\tilde{K},(A\cup B)\cup C)$ and $(\tilde{F},A)\,\tilde{\sqcap}_{\varepsilon}\left((\tilde{G},B)\,\tilde{\sqcap}_{\varepsilon}\,(\tilde{H},C)\right)=\left(\tilde{L},A\cup(B\cup C)\right)$. It is obvious that $(A\cup B)\cup C=A\cup(B\cup C)=A\cup B\cup C$. For all $\in A\cup B\cup C$, $x\in A$ or $x\in B$ or $x\in C$. Without loss of generality, we can suppose that $x\in C$. Then,

a) If, $x\notin A$ and $x\notin B$, $\tilde{K}(x)=\tilde{H}(x)=\tilde{L}(x)$.
b) If, $x\in A$ and $x\notin B$, $\tilde{K}(x)=\tilde{F}(x)\sqcap\tilde{H}(x)=\tilde{L}(x)$.
c) If, $x\notin A$ and $x\in B$, $\tilde{K}(x)=\tilde{G}(x)\sqcap\tilde{H}(x)=\tilde{L}(x)$.
d) If, $x\in A$ and $x\in B$, $\tilde{K}(x)=\left(\tilde{F}(x)\sqcap\tilde{G}(x)\right)\sqcap\tilde{H}(x)=\tilde{F}(x)\sqcap\left(\tilde{G}(x)\sqcap\tilde{H}(x)\right)=\tilde{L}(x)$.

Proposition 3.4. $(M^kF_S^S(U),\tilde{\sqcap}_R)$ is a semilattice.

Proof. (i) Let $(\tilde{F},A)\,\tilde{\sqcap}_R\,(\tilde{F},A)=(\tilde{H},C)$, where $C=A\cap A=A$ and for all $x\in A$, $\tilde{H}(x)=\tilde{F}(x)$. Thus, $(\tilde{F},A)\,\tilde{\sqcap}_R\,(\tilde{F},A)=(\tilde{F},A)$.

(ii) Let $(\tilde{F},A)\,\tilde{\sqcap}_R\,(\tilde{G},B)=(\tilde{K},C)$ and $(\tilde{G},B)\,\tilde{\sqcap}_R\,(\tilde{F},A)=(\tilde{L},D)$. Therefore, $C=A\cap B=B\cap A=D$. If $x\in A\cap B$, $\tilde{K}(x)=\tilde{F}(x)\sqcap\tilde{G}(x)=\tilde{G}(x)\sqcap\tilde{F}(x)=\tilde{L}(x)$. So, $(\tilde{F},A)\,\tilde{\sqcap}_R\,(\tilde{G},B)=(\tilde{G},B)\,\tilde{\sqcap}_R\,(\tilde{F},A)$.

(iii) Let $\left((\tilde{F},A)\,\tilde{\sqcap}_R\,(\tilde{G},B)\right)\tilde{\sqcap}_R\,(\tilde{H},C)=(\tilde{K},(A\cap B)\cap C)$ and $(\tilde{F},A)\,\tilde{\sqcap}_R\left((\tilde{G},B)\,\tilde{\sqcap}_R\,(\tilde{H},C)\right)=\left(\tilde{L},A\cap(B\cap C)\right)$. We know that $(A\cap B)\cap C=A\cap(B\cap C)=A\cap B\cap C$.

If $x\in A\cap B\cap C$, then $x\in A$ and $x\in B$ and $x\in C$. Therefore, $\tilde{K}(x)=\left(\tilde{F}(x)\sqcap\tilde{G}(x)\right)\sqcap\tilde{H}(x)=\tilde{F}(x)\sqcap\left(\tilde{G}(x)\sqcap\tilde{H}(x)\right)=\tilde{L}(x)$.

Proposition 3.5. Let $(\tilde{F},A),(\tilde{G},B)\in M^kF_S^S(U)$. Then,

(i) $\left((\tilde{F},A)\,\tilde{\sqcup}_{\mathcal{E}}\,(\tilde{G},B)\right)\tilde{\sqcap}_R\,(\tilde{F},A)=(\tilde{F},A)$,
(ii) $\left((\tilde{F},A)\,\tilde{\sqcap}_R\,(\tilde{G},B)\right)\tilde{\sqcup}_{\mathcal{E}}\,(\tilde{F},A)=(\tilde{F},A)$.

Proof.

(i) Let $\left((\tilde{F},A)\,\tilde{\sqcup}_{\mathcal{E}}\,(\tilde{G},B)\right)=(\tilde{H},A\cup B)$ and $\left((\tilde{F},A)\,\tilde{\sqcup}_{\mathcal{E}}\,(\tilde{G},B)\right)\tilde{\sqcap}_R\,(\tilde{F},A)=(\tilde{K},(A\cup B)\cap A)=(\tilde{K},A)$. Let $x\in A$.

a) If $x\in B$, then $\tilde{K}(x)=\tilde{H}(x)\sqcap\tilde{F}(x)=\left(\tilde{F}(x)\sqcup\tilde{G}(x)\right)\sqcap\tilde{F}(x)=\tilde{F}(x)$.
b) If $x\notin B$, then $\tilde{K}(x)=\tilde{H}(x)\sqcap\tilde{F}(x)=\tilde{F}(x)\sqcap\tilde{F}(x)=\tilde{F}(x)$.

(ii) Let $\left((\tilde{F},A)\,\tilde{\sqcap}_R\,(\tilde{G},B)\right)=(\tilde{H},A\cap B)$ and

$\left(\left(\tilde{F},A\right)\tilde{\sqcap}_R\left(\tilde{G},B\right)\right)\tilde{\sqcup}_\mathcal{E}\left(\tilde{F},A\right)=\left(\widetilde{K},(A\cap B)\cup A\right)$
$=(\widetilde{K},A).$

Let $x\in A$.

a) If $x\in B$, then, $\widetilde{K}(x)=\widetilde{H}(x)\sqcup\tilde{F}(x)$
$=\left(\tilde{F}(x)\sqcap\tilde{G}(x)\right)\sqcup\tilde{F}(x)=\tilde{F}(x).$

b) If $x\notin B$, then, $\widetilde{K}(x)=\widetilde{H}(x)\sqcup\tilde{F}(x)$
$=\tilde{F}(x)\sqcup\tilde{F}(x)=\tilde{F}(x).$

Proposition 3.6. Let $(\tilde{F},A),(\tilde{G},B)\in M^kF_S^S(U)$. Then,

(i) $\left(\left(\tilde{F},A\right)\tilde{\sqcup}_R\left(\tilde{G},B\right)\right)\tilde{\sqcap}_\mathcal{E}\left(\tilde{F},A\right)=(\tilde{F},A)$,

(ii) $\left(\left(\tilde{F},A\right)\tilde{\sqcap}_\mathcal{E}\left(\tilde{G},B\right)\right)\tilde{\sqcup}_R\left(\tilde{F},A\right)=(\tilde{F},A)$.

Proof. **(i)** Let $\left(\left(\tilde{F},A\right)\tilde{\sqcup}_R\left(\tilde{G},B\right)\right)=\left(\widetilde{H},A\cap B\right)$ and
$\left(\left(\tilde{F},A\right)\tilde{\sqcup}_R\left(\tilde{G},B\right)\right)\tilde{\sqcap}_\mathcal{E}\left(\tilde{F},A\right)$
$=\left(\widetilde{K},(A\cap B)\cup A\right)=(\widetilde{K},A).$

Let $x\in A$.

a) If $x\in B$, then $\widetilde{K}(x)=\widetilde{H}(x)\sqcap\tilde{F}(x)$
$=\left(\tilde{F}(x)\sqcup\tilde{G}(x)\right)\sqcap\tilde{F}(x)=\tilde{F}(x).$

b) If $x\notin B$, then we have $x\notin A\cap B$.
Therefore $\widetilde{K}(x)=\tilde{F}(x)$.

(ii) Let $\left(\left(\tilde{F},A\right)\tilde{\sqcap}_\mathcal{E}\left(\tilde{G},B\right)\right)=(\widetilde{H},A\cup B)$ and

$\left(\left(\tilde{F},A\right)\tilde{\sqcap}_\mathcal{E}\left(\tilde{G},B\right)\right)\tilde{\sqcup}_R\left(\tilde{F},A\right)$

$=\left(\widetilde{K},(A\cup B)\cap A\right)=(\widetilde{K},A).$

Let $x\in A$.

a) If $x\in B$, then $\widetilde{K}(x)=\widetilde{H}(x)\sqcup\tilde{F}(x)$
$=\left(\tilde{F}(x)\sqcap\tilde{G}(x)\right)\sqcup\tilde{F}(x)=\tilde{F}(x).$

b) If $x\notin B$, then $\widetilde{K}(x)=\tilde{F}(x)$.

Corollary 3.7. $(M^kF_S^S(U),\tilde{\sqcap}_R,\tilde{\sqcup}_\mathcal{E})$ is a complete lattice.

Proof. It is straightforward from Proposition 3.1, Proposition 3.4, Proposition 3.5 and Theorem 2.6.

Theorem 3.8. Let $\tilde{\sqsubseteq}_1$ be the ordering relation in the lattice $(M^kF_S^S(U),\tilde{\sqcap}_R,\tilde{\sqcup}_\mathcal{E})$ and $\left(\tilde{F},A\right),(\tilde{G},B)\in M^kF_S^S(U)$. Then $(\tilde{F},A)\ \tilde{\sqsubseteq}_1\ (\tilde{G},B)$ if and only if $A\subseteq B$ and $\tilde{F}(x)\sqsubseteq\tilde{G}(x)$ for all $x\in A$.

Proof. Let $(\tilde{F},A)\ \tilde{\sqsubseteq}_1\ (\tilde{G},B)$. Therefore,
$\left(\tilde{F},A\right)\tilde{\sqcup}_\mathcal{E}\left(\tilde{G},B\right)=(\tilde{G},B)$ and $\left(\tilde{F},A\right)\tilde{\sqcap}_R\left(\tilde{G},B\right)=(\tilde{F},A)$.
Using Definition 2.22 and Definition 2.25, we have
$A\cup B=B$ and $A\cap B=B$. Then $A\subseteq B$. Therefore,
for each $x\in A$, $\tilde{F}(x)\sqcup\tilde{G}(x)=\tilde{G}(x)$ and $\tilde{F}(x)\sqcap\tilde{G}(x)=\tilde{F}(x)$.
Conversely, let $A\subseteq B$ and $\tilde{F}(x)\sqsubseteq\tilde{G}(x)$, for all $x\in A$. Therefore, $\left(\tilde{F},A\right)\tilde{\sqcup}_\mathcal{E}\left(\tilde{G},B\right)=(\tilde{G},B)$ and $\left(\tilde{F},A\right)\tilde{\sqcap}_R\left(\tilde{G},B\right)=(\tilde{F},A)$. Thus $(\tilde{F},A)\ \tilde{\sqsubseteq}_1\ (\tilde{G},B)$.

Theorem 3.9. The complete lattice $\left(M^kF_S^S(U),\tilde{\sqcap}_R,\tilde{\sqcup}_\mathcal{E}\right)$ is distributive.

Proof. Let $\left(\tilde{F},A\right),\left(\tilde{G},B\right),(\widetilde{H},C)\in M^kF_S^S(U)$. It is enough to prove that
$\left(\tilde{F},A\right)\tilde{\sqcup}_\mathcal{E}\left(\left(\tilde{G},B\right)\tilde{\sqcap}_R\left(\widetilde{H},C\right)\right)$
$=\left(\left(\tilde{F},A\right)\tilde{\sqcup}_\mathcal{E}\left(\tilde{G},B\right)\right)\tilde{\sqcap}_R\left(\left(\tilde{F},A\right)\tilde{\sqcup}_\mathcal{E}\left(\widetilde{H},C\right)\right).$
Let $\left(\tilde{F},A\right)\tilde{\sqcup}_\mathcal{E}\left(\left(\tilde{G},B\right)\tilde{\sqcap}_R\left(\widetilde{H},C\right)\right)=\left(\widetilde{K},A\cup(B\cap C)\right)$ and
$\left(\left(\tilde{F},A\right)\tilde{\sqcup}_\mathcal{E}\left(\tilde{G},B\right)\right)\tilde{\sqcap}_R\left(\left(\tilde{F},A\right)\tilde{\sqcup}_\mathcal{E}\left(\widetilde{H},C\right)\right)$
$=\left(\widetilde{L},(A\cup B)\cap(A\cup C)\right)=\left(\widetilde{L},A\cup(B\cap C)\right).$

For all $x\in A\cup(B\cap C)$, we have that $x\in A$ or $x\in B\cap C$.

a) If $x\in A$ and $x\in B\cap C$, then
$\widetilde{K}(x)=\tilde{F}(x)\sqcup\left(\tilde{G}(x)\sqcap\widetilde{H}(x)\right)$
$=\left(\tilde{F}(x)\sqcup\tilde{G}(x)\right)\sqcap\left(\tilde{F}(x)\sqcup\widetilde{H}(x)\right)=\widetilde{L}(x).$

b) If $x\in A$ and $x\notin B\cap C$, then $x\notin B$ or $x\notin C$.

- If $x\notin B$ and $x\in C$, $\widetilde{K}(x)=\tilde{F}(x)=\tilde{F}(x)\sqcap\left(\tilde{F}(x)\sqcup\widetilde{H}(x)\right)=\tilde{F}(x)=\widetilde{L}(x)$.
- If $x\in B$ and $x\notin C$, $\widetilde{K}(x)=\tilde{F}(x)=\left(\tilde{F}(x)\sqcup\tilde{G}(x)\right)\sqcap\tilde{F}(x)=\tilde{F}(x)=\widetilde{L}(x)$.
- If $x\notin B$ and $x\notin C$, $\widetilde{K}(x)=\tilde{F}(x)=\tilde{F}(x)\sqcap\tilde{F}(x)=\tilde{F}(x)=\widetilde{L}(x)$.

c) If $x\notin A$ and $x\in B\cap C$, we have that $x\in B$ and $x\in C$, $\widetilde{K}(x)=\tilde{G}(x)\sqcap\widetilde{H}(x)=\widetilde{L}(x)$.

Corollary 3.10. The complete lattice $\left(M^kF_S^S(U),\tilde{\sqcap}_R,\tilde{\sqcup}_\mathcal{E}\right)$ is modular.

Proof. Since every distributive lattice is modular, the proof easily comes from Theorem 3.9.

Corollary 3.11. $(M^kF_S^S(U),\tilde{\sqcap}_\mathcal{E},\tilde{\sqcup}_R)$ is a complete lattice.

Proof. It easily comes from Proposition 3.2, Proposition 3.3, Proposition 3.6 and Theorem 2.6.

Theorem 3.12. Let $\tilde{\sqsubseteq}_2$ be ordering the relation in the lattice $(M^kF_S^S(U),\tilde{\sqcap}_\mathcal{E},\tilde{\sqcup}_R)$ and $\left(\tilde{F},A\right),(\tilde{G},B)\in M^kF_S^S(U)$. Then, $(\tilde{F},A)\ \tilde{\sqsubseteq}_2\ (\tilde{G},B)$ if and only if $B\subseteq A$ and $\tilde{F}(x)\sqsubseteq\tilde{G}(x)$ for all $x\in A$.

Proof. Let $(\tilde{F},A)\ \tilde{\sqsubseteq}_2\ (\tilde{G},B)$. Thus $\left(\tilde{F},A\right)\tilde{\sqcup}_R\left(\tilde{G},B\right)=(\tilde{G},B)$ and $\left(\tilde{F},A\right)\tilde{\sqcap}_\mathcal{E}\left(\tilde{G},B\right)=(\tilde{F},A)$. According to Definition 2.23 and Definition 2.24, we get that $A\cap B=B$ and $A\cup B=A$, so $B\subseteq A$. For all $x\in B$, $\tilde{F}(x)\sqcup\tilde{G}(x)=\tilde{G}(x)$ and $\tilde{F}(x)\sqcap\tilde{G}(x)=\tilde{F}(x)$. Therefore, $\tilde{F}(x)\sqsubseteq\tilde{G}(x)$.
Conversely, let $B\subseteq A$ and $\tilde{F}(x)\sqsubseteq\tilde{G}(x)$ for all $x\in B$. Therefore, $\left(\tilde{F},A\right)\tilde{\sqcup}_R\left(\tilde{G},B\right)=(\tilde{G},B)$ and $\left(\tilde{F},A\right)\tilde{\sqcap}_\mathcal{E}\left(\tilde{G},B\right)=(\tilde{F},A)$. Then, $(\tilde{F},A)\ \tilde{\sqsubseteq}_2\ (\tilde{G},B)$.

Theorem 3.13. The complete lattice $(M^kF_S^S(U),\tilde{\sqcap}_\mathcal{E},\tilde{\sqcup}_R)$ is distributive.

Proof. Let $\left(\tilde{F},A\right),\left(\tilde{G},B\right),(\widetilde{H},C)\in M^kF_S^S(U)$. It is enough to prove that
$\left(\tilde{F},A\right)\tilde{\sqcup}_R\left(\left(\tilde{G},B\right)\tilde{\sqcap}_\mathcal{E}\left(\widetilde{H},C\right)\right)$
$=\left(\left(\tilde{F},A\right)\tilde{\sqcup}_R\left(\tilde{G},B\right)\right)\tilde{\sqcap}_\mathcal{E}\left(\left(\tilde{F},A\right)\tilde{\sqcup}_R\left(\widetilde{H},C\right)\right).$
Let $\left(\tilde{F},A\right)\tilde{\sqcup}_R\left(\left(\tilde{G},B\right)\tilde{\sqcap}_\mathcal{E}\left(\widetilde{H},C\right)\right)=\left(\widetilde{K},A\cap(B\cup C)\right)$ and
$\left(\left(\tilde{F},A\right)\tilde{\sqcup}_R\left(\tilde{G},B\right)\right)\tilde{\sqcap}_\mathcal{E}\left(\left(\tilde{F},A\right)\tilde{\sqcup}_R\left(\widetilde{H},C\right)\right)$
$=\left(\widetilde{L},(A\cap B)\cup(A\cap C)\right)=\left(\widetilde{L},A\cap(B\cup C)\right).$

We need to show that $\widetilde{K}(x)=\widetilde{L}(x)$ for all $x\in A\cap(B\cup C)$. Let $x\in A\cap(B\cup C)$. Then we have $x\in A$ and $x\in B\cup C$.

Let $x\in A$.

a) If $x\in B$ and $x\in C$,
$\widetilde{K}(x)=\tilde{F}(x)\sqcup\left(\tilde{G}(x)\sqcap\widetilde{H}(x)\right)$
$=\left(\tilde{F}(x)\sqcup\tilde{G}(x)\right)\sqcap\left(\tilde{F}(x)\sqcup\widetilde{H}(x)\right)=\widetilde{L}(x).$

b) If $x \in B$ and $x \notin C$, $\widetilde{K}(x) = \tilde{F}(x) \sqcup \tilde{G}(x) = \tilde{L}(x)$.

c) If $x \notin B$ and $x \in C$, $\widetilde{K}(x) = \tilde{F}(x) \sqcup \widetilde{H}(x) = \tilde{L}(x)$.

Corollary 3.14. The complete lattice $(M^kF_S^S(U), \widetilde{\sqcap}_\mathcal{E}, \widetilde{\sqcup}_R)$ is modular.

Proof. Since every distributive lattice is modular, the proof easily comes from Theorem 3.13.

Let $(\tilde{F}, A), (\tilde{G}, B) \in M^kF_S^S(U)$. Note that the following equalities don't hold in general:

(i) $\left((\tilde{F}, A)\ \widetilde{\sqcup}_\mathcal{E}\ (\tilde{G}, B)\right) \widetilde{\sqcap}_\mathcal{E}\ (\tilde{F}, A) = (\tilde{F}, A)$,

(ii) $\left((\tilde{F}, A)\ \widetilde{\sqcap}_R\ (\tilde{G}, B)\right) \widetilde{\sqcup}_R\ (\tilde{F}, A) = (\tilde{F}, A)$.

Example 3.15. Let L be a lattice with the diagram in Figure 1. Let $A = \{e_1, e_2\}$ and $B = \{e_2, e_3, e_4\}$ be the set of parameters. We define the multi-fuzzy soft set

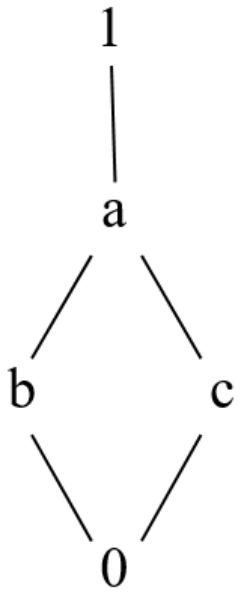

Figure 1. Lattice diagram.

$\tilde{F}: A \to M^2FS(L)$ as follows.

$\tilde{F}(e_1) = \{0/(0.4,0.7), a/(0.4,0.8), b/(0.7,0.2), c/(0.3,0.6), 1/(0.5,0.9)\}$,

$\tilde{F}(e_2) = \{0/(1.0,0.3), a/(0.4,0.5), b/(0.9,0.3), c/(0.2,0.1), 1/(0.6,0.7)\}$.

We define the multi-fuzzy soft set

$\tilde{G}: B \to M^2FS(L)$ as follows.

$\tilde{G}(e_2) = \{0/(0.5,0.8), a/(0.4,0.7), b/(0.5,0.7), c/(0.3,0.6), 1/(0.4,0.6)\}$,

$\tilde{G}(e_3) = \{0/(0.3,0.6), a/(0.8,0.6), b/(0.7,0.5), c/(0.2,0.3), 1/(0.1,0.1)\}$,

$\tilde{G}(e_4) = \{0/(0.8,1.0), a/(0.3,0.1), b/(0.8,0.4), c/(0.1,0.1), 1/(0.9,0.6)\}$.

(i) Let $\left((\tilde{F}, A)\ \widetilde{\sqcup}_\mathcal{E}\ (\tilde{G}, B)\right) \widetilde{\sqcap}_\mathcal{E}\ (\tilde{F}, A)$ $= (\widetilde{H}, (A \cup B) \cup A) = (\widetilde{H}, A \cup B)$. Then $\widetilde{H}(e_1) = \tilde{F}(e_1)$, $\widetilde{H}(e_2) = \tilde{F}(e_2)$, $\widetilde{H}(e_3) = \tilde{G}(e_3)$, $\widetilde{H}(e_4) = \tilde{G}(e_4)$. Therefore, $\left((\tilde{F}, A)\ \widetilde{\sqcup}_\mathcal{E}\ (\tilde{G}, B)\right) \widetilde{\sqcap}_\mathcal{E}\ (\tilde{F}, A) \neq (\tilde{F}, A)$.

(ii) Let $\left((\tilde{F}, A)\ \widetilde{\sqcup}_R\ (\tilde{G}, B)\right) \widetilde{\sqcap}_R\ (\tilde{F}, A) = (\widetilde{K}, (A \cap B) \cap A)$ $= (\widetilde{K}, A \cap B)$. $\widetilde{K}(e_2) = \tilde{F}(e_2)$. Therefore, $\left((\tilde{F}, A)\ \widetilde{\sqcup}_R\ (\tilde{G}, B)\right) \widetilde{\sqcap}_R\ (\tilde{F}, A) \neq (\tilde{F}, A)$.

4. Conclusion

In this paper, we deal with the lattice structure of multi-fuzzy soft sets. We give two lattice constructions on multi-fuzzy soft sets and investigate some related properties.

Author Contributions

The percentages of authors' contributions are presented below. All authors reviewed and approved the final version of the manuscript.

	R.İ.	Ş.Y.
C	30	70
D	55	45
S	30	70
DCP	70	30
DAI	55	45
L	60	40
W	80	20
CR	40	60
SR	45	55
PM	55	45
FA	55	45

C=Concept, D=Design, S=Supervision, DCP=Data Collection and/or Processing, DAI=Data analysis and/or interpretation, L=Literature search, W= Writing, CR=Critical Rewiew, SR=Submission and Revision, PM=Project Management, FA=Funding Acquisition.

Conflict of Interest

The authors declared that there is no conflict of interest.

Ethical Consideration

Ethics committee approval was not required for this study because of there was no study on animals or humans.

References

Akın C. 2021. Multi-fuzzy soft groups. Soft Comput, 25: 137-145.

Aygünoğlu A, Aygün H. 2009. Introduction to fuzzy soft groups. Comput Math Appl, 58: 1279-1286.

Birkhoff G. 1984. Lattice theory. American Math Soc, Providence, US.

Feng F, Jun YB, Zhao XZ. 2008. Soft semirings. Comput Math Appl, 56: 2621-2628.

Gratzer G. 1978. General lattice theory. Birkhauser Verlag, Basel, Switzerland.

Jun YB. 2008. Soft BCK/BCI-algebras. Comput Math Appl, 56: 1408-1413.

Kazancı O, Mayerova S, Davvaz B. 2022. Algebraic hyperstructure of multi-fuzzy soft sets related to polygroups. Mathematics, 10: 2178.

Kazancı O, Yılmaz Ş, Yamak S. 2010. Soft sets and soft BCH-algebras. Hacettepe J Math Stat, 39(2): 205 – 217.

Maji PK, Biswas R, Roy AR. 2001. Fuzzy soft sets. J Fuzzy Math, 9: 589-602.

Majumdar P, Samanta SK. 2010. Generalised fuzzy soft sets. Comput Math Appl, 59: 1425-1432.

Molodtsov D. 1999. Soft set theory-first results. Comput Math Appl, 37: 19-31.

Pawlak Z. 1982. Rough sets. Int J Info Comput Sci, 11: 341-356.

Qin K, Hong Z. 2010. On soft equality. J Comput Appl Math, 234: 1347-1355.

Sebastian S, Ramakrishnan TV. 2011a. Multi-fuzzy sets: an extension of fuzzy sets. Fuzzy Info Eng, 1: 35-43.

Sebastian S, Ramakrishnan TV. 2011b. Multi-fuzzy subgroups. Int J Contemp Math Sci, 8: 365-372.

Shao Y, Qin K. 2012. Fuzzy soft sets and fuzzy soft lattices. Int J Comput Intel Syst, 5 (6): 1135-1147.

Skornjakov LA. 1977. Elements of lattice theory. Hindustan Publishing Corporation, New Delhi, India.

Sun QM, Zhang ZL, Liu J. 2008. Soft sets and soft modules. Lecture Notes Comput Sci, 5009: 403-409.

Yang C. 2011. Fuzzy soft semigroups and fuzzy soft ideals. Comput Math Appl, 61: 255-261.

Yang Y, Tan X, Meng C. 2013. The multi-fuzzy soft set and its application in decision making. Appl Math Model, 37: 4915-4923.

Zadeh LA. 1965. Fuzzy sets. Info Cont, 8: 338-353.

Black Sea Journal of Engineering and Science
doi: 10.34248/bsengineering.1575776

Open Access Journal
e-ISSN: 2619 – 8991

Research Article
Volume 8 - Issue 1: 179-184 / January 2025

EXACT SOLUTIONS OF TIME-FRACTIONAL THIN-FILM FERROELECTRIC MATERIAL EQUATION WITH CONFORMABLE FRACTIONAL DERIVATIVE

Mustafa EKİCİ[1]*

[1]*Çanakkale Onsekiz Mart University, Faculty of Education, Department of Mathematics and Science, 17100, Çanakkale, Türkiye*

Abstract: This study employs the unified method, a powerful approach, to address the intricate challenges posed by fractional differential equations in mathematical physics. The principal objective of this study is to derive novel exact solutions for the time-fractional thin-film ferroelectric material equation. Fractional derivatives in this study are defined using the conformable fractional derivative, ensuring a robust mathematical foundation. Through the unified method, we derive solitary wave solutions for the governing equation, which models wave dynamics in these materials and holds significance in various fields of physics and hydrodynamics. The behavior of these solutions is analyzed using the conformable derivative, shedding light on their dynamic properties. Analytical solutions, formulated in hyperbolic, periodic, and trigonometric forms, illustrating the impact of fractional derivatives on these physical phenomena. This paper highlights the capability of the unified method in tackling complex issues associated with fractional differential equations, expanding both mathematical techniques and our understanding of nonlinear physical phenomena.

Keywords: The thin-film ferroelectric material equation, The unified method, Conformable fractional derivative

***Corresponding author:** Canakkale Onsekiz Mart University, Faculty of Education, Department of Mathematics and Science, 17100, Canakkale, Türkiye
E mail: mustafa.ekici@comu.edu.tr (M. EKİCİ)
Mustafa EKİCİ https://orcid.org/ 0000-0003-2494-8229

Received: October 29, 2024
Accepted: December 16, 2024
Published: January 15, 2025

Cite as: Ekici M. 2025. Exact solutions of time-fractional thin-film ferroelectric material equation with conformable fractional derivative. BSJ Eng Sci, 8(1): 179-184.

Introduction

Nonlinear partial differential equations (NLPDEs) are fundamental in the fields of science and engineering, providing critical frameworks for modeling and analyzing real-world phenomena (Sun et al., 2018). PDEs are widely applied across diverse disciplines, from physics and chemistry to engineering and finance, where they enable a more nuanced understanding of complex physical and dynamical systems. In recent years, fractional differential equations (FDEs) have attracted substantial attention due to their generalization of classical integer-order models, offering enhanced flexibility and accuracy in representation (Ray et al., 2014). The introduction of fractional order derivatives introduces additional degrees of freedom, allowing these models to more precisely capture the intricacies of physical processes and yielding improved results in practical applications when compared to traditional integer-order models.

Fractional partial differential equations (FPDEs) have thus become instrumental across multiple domains, such as physics, chemistry, control theory, acoustics, viscoelasticity, electrochemistry, fluid dynamics, and engineering. These equations support a more accurate modeling of real-world phenomena, especially those with memory and hereditary properties, by reflecting the temporal and spatial dependencies in a system more comprehensively. Nonlinear FDEs, in particular, allow for exact solutions that describe a variety of complex nonlinear behaviors, offering essential insights into the dynamics of sophisticated systems. The expanded capability of FPDEs to capture and interpret complex behaviors highlights their growing importance in advancing scientific understanding across these diverse fields (Mainardi, 2018; Wang et al., 2023).

The quest to find reliable and exact solutions for nonlinear FDEs has spurred significant research efforts; as such solutions are essential for a complete understanding of the physical implications of these equations. Researchers have developed various methods to tackle nonlinear FDEs, providing a rich set of tools for analyzing and modeling intricate phenomena. Solitary wave solutions, in particular, have garnered attention for their effectiveness in elucidating the fundamental physics behind a wide range of phenomena, contributing to fields as varied as hydrodynamics, optics, and materials science. This pursuit has not only enriched the repertoire of mathematical techniques available but has also deepened our understanding of nonlinear physical phenomena, marking nonlinear FDEs as a vital element in modern scientific and engineering research (Wang et al., 2023).

Thin-film ferroelectric materials are characterized by unique dielectric properties, notably their ability to retain polarization even after an external electric field is removed. The mathematical modeling of these materials often involves a complex set of equations to describe the relationship between the electric displacement field, polarization, and electric field within the thin film structure. The governing equation, typically derived from the Landau-Ginzburg-Devonshire theory, incorporates a nonlinear polarization term, accounting for ferroelectric hysteresis, as well as gradient energy terms that describe domain wall behavior. This equation is crucial for understanding the dynamic response and stability of polarization in thin films, which are widely used in memory storage devices, sensors, and actuators. Furthermore, solving these equations provides insights into optimizing ferroelectric material properties at nanoscale dimensions, where size-dependent effects play a significant role. The thin-film ferroelectric equation, therefore, serves not only as a theoretical framework but also as a practical tool in engineering next-generation electronic devices (Martin and Rappe, 2016).

Further the time-fractional thin-film ferroelectric material equation (TFFEME) holds a significant role across various branches of physics and thermodynamics, providing critical insights into the behavior and optimization of thin-film materials. Thin films, characterized by material layers with thicknesses typically in the micrometer range, are profoundly influenced by the deposition process, which largely determines their properties. Recent advancements in optimizing the performance of these materials have greatly expanded their applications, enhancing their relevance in contemporary technology (Setter et al., 2006). The TFFEME finds practical utility across multiple domains, with applications ranging from memory devices and actuators to sensors, each with unique performance requirements tailored to specific contexts. For instance, ferroelectric sensors prioritize high spontaneous polarization, while ferroelectric memory devices demand enhanced fatigue resistance (Gruverman et al., 1997).

In response to the increasing demand for miniaturization within microelectronics, TFFEME-based devices have been scaled down in feature size, now approaching the nanoscale (Qin et al., 2008). Such advancements underscore the adaptability of TFFEME across diverse applications, reinforcing its importance within modern technological landscapes. The one-dimensional time-fractional form of the TFFEME is given by (Zahran et al., 2022) (equation 1).

$$\frac{n_c}{q_d^2}\frac{\partial^\beta G(x,t)}{\partial t^\beta} + [(g_2 - 2\alpha)G + g_4 G^3 + g_6 G^5] - w\Delta G = 0, \quad (1)$$

where n_c and q_d are density of mass and particles. g_2, g_4, g_6 are indicating both pressure and temperature. w is the space non-uniformity coefficient, and α is the reciprocal of the electric susceptibility.

These phenomena can be effectively modeled using NLPDEs. Consequently, obtaining traveling wave solutions of NLPDEs is of significant importance. In order to gain insight into the underlying mechanisms of these physical phenomena, it is imperative to investigate their solutions. Solutions to NLPDEs not only address specific problems but also provide profound insights into the fundamental physical aspects within related fields. As a result, numerous powerful methodologies have been developed to obtain exact solutions for nonlinear equations. These methods, including the tanh-function expansion method (Fan, 2000), Jacobi elliptic function expansion method (Liu et al., 2001), homogeneous balance method (Wang et al., 1996), exponential function method (He and Wu, 2006; Ekici and Unal 2020), (G'/G)-expansion method (Zhang et al., 2008; Ekici and Unal, 2022), Adomian decomposition method (El-Sayed and Gaber, 2006), homotopy analysis method (Arafa et al., 2011), differential transformation method (Odibat and Momani, 2008; Ekici and Ayaz 2017), unified method (Akcagil and Aydemir, 2018), and Kudryashov's method (Kaplan et al., 2016; Ekici, 2023), among others, have been widely employed in exploring nonlinear phenomena across various scientific disciplines.

This study can be summarized as follows: Section 2 provides an overview of the conformable fractional derivative and its fundamental properties, along with a step-by-step explanation of the unified method. In Section 3, the unified method, a key approach in solving fractional partial differential equations and the central focus of this work, is given. Additionally, exact solutions for fractional partial differential equations are obtained using the unified method in Section 3. Finally, a comprehensive discussion of the findings is presented, along with suggestions for future research directions.

2. Materials and Methods

We give with a brief overview of the conformable fractional derivative, emphasizing its fundamental properties.

Definition; Let $\beta \in (0,1]$ and $\varpi: \mathbb{R}^+ \cup \{0\} \to R$ are be given. The conformable fractional derivative of ϖ of order β is defined as follows (equation 2):

$$\left(T_\beta \varpi\right)(t) = \lim_{\varepsilon \to 0} \frac{\varpi\left(t + \varepsilon t^{1-\beta}\right) - \varpi(t)}{\varepsilon}, (t > 0). \quad (2)$$

Theorem; Let $\beta \in (0,1], t > 0$ and ϖ, ψ be β −differentiable. Then we can write the following properties.

* $T_\beta(k\varpi + s\psi) = k(T_\beta \varpi) + s(T_\beta \psi)$, for all $k, s \in \mathbb{R}$.
* $T_\beta(t^m) = mt^{m-\beta}$ for all $m \in \mathbb{R}$.
* $T_\beta(\lambda) = 0$, for all constant functions $\varpi(t) = \lambda$.
* $T_\beta(\varpi\psi) = \varpi(T_\beta \psi) + \psi(T_\beta \varpi)$.
* $T_\beta\left(\frac{\varpi}{\psi}\right) = \frac{\psi(T_\beta \varpi) - \varpi(T_\beta \psi)}{\psi^2}$.

* If, in addition, ϖ is differentiable, then (equation 3);

$$\left(T_\beta \varpi\right)(t) = t^{1-\beta}\left(\frac{d\varpi}{dt}\right). \quad 3$$

The derivative of order β for a constant is zero. Derivatives can be applied to both differentiable and non-differentiable functions (Abdeljawad, 2015; Li and Peng, 2023).

The unified method is an advanced analytical approach that has gained considerable recognition in mathematical physics for its effectiveness in solving nonlinear fractional differential equations. The method has gained renown for its capacity to produce precise analytical solutions to complex and nonlinear equations, thus providing researchers with a robust instrument with which to address a wide range of challenging problems. A key strength of the unified method lies in its flexibility and adaptability, making it especially valuable for cases involving fractional derivative equations and complex boundary conditions.

In this study, we apply the unified method to derive stable and explicit soliton solutions for FDEs. This method accommodates a general form of nonlinear evolution equations, offering a structured approach for exploring the intricate dynamics inherent in fractional models, as outlined below. By employing the unified method, we aim to advance our understanding of these equations and highlight its potential as a powerful framework for future research in nonlinear fractional systems.

In this section we illustrate the unified method for solving NPDEs. Suppose that a NPDEs are in the following form (equation 4):

$$P(u, D_t^\beta u, u_x, D_t^\beta u_x, D_t^{2\beta} u, \dots) = 0, \quad 4$$

where β denotes the conformable fractional derivative, while P denotes a polynomial involving u and its various partial derivatives, encompassing the highest order derivative and nonlinear terms. The unified method will be elucidated to derive typical and broad-spectrum soliton solutions for NFDEs. The fundamental phases of the unified method are outlined as follows:

Step 1: Assign a compound variable ξ with the real variables x and t by the following transformation(equation 5):

$$u(x, t) = U(\xi), \xi = x - \frac{k}{\Gamma(1+\beta)} t^\beta, \quad 5$$

where k is wave velocity. The wave variable assigned in equation 5 transforms equation 4 into the following ordinary differential equation (ODE);

$$Q(U, -kU', U', -kU'', k^2U'', \dots) = O. \quad 6$$

Here, Q represents a polynomial involving U and its derivatives with respect to ξ. We integrate equation 6 as many times as feasible, and for the sake of simplicity, we set the constant(s) of integration to zero.

Step 2: We express the exact solution of equation 6 in the following form (equation 7):

$$U(\xi) = a_0 + \sum_{i=1}^{M}\left[a_i \varphi^i + b_i \varphi^{-i}\right], \quad 7$$

where M is positive integers, a_0, a_i, b_i $(i = 1, 2, 3, \dots, M)$ are constants to be determined and $\varphi = \varphi(\xi)$ satisfies following the Riccati differential equation 8.

$$\varphi'(\xi) = \varphi^2(\xi) + \lambda, \quad 8$$

where $\varphi' = \frac{d\varphi}{d\xi}$ and λ is a constant. The general solution of equation 8 as follows:

Set 1: When $\lambda < 0$, the solutions of equation 8

$$\varphi(\xi) = \begin{cases} \frac{\sqrt{-(A^2+B^2)\lambda} - A\sqrt{-\lambda}\cosh\left(2\sqrt{-\lambda}(\xi+\xi_0)\right)}{A\sinh\left(2\sqrt{-\lambda}(\xi+\xi_0)\right)+B}, \\ \frac{-\sqrt{-(A^2+B^2)\lambda} - A\sqrt{-\lambda}\cosh\left(2\sqrt{-\lambda}(\xi+\xi_0)\right)}{A\sinh\left(2\sqrt{-\lambda}(\xi+\xi_0)\right)+B}, \\ \sqrt{-\lambda} - \frac{2A\sqrt{-\lambda}}{A+\cosh\left(2\sqrt{-\lambda}(\xi+\xi_0)\right)-\sinh\left(2\sqrt{-\lambda}(\xi+\xi_0)\right)}, \\ -\sqrt{-\lambda} + \frac{2A\sqrt{-\lambda}}{A+\cosh\left(2\sqrt{-\lambda}(\xi+\xi_0)\right)+\sinh\left(2\sqrt{-\lambda}(\xi+\xi_0)\right)}, \end{cases}$$

where A, B and ξ_0 are arbitrary constants.

Set 2: When $\lambda > 0$, the solutions of equation 8

$$\varphi(\xi) = \begin{cases} \frac{\sqrt{(A^2-B^2)\lambda} - A\sqrt{\lambda}\cos\left(2\sqrt{\lambda}(\xi+\xi_0)\right)}{A\sin\left(2\sqrt{\lambda}(\xi+\xi_0)\right)+B}, \\ \frac{-\sqrt{(A^2-B^2)\lambda} - A\sqrt{\lambda}\cos\left(2\sqrt{\lambda}(\xi+\xi_0)\right)}{A\sin\left(2\sqrt{\lambda}(\xi+\xi_0)\right)+B}, \\ i\sqrt{\lambda} - \frac{2Ai\sqrt{\lambda}}{A+\cos\left(2\sqrt{\lambda}(\xi+\xi_0)\right)-i\sin\left(2\sqrt{\lambda}(\xi+\xi_0)\right)}, \\ -i\sqrt{\lambda} + \frac{2A\sqrt{\lambda}}{A+\cos\left(2\sqrt{\lambda}(\xi+\xi_0)\right)+i\sin\left(2\sqrt{\lambda}(\xi+\xi_0)\right)}, \end{cases}$$

where A, B and ξ_0 are arbitrary constants.

Set 3: When $\lambda = 0$, the solutions of equation 8

$$\varphi(\xi) = -\frac{1}{\xi + \xi_0},$$

where ξ_0 arbitrary constant (Akter et al., 2020)

Step 3: Employing the homogeneous balance method outlined in equation 6 enables us to determine the positive integer values of M corresponding to the solution described in equation 7. By substituting the solution from equation 7 into equation 6 and incorporating the Riccati equation depicted in equation 8, we obtain a polynomial expression in terms of $U(\xi)$. This polynomial, upon equating coefficients of similar powers of U(ξ) to zero, yields specific sets of algebraic equations.

Step 4: Upon substituting equation 7 into equation 6 alongside equation 8, a polynomial expression in terms of $U(\xi)$ is derived. Equating all coefficients of $U(\xi)$ to zero leads to a system of algebraic equations. By employing the Maple program, we can effectively solve this system to determine the values of parameters such as a_0, a_i, b_i $(i = 1, 2, 3, \dots, M)$, and λ. Subsequently, upon substituting these values and equation 8 into equation 7, exact solutions for the reduced equation 4 can be obtained.

3. Application

Now we apply the unifed method to obtain for analytic solution of the time-fractional thin-film ferroelectric material equation. This equation can be written as (equation 9);

$$\frac{n_c}{q_d^2}\frac{\partial^\beta G(x,t)}{\partial t^\beta}+[(g_2-2\alpha)G+g_4G^3+g_6G^5] - w\frac{\partial^2 G(x,t)}{\partial x^2}=0. \quad 9$$

Using the wave variable, substituting equation 5 into equation 9 reduces to the nonlinear ODE;

$$\left(\frac{k^2n_c}{q_d^2}-w\right)U''+[(g_2-2\alpha)U+g_4U^3+g_6U^5]=0, \quad 10$$

where $k, w, \alpha, g_2, g_4, g_6, n_c$ and q_d are constants (Zahran et al., 2022). By comparing the term U'' with U^5, utilizing the homogeneous balance principle (Wang et al., 2023), $N+2=5N$ is generated. Hence, $N=\frac{1}{2}$. When the transformation is $U(\xi)=\sqrt{P(\xi)}$ used, equation 10 can be decreased, as:

$$\left(\frac{k^2n_c}{q_d^2}-w\right)\left[\frac{1}{2}PP''-\frac{1}{4}(P')^2\right] - [(g_2-2\alpha)P^2+g_4P^3+g_6P^4]=0, \quad 11$$

where $P'=\frac{dP}{d\xi}$. Balancing the highest order term PP'' and P^4 in equation 11 we have $N=1$.

$$P(\xi)=a_0+a_1\varphi+b_1\varphi^{-1}. \quad 12$$

We substitute equation 12 into equation 11 and collect all the terms with the same power of $P^i(\xi)\,(i=0,1,2,\ldots,8)$, and equating each coefficient to zero, yields a set of algebraic equations. Solving these equations with the aid of the mathematical software Maple, yields the following solutions for k, s, b_1, a_0, a_1 :

Case 1:

$$a_0=\frac{-3g_4}{8g_6}, b_1=\frac{9g_4^2}{256a_1g_6^2}, \lambda=-\frac{9g_4^2}{256a_1g_6^2},$$
$$w=-\frac{4}{3}a_1^2g_6+k^2\frac{n_c}{q_d^2}, \alpha=\frac{g_2}{2}-\frac{3}{2}\frac{g_4^2}{g_6}.$$

Substituting these results into equation 12, we reach the results:

(a) Hyperbolic function solutions (when $\lambda<0$):

$$P_{11}(\xi)=\frac{-3g_4}{8g_6}+\frac{9g_4^2\left\{Asinh\left(2\sqrt{-\lambda}(\xi+\xi_0)\right)+B\right\}}{256a_1g_6^2\left\{A\sqrt{-(A^2+B^2)\lambda}-A\sqrt{-\lambda}cosh\left(2\sqrt{-\lambda}(\xi+\xi_0)\right)\right\}},$$

$$P_{12}(\xi)=\frac{-3g_4}{8g_6}-\frac{9g_4^2\left\{Asinh\left(2\sqrt{-\lambda}(\xi+\xi_0)\right)+B\right\}}{256a_1g_6^2\left\{\sqrt{-(A^2+B^2)\lambda}+A\sqrt{-\lambda}cosh\left(2\sqrt{-\lambda}(\xi+\xi_0)\right)\right\}},$$

$$P_{13}(\xi)=\frac{-3g_4}{8g_6}+\frac{9g_4^2\left\{A+cosh\left(2\sqrt{-\lambda}(\xi+\xi_0)\right)-sinh\left(2\sqrt{-\lambda}(\xi+\xi_0)\right)\right\}}{256a_1g_6^2\sqrt{-\lambda}\left\{cosh\left(2\sqrt{-\lambda}(\xi+\xi_0)\right)-sinh\left(2\sqrt{-\lambda}(\xi+\xi_0)\right)-A\right\}},$$

$$P_{14}(\xi)=\frac{-3g_4}{8g_6}+\frac{9g_4^2\left\{A+cosh\left(2\sqrt{-\lambda}(\xi+\xi_0)\right)+sinh\left(2\sqrt{-\lambda}(\xi+\xi_0)\right)\right\}}{256a_1g_6^2\sqrt{-\lambda}\left\{A-cosh\left(2\sqrt{-\lambda}(\xi+\xi_0)\right)-sinh\left(2\sqrt{-\lambda}(\xi+\xi_0)\right)\right\}}.$$

(b) Trigonometric function solutions (when $\lambda>0$):

$$P_{15}(\xi)=\frac{-3g_4}{8g_6}+\frac{9g_4^2\left\{Asin\left(2\sqrt{\lambda}(\xi+\xi_0)\right)+B\right\}}{256a_1g_6^2\left\{\sqrt{\left(A^2-B^2\right)\lambda}-A\sqrt{\lambda}cos\left(2\sqrt{\lambda}(\xi+\xi_0)\right)\right\}},$$

$$P_{16}(\xi)=\frac{-3g_4}{8g_6}-\frac{9g_4^2\left\{Asin\left(2\sqrt{\lambda}(\xi+\xi_0)\right)+B\right\}}{256a_1g_6^2\left\{\sqrt{\left(A^2-B^2\right)\lambda}+A\sqrt{\lambda}cos\left(2\sqrt{\lambda}(\xi+\xi_0)\right)\right\}},$$

$$P_{17}(\xi)=\frac{-3g_4}{8g_6}+\frac{9g_4^2\left\{A+cos\left(2\sqrt{\lambda}(\xi+\xi_0)\right)-i\,sin\left(2\sqrt{\lambda}(\xi+\xi_0)\right)\right\}}{256a_1g_6^2\sqrt{\lambda}\left\{icos\left(2\sqrt{\lambda}(\xi+\xi_0)\right)+\,sin\left(2\sqrt{\lambda}(\xi+\xi_0)\right)-iA\right\}},$$

$$P_{18}(\xi)=\frac{-3g_4}{8g_6}+\frac{9g_4^2\left\{A+cos\left(2\sqrt{\lambda}(\xi+\xi_0)\right)+i\,sin\left(2\sqrt{\lambda}(\xi+\xi_0)\right)\right\}}{256a_1g_6^2\sqrt{\lambda}\left\{-icos\left(2\sqrt{\lambda}(\xi+\xi_0)\right)+\,sin\left(2\sqrt{\lambda}(\xi+\xi_0)\right)+iA\right\}}.$$

(c) Rational function solutions (when $\lambda=0$)

$$P_{19}(\xi)=\frac{-3g_4}{8g_6}-\frac{9g_4^2}{256a_1g_6^2(\xi+\xi_0)},$$

where $\xi=x-\frac{k}{\Gamma(1+\beta)}t^\beta$.

Other cases of solutions can be obtained in a similar manner to the above case; however, these are omitted here for simplicity.

Case 2:

$$a_0=\frac{-3g_4}{8g_6}, b_1=\frac{9g_4^2}{256a_1g_6^2}, \lambda=\frac{9g_4^2}{256a_1^2g_6^2},$$
$$w=-\frac{4}{3}a_1^2g_6+k^2\frac{n_c}{q_d^2}, \alpha=\frac{g_2}{2}-\frac{15}{128}\frac{g_4^2}{g_6}.$$

Case 3:

$$a_0=\frac{-3g_4}{8g_6}, b_1=0, \lambda=-\frac{9}{64}\frac{g_4^2}{a_1^2g_6^2},$$
$$w=-\frac{4}{3}a_1^2g_6+k^2\frac{n_c}{q_d^2}, \alpha=\frac{g_2}{2}-\frac{3}{32}\frac{g_4^2}{g_6}.$$

Case 4:

$$a_0=\frac{-3g_4}{8g_6}, a_1=0, \lambda=-\frac{64}{9}\frac{b_1^2g_6^2}{g_4^2},$$
$$w=k^2\frac{n_c}{q_d^2}-\frac{27}{1024}\frac{g_4^4}{b_1^2g_6^3}, \alpha=\frac{g_2}{2}-\frac{3}{32}\frac{g_4^2}{g_6}.$$

4. Conclusion

In this study, the time-fractional TFFEME problem was tackled using the unified method, which provided exact solutions. Through the unified method, intricate solutions

for rational, trigonometric and hyperbolic function types were derived, allowing for the identification of periodic, w-shaped, dark, and bright soliton structures in closed-form solutions that characterize the governing model. The findings confirm that the unified method serves as an efficient and adaptable mathematical approach for deriving a range of solitary wave solutions under the influence of temporal fractional operators. All computations were conducted using Maple, demonstrating the method's capability in extracting complex wave profiles with high accuracy and consistency. These solutions offer valuable insights into the intricate mechanisms underlying nonlinear physical phenomena, particularly in the context of wave collaboration. Our findings underscore the directness and efficiency of the unified method, highlighting its applicability to a wide array of nonlinear PDEs in mathematical physics.

Author Contributions

The percentages of the author contributions are presented below. The author reviewed and approved the final version of the manuscript.

	M.E.
C	100
D	100
S	100
DCP	100
DAI	100
L	100
W	100
CR	100
SR	100
PM	100
FA	100

C=Concept, D= design, S= supervision, DCP= data collection and/or processing, DAI= data analysis and/or interpretation, L= literature search, W= writing, CR= critical review, SR= submission and revision, PM= project management, FA= funding acquisition.

Conflict of Interest

The author declared that there is no conflict of interest.

Ethical Consideration

Ethics committee approval was not required for this study because of there was no study on animals or humans.

Acknowledgements

This study is not funded by any institution. The author expresses their sincere thanks for the reviewer's suggestions and comments.

References

Abdeljawad T. 2015. On conformable fractional calculus. J Comput Appl Math, 279: 57-66.

Akcagil S, Aydemir T. 2018. A new application of the unified method. New Trends Mathl Sci, 2018: 6(1).

Akter S, Sen RK, Roshid HO. 2020. Dynamics of interaction between solitary and rogue wave of the space-time fractional Broer–Kaup models arising in shallow water of harbor and coastal zone. SN Appl Sci, 2: 1-12.

Arafa AAM, Rida SZ, Mohamed H. 2011. Homotopy analysis method for solving biological population model. Commun Theor Phys, 56(5): 797.

Ekici M, Ünal M. 2020. Application of the exponential rational function method to some fractional soliton equations. IGI Global, Newyork, USA, pp: 13-32.

Ekici M, Ayaz F. 2017. Solution of model equation of completely passive natural convection by improved differential transform method. Res Eng Struct Mat, 3(1): 1-10.

Ekici M, Ünal M. 2022. Application of the rational (G'/G)-expansion method for solving some coupled and combined wave equations. Commun Fac Sci Univ Ank Ser A1 Math Stat, 71(1): 116-132.

Ekici M. 2023. Exact solutions to some nonlinear time-fractional evolution equations using the generalized Kudryashov method in mathematical physics. Symmetry, 15(10): 1961.

El-Sayed AMA, Gaber M. 2006. The Adomian decomposition method for solving partial differential equations of fractal order in finite domains. Phys Lett A, 359(3): 175-182.

Fan E. 2000. Extended tanh-function method and its applications to nonlinear equations. Phys Lett A, 277(4): 212-218.

Gruverman A, Tokumoto H, Prakash AS, Aggarwal S, Yang B, Wuttig M, Venkatesan T. 1997. Nanoscale imaging of domain dynamics and retention in ferroelectric thin films. Appl Phys Lett, 71(24): 3492-3494.

He JH, Wu XH. 2006. Exp-function method for nonlinear wave equations. Chaos Solitons Fract, 30(3): 700-708.

Kaplan M, Bekir A, Akbulut A. 2016. A generalized Kudryashov method to some nonlinear evolution equations in mathematical physics. Nonlinear Dyn, 85(4): 2843-2850.

Li Z, Peng C. 2023. Bifurcation, phase portrait and traveling wave solution of time-fractional thin-film ferroelectric material equation with beta fractional derivative. Phys Lett A, 484: 129080.

Liu S, Fu Z, Liu S, Zhao Q. 2001. Jacobi elliptic function expansion method and periodic wave solutions of nonlinear wave equations. Phys Lett A, 289(1): 69-74.

Mainardi F. 2018. Fractional calculus: Theory and applications. Mathemat, 6(9): 145.

Martin LW, Rappe AM. 2016. Thin-film ferroelectric materials and their applications. Nat Rev Mater, 2(2): 1-14.

Odibat Z, Momani S. 2008. A generalized differential transform method for linear partial differential equations of fractional order. Appl Math Lett, 21(2): 194-199.

Qin M, Yao K, Liang YC. 2008. High efficient photovoltaics in nanoscaled ferroelectric thin films. Appl Phys Lett, 2008: 93(12).

Ray SS, Atangana A, Noutchie SC, Kurulay M, Bildik N, Kilicman A. 2014. Fractional calculus and its applications in applied mathematics and other sciences. Math Probl Eng, 2014(2): 849395.

Setter N, Damjanovic D, Eng L, Fox G, Gevorgian S, Hong S, Streiffer S. 2006. Ferroelectric thin films: Review of materials, properties, and applications. J Appl Phys, 2006: 100(5).

Sun H, Zhang Y, Baleanu D, Chen W, Chen Y. 2018. A new collection of real world applications of fractional calculus in science and engineering. Commun Nonlinear Sci Numer Simul, 64: 213-231.

Wang X, Ehsan H, Abbas M, Akram G, Sadaf M, Abdeljawad T. 2023. Analytical solitary wave solutions of a time-fractional thin-film ferroelectric material equation involving beta-derivative using modified auxiliary equation method. Results Phys, 48: 106411.

Wang M, Zhou Y, Li Z. 1996. Application of a homogeneous balance method to exact solutions of nonlinear equations in mathematical physics. Phys Lett A, 216(1-5): 67-75.

Zahran E H, Mirhosseini-Alizamini SM, Shehata MS, Rezazadeh H, Ahmad H. 2022. Study on abundant explicit wave solutions of the thin-film Ferro-electric materials equation. Opt Quantum Electron, 54(1): 48.

Zhang S, Tong J L, Wang W. 2008. A generalized (G'/G)-expansion method for the mKdV equation with variable coefficients. Phys Lett A, 372(13): 2254-2257.

Black Sea Journal of Engineering and Science
doi: 10.34248/bsengineering.1535503

Open Access Journal
e-ISSN: 2619 – 8991

Research Article
Volume 8 - Issue 1: 185-190 / January 2025

ENHANCING MAMMOGRAPHY IMAGES WITH ARTIFICIAL INTELLIGENCE TO IMPROVE RADIOLOGICAL DIAGNOSIS IN BREAST CANCER

Fatih GÜL[1]*, Muhammed UÇAR[1], Nur HÜRSOY[2]

[1]*Recep Tayyip Erdoğan University, Faculty of Engineering and Architecture, Department of Electrical-Electronics Engineering, 53100, Rize, Türkiye*
[2]*Recep Tayyip Erdoğan University, Faculty of Medicine, Department of Radiology, 53100, Rize, Türkiye*

Abstract: Breast cancer is one of the most common types of cancer in women, and early diagnosis is life-saving. The aim of this study is to enhance the resolution of mammography images, thereby improving the contrast resolution, spatial resolution, and the detectability of calcifications, distortions, and opacities in the images. For this purpose, mammography images obtained from the open-access mini-MIAS dataset were used. Both the original dataset and the images processed with the CLAHE (Contrast Limited Adaptive Histogram Equalization) algorithm underwent resolution enhancement using the Stable Diffusion artificial intelligence system. The results were evaluated by an expert radiologist, and it was determined that the diagnostic quality of the images significantly increased. These improvements aim to support early diagnosis in breast cancer and enhance diagnostic accuracy. Additionally, the applicability and effectiveness of these methods were emphasized, and the potential benefits of resolution enhancement techniques in clinical practice were discussed. The results have the potential to allow for more detailed and accurate analysis of mammography images, thereby improving patient care and treatment planning.

Keywords: Mammography, Image processing, Resolution enhancement, Artificial intelligence, Clahe algorithm

***Corresponding author:** Recep Tayyip Erdoğan University, Faculty of Engineering and Architecture, Department of Electrical-Electronics Engineering, 53100, Rize, Türkiye
E mail: fatih.gul@erdogan.edu.tr (F. GÜL)
Fatih GÜL https://orcid.org/0000-0001-5072-2122
Muhammed UÇAR https://orcid.org/0009-0007-0445-6637
Nur HÜRSOY https://orcid.org/0000-0001-5059-2268

Received: August 19, 2024
Accepted: December 16, 2024
Published: January 15, 2025

Cite as: Gül F, Uçar M, Hürsoy N. 2025. Improving mammography images with artificial intelligence support to improve radiological diagnostic processes in breast cancer. BSJ Eng Sci, 8(1): 185-190.

1. Introduction

Cancer, as one of the most common causes of death worldwide, is particularly prevalent among women. Breast cancer, in particular, holds a significant place among these diseases. One critical factor in combating breast cancer is early diagnosis. Various imaging technologies, such as Magnetic Resonance Imaging (MRI), Ultrasonography (US), and Mammography, have been developed and are used for the treatment of this disease (Avcı and Karakaya 2023). Among these techniques, mammography is the most commonly used method. Due to its cost-effectiveness and applicability, mammography plays an important role in the early diagnosis of cancer (Li et al. 2016).

Of the early signs of breast cancer, microcalcifications are a significant indicator that can be detected through screening methods (Mehdy et al. 2017). Mammography is a commonly used technique to identify masses in breast tissue. However, since these masses often have low contrast, the diagnostic process can be challenging. Images can be degraded by random noise due to environmental factors or device errors. Various algorithms have been developed to reduce this unwanted noise and improve image quality. Medical image processing techniques can be effective in enhancing these images through the use of Computer-Aided Diagnosis (CAD) systems.

Today, medical image processing is one of the fastest-growing fields in the healthcare sector, continuously advancing by offering new opportunities and solutions (Avcı and Karakaya 2023; Dhawan et al. 1991).

The primary goal of image processing is to enhance the reliability and comprehensibility of medical images used in diagnostic and treatment processes. Regarding breast cancer diagnosis, the presence of masses can be determined, and benign (non-cancerous) and malignant (cancerous) lesions can be distinguished using various image processing algorithms and statistical methods. These methods also support Computer-Aided Diagnosis (CAD) systems, making significant contributions to the diagnostic process (Mehdy et al. 2017).

To increase the visibility of microcalcifications, one of the earliest signs of breast cancer, in mammography images, various algorithms have been proposed (Besl and Jain 1988). Among these algorithms, techniques such as Mean Filter, Median Filter, Gaussian Filter, Contrast Limited Adaptive Histogram Equalization (CLAHE), Unsharp Masking, and Laplacian Sharpening are used in the

preprocessing stage. The effectiveness of different preprocessing methods on various images has been examined in numerous studies in the literature (Al-Najdawi et al., 2015; Ganvir and Yadav 2019; Swathi et al. 2017). However, a review of the literature reveals that most studies focus on filtering methods and deep learning. Research aimed at enhancing the resolution of radiological images with current artificial intelligence systems is quite limited. This underscores the need for more research in this area.

In the rapidly advancing world of technology, the importance of artificial intelligence (AI) is becoming increasingly evident. Over time, interest in AI and research in this field are growing. Artificial neural networks, designed similarly to biological neural networks, have the capacity to solve a range of problems today by being used in learning and application processes. These systems provide significant advancements in various sectors due to their ability to analyze complex datasets, recognize patterns, and make predictions. This emphasizes the potential and importance of AI in the future.

In this study, a system called Stable Diffusion (SD) is used as the artificial intelligence model. Stable Diffusion allows users to create and train their own models and then utilize them. The trained models can be used for free with the Stable Diffusion AI model, which is installed on a computer and runs on a browser. This system offers the ability to generate images from text descriptions, make modifications to images, adjust the size of uploaded images, and enhance image resolution through various methods. The main material of this study comprises sections used to enhance image resolution.

The aim of this study is to enhance the resolution of mammography images and present the obtained results to an expert radiologist to examine the ease provided by image enhancement in evaluating image contrast resolution, spatial resolution, and the detectability of calcifications, distortions, and opacities. Section 2 covers the materials and methods. Section 3 discusses how the results presented to the expert radiologist were evaluated and the discussions made on these results.

2. Materials and Methods

In this study, a web-based Stable Diffusion artificial intelligence system was used to enhance the resolution of mammography images and to examine the ease provided by image enhancement for the image analysis parameters mentioned in the introduction section.

2.1. Data Collection

The study used an open-access dataset consisting of mini-MIAS mammography images (Avcı and Karakaya 2023). Additionally, a different version of this dataset created from the original was also used for this study. The images in the original dataset were converted to PNG format and processed using the CLAHE algorithm. The original dataset is the mini-MIAS dataset, which includes 322 digitized mammography images from 161 patients, including both left and right breast images (Avcı and Karakaya 2023). The images were used in PNG format and have a size of 1024x1024 pixels.

The first dataset used in this study consists of images from the original mini-MIAS dataset that were converted to PNG format, processed through the CLAHE algorithm, and cropped to a smaller size. Due to the functionality of the CLAHE algorithm, as seen in the studies by (Al-Najdawi, Biltawi, and Tedmori 2015; Avcı and Karakaya 2023), images processed through this algorithm were primarily used. Similar processes were applied to the original mini-MIAS dataset, and studies were conducted according to the requests of the expert radiologist.

Ethical committee approval was not required for this study since the data used is open-access. Due to the public availability of the data, obtaining informed consent from patients was not necessary.

2.1.1. Examination of the Mini-MIAS Dataset by Tissue and Abnormality Classes

Based on discussions with the expert radiologist, certain characteristics and classifications were emphasized for the labeled datasets to be used in this study. The background tissue of the mammography images was classified as follows:

- F: Fatty
- G: Fatty-glandular
- D: Dense-glandular

The abnormality classes were categorized as follows:

- CALC: Calcification
- CIRC: Well-defined/circumscribed masses
- SPIC: Spiculated masses
- MISC: Other, ill-defined masses
- ARCH: Architectural distortion
- ASYM: Asymmetry
- NORM: Normal

These classifications form the methodological basis of the study, ensuring accurate and effective evaluation of the mammography images.

Following consultations with the radiologist, studies were primarily conducted on images labeled as dense-glandular (D), which are considered the most important today. Examples were selected from the abnormality classes of calcification (CALC), architectural distortion (ARCH), and asymmetry (ASYM), with the background tissue character of these images chosen as dense-glandular (D) based on the expert radiologist's guidance.

The resolution of the first 30 images in the CLAHE-processed mini-MIAS database was enhanced to continue the studies. These initial 30 images include the NORM, MISC, and SIRC abnormality classes. Additionally, the images represent three different tissue characters: fatty (F), fatty-glandular (G), and dense-glandular (D).

In the original mini-MIAS dataset, three examples each of normal (NORM), benign (BENIGN-B), and malignant (MALIGN-M) for the fatty (F), fatty-glandular (G), and dense-glandular (D) background tissue classes were studied. For the abnormality class studies, a total of 27 images were prepared, consisting of three benign and

three malignant examples for each of the CALC, ARCH, and ASYM classes, and these studies were presented to the expert radiologist.

2.2. Methods

Stable Diffusion is a deep learning-based text-to-image conversion model. This model is primarily designed to create detailed images based on text descriptions. However, the capabilities of Stable Diffusion are not limited to this. It can also be successfully used for various tasks such as altering the content of an image or expanding the image (Guide, 2024). This demonstrates that Stable Diffusion is a significant tool in the field of image processing and synthesis. In this study, this artificial intelligence system was chosen to enlarge images, prevent quality loss during the enlargement process, and increase the resolution of the uploaded mammography images. The methods applied to the images and the values of these methods are explained in detail under the "Methods" section.

The study continued in the img2img (image to image) section of the SD web interface. The settings applied to the uploaded image were adjusted from the menus generated at the initial settings using SD interface. The values and contents of the methods used for both data sets are presented in Table 1.

Table 1. Methods and values used in the SD interface, the artificial intelligence used for this study

	1. Dataset	2. Dataset
Sampling Methods	DPM++2M KARRAS	DPM++2M KARRAS
Sampling Steps	40	100
CFG Scale	10	7
Denoising Strength	0.1	0.1
Script	Ultimate SD Upscale	Ultimate SD Upscale
Target Size Type to Scale from Image Size	1.5	1.5
Upscaler	ESRGAN_4x	ESRGAN_4x

Sampling Methods are algorithms that guide the process by which an artificial intelligence model transforms random noise into a coherent image. This process can be likened to a painter who starts with a blank canvas and gradually adds layers of paint, eventually creating a picture. These methods determine how each 'brush stroke' is applied, affecting the final appearance, detail, and accuracy of the image (Steins 2023). In this study, the DPM++ 2M Karras method was chosen as the sampling method due to its high level of detail.

Sampling Steps correspond to individual brush strokes in our painting analogy. Each step is a phase where the AI makes adjustments to the image, bringing it closer to the final result. Fewer steps allow the process to progress faster but may result in less detail. Conversely, more steps enable finer details but make the process take longer. The key is to find the right balance for the desired outcome (Steins 2023). Initially, 40 steps were applied for the processed dataset and 100 steps for the original dataset.

CFG Scale is an important concept in the field of Stable Diffusion (SD). This scale is used to control how closely the generated image aligns with the input prompt. Essentially, the CFG Scale functions as a control knob that determines how closely the AI follows the specific details and instructions specified in the user's prompt (Steins 2023). For the initial dataset, a CFG Scale value of 10 was chosen. For the original dataset, this value was set to 7.

Denoising Strength is a parameter that determines how much noise is added to the image before the sampling steps. This parameter is commonly used in image-to-image transformation applications in Stable Diffusion. The value of Denoising Strength ranges from 0 to 1. A value of 0 means no noise is added to the input image, while a value of 1 means the input image is completely replaced by noise. This parameter balances between preserving the original image and creating a completely new image (Rombach et al. 2022). In this study, a Denoising Strength value of 0.1 was used for both datasets to ensure that the image was not distorted.

Target Size Type is either taken from the img2img settings mentioned above or the initially uploaded image is scaled up by the entered factor. This is an optional method that can be adjusted as needed. In this study, all uploaded images were scaled from their image size and increased by a factor of 1.5.

The Upscaler model used was ESRGAN_4x, and all other settings were left at their default values. These methods were applied to all images, and the results were obtained. This approach has allowed for more detailed analyses by increasing the resolution of the images.

2.2.1. Resolution Enhancement Applications

Selected images from the dataset processed with the CLAHE algorithm and cropped were uploaded to the system, and the specified methods were applied to obtain an output. This output was then re-uploaded to the system, and the same processes were applied a second time. Thus, the image was enhanced by enlarging it 1.5 times twice. As an example of the studies in this dataset, the steps shown in Figure 1 were obtained by applying these methods, and the processes were applied separately to each of the selected 30 images. In the size process of the sample image, the image was enlarged from 512x512 pixels to 768x768 pixels in the first application, and then to 1152x1152 pixels when applied again, obtaining the final image.

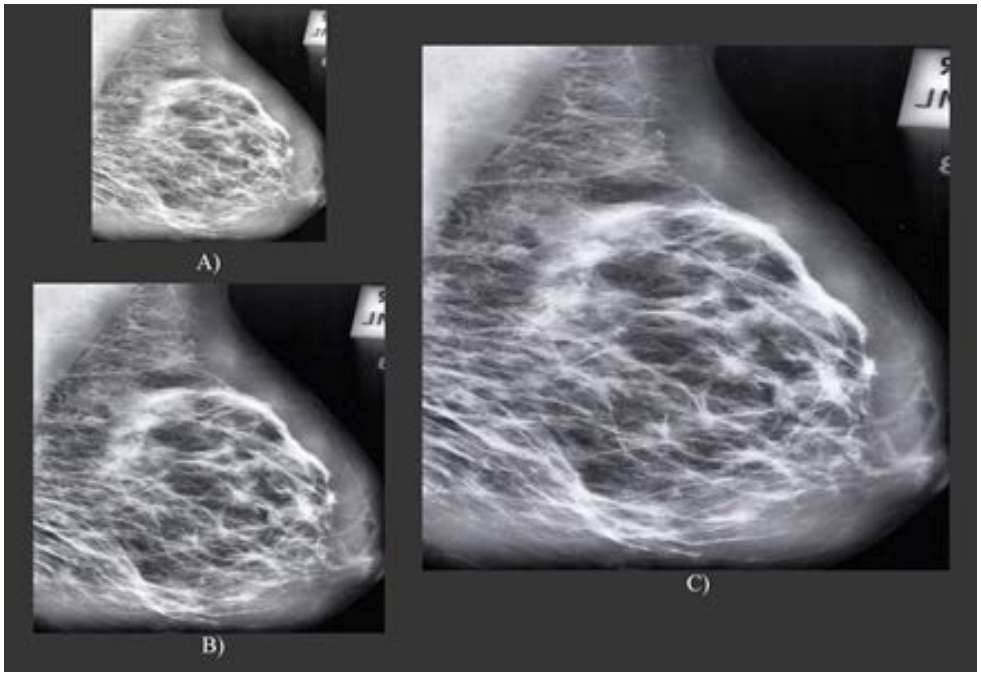

Figure 1. The normal state of a mammogram image from the processed dataset (A). The first result of applying the methods (B). The result of applying the methods a second time (C).

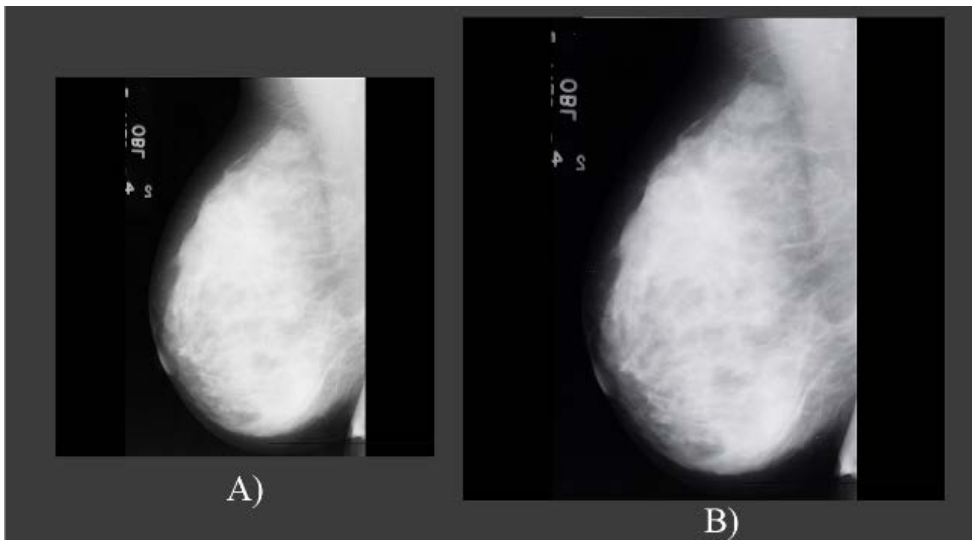

Figure 2. A sample image from the original dataset in its normal state (A), and the output obtained after the first application of the methods (B).

For the mammogram images in the original mini-MIAS dataset, images selected for categories preferred by the radiologist were converted from PGM format to PNG format. These images were then processed once, as explained in the "Methods" section, and enlarged from 1024x1024 pixels to 1536x1536 pixels. Figure 2 shows the process of the studies using one of these applications.

3. Results and Discussion

The enhanced images were evaluated by a radiology specialist with five years of experience in breast radiology using a 23.8-inch screen with a resolution of 1920x1080. The contributions of the enhanced images to the evaluation process, including contrast resolution, spatial resolution, detectability of calcifications, distortions, and opacities, were examined. Table 2 compares key image metrics before and after enhancement using artificial intelligence.

In the evaluation of the first dataset, which consisted of CLAHE-applied and cropped images, an increase in spatial and contrast resolution was detected in all images. This increase in resolution facilitated the detection of calcifications and the identification of distortions and nodular opacities. However, no differences were found in the BI-RADS category assessments by the radiology specialist. It was concluded that the image improvements could shorten the evaluation time but did not change the diagnosis made by the specialist.

Table 2. Image Metric Comparison

Metric	Before Enhancement	After Enhancement
Contrast Resolution	0.75	0.90
Spatial Resolution (pixels)	1024x1024	1536x1536
Detectability of Calcifications	Low (Score: 3/10)	High (Score: 8/10)
Detectability of Distortions	Moderate (Score: 5/10)	High (Score: 9/10)
Detectability of Opacities	50%	90%

In the second phase of the study, images from different subgroups of the unprocessed dataset (mini-MIAS dataset) were selected, as previously mentioned. Enhancements were made on images with findings of calcifications, asymmetry, and distortions in different parenchymal types in the benign and malignant labeled groups. These enhanced images were evaluated by the same radiology specialist. No obvious differences were found between the images processed by the AI system, which allows various modifications, and the raw images. The detectability of the findings indicated in the labels was similar. The reason for not detecting differences in the second study may be that the original dataset images were of higher quality compared to the images in the first phase, and image enhancement did not lead to significant changes.

Table 3 provides a summary of all categories studied in this work and the criteria considered by the radiologist during the evaluation process.

Table 3. Categories used throughout the study and the results of the examination criteria

	Contrast Resolution	Spatial Resolution	Eligibility of Calcifications	Selectability of Distortions	Selectability of Opacities	Diagnosis
Fatty (F)	✓	✓	✓	✓	✓	∼
Fatty Glandular (G)	✓	✓	✓	✓	✓	∼
Dense Glandular (D)	✓	✓	✓	✓	✓	∼
MISC	✓	✓	✓	✓	✓	∼
CIRC	✓	✓	✓	✓	✓	∼
CALC	○	○	○	○	○	∼
ARCH	○	○	○	○	○	∼
ASYM	○	○	○	○	○	∼

✓= Indicates that visible improvement with the observation of the expert mammography radiologist. ○= Indicates that there is no visible change as observed by the radiologist. ∼: Indicates that the procedure performed slight change the diagnosis made by the radiologist.

In the academic literature, the preprocessing step plays a critical role in the segmentation and feature extraction processes for identifying suspicious regions. Among preprocessing techniques, Contrast Limited Adaptive Histogram Equalization (CLAHE), Median Filtering, and Unsharp Masking algorithms are widely preferred (Al-Najdawi, Biltawi, and Tedmori 2015; Ramani et al., 2013). However, no similar studies directly overlapping with the processes performed in this study have been found. Upon examining the first dataset used, it was observed that the images were already processed with the CLAHE algorithm, which is believed to have positively contributed to the study's results.

The use of image enhancement algorithms has been found to accelerate the evaluation processes of radiologists. These algorithms, particularly in detecting calcifications, distortions, and nodular opacities, have increased the detectability rate. This suggests that the algorithms have potential value in clinical applications.

4. Conclusion

In conclusion, various methods were used in an AI model implemented on a computer system to enhance mammography images. These methods facilitated the evaluation process by increasing the resolution of the images. However, it was observed that these enhancements did not lead to a significant improvement in the diagnostic processes of radiologists. Studies conducted on images processed using the CLAHE algorithm concluded that they provided more effective decision-making capabilities and could shorten the evaluation process compared to the original images.

Future research is recommended to be conducted with expanded datasets, including filtering algorithms used in the literature, in addition to this AI system. This approach is believed to not only increase the resolution of the images but also aid radiologists more in detecting benign and malignant lesions. This could be an important step in improving the evaluation and diagnostic processes of mammography images.

Author Contributions

The percentages of the authors' contributions are presented below. All authors reviewed and approved the final version of the manuscript.

	F.G.	M.U.	N.H.
C	30	30	40
D	30	40	30
S	50	10	40
DCP	30	40	40
DAI	40	40	30
L	40	30	30
W	40	40	20
CR	30	30	40
SR	60	30	10
PM	60	30	10
FA	60	30	10

C=Concept, D= design, S= supervision, DCP= data collection and/or processing, DAI= data analysis and/or interpretation, L= literature search, W= writing, CR= critical review, SR= submission and revision, PM= project management, FA= funding acquisition.

Conflict of Interest

The authors declared that there is no conflict of interest.

Ethical Consideration

Ethics committee approval was not required for this study because of there was no study on animals or humans.

Acknowledgements

This article was produced from the thesis of the second author, supervised by the first and co-supervised by the third author, a radiology specialist with expertise in mammography. All of the research accomplished in "Artificial Intelligence/Internet of Things Research Laboratory (AIIoT Lab), Recep Tayyip Erdogan University", supported under the TÜBİTAK-121E544 project. The authors thank TÜBİTAK for contributions.

References

Al-Najdawi N, Mariam B, Sara T. 2015. Mammogram image visual enhancement, mass segmentation and classification. Applied Soft Comput, 35: 175–85. doi:10.1016/J.ASOC.2015.06.029

Avcı H, Karakaya J. 2023. A novel medical image enhancement algorithm for breast cancer detection on mammography images using machine learning. Diagnostics, 13(3): 348. doi:10.3390/DIAGNOSTICS13030348

Besl PJ, Jain RC. 1988. Segmentation through variable-order surface fitting. IEEE Transact Pattern Analys Mach Intellig, 10(2): 167–92. doi:10.1109/34.3881

Dhawan AP, Yateen SC, Myron M, Eric G. 1991. Classification of mammographic microcalcification and structural features using an artificial neural network. https://researchwith.njit.edu/en/publications/classification-of-mammographic-microcalcification-and-structural- (accessed date: August 12, 2024).

Ganvir NN, Yadav DM. 2019. Filtering method for pre-processing mammogram images for breast cancer detection. Inter J Engin Adv Technol, 9(1): 4222–29. doi:10.35940/ijeat.A1623.109119

Guide. 2024. What denoising strength does and how to use it in stable diffusion. https://onceuponanalgorithm.org/guide-what-denoising-strength-does-and-how-to-use-it-in-stable-diffusion/ (accessed date: August 12, 2024).

Li H, Shanhua Z, Qingyuan W, Rongguang Z. 2016. Clinical value of mammography in diagnosis and identification of breast mass. Pakistan J Med Sci, 32(4): 1020. doi:10.12669/PJMS.324.9384.

Mehdy MM, PY Ng, EF Shair, NI Md Saleh, C Gomes. 2017. Artificial neural networks in image processing for early detection of breast cancer. Comput Math Meth Med, 2017(1): 2610628. doi:10.1155/2017/2610628

Ramani R, Suthanthira NV, Valarmathy S. 2013. The pre-processing techniques for breast cancer detection in mammography images. Inter J Image, Graph Signal Proc, (5): 47–54. doi:10.5815/ijigsp.2013.05.06

Rombach R, Andreas B, Dominik L, Patrick E, Bjorn O. 2022. High-resolution image synthesis with latent diffusion models. Proceedings of the IEEE Computer Society Conference on Computer Vision and Pattern Recognition, 5-6 June, Dubai, UAE, pp: 10674–106785. doi:10.1109/CVPR52688.2022.01042

Steins. 2023. Stable Diffusion clearly explained! Medium. http://anakin.ai/blog/stable-diffusion-sampling-steps/ (accessed date: August 12, 2024).

Swathi C, Anoop BK. Anto Sahaya Dhas D, Perumal Sanker S. 2017. Comparison of different image preprocessing methods used for retinal fundus images. 2017 Conference on Emerging Devices and Smart Systems, ICEDSS 2017: 175–79. doi:10.1109/ICEDSS.2017.8073677

Black Sea Journal of Engineering and Science
doi: 10.34248/bsengineering.1571404

Open Access Journal
e-ISSN: 2619 – 8991

Research Article
Volume 8 - Issue 1: 191-198 / January 2025

BIOFUEL PELLETS AS A SUSTAINABLE ENERGY SOLUTION: EXPLORING THE ROLE OF BIOMASS AND REGIONAL WASTE MANAGEMENT IN TURKIYE'S TR63 REGION

Serdar ÜÇOK[1]*

[1]*Kahramanmaraş Sütcü İmam University, Faculty of Agriculture, Biosystems Engineering, 46000, Kahramanmaras, Türkiye*

Abstract: In recent years, the increasing demand for sustainable and renewable energy sources has led to significant interest in biofuels. Bifuel pellets, which combine biomass materials with fossil fuels, have emerged as an innovative and environmentally friendly energy solution. Typically made from agricultural residues, wood waste, or energy crops, blended with fossil fuels such as coal or oil derivatives, bifuel pellets offer improved energy efficiency and combustion properties. By bridging the gap between traditional fossil fuels and renewable energy alternatives, bifuel pellets provide a transitional solution that enhances both calorific value and combustion efficiency. The dual composition of these pellets allows for better adaptation to existing energy infrastructures while supporting reductions in greenhouse gas emissions. In Türkiye, regional development and waste management strategies have been shaped by the adoption of the Nomenclature of Territorial Units for Statistics (NUTS) system since 2002. The TR63 NUTS Level 2 Region, which includes the provinces of Hatay, Kahramanmaraş, and Osmaniye, plays a critical role in agriculture and livestock production. Due to these activities, the region contributes significantly to waste generation. This research highlights the potential of bifuel pellets as a viable energy option for the TR63 Region, where agricultural and livestock residues could serve as essential feedstock for sustainable energy production. The integration of bifuel pellets into regional energy policies could help address environmental goals while reducing dependence on conventional fossil fuels.

Keywords: TR63 region, Biofuel, Pellet, Energy

Corresponding author: Kahramanmaraş Sütcü İmam University, Faculty of Agriculture, Biosystems Engineering, 46000, Kahramanmaras, Türkiye
E mail: sucok@ksu.edu.tr (S. ÜÇOK)
Serdar ÜÇOK https://orcid.org/0000-0002-7158-669X

Received: October 22, 2024
Accepted: December 17, 2024
Published: January 15, 2025

Cite as: Üçok S. 2025. Biofuel pellets as a sustainable energy solution: exploring the role of biomass and regional waste management in Türkiye's TR63 region. BSJ Eng Sci, 8(1): 191-198.

1. Introduction

In recent years, the growing demand for sustainable and renewable energy sources has fueled considerable interest in biofuels. Bifuel pellets, an innovative development in this field, represent a versatile and environmentally friendly solution. These pellets are typically composed of biomass materials, such as agricultural residues, wood waste, or energy crops, combined with fossil fuels, such as coal or oil derivatives, to enhance their energy efficiency and combustion properties (Yang et al., 2019; Ståhl et al., 2016). By merging renewable biomass with conventional fuels, bifuel pellets offer a transitional energy solution, bridging the gap between traditional fossil fuels and fully renewable alternatives (Kovač et al., 2021).

The dual composition of biofuel pellets provides several benefits. Biomass, as a renewable resource, is readily available and helps reduce greenhouse gas emissions by absorbing CO_2 during its growth phase, making the combustion of these pellets nearly carbon neutral (Wang et al., 2023). Additionally, the inclusion of fossil fuel components improves the calorific value, combustion efficiency, and stability, making bifuel pellets more adaptable to existing energy infrastructures, particularly for power generation and heating systems (Luo et al., 2010; Karka et al., 2021; Samuelsson et al., 2012).

Biofuel is a type of renewable energy derived from organic materials, known as biomass, including plants, agricultural residues, and waste products. It offers a cleaner alternative to fossil fuels, reducing greenhouse gas emissions and dependence on non-renewable energy sources. Key Types of Biofuels consist of six parts: those are;

Ethanol; Produced from fermentation of sugars or starches. Commonly blended with gasoline.

Biodiesel; Made from vegetable oils, animal fats, or recycled grease. Can be used in diesel engines without modification.

Biogas; Produced from anaerobic digestion of organic waste. Primarily methane and carbon dioxide, used for heating or electricity.

Bioethanol; Similar to ethanol but produced from lignocellulosic biomass like straw or wood.

Biojet fuel; Designed for aviation, derived from oils, fats, or algae. Solid biofuel (Sing et al., 2024).

Biofuel production typically uses biochemical and

thermochemical methods, depending on the feedstock's properties. Biochemical processes like fermentation are ideal for wet biomass, while thermochemical methods like pyrolysis are better suited for dry biomass. Each method has varying costs and efficiencies, requiring tailored approaches for sustainable implementation (Rodionova et al., 2017).

The development of bifuel pellets not only reduces reliance on conventional fossil fuels but also addresses limitations often associated with pure biomass fuels, such as low energy content, moisture sensitivity, and inconsistent quality (Kheshgi et al., 2000). This hybrid fuel offers a practical and economically viable option for both industries and households, providing a cleaner, more efficient energy alternative that supports both environmental and energy security goals (Stattman et al., 2018).

Since 2002, Türkiye has implemented the Nomenclature of Territorial Units for Statistics (NUTS) to collect and develop regional statistics, conduct socio-economic analyses, define regional policy frameworks, and create a comparable statistical database aligned with the European Union's regional statistical system. Türkiye is divided into 12 NUTS Level 1, 26 NUTS Level 2, and 81 NUTS Level 3 regions. The provinces of Hatay, Kahramanmaraş, and Osmaniye, located in the southern part of Türkiye, are defined as the "TR63 NUTS Level 2 Region," within the TR6 Mediterranean NUTS Level 1 Region.

The TR63 Region, located in southern Türkiye, is bordered by the TR62 Adana-Mersin region and the Mediterranean Sea to the west, the TR72 Kayseri, Sivas, Yozgat region to the north, the TRC1 Gaziantep, Kilis, Adıyaman region to the east, and Syria to the south. Covering a total area of 23,607 km^2, the TR63 Region accounts for 3% of Turkiye's total land area. With the enactment of Law No. 6360 on the establishment of metropolitan municipalities in thirteen provinces and the creation of twenty-six new districts, Hatay and Kahramanmaraş gained metropolitan status. There are 32 districts in total: 15 in Hatay, 11 in Kahramanmaraş, and 6 (excluding the central district) in Osmaniye.

Due to its significant role in agriculture and livestock production, the TR63 Region is a major contributor to waste generation (DOGAKA, 2024).

The aim of this study was to determine some agricultural wastes and their waste potential in the TR63 region and to investigate their usability as pellets.

2. Materials and Methods

2.1. Some Materials That Can Be Used for Biofuel in the TR63 Region

The materials identified for potential use as biofuels in the TR63 region include olive pomace, peanut shells, walnut husks, pepper stalk and seed residues, pistachio shells, vineyard pruning waste, forest residues, cotton gin waste, corn residues, barley residues, sunflower residues, wheat residues, and chicken manure.

2.2. Method

Total pellet energy value (TEV) was calculated by multiplying the existing pellet caloric (EPC) value of each product with the total waste potential (TWP). Total energy value is shown in equation 1.

$$TEV=EPC*TWP \quad (1)$$

3. Results

3.1. Properties of Materials and Total Amount of Energy

3.1.1. Olive pomace

Olive residues consist of pomace and wastewater produced during olive oil extraction. Among these, the most important input for energy production is olive pomace. After the olives are pressed to extract olive oil in olive oil factories, the remaining mixture of pits, skins, and pulp is known as olive pomace. The quality of pomace varies depending on the olive oil processing method. The quality of the pomace directly affects the time and cost of processing it for biofuel production.

Table 1. Number and olive pomace production capacity of Olive Oil Facilities in the TR63 Region (TOBB, 2024)

Provinces	Number of Facilities (units)	Production Capacity (tons)
Hatay	28	158,977
Kahramanmaraş	7	26,755
Osmaniye	8	3,500
Total	37	189,232

Looking at the TR63 Region as a whole, this figure averages 189,232 tons per year. Since a significant portion of the olive oil processing facilities operate using a three-phase system, this method has been taken into account when calculating the annual average pomace yield. In this system, 20-25% of olive oil is produced from 100 kg of olives, 45-50% of pomace is obtained, and the remainder is released as wastewater (Hocaoğlu et al, 2015). Therefore, it is possible to obtain an average of 189,232 tons of pomace with a moisture content of 45-55% per year from the region. When olive pomace is produced in pellet form, it generates 4,000-5000 calories/kg of heat (Develi et al., 2021; Miranda et al., 2012). The amount of energy that can be produced from these wastes as pellets is 803 (GJ)/year (Table 2).

3.1.2. Peanut shells

Peanut (Arachis hypogaea) is an annual summer plant belonging to the legume family. It is a highly valuable oilseed crop globally and is recognized as a snack crop in Turkiye. Among the approximately eight oilseed crops used in vegetable oil production worldwide, it ranks among the top three. Its significance lies in its use as both human food and animal feed, as well as its ability to enrich the soil with nitrogen. The composition of peanuts includes approximately 45-55% oil, 20-25% protein, 16-18% carbohydrates, and 5% mineral content.

Peanut shells possess significant potential, with a global production of 6.49 million tons per year and 24.50 000 tons per year in Türkiye. In this regard, peanut shells play an important role among waste plant biomass resources (Taşar et al., 2015). Additionally, peanut production in with a large portion coming from Osmaniye (44 060 tons/year), Hatay (4 411 tons/year), Kahramanmaraş (5 177 tons/year) (TUIK, 2023). The provinces where peanut farming is most prevalent in Türkiye are Osmaniye and Adana, where approximately 88% of the production occurs in the Çukurova region, translating to approximately 200,000 tons/year of production (TUIK, 2023). About 35% of the produced peanuts are generated as waste, which means approximately 70 000 tons of waste is formed annually. In the TR63 region, approximately 54,000 tons of peanuts are produced, resulting in around 19,000 tons of waste. There are 116 peanut processing facilities in Osmaniye, 103 of which are located in the center. Among these 103 facilities, 48 are concentrated in the town of Cevdetiye. The shells remaining after the seeds are extracted from the peanut fruit contain 6-7% crude protein, 1-2% oil, 60-67% crude fiber, 35-45% cellulose, 27-33% lignin, and 2-4% ash. When used as pellets, peanut shell waste produces an average of 4,000-4,300 cal/kg (Moreno et al., 2018). The amount of energy that can be produced from these wastes as pellets is 79 GJ/year (Table 2).

3.1.3. Walnut shells

Türkiye holds a significant position in the global walnut (Juglans regia L.) production landscape. In 2023, Türkiye achieved a walnut production of 360,000 tons per year (TUIK, 2023), placing it fourth in the world for walnut production (FAO, 2023). Kahramanmaraş Province ranks among the top walnut-producing areas in Turkiye, with an annual production of 18,330 tons (TUIK, 2023). Other provinces contribute as follows: Hatay with 2,029 tons/year, and Osmaniye with 1,418 tons/year (TUIK, 2023). The unused outer shell of walnuts accounts for 45% of the waste. In the TR63 region, the total production amount is 21,777 tons per year, resulting in approximately 9,799 tons per year of waste. When walnut shell waste is processed into pellets, it produces an average of 4,000-4500 calories/kg (Kantova et al., 2022). The amount of energy that can be produced from these wastes as pellets is 41 GJ/year (Table 2).

3.1.4. Pepper stems and seed residues

Pepper is a vegetable belonging to the Capsicum genus in the Solanaceae family and is grown as an annual crop in warm climates. In 2023, pepper production figures were as follows: Hatay produced 2,550 tons/year, Kahramanmaraş produced 28,850 tons/year, and the total production in Türkiye is approximately 287,322 tons/year (TUIK, 2023). About 27% of this production occurs in Gaziantep (82,609 tons/year), and approximately 55% of Türkiye's spice pepper production (155,000 tons/year) is sourced from this region. According to information from the Kahramanmaraş Red Pepper Growers Association, around 20% of processed peppers result in waste. Based on this data, the total production of red pepper stems and seeds in the TR63 region amounts to 31,400 tons/year, resulting in approximately 6,280 tons/year of waste. When red pepper stem and seed residues are used as pellets, they generate an average of 3,700-4,000 calories/kg (Başıbüyük et al, 2020). The amount of energy that can be produced from these wastes as pellets is 23 GJ/year (Table 2).

3.1.5. Pistachio shells

Pistachio (*Pistacia vera* L.) belongs to the Anacardiaceae family and is known for its edible, hard-shelled fruit, which comes in 11 different varieties (Zohary, 1952). In 2023, Türkiye's total pistachio production reached 176,000 tons (TUIK, 2023). Approximately 35-40% of the produced pistachios become waste, resulting in about 77,000 to 88,000 tons of waste annually. According to TOBB 2023 data, there are a total of 163 registered pistachio processing facilities in Türkiye, with 64 located in Gaziantep, 1 in Kahramanmaraş and 3 in Osmaniye. Given its proximity to the TR63 region, pistachio shells can be considered an alternative waste resource.

4325 tons of production occurred in Kahramanmaraş and 6 tons in Hatay. The amount of waste that may occur is 2165 tons. When processed into pellets, pistachio shell waste yields an average of 4,100 to 4,300 cal/kg and the waste rate is estimated to be fifty percent (Develi et al, 2021). The amount of energy that can be produced from these wastes as pellets is 8 GJ/year (Table 2).

3.1.6. Vine pruning residues

In the region, with approximately Hatay with about 47,967 decares; Kahramanmaraş with around 114,885 decares and Osmaniye with roughly 1,036 decares of vineyard area (TUIK, 2023). When considering the TR63 region, there is approximately 166,888 hectares of vineyards. In a study by Cavalaglio and Cotana (2007), it was noted that 2.9 tons/ha of vine pruning residues are obtained, while Sanchez et al. (2002) indicated that between 1 to 7.5 tons can be collected per hectare of vineyard. According to a study by Arık (2023), the amount of vine pruning residues is estimated at 3 tons/ha. Thus, the TR63 region generates around 500 664 tons of pruning waste. When collected, the moisture content of pruning residues is around 30-40%, indicating they do not possess excessively high moisture levels. When processed into pellets, vine pruning residues produce an average of 4,000 to 4,300 calories/kg (Akkuş, 2018). The amount of energy that can be produced from these wastes as pellets is 2079 GJ/year (Table 2).

3.1.7. Forest residues

Among biomass resources, forest residues hold significant importance. Biomass that results from the cutting of trees includes fine branches, tops, roots, cones, bark, understory vegetation, and shrub types. In certain Forest Regional Directorates (OBG), woody biomass obtained from forest maintenance and thinning activities is processed into wood chips for particle board

production or prepared for use as fuel in heating systems. The potential of woody biomass available for bioenergy, as estimated by the General Directorate of Forestry (OGM), is approximately 5 million tons annually. The largest potential is concentrated in the western and southern regions, particularly in the Mediterranean Region. In Kahramanmaraş, the production of industrial wood is 219,000 tons, and firewood is 48,000 tons, totaling 267,000 tons. In Hatay, the figures are 229,000 tons of industrial wood and 41,000 tons of firewood, resulting in a total of 260,000 tons. In Osmaniye, industrial wood production stands at 251,000 tons, and firewood at 37,000 tons, giving a total of 288,000 tons of unprocessed wood products (OGM, 2024). The total forest product generation in the TR63 region is estimated to be around 715,000 tons/year. When processed into pellets, forest residues yield an average of 4,350 to 4,850 calories/kg (Özdemir and Er, 2018). The amount of energy that can be produced from these wastes as pellets is 3289 GJ/year (Table 2).

3.1.8. Cotton gin waste

Cotton is sent to ginning factories for the separation of seeds from the cotton fiber. After the ginning process, a substantial amount of waste is generated. The processing waste from cotton, particularly from the ginning and oil production industries, poses significant storage and disposal challenges. In the TR63 region, approximately 280,000 tons of cotton waste is generated. This production consists of 254,000 tons in Hatay, 23,000 tons in Kahramanmaraş and 3,000 tons in Osmaniye (TUIK, 2023). The energy production from ginning waste when used in pellet form is estimated at around 3.900 to 4.250 calories/kg (Karaca and Başçetinçelik, 2010). The amount of energy that can be produced from these wastes as pellets is 1148 GJ/year (Table 2).

3.1.9. Corn residues

The corn generated in 2023 was 175,828 tons in Kahramanmaraş, 210,257 tons in Hatay, 383,067 tons in Osmaniye. The areas used for corn production are approximately 247,080 dekar in Kahramanmaraş, 205,782 dekar in Hatay and 406,296 dekar in Osmaniye. The amount of usable corn waste generated per hectare of corn production has been estimated at 527 kg/dekar (Bascetincelik et al., 2006; Avcıoglu et al., 2019). Based on these figures, the estimated usable corn waste generated in 2023 was around 130,020 tons in Kahramanmaraş, 106,232 tons in Hatay and 211,415 tons in Osmaniye. In total, approximately 448,000 tons of corn waste were produced in the TR63 region. Literature indicates that the calorific value of pellets made from corn residues ranges from 3,817 to 4,287 cal/kg (Özdemir and Er, 2018). The amount of energy that can be produced from these wastes as pellets is 1793 GJ/year (Table 2).

3.1.10. Barley residues

According to TUIK data from 2023, the areas used for barley production are approximately 438,720 dekar in Kahramanmaraş, 33,398 dekar in Hatay and 41,697 dekar in Osmaniye. The amount of usable barley waste generated per hectare has been estimated at 36 kg/dekar (Bascetincelik et al., 2006; Avcıoglu et al., 2019). Based on these estimates, the amount of usable barley waste produced in 2023 was approximately 15,793 tons in Kahramanmaraş, 1,501 tons in Hatay and 1,202 tons in Osmaniye. Overall, about 18,496 tons of barley waste were produced in the TR63 region. The calorific value of pellets made from barley residues is reported to range from 3,600 to 4,100 calories/kg (Serrano et al., 2011). The amount of energy that can be produced from these wastes as pellets is 71 GJ/year (Table 2).

3.1.11. Sunflower residues

According to TUIK data from 2023, sunflower production areas are approximately 85,767 dekar in Kahramanmaraş, 3010 dekar in Hatay, and 87,910 dekar in Osmaniye. The amount of usable sunflower waste generated per hectare is estimated at 550 kg/dekar (Aybek et al., 2015a). Based on this, the estimated usable sunflower waste for 2023 is about 47,171 tons in Kahramanmaraş, 1,655 tons in Hatay, and 48,350 tons in Osmaniye. In total, approximately 97,176 tons of sunflower wastes were produced in the TR63 region. The calorific value of pellets made from sunflower residues ranges from 3,600 to 4,700 calories/kg (Topkoç, 2023). The amount of energy that can be produced from these wastes as pellets is 403GJ/year (Table 2).

3.1.12. Wheat residues

According to TUIK data from 2023, wheat production areas are approximately 879,300 dekar in Kahramanmaraş, 522,370 dekar in Hatay, and 365,398 dekar in Osmaniye. The amount of usable wheat waste generated per hectare is estimated at 37 kg/dekar (Aybek et al., 2015a). Based on this, the estimated usable wheat waste for 2023 is about 32,534 tons in Kahramanmaraş, 19,327 tons in Hatay, and 13,519 tons in Osmaniye. In total, around 65,380 tons of wheat waste were produced in the TR63 region. The calorific value of pellets made from wheat residues ranges from 4,000 to 4,200 calories/kg (Jóvér et al., 2018; Bradna et al., 2016). The amount of energy that can be produced from these wastes as pellets is 273 GJ/year (Table 2).

3.1.13. Chicken manure residues

According to TUIK data from 2023, the total number of meat and egg chickens is approximately 1 568,279 in Kahramanmaraş, 869,273 in Hatay, and 1 124,164 in Osmaniye. Each chicken produces an average of 0.13 kg of waste per day (Aybek et al., 2015b). The total amount of manure generated from chicken waste is approximately 203 tons/day in Kahramanmaraş, 112 tons/day in Hatay, and 146 tons/day in Osmaniye. Overall, the total chicken manure production in the TR63 region is about 461 tons/day and 168, 265 tons. The calorific value of energy produced from chicken manure ranges from 3,100 to 3,500 calories/kg (Özdemir and Er, 2018). The amount of energy that can be produced from these wastes as pellets is 554 GJ/year (Table 2).

3.1.14. Total energy

High potential for energy generation

Forest Residues: With 3,289 GJ, forest residues provide the highest energy potential, making them a leading candidate for biofuel pellet production. Forest residues are widely available, particularly in areas with sustainable forest management, and their high caloric value (4,600 cal/kg) makes them efficient for producing energy-dense pellets. Vine Pruning Waste, Corn Waste, Chicken Manure Residues and Cotton Ginning Waste These materials also stand out due to their considerable mass and substantial energy contributions (2,079 GJ, 1792 GJ, 1521 and 1148 GJ). Those are commonly available in agricultural regions, providing a sustainable means of utilizing otherwise underused residues.

Table 2. Amounts of energy that can be produced from residue TR63 region

Material	Average Material Amount (106 kg)	Average Caloric Value (cal/kg)	Average Energy Amount (GJ)
Olive Pomace	189	4250	803
Peanut Shell Residue	19	4150	79
Walnut Shell Residue	10	4100	41
Pepper Stem and Seed	6	3850	23
Pistachio Shell Residue	2	4200	8
Vine Pruning Waste	501	4150	2079
Forest Residues	715	4600	3289
Cotton Ginning Waste	280	4100	1148
Corn Residues	448	4000	1792
Barley Residues	18	3850	71
Sunflower Residues	97	4150	403
Wheat Residues	65	4200	273
Chicken Manure Residues	168	3300	554
TOTAL	2518		10563

Moderate Energy Contributors

Olive pomace 803 GJ, Sunflower Residues (403 GJ) and Wheat waste (273 GJ), offer decent energy potential. Although their caloric values vary, they are available in significant quantities, making them feasible for biofuel pellet production, especially in regions where these crops and livestock are prevalent. For instance, sunflower residues are a natural by-product of oil production, while corn residues come from large-scale farming operations, and chicken manure addresses waste management challenges in poultry farming. Specialized Residues with Lower Contributions: Peanut Shell Residue, peper stem and seed, Walnut Shell Residue, and Pistachio Shell Residue provide lower overall energy contributions due to their smaller quantities, but they have relatively high caloric values, especially olive pomace (4,250 cal/kg) and pistachio shell (4,200 cal/kg). These residues are most relevant in specific regions where olives, peanuts, walnuts, and pistachios are processed. Their small-scale availability limits their broader application, but they offer valuable localized solutions for biofuel pellet production.

4. Discussion

Celma et al. (2007) used olive and grape wastes in their study in Extremadura, approximately 21,106 tons of waste was obtained from olive waste and 89,106 tons of waste was obtained from grape waste. The amount of energy that could be produced was 369 GJ from grape waste and 89 GJ from olive waste. Moreno et al., 2018, in their study, stated that peanut production in the world is 43,982,066 tons and the average amount of waste that could be generated is 11,000,000 tons. The amount of energy that could be produced from these wastes is calculated as 45,000 GJ on average. Shah et al., 2018, in their study, reported that walnut shells would create 100,000 t of waste in India. The average amount of energy that could be produced from these wastes is 4100 GJ. In addition, a total of 360,000 tons of walnuts were produced in Türkiye in 2023 and 22,000 tons occurred in the TR63 region. 6% of the energy to be produced from these wastes in Türkiye may come from this region (TUIK, 2023). Uzundumlu et al., 2024, Global Pistachio Production Forecasts for 2020–2025, estimated that the amount of Pistachio produced between these years will be 1,078,490 tons and 161,930 tons in Türkiye. This amount is 15% of the amount of Pistachio produced in the world in Türkiye. The amount of waste and energy that may be generated from this product will constitute approximately 15% of the world. In 2023, pepper produced in Türkiye was 287,322 tons and 31,400 tons were produced in the TR63 region. This region constitutes approximately 11% of Türkiye's production. The amount of energy that can be produced from these wastes will constitute approximately 11% of Türkiye's production and has an important place (TUIK, 2023). In a study conducted in 2017, Toklu reported the forest waste that could be generated in Türkiye as 20,000,000 t/year. It is approximately 715,000 tons/year in the TR63 region. This shows that 4% of the energy that can be generated from forest waste in Türkiye can be generated from this region. In 2023, approximately 368,624,420 chickens were raised in Türkiye and 3,561,716 chickens were raised in the TR63 region (TUIK, 2023). The amount of energy that can be generated in this region can constitute 1% of Turkiye. A total of 2,877,000 tons of waste was generated in cotton waste in Türkiye and 279,240 t of waste was generated in the TR63 region

(TUIK, 2023). Approximately 10% of the energy that can be generated from these wastes can be generated from this region. In 2023, corn production was in approximately 9,580,171 decares in Türkiye and 859,159 decares of corn was produced in the TR63 region (TUIK, 2023). This means that 9% of the energy that can be produced from this product in Türkiye can be from this region. In 2023, barley production was in approximately 31,702,723 decares in Türkiye and 513,815 decares in the TR63 region (TUIK, 2023). This means that 1.62% of the energy that can be produced from this product in Türkiye can be from this region. In 2023, sunflower production was in approximately 86,446,679 decares in Türkiye and 151,498 decares of sunflower was produced in the TR63 region (TUIK, 2023). This means that 1.75% of the energy that can be produced from this product in Türkiye can be from this region. In 2023, wheat production was approximately 81,767,068 decares in Türkiye and 151,498 decares of wheat was produced in the TR63 region (TUIK, 2023). This means that 3.2% of the energy that can be produced from this product in Türkiye can be from this region. This study shows that certain agricultural residues, particularly from pistachio, peanut, and olive production, are abundant in the TR63 region of Türkiye. For instance, 6% of walnut waste, 11% of pepper waste, 4% of forest waste, 10% of cotton waste, 9% of corn waste, and 3.2% of wheat waste originate from this region. Due to the sustainability and continuity of these residues, they represent a significant energy resource, with energy potential varying according to waste amounts, as compared to other global studies. The results of this study highlight the importance of agricultural waste in the TR63 region of Türkiye as a significant energy source, particularly from pistachio, peanut, olive, walnut, and pepper residues. With a focus on sustainability, these wastes can contribute to energy production, with energy potential varying by waste amount. Comparisons with global studies show that the TR63 region holds considerable potential for biogas and energy production from agricultural and forest residues, reinforcing the need for strategies to harness these renewable resources efficiently.

5. Conclusion and Suggestions

In conclusion, bifuel pellets represent a promising and innovative solution for addressing Turkiye's energy challenges, particularly in the TR63 region. By integrating biomass materials such as agricultural residues with fossil fuels, these pellets offer a transitional energy source that enhances energy efficiency and reduces greenhouse gas emissions. The TR63 region, characterized by its rich agricultural and livestock production, generates significant amounts of waste, which can be effectively utilized as feedstock for bifuel pellet production.

The diverse range of available materials, including olive pomace, peanut shells, walnut husks, and various crop residues, not only contributes to waste management and environmental sustainability but also enhances the region's energy security. Incorporating bifuel pellets into the regional energy policies aligns with Türkiye's broader environmental goals, promoting the use of renewable resources while reducing reliance on conventional fossil fuels.

Ultimately, the development and implementation of bifuel pellet technology in the TR63 region can lead to a more sustainable energy future, create economic opportunities in biomass processing, and contribute to local job creation. As the demand for renewable energy continues to grow, leveraging the potential of bifuel pellets can play a critical role in advancing Türkiye's transition towards a sustainable and resilient energy system.

In conclusion, this study highlights the significant energy potential of agricultural and forest residues in Türkiye's TR63 region. By utilizing waste from products such as pistachio, peanut, olive, and cotton, substantial amounts of energy can be generated. The TR63 region alone contributes a notable percentage to Türkiye's total energy potential from these wastes. This emphasizes the need for sustainable waste management practices, as increasing waste utilization could enhance energy production and contribute to environmental sustainability in the region.

The study highlights the potential of bifuel pellets as a sustainable energy solution for the TR63 region, emphasizing their role in promoting a sustainable energy future, creating economic opportunities, and generating local employment. To strengthen the impact of the findings, the conclusion could explicitly recommend the following future actions and research directions:

Economic Feasibility and Scalability Studies: Conduct detailed analyses to evaluate the cost-effectiveness and scalability of bifuel pellet production in the TR63 region, ensuring practical implementation.

Policy Recommendations: Develop and advocate for policies that encourage the adoption of bifuel pellet technology, including incentives for producers and users.

Diverse Feedstock Exploration: Investigate alternative feedstock options to broaden the range of materials used for bifuel pellet production, enhancing sustainability and resource utilization.

Pilot Projects: Initiate pilot programs to test and refine bifuel pellet technology on a larger scale, addressing potential challenges and optimizing processes.

Incorporating these suggestions would provide a clear roadmap for advancing bifuel pellet technology and maximizing its benefits for the TR63 region.

Author Contributions

The percentages of the author contributions are presented below. The author reviewed and approved the final version of the manuscript.

	S.Ü.
C	100
D	100
S	100
DCP	100
DAI	100
L	100
W	100
CR	100
SR	100
PM	100
FA	100

C=Concept, D= design, S= supervision, DCP= data collection and/or processing, DAI= data analysis and/or interpretation, L= literature search, W= writing, CR= critical review, SR= submission and revision, PM= project management, FA= funding acquisition.

Conflict of Interest Statement

The author declare that there is no conflict of interest in this study.

Ethical Consideration

Ethics committee approval was not required for this study because of there was no study on animals or humans.

References

Akkuş G. 2018. Bağ budama artıklarından torrefaksiyon ile katı yakıt üretimi.Yüksek Lisans Tezi, Fırat Üniversitesi, Fen Bilimleri Enstitüsü, Kimya Mühendisliği, Elâzığ, Türkiye, ss: 86.

Avcıoğlu AO, Dayıoğlu MA, Türker U. 2019. Assessment of the energy potential of agricultural biomass residues in Türkiye. Renew Energy, 138: 610-619.

Aybek A, Üçok S, İspir MA, Bilgili ME. 2015a. Türkiye'de kullanılabilir hayvansal gübre ve tahıl sap atıklarının biyogaz ve enerji potansiyelinin belirlenerek sayısal haritalarının oluşturulması. Tekirdağ Ziraat Fak Derg, 12(03): 111-120.

Aybek A, Üçok S, Bilgili ME, İspir MA. 2015b. Kahramanmaraş ilinde bazı tarımsal atıkların biyogaz enerji potansiyelinin belirlenerek sayısal haritalarının oluşturulması. Uludağ Üniv Zir Fak Derg, 29(2): 25-37.

Arık C. 2023. Bağ budama atıklarının mevcut ve olası değerlendirilme şekilleri. Bah Derg, 52(1): 401-417.

Bascetincelik A, , Ozturk HH, Karaca C, Ekinci K, Kaya D, Kacıra M. 2006. A guide on exploitation of agricultural residues in Turkey. EU Life Program Project, LIFE03 TCY/TR/000061, pp: 761.

Başıbüyük ÜF, Aybek A, Üçok S. 2021. Pamuk çiğidi küspesi ve kırmızı biber işleme atıklarından biyoyakıt amaçlı pelet elde edilmesi. ÇÜ Müh Fak Derg, 36(4): 879-890.

Bradna J, Malaťák J, Hájek D. 2016. The properties of wheat straw combustion and use of fly ash as a soil amendment. Agron Res, 14(4): 1257-1265.

Cavalaglio G, Cotana S. 2007. Recovery of vineyards pruning residues in an agro-energetic chain. Peach, 2(6): 1-11.

Celma AR, Rojas S, López RF. 2007. Waste-to-energy possibilities for industrial olive and grape by-products in Extremadura. Biomass Bioenerg, 31(7): 522-534.

Develi HC, Aybek A, Üçok S. 2021. Pellet production from pistachio shell and olive cake for biofuels. Tekirdağ Ziraat Fak Derg, 18(4): 689-701.

Dogaka, 2024. https://www.dogaka.gov.tr/dokuman-merkezi/kurumsal-dokumanlar/tr63-bolge-plani-2014-2023, (accesed date: October 10, 2024).

FAO, 2023. http://www.fao.org/faostat/en/#data/QC. (Erişim tarihi: .09.11.2023).

Hocaoğlu SM, Haksevenler P, Talazan C, Aydöner G, Karahan A, Günay G. Bağtürk ET, Budak T. 2015. Zeytin sektörü atıklarının yönetimi. Proje nihai rapor, Proje No: 5148602, Ankara, Türkiye, ss: 145.

Jóvér J, Antal K, Zsembeli J, Blaskó L, Tamás J. 2018. Assessment of gross calorific value of crop and bio-energy residues. Res Agri Eng, 64(3): 121-127.

Karaca C, Başçetinçelik A. 2010. Pamuk çırçır atıklarının briketleme özelliklerinin ve yanma emisyonlarının belirlenmesi. VII. Ulusal Temiz Enerji Sempozyumu, UTES, 1-5 Aralık, Samsun, Türkiye, ss: 1-5.

Karka P, Johnsson F, Papadokonstantakis S. 2021. Perspectives for greening European fossil-fuel infrastructures through use of biomass: the case of liquid biofuels based on lignocellulosic resources. Front Energy Res, 9(1): 1-22

Kheshgi HS, Prince RC, Marland G. 2000. The potential of biomass fuels in the context of global climate change: focus on transportation fuels. Annu Rev Energy Environ, 25(1): 199-244.

Kantova NC, Caja A, Belány P, Kolková Z, Hrabovsky P, Hecko D, Micko P. 2022. Mechanical and energy properties of pellets formed from walnut shells blended with spruce sawdust. Bioresour Technol, 17(1): 1881-1891.

Kovač A, Paranos M, Marciuš D. 2021. Hydrogen in energy transition: A review. Int J Hyd Energy, 46(16): 10016-10035.

Luo J, Hou S, Zhao L, Meng H, Tian Y. 2010. Experimental study on combustion and emission characteristics of biomass pellets. Tran Chin Soc Agri Eng, 26(5): 220-226.

Miranda T, Arranz JI, Montero I, Román S, Rojas CV, Nogales S. 2012. Characterization and combustion of olive pomace and forest residue pellets. Fuel Proc Tech, 103(1): 91-96.

Moreno MA, Manzano-Agugliaro F, Hernandez-Escobedo Q, Perea-Moreno AJ. 2018. Peanut shell for energy: properties and its potential to respect the environment. Sustain, 10(9): 3254-3264.

OGM, 2024. https://www.ogm.gov.tr/tr/e-kutuphane/resmi-istatistikler (accessed date: December 9, 2024).

Özdemir S, Er A. 2018. Tavuk gübresi ve tarımsal atıkların biyoyakıt karakterlerinin incelenmesi. Sak Univ J Sci, 22(2): 489-494.

Rodionova MV, Poudyal RS, Tiwari I, Voloshin RA, Zharmukhamedov SK, Nam, HG, Allakhverdiev SI. 2017. Biofuel production: challenges and opportunities. Int J Hydrog Energy, 42(12): 8450-8461.

Shah MA. Khan MNS, Kumar V. 2018. Biomass residue characterization for their potential application as biofuels. J Therm Anal Calor, 134(10): 2137-2145.

Sanchez A, Ysunza F, Beltran-Garcia MJ, Esqueda M. 2002. Biodegradation of viticulture wastes by Pleurotus: A source of microbial and human food and its potential use in animal feeding. J Agric Food Chem, 50(9): 2537-2542.

Samuelsson R, Larsson SH, Thyrel M, Lestander TA. 2012. Moisture content and storage time influence the binding mechanisms in biofuel wood pellets. Appl Energy, 99(5): 109-115.

Serrano C, Monedero E, Lapuerta M, Portero H. 2011. Effect of moisture content, particle size and pine addition on quality parameters of barley straw pellets. Fuel Proc Tech, 92(3), 699-706.

Sing N, Mahali K, Roy S. 2024. An Overview on Biofuels: Advantages and Disadvantages. In: Karaman R. editor. Recent Developments in Chemistry and Biochemistry. BP International. London, England, 7th ed., pp: 98-116.

Ståhl M, Berghel J, Williams H. 2016. Energy efficiency, greenhouse gas emissions and durability when using additives in the wood fuel pellet chain. Fuel Proc Tech, 152(6): 350-355.

Stattman SL, Gupta A, Partzsch L, Oosterveer P. 2018. Toward sustainable biofuels in the European Union? Lessons from a decade of hybrid biofuel governance. Sustain, 10(11): 4111-4122.

Taşar Ş, Kaya F, Özer A. 2015. A study on the pyrolysis of peanut shells at different isothermal conditions and determination of the kinetic parameters. Pamuk. Üni Müh Bil Derg, 21(7): 306-313.

TOBB, 2024. Türkiye Odalar ve Borsalar Birliği Sanayi Veri Tabanı, http://sanayi.tobb.org.tr/ksorgu_harita5.php?kodu=10.39.17.70.00 (accesed date: October 10, 2024).

Topkoç E. 2023. Çeşitli tarımsal atıklardan elde edilen biyopeletlerin bazı yakıt özelliklerinin değerlendirilmesi. Yüksek Lisans Tezi, Tarsus Üniversitesi, Lisansüstü Eğitim Enstitüsü Müdürlüğü, Mersin, Türkiye, pp: 105.

Toklu, E. 2017. Biomass energy potential and utilization in Turkey. Ren Ener, 107(7): 235-244.

TUIK, 2021. https://data.tuik.gov.tr/Kategori/GetKategori?p=tarim-111&dil=1 (accesed date: October 10, 2024).

Uzundumlu AS, Pınar V, Tosun NE, Kumbasaroğlu, H. 2024. Global pistachio production forecasts for 2020–2025. Kah Süt İm Üniv Tar Doğ Der, 27(5): 1105-1115.

Zohary M. 1952. Ecological studies in the vegetation of the near eastern deserts: Environment and vegetation classes. Isr Exp J, 2(4): 201-215.

Yang Z, Wu Y, Zhang Z, Li H, Li X, Egorov RI, Gao X. 2019. Recent advances in co-thermochemical conversions of biomass with fossil fuels focusing on the synergistic effects. Renew Sustain Energy Rev, 103(8): 384-398.

Wang J, Fu J, Zhao Z, Bing L, Xi F, Wang F, Hu Q. 2023. Benefit analysis of multi-approach biomass energy utilization toward carbon neutrality. The Innov, 4(3): 1-11.

Black Sea Journal of Engineering and Science
doi: 10.34248/bsengineering.1476268

Open Access Journal
e-ISSN: 2619 – 8991

Araştırma Makalesi (Research Article)
Cilt 8 - Sayı 1: 199-205 / Ocak 2025
(Volume 8 - Issue 1: 199-205 / January 2025)

AB ÜLKELERİNİN DİJİTALLEŞME SEVİYELERİNİN YENİ BİR VIKOR UZANTISIYLA KARŞILAŞTIRILMASI

Furkan GÖKTAŞ[1]*, Sümeyra Sezer KAPLAN[2]

[1]*Karabuk University, Faculty of Business, Department of Business Administration, 78050, Karabük, Türkiye*
[2]*Karabuk University, Faculty of Business, Department of Actuarial Sciences, 78050, Karabük, Türkiye*

Özet: Dijitalleşme kavramı gün geçtikçe önem kazanmaktadır. Bu çalışmanın amacı Avrupa Birliği (AB) ülkelerinin 2017-2022 dönemindeki dijitalleşme seviyelerinin bütüncül bir bakış açısıyla karşılaştırılmasıdır. Bu nedenle VIKOR yönteminin norm minimizasyonuna dayalı bir uzantısı (NM-VIKOR) bu çalışmada önerilmiştir ve bu uzantı grup karar verme problemleri için genelleştirilmiştir. Bu genel hal NMG-VIKOR olarak adlandırılmıştır. Bu yaklaşımlar tanımları gereği tek çözüm vermektedir. NM-VIKOR kullanılarak yapılan karşılaştırmalara göre; 2021 ve 2022 yıllarında Danimarka ilk sırada iken 2017, 2018, 2019 ve 2020 yıllarında Finlandiya ilk sıradadır. Tüm periyot için NMG-VIKOR kullanılarak yapılan karşılaştırmaya göre; Finlandiya ve Danimarka sıralaması vardır. Buna karşın diğer AB ülkeleri dijital gelişim açısından görece yetersizdir.

Anahtar kelimeler: Avrupa Birliği, Çok kriterli karar verme, DESI, Dijitalleşme, Konveks optimizasyon, VIKOR

The Comparison of Digitalization Levels of EU Countries with a Novel VIKOR Extension

Abstract: The concept of digitalization is gaining importance day by day. This study aims to compare the digitalization levels of European Union (EU) countries in the 2017-2022 period from a holistic perspective. Thus, in this study, the extension of the VIKOR method based on norm minimization (NM-VIKOR) is proposed, and this extension is generalized for group decision-making problems. This general case is called NMG-VIKOR. These approaches give unique solutions by definitions. As a result of the comparisons made using NM-VIKOR, Finland is first ranked in the years 2017, 2018, 2019, and 2020 whereas Denmark is first ranked in the years 2021 and 2022. As a result of the comparison using NMG-VIKOR for the whole period, Finland and Denmark rankings are obtained. In contrast, other EU countries are relatively inadequate in terms of digital development.

Keywords: European Union, Multi-criteria decision-making, DESI, Digitalization, Convex optimization, VIKOR

***Sorumlu yazar (Corresponding author):** Karabuk University, Faculty of Business, Department of Business Administration, 78050, Karabük, Türkiye
E mail: furkangoktas@karabuk.edu.tr (F. GÖKTAŞ)
Furkan GÖKTAŞ https://orcid.org/0000-0001-9291-3912
Sümeyra Sezer KAPLAN https://orcid.org/0000-0002-7920-9389

Gönderi: 01 Mayıs 2024 **Received:** May 01, 2024
Kabul: 17 Aralık 2024 **Accepted:** December 17, 2024
Yayınlanma: 15 Ocak 2025 **Published:** January 15, 2025

Cite as: Göktaş F, Kaplan SS. 2025. The comparison of digitalization levels of EU countries with a novel VIKOR extension. BSJ Eng Sci, 8(1): 199-205.

1. Giriş

Dijitalleşme, yeni teknolojilerin hayatın tüm unsurlarına uyarlanmasını ifade eder. Bir dönüştürme süreci olan dijitalleşme, insanların yaşam kalitesini artırmaktadır (Kumar vd., 2018). Dijital teknolojiler, dünyanın farklı alanlarında sosyal alanları bağlamak ve dijital verileri gerçek zamanlı olarak toplamak, analiz etmek ve manipüle etmek için kullanılır. Karmaşık ve dinamik bir süreç olan dijitalleşmenin faydaları açıktır, ancak bunların doğru bir şekilde ölçülmesi gerekmektedir. Bu nedenle teknolojinin belirli bir alanındaki ilerlemenin ölçüldüğü çok sayıda endeks oluşturulmuştur. Dijital Hükümet Endeksi (DGI), Dijital Benimseme Endeksi (DAI), Dijital Yoğunluk Endeksi (DII), Dijital Ekonomi ve Toplum Endeksi (DESI) bunlara örnek olarak verilebilir. Çalışma kapsamında kullanılan DESI, Avrupa Komisyonu tarafından geliştirilmiştir (Stankovic vd., 2021; Ionescu-Feleagă vd., 2023).

Ülkelerin dijitalleşme seviyelerini DESI verileriyle karşılaştıran bazı çalışmalar şunlardır. Stankovic vd. (2021) Avrupa ülkelerinin dijital gelişimlerini CRITIC ağırlıklı TOPSIS kullanarak karşılaştırmıştır. Kiselakova vd. (2022) AB ülkelerini DESI ve Küresel Dijital Rekabetçilik Endeksi verileriyle karşılaştırmıştır. Georgescu vd. (2023) Avrupa ülkelerinin dijital gelişimlerini DEA kullanarak karşılaştırmıştır. Marti ve Puertas (2023) Küresel İnovasyon Endeksi tarafından ölçülen yenilik faktörlerini ve DESI'nin boyutlarını içeren sentetik bir gösterge üreterek AB ülkelerinin rekabet gücünü analiz etmiştir. Banhidi ve Dobos (2023a) Brexit öncesi AB'nin yirmi sekiz ülkesinin dijital gelişimlerini DEA kullanarak karşılaştırmıştır. Banhidi ve Dobos (2023b) üç farklı yöntem kullanarak AB ülkelerini dijital gelişim açısından gruplandırmıştır. Banhidi ve Dobos (2024) TOPSIS kullanılarak bulunan, AB ülkelerin dijital gelişim sıralamalarının kriter ağırlıklarına ve veri normalizasyonuna olan hassaslığını analiz etmiştir. Bunlardan farklı olarak Zerhouni ve Özarı (2022) I-DESI (uluslararası DESI) verileriyle 45 ülkenin dijital gelişimlerini Entropi ağırlıklı TOPSIS kullanarak karşılaştırmıştır.

Yukarıdaki çalışmalarda, birden çok yıl için dijitalleşme

seviyesi karşılaştırması yapılmışsa periyottaki her bir yıl için ayrı ayrı analiz yapılması ve sonrasında periyotun geneli için bir değerlendirme yapılması yaklaşımı tercih edilmiştir. Öte yandan bu yaklaşımla tüm periyot için tek bir sonuç bulunamamaktadır. Literatürdeki bu boşluğu doldurmak ve AB ülkelerinin 2027-2022 dönemindeki dijitalleşme seviyelerinin bütüncül bir şekilde karşılaştırılması çalışmada amaçlanmıştır. Bu amaca ulaşmak için popüler çok kriterli karar verme (ÇKKV) yöntemlerinden biri olan VIKOR'un, norm minimizasyonuna dayalı uzantısı (NM-VIKOR) çalışmada önerilmiştir ve sonrasında söz konusu uzantı grup karar verme problemleri için genelleştirilmiştir. Göktaş (2024) TOPSIS yöntemini baz alarak benzer yaklaşım uygulamıştır. Çalışmanın orijinalliği önerilen uzantıdan ve bunun genel halinden (NMG-VIKOR) kaynaklanmaktadır. NM-VIKOR, iki farklı kesin konveks minimizasyon problemine dayanmaktadır ve alternatiflerin uzlaşık performans değerini bir kapalı aralık olarak belirlemektedir. NMG-VIKOR için de bu bilgiler geçerlidir. Bununla birlikte NMG-VIKOR, periyottaki her bir yılın ayrı bir karar verici olarak belirlenmesine imkân verdiğinden daha kapsamlı analizlerde kullanılabilmektedir. Söz konusu yaklaşımlar; sıralamaya ek olarak gruplandırmada ve kaynak dağıtımında kullanılabildiğinden, VIKOR'a oranla daha fazla bilgi taşımaktadır.

Çalışmanın devamı şu şekilde organize edilmiştir. Bölüm 2'de DESI metodolojisi ile ilgili bilgiler verilmiştir. Bölüm 3'te VIKOR kısaca açıklandıktan sonra, çalışmada önerilen NM-VIKOR ve NMG-VIKOR tanıtılmıştır. Bölüm 4'te AB ülkelerinin 2017-2022 dönemindeki dijitalleşme seviyeleri NMG-VIKOR kullanılarak karşılaştırılmıştır (DESI, 2022a). Ayrıca NM-VIKOR kullanılarak AB ülkelerinin dijitalleşme seviyeleri her bir yıl için analiz edilmiştir. Bölüm 5'teki son değerlendirmelerle çalışma sonuçlandırılmıştır.

2. Kavramsal Çerçeve

DESI, AB ülkelerinin dijital rekabet gücündeki genel performansını değerlendirmek ve bu alandaki ilerlemelerini izlemek için kullanılmaktadır (DESI, 2022b). Bu endeks ilk kez 2014 yılında hesaplanmıştır ve 2021'de, dijital politik bir program olan Dijital On yıl Pusulası ile uyumlu hale getirilmiştir (Skvarciany vd., 2023). Bu program, dijital hedefleri sunmaktadır ve 2030 için ana hedefleri dört ana noktada belirlemiştir. Bunlar; yetkinlikler, altyapı, şirketlerin ve kamu hizmetlerinin dijital dönüşümü olarak sıralanabilir. DESI'yi oluşturan dört boyut, on alt boyut, otuz üç gösterge vardır. DESI'nin dört boyutu; insan sermayesi, bağlantı, dijital teknolojinin entegrasyonu, dijital kamu hizmetleri olarak sıralanabilir (Stankovic vd., 2021; DESI, 2022b; Ionescu-Feleagă vd., 2023).

İnsan sermayesi boyutu, internet kullanım becerilerini ve gelişmiş dijital becerileri kapsamaktadır. Bu tür becerilerin değerlendirilmesi gereklidir, çünkü dijital beceriler günümüz dünyası için vazgeçilmez unsurlardandır. Bilgi tabanlı iş gücüne katılmayı hedefleyen insanlar, Bilgi ve İletişim Teknolojilerini (BİT) verimli bir şekilde kullanmalıdır (Van Laar vd., 2017). Bağlantı boyutu, ekonomik kalkınma ve toplumun refahı için hayati öneme sahiptir. Dünya genelinde internet kullanımı %50'yi aşmıştır. Dünya nüfusunun %75'i aktif mobil geniş bant aboneliğine sahiptir ve bunun %57'den fazlası evde internet erişimine sahiptir (ITU, 2019). Dijital teknolojinin entegrasyonu boyutu, işletmelerin dijital göstergeleri ile ilgilidir. Yapay Zekâ (AI) kullanımı da bu boyuta dahildir. AI, işletmelerin dijital dönüşümünün önemli bir unsurudur ve şirketlerin verimliliğini artırmaktadır (Calp, 2020). Dijital kamu hizmetleri boyutu, vatandaşlar ve işletmeler için dijital kamu hizmetlerini değerlendirmektedir. Bu tür hizmetlerin sayısı ve verimliliği dijitalleşme ile birlikte artmıştır (DESI, 2022b). Tüm boyutlar Tablo 1'de sunulmuştur.

Tablo 1. DESI yapısı (DESI, 2022b, Ionescu-Feleagă vd., 2023).

Boyut	Alt Boyut ve Gösterge Sayıları
İnsan sermayesi (K1)	İnternet kullanım becerileri, ileri düzey beceriler ve gelişim (2 alt boyut ve 7 gösterge)
Bağlantı (K2)	Sabit geniş bant, sabit geniş bant kapsama alanı, mobil geniş bant, geniş bant fiyatları (4 alt boyut ve 10 gösterge)
Dijital teknolojinin entegrasyonu (K3)	Dijital yoğunluk, iş için dijital teknolojiler, e-ticaret (3 alt boyut ve 11 gösterge)
Dijital kamu hizmetleri (K4)	E-devlet (1 alt boyut ve 5 gösterge)

DESI metodolojisine göre; göstergelerden alınan puanların alt boyut puanlarını oluşturmasında, alt boyutlardan alınan puanların boyut puanlarını oluşturmasında ve dört boyuttan alınan puanların genel puanı oluşturmasında basit toplamlı ağırlıklandırma yöntemini kullanılır. Genel puan hesaplanırken, dört boyutun ağırlıkları eşit alınır (DESI, 2022b).

3. Materyal ve Yöntem

VIKOR yönteminin adımları aşağıdaki gibi sıralanabilir (Chatterjee ve Chakraborty, 2016). Anlaşılırlığı artırmak amacıyla söz konusu adımlar basitleştirilmiştir.

Adım 1: i. alternatifin j. kriter bazında performans değeri a_{ij} olmak üzere karar matrisi $A_{nxm}=(a_{ij})$ oluşturulur. Bununla birlikte kriterlerin ağırlık vektörü $w=(w_j)$ belirlenir. (Burada n alternatif sayısı iken, m kriter

sayısıdır.)

Adım 2: j. kriterin fayda veya maliyet yönlü kriter olması dikkate alınıp, C=(c_{ij}) matrisi eşitlik 1 ile oluşturulur. Burada $c_{ij} \in [0, w_j]$ kapalı aralığındadır. Bu değer küçüldükçe i. alternatifin j. kriter bazındaki performansı artar.

$$c_{ij} = \begin{cases} w_j \dfrac{\underset{i}{\text{maks}}\, a_{ij} - a_{ij}}{\underset{i}{\text{maks}}\, a_{ij} - \underset{i}{\min}\, a_{ij}}, & \textit{fayda yönlü kriterse} \\ w_j \dfrac{a_{ij} - \underset{i}{\min}\, a_{ij}}{\underset{i}{\text{maks}}\, a_{ij} - \underset{i}{\min}\, a_{ij}}, & \textit{maliyet yönlü kriterse} \end{cases} \quad (1)$$

Adım 3: C matrisinin i. satırının 1-normu olarak tanımlanan s_i, yine bunun i. satırının sonsuz-normu olarak tanımlanan r_i eşitlik 2 ile hesaplanır.

$$s_i = \sum_{j=1}^{m} c_{ij}$$
$$r_i = \underset{j}{\text{maks}}\, c_{ij} \quad (2)$$

Uyarı: $c_{ij} \in [0, w_j]$ olduğundan negatif ideal çözüm w=(w_j) vektörü olarak, pozitif ideal çözüm tüm elemanları 0 olan m elemanlı vektör yani sıfır vektörü olarak tanımlansın. Buna göre i. alternatifin pozitif ideal çözüme Manhattan uzaklığı s_i iken, buna Çebişev uzaklığı r_i olarak bulunur.

Adım 4: i. alternatif için q_i, eşitlik 3 ile hesaplanır. $v \in [0,1]$ genellikle 0.5 olarak alınır.

$$q_i = v \frac{s_i - \underset{i}{\min}\, s_i}{\underset{i}{\text{maks}}\, s_i - \underset{i}{\min}\, s_i} + (1-v) \frac{r_i - \underset{i}{\min}\, r_i}{\underset{i}{\text{maks}}\, r_i - \underset{i}{\min}\, r_i} \quad (3)$$

Adım 5: s_i, r_i ve q_i değerleri ayrı ayrı kullanılarak küçükten büyüğe sıralamalar yapılır. q_i değerleri kullanılarak yapılan sıralamada ilk sırada olan alternatif (a^*) eğer diğer iki sıralamadan birinde de ilk sıradaysa ve bu alternatifin q_i değeri ile en düşük ikinci q_i değeri arasındaki fark 1/(n-1) değerinden büyük eşitse a^* en iyi alternatif olarak belirlenir ve seçilir.

VIKOR yönteminin çok sayıda uzantısı vardır (Chatterjee ve Chakraborty, 2016). Çalışmada önerilen NM-VIKOR adlı VIKOR uzantısı, iki farklı norm minimizasyonu problemi ile tanımlanmıştır. Alternatiflerin ağırlık vektörü p=(p_i) ile gösterilsin. Bu vektöre karşı gelen kaynak dağıtım planı için kriter bazında performans vektörü, ağırlıklı toplam ifadesine karşı gelen C^Tp vektörüne eşittir. (C^T matrisi, C matrisinin transpozudur.) C^Tp vektörünün 1-normu eşitlik 4 ile minimize edilir. Geometrik olarak eşitlik 4, C^Tp vektörü ve pozitif ideal çözüm (sıfır vektörü) arasındaki Manhattan uzaklığının minimize edilmesine karşı gelir. Burada 1-norm yerine sonsuz-norm kullanıldığında, bu ikisi arasındaki Çebişev uzaklığı minimize edilir. eşitlik 4 konveks minimizasyon problemidir. Bu nedenle bunun optimal çözüm kümesi (F) konvekstir (Boyd ve Vandenberghe, 2004).

$$\min \left\| C^T p \right\|_1$$
$$k.a. \sum_{i=1}^{n} p_i = 1 \quad (4)$$
$$p_i \geq 0, \forall i$$

Öklid uzaklığı ile ilişkili olan 2-norm, argümanının kesin konveks fonksiyonu olduğundan konveks küme üzerinde minimize edilirse tek çözüm verir (Boyd ve Vandenberghe, 2004). F üzerinde 2-normu minimum olan yani orijine en yakın olan tek optimal çözümü yaklaşık olarak bulmak amacıyla çalışmada eşitlik 4 yerine eşitlik 5 kullanılmıştır. eşitlik 5, Tikhonov'un düzenlenmiş problemi olarak adlandırılır. Burada p^Tp ifadesi p vektörünün 2-normunun karesine eşittir ve ε, 0'a oldukça yakın pozitif bir sayıdır (Beck ve Sabach, 2014). (Çalışmada $\varepsilon = 2^{-23}$ olarak alınmıştır.) eşitlik 5 kesin konveks minimizasyon problemidir ve tek çözüm vermektedir.

$$\min \left\| C^T p \right\|_1 + \frac{\varepsilon}{2} p^T p$$
$$k.a. \sum_{i=1}^{n} p_i = 1 \quad (5)$$
$$p_i \geq 0, \forall i$$

eşitlik 5, MATLAB yazılımı olan CVX yardımıyla çözülebilir (Grant ve Boyd, 2008). Bunun için CVX kodu eşitlik 6'daki gibidir. 1-norm yerine sonsuz-norm kullanıldığında, norm(x,1) yerine norm(x,inf) ifadesi kullanılır.

```
cvx_solver mosek
cvx_begin
variables p(n);
d = 0.5*eps("single");
minimize( norm( transpose(C)* p,1) + d*transpose( p)* p)        (6)
subject to
    ones(1,n)* p == 1;
    p >= zeros(n,1);
cvx_end
```

NM-VIKOR'un ilk iki adımı VIKOR'un ilk iki adımı ile aynıdır. NM-VIKOR'un diğer adımları aşağıdaki gibi sıralanabilir.

Adım 3: eşitlik 5'in tek optimal çözümü $p^*=(p_i^*)$, eşitlik 6'daki CVX koduyla ya da başka bir şekilde bulunur. Her i için $s_i=1-p_i^*$ olmak üzere s=(s_i) vektörü oluşturulur. eşitlik 5 ve eşitlik 6'da 1-norm yerine sonsuz-norm kullanıldığında her i için $r_i=1-p_i^*$ olmak üzere r=(r_i) vektörü oluşturulur.

Adım 4: i. alternatif için aralık değerli uzlaşık performans olan 1-q_i, eşitlik 7'deki gibi belirlenir.

$$1 - q_i := \left[\min\left(1-s_i, 1-r_i\right), \text{maks}\left(1-s_i, 1-r_i\right) \right] \quad (7)$$

Adım 5: Alternatifler büyükten küçüğe sıralanırken ve alternatiflere kaynak dağıtımı yapılırken eşitlik 7'deki kapalı aralığın orta noktası kullanılır. 1-q_i=0 ise ilgili alternatif görece yetersiz alternatif olarak adlandırılır.

ÇKKV yöntemleri grup karar verme problemleri için genelleştirildiğinde, aynı anda birden çok yılın bir bütün olarak ve herhangi bir bilgi kaybı olmadan analiz edilebilmesine imkân verir. NM-VIKOR'un grup karar verme problemleri için genel hali olan NMG-VIKOR'un adımları aşağıdaki gibidir.

Adım 1: Her bir karar verici için karar matrisi (A^k) ve kriterlerin ağırlık vektörü (w^k) ayrı ayrı belirlenir.

Adım 2: Her bir karar verici için C^k matrisi, eşitlik 1 kullanılarak ayrı ayrı oluşturulur.

Karar verici sayısı t olmak üzere eşitlik 5'in NMG-VIKOR'daki karşılığı eşitlik 8'deki gibi belirlenmiştir. eşitlik 5'te tek bir karar verici için pozitif ideal çözüme olan Manhattan uzaklığı kullanılırken, eşitlik 8'de farklı karar vericiler için pozitif ideal çözüme olan Manhattan uzaklıklarının toplamı kullanılmıştır.

$$\begin{aligned} &\min \ \frac{\varepsilon}{2} p^T p + \sum_{k=1}^{t} \left\| \left(C^k\right)^T p \right\|_1 \\ &k.a. \sum_{i=1}^{n} p_i = 1 \\ &\quad p_i \geq 0, \forall i \end{aligned} \tag{8}$$

eşitlik 8 için CVX kodu eşitlik 9'daki gibidir.

```
cvx_solver mosek
cvx_begin
variables p(n) y(t);
d = 0.5*eps("single");
minimize (sum(y) + d*transpose(p)*p)
subject to
    ones(1,n)*p == 1;
    p >= zeros(n,1);
   y(k,1)>=norm(transpose(C^k)*p,1), ∀k
cvx_end
```

(9)

Adım 3: eşitlik 8'in tek optimal çözümü $p^*=(p_i^*)$, eşitlik 9'daki CVX koduyla ya da başka bir şekilde bulunur. Her i için $s_i=1-p_i^*$ olmak üzere $s=(s_i)$ vektörü oluşturulur. eşitlik 8 ve eşitlik 9'da 1-norm yerine sonsuz-norm kullanıldığında, her i için $r_i=1-p_i^*$ olmak üzere $r=(r_i)$ vektörü oluşturulur.

NMG-VIKOR'un son iki adımı, NM-VIKOR'un son iki adımı ile aynıdır. Başka bir deyişle NMG-VIKOR alternatiflerin uzlaşık performanslarını ($1-q_i$) bir kapalı aralık olarak belirler. Alternatifler büyükten küçüğe sıralanırken ve alternatiflere kaynak dağıtımı yapılırken bu aralığın orta noktası kullanılır.

Uyarı: Tanımları gereği NM-VIKOR ve NMG-VIKOR, tüm alternatifleri değerlendirerek ideal bir alternatif portföyü oluşturur. Her i için $1-s_i$, $1-r_i$ ve $1-q_i$ değerleri, i. alternatifin bu ideal alternatif portföyündeki ağırlığı ile ilişkilidir. Görece yetersiz olan alternatiflerin bu portföydeki ağırlıkları sıfırdır.

4. Bulgular ve Tartışma

Bu bölümde öncelikle 2022 yılı DESI verileri kullanılarak NM-VIKOR'un uygulama adımları gösterilmiştir. Ayrıca 2017-2022 dönemindeki her bir yıl için yirmi yedi AB ülkesinin dijitalleşme seviyelerinin karşılaştırılmasında NM-VIKOR kullanılarak elde edilen sonuçlar, yine bu kapsamda ama bu kez 2017-2022 döneminin geneli için NMG-VIKOR kullanılarak elde edilen sonuçlar sunulmuştur. Ayrıca elde edilen tüm sonuçlar, birbirleriyle ve literatürdeki sonuçlarla karşılaştırılmıştır. DESI'nin dört boyutu olarak belirlenen ve Tablo 1'de açıklanan fayda yönlü kriterler (K1, K2, K3 ve K4) bu karşılaştırmada kullanılmıştır. DESI metodolojinde bu boyutların ağırlıkları eşit olduğundan çalışmada kriter ağırlıkları eşit olarak alınmıştır. Sonuçları özel olarak belirtilmeyen ülkeler için bulunan uzlaşık performans değerleri ($1-q_i$) 2017-2022 döneminin tüm yılları için 0'dır. Yani bu ülkeler 2017-2022 dönemindeki tüm yıllarda dijitalleşme seviyesi açısından görece yetersiz ülke olarak bulunmuştur. NM-VIKOR, 2022 yılı DESI verileri kullanılarak aşağıdaki adımlarla uygulanmıştır.

Adım 1: Karar matrisi (A) Tablo 2'deki gibi oluşturulmuştur. Kriter ağırlıkları eşit alınmıştır.

Tablo 2. Karar matrisi

	K1	K2	K3	K4
Avusturya	50,95	56,47	39,17	72,12
Belçika	48,69	39,83	47,96	64,75
Bulgaristan	32,59	50,70	15,53	51,90
G. Kıbrıs	41,77	58,78	35,35	57,52
Çekya	45,59	52,69	33,84	64,46
Almanya	44,97	67,32	35,84	63,41
Danimarka	59,19	77,09	57,99	83,07
Estonya	53,95	44,45	36,47	91,18
Yunanistan	40,13	49,58	26,63	39,39
İspanya	51,32	69,71	38,54	83,52
Finlandiya	71,39	60,55	59,09	87,37
Fransa	49,87	64,19	31,91	67,35
Hırvatistan	51,83	48,06	36,73	53,57
Macaristan	38,45	57,60	21,58	57,40
İrlanda	62,64	61,54	43,32	83,45
İtalya	36,57	61,23	40,74	58,48
Litvanya	42,46	49,35	37,25	81,80
Lüksemburg	57,77	59,30	34,96	83,37
Letonya	44,14	50,07	25,83	78,81
Malta	56,60	53,00	48,13	85,81
Hollanda	63,13	70,10	52,07	84,19
Polonya	37,03	46,52	22,88	55,76
Portekiz	45,94	51,59	37,59	67,91
Romanya	30,92	55,23	15,15	21,04
İsveç	61,98	60,25	56,24	82,42
Slovenya	44,25	59,90	39,84	69,49
Slovakya	44,13	49,82	27,83	52,00

Adım 2: eşitlik 1 kullanılarak, C matrisi Tablo 3'teki gibi oluşturulmuştur.

Tablo 3. C matrisi

	K1	K2	K3	K4
Avusturya	0,1262	0,1384	0,1133	0,0679
Belçika	0,1402	0,2500	0,0633	0,0942
Bulgaristan	0,2397	0,1770	0,2479	0,1400
G. Kıbrıs	0,1830	0,1229	0,1351	0,1200
Çekya	0,1594	0,1637	0,1437	0,0953
Almanya	0,1632	0,0655	0,1323	0,0990
Danimarka	0,0754	0,0000	0,0062	0,0289
Estonya	0,1077	0,2190	0,1287	0,0000
Yunanistan	0,1931	0,1846	0,1847	0,1846
İspanya	0,1240	0,0495	0,1169	0,0273
Finlandiya	0,0000	0,1110	0,0000	0,0136
Fransa	0,1329	0,0866	0,1546	0,0849
Hırvatistan	0,1208	0,1948	0,1272	0,1341
Macaristan	0,2035	0,1307	0,2134	0,1204
İrlanda	0,0540	0,1043	0,0897	0,0276
İtalya	0,2151	0,1064	0,1044	0,1166
Litvanya	0,1787	0,1861	0,1243	0,0334
Lüksemburg	0,0841	0,1193	0,1373	0,0278
Letonya	0,1684	0,1812	0,1893	0,0441
Malta	0,0914	0,1616	0,0624	0,0191
Hollanda	0,0510	0,0469	0,0400	0,0249
Polonya	0,2122	0,2051	0,2060	0,1262
Portekiz	0,1572	0,1711	0,1223	0,0830
Romanya	0,2500	0,1467	0,2500	0,2500
İsveç	0,0581	0,1129	0,0162	0,0312
Slovenya	0,1676	0,1153	0,1095	0,0773
Slovakya	0,1684	0,1829	0,1778	0,1397

Adım 3: eşitlik 5'in tek çözümü eşitlik 6 kullanılarak bulunmuştur. Buna göre $1\text{-}s_i$ değerleri; Danimarka için 1 iken, diğer ülkeler için 0'dır. eşitlik 5 ve eşitlik 6'da 1-norm yerine sonsuz-norm kullanılarak bulunan tek optimal çözüme göre $1\text{-}r_i$ değerleri; Danimarka için 0,595, Finlandiya için 0,405 ve diğer ülkeler için 0'dır.

Adım 4: i. alternatifin uzlaşık performans değeri **(**$1\text{-}q_i$), eşitlik 7 kullanılarak belirlenmiştir. Buna göre Danimarka için $1\text{-}q_i$=[0,595,1], Finlandiya için $1\text{-}q_i$=[0,0,405] ve diğer ülkeler için $1\text{-}q_i$=0 olarak bulunmuştur.

Adım 5: Uzlaşık performans değerlerinin orta noktaları kullanılarak 2022 yılındaki sıralama, Danimarka ve Finlandiya olarak bulunmuştur. Diğer ülkelerin uzlaşık performans değerleri 0 olduğundan bu ülkeler görece yetersiz ülke (Y) olarak bulunmuştur. Söz konusu bilgiler Tablo 4'te özetlenmiştir.

Tablo 4. 2022 yılı için sonuçlar

	$1\text{-}s_i$	$1\text{-}r_i$	$1\text{-}q_i$	Sıra
Danimarka	1	0,595	[0,595, 1]	1
Finlandiya	0	0,405	[0, 0,405]	2
Lüksemburg	0	0	0	Y
İsveç	0	0	0	Y

2021 yılına ait verilerle yapılan karşılaştırmada, Tablo 5'teki sonuçlar elde edilmiştir. 2021 yılı için bulunan sıralama; Danimarka ve Finlandiya şeklindedir. Diğer ülkeler, dijitalleşme seviyesi açısından görece yetersiz ülke olarak bulunmuştur.

Tablo 5. 2021 yılı için sonuçlar

	$1\text{-}s_i$	$1\text{-}r_i$	$1\text{-}q_i$	Sıra
Danimarka	1	0,663	[0,663, 1]	1
Finlandiya	0	0,337	[0, 0,337]	2
Lüksemburg	0	0	0	Y
İsveç	0	0	0	Y

2020 yılına ait verilerle yapılan karşılaştırmada, Tablo 6'daki sonuçlar elde edilmiştir. 2020 yılı için bulunan sıralama; Finlandiya ve İsveç şeklindedir. Diğer ülkeler, dijitalleşme seviyesi açısından görece yetersiz ülke olarak bulunmuştur.

Tablo 6. 2020 yılı için sonuçlar

	$1\text{-}s_i$	$1\text{-}r_i$	$1\text{-}q_i$	Sıra
Danimarka	0	0	0	Y
Finlandiya	1	0,430	[0.430, 1]	1
Lüksemburg	0	0	0	Y
İsveç	0	0,570	[0, 0,570]	2

2019 yılına ait verilerle yapılan karşılaştırmada, Tablo 7'deki sonuçlar elde edilmiştir. 2019 yılı için bulunan sıralama; Finlandiya ve İsveç şeklindedir. Diğer ülkeler, dijitalleşme seviyesi açısından görece yetersiz ülke olarak bulunmuştur.

2018 yılına ait verilerle yapılan karşılaştırmada, Tablo 8'deki sonuçlar elde edilmiştir. 2018 yılı için bulunan sıralama; Finlandiya ve İsveç şeklindedir. Diğer ülkeler, dijitalleşme seviyesi açısından görece yetersiz ülke olarak bulunmuştur.

2017 yılına ait verilerle yapılan karşılaştırmada, Tablo 9'daki sonuçlar elde edilmiştir. 2017 yılı için bulunan sıralama; Finlandiya, Lüksemburg ve Danimarka şeklindedir. Diğer ülkeler, dijitalleşme seviyesi açısından görece yetersiz ülke olarak bulunmuştur.

Tablo 7. 2019 yılı için sonuçlar

	$1-s_i$	$1-r_i$	$1-q_i$	Sıra
Danimarka	0	0	0	Y
Finlandiya	1	0,441	[0,441, 1]	1
Lüksemburg	0	0	0	Y
İsveç	0	0,559	[0, 0,559]	2

Tablo 8. 2018 yılı için sonuçlar

	$1-s_i$	$1-r_i$	$1-q_i$	Sıra
Danimarka	0	0	0	Y
Finlandiya	1	0,307	[0,307, 1]	1
Lüksemburg	0	0	0	Y
İsveç	0	0,693	[0, 0,693]	2

Tablo 9. 2017 yılı için sonuçlar

	$1-s_i$	$1-r_i$	$1-q_i$	Sıra
Danimarka	0	0,226	[0, 0,226]	3
Finlandiya	1	0,423	[0,423, 1]	1
Lüksemburg	0	0,351	[0, 0,351]	2
İsveç	0	0	0	Y

2017, 2018, 2019 ve 2020 yıllarında Finlandiya dijitalleşme seviyesi açısından ilk sırada iken 2021 ve 2022 yıllarında yerini Danimarka'ya kaptırmıştır ve ikinci sıraya düşmüştür. 2017 yılında Danimarka üçüncü sırada iken 2018, 2019 ve 2020 yıllarında görece yetersiz ülke olarak bulunmuştur. 2017 yılında görece yetersiz ülke konumunda olan İsveç; 2018, 2019 ve 2020 yıllarında ikinci sıraya yükselse de 2021 ve 2022 yıllarında tekrardan görece yetersiz ülke konumuna düşmüştür. Lüksemburg 2017 yılında ikinci sırada iken sonraki yıllarda görece yetersiz ülke konumuna düşmüştür. Özetle, yıldan yıla AB ülkelerinin dijitalleşme seviyeleri değişmektedir. Öte yandan öne çıkan iki ülke Finlandiya ve Danimarka'dır.

2017-2022 döneminin geneli için bulunan sıralama Tablo 10'da sunulmuştur. Burada Finlandiya ilk sırada, Danimarka ikinci sıradadır. Diğer ülkeler ise görece yetersiz ülke olarak bulunmuştur. Söz konusu sonuçlar, periyottaki her bir yıl için ayrı ayrı bulunan sonuçlarla uyumludur.

Tablo 10. 2017-2022 dönemi için sonuçlar

	$1-s_i$	$1-r_i$	$1-q_i$	Sıra
Danimarka	0	0,665	[0, 0,665]	2
Finlandiya	1	0,335	[0,335, 1]	1
Lüksemburg	0	0	0	Y
İsveç	0	0	0	Y

AB ülkelerini karşılaştıran literatürdeki çalışmalarda elde edilen ilk üç sıra Tablo 11'de sunulmuştur. Görüldüğü üzere bu çalışmanın sonuçları, literatürdeki sonuçlarla uyumludur.

Tablo 11. Literatürdeki sonuçlar

	1. sıra	2. sıra	3. sıra
Stankovic vd. (2021)	Finlandiya	Hollanda	Danimarka
Bandhi ve Dubos (2023a)	Danimarka	Finlandiya	İsveç
Bandhi ve Dubos (2023b)	Danimarka	Finlandiya	-
Bandhi ve Dubos (2024)	Finlandiya	İsveç	Danimarka
Marti ve Puertas (2023)	İsveç	Hollanda	Finlandiya
Kiselakova vd. (2022)	Danimarka	Finlandiya	Hollanda
Georgescu vd. (2023)	Finlandiya	İsveç	Danimarka
Bu çalışma	Finlandiya	Danimarka	-

5. Sonuç

Çalışmada, AB ülkelerinin 2017-2022 dönemindeki dijitalleşme seviyelerini bütüncül bir şekilde karşılaştırmak amacıyla VIKOR'un norm minimizasyonuna dayalı uzantısı (NM-VIKOR) önerilmiştir ve bu uzantı grup karar verme problemleri için genelleştirilmiştir. Bu uzantı ile yapılan karşılaştırmada farklı yıllar için farklı sonuçlar bulunmuştur. Örneğin, 2017, 2018, 2019 ve 2020 yıllarında Finlandiya ilk sıradadır. 2021 ve 2022 yıllarında ise Danimarka ilk sıradadır. Bu uzantının genel hali olan NMG-VIKOR kullanıldığında ise 2017-2022 dönemi için ilk iki sıra; Finlandiya ve Danimarka olarak bulunmuştur. Diğer AB ülkeleri, dijitalleşme seviyesi açısından görece yetersizdir. Çalışmada elde edilen sonuçlar, dijitalleşme seviyesi açısından görece yetersiz olarak bulunan AB ülkelerinin ve ülkemiz gibi AB'ye aday, gelişmekte olan ülkelerin dijital gelişimlerinin iyileştirilmesi için söz konusu iki ülkeyi örnek alması gerektiğini göstermektedir.

Çalışmanın üç önemli sınırlılığı vardır. İlk olarak, DESI metodolojisi 2023 yılında kısmen değiştiği için 2023 yılı çalışma kapsamına dahil edilememiştir. Bununla birlikte çalışmada tek bir yöntem (NM-VIKOR) ve bunun genel hali (NMG-VIKOR) kullanılmıştır. Ayrıca AB'ye üye olmadıklarından ülkemiz gibi birçok ülke çalışmaya dahil edilmemiştir. İlerideki çalışmalarda dijitalleşme seviyelerinin karşılaştırılmasında kullanılan yöntem sayısı artırılabilir. Ayrıca I-DESI verileri kullanılarak çalışma kapsamı genişletilebilir. Bununla birlikte ülkelerin dijital gelişimlerinin karşılaştırılmasından farklı ÇKKV problemleri için bu yöntemler kullanılabilir. Öte yandan bu yöntemler, görece yetersiz olan alternatifleri kendi içlerinde sıralayamaz. Ayrıca orijinal problemler yerine Tikhonov'un düzenlenmiş problemlerini kullandıklarından yaklaşık sonuçlar verir. Bununla birlikte kullanılabilmeleri için özel yazılımlara ihtiyaç duyulur. Öte yandan VIKOR'dan farklı olarak bu yöntemler, alternatiflerin gruplandırılmasında ve alternatiflere kaynak dağıtımında kullanılabilir. Başka bir deyişle bu yöntemlerden daha az bilgi taşısa da VIKOR, bunlara oranla daha pratik bir yöntemdir.

Katkı Oranı Beyanı

Yazarların katkı yüzdeleri aşağıda verilmiştir. Yazarlar makaleyi incelemiş ve onaylamıştır.

	F.G.	S.S.K.
K	50	50
T	50	50
Y	50	50
VTI	50	50
VAY	50	50
KT	50	50
YZ	50	50
KI	50	50
GR	50	50
PY	50	50
FA	50	50

K= kavram, T= tasarım, Y= yönetim, VTI= veri toplama ve/veya işleme, VAY= veri analizi ve/veya yorumlama, KT= kaynak tarama, YZ= Yazım, KI= kritik inceleme, GR= gönderim ve revizyon, PY= proje yönetimi, FA= fon alımı.

Çatışma Beyanı

Yazarlar bu çalışmada hiçbir çıkar ilişkisi olmadığını beyan etmektedirler.

Etik Onay Beyanı

Bu araştırmada hayvanlar ve insanlar üzerinde herhangi bir çalışma yapılmadığı için etik kurul onayı alınmamıştır.

Kaynaklar

Bánhidi Z, Dobos I. 2023a. A Data Envelopment Analysis model for ranking digital development in the countries of the European Union without explicit inputs and common weights analysis. Decis Anal J, 6: 100167. https://doi.org/10.1016/j.dajour.2023.100167

Bánhidi Z, Dobos I. 2023b. Measurement of digital development with partial orders, Tiered DEA, and cluster analysis for the European Union. Int Rev Appl Sci Eng, 14(3): 392-401. https://doi.org/10.1556/1848.2023.00612

Bánhidi Z, Dobos I. 2024. Sensitivity of TOPSIS ranks to data normalization and objective weights on the example of digital development. Cent Eur J Oper Res, 32(1): 29-44. https://doi.org/10.1007/s10100-023-00876-y

Beck A, Sabach S. 2014. A first order method for finding minimal norm-like solutions of convex optimization problems. Math Program, 147(1): 25-46. http://dx.doi.org/10.1007/s10107-013-0708-2

Boyd SP, Vandenberghe L. 2004. Convex optimization. Cambridge University Press.

Calp MH. 2020. The role of artificial intelligence within the scope of digital transformation in enterprises. In Advanced MIS and digital transformation for increased creativity and innovation in business. IGI Global, pp: 122-146.

Chatterjee P, Chakraborty S. 2016. A comparative analysis of VIKOR method and its variants. Decis Sci Lett, 5(4): 469-486. http://dx.doi.org/10.5267/j.dsl.2016.5.004

DESI. 2022a. Metadata. URL: https://digital-decade-desi.digital-strategy.ec.europa.eu/datasets/desi-2022/metadata (erişim tarihi: 20 Şubat 2024).

DESI. 2022b. Thematic chapters and methodological note. URL: https://digital-strategy.ec.europa.eu/en/policies/desi (erişim tarihi: 20 Şubat 2024).

Georgescu MR, Lungu AE, Bogoslov IA, Stoica EA. 2023. European Efficiency or Inefficiency in Economic Growth Through Digital Transformation. Sci Ann Econ Bus, 70: 19-31. https://doi.org/10.47743/saeb-2023-0010

Göktaş F. 2024. İskandinav ülkelerinin dijital toplum seviyelerinin yeni bir TOPSIS uzantısı ile karşılaştırılması. J Innov Eng Nat Sci, 4(2): 482-494. https://doi.org/10.61112/jiens.1461755

Grant MC, Boyd SP. 2008. Graph implementations for nonsmooth convex programs. In Recent advances in learning and control. Springer London, pp: 95-110. https://doi.org/10.1007/978-1-84800-155-8_7

Ionescu-Feleaga L, Ionescu BŞ, Stoica OC. 2023. The Link between Digitization and the Sustainable Development in European Union Countries. Electronics, 12(4): 961. https://doi.org/10.3390/electronics12040961

ITU. 2019. Measuring digital development facts and figures. URL: https://www.itu.int/en/ITU-D/Statistics/Pages/facts/default.aspx (erişim tarihi: 20 Şubat 2024).

Kiselakova D, Sofrankova B, Sira E, Fedorcíkova R. 2022. Assessment of the digital economy's level among the EU countries-an empirical study. Pol J Manag Stud, 26(1): 107-124. https://doi.org/10.17512/pjms.2022.26.1.07

Kumar R, Sachan A, Mukherjee A. 2018. Direct vs indirect e-government adoption: an exploratory study. Dig Policy Regul, 19(1): 77-100. https://doi.org/10.1108/DPRG-05-2021-0060

Marti L, Puertas R. 2023. Analysis of European competitiveness based on its innovative capacity and digitalization level. Technol Soc, 72: 102206. https://doi.org/10.1016/j.techsoc.2023.102206

Skvarciany V, Lapinskaitė I, Stasytytė V. 2023. Efficiency of digital economy in the context of sustainable development: DEA-Tobit approach. Prague Econ Pap, 32(2): 129-158. https://doi.org/10.18267/j.pep.824

Stankovic JJ, Marjanovic I, Drezgic S, Popovic Z. 2021. The digital competitiveness of European countries: A multiple-criteria approach. J Compet, 13(2): 117-134. https://doi.org/10.7441/joc.2021.02.07

Van Laar E, Van Deursen AJ, Van Dijk JA, De Haan J. 2017. The relation between 21st-century skills and digital skills: A systematic literature review. Comput Hum Behav, 72: 577-588. https://doi.org/10.1016/j.chb.2017.03.010

Zerhouni MN, Özarı Ç. 2022. Assessment of international digital economy and society index using entropy based TOPSIS methods. Int J Rec Res Commerce Economics Manag, 9(2): 70-77. https://doi.org/10.5281/ZENODO.6579884.

Black Sea Journal of Engineering and Science
doi: 10.34248/bsengineering.1582756

Open Access Journal
e-ISSN: 2619 – 8991

Research Article
Volume 8 - Issue 1: 206-213 / January 2025

TUBULAR SURFACES OF ADJOINT CURVES ACCORDING TO THE MODIFIED ORTHOGONAL FRAME

Esra DAMAR [1]*, Burçin SALTIK BAEK [2], Nural YÜKSEL[2], Nurdan OĞRAŞ[2]

[1]*Hitit University, Vocational School of Technical Sciences, Department of Motor Vehicles and Transportation Technologies, 19100, Çorum, Türkiye*
[2]*Erciyes University, Faculty of Science, Department of Mathematics, 38030, Kayseri, Türkiye*

Abstract: In this paper, we study tubular surfaces defined by adjoint curves which have a wide range of applications. In three-dimensional Euclidean space, we consider tubular surfaces in modified orthogonal frame generated by a curve β whose center curve is adjoint of a curve α. We give some characterizations for tubular surfaces constructed according to with curvature and with torsion modified orthogonal frames. Through these characterizations we obtain some important results. We also study asymptotic and geodesic curves as well as flat, minimal, Weingarten and linear-Weingarten surfaces using conventional differential geometry techniques. Finally, we present case examples for both versions of the frame to validate our theoretical results.

Keywords: Tubular surface, Adjoint curve, Modified orthogonal frame

***Corresponding author:** Hitit University, Department of Motor Vehicles and Transportation Technologies, 19200, Çorum, Türkiye
E mail: esradamar@hitit.edu.tr (E. DAMAR)
Esra DAMAR https://orcid.org/0000- 0002-0743-8545
Burçin SALTIK BAEK https://orcid.org/0000-0001-5174-6484
Nural YÜKSEL https://orcid.org/0000- 0003-3360-5148
Nurdan OĞRAŞ https://orcid.org/0000-0002-5539-4890

Received: November 12, 2024
Accepted: December 19, 2024
Published: January 15, 2025

Cite as: Damar E, Saltık Baek B, Yüksel N, Nurdan O. 2025. Tubular surfaces of adjoint curves according to the modified orthogonal frame. BSJ Eng Sci, 8(1): 206-213.

1. Introduction

The Frenet frame has not always been sufficient for solving all problems in studies involving curves and surfaces. Therefore, alternative frames have been developed to address such issues. While the Serret-Frenet frame is a useful tool for the analysis of curves, it cannot be defined at points where the second derivative of the curve is zero. Moreover, at these points, the principal normal vector may exhibit discontinuities, making computations more challenging. To address these problems, Sasai introduced the modified orthogonal frame as an alternative to the Frenet frame. In this frame, the curvature function is used to multiply each Frenet vector, resulting in a new set of vectors. This approach allows the application of a new formula corresponding to the Frenet differentiation equations for the aforementioned cases (Sasai, 1984).

In computer-aided design (CAGD), the envelope of a moving sphere with a changeable radius is called a canal surface, and it is commonly used for surface and solid modeling. The combination of the spheres that are determined by the radius function $r(s)$ and the center curve $\alpha(s)$ yields the canal surface $\psi(s,\theta)$. ψ canal surface can be parameterized as follows (equation 1):

$$\begin{aligned}&\psi(s,\theta)\\&=\alpha(s)-r'(s)r(s)t(s)\\&\pm r(s)\sqrt{1-r'(s)^2}(\cos\theta n(s)+\sin\theta b(s))\end{aligned} \quad (1)$$

where $\alpha(s)$ is a unit speed curve parameterized by arc-lenght s. $\{t,n,b\}$ is the Frenet frame of $\alpha(s)$ (Xu et al., 2006). These canal surfaces are known as tubular surfaces if the radius function $r(s)=r$. In addition, it is useful for reconstructing shapes, planning robot motion, creating blending surfaces, and observing long, thin things like pipes, ropes, poles, even living intestines. Research on tube surfaces in various frames and spaces can be found in (Karacan et al., 2006; Karacan and Yayli, 2008; Yüksel et al., 2011; Karacan and Tuncer, 2013; Saad et al., 2024).

The theory of curves has been one of the main fields of study in differential geometry (Bükçü and Karacan, 2016; Mazlum et al., 2022; Yüksel et al., 2022). Involute-evolute curves, adjoint curves, Bertrand curves, Manheimm curves, and helices have been the most common intersecting curves in recent years. As stated in (Kühnel and Hunt, 2005), an adjoint curve is the integral of a binormal vector of a curve $\alpha(s)$ with any parameter s. In numerous applications, including number theory, coding theory, algebraic geometry, etc., the adjoint curves are crucial. Moreover, adjoint curves are the subject of numerous investigations in (Nurkan et al., 2019; Arıkan and Nurkan, 2020; Cakmak and Şahin, 2022; Nurkan and Güven, 2022).

This study examines tubular surfaces whose centers are adjoint curves defined with respect to the modified

orthogonal frame in E. First, the modified orthogonal frame is used to create the adjoint curve and establish the link between the Frenet vectors (Arıkan and Nurkan, 2020). Next, the geometric properties of these surfaces are obtained, along with some significant findings. Finally, using an example, we demonstrate the visualizations of provided surfaces and tubular surfaces.

2. Materials and Methods

The mathematical definitions for the curvature and torsion of a curve in $E^3$are provided in (O'Neill, 1996). To begin, let us consider unit-speed curves. A key element in the differential geometry of a curve is the use of the Frenet frame field $\{t, n, b\}$. The Frenet differentiation formulas, constructed using these vectors, are expressed as follows:

$t' = \kappa n, n' = -\kappa t + \tau b, b' = -\tau n,$

where κ, τ represent the first and second curvature of the curve, respectively.

Let $\alpha: I \to E^3$ be a space curve. We assume that the curvature κ of α is not identically zero. As a result, the modified orthogonal frame $\{T, N, B\}$ with the curvature κ of the curve α can be defined. Now we define the modified orthogonal frame $\{T, N, B\}$ as follows:

$T = \frac{d\alpha}{ds}, N = \frac{dT}{ds}, B = T \wedge N.$

The following represents the relationships between the modified orthogonal frame $\{T, N, B\}$ and Frenet frame $\{t, n, b\}$ at non-zero positions of κ

$T = t, N = \kappa n, B = \kappa b.$

The modified orthogonal frame $\{T, N, B\}$ satisfies the below relations

$\langle N, T\rangle = \langle B, T\rangle = \langle B, N\rangle = 0,$

$\langle T, T\rangle = 1, \langle N, N\rangle = \langle B, B\rangle = \kappa^2,$

where $\langle , \rangle$ is the inner product. Due to these equations, the derivative equations of the modified orthogonal frame $\{T, N, B\}$ are given as

$T' = N,$

$N' = -\kappa^2 T + \frac{\kappa'}{\kappa} N + \tau B,$

$B' = -\tau N + \frac{\kappa'}{\kappa} B,$

where $\tau = \frac{det(\alpha', \alpha'', \alpha''')}{\kappa^2}$ is the torsion of α (Bükçü and Karacan, 2016).

Now let's talk about the modified orthogonal modified frame with torsion.

The following represents the relationships between the modified orthogonal frame with torsion $\{T, N, B\}$ and Frenet frame $\{t, n, b\}$ at non-zero positions of

$T = t, N = \tau n, B = \tau b$

where

$\langle N, T\rangle = \langle B, T\rangle = \langle B, N\rangle = 0,$

$\langle T, T\rangle = 1, \langle N, N\rangle = \langle B, B\rangle = \tau^2.$

In this case, the following modified orthogonal frame with torsion hold:

$T' = \frac{\kappa}{\tau} N,$

$N' = -\kappa\tau T + \frac{\tau'}{\tau} N + \tau B,$

$B' = -\tau N + \frac{\tau'}{\tau} B$ (Bükçü and Karacan, 2016).

Let $\psi(s, \theta)$ a surface in E and $U(s, \theta)$ be the typical unit normal vector field on $\psi(s, \theta)$ defined by $U = \frac{\psi_s \times \psi_\theta}{\|\psi_s \times \psi_\theta\|}$ where $\psi_s = \frac{\partial \psi}{\partial s}$ and $\psi_\theta = \frac{\partial \psi}{\partial \theta}$ are the tangent vectors of $\psi(s, \theta)$. Then, the first fundamental form I of $\psi(s, \theta)$ is defined by

$I = g_{11} ds^2 + 2 g_{12} ds d\theta + g_{22} d\theta^2$

where

$g_{11} = \langle \psi_s, \psi_s\rangle, g_{12} = \langle \psi_s, \psi_\theta\rangle, g_{22} = \langle \psi_\theta, \psi_\theta\rangle.$

The second fundamental form of $\psi(s, \theta)$ can be defined as follows:

$II = h_{11} ds^2 + 2 h_{12} ds d\theta + h_{22} d\theta^2$

where

$h_{11} = \langle \psi_{ss}, U\rangle, h_{12} = \langle \psi_s, U\rangle, g_{22} = \langle \psi_{\theta\theta}, U\rangle$

The mean curvature H and the Gaussian curvature K are both represented as follows:

$$K = \frac{h_{11} h_{22} - h_{12}^2}{g_{11} g_{22} - g_{12}^2}, H = \frac{h_{11} g_{22} - 2 g_{12} h_{12} + g_{11} h_{22}}{2(g_{11} g_{22} - g_{12}^2)}. \quad (1)$$

Definition 1; Let α be a unit speed curve in E^3 with $\tau \neq 0$ and the Frenet frame of α be $\{T_\alpha, N_\alpha, B_\alpha\}$. The adjoint curve of α is defined in as

$\beta(s) = \int_{s_0}^{s} B_\alpha(s) ds$ (Kühnel and Hunt, 2005).

Theorem 1; Let α be a curve with an arc length parameter s and β be the adjoint curve of α. If the Frenet vectors of α and β are $\{T_\alpha, N_\alpha, B_\alpha\}$ and $\{T_\beta, N_\beta, B_\beta\}$ the curvature and torsion are $\{\kappa_\alpha, \tau_\alpha\}$ and $\{\kappa_\beta, \tau_\beta\}$ respectively, then the following relations hold (Arıkan and Nurkan, 2020):

$$\begin{cases} T_\beta = B_\alpha, \\ N_\beta = -N_\alpha, \kappa_\beta = \tau_\alpha, \tau_\beta = \kappa_\alpha. \\ B_\beta = T_\alpha, \end{cases}$$

Theorem 2; Let α be a unit speed regular curve in E^3 and β is the adjoint curve of α according to the modified orthogonal frame with curvature. If the modified orthogonal frames of α and β are $\{T_\alpha, N_\alpha, B_\alpha\}$ and $\{T_\beta, N_\beta, B_\beta\}$, the curvature and torsion are $\{\kappa_\alpha, \tau_\alpha\}$ and $\{\kappa_\beta, \tau_\beta\}$ respectively, the following relations hold (Arıkan and Nurkan, 2020):

$$\begin{cases} T_\beta = \left(\frac{1}{\kappa_\alpha}\right) B_\alpha, \\ N_\beta = -\left(\frac{\tau_\alpha}{\kappa_\alpha^2}\right) N_\alpha, \kappa_\beta = \frac{\tau_\alpha}{\kappa_\alpha}, \tau_\beta = 1. \\ B_\beta = \left(\frac{\tau_\alpha}{\kappa_\alpha}\right) T_\alpha, \end{cases}$$

Theorem 3; Let α be a unit speed regular curve in E^3 and β is the adjoint curve of the modified orthogonal frame with torsion. If the modified orthogonal frames of α and β are $\{T_\alpha, N_\alpha, B_\alpha\}$ and $\{T_\beta, N_\beta, B_\beta\}$ the curvature and torsion are $\{\kappa_\alpha, \tau_\alpha\}$ and $\{\kappa_\beta, \tau_\beta\}$ respectively, consequently, the following relationships exist (Arıkan and Nurkan, 2020):

$$\begin{cases} T_\beta = \left(\frac{1}{\tau_\alpha}\right) B_\alpha \\ N_\alpha = -\left(\frac{\kappa_\alpha}{\tau_\alpha^2}\right) N_\alpha,\ \kappa_\beta = 1, \tau_\beta = \frac{\kappa_\alpha}{\tau_\alpha}. \\ B_\alpha = \left(\frac{\kappa_\alpha}{\tau_\alpha}\right), \end{cases}$$

Definition 2; If $\Phi(X,Y) = 0$, where the Jacobi function Φ is defined as $X_S Y_\Theta - Y_S X_\Theta = 0$ then the pair $(X,Y), X \neq Y$ of the curvatures K, H of a tubular surface $\psi(s,\theta)$ is said to be a (X,Y)-Weingarten surface (Kim et al., 2016).

Definition 3; If $\psi(s,\theta)$ satisfies the following relation, then the pair $(X,Y), X \neq Y$ of the curvatures K, H of the tubular surface $\psi(s,\theta)$ is said to be a (X,Y)-linear Weingarten surface:

$a_1 X + a_2 Y = a_3$

where $a_1, a_2, a_3 \in \mathbb{R}$ and $(a_1, a_2, a_3) \neq (0,0,0)$ (López, 2009).

3. Results

3.1. Tubular Surfaces Whose Center Curve is an Adjoint Curve in a Modified Orthogonal Frame with Curvature

The tubular surface whose center curve adjoint curve β of the α using to the modified orthogonal frame with curvature in E^3 is examined in this section. Concerning the modified orthogonal frame, the parameterization of the tubular surface exists.

$$\psi(s,\theta) = \alpha(s) + \frac{r}{\kappa(s)}(\cos\theta N(s) + \sin\theta B(s)) \quad (2)$$

where $r = const.$ and $\kappa \neq 0$. The center curve β of the curve α is considered to be the adjoint curve of this surface. So from equation 2 we get

$$\psi(s,\theta) = \beta(s) + \frac{r}{\kappa(s)}\left(\cos\theta N_\beta(s) + \sin\theta B_\beta(s)\right)$$

$$\psi(s,\theta) = \int_{s_0}^{s} B_\alpha(s)ds + r\left(-\frac{\cos\theta}{\kappa_\alpha(s)} N_\alpha(s) + \sin\theta T_\alpha(s)\right).$$

The derivatives according to s and θ concerning the tubular surface $\psi(s,\theta)$ are (equation 3)

$$\psi_s = (r\kappa_\alpha\cos\theta)T_\alpha + (r\sin\theta)N_\alpha + \left(1 - \frac{r\tau_\alpha}{\kappa_\alpha}\cos\theta\right)B_\alpha,$$

$$\psi_\theta = (r\cos\theta)T_\alpha + \left(\frac{r}{\kappa_\alpha}\sin\theta\right)N_\alpha,$$

$$\psi_{ss} = (r\kappa_\alpha'\cos\theta - r\kappa_\alpha^2\sin\theta)T_\alpha + \left(\left(r\kappa_\alpha\cos\theta + r\frac{\kappa_\alpha'}{\kappa_\alpha}\sin\theta\right) - \left(\frac{\tau_\alpha}{\kappa_\alpha}\right)(\kappa_\alpha - r\tau_\alpha\cos\theta)\right)N_\alpha + \left(r\tau_\alpha\sin\theta + \frac{r\cos\theta}{\kappa_\alpha^2}(\tau_\alpha\kappa_\alpha' - \kappa_\alpha\tau_\alpha') + \frac{\kappa_\alpha'}{\kappa_\alpha^2}(\kappa_\alpha - r\tau_\alpha\cos\theta)\right)B_\alpha,$$

$$\psi_{\theta\theta} = (-r\sin\theta)T_\alpha + \left(\frac{r}{\kappa_\alpha}\cos\theta\right)N_\alpha. \quad (3)$$

Hence we obtain

$g_{11} = r^2\kappa_\alpha^2 + r^2\tau_\alpha^2\cos^2\theta + \kappa_\alpha^2 - 2r\,\kappa_\alpha\tau_\alpha\cos\theta,$

$g_{12} = r^2\kappa_\alpha,$

$g_{12} = r^2,$

$g = g_{11}g_{22-}g_{12}^2 = r^2(\kappa_\alpha - r\tau_\alpha\cos\theta)^2 \neq 0.$

The normal vector field the unit U is provided by (equation 4)

$$U(s) = -\sin\theta T_\alpha + \frac{1}{\kappa_\alpha}\cos\theta\, N_\alpha \quad (4)$$

as well as the second fundamental form's coefficients, which are as follows:

$h_{11} = r\kappa_\alpha^2 - \tau_\alpha\cos\theta\,(\kappa_\alpha - r\tau_\alpha\cos\theta),$

$h_{12} = r\kappa_\alpha,$

$h_{22} = r,$

from equation 1, the Gaussian and the mean curvatures are provided by (equations 5 and 6)

$$K = -\frac{\tau_\alpha\cos\theta}{r(\kappa_\alpha - r\tau_\alpha\cos\theta)} \quad (5)$$

$$H = \frac{\kappa_\alpha - 2r\tau_\alpha\cos\theta}{2r(\kappa_\alpha - r\tau_\alpha\cos\theta)}. \quad (6)$$

The mean curvature H and the Gaussian curvature K of tubular surface $\psi(s,\theta)$ satisfy the following relationship

$$H = \frac{1}{2}\left(Kr + \frac{1}{r}\right) \quad (7)$$

it follows that, the principal curvatures of $\psi(s,\theta)$ are obtained as follows:

$k_1 = \frac{1}{r}$, $k_2 = Kr.$

Proposition 1; In Euclidean 3-space, let $\psi(s,\theta)$ be a tubular surface. $\psi(s,\theta)$ is not a flat surface in such case.

Proof; We presume that $\psi(s,\theta)$ is flat. In this case, $\kappa = 0$ from equation 5, we get

$-\tau_\alpha\cos\theta = 0$, since $\tau_\alpha \neq 0$ from the definition of adjoint curve $\psi(s,\theta)$ the tube surface is not flat.

Proposition 2; In Euclidean 3-space, let $\psi(s,\theta)$ be a tubular surface. Then $\psi(s,\theta)$ is minimal if and only if $r = \frac{\kappa_\alpha}{2\tau_\alpha\cos\theta}$.

Proof; Equation 6 provides the result immediately.

Theorem 1; Let $\psi(s,\theta)$ be a tubular surface with a modified orthogonal frame in E^3. Then

i) Asymptotic curves are s-parameter curves of $\psi(s,\theta)$ if and only if $r = \frac{\tau_\alpha\kappa_\alpha\cos\theta}{\tau_\alpha^2\cos^2\theta + \kappa_\alpha^2}$.

ii) Asymptotic curves cannot be θ-parameter curves of $\psi(s,\theta)$.

Proof; We can infer from the definition of asymptotic curves that

$\langle\psi_{ss}, U\rangle = 0$, $\langle\psi_{\theta\theta}, U\rangle = 0$

i) From equations 3 and 4, we can get

$h_{11} = r\kappa_\alpha^2 - \tau_\alpha\cos\theta\,(\kappa_\alpha - r\tau_\alpha\cos\theta) = 0$

$r = \frac{\tau_\alpha\kappa_\alpha\cos\theta}{\tau_\alpha^2\cos^2\theta + \kappa_\alpha^2}$.

ii) Since $h_{22} \neq 0$, θ-parameter curves of the $\psi(s,\theta)$ cannot be asymptotic.

Theorem 2; In E, let $\psi(s,\theta)$ be a tubular surface with a modified orthogonal frame. Then

i) Geodesic curves cannot be s-parameter curves of $\psi(s,\theta)$.

ii) The curves for the θ -parameter of $\psi(s,\theta)$ are geodesic.

Proof; In order to define the parameter curves s and, it is necessary to provide the values of $\psi_{ss} \times U = 0$ and $\psi_{\theta\theta} \times U = 0$ for the geodesic curves.

i) According to equations 3 and 4, we obtain

$\psi_{ss} \times U = (r\tau'_\alpha \cos^2\theta - r\cos\theta \sin\theta\, \kappa_\alpha\tau_\alpha - \kappa'_\alpha \cos\theta)T_\alpha$
$+\left(r\cos\theta \sin\theta \frac{\tau'_\alpha}{\kappa_\alpha} - r\sin^2\theta\tau_\alpha - \frac{\kappa'_\alpha}{\kappa_\alpha}\sin\theta\right)N_\alpha$
$+\left(r\frac{\kappa'_\alpha}{\kappa_\alpha} - \tau_\alpha \sin\theta + r\sin\theta\cos\theta\frac{\tau_\alpha^2}{\kappa_\alpha}\right)B_\alpha$.

Since T_α , N_α and B_α are linearly independent then, $\psi_{ss} \times U = 0$ if and only if $\kappa_\alpha = const.\tau_\alpha = 0$. Nevertheless, given $\tau_\alpha \neq 0$, $\psi(s,\theta)$ cannot be a geodesic curve.

ii) Furthermore, we obtain $\psi_{\theta\theta} \times U = 0$ from equations 3 and 4. θ-parameter curves are geodesic curves.

We now define the mean curvature and the partial derivative of the Gaussian curvature of the tubular surface as follows:

$$K_s = -\frac{\cos\theta(\kappa_\alpha\tau'_\alpha - \tau_\alpha\kappa'_\alpha)}{r(\kappa_\alpha - r\tau_\alpha\cos\theta)^2},$$
$$H_s = -\frac{\cos\theta(\kappa_\alpha\tau'_\alpha - \tau_\alpha\kappa'_\alpha)}{2(\kappa_\alpha - r\tau_\alpha\cos\theta)^2},$$
$$K_\theta = \frac{\kappa_\alpha\tau_\alpha\sin\theta}{r(\kappa_\alpha - r\tau_\alpha\cos\theta)^2},$$
$$H_\theta = \frac{\kappa_\alpha\tau_\alpha\sin\theta}{2(\kappa_\alpha - r\tau_\alpha\cos\theta)^2}. \quad (8)$$

Theorem 3; Let $\psi(s,\theta)$ be a tubular surface with a modified orthogonal frame in E. The surface $\psi(s,\theta)$ is a (K,H) −Weingarten surface.

Proof; If the derivatives of the mean curvature and the Gaussian curvature of the surface $\psi(s,\theta)$, given by equation 8, are substituted into the Jacobi equation

$H_sK_\theta - H_\theta K_s = 0$

is obtained. Therefore, the surface $\psi(s,\theta)$ is a (K,H) −Weingarten surface.

Theorem 4; Let $\psi(s,\theta)$ be a tubular surface in $\mathbb{E}^3$ equipped with a modified orthogonal frame. If ψ is (K,H) -linear Weingarten surface, then for $a_3 = 1$, the following relations hold $a_1 = -3r^2$ and $a_2 = 2r$, hold.

Proof; Let us assume that ψ is a (K,H) -linear Weingarten surface. In this case, the following equation is satisfied

$a_1K + a_2H = 1$

where $a_1, a_2 \in \mathbb{R}$ and $(a_1, a_2) \neq 0$. From equation 7, the following relations are derived

$$2r - a_2 = \frac{-\tau_\alpha\cos\theta}{\kappa_\alpha - r\tau_\alpha\cos\theta}(a_2r + 2a_1)$$

and

$2\tau_\alpha\cos\theta\,(r^2 + a_2r + a_1) + \kappa_\alpha(2r - a_2) = 0$.

Consequently, $a_1 = -3r^2$ is obtained when $a_2 = 2r$.

Example 1; The parametric equation of curve α_1 is provided by

$$\alpha_1(s) = \left(\cos\left(\frac{\sqrt{7}s}{4}\right), \sin\left(\frac{\sqrt{7}s}{4}\right), \frac{3s}{4}\right).$$

The parametric equation of the adjoint curve of α is given by

$$\beta_1(s) = \left(-\frac{3\sqrt{7}}{16}\cos\left(\frac{\sqrt{7}}{4}s\right), -\frac{3\sqrt{7}}{16}\sin\left(\frac{\sqrt{7}}{4}s\right), -\frac{7\sqrt{7}}{64}s\right).$$

The tube surface whose center curve is α_1 according to the modified orthogonal frame with curvature is given by

$\psi_{\alpha_1}(s,\theta) = \left(\frac{3}{4}\sin\theta\sin\left(\frac{\sqrt{7}}{4}s\right) - \cos\theta\cos\left(\frac{\sqrt{7}}{4}s\right) +\right.$
$+\cos\left(\frac{\sqrt{7}}{4}s\right), -\cos\theta\sin\left(\frac{\sqrt{7}}{4}s\right) - \frac{3}{4}\sin\theta\cos\left(\frac{\sqrt{7}}{4}s\right)$
$\left.+\sin\left(\frac{\sqrt{7}}{4}s\right), \frac{\sqrt{7}}{4}\sin\theta + \frac{3s}{4}\right)$.

The graph of the tube surface, whose center curve is according to the modified orthogonal frame with curvature, is illustrated in Figure 1.

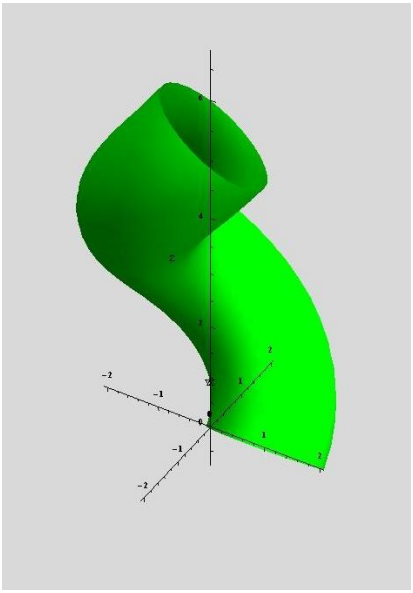

Figure 1 The tube surface, whose center curve is α_1 according to the modified orthogonal frame with curvature.

The tube surface whose center curve is $\beta_1(s)$ according to the modified orthogonal frame with curvature is given by

$\psi_{\beta_1(s)}(s,\theta) = \left(-\frac{3\sqrt{7}}{16}\cos\left(\frac{\sqrt{7}s}{4}\right) + \cos\theta\cos\left(\frac{\sqrt{7}s}{4}\right)\right.$
$\left.-\frac{\sqrt{7}}{4}\sin\theta\sin\left(\frac{\sqrt{7}s}{4}\right), -\frac{3\sqrt{7}}{16}\sin\left(\frac{\sqrt{7}s}{4}\right) + \cos\theta\sin\left(\frac{\sqrt{7}s}{4}\right)\right.$

$$+\frac{\sqrt{7}}{4}\sin\theta\cos\left(\frac{\sqrt{7}s}{4}\right),\frac{7\sqrt{7}}{64}s+\frac{3}{4}\sin\theta\Big)$$

The graph of the tube surface $\psi_{\beta_1(s)}(s,\theta)$ whose center curve is $\beta_1(s)$ according to the modified orthogonal frame with curvature is illustrated in Figure 2.

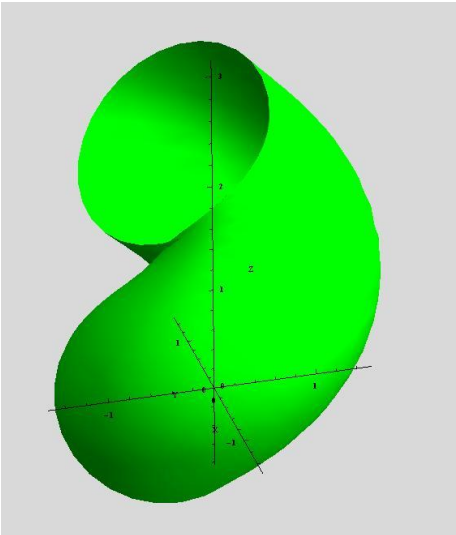

Figure 2. The tube surface whose center curve is β_1 according to the modified orthogonal frame with curvature.

3.2 Tubular Surfaces Whose Center Curve is Adjoint Curve in Modified Orthogonal Frame with Torsion

This section is dedicated to the analysis of the tubular surface whose center curve is the adjoint curve β of the α, according to the modified orthogonal frame with torsion in E^3. The parameterization of the tubular surface exists with respect to the modified orthogonal frame.

$$W(s,\theta)=\alpha(s)+\frac{r}{\tau(s)}(\cos\theta N(s)+\sin\theta B(s)) \quad (9)$$

where $r=const.$ and $\tau\neq 0$. The adjoint curve of this surface is defined as the center curve β of the curve α. Thus, we derive equation 9 and

$$W(s,\theta)=\beta(s)+\frac{r}{\kappa_\beta}\big(\cos\theta\, N_\beta(s)+\sin\theta B_\beta(s)\big),$$

$$W(s,\theta)=\int_{s_0}^{s}B_\alpha(s)ds+r\left(-\frac{\cos\theta}{\tau_\alpha(s)}N_\alpha(s)+\sin\theta T_\alpha(s)\right),$$

$$W_s=(r\kappa_\alpha\cos\theta)T_\alpha+\left(\frac{r\kappa_\alpha}{\tau_\alpha}\sin\theta\right)N_\alpha+(1-r\cos\theta)B_\alpha,$$

$$W_\theta=(r\cos\theta)T_\alpha+\left(\frac{r}{\tau_\alpha}\sin\theta\right)N_\alpha,$$

$$W_{ss}=(r\kappa_\alpha'\cos\theta-r\kappa_\alpha^2\sin\theta)T_\alpha$$
$$+\left(\frac{r\kappa_\alpha\cos\theta}{\tau_\alpha}+\frac{r\kappa_\alpha'\sin\theta}{\tau_\alpha}-\tau_\alpha(1-r\cos\theta)\right)N_\alpha$$
$$+\left(r\kappa_\alpha^2\sin\theta+\frac{\tau_\alpha'(1-r\cos\theta)}{\tau_\alpha}\right)B_\alpha,$$

$$W_{\theta\theta}=(-r\sin\theta)T_\alpha+\left(\frac{r\cos\theta}{\tau_\alpha}\right)B_\alpha. \quad (10)$$

Thus, we get at

$$g_{11}=r^2\kappa_\alpha^2+r^2\tau_\alpha^2\cos^2\theta+\tau_\alpha^2-2r\tau_\alpha^2\cos\theta,$$
$$g_{12}=r^2\kappa_\alpha,$$
$$g_{22}=r^2,$$
$$g=g_{11}g_{22}-g_{12}^2=r^2\tau_\alpha^2(1-r\cos\theta)^2\neq 0.$$

The unit normal vector field U^* is given by,

$$U^*=-\sin\theta\, T_\alpha+\frac{\cos\theta}{\tau_\alpha}N_\alpha, \quad (11)$$

$$h_{11}=r\kappa_\alpha^2-\tau_\alpha^2\cos\theta(1-r\cos\theta),$$
$$h_{12}=r\kappa_\alpha,$$
$$h_{22}=r.$$

According to equations 5 and 6, the mean and the Gaussian curvatures are given, respectively, by

$$K=-\frac{\cos\theta}{(1-r\cos\theta)},H=\frac{1-2r\cos\theta}{2r(1-r\cos\theta)}. \quad (12)$$

Proposition 3; In Euclidean 3-space, let $W(s,\theta)$be a tubular surface. $W(s,\theta)$ is not a flat surface in such case.

Proof; It is similar to Proof 1.

Proposition 4; In Euclidean 3-space, let $W(s,\theta)$ be a tubular surface. Then $W(s,\theta)$ is minimal if and only if $r=\frac{1}{2\sec\theta}$.

Proof; Equation 12 provides the result explicitly.

Theorem 4; Let $W(s,\theta)$ be a tubular surface with a modified orthogonal frame in E^3. Then

i) Asymptotic curves are s-parameter curves of $W(s,\theta)$ if and only if $r=\frac{\tau_\alpha^2\cos\theta}{\kappa_\alpha^2+\tau_\alpha^2\cos\theta}$.

ii) Asymptotic curves cannot be θ -parameter curves of $W(s,\theta)$.

Proof; We can infer from the definition of asymptotic curves that $\langle W_{ss},U^*\rangle=0$, $\langle W_{\theta\theta},U^*\rangle=0$.

i) From equations 10 and 11 we obtain results

$r\kappa_\alpha^2-\tau_\alpha^2\cos\theta\,(1-r\cos\theta)=0$

and

$r=\frac{\tau_\alpha^2\cos\theta}{\tau_\alpha^2\cos^2\theta+\kappa_\alpha^2}$.

ii) Since $r\neq 0$, θ-parameter curves of the $W(s,\theta)$ cannot be asymptotic.

Theorem 5; Let $W(s,\theta)$ be a tubular surface with modified orthogonal frame in E^3 . Then

i) s-parameter curves of $W\ (s,\theta)$ cannot be geodesic curves.

ii) θ- parameter curves of $W(s,\theta)$ are geodesic.

Proof; According to the definition of the geodesic curve, the conditions $W_{ss}\times U=0$ and $W_{\theta\theta}\times U=0$ must be satisfied for the s - and θ - parameter curves.

i) According to equations 10 and 11 we obtain

$$W_{ss}\times U=\big(-\tau_\alpha r\kappa_\alpha\sin\theta-\tau_\alpha'\cos\theta\,(1-r\cos\theta)\big)T_\alpha$$
$$+\left(\frac{\tau_\alpha'(1-r\cos\theta)}{\tau_\alpha}-r\kappa_\alpha\sin^2\theta\right)N_\alpha$$
$$+\left(\frac{r\kappa_\alpha'}{\tau_\alpha}-\tau_\alpha(1-r\cos\theta)\sin\theta\right)B_\alpha$$

Since T_α,N_α and B_α are linearly independent then, $W_{ss}\times U=0$ if and only if $\kappa_\alpha=0$, $\tau_\alpha=0$. Nevertheless, given $\kappa_\alpha\neq 0$, $\tau_\alpha\neq 0$, $W(s,\theta)$ cannot be a geodesic curve.

ii) Furthermore, we obtain $W_{\theta\theta}\times U=0$ from equations 10 and 11. θ-parameter curves are hence geodesic curves.

We now define the mean curvature H and the partial derivative of the Gaussian curvature K of the tubular surface $W(s,\theta)$ as follows

$K_s = 0,$ (13)

$K_\theta = \frac{-\sin\theta}{r(1-r\cos\theta)^2},$

$H_s = 0,$

$H_\theta = \frac{-\sin\theta}{2(1-r\cos\theta)}$

Theorem 6 ; Let $W(s,\theta)$ be a tubular surface with a modified orthogonal frame in E^3. The surface $W(s,\theta)$ is a (K,H) −Weingarten surface.

Proof; If the derivatives of the mean curvature and the Gaussian curvature of the surface $W(s,\theta)$, given by equation 13, are substituted into the Jacobi equation

$H_s K_\theta - H_\theta K_s = 0$

is obtained. Therefore, the surface $W(s,\theta)$ is a (K,H) −Weingarten surface.

Theorem 7; Let $W(s,\theta)$ be a tubular surface in $\mathbb{E}^3$ equipped with a modified orthogonal frame If W is (K,H) -linear Weingarten surface, then for $a_3 = 1$, the following relations hold $a_1 = -r^2$ and $a_2 = 2r$, hold.

Proof; Let us assume that W is a (K,H) -linear Weingarten surface. In this case, the following equation is satisfied

$a_1 K + a_2 H = 1$

where $a_1, a_2 \in \mathbb{R}$ and $(a_1, a_2) \neq 0$. From equation 12, we have the following relation

$2\cos\theta\,(-r^2 + a_r r + a_1) + (2r - a_2) = 0.$

Consequently, $a_1 = -r^2$ is obtained when $a_2 = 2r$.

Example 2; The parametric equation of the curve α_2 is given by

$\alpha_2(s) = \left(2\cos\left(\frac{s}{3}\right), 2\sin\left(\frac{s}{3}\right), \frac{\sqrt{5}s}{3}\right)$

The parametric equation of the adjoint curve of α_2 is given by

$\beta_2(s) = \left(\frac{5}{27}\cos\left(\frac{s}{3}\right), -\frac{5}{27}\sin\left(\frac{s}{3}\right), \frac{2\sqrt{5}}{27}s\right)$

The tube surface whose center curve is α_2 according to the modified orthogonal frame with torsion is given by

$W_{\alpha_2}(s,\theta) = \left(\frac{\sqrt{5}}{3}\sin\theta\sin\left(\frac{s}{3}\right) - \cos\theta\cos\left(\frac{s}{3}\right) + 2\cos\left(\frac{s}{3}\right),\right.$

$-\cos\theta\sin\left(\frac{s}{3}\right) - \frac{\sqrt{5}}{3}\sin\theta\cos\left(\frac{s}{3}\right) + 2\sin\frac{s}{3},$

$\left.\frac{2}{3}\sin\theta + \frac{\sqrt{5}s}{3}\right)$

The graph of the tube surface that $W_{\alpha_2}(s,\theta)$ whose center curve is α_2 according to the modified orthogonal frame with torsion is illustrated in Figure 3.

The tube surface whose center curve is β_2 according to the modified orthogonal frame with torsion is given by

$W_{\beta_2}(s,\theta) = \left(-\frac{5}{9}\cos\left(\frac{s}{3}\right) + \cos\theta\cos\left(\frac{s}{3}\right) - \frac{2}{3}\sin\theta\sin\left(\frac{s}{3}\right),\right.$

$-\frac{5}{9}\sin\left(\frac{s}{3}\right) + \cos\theta\sin\left(\frac{s}{3}\right) + \frac{2}{3}\sin\theta\cos\left(\frac{s}{3}\right),$

$\left.\frac{2\sqrt{5}}{27}s + \frac{\sqrt{5}}{3}\sin\theta\right)$

The graph of the tube surface that $W_{\beta_2}(s,\theta)$ whose center curve is β_2 according to the modified orthogonal frame with torsion is illustrated in Figure 4.

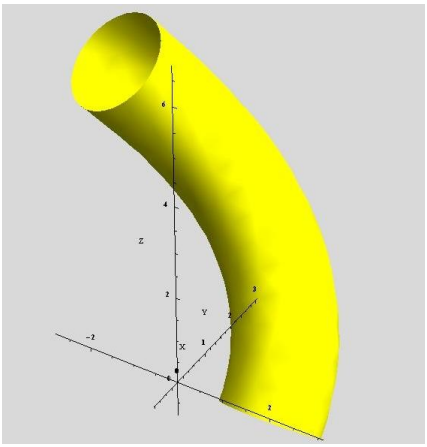

Figure 3. The tube surface, whose center curve is α_2 according to the modified orthogonal frame with torsion.

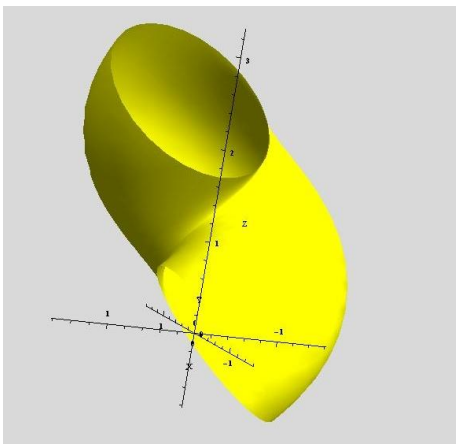

Figure 4. The tube surface, whose center curve is β_2 according to the modified orthogonal frame with torsion.

4. Discussion

The geometry of tubular surfaces in a modified orthogonal frame was investigated in this work, with particular attention to situations in which the center curve in Euclidean 3-space is the adjoint curve of another curve. By using this method, we were able to determine important properties such as Gaussian and mean curvature, which showed that the geometric qualities of these surfaces, such as minimality and flatness, are dependent on certain center curve-related requirements. We discovered that the non-zero Gaussian curvature of these surfaces prevents them from being flat, and minimality is only achievable when the mean curvature is zero. Furthermore, we examined the behavior of asymptotic and geodesic curves, demonstrating that depending on how they relate to curvature and torsion, some parameter curves display asymptotic or geodesic characteristics. Ultimately, we expanded our knowledge of the structural and geometric behavior of these tubular surfaces by classifying them as Weingarten surfaces under particular circumstances.

5. Conclusion

In the modified orthogonal frame, tubular surfaces with center curves that are adjoint curves are thoroughly examined in this work. The importance of the modified orthogonal frame in comprehending the specifics of tubular surface geometry was highlighted when we discovered crucial geometric criteria for the flatness, minimality, asymptotic behavior, and geodesicity of these surfaces by exact mathematical deductions. Our findings show the usefulness of adjoint curves in creating a more comprehensive framework for describing tubular surfaces by exposing unique characteristics not seen in traditional frames. These results provide a more thorough understanding of tubular surface geometry, and the techniques discussed here could be used for additional research in differential geometry, especially in situations where the interplay between curvature and frame structures is essential.

Author Contributions

The percentages of the authors' contributions are presented below. All authors reviewed and approved the final version of the manuscript.

	E.D.	B.S.B.	N.Y.	N.O.
C	25	25	25	25
D	40	20	20	20
S	40	20	20	20
DCP	40	20	20	20
DAI	40	20	20	20
L	40	20	20	20
W	40	20	20	20
CR	40	20	20	20
SR	40	20	20	20
PM	40	20	20	20
FA	0	0	0	0

C=Concept, D= design, S= supervision, DCP= data collection and/or processing, DAI= data analysis and/or interpretation, L= literature search, W= writing, CR= critical review, SR= submission and revision, PM= project management, FA= funding acquisition.

Conflict of Interest

The authors declared that there is no conflict of interest.

Ethical Consideration

Ethics committee approval was not required for this study because of there was no study on animals or humans.

References

Arıkan M, Nurkan KS. 2020. Adjoint curve according to modified orthogonal frame with torsion in 3-space. Uşak Üniv Fen Doğa Bilim Derg, 4: 54-64.

Bükcü B, Karacan M. K. 2016. On the modified orthogonal frame with curvature and torsion in 3-space. Math Sci Applicat E-Notes, 4: 184-188.

Cakmak A, Şahin V. 2022. Characterizations of adjoint curves according to alternative moving frame. Fundamen J Math Applicat, 5: 42-50.

Karacan MK, Es H, Yayli Y. 2006. Singular points of tubular surfaces in Minkowski 3-space. Sarajevo J Math, 2: 73-82.

Karacan MK, Yayli Y. 2008. On the geodesics of tubular surfaces in Minkowski 3-space. Bullet Malaysian Math Sci Soc Second Series, 31: 1-10.

Karacan MK, Tuncer Y. 2013. Tubular surfaces of Weingarten types in Galilean and pseudo-Galilean. Bull Math Anal Appl, 5: 87-100.

Kim Y. H, Liu H, Qian J. 2016. Some characterizations of canal surfaces. Bull Korean Math Soc, 53: 461-477.

Kühnel W, Hunt B. 2005. Differential geometry: curves-surfaces-manifolds. Providence, Rhode Island: American Mathematical Society 3rd ed., New York, USA, pp: 402.

López R. 2009. Linear Weingarten surfaces in Euclidean and hyperbolic space. arXiv preprint arXiv: 0906.3302.

Mazlum GS, Şenyurt S, Bektaş M. 2022. Salkowski curves and their modified orthogonal frames in J New Theory, 40: 12-26.

Nurkan KS, Güven Aİ, Karacan M. K. 2019. Characterizations of

adjoint curves in Euclidean 3-space. Proc National Acad Sci, India Section A: Phys Sci, 89: 155-161.

Nurkan KS. Güven Aİ. 2022. A new approach for Smarandache curves. Turkish J Math Comput Sci, 14: 155-165.

O'Neill B. 1996. Elementary differential geometry. Academic Press, Inc, New York, USA, pp: 154.

Saad MK, Yüksel N, Oğraş N, Alghamdi F, Abdel-Salam AA. 2024. Geometry of tubular surfaces and their focal surfaces in Euclidean 3-space. AIMS Math, 9: 12479-12493.

Sasai T. 1984. The fundamental theorem of analytic space curves and apparent singularities of Fuchsian differential equations. Tohoku Math J, Second Series, 36(1):17-24.

Yuksel N, Tuncer Y, Karacan MK. 2011. Tabular surfaces with Bishop frame of Weingarten types in Euclidian 3-Space. Acta Univer Apulensis, 27: 39-50.

Yüksel N, Saltık B, Damar E. 2022. Parallel curves in Minkowski 3-space. Gümüşhane Üniv Fen Bilim Derg, 12: 480-486.

Xu Z, Feng R, Sun J. G. 2006. Analytic and algebraic properties of canal surfaces. J Comput Appl Math, 195: 220-228.

Black Sea Journal of Engineering and Science
doi: 10.34248/bsengineering.1527551

Open Access Journal
e-ISSN: 2619 – 8991

Research Article
Volume 8 - Issue 1: 214-224 / January 2025

FAKE NEWS DETECTION ON MAINSTREAM MEDIA USING NATURAL LANGUAGE PROCESSING

İsa KULAKSIZ[1]*, Ahmet COŞKUNÇAY[1]

[1]Atatürk University, Faculty of Engineering, Department of Computer Engineering, 25000, Erzurum, Türkiye

Abstract: In light of recent advances in online journalism, the diversity, abundance, and accessibility of news have increased exponentially. However, the growth of online journalism also brings issues, especially regarding the reliability of the news. Notably, news widely shared on social media during the US presidential election campaign and the UK Brexit referendum caused millions of reactions from the public. This concerning scenario prompted industry and academia to address the pressing issue of fake news. Detecting fake news is a meticulous, time-consuming, and labor-intensive task that requires expert judgment. To mitigate this challenge, this study proposes a linguistic based model for Turkish fake news detection. In this dataset was collected from TRT's RSS service and through web scraping from the Teyit.org platform. It contains news titles and summaries related to significant events in Türkiye between 2015 and 2023. The research compares classical machine learning classifiers including SVM, Logistic Regression, Random Forest, k-NN, Decision Tree, and Naive Bayes, against a neural based sequential learning model such as LSTM using real world datasets. Furthermore, the research investigates the impacts of different word representation techniques, including TF-IDF and CountVectorizer, and also hyperparameter optimization on the classification results. The findings revealed that using hyperparameter tuning, the TF-IDF method yielded the highest accuracy rate of 93.12% on the SVM model and that TF-IDF is more effective.

Keywords: Fake news detection, Machine learning, Classification, LSTM, NLP

***Corresponding author:** Ataturk University, Faculty of Engineering, Department of Computer Engineering, 25000, Erzurum, Türkiye
E mail: isakulaksiz@outlook.com (İ. KULAKSIZ)
İsa KULAKSIZ https://orcid.org/0009-0000-1138-7130
Ahmet COŞKUNÇAY https://orcid.org/0000-0002-7411-310X

Received: August 07, 2024
Accepted: December 19, 2024
Published: January 15, 2025

Cite as: Kulaksız İ, Coşkunçay A. 2025. Fake news detection on mainstream media using natural language processing. BSJ Eng Sci, 8(1): 214-224.

1. Introduction

In the initial phase of the World Wide Web or Web 1.0 (1995 -onwards), its content primarily consisted of monologues meant to convey ideas mainly generated by mainstream media agencies (i.e. Haberturk, TRT). However, Web 2.0 (2000 -onwards) facilitated the sharing of news by ordinary users by empowering them to create large-scale interactive content on social media platforms (Choudhury, 2014; Lazer et al., 2018) such as Facebook and X. The consequential impact of news production is significant; it spreads rapidly throughout society and generates both positive and negative information regarding journalism, democracy, and political agendas. In addition, certain entities with opposing viewpoints have used similar platforms to make money (Kucharski, 2016; Garcia et al., 2020) or to create biased opinions on social media platforms. The events surrounding the 2016 United Kingdom's withdrawal from the European Union (i.e. Brexit) and the results of the US presidential election notably heightened the prevalence of fake news in society (Kucharski, 2016). While numerous studies in Indo-European languages focus on detecting fake news, the analysis of Turkish presents a significant challenge due to its distinctive morphological structure. This is primarily because Turkish's classification within the Ural-Altaic language family allows for the addition of multiple suffixes to a word root, resulting in the formation of intricate "beads-on-a-string" structures (Oflazer, 2014; Yamanan, 2016).

- Çekoslovakyalılaştıramadıklarımızdan mısınız?
- "Are you one of those who we could not make czechoslovakian?"

This example highlights the complexity, but native speakers can readily understand many words of similar size (Çöltekin, 2014). Distinguishing the fakeness of a news story requires an expert's meticulous attention. Fake news spreads misleading claims in its content, so the best way to detect it is to inspect news articles for hints. In (Shu et al., 2017), the topic of fake and real news articles is discussed. TRT dataset includes real news has a stronger relationship with the agenda. The articles collected from TRT news sources were cross-validated. This necessitates using Natural Language Processing (NLP) techniques to automate it. This technique eliminates stopwords (prepositions, conjunctions), stemming, and word representation. In order to understand how news can influence society, it is essential to examine the relationship between journalistic language and media tools. Although television and newspaper news presentations use formal and professional language, ordinary users share news via social media using casual language. These studies contributed to the depth and comprehensiveness of the study. Figure 1 shows a screenshot of the TRT and Teyit websites.

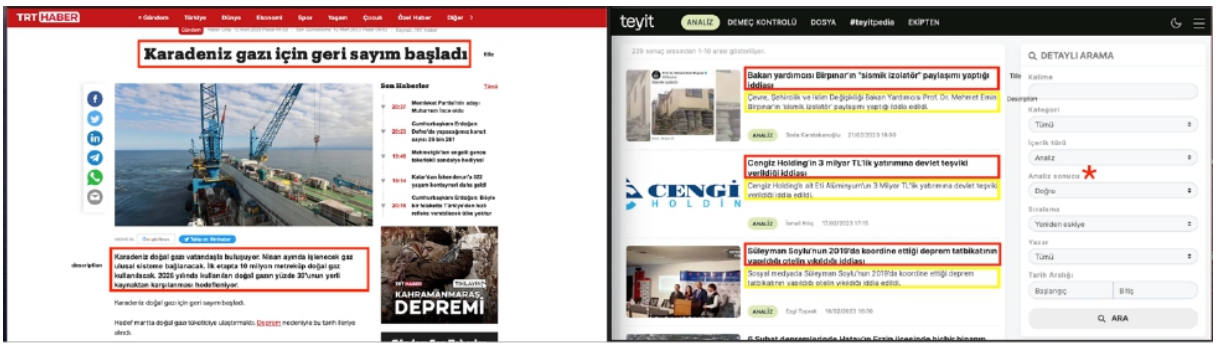

Figure 1. An example of news shared by TRT and Teyit.org platform.

Several communities are involved in this effort, including Teyit.org, which utilizes an expert-oriented fact-checking method. This platform verifies whether the news item is real or fake and that a reputable news source issues it. Notably, Teyit.org is part of IFCN (Ünver, 2023). In this study, the open source library Zemberek is used for stemming and lemmatization in Turkish NLP (Akın and Akın, 2007).

This research investigates the classification performance of the classical machine learning (i.e., SVM, Logistic Regression, Random Forest, k-NN, Decision Tree, and Naive Bayes) and Long Short-Term Memory (LSTM) algorithms using real world dataset including TRT and Teyit.org. It also uses n-gram, bag of words, and word representation methods (TF-IDF and CountVectorizer) for feature extraction. Furthermore, pre-processing steps are performed using the Zemberek library, and structural similarity is calculated to illustrate this difference. For classification tasks, classical machine learning algorithms were preferred over transformer-based models (e.g., BerTurk, Roberta) due to their lower resource requirements.

In section 3. The collection and preprocessing stages of datasets were explained. The rest of the paper contains experimental results, a discussion of this research and future natural language processing studies in fake news in section 4, and the conclusion in section 5.

2. Related Works

In the field of NLP, research focuses on facilitating communication between people and machines by providing translation, summarization, and the creation of chatbots and other tools to enhance interaction. The studies in this topic area include those that analyze and compare the use of machine learning, LSTM, and transformer algorithms to detect fake news in mainstream and social media. Reis et al, (2019) have achieved the best classification with XGB 86% according to the BuzzFeed set of tagged posts by journalists during the 2016 US presidential campaign. In contrast, Kaliyar et al. (2021a, 2021b) proposed an EchoFakeD model based on ANN, which reached 92.30% accuracy and the CNN and Bert models reached 98.90% accuracy. In addition to studies using XGB and machine learning algorithms (Khanam et al., 2021), the BI-LSTM deep learning algorithm was also used (Aslam et al., 2021) in the public LIAR dataset collected from news sites such as Politifact and FactCheck.org. The BI-LSTM model achieved the highest accuracy of 89%, followed by XGBoost at 75% and Random Forest at 73%. In a study on detecting fake news from English news shared on X, Monti et al. (2019) CNN achieved a remarkable 92.7% accuracy, significantly higher than Random Forest 87% and Geometric Deep Learning 73% by Meyers et al. (2020). Another deep learning method is LSTM 82% by Ajao et al. (2018). These results indicate that deep learning methods provide higher accuracy. Ahmad et al. (2020) presented a study on the effects of machine learning algorithms compared on DS4 created by combining DS2, DS3 and ISOT datasets taken by the Kaggle platform. In terms of results, Random Forest and Perez-LSVM achieved 99% on the ISOT dataset, Decision Tree and XGBoost achieved 94% on DS2, Perez-LSVM achieved 96% on DS3 and Random Forest achieved 91% on DS4. In 2020, Mertoğlu and Genç (2020) proposed an innovative method of detecting fake news in digital libraries by automating the classification of news to be included therein. On the TRFN dataset created with GDELT, Teyit.org and MVN, the model trained on classification algorithms (K-Nearest Neighbor, Decision Trees, Gaussian Naive Bayes, Random Forest, Support Vector Machines, ExtraTrees Classifier, Logistic Regression) found that the ExtraTrees algorithm provided the best performance with an accuracy of 96.81%. Taskin et al. (2022) presented work on the two most shared topics on social media in Türkiye (i.e., Galatasaray's Falcao transfer). They collected data using Teyit.org and X API and compared the performance of supervised and unsupervised machine learning and deep learning (DL) algorithms in detecting fake news. This study focusing on social media contributed to developing our model for mainstream media. Based on the model's classification results, the SVM algorithm achieved the highest accuracy at 90%. Bozuyla and Özçift (2022) presented a model analysis of COVID-19 fake news during the pandemic, which analyzed data collected through X API and several Turkish expert-oriented fact-checking systems (i.e. Teyit, Malumatfurus, and Dogrulugune), using machine and deep learning algorithms and transformers to improve accuracy. In the study, BerTURK Turkish transformer detected fake

COVID-19 news with 98.5% accuracy. Güler and Gündüz (2023) investigated the comparison of CNN and RNN-LSTM deep learning algorithms with Word2vec word representation approaches using datasets collected from social media using English BuzFeed, ISOT, and SOSYalan via X APIs. The results showed that the RNN-LSTM algorithm achieved 93.41% and 85.66% CNN accuracy. Koru and Uluyol (2024) achieved 90% to 94% accuracy using BERT and BERTurk+CNN models on the TR_FaRe_News dataset created from tweets of Turkish fake news and BuzzFeedNews, LIAR, GossipCop, ISOT, Twitter15 and Twitter16 datasets pre-processed. Güler and Gündüz (2023) compared a set of Turkish tweets called SOSYalan using CNN and RNN-LSTM algorithms in comparison with BuzzFeed and ISOT. The results showed that the English-based model achieved an accuracy ranging from 85.16% to 99.9% while the Turkish-based model achieved an accuracy ranging from 87.14% to 92.48%. Kaliyar et al. (2020). proposed a convolutional neural network (CNN) based FDNet model for fake news spread during the controversial US presidential election in 2016. The proposed model achieved a performance of 98.36% on the test dataset Natural Language Processing has proved successful in data mining, summarization and sentiment analysis thanks to classification algorithms and transformer models. NLP has been revolutionized by the development of transformer models such as BERT and GPT which provide advanced capabilities for analyzing and generating human language. These technologies play a critical role in the news verification process by analyzing text and evaluating the accuracy of the information presented.

3. Materials and Methods

The flowchart in Figure 2 illustrates the process of detecting Turkish fake news using machine learning algorithms and LSTM, a modified RNN architecture developed by Hochreiter and Schmidhuber (1997). It involves collecting data, extracting features, training the model with linguistic and similarity analysis, and using the trained model for classification.

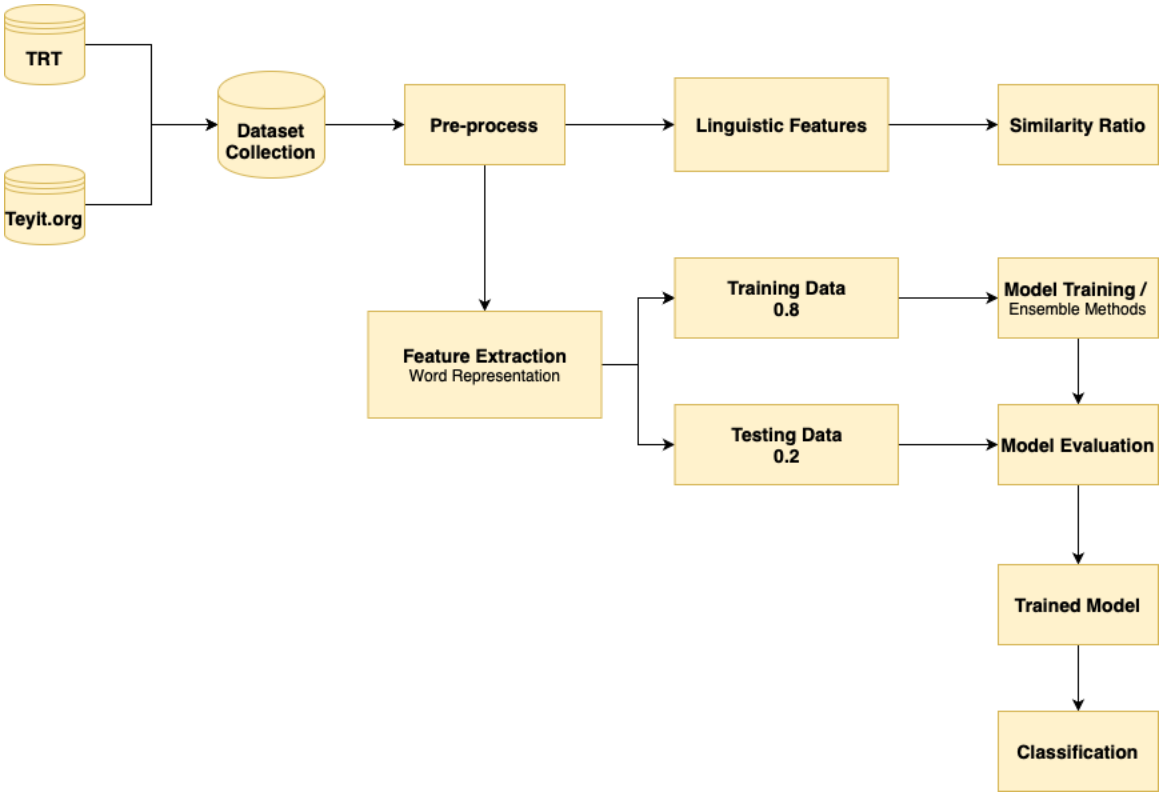

Figure 2. Flowchart for fake news detection.

3.1. Dataset Collection

This study employed supervised learning, utilizing a model trained on the titles and summaries of news articles sourced from TRT Agenda's RSS service and Teyit.org, an expert-oriented fact-checking platform. The news articles from TRT, the official broadcasting organ of the Republic of Türkiye, were collected a few days after the incident. Therefore, if errors or misleading information are detected after publication, necessary corrections will be made to the news. Consequently, it will be possible to include only the real news instead of those removed from the official Turkish broadcasting channel TRT. As a result of these factors, TRT, the official state broadcaster, was assumed to provide real news. Teyit.org is a platform in Türkiye that verifies the accuracy of claims made in the news. As a member of the International Fact-Checking Network (IFCN), Teyit.org maintains its neutralism by relying on transparent sources and sharing its methodology with the public. Fact-checking is performed by experts and volunteers, as

well as machine and deep learning algorithms (Ünver, 2023). The news dataset established and preprocessed in this study contains 5325 records. The amount of fake news received from Teyit.org is significantly higher than that of real news with a ratio of 211 to 2845. Overfitting might happen in cases where some possible outcomes are not represented with enough number samples in the dataset. This is because the overfitted model memorizes the training set without generalizing on the test set, which may negatively affect the classification result. Several methods are available for reducing the risk of overfitting (e.g., early stopping, network reduction, data expansion and regularization) (Ying, 2019). The distribution of resources, rates, and dates within the dataset is illustrated in Figure 3.

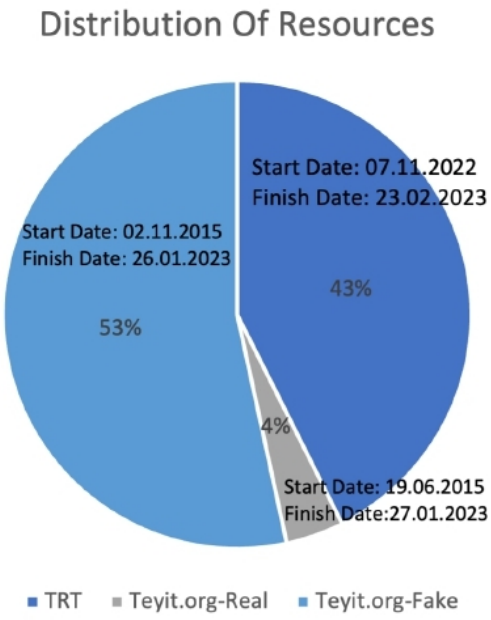

Figure 3. Information about the dataset.

In order to reduce overfitting, the dataset has been expanded with TRT news to ensure better classification results. Additionally, stopwords have been removed from the dataset to prevent the model from memorizing frequently used words during training. Determining whether different data sources have structural similarities will explain why the data collected in the study were combined. Several models for the distance-based measure of similarities between documents are frequently used in natural language processing, including cosine similarity and the Levenshtein distance metrics (Siahaan et al., 2018). The Cosine Similarity uses vector modeling to determine the structural similarity between two text documents. It can take values ranging from 0 to 1 with 0 indicating that the documents are unrelated and 1 indicating identical (Rahutomo et al., 2012; Falah and Suryawan, 2022). The internal similarities between TRT and Teyit.org were calculated by dividing this dataset into two parts and comparing them. TRT's internal similarity was calculated as 0.53 and Teyit.org's internal similarity was calculated as 0.37. This shows that the similarity of news texts within news sources is low. Then, TRT and Teyit.org news texts were compared and their similarities were calculated. The news text similarity of these two news sources is 0.23 as shown in Figure 4.

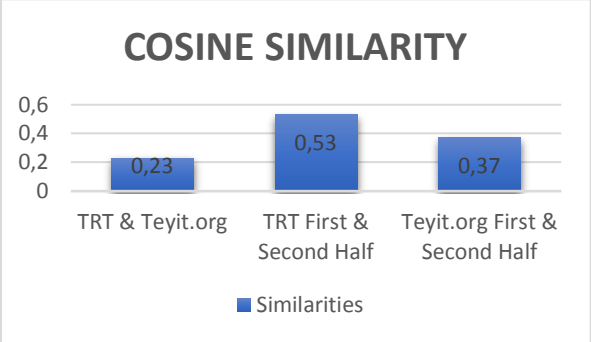

Figure 4. The Cosine similarity ratio.

3.2. Data Preprocessing

Data preprocessing refers to a series of processes that are performed before training machine learning models. In order to achieve these processes, Turkish stopwords were removed, data was transformed, and stemming was applied to ensure consistency and high quality. Noise reduction is one of the most critical steps in data preprocessing. Noise in a dataset refers to inconsistent and inaccurate data. For example, there may be inconsistencies caused by incorrect or missing data. The data must be cleaned of these problems (Han and Kamber, 2011). The steps used are shown in Figure 5.

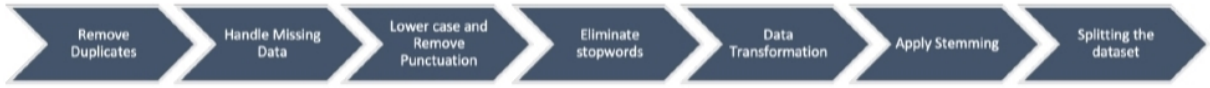

Figure 5. Data preprocessing steps.

One of the most frequent issues of the dataset was regarding the use of the wording "claimed" (i.e., in Turkish, "iddia edildi"). There might be a bias in that many of the news containing this expression are fake news. Since this would cause memorization on the training set, the places where this expression was used were replaced with more neutral and unpretentious expressions. Therefore, the places where this expression was used were replaced with more neutral and unpretentious expressions.

Figure 6. Most frequently used words with WordCloud.

During preprocessing, stopwords are often removed from texts in studies of NLP. By removing words that do not add much valuable information to the language (prepositions, conjunctions, etc.), dimension reduction brings attention to the critical information within the texts. The Turkish stopwords were removed from our dataset. Furthermore, in order not to possibly harm the dignity of individuals and to avoid conflict of interest, proper names have been removed from Wordcloud. In Figure 5, the final preprocessing step is stemming. Stemming is the most common morphological technique in NLP to determine a word's root. Stemming uses a method that allows words with similar meanings to be represented as the same, with the correct cutoff point and hence the size is reduced (Korenius et al., 2004). Many open source NLP libraries work with Indo-European texts. NLP researchers face a challenge due to the excessive use of affixes in Turkish, an agglutinative language. Therefore, linguistic feature based approaches were used to extract the texts' characters, terms and sentences based on the Zemberek library (Akın and Akın, 2007). The dataset is divided into training and testing sets with an 80 to 20 split.

3.3. Feature Extraction

When dealing with very high dimensional datasets, text grouping poses a challenge. The classification results can be adversely affected by unimportant or unconnected words. Therefore, the frequency and importance of words in a document can be measured by several word representation approaches that convert words into numerical vectors (Kaur et al., 2020). In this study, it was transformed into numerical vectors using both TF-IDF and CountVectorizer methods.

TF-IDF (Term Frequency-Inverted Document Frequency)

is a metric used to determine the importance of each word in a text. In this method, the importance of a word in a document increases as its frequency increases. The TF-IDF metric consists of two metrics: term frequency (TF) and inverse document frequency (IDF). The equations 1 and 2 formulas used to compute the tf-idf for a term t within a document set are as follows:

$$tf - idf = tf(t,d) * idf(t) \quad (1)$$

N is the number of documents in the document set and df(t) is the document frequency at t;

$$idf(t) = log\frac{n}{df(t)} + 1 \quad (2)$$

In order to identify fake news, researchers have employed a variety of methods. Bag of Words (BoW) is one of their most essential methods for feature extraction (Ahmed et al., 2017). In one respect, it is similar to Term Frequency (TF) in that word groups (n-grams) can be extracted from the text content based on word frequencies.

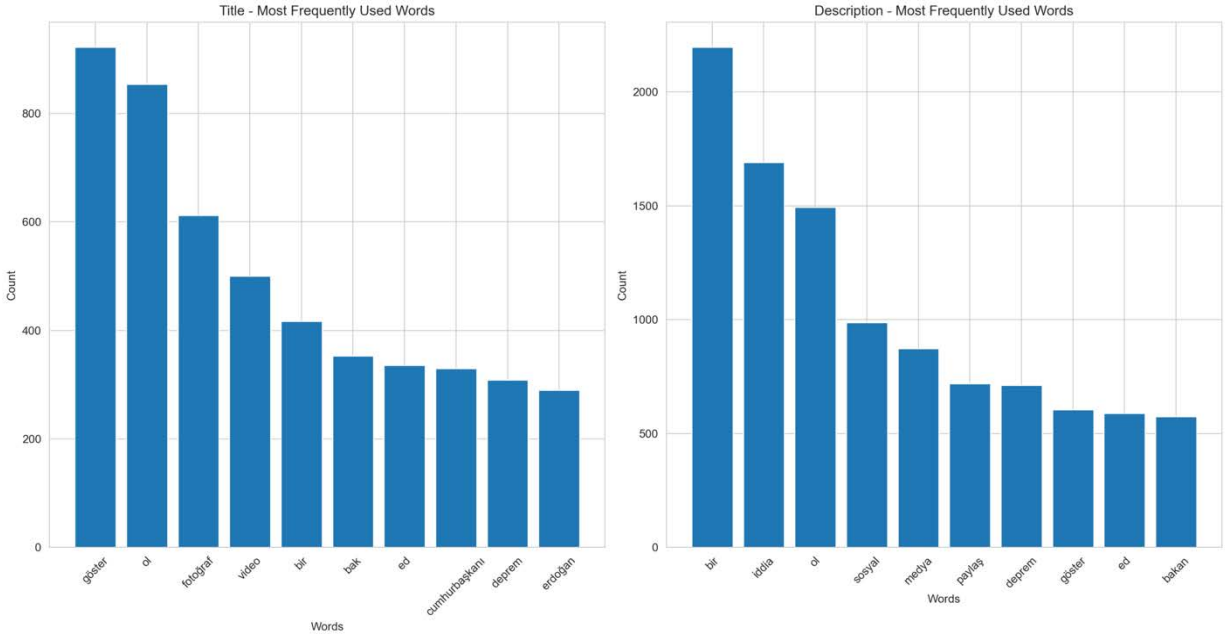

Figure 7. Title and summary: Identifying most frequent words using Bag of Words (BoW) approach.

CountVectorizer is based on word frequency in a text document. It is used for fragmentation (i.e. tokenization) in text processing. CountVectorizer provides many parameters to improve the selection of features. There are three parameters available for building features: unigrams (min d f = 1), bigrams (min d f = 2) and trigrams (min d f = 3) (Korenius et al., 2004). In this study, min d f as 3 was used. To facilitate understanding of the occurrence of each feature in a document, each vector (term) represents the feature name shown in Figure 8.

3.4. Evaluation Metrics

Several evaluation metrics are used to identify fake news, real news, misclassified real news, and undetected fake news. These metrics include True Positive (TP), True Negative (TN), False Positive (FP), False Negative (FN). They provide valuable insights into models' performance and effectiveness in distinguishing between different types of news. Significantly, the Accuracy value is the percentage of accurate predictions to be made based on the algorithm over the total number of predictions. Each evaluation metrics: accuracy is equation 3, precision is equation 4, recall (or sensitivity) is equation 5, and f1 is equation 6 is represented below by a mathematical formula.

$$Accuracy = \frac{TP + TN}{TP + TN + FP + FN} \quad (3)$$

$$Precision = \frac{TP}{TP + FP} \quad (4)$$

$$Recall = \frac{TP}{TP + FN} \quad (5)$$

$$F1 = 2 \times \frac{Precision \text{ x } Recall}{Precision + Recall} \quad (6)$$

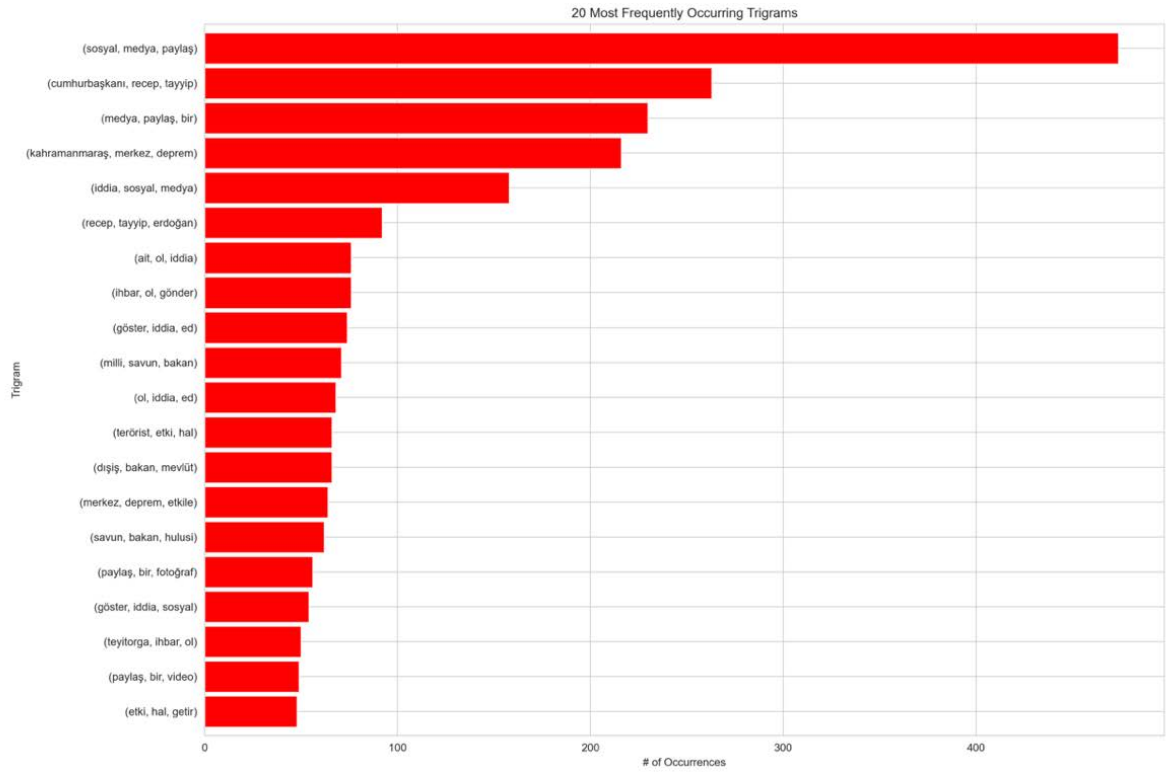

Figure 8. Twenty most frequently used trigram.

4. Results and Discussion

In mainstream media with widespread of fake news the need for artificial intelligence systems to fact-check news has become inevitable. TF-IDF and CountVectorizer word representation methods are evaluated to improve classification accuracy, and hyperparameters are optimized in this study. Additionally, many methods were applied to ensure that the model was free from the effects of extinction gradients and overfitting. This is prevented by randomization, data transformation, removing Turkish stopwords, and stemming. For LSTM, regularization techniques (L2), dropout, and early stopping were applied. In Table 1, illustrates a detailed of the hyperparameters used, which yielded the best-tuned parameters across various algorithms.

In Table 2, illustrates the classifiers with the highest hyperparameter tuning and accuracy using bold characters. Figure 9 and Figure 10 show charts of all evaluation metrics obtained using the tf-idf and countvectorizer methods.

The findings revealed that among the methods evaluated in the research, SVM achieved the highest accuracy rate of SVM (tf-idf 93.12%, countvectorizer 92.86%), followed by LSTM (tf-idf 92.21%, 92.40%) and Logistic Regression (tf-idf 92.72%, countvectorizer 92.75%). Decision Tree and Naive Bayes exhibited lower accuracy, with Decision Tree achieving 87.35% (tf-idf) and 88.40% (CountVectorizer) and Naive Bayes reaching 74.39% (tf-idf) and 75.33% (CountVectorizer). Mainly, LSTM, Logistic Regression, and Random Forest, one of the classification learning algorithms used in the study, were very close competitors to SVM in terms of performance. The findings revealed that TF-IDF had a relatively better effect on classification results than CountVectorizer. Consequently, the best classification algorithm, SVM, has detected 93.12% of fake news. In addition, the model trained with the best-fine-tuned parameters obtained through hyperparameter optimization demonstrated relatively better accuracy. Consequently, SVM and Logistic Regression have been effective for classification problems, producing binary outputs, while LSTM has shown effectiveness through its forget gates.

Table 1. Model hyperparameters and best parameters

Model Name	Default Parameters	Best Parameters
SVM	C: 1.0 Kernel: RBF Gamma: Scale Degree: 3	C: 1 Kernel: RBF
k-NN	Number of Neighbors: 5 Weight: Uniform Algorithm: Auto	Number of Neighbors: 7 Weight: Distance Algorithm: Auto
Logistic Regression	C: 1.0 Penalty: l2 Solver: lbfgs Max Iterations: 100	C: 1 Penalty: l2
Decision Tree	Criterion: Gini Max Depth: None Min Samples Split: 2 Min Samples Leaf: 1	Criterion: Gini Max Depth: 20 Min Samples Split: 10 Min Samples Leaf: 4
Random Forest	Number of Estimators: 100 Max Depth: None Min Samples Split: 2 Min Samples Leaf: 1 Criterion: Gini Bootstrap: True	Number of Estimators: 100 Max Depth: None Min Samples Split: 2 Min Samples Leaf: 1
Naive Bayes	-	-
LSTM	Optimizer: Adam Activation: Relu & Sigmoid Loss: Categorical Crossentropy Epochs: 10/7 (Early Stopping) Dropout: 0.2 Batch Size: 32	

Table 2. Model evaluation metrics with hyperparameter tuning and test accuracy

Model	Hyperparameter Tuning (%)		Test Accuracy (%)	
	TF-IDF	CountVectorizer	TF-IDF	CountVectorizer
SVM	93.12	92.86	92.40	91.65
Logistic Regression	92.72	92.75	91.74	91.46
Random Forest	92.61	92.72	92.12	91.56
k-NN	87.86	84.23	84.62	82.93
Decision Tree	87.74	88.15	85.74	86.30
Naive Bayes	74.39	75.33	74.39	75.33
LSTM	92.21	92.40	92.21	92.40

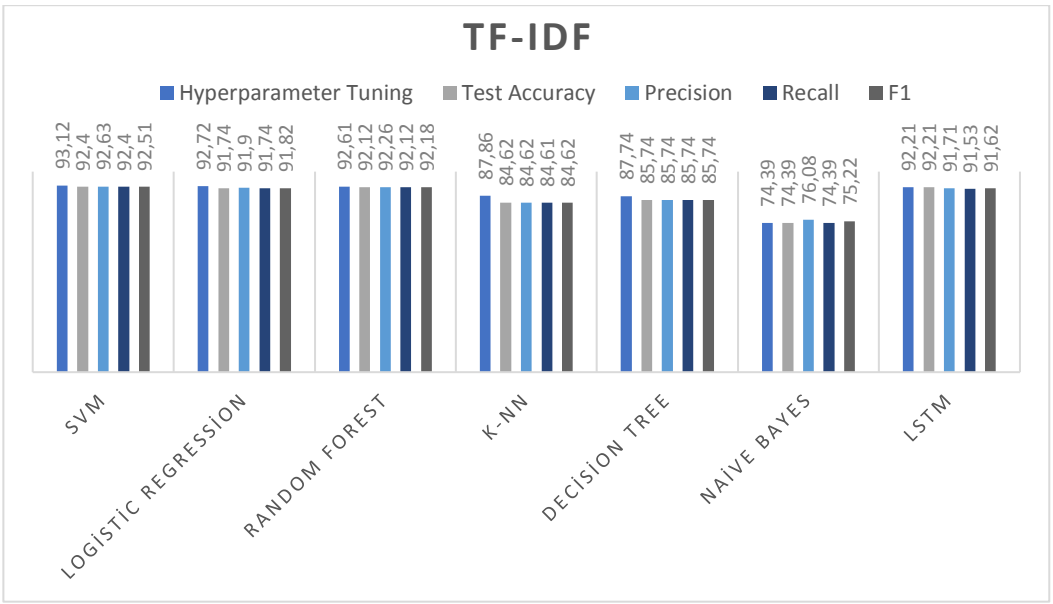

Figure 9. Evaluation metrics obtained by TF-IDF vectorization method.

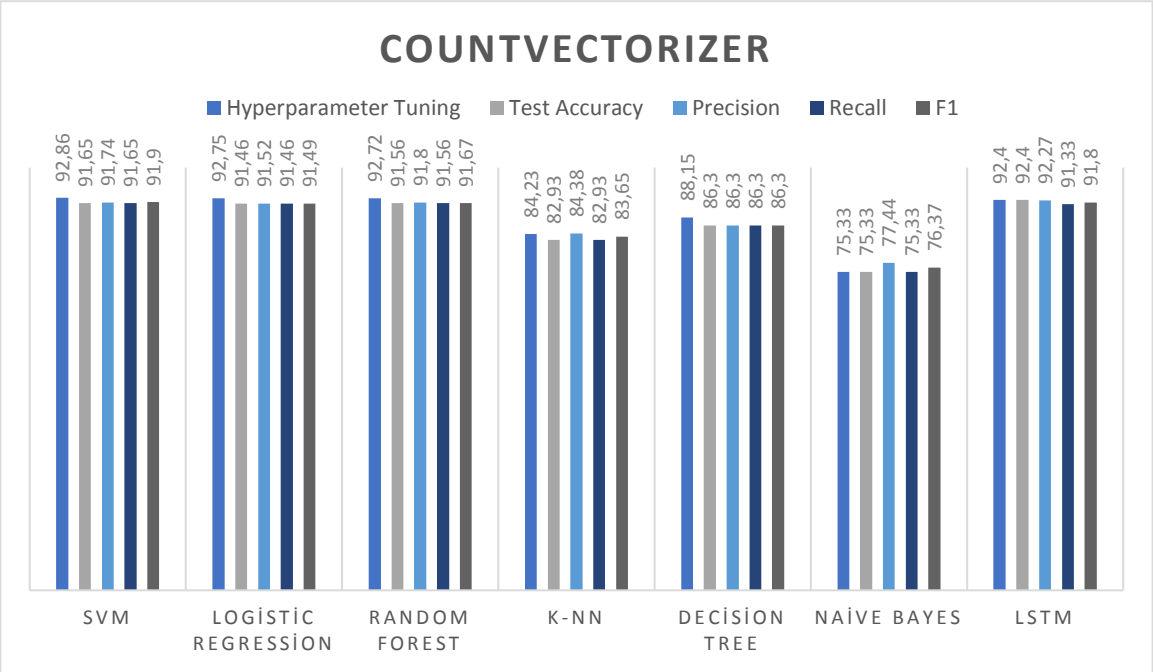

Figure 10. Evaluation metrics obtained by Countvectorizer vectorization method.

This study evaluated the performance of previous research conducted in the Turkish language and the algorithms used. Taskin et al. (2022) achieved 90% accuracy with the SVM algorithm. Bozuyla and Özçift (2022) achieved an accuracy of 98.5% using the BerTURK model. Güler and Gündüz (2023) obtained accuracies ranging from 85.66% to 93.41% with CNN and RNN-LSTM. Koru and Uluyol (2024) demonstrated that The_News dataset showed performance between 90% and 94% with BERT and BERTurk+CNN algorithms. Using the SOSYalan dataset, Koru and Uluyol (2024) achieved 87.14% and 92.48% accuracy with CNN and RNN-LSTM algorithms, respectively. This study has demonstrated that the SVM algorithm achieved an accuracy of 93.12%, which is better than many other models. This model outperformed other approaches in several studies, except for the BerTURK approach by Bozuyla and Özçift (2022). Therefore, SVM algorithms have indicated effectiveness in detecting Turkish fake news.

In addition, future studies are planned to increase the quality and quantity of the datasets used for model training, which will likely result in continuous improvements in the performance of supervised learning classification algorithms. These studies are purposed to improve the accuracy and reliability of fake news detection on mainstream and social media by using their results. Furthermore, this work may be extended to other ensemble methods.

5. Conclusion

Traditional and social media contains substantial news that damages society and the economy psychologically and materialistically. In recent years, it has been seen that the need for expert-based control systems to distinguish the accuracy of news has decreased with the developments in the field of artificial intelligence. In this study, the data collected from TRT and Teyit.org news sources were classified as fake and real news using hyperparameter tuning with machine learning and LSTM algorithms. Furthermore, Zemberek, one of the best libraries on Turkish texts, was used in the data pre-processing stage for stemming and lemmatization. When the results were investigated, it was seen that the highest classification accuracy was achieved with tf-idf 93.12% SVM. In addition to feature extraction using tf-idf and counvectorizer, n-gram and BoW methods are also applied. In future studies, transformer models (GPT or BERT) or boosting algorithms can be trained and compared on the dataset.

Author Contributions

The percentages of the authors contributions are presented below. All authors reviewed and approved the final version of the manuscript.

	İ.K.	A.C.
C	70	30
D	70	30
S	40	60
DCP	70	30
DAI	70	30
L	80	20
W	70	30
CR	70	30
SR	80	20
PM	70	30

C=Concept, D= design, S= supervision, DCP= data collection and/or processing, DAI= data analysis and/or interpretation, L= literature search, W= writing, CR= critical review, SR= submission and revision, PM= project management, FA= funding acquisition.

Conflict of Interest

The authors declared that there is no conflict of interest.

Ethical Consideration

Ethics committee approval was not required for this study because of there was no study on animals or humans.

Acknowledgments

This research is based on a master's thesis.

References

Ahmad I, Yousaf M, Yousaf S, Ahmad M. 2020. Fake news detection using machine learning ensemble methods. Complexity, 2020: 8885861. https://doi.org/10.1155/2020/8885861

Ahmed H, Traore I, Saad S. 2017. Detection of online fake news using n-gram analysis and machine learning techniques. International Conference On Intelligent, Secure, And Dependable Systems In Distributed And Cloud Environments, 28-30 November; Vancouver, Canada, pp: 127-138.

Akın A, Akın M. 2007. Zemberek, an open source NLP framework for Turkic languages. Structure, 10(2007): 1-5.

Ajao O, Bhowmik D, Zargari S. 2018. Fake news identification on twitter with hybrid cnn and rnn models. SMSociety '18: International Conference on Social Media and Society, July 18-20, New York USA, pp: 226-230.

Aslam N, Khan I, Alotaibi F, Aldaej L, Abdulbaikil A. 2021. Fake detect: A deep learning ensemble model for fake news detection, Complexity, 2021(4): 1-8.

Bozuyla M, Özçift A. 2022. Developing a fake news identification model with advanced deep language transformers for Turkish COVID-19 misinformation data. Turk J Electr Eng Comput Sci, 30(3): 908–926.

Choudhury N. 2014. World wide web and its journey from web 1.0 to web 4.0. Int J Comput Sci Inf Technol, 5(6): 8096–8100.

Çöltekin Ç. 2014. A set of open source tools for Turkish natural language processing. In Proceedings of the Ninth International Conference on Language Resources and Evaluation (LREC'14), 26-31 May, Reykjavik Iceland, pp: 1079–1086.

Falah Z, Suryawan F. 2022. Recommendation system to propose final project supervisors using cosine similarity matrix. Khazanah Informatika: Jurnal Ilmu Komputer dan Informatika, 8(2).

García S, Garcia G, Prieto M, Guerrero A, Jimenez, C. 2020. The impact of term fake news on the scientific community. Scientific performance and mapping in web of science. Soc Sci, 9(5): 73.

Güler G, Gündüz S. 2023. Deep learning based fake news detection on social media. Int J Inf Secur, 12(2): 1-21.

Han J, Kamber M. 2011. Data mining: concepts and techniques. Morgan Kaufmann, Elsevier, Waltham, MA 02451, USA, pp: 47-67.

Hochreiter S, Schmidhuber J. 1997. Long short-term memory. Neural Comput, 9(8), 1735–1780.

Kaliyar R, Goswami A, Narang P. 2021a. FakeBERT: Fake news detection in social media with a BERT-based deep learning approach. Multimed Tools Appl, 80(8): 11765-11788.

Kaliyar R, Goswami A, Narang P. 2021b. EchoFakeD: improving fake news detection in social media with an efficient deep neural network. Neural Comput Appl, 33(14): 8597-8613.

Kaliyar R, Goswami A, Narang P. 2020. FNDNet – A deep convolutional neural network for fake news detection, Cogn Syst Res, 61: 32-44.

Kaur S, Kumar P, Kumaraguru P. 2020. Automating fake news detection system using multi-level voting model. Soft Comput, 24(12): 9049-9069.

Khanam Z, Alwasel B, Sirafi H, Rashid M. 2021. Fake news detection using machine learning approaches. International Conference on Applied Scientific Computational Intelligence using Data Science (ASCI 2020), 22-23 December, Jaipur India.

Korenius T, Laurikkala J, Jarvalin K, Juhola M. 2004. Stemming and lemmatization in the clustering of Finnish text documents. Proceedings of the thirteenth ACM international conference on Information and Knowledge Management, 13 November, New York USA, pp: 625–633.

Koru G, Uluyol Ç. 2024. Detection of Turkish fake news from tweets with BERT models. IEEE, 12: 14918-14931.

Kucharski A. 2016. Study epidemiology of fake news. Nature, 540(7634): 525-525.

Lazer D, Baum M, Benkler Y, Berinsky A, Greenhill K, Menczer F, Metzger M, Nyhan B, Pennycook G, Rothschild D, Schudson M, Sloman S, Sunstein C. Thorson E, Watts D, Zittrain J. 2018. The science of fake news. Sci, 359(6380): 1094-1096.

Mertoğlu U, Genç B. 2020. Automated fake news detection in the age of digital libraries, Inf Technol Libr, 39(4).

Meyers M, Weiss G, Spanakis G. 2020. Fake news detection on twitter using propagation structures. Disinformation in Open Online Media, 26-27 October, Leiden Netherlands, pp: 138-158.

Monti F, Frasca F, Eynard D, Mannion D, Bronstein M. 2019. Fake news detection on social media using geometric deep learning. URL: https://arxiv.org/abs/1902.06673 (access date: December 17, 2023).

Oflazer K. 2014. Turkish and its challenges for language processing. Lang Resour Eval, 48(4): 639-653.

Rahutomo F, Kitasuka T, Aritsugi M. 2012. Semantic cosine similarity. The 7th International Student Conference on Advanced Science and Technology ICAST 2012, October 29-30, Seoul, South Korea, pp: 54.

Reis J, Correia A, Murai F, Veloso A, Benevenuto F. 2019. Supervised learning for fake news detection. IEEE Intell Syst, 34(2): 76-81.

Shu K, Amy S, Wang S, Tang J, Liu H. 2017. Fake news detection on social media: a data mining perspective. ACM SIGKDD Explor Newsl, 19(1): 22-36.

Siahaan A, Aryza S, Hariyanto E, R, Lubis A. 2018. Combination of Levenshtein distance and Rabin-Karp to improve the accuracy of document equivalence level. Int J Eng Technol, 7(27): 17-21.

Taskin S, Kucuksille E, Topal K. 2022. Detection of Turkish fake news in twitter with machine learning algorithms. Arab J Sci Eng, 47(2): 2359-2379.

Ünver A. 2023. Emerging technologies and automated fact-checking: tools, techniques and algorithms. URL: https://ssrn.com/abstract=4555022 (accessed date: August 29, 2023).

Yamanan E. 2016. Türkçenin güncel söz varliği. Mill Eğ Derg, 45(210): 85-91.

Ying X. 2019. An overview of overfitting and its solutions. J Phy Conf Ser, 1168: 022022.

Black Sea Journal of Engineering and Science
doi: 10.34248/bsengineering.1571843

Open Access Journal
e-ISSN: 2619 – 8991

Research Article
Volume 8 - Issue 1: 225-233 / January 2025

PRACTICAL AND ESTIMATED EFFICIENCIES OF SOLAR PHOTOVOLTAIC POWER PLANTS

Turhan KOYUNCU[1], Fuat LÜLE[1]*

[1]*Adıyaman University, Vocational School of Technical Sciences, 02040, Adıyaman, Türkiye*

Abstract: Practical and estimated efficiencies of three (A, B and C) solar photovoltaic power plants (SPVPs) has been determined in this paper. Each of this SPVPs mainly has steel frame constructions for panel placing, polycrystalline silicon type solar PV (photovoltaic) panels, combinations of MPPT (maximum power point tracker) + inverter boxes, collecting busbar, transformer boxes, distributor busbar, kWh meter (output counter), underground cable line and mechanical components for external grid connection, control building, lighting and camera monitoring system. Selected SPVPs were installed in location of Adıyaman City, Türkiye (Latitude: 37.45°, Longitude: 38.17° and Altitude: 672 m), in 2017. Installed power capacity per SPVP is 1.025 MW. The results of the work showed us that the first year average electric energy production is 1691642 kWh and average practical and estimated efficiencies are 15.00% and 14.783%, respectively.

Keywords: Solar PV plant, Practical efficiency, Estimated efficiency

***Corresponding author:** Adıyaman University, Vocational School of Technical Sciences, 02040, Adıyaman, Türkiye
E mail: flule@adiyaman.edu.tr (F. LÜLE)
Turhan KOYUNCU https://orcid.org/0000-0003-2279-9899
Fuat LÜLE https://orcid.org/0000-0002-9332-0761

Received: October 22, 2024
Accepted: December 25, 2024
Published: January 15, 2025

Cite as: Koyuncu T, Lüle F. 2025. Practical and estimated efficiencies of solar photovoltaic power plants. BSJ Eng Sci, 8(1): 225-233.

1. Introduction

Increasing demand and scarcity in conventional sources have triggered the scientist to pave way for the development of research in the field of renewable energy sources especially solar energy (Goura, 2015; Kumar and Sudhakar, 2015).

Renewable energy sources are considered as alternative energy sources due to environmental pollution, global warming and depletion of ozone layer caused by greenhouse effect. Earth receives about 3.8×10^{24} J of solar energy on an average which is 6000 times greater than the world consumption. Solar energy is most readily available source of energy. Solar energy is Non-polluting and maintenance free. Solar energy is becoming more and more attractive especially with the constant fluctuation in supply of grid electricity. Solar power plant is commonly based on the conversion of sunlight into electricity directly using photovoltaic (PV) panel (Aliman et al., 2007; Shukla et al., 2016).

In this work, practical and estimated efficiencies of three 1.025 MW solar photovoltaic power plants (SPVPs) that located in Adıyaman City, Türkiye, has been determined. The results of the work showed us that the first year average electric energy production is 1691642 kWh and average practical and estimated efficiencies are 15.00% and 14.783 %, respectively.

2. Materials and Methods

Three (A, B and C) 1.025 MW solar photovoltaic power plants (SPVPs) has been selected for this work. These SPVPs were installed in location of Adiyaman City, Türkiye (Latitude: 37.45°, Longitude: 38.17° and Altitude: 672 m). Installed power capacity per SPVP is 1.025 MW. Each selected solar photovoltaic power plant mainly has steel frame constructions for panel placing, polycrystalline silicon type solar PV (photovoltaic) panels, combinations of MPPT (maximum power point tracker) + inverter boxes, collecting busbar, transformer boxes, distributor busbar, kWh meter (output counter), underground cable line and mechanical components for external grid connection, control building, lighting and camera monitoring system (Figure 1). In addition, the Current (I) – Voltage (V) curve of the polycrystalline silicon photovoltaic cell (Figure 2), the technical drawings of the polycrystalline silicon photovoltaic module (Figure 3) and the installation angle and direction of the PV panels (Figure 4) are given in Figure 2-4.

Technical specifications of polycrystalline silicon PV module are given in Table 1 and some other technical features regarding the three 1.025 MW solar photovoltaic power plants are also seen in Table 2. As seen from these tables that each PV module has 60 cells, 16.32 % peak efficiency (under STC: Standard Test Conditions: irradiance @ 1000 W/m^2 with an air mass 1.5, module temperature @ 25 °C and @ 0 m/s wind speed), 1.6236 m^2 area, 18.5 kg mass, 45±2 °C nominal operating cell temperature and 97.5%, 90.0%, 80.0% of overall efficiency for first year, 10 years and 25 years, respectively.

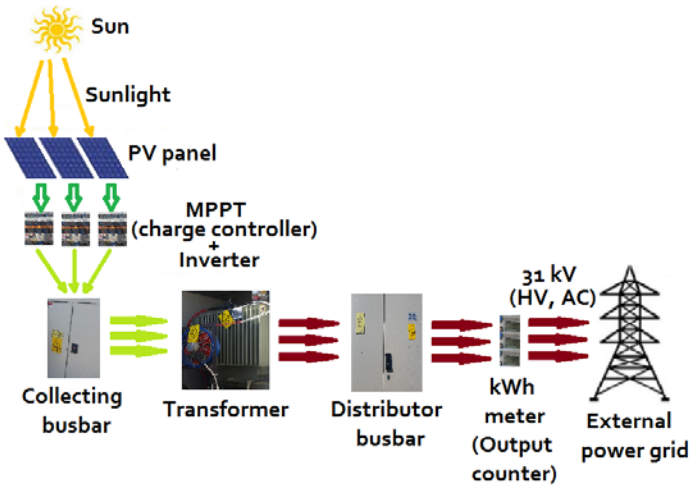

Figure 1. Schematic presentation of working principle of three identical SPVPs.

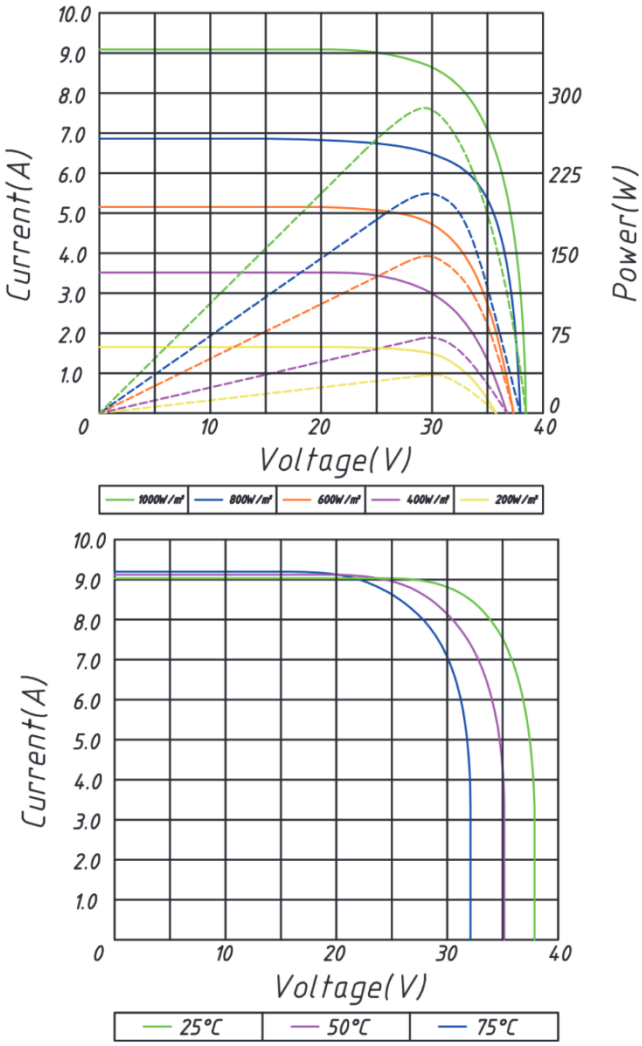

Figure 2. Current (I) – Voltage (V) curve of the polycrystalline silicon photovoltaic cell.

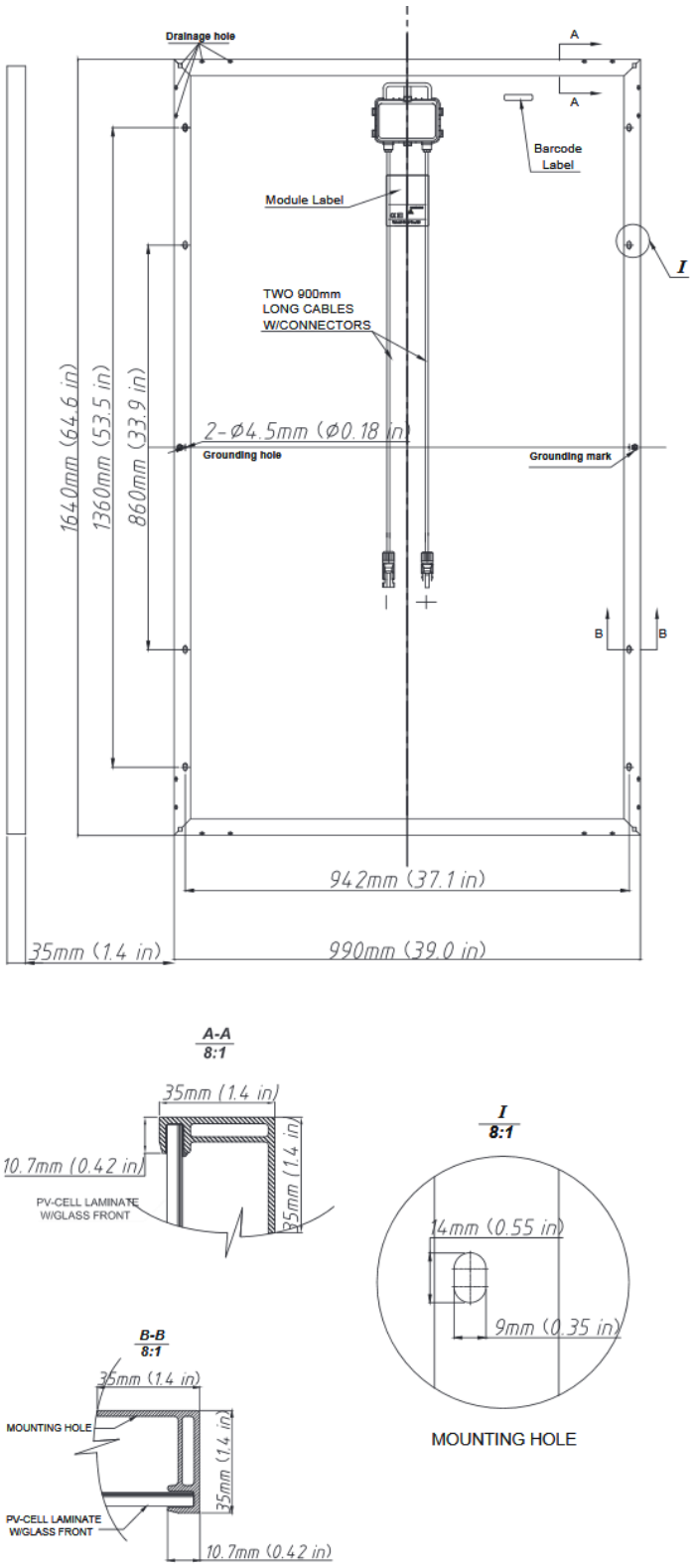

Figure 3. Technical drawings of the polycrystalline silicon photovoltaic module.

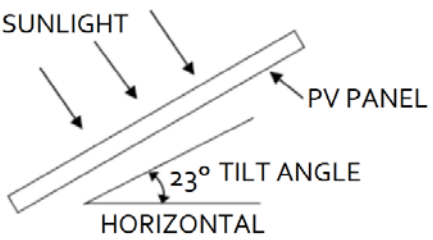

Figure 4. All PV panels were installed at the same orientation and angle.

Besides, it should be noted that the efficiency of solar PV panels are affected by environmental and climatic conditions, temperature, dust and using time (Darwish et al., 2015; Maghami et al., 2016; Costa et al., 2016; Ketjoy and Konyu, 2014; Menoufi et al., 2017; Kumar et al., 2013). In addition to this, other components of the SPVPs such as MPPT, inverter, and transformer has also efficiencies that commonly changing between 95 % ... 99 % (Koyuncu, 2017). The maximum possible efficiency of solar panels can also be obtained in first year.

Table 1. Technical specifications of polycrystalline silicon PV module

Type	Polycrystalline silicon
Number of cells	60
Peak efficiency (%)	16.32
Length (mm)	1640
Width (mm)	990
Depth (mm)	35
Module mass (kg)	18.5
STC power rating (Pmax) (W)	265
STC power per unit of area (W/m^2)	163.2
Maximum system voltage (V, DC)	1000
Operating voltage (Vmpp) (V)	30.8
Operating current (Impp) (A)	8.62
Open – circuit voltage (Voc) (V)	37.9
Short – circuit current (Isc) (A)	9.25
Maximum series fuse (A)	15

Table 1. Technical specifications of polycrystalline silicon PV module (continuing)

Type	Polycrystalline silicon
Power tolerance	+ 3%
Operating temperature (°C)	-40 ... +85
Nominal operating cell temperature (NOCT) (°C)	45 ± 2
Temperature coefficienct	Pmax : - 0.40 % / °C Voc : - 0.31 % / °C
Front glass	3.2 mm high transmission tempered glass
Frame	Anodized aluminium alloy
Installation method	Rack - mounted
Static loading (Pa)	5400
80% power output warranty period (Year)	25
90% power output warranty period (Year)	10
Workmanship warranty period (Year)	10
Company performance warranty	During the first year, the company guarantees the nominal power output of the product will be no less than 97.5% of the labeled power output. From year 2 to year 24, the nominal power decline will be no more than 0.7% in each year; by the end of year 25, the nominal power output will be no less than 80.7% of the labeled power output.
STC (Standard Test Conditions)	Irradiance @ 1000 W/m^2 with an air mass 1.5 (AM 1.5 g)spectrum, modüle temperature @ 25 °C and @ 0 m/s wind speed

Table 2. Some technical features regarding selected solar photovoltaic power plants

Names of SPVP	A, B, C
Location	Adiyaman City, Türkiye (Latitude : 37,45°, Longitude : 38,17° and Altitude : 672 m)
Installed power capacity per SPVP	1025 MW
Power of each module	265 W
Number of module per SPVP	3868
Total area of panel per SPVP	6280 m^2
Installation cost per SPVP	$ 1000000
Date of commencement of operation	November 27, 2017
PV module type	Polycrystalline silicon
Maximum labeled efficiency of module	$\eta_{MODULE} = 16.32\ \% = 0.1632$
Labeled power output warranty during first year	$\eta_{MODULE-FIRST\ YEAR} = 0.975 \times 0.1632 = 0.15912$
Labeled power output warranty during 10 years	$\eta_{MODULE-10\ YEARS} = 0.90 \times 0.1632 = 0.14688$
Labeled power output warranty during 25 years	$\eta_{MODULE-25\ YEARS} = 0.80 \times 0.1632 = 0.13056$
MPPT and Inverter numbers per SPVP	17
Estimated lifetime of MPPT, inverter and transformer	10 Years
Estimated total efficiency of MPPT, inverter and transformer	$\eta_{MPPT} = 98\ \% = 0.98$ $\eta_{INVERTER} = 98\ \% = 0.98$ $\eta_{TRANSFORMER} = 97\ \% = 0.97$ $\eta_{TOTAL-DEVICE} = 0.98 \times 0.98 \times 0.97 = 0.9316$

Table 2. Some technical features regarding selected solar photovoltaic power plants (continue)

Names of SPVP	A, B, C
Estimated average efficiency due to losses of power cut	Power cut losses = 2 h/Month = 24 h/Year = 1 Day/Year = 1 Day/365 Day = 0.00274 = 0.274 % $\eta_{\text{POWER CUT}} = 1.00 - 0.00274 = 0.99726$
Estimated average efficiency due to losses of dust (Assume that panels are periodically cleaned)	First year : very less and negligible From year 2 to 25 = 0.5 % = 0.005 $\eta_{\text{DUST}} = 99.50$
Estimated system total efficiency	$\eta_{\text{ESTIMATED-SYSTEM-FIRST YEAR}} = \eta_{\text{MODULE-FIRST YEAR}} \text{ x } \eta_{\text{TOTAL-DEVICE}} \text{ x } \eta_{\text{POWER CUT}}$ $\eta_{\text{ESTIMATED-SYSTEM-FIRST YEAR}} = 0.15912 \text{ x } 0.9316 \text{ x } 0.99726$ $= 0.14783 = 14.783\ \%$ $\eta_{\text{ESTIMATED-SYSTEM-10 YEARS}} = \eta_{\text{MODULE-10 YEARS}} \text{ x } \eta_{\text{TOTAL-DEVICE}} \text{ x } \eta_{\text{POWER CUT}} \text{ x } \eta_{\text{DUST}}$ $\eta_{\text{ESTIMATED-SYSTEM-10 YEARS}} = 0.14688 \text{ x } 0.9316 \text{ x } 0.99726 \text{ x } 0.9950$ $= 0.13577 = 13.577\ \%$ $\eta_{\text{ESTIMATED-SYSTEM-25 YEARS}} = \eta_{\text{MODULE-25 YEARS}} \text{ x } \eta_{\text{TOTAL-DEVICE}} \text{ x } \eta_{\text{POWER CUT}} \text{ x } \eta_{\text{DUST}}$ $\eta_{\text{ESTIMATED-SYSTEM-25 YEARS}} = 0.13056 \text{ x } 0.9316 \text{ x } 0.99726 \text{ x } 99.50$ $= 0.12069 = 12.069\ \%$

Practical and estimated efficiencies of SPVPs can simply be calculated by using Equations 1 - 5. Practical system total efficiency is equal to annual (first year) generated electric energy divided by annual incident solar energy (Equation 1, 2). Estimated system total efficiency during 10 and 25 years (life time) can also be calculated by using MPPT, inverter, transformer efficiencies and efficiencies due to losses of power cut and dust (Equations 3, 4, 5). The results showed that average practical and estimated efficiencies are 15.00% and 14.783%, respectively, for first year. Both practical and estimated efficiencies are about same and there is negligible differences between them. These data clearly shows that estimated values of efficiencies for 10 and 25 years are quite reliable.

Practical system total efficiency:

$$\eta_{PRACTICAL-SYSTEM}\ (\%) = \frac{E_{GEN}\ (kWh/Year)}{E_{SOL}\ (kWh/Year)} \quad (1)$$

$$E_{SOL}\ (kWh) = I_R\ (kWh/m^2\ x\ Day)\ x\ A_{PV}\ (m^2)\ x\ 365\ (Day/Year) \quad (2)$$

Estimated system total efficiency:

$$\eta_{ESTIMATED-SYSTEM-FIRST\ YEAR}\ (\%) = \eta_{MODULE-FIRST\ YEAR}\ x\ \eta_{TOTAL-DEVICE}\ x\ \eta_{POWER\ CUT} \quad (3)$$

$$\eta_{ESTIMATED-SYSTEM-FIRST\ YEAR} = 0.15912\ x\ 0.9316\ x\ 0.99726 = 0.14783 = 14.783\ \%$$

$$\eta_{ESTIMATED-SYSTEM-10\ YEARS}\ (\%) = \eta_{MODULE-10\ YEARS}\ x\ \eta_{TOTAL-DEVICE}\ x\ \eta_{POWER\ CUT}\ x\ \eta_{DUST} \quad (4)$$

$$\eta_{ESTIMATED-SYSTEM-10\ YEARS} = 0.14688\ x\ 0.9316\ x\ 0.99726\ x\ 0.9950 = 0.13577 = 13.577\ \%$$

$$\eta_{ESTIMATED-SYSTEM-25\ YEARS}\ (\%) = \eta_{MODULE-25\ YEARS}\ x\ \eta_{TOTAL-DEVICE}\ x\ \eta_{POWER\ CUT}\ x\ \eta_{DUST} \quad (5)$$

$$\eta_{ESTIMATED-SYSTEM-25\ YEARS} = 0.13056\ x\ 0.9316\ x\ 0.99726\ x\ 99.50 = 0.12069 = 12.069\ \%$$

where :

$\eta_{PRACTICAL-SYSTEM}$: Practical system total efficiency, %
E_{GEN} : Annual (first year) generated electric energy, kWh
E_{SOL} : Annual incident solar energy, kWh
I_R : Incident solar radiation, kWh/m^2.Day
A_{PV} : Solar PV panel surface area, m^2
$\eta_{ESTIMATED-SYSTEM-FIRST\ YEAR}$: Estimated system total efficiency during first year, %
$\eta_{ESTIMATED-SYSTEM-10\ YEARS}$: Estimated system total efficiency during 10 years, %
$\eta_{ESTIMATED-SYSTEM-25\ YEARS}$: Estimated system total efficiency during 25 years, %
$\eta_{MODULE-1FIRST\ YEAR}$: Labeled power output warranty of the module during first year, 97.5 %
$\eta_{MODULE-10\ YEARS}$: Labeled power output warranty of the module during 10 years, 90 %
$\eta_{MODULE-25\ YEARS}$: Labeled power output warranty of the

module during 25 years, 80%

$\eta_{TOTAL-DEVICE}$: Estimated total efficiency of MPPT, inverter and transformer, 93.16%

$\eta_{POWER\,CUT}$: Estimated average efficiency due to losses of power cut, 99.726%

η_{DUST} : Estimated average efficiency due to losses of dust, 99.50%.

3. Results and Discussion

Average solar radiation or solar energy intensity of Adıyaman City, Türkiye for first year and for many years are given in Figure 5 and 6 (Anonymous, 2019). Average values regarding these years are 4.919 kWh/m² Day and 4.941 kWh/m² Day. Both of these data are about same and negligible differences between them. Measured electric energy from kWh-meters for first year and for three SPVP are given in Figure 7. Average measured electricity generation of three SPVPs for first year is 1696665 kWh. Changing of efficiency of polycrystalline silicon module and changing of system sverage efficiency of SPVPs during lifetime are seen in Figure 8 and 9. Average efficiency of polycrystalline silicon module is starting with efficiency of 15.912 % and finishing with 13.443%. Average SPVP system total efficiency is starting with efficiency of 14.783 % and finishing with 12.427 %. Practical system total efficiencies for three 1.025 MW SPVP are given in Figure 10. As seen from this figure that average practical system efficiency and estimated efficiency are 14.783 % and 15.047 % , respectively. Both of these data are about same and negligible differences between them. Labeled efficiency and estimated system total efficiencies for first year, 10 years and 25 years (lifetime) are seen in Figure 11 for comparison. As seen from this figure that data regarding label, first year, 10 years and 25 years (lifetime) are 16.320 %, 14.783 %, 13.577 % and 12.069 %, respectively.

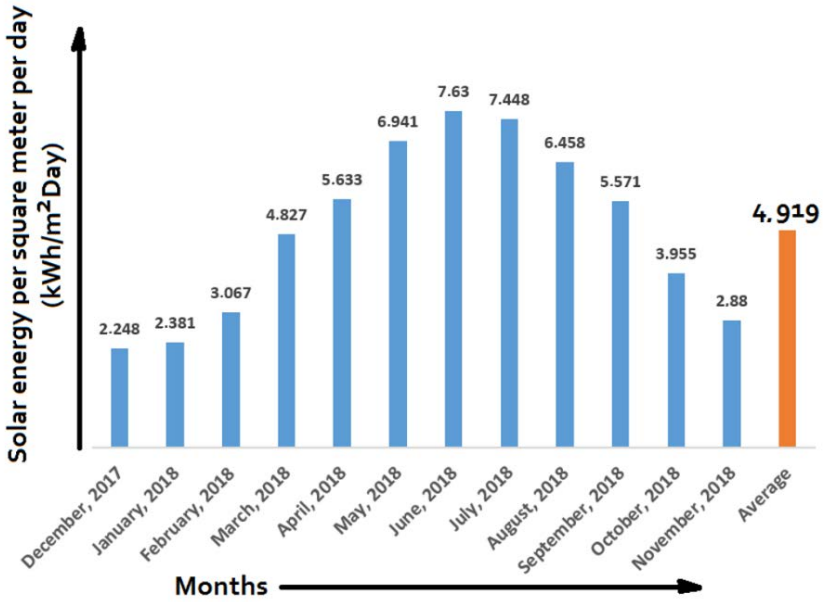

Figure 5. Solar radiation or solar energy intensity of Adiyaman City, Türkiye for first year of SPPs (Anonymous, 2019).

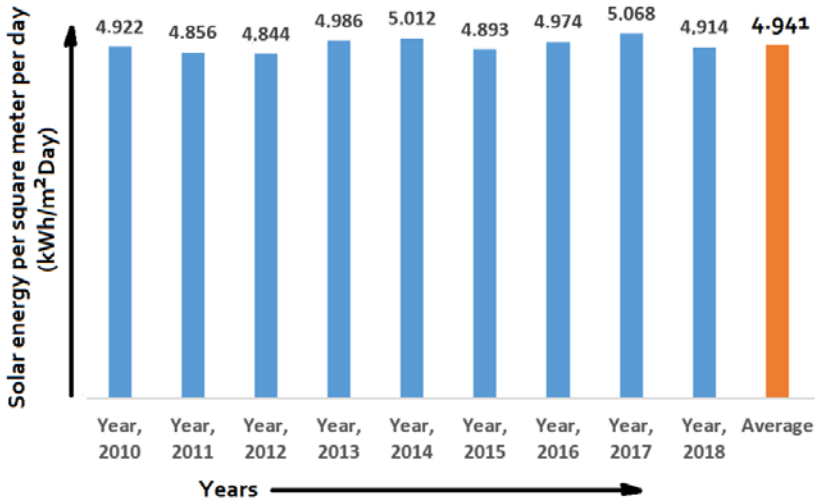

Figure 6. Solar radiation or solar energy intensity of Adiyaman City, Türkiye (Anonymous, 2019).

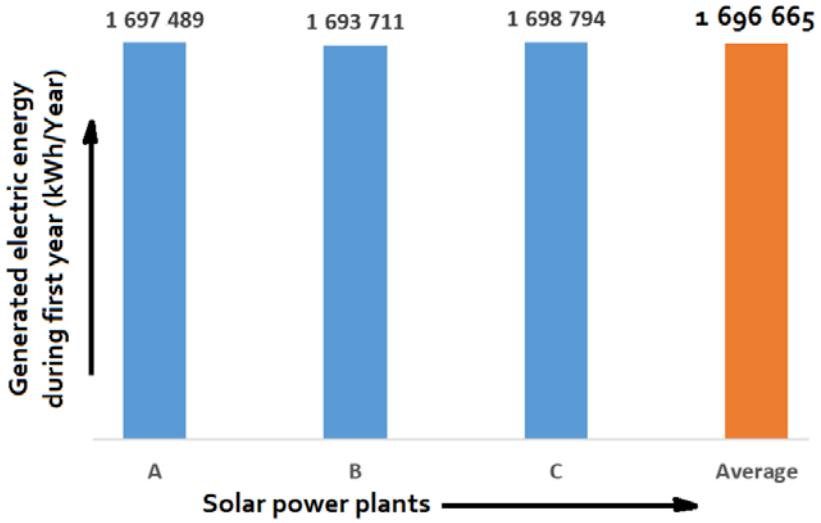

Figure 7. Measured electricity generation of three SPVPs for first year.

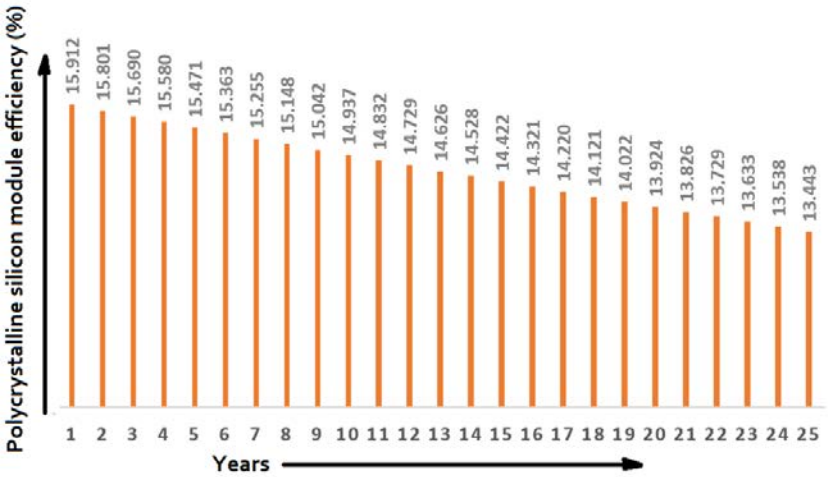

Figure 8. Changing of efficiency of polycrystalline silicon module during lifetime.

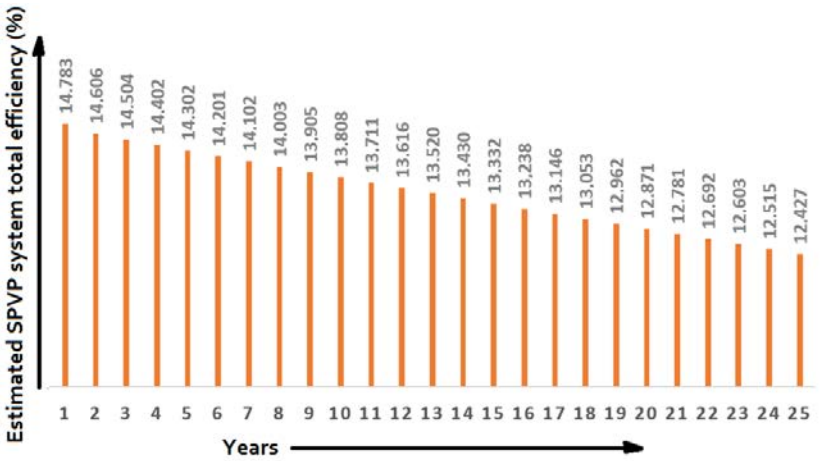

Figure 9. Changing of system total efficiency of SPVPs during lifetime.

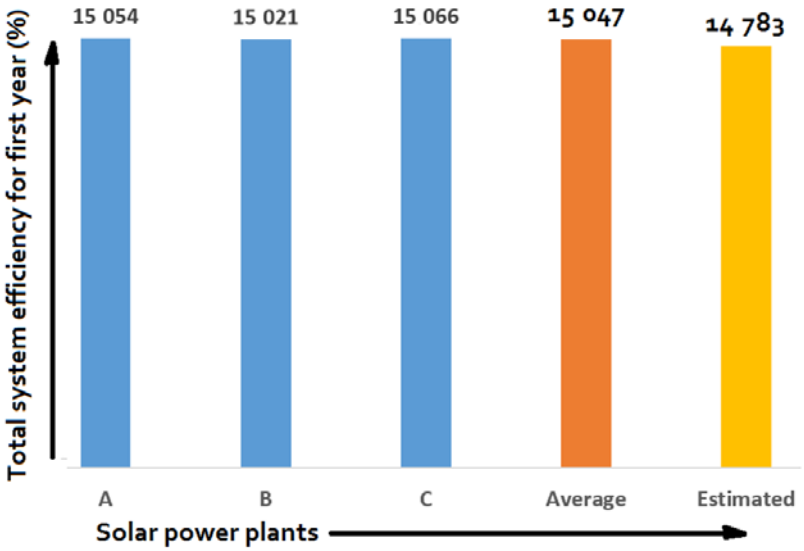

Figure 10. Practical system efficiency for first year.

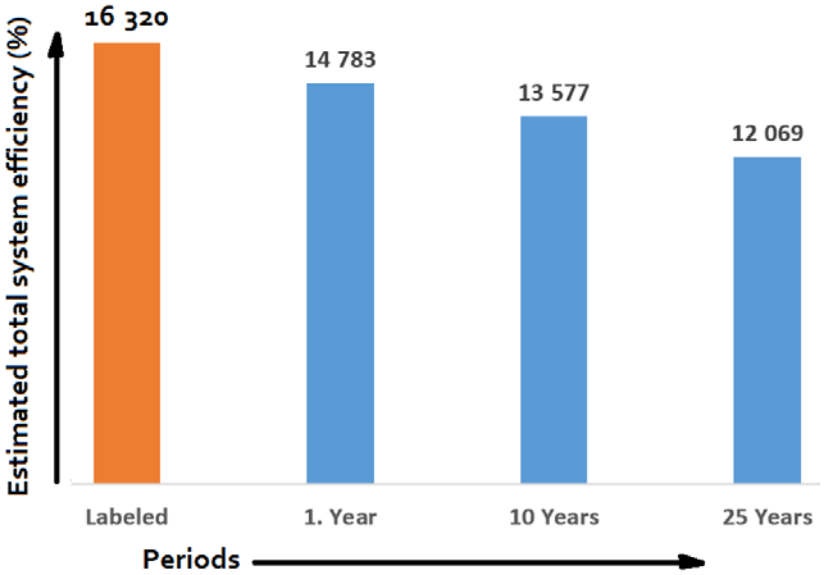

Figure 11. Estimated total system efficiency for first year, 10 years and 25 years (lifetime).

4. Conclusion

Briefly, the results of this work showed us that the average labeled efficiency of polycrystalline silicon module, average practical system efficiency and average estimated system efficiency of these three 1.025 MW SPVPs are 16.320 %, 15.047 % and 14.783 %, respectively for first year. Estimated average system efficiency for 10 years and 25 years (lifetime) are also determined as 13.577% and 12.069 %.

Author Contributions

The percentages of the authors' contributions are presented below. The author reviewed and approved the final version of the manuscript.

	T.K.	F.L.
C	50	50
D	50	50
S	50	50
DCP	50	50
DAI	50	50
L	50	50
W	50	50
CR	50	50
SR	50	50
PM	50	50

C=Concept, D= design, S= supervision, DCP= data collection and/or processing, DAI= data analysis and/or interpretation, L= literature search, W= writing, CR= critical review, SR= submission and revision, PM= project management.

Conflict of Interest

The authors declared that there is no conflict of interest.

Ethical Consideration

Ethics committee approval was not required for this study because of there was no study on animals or humans.

References

Aliman O, Daut I, Isa M, Adzman MR. 2007. Simplification of sun tracking mode to gain high concentration solar energy. Amer J Appl Sci, 4(3): 171-175. https://doi.org/10.3844/ajassp.2007.171.175

Anonymous. 2019. T.C. Çevre, Şehircilik ve İklim Değişikliği Bakanlığı, Meteo. Gen. Müd., URL: https://www.mgm.gov.tr/kurumici/radyasyon_iller.aspx?il=adiyaman (accessed date: May 15, 2024).

Costa SCC, Diniz ASAC, Kazmerski LL. 2016. Dust and soiling issues and impacts relating to solar energy systems: Literature review update for 2012–2015. Renew Sustain Ener Rev, 63: 33-61.

Darwish ZA, Kazem HA, Sopian K, Al-Goul MA, Alawadhi H. 2015. Effect of dust pollutant type on photovoltaic performance. Renew Sustain Ener Rev, 41: 735-744.

Goura R. 2015. Analyzing the on-field performance of a 1-Megawatt-Grid-Tied PV system in south India. Int J Sustain Ener, 34(1): 1-9.

Ketjoy N, Konyu M. 2014. Study of dust effect on photovoltaic module for photovoltaic power plant. Ener Proced, 52: 431-437.

Koyuncu T. 2017. Practical efficiency of photovoltaic panel used for solar vehicles. 2nd Int Conf on Green Energy Tech (ICGET 2017), July 18-20, Rome, Italy, pp: 48.

Kumar BS, Sudhakar K. 2015. Performance evaluation of 10 MW Grid connected solar photovoltaic power plant in India. Ener Rep, 1: 184-192.

Kumar ES, Sarkar B, Behera DK. 2013. Soiling and dust impact on the efficiency and the maximum power point in the photovoltaic modules. Int J Eng Res Technol, 2(2): 1-8.

Maghami MR, Hizam H, Gomes C, Radzi MA, Rezadad MI, Hajighorbani S. 2016. Power loss due to soiling on solar panel: A review. Renew Sustain Ener Rev, 59: 1307-1316.

Menoufi K, Farghal HF, Farghali AA, Khedr MH. 2017. Dust accumulation on photovoltaic panels: A case study at the east bank of the Nile (Beni-Suef, Egypt). Ener Proced, 128: 24-31.

Shukla AK, Sudhakar K, Baredar P. 2016. Simulation and performance analysis of 110 kWp grid-connected photovoltaic system for residential building in India: A comparative analysis of various PV technology. Ener Rep, 2: 82-88.

Black Sea Journal of Engineering and Science
doi: 10.34248/bsengineering.1590228

Open Access Journal
e-ISSN: 2619 – 8991

Araştırma Makalesi (Research Article)
Cilt 8 - Sayı 1: 234-242 / Ocak 2025
(Volume 8 - Issue 1: 234-242 / January 2025)

KAZIK-ZEMİN ETKİLEŞİMİNİN RÜZGÂR TÜRBİNLERİNİN DEPREM DAVRANIŞI VE KIRILGANLIK EĞRİSİ ÜZERİNDEKİ ETKİSİ

Abdullah DİLSİZ[1]*, Ali Ruzi ÖZUYGUR[2]

[1]*Ankara Yıldırım Beyazıt University, Faculty of Engineering and Natural Sciences, Department of Civil Engineering, 06010, Ankara, Türkiye*
[2]*Yapı Proje Uygulama A.Ş., 34349, İstanbul, Türkiye*

Özet: Bir yapı konumunda, taban kayasına ulaşan sismik dalgalar, üstündeki zemin aracılığıyla temele doğru yayılır ve dalganın bir kısmı temel ara yüzünden zemine geri yansırken, diğer bir kısmı ise yapıya iletilir ve yapının tepesinden tekrar zemine yansır. Bu süreç hem zeminin ve hem de yapının dinamik davranış özellikleri ile de etkileşim içerisindedir. Bu olayın tamamına Zemin-Yapı Etkileşimi (ZYE) denilmektedir. ZYE hakkında çok sayıda akademik araştırma mevcuttur. Türkiye Bina Deprem Yönetmeliği (TBDY) kazıklı temellerinin ZYE ile deprem etkisi altında gerçekleştirilen analiziyle ilgili ayrıntılı hükümler içermektedir. TBDY tarafından benimsenen en basit yöntemde, kazıklar çubuk elemanlar olarak modellenir; çubuk elemanların düğüm noktalarına zeminin yatay ve düşey basınçlarını temsilen doğrusal olmayan yatay ve düşey yaylar tanımlanır; ayrıca kazığın alt ucuna zeminin düşey basıncını temsilen doğrusal olmayan düşey yay tanımlanır. Zeminin yatay, düşey ve kazık uç direnci için basınç-yerdeğiştirme ilişkisi sırasıyla *p-y, t-z* ve *Q-z* ile gösterilir. Bu çalışmada, kazıklı temele sahip bir rüzgâr türbininin dinamik davranışı, i) yukarıda açıklanan doğrusal olmayan zemin yaylarının dikkate alındığı ve ii) temelin ankastre mesnet kabul edildiği durumlar için incelenmiştir. Bu iki durum için ayrıca yatay yerdeğiştirmenin esas alındığı kırılganlık eğrileri elde edilmiştir. Yapılan sayısal analizler sonucunda rüzgâr türbini kulesi iç kuvvet istemlerinde önemli sayılabilecek farklılıkların oluştuğu, ancak kulenin yatay yerdeğiştirme istemindeki farkın ihmal edilebilir mertebede olduğu görülmüştür.

Anahtar kelimeler: Zemin-yapı etkileşimi, Kazık-zemin etkileşimi, Kazıklı temel, Rüzgâr türbini

Effect of Pile-Soil Interaction on Earthquake Behavior and Fragility Curve of Wind Turbines

Abstract: The seismic wave reached to the bedrock propagates toward the foundation through the soil above it. While part of the wave reflects back into the soil from the foundation interface, the rest is transmitted into the structure and reflects back to the ground from the top of the structure. This phenomenon interacts both the dynamic behaviors of the structure as well as the soil. This entire phenomenon is referred to as Soil-Structure Interaction (SSI). There are numerous academic studies on SSI. The Turkish Building Earthquake Code (TBEC) includes detailed provisions regarding the seismic analysis of piled foundations considering SSI. In the simplest method adopted by TBEC, piles are modeled as frame elements; nonlinear horizontal and vertical springs are assigned at the nodes of these frame elements to represent the horizontal and vertical resistance of the soil; additionally, a nonlinear vertical spring is assigned at the bottom tip of the pile to represent the vertical resistance of the soil. The horizontal, vertical, and pile-tip resistance of the soil and their relating displacement properties are represented as *p-y, t-z,* and *Q-z*, respectively. In this study, the dynamic behavior of a wind turbine with a piled foundation has been examined for the following conditions: i) the case that the nonlinear soil springs described above are used, and ii) the case that the foundation is assumed to be a fixed support. For these two cases, fragility curves based on the lateral displacement of the turbine tower have also been derived. Numerical analyses have revealed that there are significant differences in the internal force demands of the tower, while the difference in the lateral displacement demands of the tower is negligible.

Keywords: Soil-structure interaction, Pile-soil interaction, Pile foundation, Wind turbine

***Sorumlu yazar (Corresponding author):** Abdullah DİLSİZ, Ankara Yıldırım Beyazıt University, Faculty of Engineering and Natural Sciences, Department of Civil Engineering, 06010, Ankara, Türkiye
E mail: adilsiz@aybu.edu.tr (A. DİLSİZ)
Abdullah DİLSİZ https://orcid.org/0000-0002-1750-9327
Ali Ruzi ÖZUYGUR https://orcid.org/0000-0002-7145-8065

Gönderi: 23 Kasım 2024
Kabul: 25 Aralık 2024
Yayınlanma: 15 Ocak 2025
Received: November 23, 2024
Accepted: December 25, 2024
Published: January 15, 2025

Cite as: Dilsiz A, Özuygur AR. 2025. Effect of pile-soil interaction on earthquake behavior and fragility curve of wind turbines. BSJ Eng Sci, 8(1): 234-242.

1. Giriş

Yapıların bulunduğu konumda, taban kayasına ulaşan sismik dalgalar, üstündeki zemin aracılığıyla temele doğru yayılır ve dalganın bir kısmı temel ara yüzünden zemine geri yansırken, diğer bir kısmı ise yapıya iletilir ve yapının tepesinden tekrar zemine yansır. Bu süreç hem zeminin ve hem de yapının dinamik davranış özellikleri ile de etkileşim içerisindedir. Bu olayın tamamı Zemin-Yapı Etkileşimi (ZYE) olarak tanımlanır. Yapı-Deprem Mühendisliği alanında ZYE'nin çeşitli boyutları üzerine önemli sayıda akademik araştırma mevcuttur. Hali hazırda yürürlükte bulunan Türkiye Bina Deprem Yönetmeliği (TBDY, 2018) de kazıklı temellerinin ZYE ile deprem etkisi altında gerçekleştirilen analiziyle ilgili

ayrıntılı hükümler içermektedir. TBDY tarafından benimsenen en basit yöntemde, kazıklar çubuk elemanlar olarak modellenir; çubuk elemanların düğüm noktalarına zeminin yatay ve düşey basınçlarını temsilen doğrusal olmayan yatay ve düşey yaylar tanımlanır; ayrıca kazığın alt ucuna zeminin düşey basıncını temsilen doğrusal olmayan düşey yay tanımlanır. Zeminin yatay, düşey ve kazık uç direnci için basınç-yerdeğiştirme ilişkisi sırasıyla *p-y, t-z* ve *Q-z* ile gösterilir. Buradaki *p-y, t-z* ve *Q-z* yayları genellikle Amerikan Petrol Enstitüsü (American Petroleum Institute, API) tarafından yayınlanan "Recommended Practice for Planning, Designing and Constructing Fixed Offshore Platforms-Working Stress Design (2002)" isimli doküman referans alınarak hesaplanır. Dolayısıyla, bu yaylar API yayları olarak da anılır.

Türkiye'de mühendislik uygulamalarında kazıklı temeller için ZYE analizi yapmak nispeten yenidir. Polat (2008), kazık destekli deniz yapılarının deformasyona dayalı sismik analizinde doğrusal olmayan kazık-zemin etkileşim analizini kullanmıştır. Aydınoğlu (2011), zayıf zeminlerde inşa edilecek binalar için dinamik kazık-zemin etkileşim analizi ile uygulamaya yönelik bir yöntem önermiştir. Aydınoğlu vd. (2014), dinamik kazık-zemin etkileşim analizi için uygulamaya yönelik başka bir yöntem önermiştir. Bildik vd. (2017) ise kazıkların davranışının kinematik etkileşim analizi ile incelenmesine ilişkin bir vaka çalışması sunmuştur.

Bu çalışmada, kazıklı temele sahip bir rüzgâr türbininin dinamik davranışı, i) yukarıda açıklanan doğrusal olmayan zemin yaylarının dikkate alındığı ve ii) temelin ankastre mesnet kabul edildiği durumlar için incelenmiştir. Bu iki durum için ayrıca yatay yerdeğiştirmenin esas alındığı kırılganlık eğrileri elde edilmiştir. Yapılan sayısal analizler sonucunda rüzgâr türbini kule iç kuvvet istemlerinde önemli sayılabilecek farklılıkların ortaya çıktığı, ancak kulenin yatay yerdeğiştirme istemlerindeki farkın ihmal edilebilir mertebede olduğu görülmüştür. Çalışmanın aşağıda yer alan bölümlerinde bahsi geçen rüzgâr türbini yapısal özellikleri ile birlikte TBDY (2018) doğrultusunda uygulanan ZYE analizleri detaylı şekilde sunulmuş ve sonuçlar tartışılmıştır.

2. Rüzgâr Türbininin Yapısal Özellikleri

Çalışmada ZYE analizlerinin uygulanması amacıyla ülkemizde kullanılanlara benzer bir rüzgâr türbini ele alınmıştır. Rüzgâr türbininin temel planı ve kesiti Şekil 1'de verilmiştir. Temel, toplam genişliği 20 m olan sekizgen bir şekle sahiptir. Temel kalınlığı, orta bölgede 3 m'den kenarda 1,4 m'ye kadar değişmektedir. Temel, çapı 0,8 m ve uzunluğu 20 m olan 16 adet kazık tarafından desteklenmektedir. Toplam 1493 kN ağırlığındaki motor ve diğer aksamları, ağırlığı 1463 kN olan dairesel bir çelik kule tarafından taşınmaktadır. Çelik kulenin yüksekliği 80 m olup, çapı altta 4 m'den başlayarak, üstte 3 m'ye kadar azalacak şekilde değişmektedir. Bununla birlikte, çelik kule bölümlerinin duvar kalınlığı da altta 25 mm'den üstte 13 mm'ye kadar değişmektedir. Temel ve kazıkların beton sınıfı C30, dairesel kulenin çelik sınıfı ise S275'tir.

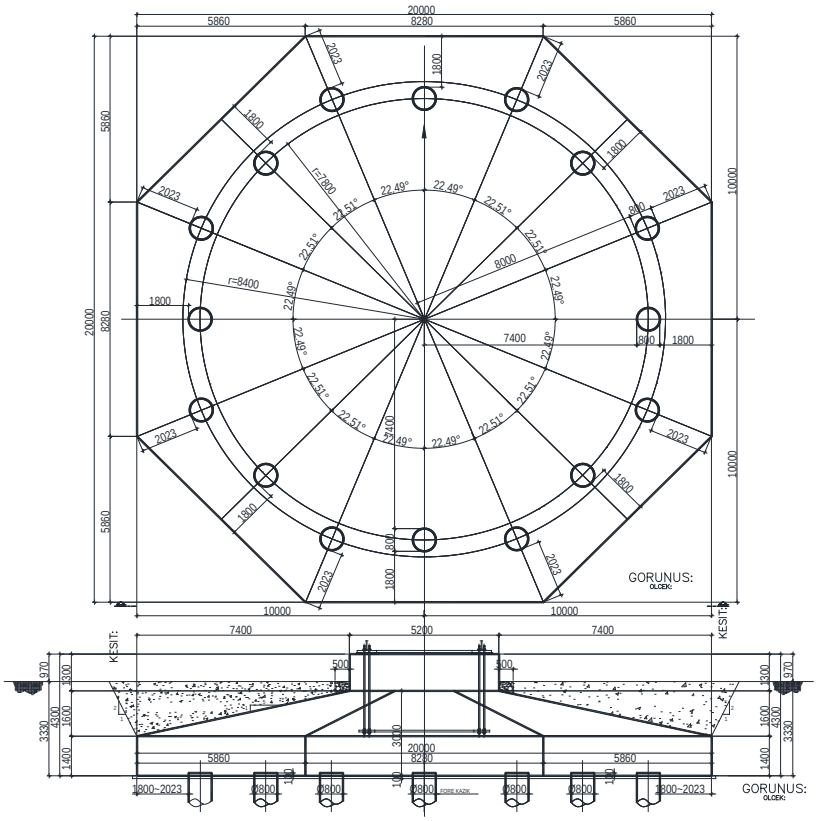

Şekil 1. Seçilen rüzgâr türbininin temel planı.

3. Zemin Özellikleri ve *p-y, t-z, Q-z* Eğrileri

Temel zemininin, içsel sürtünme açısı $\phi = 20^o$, birim hacim ağırlığı $\gamma = 19$ kN/m^3 ve drenajsız kesme dayanımı $c_u = 90$ kN/m^2 olan kohezyonlu zemin olduğu varsayılmıştır.

Zeminin doğrusal olmayan yay parametrelerini, başka bir deyişle *p-y, t-z* ve *Q-z* eğrilerini tanımlamak için çok sayıda araştırma yapılmıştır. *p-y* eğrisinin tayini için zemin türüne bağlı olarak şu yöntemler kullanılabilir: Matlock (1970) yöntemi yumuşak kil ($c_u < 50$ kPa) için uygundur; Reese vd. (1975) yöntemi su tablasının altındaki sert kil için uygundur; Welch ve Reese (1972) yöntemi su tablasının üzerindeki sert kil için uygundur; Reese vd. (1974) yöntemi kum için uygundur. *t-z* ve *Q-z* eğrileri genellikle API (2002) dokümanı esas alınarak elde edilir.

Kohezyonlu zemindeki yanal *p-y* yayları, kazık kesitinin kama etki bölgesinde olup olmadığına bağlı olarak tanımlanır. Kama etkisi bölgesi, kazık yakınındaki zeminin, yatay yükleme nedeniyle kama şeklinde bir göçme mekanizmasına maruz kaldığı bölgeyi ifade eder. Kama etki bölgesindeki yanal *p-y* yaylarının hesaplanması için gerilme birimindeki (kN/m^2) nihai yanal zemin direnci eşitlik 1'de verildiği şekilde ifade edilir:

$$p_u = 3c_u + \gamma X + J\frac{c_u X}{D} \quad (1)$$

Burada; X derinlik (m), γ etkin zemin birim ağırlığı (kN/m^3), D kazık çapı (m), c_u örselenmemiş kohezyonlu zeminin drenajsız kesme dayanımı ve J de 0.25 ile 0.5 arasında değişen boyutsuz ampirik bir sabittir.

Kama etki bölgesinin dışında kalan derinlikteki nihai yanal zemin direnci eşitlik 2'de verilmiştir:

$$p_u = 9c_u \quad (2)$$

Çevrimsel yükleme altında kohezyonlu bir zemin için, doğrusal olmayan yanal zemin direnci ve yanal yerdeğiştirme ilişkisi, Tablo 1 ve Şekil 2'de verildiği gibi önerilmektedir. Burada p gerçek direnç, y gerçek yanal yerdeğiştirme ve $y_c = 2{,}5\varepsilon_{50}D$'dir. ε_{50}, bu çalışmada 0.005 olarak alınan maksimum gerilmenin %50'sindeki zemin şekil değiştirmesidir. Bu çalışmada verilen zemin özellikleri için zemin direnci ve yanal yerdeğiştirme ilişkisi Şekil 3'te gösterilmiştir. Kama etkisi bölgesinin, eşitlik 1 ve 2'nin sayısal sonuçlarının birbirine yakınsadığı 7 m derinlikte sona erdiği görülmektedir.

Tablo 1. Yanal zemin direnci ve yanal yerdeğiştirme ilişkisi (*p-y* eğrisi) (API, 2002)

Kama etki bölgesi dışında		Kama etki bölgesinde	
p/p_u	y/y_c	p/p_u	y/y_c
0,5	1	0,5	1
0,72	3	0,72	3
0,72	∞	$0{,}72X/X_r$	∞

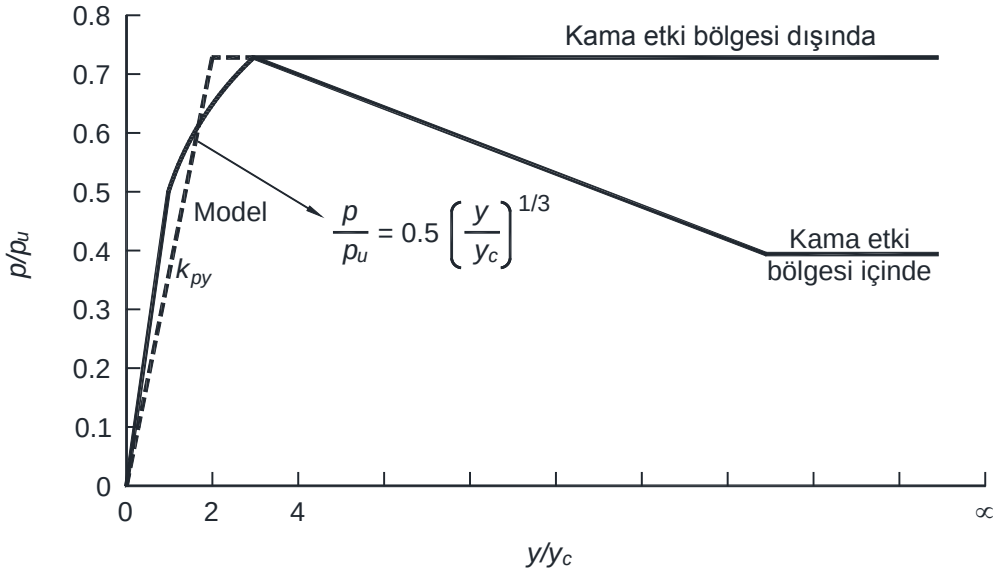

Şekil 2. Çevrimsel yükleme altında kohezyonlu zeminin *p-y* eğrisi (API, 2002).

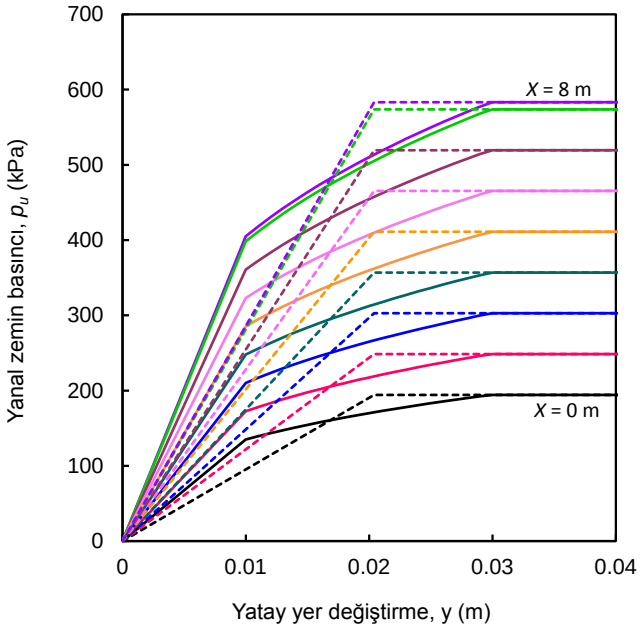

Şekil 3. Çevrimsel yükleme altında, verilen kohezyonlu zeminin *p-y* eğrisi.

Doğrusal olmayan *p-y* yaylarının kuvvet-deplasman özelliği, akma gerilmesi p_{sy} ve etkin elastik rijitlik $k_{py} = p_{sy} / y_y$ ile tanımlanan elastoplastik bir eğri kullanılarak idealize edilebilir. Burada y_y, elastoplastik doğrusal olmayan yay elemanının akma deplasmanını ifade eder.

Düşey yönde, kazık yüzey sürtünmesi direnci ile düşey yerdeğiştirmesi arasındaki ilişkiyi temsil etmek için doğrusal olmayan *t-z* yayları kullanılır. Uç direnci ile düşey yerdeğiştirme arasındaki ilişkiyi temsil etmek için ise doğrusal olmayan *Q-z* yayları kullanılır.

Kohezyonlu zemindeki kazıklar için, nihai kazık yüzey sürtünmesi t_{max} eşitlik 3 ile elde edilebilir:

$$t_{\max} = \alpha c_u \tag{3}$$

Burada α boyutsuz bir katsayıdır ve c_u zeminin drenajsız kayma dayanımıdır. Boyutsuz katsayı α hesabı eşitlik 4 ve 5 ile yapılabilir:

$$\psi \le 1.0 \quad \text{için} \quad \alpha = \psi^{0.5} \tag{4}$$

$$\psi > 1.0 \quad \text{için} \quad \alpha = \psi^{0.25} \tag{5}$$

Burada, ψ katsayısı eşitlik 6 kullanılarak hesaplanır:

$$\psi = \frac{c_u}{\sigma_0} \tag{6}$$

Bu denklemde, σ_0 etkin aşırı yüklenmiş basınç (kPa) değeridir.

Şekil 4'te, kazık yüzey sürtünme direnci ve düşey yerdeğiştirme ilişkisi gerilme birimi (kN/m²) cinsinden gerçek ve idealize edilmiş üç-doğrusal biçim için verilmiştir. Şekil 4'te, t_{max} zeminin maksimum birim yüzey sürtünme direnci, *z* düşey yerdeğiştirme ve *D* kazık çapıdır.

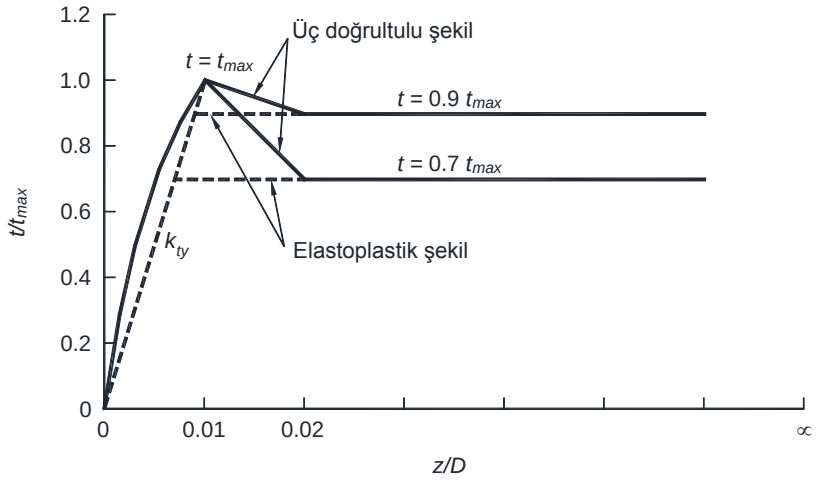

Şekil 4. Kohezyonlu zemin için *t-z* eğrisi (API, 2002).

İdealize edilmiş formun elastik rijitliği eşitlik 7 ile tanımlanabilir:

$$k_{ty} = \frac{t_{\max}}{z_y} \tag{7}$$

Burada z_y kohezyonlu zeminlerde *0,01*D*'ye eşit olan akma yerdeğiştirmesidir. Doğrusal olmayan yüzey sürtünmesi, $t = 0{,}7t_{max}$ veya $0{,}9t_{max}$'a eşit elastoplastik formda veya Şekil 4'te gösterildiği gibi üç doğrusal eğri şeklinde olabilir. Bu çalışmadaki rüzgâr türbininin kazıkları için hesaplanan $0{,}7t_{max}$ ile idealize edilmiş olan elastoplastik yüzey sürtünme yayları Şekil 5'te gösterilmiştir.

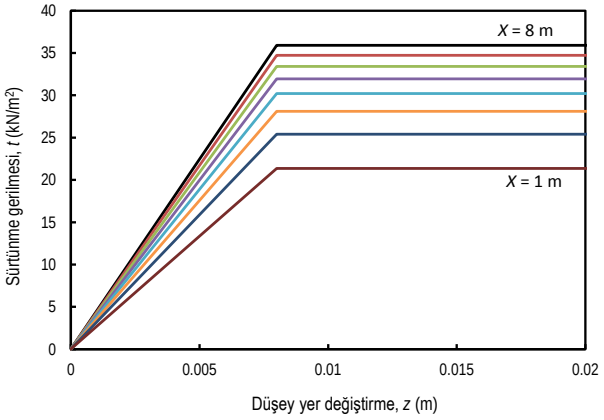

Şekil 5. Kohezyonlu zemin için *t-z* eğrisi.

Kohezyonlu zemindeki bir kazık için, kuvvet birimindeki (kN) nihai uç direnci eşitlik 8 ile hesaplanabilir:

$$Q_u = 9c_u A_p \tag{8}$$

Burada c_u zeminin drenajsız kesme dayanımı ve A_p kazığın kesit alanıdır.

Önerilen değerlere sahip *Q-z* eğrisi ve idealize edilmiş elastoplastik formu Şekil 6'da gösterilmiştir. Şekil 6'da *z* düşey uç yerdeğiştirmesi, *D* ise kazık çapıdır. İdealize edilmiş *Q-z* yayının elastik rijitliği de eşitlik 9'da tanımlanmıştır:

$$k_{qy} = \frac{Q_u}{z_y} \tag{9}$$

Burada z_y elastoplastik yayın akma yerdeğiştirmesidir.

Rüzgâr türbininin kazıkları için hesaplanan idealize edilmiş elastoplastik *Q-z* yayı Şekil 7'de gösterilmiştir.

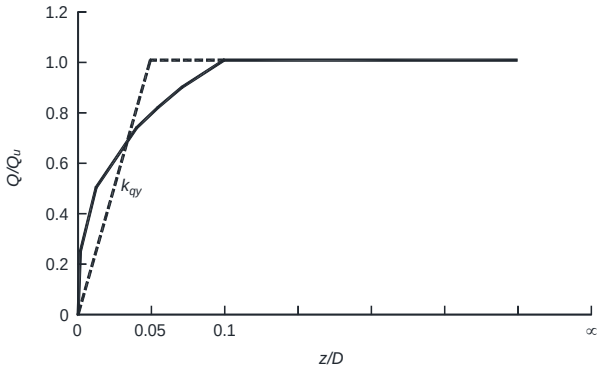

Şekil 6. Kohezyonlu zemin için *Q-z* eğrisi (API, 2002).

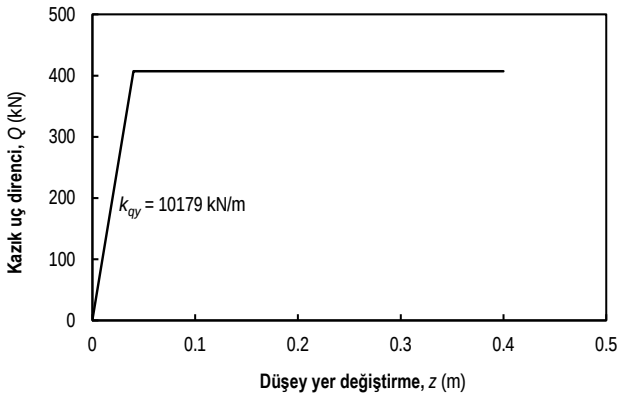

Şekil 7. Kohezyonlu zemin için *Q-z* eğrisi.

4. Deprem Parametreleri

Doğrusal olmayan zaman geçmişi analizleri TBDY'de DD1 olarak tanımlanan, tekrarlanma periyodu 2475 yıl ve 50 yılda aşılma olasılığı %2 olan deprem seviyesi altında gerçekleştirilmiştir. Varsayılan, ZC zemin sınıfına sahip bir konum için depremin kısa periyot spektral ivmesi ve 1 saniyelik periyot spektral ivmesi sırasıyla S_{DS} = 2,092 g ve S_{D1} = 0,757 g olarak elde edilmiştir. Seçilen DD1 depreminin %5 sönümlü tepki spektrumu Şekil 8'de verilmiştir.

Deprem yer hareketleri, seçilen sahanın deprem tehlikesini yansıtan moment büyüklüğü M_w, fay mesafesi R_{jb} ve saha zemininin en üst 30 m'sindeki zaman ortalamalı kayma dalgası hızı V_{S30} gibi varsayılan kriterlere göre TBDY'ye uygun olarak seçilmiş ve ölçeklendirilmiştir. Yedi adet çift yönlü deprem yer hareketi kaydı, Pasifik Deprem Mühendisliği Araştırma Merkezi'nin NGA-West2 Veritabanı (PEER, 2024) kullanılarak elde edilmiştir. Ölçeklendirme, DD1 hedef spektrumuna uyacak şekilde ortalama karesel hatanın en aza indirilmesiyle gerçekleştirilmiştir ve çift yönlü spektrumların karelerinin toplamının karekökünün aritmetik ortalaması Şekil 8'de gösterilmiştir. Seçilen deprem yer hareketi zaman geçmişlerinin özellikleri ve ölçeklendirme katsayıları Tablo 2'de verilmiştir. M_w, R_{jb} ve V_{S30}'un ortalama değerleri M_w = 6,86, R_{jb} = 12 km ve V_{S30} = 229 m/s olarak hesaplanmıştır.

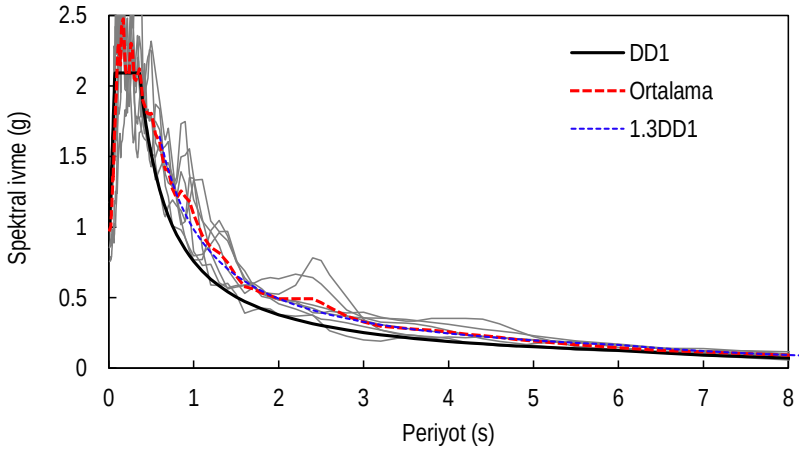

Şekil 8. Seçilen yer hareketleri için DD1 spektrumu ve %5 sönümlü tepki spektrumları.

Tablo 2. PEER'den (2024) alınan deprem kayıtları

Kayıt sıra numarası	Ölçekl katsayısı	T_p-Darbe periyodu (s)	Deprem adı	Yıl	Kayıt istasyonu	Büyüklük	Fay	R_{jb} (km)	V_{s30} (m/s)
183	1.5152	-	Imperial Valley-06	1979	El Centro Array #8	6.53	yatay atımlı	3.86	206
184	1.4348	6.265	Imperial Valley-06	1979	El Centro Differential Array	6.53	yatay atımlı	5.09	202
719	5.7099	-	Superstition Hills-02	1987	Brawley Airport	6.54	yatay atımlı	17.03	209
5827	1.4507	-	El Mayor-Cucapah_ Mexico	2010	Michoacan De Ocampo	7.2	yatay atımlı	13.21	242
5829	1.546	-	El Mayor-Cucapah_ Mexico	2010	RIITO	7.2	yatay atımlı	13.7	242
6890	2.2227	-	Darfield_ New Zealand	2010	Christchurch Cash. H. School	7	yatay atımlı	17.64	204
6961	4.6272	-	Darfield_ New Zealand	2010	RKAC	7	yatay atımlı	13.37	296

5. Doğrusal Olmayan Dinamik Analizler ve Sonuçları

Rüzgâr türbini, yapısal analiz ve tasarım yazılımı SAP2000 V.25 (2024) kullanılarak modellenmiştir. Modelde *p-y, t-z* ve *Q-z* yayları doğrusal olmayan link elemanları olarak modellenmiştir. Doğrusal olmayan zaman geçmişi analizleri, Hızlı Doğrusal Olmayan Analiz yöntemi ile gerçekleştirilmiştir. Aşağıda sunulan analiz sonuçları, seçilmiş olan yedi adet çift yönlü yer hareketi altındaki zaman geçmişi analizlerinin ortalaması olarak elde edilmiştir.

Tablo 2'de kayıt sıra numarası 5829 olan deprem için 3 m derinlikteki *p-y* yayının kuvvet-yerdeğiştirme geçmişi Şekil 9'da örnek olarak sunulmuştur.

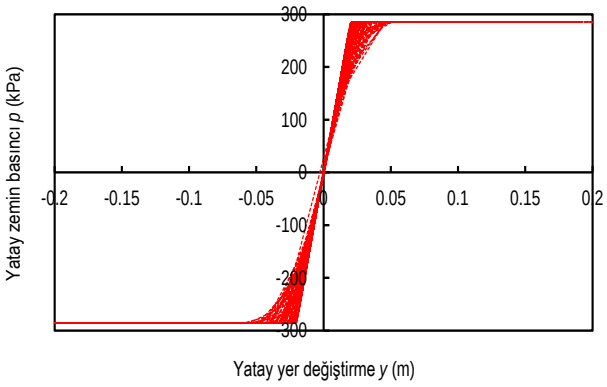

Şekil 9. Örnek *p-y* yayının kuvvet-yerdeğiştirme geçmişi.

Türbinin çelik kulesinin moment ve kesme kuvveti istem sonuçları, doğrusal olmayan *p-y* yayları ve temelin ankastre mesnet alınması durumları için Şekil 10'da karşılaştırmalı olarak verilmiştir. Görüldüğü gibi, kazık etrafındaki zeminin doğrusal olmayan yay olarak modellenmesi, kulenin iç kuvvet istemlerinin büyüklüğünü ve dağılımını önemli ölçüde etkilemektedir. Kulenin iç kuvvet değerleri zeminin doğrusal olmayan yay olarak modellenmesi durumunda azalmaktadır.

Türbinin çelik kulesinin moment tasarımında enkesitin moment kapasitesine ek olarak, yerel elastik ve yerel plastik burkulma (buruşma) durumları da önemli olmaktadır. Bu çalışmada dikkate alınan türbin kulesinin enkesit mekanik değerleri dikkate alındığında moment tasarımında yerel plastik burkulmanın belirleyici olduğu, yerel plastik burkulmanın, kesitin akma veya plastik moment kapasitesinden önce meydana geldiği görülmüştür. API (2002)'ye göre yerel plastik burkulmaya neden olan malzeme gerilme sınırı hesabı eşitlik 10'da verilmiştir:

$$F_{xc} = F_y\left(1.64 - 0.23\left(\frac{D}{t}\right)^{1/4}\right) \tag{10}$$

Burada F_y malzeme akma gerilmesi, D kesitin dış çapı, t ise kesitin et kalınlığıdır. Bu ifade yardımıyla hesaplanan yerel burkulmaya neden olacak gerilme sınırları ve enkesit moment değerleri Şekil 10a'a gösterilmiştir. Görüldüğü gibi *p-y* yayı ve ankastre mesnet durumları için elde edilen momentler yerel plastik burkulma değerlerinden, aynı şekilde plastik moment

kapasitesinden daha küçüktür. Başka bir deyişle seçilen deprem seviyesinde kule kesitinde plastikleşme meydana gelmemektedir. Buna paralel olarak kule kesiti doğrusal elastik modellenmiştir.

Türbinin çelik kulesinin yatay yerdeğiştirmeleri, doğrusal olmayan *p-y* yayları ve temelin ankastre mesnet alınması durumları için Şekil 11'de karşılaştırmalı olarak verilmiştir. Görüldüğü gibi her iki durum için yatay yerdeğiştirmeler benzer mertebede elde edilmiştir. Türbin kulelerinin tasarımında yatay yerdeğiştirmenin sınırlanması belirleyici tasarım konularındandır. Yatay yerdeğiştirmenin sınırı konusunda API (2002) vb. kaynaklarda kesin bir değer verilmemiştir. Asareh (2015) ve Mo vd. (2017) yaptıkları çalışmada türbin kulelerinin yatay yerdeğiştirmesi için yüksekliğin %1.25 ötelenme sınırını önermiştir. Analiz sonuçlarında *p-y* yayı ve ankastre mesnet durumları için elde edilen kule yatay ötelenmeleri %1.25 ötelenme sınırının altında gerçekleşmiştir.

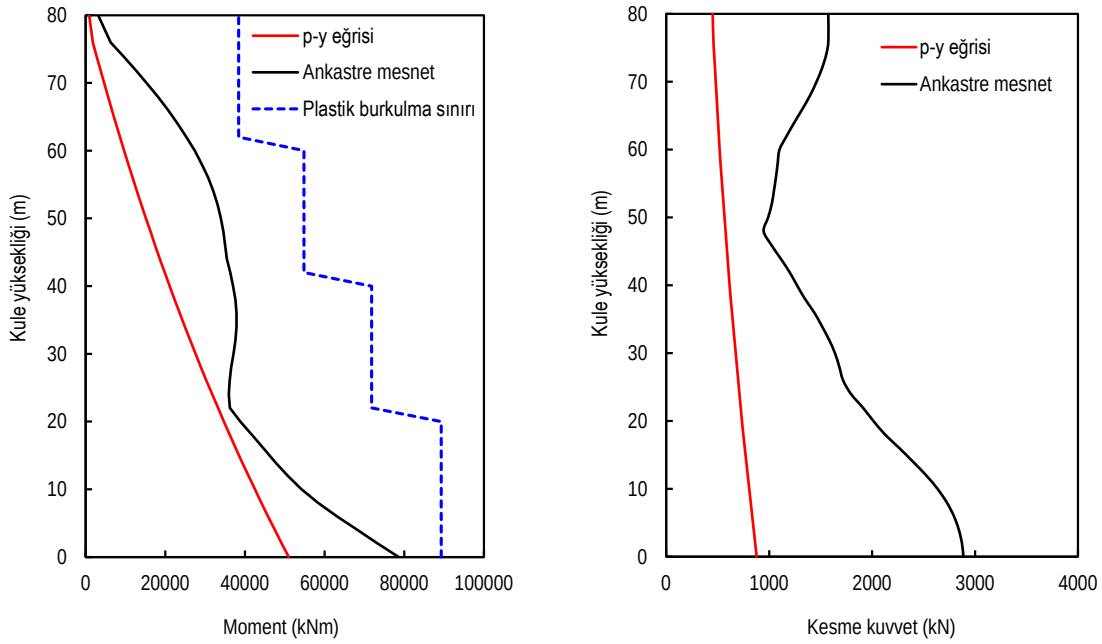

(a) (b)

Şekil 10. *p-y* yayı ve ankastre mesnet durumları için çelik kulenin iç kuvvetleri; (a) moment, (b) kesme kuvveti.

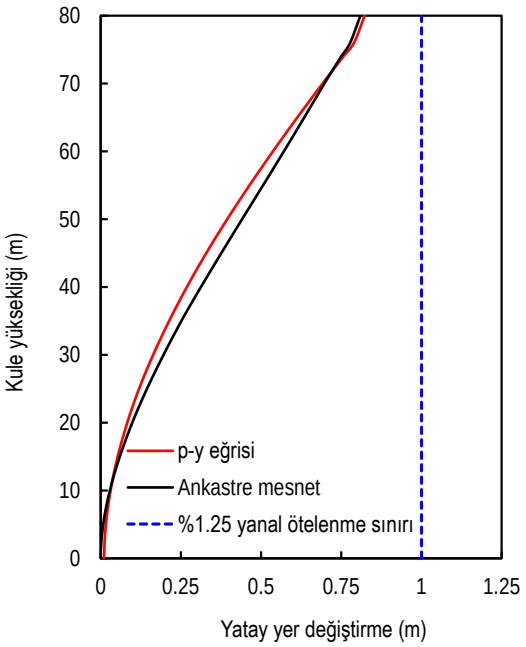

Şekil 11. *p-y* yayı ve ankastre mesnet durumları için çelik kulenin yatay yerdeğiştirmesi.

6. Kırılganlık Eğrileri

Kırılganlık eğrisi, bir sistemin göçme veya belirli bir hasar durumunun gerçekleşme olasılığını, en büyük zemin ivmesi (PGA), belirli bir periyottaki spektral ivme veya katlar arası ötelenme oranı gibi bir tehlike şiddet ölçüsünün (*IM*) bir fonksiyonu olarak ifade eder. Kırılganlık fonksiyonu genellikle eşitlik 11'de verildiği şekilde bir lognormal kümülatif dağılım fonksiyonu ile ifade edilir (Baker, 2015):

$$P\left(C\middle|IM=x\right)=\Phi\left(\frac{\ln\left(x/\theta\right)}{\beta}\right) \tag{11}$$

Burada $P(C|IM = x)$, $IM = x$ olan bir yer hareketinin yapının göçmesine neden olma olasılığı; Φ standart normal kümülatif dağılım fonksiyonu (CDF); θ kırılganlık fonksiyonunun medyanı (%50 göçme olasılığı olan *IM* seviyesi); ve β, ln(*IM*)'nin standart sapmasıdır. Artımsal dinamik analiz (IDA) (Vamvatsikos ve Cornell 2002; Federal Emergency Management Agency - FEMA 2009) genellikle kırılganlık fonksiyonunu tahmin etmek için veri toplamak amacıyla kullanılır.

Rüzgâr türbininin temel titreşim periyodu T = 3,22 s'deki spektral ivme, bu çalışma için Şiddet Ölçüsü (*IM*) olarak

belirlenmiştir. Kulenin temel titreşim periyoduna ait 1. modda %73 modal kütle katılım sağlanmıştır; dolayısıyla 1. Mod kulenin dinamik davranışını yeteri ölçüde temsil etmektedir. Kulenin yanal ötelenmesi talep parametresi olarak seçilmiştir. %1,25'lik bir yanal ötelenme, göçmenin eşiği olarak belirlenmiştir.

Türbin kulesinin kırılganlık eğrilerinin elde edilmesi için Tablo 2'de verilen deprem kayıtları kullanılmıştır. Seçilen deprem kayıtlarının kaynak fayına olan mesafeleri, genelde yakın fay sınırı olarak kabul edilen 15 km'den büyük veya küçüktür. Dolayısıyla deprem kayıtlarının hem yakın fay, hem uzak fay depremlerini temsil ettiği söylenebilir. Deprem kayıtları, seçilen tasarım spektrumunun T = 3,22 s'deki değeri olan 0,23 g'ye Tablo 3'te verilen ölçeklendirme katsayılarıyla ölçeklendirilmiştir. Türbinin çelik kulesinin yatay yerdeğiştirme parametresi kullanılarak, doğrusal olmayan *p-y* yayları ve temelin ankastre mesnet alınması durumları için elde edilen kırılganlık eğrileri Şekil 12'de karşılaştırmalı olarak verilmiştir. Görüldüğü gibi her iki durum için elde edilen kırılganlık eğrileri aynıdır. Kırılganlık eğrilerinde dikkat çeken diğer bir husus, tasarım spektrumuna ölçeklenen 7 adet depremin ortalaması olarak elde edilen yatay ötelenme %1,25 ötelenme sınırının altındayken, tasarım spektrumunun T = 3,22 s'deki değeri olan 0,23 g'deki sistemin göçme olasılığı %100 olmasıdır.

Tablo 3. Deprem kayıtlarının *T* = 3,22 s'deki spektral ivme 0,23 g'ye ölçeklendirme katsayıları

DKSN	Ölçeklendirme katsayısı
183	1,4744
184	1,8965
719	6,6389
5827	1,8468
5829	2,7533
6890	3,4656
6961	5,7578

DKSN= deprem kaydı sıra numarası.

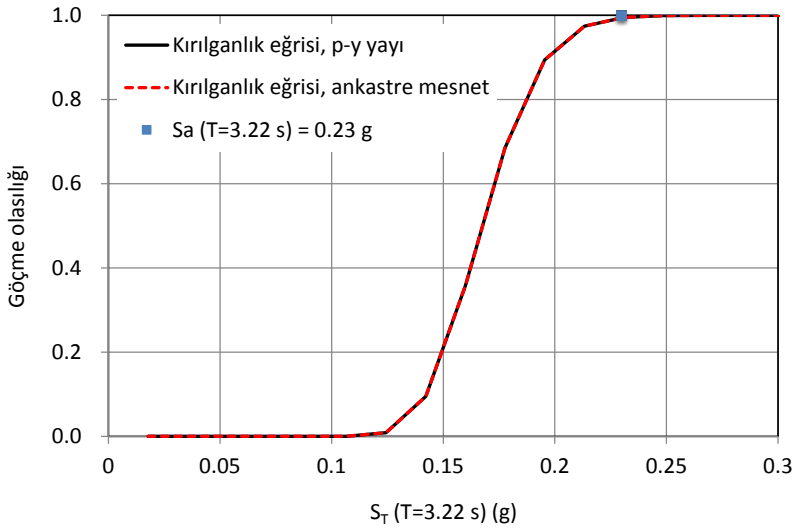

Şekil 12. *p-y* yayı ve ankastre mesnet durumları için çelik kulenin kırılganlık eğrileri.

7. Sonuçlar

Bu çalışmada, kazıklı temele sahip bir rüzgâr türbini seçilerek dinamik davranışı, i) doğrusal olmayan zemin yaylarının dikkate alındığı ve ii) temelin ankastre mesnet kabul edildiği durumlar için incelenmiştir. Bu iki durum için ayrıca yatay yerdeğiştirmenin esas alındığı kırılganlık eğrileri de elde edilmiştir. Elde edilen sonuçlar aşağıda özetlenmiştir:

1) Kazık etrafındaki zeminin doğrusal olmayan yay olarak modellenmesi, kulenin iç kuvvet istemlerinin büyüklüğünü ve dağılımını önemli ölçüde etkilemektedir. Kulenin iç kuvvet değerleri ise zeminin doğrusal olmayan yay olarak modellenmesi durumunda azalmaktadır. Bu durum, türbin kulesi tasarımında ankastre mesnetli durumun dikkate alınmasının yeterli olduğunu göstermektedir. Bununla birlikte, bu çalışmada kapsam dışı tutulan kazık tasarımında, kazık-zemin etkileşiminin önemli olabileceği unutulmamalıdır.

2) Doğrusal olmayan *p-y* yayları ve temelin ankastre mesnet alınması durumları için yatay yerdeğiştirme istemleri benzer mertebede elde edilmiştir.

3) Yatay yerdeğiştirme parametresi kullanılarak, doğrusal olmayan *p-y* yayları ve temelin ankastre mesnet alınması durumları için kırılganlık eğrileri benzer olarak elde edilmiştir.

Katkı Oranı Beyanı

Yazarların katkı yüzdeleri aşağıda verilmiştir. Yazarlar makaleyi incelemiş ve onaylamıştır.

	A.D.	A.R.O.
K	50	50
T	50	50
VTI	50	50
VAY	40	60
KT	50	50
YZ	50	50
KI	60	40
GR	70	30

K= kavram, T= tasarım, VTI= veri toplama ve/veya işleme, VAY= veri analizi ve/veya yorumlama, KT= kaynak tarama, YZ= Yazım, KI= kritik inceleme, GR= gönderim ve revizyon.

Çatışma Beyanı

Yazarlar bu çalışmada hiçbir çıkar ilişkisi olmadığını beyan etmektedirler.

Etik Onay Beyanı

Bu araştırmada hayvanlar ve insanlar üzerinde herhangi bir çalışma yapılmadığı için etik kurul onayı alınmamıştır.

Kaynaklar

API - American Petroleum Institute. 2002. Recommended practice for planning, designing and constructing fixed offshore platforms – working stress design, API- RP 2A-WSD. URL: https://www.api.org/~/media/files/publications/whats%20new/2a-wsd_e22%20pa.pdf (accessed date: March 18, 2024).

Asareh MA. 2015. Dynamic behavior of operational wind turbines considering aerodynamic and seismic load interaction, Ph.D. Thesis, Missouri University of Science and Technology, Missouri, USA, pp: 148.

Aydınoğlu MN. 2011. Zayıf zeminlerde yapılan binalarda dinamik yapı-kazık-zemin etkileşimi için uygulamaya yönelik bir hesap yöntemi. Boğaziçi Üniversitesi Kandilli Rasathanesi ve Deprem Araştırma Enstitüsü Rapor No. 2011/1, İstanbul, Türkiye, ss: 15.

Aydınoğlu MN, Celep UU, Önem G. 2014. A practical method for structure – pile – soil interaction under seismic action. Symposium on Developments and Experiences in Geotechnics, in honour of Prof. Dr. Kutay ÖZAYDIN, Yıldız Technical University, June 2, Istanbul, Türkiye, pp:68.

Baker JW. 2015. Efficient analytical fragility function fitting using dynamic structural analysis. Earthquake Spectra. 31(1):579-599.

Bildik S, Savaşeri K, Polat ŞŞ, Laman M. 2017. A case study on the investigation of the behavior of piles by kinematic interaction analysis. 7. Geoteknik Sempozyumu, November 22-24, İstanbul, Türkiye, pp: 54.

Federal Emergency Management Agency – FEMA. 2009. quantification of building seismic performance factors (FEMA P695, ATC-63). FEMA, Washington, USA, pp: 421.

Matlock H. 1970. Correlation for design of laterally loaded piles in soft clay. 2nd Annual Offshore Technology Conference, Paper No. OTC 1204, 31 March–2 April, Houston, Texas, USA, pp: 577-594

Mo R, H Kang and M Li. 2017. Seismic fragility analysis of monopile offshore wind turbines under different operational conditions. Energies, 10: 109414.

PEER 2024. NGA-West2 Database of Pacific earthquake engineering research center. URL: http://ngawest2.berkeley.edu. (accessed date: March 18, 2024).

Polat ŞŞ. 2008. Deformation based seismic design of pile supported marine facilities. Ph.D. Thesis, Boğaziçi University, İstanbul, Türkiye, pp: 148.

Reese LC, Cox WR and Koop FD. 1974. Analysis of laterally loaded piles in sand. 6th Offshore Technology Conference, 6–9 May, Paper 2080, Houston, Texas, USA, pp: 473-483.

Reese LC, Cox WR and Koop FD. 1975. Field testing and analysis of laterally loaded piles in stiff clay, 7th Offshore Technology Conference, 1-4 May, Paper No. OTC 2321, Houston, Texas, USA, pp: 671-690.

SAP2000 V25. 2024. Structural Analysis Program. Computers and Structures, Inc., Berkeley, CA, USA.

TBDY 2018. Turkish building seismic code, disaster and emergency management presidency. Republic of Turkey Prime Ministry, Ankara, Türkiye.

Vamvatsikos D and Cornell CA. 2002. Incremental dynamic analysis. Earthquake Engin Struct Dynamics 31: 491–514.

Welch RC and Reese LC. 1972. Laterally loaded behavior of drilled shafts. Research Report, Center for Highway Research, University of Texas, Austin, USA, pp: 3-5-65-89.

Black Sea Journal of Engineering and Science
doi: 10.34248/bsengineering.1574470

Open Access Journal
e-ISSN: 2619 – 8991

Research Article
Volume 8 - Issue 1: 243-248 / January 2025

PREDICTING AND REDUCING PATIENT WAITING TIMES IN DENTAL CLINICS USING MACHINE LEARNING: A CASE STUDY FROM TÜRKİYE

Abdulkadir KESKİN[1]*

[1]*Istanbul Medeniyet University, Faculty of Engineering and Natural Sciences, Department of Statistics, 34674, İstanbul, Türkiye*

Abstract: Long waiting times in polyclinics are a critical factor affecting patient satisfaction and the efficient use of healthcare personnel and resources. This study applied machine learning (ML) algorithms to predict and reduce patient waiting times in a dental clinic in Türkiye. The daily data collected from the clinic included variables such as patient satisfaction, appointment patients, Walk-in patients, number of doctors and nurses, and dental technicians on duty. Six ML algorithms were tested: Decision Trees (DT), Linear Regression (LR), Support Vector Machines (SVM), Gaussian Process Regression (GPR), Kernel Regression (KR), and Neural Networks (NN). Among these, the GPR model achieved the best performance, accurately predicting patient waiting times with an R^2 value of 0.936 and RMSE of 0.075. This study highlights the potential of ML methods to enhance operational efficiency in healthcare management.

Keywords: Healthcare management, Waiting time prediction, Dental clinic, Machine learning

***Corresponding author:** *Istanbul Medeniyet University, Faculty of Engineering and Natural Sciences, Department of Statistics, 34674, İstanbul, Türkiye*
E mail: abdulkadir.keskin@medeniyet.edu.tr, (A. Keskin)
Abdulkadir KESKİN https://orcid.org/0000-0002-4795-1028

Received: October 27, 2024
Accepted: December 03, 2024
Published: January 15, 2025

Cite as: Keskin A. 2025. Predicting and reducing patient waiting times in dental clinics using machine learning: a case study from Türkiye. BSJ Eng Sci, 8(1): 243-248.

1. Introduction

Efficiency and service quality in healthcare have become increasingly important in recent years due to growing demand and a competitive environment. Patient satisfaction in a competitive market is regarded as one of the most critical indicators of a healthcare institution's success. Particularly, patient waiting times are a significant factor that directly affects patient satisfaction (Soremekun et al., 2011; Bahammam, 2023). Long waiting times hinder patients' access to services, disrupt operational processes within hospitals, and increase the workload of healthcare staff. This situation leads to a decline in the quality of healthcare services and erodes patients' trust in the healthcare institution. Delivering healthcare services promptly and managing patient flow efficiently helps patients feel better both physically and psychologically (Boudreaux and O'Hea, 2004; Mohsin et al., 2007).

A significant portion of the treatment time in hospitals impacts waiting times, directly influencing both patient satisfaction and the quality of care. Various studies on patient satisfaction have shown that waiting time has a direct effect on patients' decisions to return to the hospital (Anderson et al., 2007; Pitrou et al., 2009). Patients with long waiting times are expected to deliver lower values of overall service quality and thus, in turn, reduce the probability of returning to that hospital. Analysis of the relevant data obtained to reduce waiting times, use available resources effectively, and improve the process are important for health management. Specifically, data-driven methods like machine learning ML are highly effective tools for extracting meaningful insights from large datasets and identifying inefficiencies in service delivery (Stiglic et al., 2020; Keskin et al., 2024). ML algorithms offer various opportunities to improve service processes and enhance operational efficiency by making predictions based on historical data. Large and complex datasets that are difficult to analyze using traditional methods can be processed quickly and effectively using ML algorithms, significantly contributing to healthcare management. The applications of ML methods range from disease diagnosis and treatment to improving operational processes (Kononenko, 2001; Liao et al., 2016).

Several studies in literature have developed strategies to estimate patient waiting times. Cayirli and Veral (2003) explored the optimization of appointment systems and examined the effects of factors such as delays, service times, and patient and doctor preferences on waiting times. Similarly, Qu and Shi (2011) proposed models to manage both pre-scheduled appointments and real-time demands within the same system. These models provide valuable insights into optimizing patient demand while predicting waiting times. Another study developed a Kalman filter-based model to predict outpatient waiting times, finding that this model outperformed traditional

models (Montecinos et al., 2018). ML techniques used in dental clinics have been found to perform better than traditional methods. For instance, while Autoregressive integrated moving average (ARIMA) models predict waiting times in a specific clinic based on historical data, ML algorithms produce more dynamic and accurate results by considering current patient data and external factors (Channouf et al., 2007). In this context, studies on predicting waiting times contribute to more efficient use of resources while increasing patient satisfaction (Reid et al., 2013). Atalan and Keskin (2023) estimated patient waiting times in a dental clinic in Türkiye using a discrete-event simulation (DES) model. Komşuoğlu (2022) highlighted in a study on patient satisfaction in dental clinics that treatment duration is a significant variable influencing patient satisfaction.

The use of artificial intelligence, especially machine learning ML algorithms or artificial neural networks, is increasingly used in various fields, including healthcare management. ML-based models, such as artificial neural networks, generally provide much more accurate predictions than traditional statistical methods. For this reason, using such methods in healthcare management can improve operational efficiency, reduce costs, reduce staff workload, and increase patient satisfaction. In this study, which aims to improve patient waiting times, one of these problems, ML methods were used. Waiting time is considered one of the most critical indicators of healthcare quality and reducing it is important to increase patient satisfaction. The aim of the study was to estimate maximum waiting times and identify areas for improvement to increase operational efficiency and reduce waiting times. Six different ML algorithms were used to achieve this goal.

This study consists of four main sections. The first section emphasizes the importance of the topic and provides a comprehensive review of the relevant literature. The second section details the dataset and methodology employed in the study. In the third section, machine learning algorithms are compared to identify the ones with the best predictive performance, and the results are analyzed. Finally, the last section discusses the study's recommendations, limitations, and suggestions for future research.

2. Materials and Methods

In this study, clinical data collected over a 6-month period from an intermediate-sized dental clinic in Türkiye were utilized. Typically, for machine learning algorithms, 80% of the dataset is randomly selected for training, while the remaining 20% is used for testing. To ensure uniformity and enhance analytical accuracy, the dataset was normalized to a range between 0 and 1 prior to analysis. Table 1 presents the basic statistics related to daily appointment patients, walk-in patients, the number of doctors, nurses, and dental technicians, as well as the average waiting time (in minutes) in the dental clinic. In addition, the general satisfaction score of patients, which is critical for healthcare services, was also included in the model. The satisfaction score for the service received by the patients was obtained using a scale from one to ten. The dataset was obtained from daily records between March 1, 2024, and August 31, 2024. Descriptive statistics for the variables used are summarized in Table 1.

Before running machine learning algorithms, a feature selection analysis was conducted to assess the importance of the variables used in the models. Feature selection helps improve the accuracy of the ML model by eliminating unnecessary variables (Miao and Niu, 2016). Figure 1 shows the feature importance results of the variables based on the F-test algorithms. In the ML models predicting the average waiting time, it was found that the patient satisfaction score is the most important parameter. The second most significant parameter turned out to be the number of scheduled patients. In contrast, the number of technicians was identified as the least important parameter compared to the others. The patient satisfaction score was collected using a Likert scale ranging from 1 to 10, obtained after the patients received treatment. Waiting time was recorded in minutes.

Waiting times at the dental clinic were predicted using six different algorithms. The models used include Decision Trees (DT), Linear Regression (LR), Support Vector Machines (SVM), Gaussian Process Regression (GPR), Kernel Regression (KR), and Neural Networks (NN). In this study, various machine learning algorithms that perform well with different data structures were employed to analyze the data from the dental clinic. Decision Trees create a hierarchical model by dividing the dataset into branches, showing the effects of each variable under certain conditions (Song and Lu, 2015). Linear Regression assumes a linear relationship between the dependent and independent variables. Although it models this relationship using the least squares method and is simple and interpretable, it may be insufficient for non-linear relationships (Bertsimas and King, 2016). Support Vector Machines excel in solving non-linear problems by finding the best hyperplane that separates the data points (Gualtieri and Chettri, 2000). Gaussian Process Regression assigns distributions to each data point using a probabilistic approach, considering uncertainties. This method is particularly preferred in cases requiring high accuracy (Marrel and Iooss, 2024). Kernel Methods are effective in data analysis by projecting non-linear relationships into a higher-dimensional space (Arenas-Garcia et al., 2013). Thanks to their multilayered structures, neural networks learn from inputs, model complex relationships, and exhibit strong performance, especially with large data sets (Naskath et al., 2023). The characteristics of the six machine learning methods used in this research are detailed in Table 2. All analyses were performed with MATLAB 2024, a powerful software tool widely used in fields such as machine learning, simulation and artificial intelligence (The MathWorks, 2024).

Table 1. Descriptive statistics of the variables used to estimate patient waiting time

	Variable	Mean	Median	Maximum	Minimum	Std. Dev.	Obs.
Average waiting time	Output	12.93	13.90	29.73	4.13	8.11	158
Appointment Patients	Input	54.87	56.00	86.00	15.00	18.16	158
Walk-in patient	Input	13.46	12.00	28.00	4.00	5.67	158
Number of Dentists	Input	4.03	4.00	5.00	3.00	0.85	158
Number of Nurses	Input	2.96	3.00	4.00	2.00	0.80	158
Num Technicians	Input	1.49	1.00	2.00	1.00	0.50	158
Patient Satisfaction	Input	5.74	5.71	7.72	4.04	0.88	158

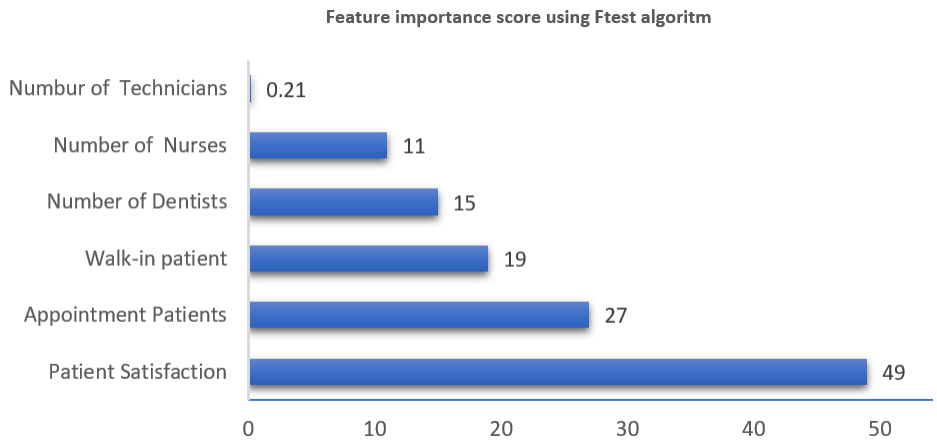

Figure 1. The feature selection information of ML model

Table 2. Parameters of machine learning algorithms used to predict waiting time

Algorithm	Parameters of the algorithm
Decision Trees (DT)	- MaxNumSplits: 100 - MinLeafSize: 1 - SplitCriterion: 'gdi' (Gini's diversity index)-Prune: 'off'
Linear Regression (LR)	- FitIntercept: true (bias term is included) - Solver: 'normal equations' (closed-form solution) - Lambda: 0 (no regularization, simple regression)
Support Vector Machines (SVM)	- KernelFunction: 'linear' - BoxConstraint: 1 (penalty parameter) - KernelScale: 'auto', Standardize: true
Gaussian Process Regression (GPR)	- KernelFunction: 'squaredexponential' - BasisFunction: 'constant' - Sigma: 1e-3 (noise variance)
Kernel Regression (KR)	- KernelFunction: 'Gaussian' - Bandwidth: 1 (kernel width)
Neural Network (NN)	- HiddenLayerSizes: 10 (single layer, 10 neurons) - ActivationFunction: 'relu' - Solver: 'adam' - MaxEpochs: 100, LearningRate: 0.01

In this study, the performance of the machine learning models was compared using commonly used evaluation metrics. To assess the accuracy and error rates of the models, the predictive performances of the algorithms were evaluated based on RMSE (Root Mean Square Error), MSE (Mean Square Error), R^2 (coefficient of determination), and MAE (Mean Absolute Error). The details are shown in the following formulas.

$$MAE = \frac{1}{n}\sum_{i=1}^{n} |y_i - \tilde{y}_i|^2 \quad (1)$$

$$MSE = \sum_{i=1}^{n} (y_i - \tilde{y}_i)^2 \quad (2)$$

$$R^2 = \sum_{i=1}^{n} \left[\frac{y_i - \tilde{y}_i}{y_i - \bar{y}_i}\right]^2 \quad (3)$$

$$RMSE = \sqrt{\frac{\sum_{i=1}^{n}(y_i - \tilde{y}_i)^2}{n}} \quad (4)$$

3. Results

The results of the machine learning models used to predict the average waiting time of patients in the dental clinic are presented in Table 3. The Decision Tree model obtained 0.087 RMSE, 0.916 R^2, 0.008 MSE and 0.065 MAE values in the training phase. In the testing phase, it showed a strong prediction performance with 0.086 RMSE and 0.917 R^2 values.

On the other hand, the Linear Regression model performed worse than the Decision Tree model. While the model reached 0.106 RMSE and 0.875 R^2 in the training phase, its performance decreased even further in the testing phase, with 0.848 R^2 and 0.116 RMSE, showing a lower accuracy than the training phase. Although the LR model performs well in linear relationships, its predictive power weakens in complex models. The Support Vector Machines model has an RMSE of 0.110 and an R^2 of 0.867 in the training phase. In the testing phase, it performed close to the LR model with 0.850 R^2 and 0.115 RMSE. Similar to the LR model, the SVM model performed worse than the DT model.

The Gaussian process regression model provided the best results during the training phase, with an RMSE of 0.075 and an R^2 of 0.938. In the testing phase, it exhibited performance nearly identical to the training phase, with an R^2 of 0.936 and an RMSE of 0.075. GPR represented the data very well, emerging as the best-performing ML model.

The kernel regression model showed similar performance to the decision tree model in the testing phase, with an RMSE of 0.087 and an R^2 of 0.916. In the testing phase, it performed almost identically to the DT model, with an R^2 of 0.915.

The neural network model had an RMSE of 0.112 and an R^2 of 0.861 during the training phase, indicating lower performance compared to other models. However, in the testing phase, it provided better results with an R^2 of 0.917 and an RMSE of 0.086.

Overall, the GPR model, alongside the DT model, has shown the best performance for predicting the average waiting time of patients in the clinic. In comparison to other models, the KR model also demonstrated strong performance. The training and testing performance of the GPR model is illustrated in Figure 2.

Table 3. Value of the measurement performance of ML models

Ml model algorithm	Train				Test			
Performance criteria	MAE	MSE	RMSE	R^2	MAE	MSE	RMSE	R^2
Decision Tree	0.065	0.008	0.087	0.916	0.063	0.007	0.086	0.916
Linear Regression	0.086	0.011	0.106	0.875	0.097	0.014	0.116	0.848
Support Vector Machines	0.085	0.012	0.110	0.867	0.094	0.013	0.115	0.850
Gaussian Process Regression	0.056	0.006	0.075	0.938	0.056	0.006	0.075	0.936
Kernel Regresion	0.067	0.008	0.087	0.916	0.060	0.008	0.087	0.915
Neural Network	0.081	0.013	0.112	0.861	0.065	0.007	0.086	0.917

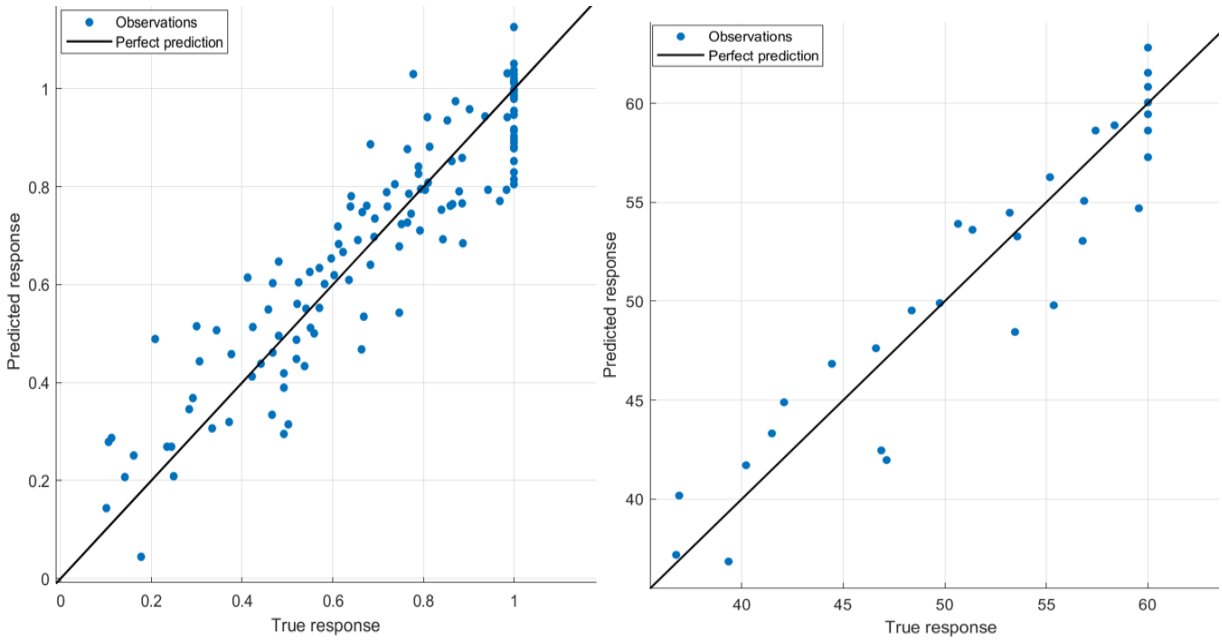

Figure 2. Performance of the train and test prediction phase of the GPR algorithm.

Health expenditures are increasingly becoming a significant economic burden on governments worldwide for various reasons, such as the rising average lifespan. A substantial portion of the expenditures is allocated to

fundamental resources in the healthcare sector, including medical personnel, facilities, equipment, and medications (Atalan and Şahin, 2024). Particularly in dental health services, the use of alternative resource allocation techniques can provide crucial data for decision-makers and policymakers by offering deeper insights into the economic impact of health expenditures.

Inefficient management of resources leads to increased costs in healthcare systems and delays in service delivery. Such inefficiencies financially and operationally challenge healthcare systems (Hung et al., 2019). Therefore, the use of increasingly popular machine learning ML methods in healthcare management is critical to achieving more efficient results. ML outperforms classical statistical methods by analyzing large data sets, detecting patterns, and optimizing resource allocation. Integrating ML techniques into healthcare management minimizes inefficient use of resources, saves costs, and improves service quality with smoother operations. This study proposes an ML algorithm that aims to increase resource management efficiency in healthcare. With ML based solutions, healthcare managers can improve decision-making processes, predict future resource needs more accurately, and support the development of sustainable healthcare systems.

4. Discussion and Conclusion

In this study, the waiting time was estimated by variables obtained using ML algorithms to minimize patient waiting times in dental clinics. Six different machine learning models were used in this context. Decision Trees DT, Linear Regression LR, Support Vector Machines SVM, Gaussian Process Regression GPR, Kernel Regression KR and Artificial Neural Networks NN were applied to the daily data obtained from dental clinics and the performance of each ML model was evaluated by means of certain criteria. Before the analysis, feature selection was used to evaluate the importance levels of the variables included in the models. According to the results obtained, it was found that the GPR model performed better than the other five ML models, while the SVM model showed the lowest performance. The obtained results show that the ML algorithm will be useful in estimating patient waiting times and improving the process. In addition, the integration of data-driven decision support systems into hospital management processes will contribute to more efficient resource use, improved service quality and optimized staff workload.

This study has two primary limitations. First, incorporating detailed information about staff shift schedules could potentially enhance the accuracy and comprehensiveness of the predictions. Second, applying the methodology to larger dental hospitals, where a broader range of parameters and average treatment durations for various procedures can be included, may yield more robust and generalizable results.

Future research can expand on the findings of this study in several ways. First, larger-scale data analyses can be conducted in bigger dental hospitals, incorporating diverse treatment types and patient densities to improve prediction accuracy. Second, multivariate models that include additional variables such as patient age, appointment time, and staff experience could provide more comprehensive insights. Third, real-time prediction systems powered by artificial intelligence could be developed to enhance operational efficiency and patient satisfaction. Fourth, international comparisons could be made by analyzing datasets from clinics in different countries to test the generalizability of the proposed methods. Lastly, optimization studies can focus on designing algorithms to minimize waiting times by optimizing patient and staff workflows.

Author Contributions

The percentages of the authors' contributions are presented below. The author reviewed and approved the final version of the manuscript.

	A.K
C	100
D	100
S	100
DCP	100
DAI	100
L	100
W	100
CR	100
SR	100
PM	100
FA	100

C=Concept, D= design, S= supervision, DCP= data collection and/or processing, DAI= data analysis and/or interpretation, L= literature search, W= writing, CR= critical review, SR= submission and revision, PM= project management, FA= funding acquisition

Conflict of Interest

The author declared that there is no conflict of interest.

Ethical Consideration:

Ethics committee approval was not required for this study because of there was no study on animals or humans.

References

Anderson RT, Camacho FT, Balkrishnan R. 2007. Willing to wait? The influence of patient wait time on satisfaction with primary care. BMC Health Serv Res, 7(1): 1-5. https://doi.org/10.1186/1472-6963-7-31/TABLES/2

Arenas-Garcia J, Petersen KB, Camps-Valls G, Hansen LK. 2013. Kernel multivariate analysis framework for supervised subspace learning: A tutorial on linear and kernel multivariate methods. IEEE Signal Proces Mag, 30(4): 16-29.

https://doi.org/10.1109/MSP.2013.2250591
Atalan A, Keskin A. 2023. Estimation of the utilization rates of the resources of a dental clinic by simulation. Sigma J Eng Nat Sci, 41(2): 423-432. https://doi.org/10.14744/sigma.2023.00045
Atalan A, Şahin H. 2024. Forecasting of the dental workforce with machine learning models. Müh Bil Araş Derg, 6(1): 125-132. https://doi.org/10.46387/bjesr.1455345
Bahammam FA. 2023. Satisfaction of clinical waiting time in ear, nose & throat departments of the Ministry of Health in Jeddah, Saudi Arabia. Health Serv Insights, 2023: 16. https://doi.org/10.1177/11786329231183315
Bertsimas D, King A. 2016. OR forum—An algorithmic approach to linear regression. Oper Res, 64(1): 2-16. https://doi.org/10.1287/opre.2015.1436
Boudreaux ED, O'Hea EL. 2004. Patient satisfaction in the Emergency Department: a review of the literature and implications for practice. J Emer Medic, 26(1): 13-26. https://doi.org/10.1016/J.JEMERMED.2003.04.003
Cayirli T, Veral E. 2003. Outpatient scheduling in health care: A review of literature. Prod Oper Manag, 12(4): 519-549. https://doi.org/10.1111/J.1937-5956.2003.TB00218.X
Channouf N, L'Ecuyer P, Ingolfsson A, Avramidis AN. 2007. The application of forecasting techniques to modeling emergency medical system calls in Calgary, Alberta. Health Care Manag Sci, 10(1): 25-45. https://doi.org/10.1007/S10729-006-9006-3/METRICS
Gualtieri JA, Chettri S. 2000. Support Vector Machines for classification of hyperspectral data. International Geoscience and Remote Sensing Symposium (IGARSS), July 24928, Honolulu, US, 2: 813-815. https://doi.org/10.1109/IGARSS.2000.861712
Hung M, Xu J, Lauren E, Voss MW, Rosales MN, Su W, Licari FW. 2019. Development of a recommender system for dental care using machine learning. SN Appl Sci, 1(7): 1-12. https://doi.org/10.1007/S42452-019-0795-7/FIGURES/1
Keskin A, Ersin İ, Atalan A. 2024. Price estimation of selected grains products based on machine learning for agricultural economic development in Türkiye. J Anim Plant Sci, 34(5): 1290-1301. https://doi.org/10.36899/japs.2024.5.0811
Komşuoğlu AF. 2022. Özel diş kliniklerinde hasta memnuniyeti ve diş sağlık hizmet kalitesi. İstat Uyg Bil Derg, 6: 1-11. https://doi.org/10.52693/JSAS.1200905
Kononenko, I. 2001. Machine learning for medical diagnosis: history, state of the art and perspective. Artif Intel Medic, 23(1): 89-109. https://doi.org/10.1016/S0933-3657(01)00077-X
Liao Z, Li D, Wang X, Li L, Zou Q. 2016. Cancer diagnosis through isomir expression with machine learning method. Curr Bioinformatics, 11(3): 57-63. https://doi.org/10.2174/1574893611666160609081155
Marrel A, Iooss B. 2024. Probabilistic surrogate modeling by Gaussian process: A review on recent insights in estimation and validation. Reliab Eng Syst Safety, 247: 110094. https://doi.org/10.1016/j.ress.2024.110094
Miao J, Niu L. 2016. A survey on feature selection. Proc Comp Sci, 91: 919-926. https://doi.org/10.1016/J.PROCS.2016.07.111
Mohsin M, Forero R, Ieraci S, Bauman AE, Young L, Santiano N. 2007. A population follow-up study of patients who left an emergency department without being seen by a medical officer. Emer Medic J, 24(3): 175-179. https://doi.org/10.1136/EMJ.2006.038679
Montecinos J, Ouhimmou M, Chauhan S. 2018. Waiting-time estimation in walk-in clinics. Int Transact Oper Res, 25(1): 51-74. https://doi.org/10.1111/itor.12353
Naskath J, Sivakamasundari G, Begum AAS. 2023. A study on different deep learning algorithms used in deep neural nets: MLP SOM and DBN. Wireless Personal Commun, 128(4): 2913-2936. https://doi.org/10.1007/S11277-022-10079-4/FIGURES/7
Pitrou I, Lecourt AC, Bailly L, Brousse B, Dauchet L, Ladner J. 2009. Waiting time and assessment of patient satisfaction in a large reference emergency department: A prospective cohort study, France. Eur J Emer Medic, 16(4): 177-182. https://doi.org/10.1097/MEJ.0B013E32831016A6
Qu X, Shi J. 2011. Modeling the effect of patient choice on the performance of open access scheduling. Int J Prod Econ, 129(2): 314-327. https://doi.org/10.1016/j.ijpe.2010.11.006
Reid RO, Ashwood JS, Friedberg MW, Weber ES, Setodji CM, Mehrotra A. 2013. Retail clinic visits and receipt of primary care. J General Internal Medic, 28(4): 504-512. https://doi.org/10.1007/S11606-012-2243-X/TABLES/5
Song Y-Y, Lu Y. 2015. Decision tree methods: applications for classification and prediction. Shanghai Arch Psychiatry, 27(2): 130-135. https://doi.org/10.11919/j.issn.1002-0829.215044
Soremekun OA, Takayesu JK, Bohan SJ. 2011. Framework for analyzing wait times and other factors that impact patient satisfaction in the emergency department. J Emer Medic, 41(6): 686-692. https://doi.org/10.1016/J.JEMERMED.2011.01.018
Stiglic G, Kocbek P, Fijacko N, Zitnik M, Verbert K, Cilar L. 2020. Interpretability of machine learning-based prediction models in healthcare. WIREs Data Mining Knowl Discov, 10(5): e1379. https://doi.org/10.1002/widm.1379
The MathWorks, Inc. 2024. MATLAB and Statistics Toolbox Release [2024a], Regression Learner. Massachusetts: The MathWorks, Inc.

Black Sea Journal of Engineering and Science
doi: 10.34248/bsengineering.1576901

Open Access Journal
e-ISSN: 2619 – 8991

Araştırma Makalesi (Research Article)
Cilt 8 - Sayı 1: 249-262 / Ocak 2025
(Volume 8 - Issue 1: 249-262 / January 2025)

AGREGA SEGREGASYONUNUN ASFALT KARIŞIMLARININ SIKIŞTIRILABİLİRLİĞİNE ETKİLERİNİN İNCELENMESİ

Ayhan Öner YÜCEL[1]*, Murat GÜLER[2]

[1]*Aydın Adnan Menderes University, Faculty of Engineering, Department of Civil Engineering, 09010, Aydın, Türkiye*
[2]*Middle East Technical University, Faculty of Engineering, Department of Civil Engineering, 06800, Ankara, Türkiye*

Özet: Asfalt karışımlarının sıkıştırılabilirliği, karışımların hedef yoğunluğa sıkıştırılmasının ne ölçüde kolay olduğunu tanımlamak için kullanılmaktadır. Asfalt karışımlarının sorunsuz şekilde sıkıştırılması, karışımdan beklenen performansı elde etmek için çok kritiktir. Agrega segregasyonu karışımdaki kaba agregaların belirli alanlarda kümelenmesi olarak tanımlanmakta olup, karışımın içyapısını etkileyen önemli bir durumdur. Bu çalışmada, agrega segregasyonunun asfalt karışımlarının hacimsel özelliklerine ve sıkıştırılabilirliğine etkileri incelenmiştir. Farklı koşulları simüle etmek için aynı sıkıştırma eforu uygulanarak ve aynı hedef yoğunlukta olmak üzere iki grup numune hazırlanmıştır. Her grup için ön koşulsuz-homojen ve iki seviyede segregasyona uğramış asfalt karışımı numuneleri Superpave yoğurmalı pres kullanılarak üretilmiştir. Segregasyona uğramış numuneler üretmek için tasarım gradasyonundaki kaba ve ince agregalar farklı oranlarda birleştirilerek hazırlanan karışımlar kalıba iki tabaka olarak yerleştirilip sıkıştırılmıştır. Üretilen numunelerin hacimsel özellikleri belirlenmiş ve numunelerin sıkışma eğrileri kullanılarak sıkıştırılabilirlik indeksleri hesaplanmıştır. Sonuçlar, agrega segregasyonunun, asfalt karışımlarının hacimsel özelliklerini ve sıkıştırılabilirliğini önemli ölçüde etkilediğini göstermektedir. Artan segregasyon seviyesi ile asfalt karışımlarının sıkıştırılabilirliğinin düştüğü ve aynı hedef yoğunlukta numune üretebilmek için çok daha fazla sıkıştırma eforu harcanması gerektiği belirlenmiştir.

Anahtar kelimeler: Asfalt karışımı, Agrega segregasyonu, Sıkıştırılabilirlik, Superpave, Sıkışma enerjisi indeksi

Investigation of the Effects of Aggregate Segregation on Asphalt Mixture Compactability

Abstract: The compactablility of asphalt mixtures refers to how easily these mixtures can be compacted to reach the target density. Proper compaction of asphalt mixtures is crucial for achieving the expected performance from the mixture. Aggregate segregation is defined as the concentration of coarse aggregates within the mixture in specific areas, and it is an important factor that affects the internal structure of the mixture. In this study, the effects of aggregate segregation on the volumetric properties and compactability of asphalt mixtures were investigated. To simulate different conditions, two groups of specimens were produced, applying the same compaction effort and targeting the same density. Unbiased-homogenous and segregated specimens at two levels were fabricated for each group using the Superpave gyratory compactor. To produce segregated samples, the mixtures prepared by combining the coarse and fine aggregates in the design gradation in different proportions and then placed in the mold in two layers before compaction. The volumetric properties of the produced samples were determined, and the compactability indices of the samples were calculated using the compaction curves. The results show that aggregate segregation significantly affects the volumetric properties and compactability of asphalt mixtures. It was also observed that the compactability of asphalt mixtures decreases with the increasing segregation level, and much more compaction effort is required to produce samples with the same target density.

Keywords: Asphalt mixture, Aggregate segregation, Compactability, Superpave, Compaction energy index

***Sorumlu yazar (Corresponding author):** Aydın Adnan Menderes University, Faculty of Engineering, Department of Civil Engineering, 09010, Aydın, Türkiye
E mail: aoyucel@adu.edu.tr (A. Ö. YÜCEL)
Ayhan Öner YÜCEL https://orcid.org/0000-0001-5888-2809
Murat GÜLER https://orcid.org/0000-0001-6939-3322

Gönderi: 31 Ekim 2024 **Received:** October 31, 2024
Kabul: 09 Aralık 2024 **Accepted:** December 9, 2024
Yayınlanma: 15 Ocak 2025 **Published:** January 15, 2025

Cite as: Yücel AÖ, Güler M. 2025. Investigation of the effects of aggregate segregation on asphalt mixture compactability. BSJ Eng Sci, 8(1): 249-262.

1. Giriş

Asfalt karışımı; agrega, bitüm ve hava boşluğu olmak üzere üç ana bileşenden oluşan heterojen bir malzemedir (Hu vd., 2022). Asfalt karışımlarının performansı birçok parametreye bağlı olmakla birlikte, içyapı özellikleri performansı etkileyen en önemli faktörlerden birisidir (Guo vd., 2022; Jing vd., 2023; Taheri-Shakib ve Al-Mayah, 2023; Yu vd., 2023). İçyapı, karışımı oluşturan bileşenlerin yerleşimi ve birbiriyle fiziksel etkileşimi olarak tanımlanmaktadır (Tashman vd., 2001; Masad ve Button, 2004). Asfalt karışımlarında içyapı, kullanılan malzemelerin özelliklerine, karıştırma-sıkıştırma sıcaklığına ve uygulanan sıkıştırma enerjine bağlı olarak değişmektedir (Sefidmazgi vd., 2013; Bessa vd. 2015; Zhang vd., 2016; Chen ve Wong, 2017).

Asfalt karışımlarının ağırlık olarak %90'ından fazlası agregalar tarafından oluşmaktadır ve bu yüzden karışımların sıkıştırılabilirliğinde agregaların büyük bir önemi vardır. Uygulanan sıkıştırma enerjisi agrega iskeletini önemli bir şekilde etkilemektedir ve farklı agrega yapısına sahip karışımlar için farklı sıkıştırma enerjisi uygulamak gerekmektedir (Gong vd., 2022; Jin vd., 2023; Selvam vd., 2023). Aynı nominal maksimum tane boyuna sahip olmasına rağmen gradasyonun farklı

olması durumunda tasarım yoğunluğuna ulaşmak için asfalt karışımlarının farklı seviyede sıkıştırılması gerekmektedir (Gao vd., 2014). İyi sıkışma performansı gösteren asfalt karışımları, tasarım yoğunluğuna kolayca sıkıştırılabilmekte ve servis koşullarında tutarlı seviyede stabilite sürdürülebilmektedir (Dubois vd., 2010). Sıcak karışım asfalt karışımlarının sıkıştırılması, hedeflenen kaliteye ulaşmadaki en önemli adımlardan birisidir. Yapılan karışım tasarımı ve kullanılan malzemelerin özelliklerine bakılmaksızın, iyi bir kaplama için asfalt karışımlarının düzgün sıkıştırılması çok önemlidir. Yapılan çalışmalar, esnek kaplamalardaki tekerlek izi, nem hasarı ve sökülme dahil olmak üzere erken dönem bozulmalarının %80'inin yetersiz sıkıştırmadan kaynaklandığını göstermektedir (Mohamed vd., 1993; Liu vd., 2007).

İyi bir agrega iskeleti, asfalt betonundan istenen performansı yakalayabilmek için önemli bir parametre olarak ortaya çıkmaktadır. Karışımdaki iri agregalar iskeleti oluştururken, çok daha ince agregalar ve bitüm birleşimi mastiği oluşturmaktadır (Onifade vd., 2016). Asfalt betonunda yük transferi, agrega iskeletini oluşturan tanecikler arasındaki temas noktaları vasıtasıyla gerçekleşmektedir. Mastik ise kaba agregalar arasında bağlayıcı bir kuvvet oluşturmakta ve aralarındaki boşlukları doldurarak yüksek dayanımlı bir karışım oluşturmaktadır (Cai vd., 2021). Yapılan çalışmalar agreganın karışım içerisindeki yerleşiminin performans ve sıkıştırılabilirlik açısından önemli olduğunu göstermektedir (Sefidmazgi vd., 2012; Dessouky vd., 2013; Jiang vd., 2017; Georgiou ve Plati, 2021).

Agrega segregasyonu, karışımdaki kaba agregaların belirli alanlarda kümelenmesi olarak tanımlanmaktadır. Asfalt karışımı içerisindeki kaba ve ince agregaların homojen olmayan dağılımı durumu laboratuvarda hazırlanan numunelerde ve sahada gerçekleşebilmektedir. Segregasyon durumunda, asfalt karışımlarının hacimsel ve mekanik özelliklerinde beklenenin dışında sonuçlarla karşılaşılmaktadır. Agrega segregasyonunun sonucu olarak genellikle karışımın alt kısımlarında kaba agrega yoğunluğu fazlayken, yüzeye yakın kısımlarda tasarım gradasyonuna göre kaba agrega miktarı azdır (Azari, 2005). Segregasyonun asfalt karışımının sıkıştırılabilirliğine ve hacimsel özelliklerine olumsuz etkileri olacağı bilinmektedir. Asfalt karışımlarının karıştırılması ve sıkıştırılması sırasında meydana gelecek agrega segregasyonunun asfalt betonunun mekanik performansı ve servis ömrü açısından kritik etkileri olduğu daha önceki çalışmalarda ortaya konulmuştur (Khedaywi ve White, 1995; Cross vd., 1998; Stroup-Gardiner ve Brown, 2000). Yapılan çalışmalar, agrega segregasyonunun, asfalt betonunun yorulma dayanımı, çekme dayanımı ve tekerlek izi direnci gibi mekanik performansını düşürdüğünü göstermektedir (Cross ve Brown, 1993; Cross vd., 1998). Segregasyon durumunda kaplamanın bakım-onarım maliyetleri de artmakta ve bu faaliyetlerin daha sık yürütülmesi gerekliliğini doğurmaktadır. Kaplamada segregasyonun gerçekleştiği bölgelerde bitüm içeriği ve asfalt betonu yoğunluğun, kaplamanın diğer kısımlarına göre daha düşük olduğu belirlenmiştir (Cross ve Brown, 1993). Buna karşın, ince agregaların yoğunlaştığı kaplama kısımlarında ise hava boşluğunun daha düşük olduğu, bitüm içeriğinin daha yüksek olduğu belirlenmiştir (Williams vd., 1996).

Asfalt kaplamalarda meydana gelen segregasyona ek olarak, laboratuvarda üretilen ve tasarım için yürütülen hacimsel ve mekanik testlerde kullanılan numunelerde meydana gelen agrega segregasyonu da kritik önem taşımaktadır (Yücel, 2019). Agrega segregasyonu gerçekleşen numuneler üzerinde yapılan testlerde, test sonuçları arasında yüksek sapmalar görülmekte ve tasarım aşamasında problemlere sebep olabilmektedir (Kwon vd., 2019; Huanan vd., 2021; Shi vd., 2023). Segregasyona uğramış numunelerdeki tutarsız sonuçlar, değişen agrega dağılımıyla etkilenen agrega temas yüzeyleri ve sıkışmada elde edilen düşük verimin sonuçları olarak yorumlanabilmektedir. Bu sebeplerle hem sahada hem de laboratuvarda meydana gelen agrega segregasyonu, asfalt karışımlarının sıkıştırılabilirliği ve performans özelliklerini önemli şekilde etkilenmekte ve bu konuyu irdeleme ihtiyacı doğmaktadır. Laboratuvar ortamında asfalt karışımlarının sıkıştırılabilirliği Superpave yoğurmalı pres kullanılarak değerlendirilebilmektedir. Üretilen numunelerin hacimsel sonuçları sıkıştırılabilirlik açısından önemli göstergeler olmakla birlikte birçok araştırmacı tarafından sıkışma indeksleri de geliştirilmiştir (Rand, 1997; Bahia vd., 1998; Mahmoud ve Bahia, 2004; Mallick, 1999). Bahia vd. (1998) Superpave yoğurmalı pres tarafından ölçülen sıkışma eğrilerinin sıkışma indekslerinin hesaplanması için kullanılabileceğini ve bu indekslerin karışımların yapım ve servis sırasındaki performansını temsil ettiğini belirlemişlerdir. Ayrıca yazarlar tarafından asfalt karışımlarının yapım ve servis sırasındaki potansiyel performanslarını değerlendirmek için, sıkışma enerjisi indeksi ve trafik sıkıştırma indeksi belirlenmiştir.

Bu çalışmada, laboratuvar teknikleri kullanılarak ön koşulsuz-homojen ve segregasyona uğramış Superpave yoğurmalı pres numuneleri üretilmiştir. Üretilen farklı segregasyon seviyesindeki numunelerin hacimsel özellikleri değerlendirilmiştir. Farklı segregasyon seviyesinde hazırlanan numunelerin; aynı sıkıştırma eforu uygulanması durumunda hacimsel özellikleri ve aynı yoğunluğa ulaşmaları için uygulanması gereken sıkıştırma enerjileri irdelenmiştir. Bu çalışmada, agrega segregasyonunun, asfalt betonu sıkıştırılabilirliğine etkilerinin ortaya konulması hedeflenmiştir. Bu sebeple, Superpave yoğurmalı pres kullanılarak üretilen numunelerinin hacimsel özellikleri ve sıkıştırma parametreleri incelenmiştir.

2. Materyal ve Yöntem

2.1. Superpave Karışım Tasarım Metodu

Superpave karışım tasarım yönteminde asfalt karışımlarını sıkıştırmak için Superpave yoğurmalı pres kullanılmaktadır (Şekil 1). Bu ekipman, sıcak karışım asfalt numunelerini sahada elde edilene benzer bir yoğunlukta sıkıştırmak için geliştirilmiştir (Roberts vd., 1996). Bu yöntemle sıkıştırılan numunelerdeki agrega doğrultuları da sahadaki duruma benzerdir (Tashman vd., 2001). Superpave yoğurmalı pres ile numune sıkıştırmak için uygulanan düşey basınç, yoğurma açısı ve sıkıştırma devir hızı gibi parametreler kullanıcı tarafından tanımlanabilmekte ve sıkıştırma enerjisinin kontrol edilmesini sağlamaktadır. Superpave tasarım yönteminde bu parametreler için sabit değerler kullanılmaktadır. Sıkıştırma işlemi için sıkıştırma başlığı tarafından uygulanacak düşey basınç 600 kPa ve sıkıştırma açısı 1.25° olarak belirlenmiştir. Yoğurma işleminin dakikada 30 devir olacak şekilde uygulanması gerekmektedir. Numuneye uygulanacak sıkıştırma devir sayısı ise trafik yüküne göre değişmektedir ve takip edilen standartta (AASHTO R35, 2010) farklı trafik hacimleri için uygulanması gereken devir sayıları belirtilmiştir. Böylelikle saha koşulları daha iyi simüle edilmiş olacaktır. Superpave yoğurmalı pres 100 mm veya 150 mm çapında numune üretmeye uygun olsa da Superpave tasarım şartnameleri 150 mm çapında numune kullanımını gerektirmektedir. Tasarımda uygulanacak sıkıştırma devir sayıları, 20 yıllık tasarım trafik hacmine göre belirlenmektedir. Farklı trafik hacimleri için uygulanması gereken sıkıştırma devir sayısı Tablo 1'de verilmiştir (AASHTO R35, 2010).

Şekil 1. Superpave yoğurmalı pres.

Tablo 1. Superpave yoğurmalı pres devir sayıları (AASHTO R35, 2010)

Tasarım ESAL (milyon)	Sıkıştırma parametreleri		
	N_i	N_d	N_m
<0,3	6	50	75
0,3 to <3	7	75	115
3 to <30	8	100	160
≥30	9	125	205

Bu tabloda; N_i: ilk sıkıştırma devir sayısı, N_d: tasarım sıkıştırma devir sayısı ve N_m: maksimum sıkıştırma devir sayısı olarak tanımlanmaktadır. N_i ve N_m devir sayıları karışımın sıkıştırılabilirliğini değerlendirmek için kullanılırken, N_d devir sayısında sıkıştırılan numuneler optimum bitüm içeriğini belirlemek için kullanılmaktadır. N_d'nin açılımı N-tasarım olup tasarım trafik hacmi sonrasında sahada gerçekleşmesi beklenen yoğunlukla aynı yoğunlukta numune üretmek için uygulanması gereken yoğurmalı pres devir sayısını göstermektedir. Karışım tasarımında seçilen N_d devir sayısında sıkıştırılan numunelerden %4 hava boşluğunu sağlayan bitüm içeriği optimum değer olarak seçilmektedir. N_i'nin açılımı N-ilk olup karışım sıkıştırılabilirliğini değerlendirmede kullanılmaktadır. Çok hızlı sıkışan numuneler sahada kolay bütünlüğünü kaybedebilmekte ve trafik yükleri altında stabilitesini koruyamamaktadır (Leiva ve West, 2008). %4 hava boşluğuna göre tasarlanan karışımlarda, N_i devir sayısında sıkıştırılan numunelerde hava boşluğu en az %11 olmalıdır. N_m'nin açılımı N-maksimum olup laboratuvarda uygulanacak ve sahada asla ulaşılamayacak yoğunlukta numune üretmek için gerekli yoğurma devir sayısıdır. Bu devir sayısında sıkıştırılacak numunelerde hava boşluğunun çok düşük olması trafik yükleri altında çok fazla sıkışıp tekerlek izi gibi problemler yaratacağının göstergesidir. N_m devir sayısıyla sıkıştırılan numunelerde minimum hava boşluğu %2 olmalıdır. Bu çalışmada, tasarım ESAL değerleri 3-30 milyon aralığında kabul edilerek N_i=8, N_d=100 ve N_m=160 sıkıştırma devir sayılarına göre karışım tasarımları yapılmıştır.

2.2. Malzemeler ve Karışım Tasarımı

Bu çalışmada, farklı saha koşullarını simüle edebilmek için iki grup numune hazırlanmıştır. İlk gruptaki numuneleri (G1) üretmek için aynı sıkıştırma eforu uygulanmıştır. Bu sıkıştırma devir sayısı, önceki bölümde tartışıldığı gibi 100 devir olarak belirlenmiştir. İkinci gruptaki numuneler (G2) ise %4 hava boşluğuna karşılık gelen yoğunlukta sıkıştırılmıştır. Bu iki grup için farklı kaynaklardan elde edilen kalker agregaları ve 50/70 penetrasyon sınıfında bitüm kullanılmış olup kullanılan agrega ve bitüm özellikleri Tablo 2'de verilmiştir.

Tablo 2. Agrega ve bitüm özellikleri

Agrega özellikleri		Şartname	G1 Tasarımı	G2 Tasarımı
			Kalker-1	Kalker-2
Kaba agrega	Hacim özgül ağırlık	AASHTO T 85	2,684	2,680
	Zahiri özgül ağırlık		2,711	2,714
	Su emme (%)		0,367	0,473
İnce agrega	Hacim özgül ağırlık	AASHTO T 84	2,664	2,630
	Zahiri özgül ağırlık		2,695	2,669
	Su emme (%)		0,432	0,553
Filler	Zahiri özgül ağırlık	AASHTO T 100	2,704	2,693
Los Angeles aşınma (%)		AASHTO T 96	32	29
Bitüm özellikleri			Bitüm-1	Bitüm-2
Penetrasyon (25°C, 0.1 mm)		AASHTO T 49	54	60
Yumuşama noktası (°C)		AASHTO T 53	50	49,5
Düktilite (cm @ 25°C)		AASHTO T 51	>100	>100
Özgül ağırlık		AASHTO T 228	1,036	1,033

Tasarım aşamasında, sıcak karışım asfalt numuneleri 150 mm çapında ve 115 mm yüksekliğinde olacak şekilde hazırlanmış ve sıkıştırılmıştır. Her bir numune için 4900 gram agrega kullanılmıştır. Tasarımlarda kullanılan agrega gradasyonu Şekil 2'de gösterilmektedir. Tasarım aşamasında her iki tasarım için de 100 devir sıkıştırma uygulanmış ve %4 hava boşluğuna karşı gelen bitüm oranları optimum değerler olarak seçilmiştir. Sıkıştırılmış numuneler hacimsel olarak değerlendirilerek karışım tasarımları yürütülmüştür. N_d sıkıştırma devir sayısına ek olarak N_i ve N_m sıkıştırma devir sayılarında hava boşluğu oranları da kontrol edilmiştir. Tasarımlarda kullanılan bitümler için Brookfield viskozite deneyleri yardımıyla karıştırma ve sıkıştırma sıcaklıkları belirlenmiştir. AASHTO T316 standardına göre yürütülen testlerde karıştırma ve sıkıştırma sıcaklıkları 0,17 Pa.s±0,02 ve 0,28 Pa.s±0,03 viskozite değerlerine karşılık gelen sıcaklıklar olarak seçilmiştir. G1 tasarımında kullanılan bitüm için karıştırma ve sıkıştırma sıcaklıkları 152°C ve 140°C seçilmişken, G2 dizaynı için kullanılan bitümde 154°C ve 143°C olarak belirlenmiştir. Agrega ve bitüm karışımı hazırlandıktan sonra sıkıştırma öncesi numuneler 2 saat boyunca sıkıştırma sıcaklığında fırında bekletilerek yaşlandırılmıştır. Bu prosedür ile karışımın hazırlanması, taşıma ve serilme safhasındaki yaşlanma durumu simüle edilmektedir. Yaşlandırma işleminin yapılmaması durumunda daha düşük bir optimum bitüm içeriği bulunacak ve kaplamada durabilite kaybına neden olacaktır. Farklı bitüm oranları için üretilen numuneler için sıkıştırılmış özgül ağırlık (G_{mb}) ve sıkıştırılmamış numuneler kullanılarak maksimum özgül ağırlık (G_{mm}) değerleri bulunmuştur. Tasarım için yapılan tüm değerlendirilmelerin sonucunda %4 hava boşluğuna karşı gelen optimum bitüm içerikleri G1 ve G2 tasarımları için sırasıyla %5 ve %4,75 olarak belirlenmiştir.

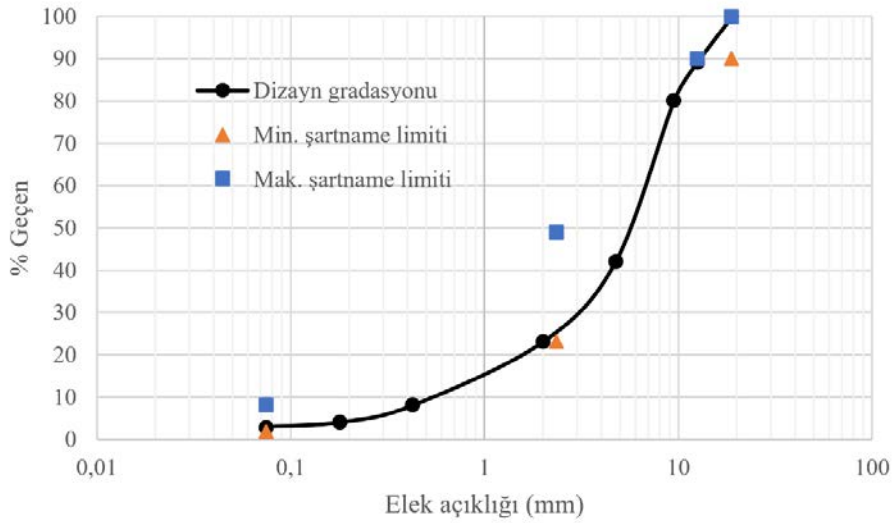

Şekil 2. Agrega gradasyon eğrisi ve şartname limitleri.

2.3. Laboratuvarda Segregasyona Uğramış Asfalt Karışımlarının Üretimi

Agrega segregasyonunun, asfalt karışımı özelliklerine etkilerini araştırmak amacıyla farklı teknikler kullanılarak laboratuvar ortamında segregasyona uğramış numuneler üretmek mümkündür. Bu tekniklerin en eskilerinden olan yöntemde, tasarım gradasyonunun kaba ve ince kısımları farklı oranlarda karıştırılarak yapay olarak segregasyona uğramış numuneler üretilmiştir (Khedaywi ve White, 1995). Bahsedilen çalışmada üretilen farklı seviyelerdeki segregasyonları temsil eden Marshall numunelerinin agrega gradasyonları tasarım gradasyonundan tamamen farklı olmaktadır ve numunelerin fiziksel ve mekanik özelliklerinde büyük farklılıklar olduğu görülmektedir. Bir başka çalışmada ise tasarım gradasyonundan ufak sapmalarla farklı gradasyonlar elde edilmiş ve bu gradasyonlarda numuneler üretilmiştir (Xuelian vd., 2018). Segregasyon derecesi ise orijinal gradasyonun her elek boyu için yüzde geçenden toplam sapma miktarına göre belirlenmektedir. Agrega gradasyonunun korunarak, numunelerde meydana gelecek düşey yöndeki agrega segregasyonunu simüle etmek için de yöntemler geliştirilmiştir. Numune içerisindeki agrega segregasyonunu temsil etmek için geliştirilen yöntemlerde, orijinal gradasyon korunarak kaba agregaların numunelerin alt kısmında yoğunlaşması hedeflenmiştir (Azari, 2005; Yücel, 2019). Bu yöntemle, aynı gradasyona sahip, düşey doğrultuda homojen olmayan agrega dağılımına sahip numuneler üretmek mümkündür. Bu metot, laboratuvarda üretilen numunelerde ve sahada asfalt karışımını yerleştirme sırasında meydana gelen düşey doğrultudaki segregasyonu başarılı şekilde temsil etmektedir. Bu yöntemde, tasarım gradasyonu No.4 (4,75 mm) elekten geçen ve kalan agregalar olarak ikiye ayrılmakta ve farklı oranlarda karıştırılarak kaba agreganın daha yoğun ve daha az yoğun olduğu iki ayrı agrega grubu elde edilmektedir. Bu agregalar ayrı olarak bitümle karıştırılmakta ve kalıba 2 tabaka şeklinde yerleştirilerek sıkıştırılmaktadır. Alt tabakaya kaba agrega yoğunluklu karışım, üst tabakaya ise ince agrega yoğunluklu karışım yerleştirilmektedir. Bu yöntemle, numunedeki toplam agrega miktarı tasarım gradasyonunda olup, faklı seviyelerde düşey agrega segregasyonuna uğramış numuneler elde edilmektedir.

Bu çalışma kapsamında G1 ve G2 grupları için 3 farklı segregasyon seviyesinde numuneler üretilmiştir. Bu segregasyon seviyeleri; homojen-ön koşulsuz (H), orta seviye segrege-ön koşullu (O) ve yüksek seviye segrege-ön koşullu (Y) olarak sınıflandırılmıştır. Her bir segregasyon seviyesinde 6 numune olmak üzere, toplamda 2 grup için 36 numune üretilip değerlendirilmiştir (Tablo 3).

Tablo 3. Laboratuvarda üretilen numune tipleri

Tasarım	Segregasyon seviyesi	Numune sayısı
G1	H	6
	O	6
	Y	6
G2	H	6
	O	6
	Y	6

Ön koşulsuz numuneler elde etmek için, asfalt karışımlarının hazırlaması ve kalıba yerleştirilmesi esnasında mümkün olduğunca homojen olmaları hedeflenmiştir. Orta ve yüksek seviyede segregasyona uğramış ön koşullu numuneler üretmek için ise asfalt karışımları kalıba iki tabaka olarak yerleştirilmiş ve sıkıştırılmıştır. Agrega segregasyonu gerçekleştiğinde genellikle kaba agregaların karışımın alt kısımlarında kaldığı, yüzeye yakın bölgelerde kaba agrega yoğunluğunun azaldığı bilinmektedir. Bu sebeple, ön koşullu numunelerde alt katmana tasarım gradasyonuna göre daha kaba, üst katmana ise daha ince bir karışım yerleştirilmesi planlanmıştır. Bu katmanlarda kullanılacak agregalar, tasarım gradasyonu temel alınarak belirlenmiştir. Tasarım gradasyonunda agregaların %58'inin 4,75 mm açıklıklı elek üzerinde kaldığı, %42'sinin ise bu elekten geçtiği görülmektedir. Numunenin alt ve üst katmanlarında kullanılacak agregaları seçmek için tasarım gradasyonundaki 4,75 mm açıklıklı elekten geçen ve kalan agregalar farklı oranlarda karıştırılmıştır. Orta seviye segrege olmuş numunelerde alt katmanı oluşturacak kaba kısım için tasarım gradasyonundaki kaba agregaların %68'i, ince agregaların ise %40'ı kullanılmıştır. Numunelerin üst kısmını oluşturacak ince kısım için ise kaba agregaların kalan %32'lik kısmı ve ince agregaların %60'ı kullanılmıştır. Yüksek seviye segrege olmuş numune üretiminde ise numunelerin alt katmanını oluşturacak kaba kısım için tasarım gradasyonundaki kaba agregaların %73'ü, ince agregaların ise %40'ı kullanılmıştır. Numunelerin üst kısmını oluşturacak ince kısım için ise kaba agregaların kalan %27'si ve ince agregaların %60'ı kullanılmıştır. Bu oranların seçilmesine laboratuvar ortamında yapılan deneme dökümleriyle karar verilmiştir. Alt ve üst katmanlarda kullanılan agregaların toplamı, tasarım agrega gradasyonuna eşittir. Tablo 4'te tasarım gradasyonu ile orta ve yüksek seviye segregasyon için hazırlanacak katmanların gradasyonları verilmiştir.

Tablo 4. Tasarım gradasyonu ve katman gradasyonları

Elek açıklığı (mm)	% Geçen				
	Tasarım gradasyonu	Orta seviye segregasyon (O)		Yüksek seviye segregasyon (Y)	
		Kaba kısım	İnce kısım	Kaba kısım	İnce kısım
19	100	100	100	100	100
12,5	89	86,7	92	86,4	92,7
9,5	80	75,8	85,4	75,3	86,8
4,75	42	29,9	57,6	28,4	61,7
2	23	16,4	31,5	15,6	33,8
0,425	8	5,7	11	5,4	11,7
0,18	4	2,8	5,5	2,7	5,9
0,075	3	2,1	4,1	2	4,4

İki katman olarak sıkıştırılan ön koşullu numunelerin kaba ve ince kısımlarında kullanılacak bitüm miktarı asfalt film kalınlıklarına göre belirlenmiştir. İlk olarak G1 ve G2 tasarımları için optimum bitüm içeriğinde asfalt film kalınlıkları hesaplanmıştır. İnce ve kaba kısımlardaki bitüm içeriği ise bu kısımlardaki asfalt film kalınlıklarının tasarım asfalt film kalınlıklarına eşit olacağı varsayımına göre yapılmıştır. Asfalt film kalınlığı eşitlik 1 yardımıyla hesaplanmaktadır (Roberts vd., 1996; Debao vd., 2013).

$$FT = 1000x\frac{P_{be}}{SAxP_sxG_b} \quad (1)$$

Burada:
FT = Asfalt film kalınlığı (µm)
P_{be} = Efektif bitüm içeriği (karışım ağırlığına göre, %)
P_s = Ağırlık cinsinden agrega yüzdesi (%)
SA = Agrega yüzey alanı (m^2/kg)
G_b = Bitüm özgül ağırlığı

Asfalt film kalınlığı hesaplamalarında tasarım aşamasında belirlenen hacimsel özelliklerin yanında agrega yüzey alanlarının da hesaplanması gerekmektedir. Agrega yüzey alanlarını hesaplamak için belirli eleklerden geçen agrega yüzdesi ile bu elekler için belirlenen katsayılar çarpılmaktadır. G1 ve G2 tasarımlarında aynı agrega gradasyonu kullanıldığından bu tasarımlar için hesaplanan agrega yüzey alanı Tablo 5'te gösterilmiştir.

Tablo 5. Agrega yüzey alanlarının hesaplanması

Elek açıklığı, mm (in)	% Geçen	Yüzey alanı faktörü	Yüzey alanı (m^2/kg)
19 (3/4)	100	0,41	
12,5 (1/2)	89	0,41	0,41x1=0,41
9,5 (3/8)	80	0,41	
4,75 (No.4)	42	0,41	0,41x0,42=0,17
2,36 (No.8)	25,5	0,82	0,82x0,255=0,21
1,18 (No.16)	15,2	1,64	1,64x0,152=0,25
0,6 (No.30)	9,7	2,87	2,87x0,097=0,28
0,3 (No.50)	6	6,14	6,14x0,06=0,37
0,15 (No.100)	3,7	12,29	12,29x0,037=0,45
0,075 (No.200)	3	32,77	32,77x0,03=0,98
Toplam			3,12 m^2/kg

G1 ve G2 tasarımları için yukarıda verilen eşitlik kullanılarak asfalt film kalınlıkları sırasıyla 13,82 µm ve 13,31 µm olarak hesaplanmıştır. G1 ve G2 numuneleri için hesaplanan ince ve kaba gradasyonlu katmanlarda kullanılacak bitüm miktarları Tablo 6'da özetlenmiştir. Bu çalışma kapsamında üretilen numuneler daha sonra tekrarlı sünme testine tabi tutulacağından numune boyutlarının bu teste uygun olması gerekmektedir. Tekrarlı sünme testi için üretilen 150 mm çapında Superpave numunelerinden karot alınarak elde edilen 100 mm çapında numuneler test için kullanılmaktadır. Numune uzunluğu ise üst ve alt noktalardan kesildikten sonra 150 mm olmalıdır. Bu yüzden, kesilmeden önceki numune boyunun 165 mm civarında olması hedeflenmektedir. Bu boyutlarda numune üretmek için her bir numune için 7000 gram agrega kullanılmıştır. Ön koşulsuz numunelerde 7000 gram agrega optimum bitüm içeriğinle karıştırılarak fırına konulmuş, 2 saatlik yaşlandırma süresinden sonra Superpave numune kalıbına mümkün olduğunca homojen olacak şekilde yerleştirilmiş ve sıkıştırılmıştır. Ön koşullu numunelerde ise kaba ve ince kısımlar ayrı ayrı hazırlanmış ve iki ayrı kapta yaşlanmaları için fırına konulmuştur. 2 saatlik sürenin ardından Superpave numune kalıbına ilk olarak kaba karışım yerleştirilmiş, daha sonra yüzeyi spatula ile düzlenerek ince karışım eklenmiştir. Kalıba yerleştirilen numunelerin alt ve üstüne filtre kağıtları ve çelik plakalar yerleştirilmektedir. Böylelikle karışımın sıkıştırma başlığına veya kalıba yapışması engellenmekte ve düzgün bir karışım hazırlanması sağlanmaktadır. Böylelikle ön koşulsuz numunelerle aynı gradasyonda ve bitüm içeriğinde olan fakat kaba ve ince agrega dağılımı homojen olmayan numunelerin üretimi sağlanmıştır.

Tablo 6. Kaba ve ince gradasyonlu katmanlarda kullanılacak bitüm miktarları

Tasarım	Parametreler	Tasarım gradasyonu	Orta seviye segregasyon		Yüksek seviye segregasyon	
			Kaba kısım	İnce kısım	Kaba kısım	İnce kısım
G1	Agrega Yüzey alanı, m^2/kg	3,12	2,34	4,13	2,25	4,39
	Bitüm içeriği, %	5	3,98	6,28	3,85	6,61
	Agrega ağırlığı, g	7000	3936,8	3063,2	4139,8	2860,2
	Bitüm ağırlığı, g	368,5	163,1	205,4	165,9	202,6
G2	Agrega Yüzey alanı, m^2/kg	3,12	2,34	4,13	2,25	4,39
	Bitüm içeriği, %	4,75	3,76	5,99	3,64	6,31
	Agrega ağırlığı, g	7000	3936,8	3063,2	4139,8	2860,2
	Bitüm ağırlığı, g	349,1	153,9	195,2	156,5	192,6

Superpave yoğurmalı pres ekipmanı bir yazılım vasıtasıyla kontrol edilebilmektedir. Bu yazılımda sıkıştırmada uygulanacak devir sayısı tanımlanarak sıkıştırma işlemi yapılabilmektedir. G1 numunelerinin aynı sıkıştırma eforu ile sıkıştırılması hedeflendiğinden tüm numuneler için yazılıma hedef sıkıştırma devir sayısı 100 devir olarak girilmiş ve cihaz bu devir sayısına ulaştığında sıkıştırma işlemini sonlandırmıştır. G2 numunelerinin ise aynı hedef yoğunlukta sıkıştırılması hedeflenmiştir. Bu yazılımda, kalıba yerleştirilen asfalt karışımın ağırlığı girilebilmekte ve numune yükseklikleri her devirde kaydedilmektedir. Kullanılan kalıpların çapı da yazılıma 150 mm olarak tanımlanmıştır. Numune ağırlığı, çapı ve yüksekliği verisini kullanarak, yazılım her sıkıştırma devrinde numunenin yoğunluğunu hesaplayabilmektedir. Bu sayede yazılıma hedef bir yoğunluk tanımlanıp numunelerin hedef yoğunluğa ulaşıncaya kadar sıkıştırılması sağlanabilmektedir. Yazılım tarafından hesaplanan yoğunluk değeri, gerçek ölçülen yoğunluk değerinden bir miktar farklıdır. Bunun sebebi numunenin alt, üst ve yan yüzeylerdeki boşlukların fazla olmasıdır (Masad vd., 2002). Numunelerin gerçek yoğunluk değerleri ancak özgül ağırlık deneyi ile bulunabilir. Deneme numuneleri üretilerek hesaplanan ve gerçek yoğunluk değerleri arasındaki ilişki incelenmiş ve düzeltme faktörü belirlenmiştir. G2 numuneleri %4 hava boşluğuna karşılık gelen yoğunlukta sıkıştırılmak istendiğinden, bu hava boşluğu için ulaşılması gereken gerçek yoğunluk değeri belirlenmiş ve düzeltme faktörü kullanılarak yazılımda tanımlanacak yoğunluk değeri belirlenmiştir. G2 numunelerinin sıkıştırılması esnasında hesaplanan yoğunluk değeri yazılıma tanımlanmış ve numuneler bu yoğunluğa ulaşıncaya kadar sıkıştırma işlemi devam etmiştir. Sonuçta, G1 numuneleri 100 devir sıkıştırma uygulanarak elde edilmişken, G2 numuneleri %4 hava boşluğuna karşı gelen yoğunluğa ulaşacak şekilde sıkıştırılmıştır. Böylelikle, farklı segregasyon seviyesindeki numunelerin aynı sıkıştırma eforu altındaki hacimsel özellikleri ve aynı yoğunluğa ulaşması için uygulanması gereken sıkıştırma eforunun incelenmesi sağlanmıştır.

2.4. Sıcak Karışım Asfaltların Sıkıştırılabilirliği

Superpave tasarım yönteminin kullanımının yaygınlaşmasıyla birlikte, asfalt karışımlarının sıkıştırılabilirliğini değerlendirmek için birçok metot geliştirilmiştir. Aynı sıkıştırma eforu altında sıkıştırılan numunelerin hacimsel özellikleri ve aynı hedef yoğunluğa ulaşmak için uygulanması gereken sıkıştırma devir sayıları karışımların sıkıştırılabilirliği bakımından önemli parametrelerdir.

Superpave yoğurmalı pres, sıkıştırma süresince elde edilen yükseklik ve sıkışma yüzdesine ek olarak numunelerin kayma direncini de kaydetmektedir. Kayma direnci parametresi, her sıkıştırma devrinde numunede ölçülen en büyük kayma gerilmesi olup yüksekliğe benzer şekilde sıkıştırma boyunca kaydedilmektedir. Guler vd. (2000) yoğurmalı pres ile sıkıştırma boyunca karışımların kayma direncini ölçmek için bir prosedür geliştirmişlerdir. Bu çalışmada kayma direncinin, gradasyon, bitüm içeriği ve sıcaklığa çok hassas olduğu görülmüştür. Ayrıca, hesaplanacak kayma direncinin karışımların sıkıştırılabilirliği ve tekerlek izi dayanımı için önemli gösterge olduğu ortaya konulmuştur. Sıkıştırılabilirlik değerlendirilmesi için önerilen parametrelerden ilki %92 G_{mm}'e ulaşıldığı sıkıştırma devrinde kaydedilen kayma direncidir. Bu değerin çok yüksek olması karışımın sıkıştırılabilirliğinin düşük olduğunun göstergesidir. İkinci parametre ise %86 ile %92 G_{mm} arasında, kayma direnci eğrisi altında kalan alanın, G_{mm} (% sıkışma) eğrisi altında kalan alana oranından elde edilen enerji değeridir (E). Bu değer, karışımı %14 hava boşluğundan %8 hava boşluğuna sıkıştırmak için gerekli enerjiyi temsil etmektedir. Sahada karışımlar %92 G_{mm} değerine ulaşıncaya kadar sıkıştırıldığından, hesaplanan bu parametre sahadaki sıkışma koşullarını temsil etmektedir.

Bunların yanında Superpave yoğurmalı pres yazılımından elde edilen sıkışma eğrilerini kullanarak hesaplanan indeksler de önemli sıkıştırılabilirlik parametreleridir. Sıkışma enerjisi indeksi (CEI) yaygın olarak kullanılan indekslerdendir (Ma vd., 2020). Superpave yoğurmalı presin kaydettiği verilerle elde edilen sıkışma eğrisinde, sıkıştırma devir sayılarına karşı gelen sıkışma yüzdesi (%G_{mm}) elde edilmektedir (Şekil

3). Sıkışma eğrisinin, 8. sıkıştırma devri ve maksimum özgül ağırlığın ($G_{mm,max}$) %92'sine karşılık gelen devir aralığında kalan alan CEI indeksini vermektedir (Mahmoud ve Bahia, 2004). CEI sayısı %92 G_{mm} değerine ulaşmak için sahada sıkıştırıcı silindirler tarafından yapılacak işi temsil etmektedir. Düşük CEI değerleri sahada daha kolay sıkıştırma gerçekleşeceğinin göstergesidir. Daha hızlı sıkışma karışımın daha işlenebilir ve sıkıştırılabilir olduğunu gösterdiğinden istenilen bir durumdur. Çok düşük CEI değeri karışımın bütünlüğünü kaybetmeye meyilli olduğunun göstergesidir ve bu durumdan kaçınılmalıdır (Mahmoud ve Bahia, 2004). 8. devirdeki G_{mm} değeri sahada serilen asfalt karışımının sericiden çıktığı durumu temsil etmektedir. %92 G_{mm} değerinin seçilme sebebi ise, yaygın uygulama olarak sıcak karışım asfaltlar silindirlerle bu yoğunluğa sıkıştırılmakta ve sıkışma trafik yükleri altında devam etmektedir.

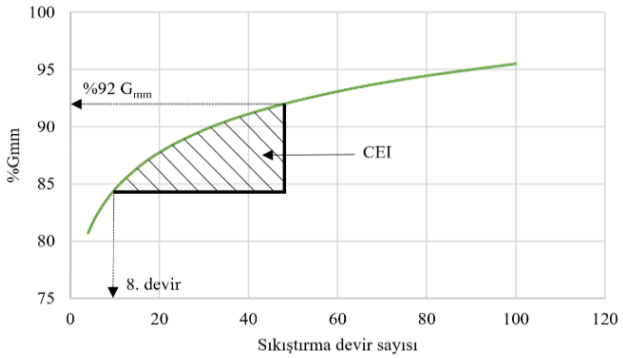

Şekil 3. Sıkışma eğrileri kullanarak CEI hesaplanması.

3. Bulgular ve Tartışma

3.1. Hacimsel Sonuçlar

Üretilen numuneler için yapılan hacim özgül ağırlık deneyleri ve tasarım aşamasında yapılan agrega özgül ağırlık ve asfalt karışımı maksimum özgül ağırlık deney sonuçları kullanılarak hacimsel özellikler belirlenmiştir. Hava boşluğu, mineral agregalar arası boşluk oranı (VMA) ve bitüm ile dolu boşluk oranı (VFA) önemli hacimsel özellikler olup karışımların yerleştirilmesi, sıkıştırılması ve servis koşulları altındaki davranışları için önemli parametrelerdir. Sıkıştırılmış numunelerin yükseklikleri de karışımların sıkıştırılabilirliği açısından önemli olup, Superpave yoğurmalı pres cihazı tarafından her numune için kaydedilmiştir. G1 ve G2 tasarımları için 3 ayrı segregasyon seviyesinde üretilen numuneler için hesaplanan hava boşluğu, VMA ve VFA değerleri Tablo 7'de verilmiştir. Bu değerler her bir sınıf için üretilen 6 numunenin sonuçlarının ortalamasıdır.

Farklı segregasyon seviyelerindeki G1 numunelerinin hava boşluğu incelendiğinde, artan segregasyon seviyesi ile hava boşluğu miktarının arttığı görülmüştür. Tablo 7'de görüleceği gibi G1-H, G1-O ve G1-Y numunelerinin ortalama hava boşlukları sırasıyla %4,47, %5,69 ve %6,46 olarak belirlenmiştir. Tasarım numuneleri 4900 gram agrega kullanılarak hazırlanmış ve optimum bitüm içeriği %4 hava boşluğu için hesaplanmıştır. Ancak test numuneleri 7000 gram agrega kullanılarak hazırlandığından aynı oranda bitüm kullanılmasına rağmen artan karışım hacmi, ön koşulsuz G1-H numunelerinin hava boşluğu değerlerinin bir miktar artışına sebep olmuştur. Segregasyona uğramış numunelerde kaba agregaların yoğunlaştığı numunelerin alt bölgelerinde hava boşluklarının oldukça yüksek olduğu gözlemlenmiştir. İnce agregaların yoğun olduğu numunelerin üst bölgelerinde ise hava boşluğu miktarı normal koşullara göre az olduğu görülmektedir. Bununla birlikte, numunelerin tamamı göz önüne alındığında agrega segregasyonun hava boşluğu miktarını arttırdığı görülmüştür. G1-H ve G1-Y numuneleri arasında %2 civarında bir hava boşluğu farklı bulunmaktadır. Buna paralel olarak VMA değeri artan segregasyon seviyesi ile artmakta iken, VFA değerleri artan segregasyon seviyesi ile azalmaktadır. Bu sonuçlar, agrega segregasyonunun derecesi arttıkça asfalt karışımlarının sıkıştırılabilirliğinin azaldığını göstermektedir. Sıkıştırılabilirlik yanında, bu durumun asfalt karışımının mekanik performansı ve durabilitesini de olumsuz etkileyeceği açıktır.

Tablo 7. Farklı segregasyon seviyesindeki numunelerin hacimsel özellikleri

Tasarım	Segregasyon seviyesi	Hava boşluğu (%)		VMA (%)		VFA (%)	
		Ortalama	Standart sapma	Ortalama	Standart sapma	Ortalama	Standart sapma
G1	H	4,47	0,20	14,5	0,18	69,2	1,02
	O	5,69	0,14	15,6	0,12	63,5	0,59
	Y	6,46	0,20	16,3	0,17	60,3	0,78
G2	H	3,94	0,08	13,6	0,07	71,1	0,44
	O	3,94	0,07	13,6	0,07	71,1	0,40
	Y	3,94	0,03	13,6	0,03	71,1	0,19

Yoğurmalı pres ile sıkıştırma esnasında numune yüksekliğinin uygulanan devir sayısına karşı düşüşü karışımın sıkışmaya karşı direncini göstermektedir. Bu veri, karışımların sıkıştırılabilirliğini değerlendirmek için kullanılmaktadır. Aynı sıkıştırma devir sayısı uygulanarak üretilmiş G1 numunelerinin her bir segregasyon seviyesi için ortalama numune yükseklikleri Şekil 4'de verilmiştir. Şekilde görüldüğü gibi G1-H, G1-O ve G1-Y numunelerinin ortalama yükseklikleri 175,7 mm, 178,9 mm ve 180,2 mm olarak belirlenmiştir. Bu

sonuçlar, agrega segregasyonun aynı sıkıştırma eforu altında numune yüksekliklerini etkilediğini göstermektedir ve agrega segregasyonu sonucu değişen asfalt betonu içyapısının göstergesidir. Homojen karışımlara kıyasla agrega temas noktalarının (toplam temas noktası toplamı, toplam agrega temas uzunluğu vb.) özellikleri de ciddi şekilde etkilenecektir. Asfalt karışımlarının yük taşıma kapasiteleri önemli ölçüde agregalar arası temasla sağlandığından, değişen agrega dağılımının performansı da etkileyeceği öngörülmektedir.

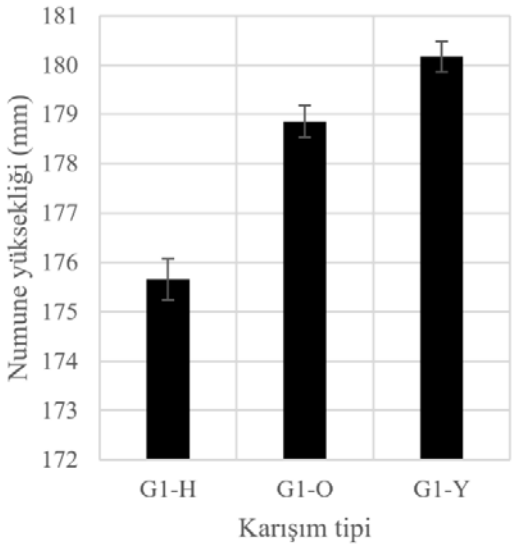

Şekil 4. Aynı sıkıştırma devir sayısı sonucu numune yükseklikleri.

Aynı yoğunlukta sıkıştırılan G2 numunelerinde numune yükseklikleri birbirine çok yakın olup ortalama numune yüksekliği 174,5 mm olarak belirlenmiştir. Farklı segregasyon seviyesindeki numuneleri, aynı hedef yoğunluğa ulaşacak şekilde sıkıştırmak için gerekli ortalama sıkıştırma pres devir sayısı G2-H, G2-O ve G2-Y numuneleri için sırasıyla 122, 238 ve 315 olarak bulunmuştur (Şekil 5). Farklı segregasyon seviyesindeki numunelerin ortalama hava boşlukları eşit olup bu değer %3,94 olarak bulunmuştur. G2-Y numunelerinde hedef yoğunluğa ulaşmak için gerekli sıkıştırma devir sayısı, G2-H için gerekli sayının neredeyse 3 katına yakındır. Bu sonuçlar artan agrega segregasyonunun, aynı hedef yoğunluğa ulaşmak için asfalt karışımlarının sıkıştırılabilirliğini önemli ölçüde zorlaştırdığını açıkça ortaya koymaktadır.

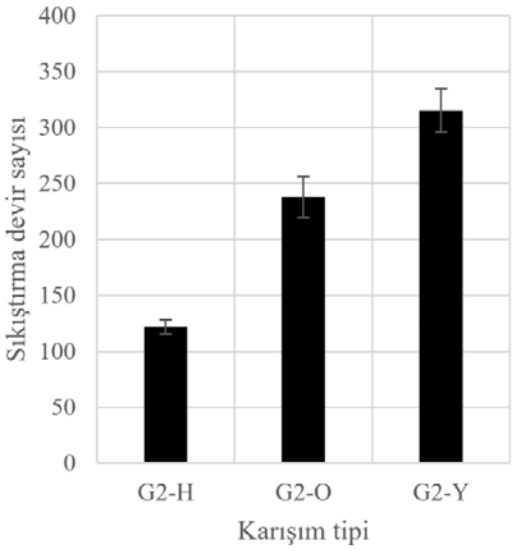

Şekil 5. Aynı yoğunluğa sıkıştırmak için gerekli sıkıştırma devir sayıları.

Asfalt karışımı numuneleri üretildikten sonra farklı performans testleri için numune merkezlerinden 100 mm çapında karotlar alınmış ve 150 mm numune uzunluğu elde etmek için numunelerin alt ve üst uçları testere ile kırpılmıştır. Her bir karışım tipi için agrega dağılımının nasıl olduğunu göstermek amacıyla örnek numune resimleri Şekil 6'da verilmiştir.

3.2. Karışımların Sıkıştırılabilirlikleri

Sıkışma eğrileri karışımların sıkıştırılabilirliğini değerlendirmek için önemli çıktılar olup, sıkıştırma esnasında Superpave yoğurmalı pres tarafından kaydedilen veriler kullanılarak oluşturulmuştur. Karışımların önceden belirlenen maksimum teorik özgül ağırlıkları (G_{mm}) ve sıkıştırılmış numunelerin hacim özgül ağırlıkları (G_{mb}) kullanılarak hacimsel özellikler belirlenmektedir. Numunelerin her devir sayısındaki yüksekliği yazılım tarafından kaydedildiğinden bu devir sayılarına karşı gelen numune yoğunluğu (%G_{mm}) hesaplanabilmektedir. Bu oran sıkışma yüzdesi olarak da tanımlanmaktadır. G1 ve G2 numunelerinin %G_{mm} - sıkıştırma devir sayısı ilişkisini temsil eden sıkışma eğrileri Şekil 7 ve Şekil 8'de gösterilmektedir. Bu eğriler, tüm sonuçlar arasından ortalamayı en iyi temsil edenlerden seçilmiştir.

Karışımların bazı önemli sıkıştırma devir sayılarındaki yoğunlukları ve kritik yoğunluklara ulaşması için gerekli sıkıştırma devir sayıları Tablo 8'de verilmiştir. Bu tabloda tüm karışımlar için sırasıyla; N_i devir sayısındaki %G_{mm}, %92 G_{mm}'deki devir sayısı, N_d devir sayısındaki %G_{mm} ve %96 G_{mm}'deki devir sayısı verilmiştir. Ni ilk sıkıştırma devir sayısı bu çalışmada 8 devir olup, bu devir sayısındaki %G_{mm} sıkıştırılabilirlik açısından anlamlı veriler sunmaktadır. Bu devir sayısında %G_{mm} değeri çok yüksekse karışımın hızlı sıkıştığını gösterir ve sahada uygulama esnasında ve trafik yükleri altında stabil davranış göstermezler. Bu çalışmadaki karışımların N_i devir sayısındaki %G_{mm} değeri kritik değer olan %89

G_{mm}'den küçük olup Superpave kriterlerini sağlamaktadır. Bu değerin daha küçük olması segregasyona uğramış karışımların daha zor sıkıştırılacağını göstermektedir. %92 G_{mm}'e ulaşmak için gerekli devir sayısının verilme sebebi, sahada sıkıştırılan asfalt karışımları %92 G_{mm}'e (%8 hava boşluğu) ulaşıncaya kadar silindirlerle sıkıştırılmakta ve bu noktada trafiğe açılmaktadır. Trafik yükleri altında kaplama sıkışmaya devam etmektedir. Bu yüzden %92 G_{mm}'e ulaşmak için gerekli devir sayısı önemli bir sıkıştırılabilirlik göstergesidir. Homojen numunelere göre orta ve yüksek seviyede segrege numunelerde sıkışma devir sayısının oldukça yüksek olduğu görülmektedir.

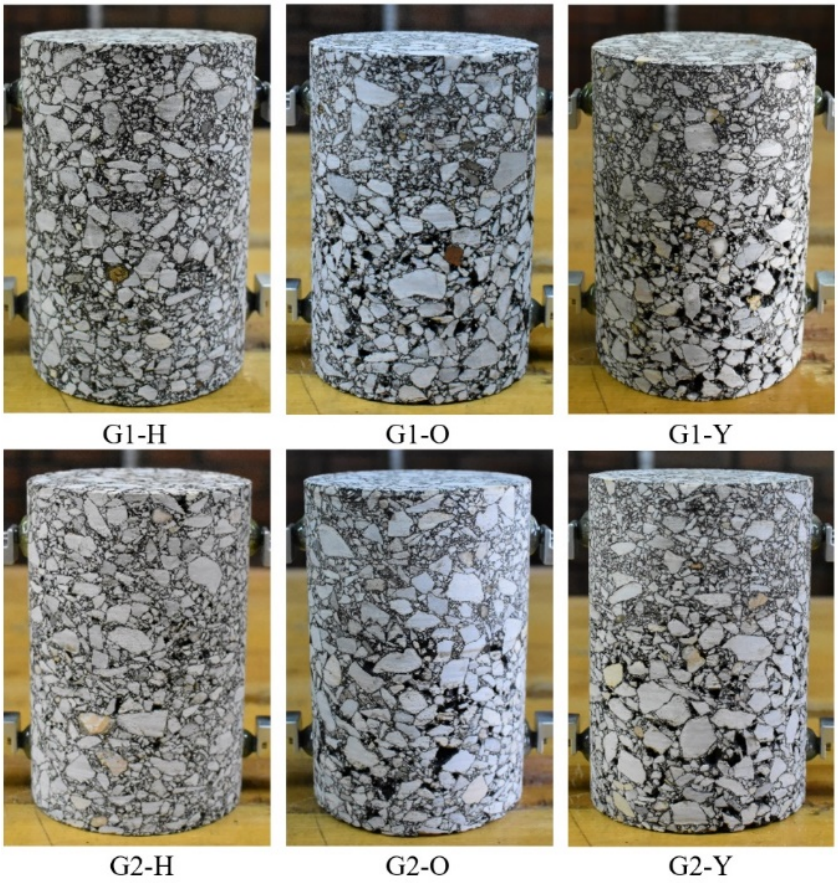

Şekil 6. Karışım tipleri için örnek numuneler.

Tablo 8. Karışımların sıkışma durumları

Tasarım	Segregasyon seviyesi	N_i'de %G_{mm}	%92 G_{mm}'de N	N_d'de %G_{mm}	%96 G_{mm}'de N
G1	H	83,67	48	95,53	-
	O	82,44	61	94,31	-
	Y	81,64	72	93,54	-
G2	H	83,80	46	-	122
	O	81,96	73	-	238
	Y	81,46	83	-	315

G1 numunelerine, tasarım sıkıştırma devir sayısı (N_d) olarak belirlenen 100 devir sıkıştırma uygulanmıştır. Şekil 7'de her bir segregasyon seviyesini temsil eden üç adet eğri gösterilmektedir. G1-H, G1-O ve G1-Y karışımları için 100 devir sıkıştırma sonucunda belirlenen ortalama %G_{mm} değerleri sırasıyla 95,53, 94,31 ve 93,54 olarak belirlenmiştir. Bu sonuçlar, farklı segregasyon seviyesindeki karışımların aynı sıkıştırma eforu altında farklı davrandığını ortaya koymaktadır. Agrega segregasyonu gerçekleştiğinde, aynı sıkıştırma eforu altında farklı yoğunlukta asfalt betonları elde edileceği görülmektedir.

G2 numuneleri %4 hava boşluğuna karşılık gelen %96 G_{mm} değerine ulaşıncaya kadar sıkıştırılmıştır. Hedef yoğunluğa ulaşmak için her numuneye uygulanan sıkıştırma devir sayıları farklılıklar göstermiştir. Farklı segregasyon seviyelerini temsil eden G2-H, G2-O ve G2-Y numunelerinin hedef yoğunluğa ulaşmaları için uygulanan ortalama sıkıştırma devir sayıları 122, 238 ve 315 olarak belirlenmiştir. Görüleceği üzere, önkoşulsuz karışımlarla karşılaştırıldığında, aynı yoğunluğa ulaşmak için orta seviyede segregasyon durumunda %95, yüksek

seviye segregasyon durumunda ise %158 daha fazla sıkıştırma devri uygulanması gerektiği görülmektedir. Laboratuvar ortamında düşük sıkıştırılabilirliği olan karışımdan sahada da aynı performans beklenmektedir. Bu tip karışımlarda, hedef yoğunluğa ulaşmak için sahada çok fazla sıkıştırma eforu gerekmekte ve sıkıştırma süresi uzamaktadır.

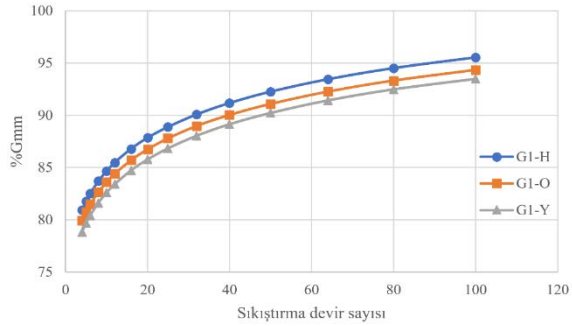

Şekil 7. Aynı devir sayısında sıkıştırılan numunelerin sıkışma eğrileri.

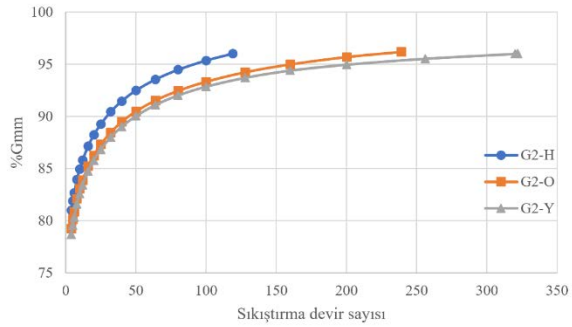

Şekil 8. Aynı hedef yoğunlukta sıkıştırılan numunelerin sıkışma eğrileri.

3.2.1. Kayma Direnci Sonuçları

Superpave yoğurmalı pres tarafından sıkıştırma boyunca kaydedilen her devir için asfalt karışımı numunesinde ölçülen kayma direnci verileri bu bölümde sunulmuştur. Önceki bölümlerle tartışıldığı gibi, kayma direnci verisi kullanılarak karışımların sıkıştırılabilirliğini değerlendirmek için iki adet parametre kullanılmıştır. Bu parametrelerden ilki karışımların %92 G_{mm} değerine ulaştığı devirde ölçülen kayma direncidir. Sahadaki sıkıştırma işlemleri bu sıkışma yüzdesine kadar yapıldığından, bu noktadaki kayma dirençlerinin karşılaştırılması hangi karışımın daha kolay sıkıştığını göstermesi açısından önemlidir. İkinci parametre ise %86 ile %92 G_{mm} arasında, kayma direnci eğrisi altında kalan alanın, G_{mm} (% sıkışma) eğrisi altında kalan alana oranından elde edilen enerji değeridir (*E*). *E* değeri %86 sıkışmadan %92 sıkışmaya ulaşmak için gerekli enerjiyi temsil ettiğinden daha düşük parametre daha kolay sıkıştırılabilirlik anlamına gelmektedir. G1 ve G2 karışımları için her bir segregasyon seviyesini temsil eden kayma direnci eğrileri Şekil 9'da verilmiştir.

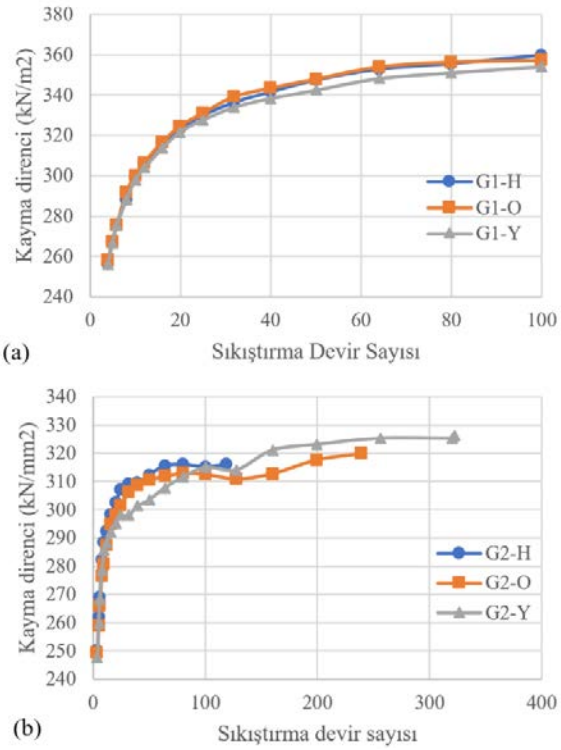

Şekil 9. Farklı segregasyon seviyeleri için kayma direnci eğrileri: a) G1, b) G2.

N_d devir sayısında (100 devir) sıkıştırılan G1 numuneleri için kayma direnci parametreleri hesaplanmış ve Tablo 9'da verilmiştir. Sıkıştırılabilirlik için kullanılan ilk parametre olan %92 G_{mm}'deki kayma dirençleri incelendiğinde homojen numuneler için 346,5 kN/mm² bulunmuşken, orta ve yüksek seviye segrege numuneler için sırasıyla 352,9 kN/mm² ve 350,0 kN/mm² olarak belirlenmiştir. G1-H için bulunan parametre segrege numunelere göre küçük olmakla birlikte, G1-O ve G1-Y için hesaplanan parametre birbirine oldukça yakındır. Bu parametrenin küçük olması daha kolay sıkışma anlamına geldiğinden G1-H numuneleri en sıkıştırılabilir karışımlar olarak ortaya çıkmaktadır. *E* parametresi ise G1-H, G1-O ve G1-Y numuneleri için sırasıyla 3,72, 3,81 ve 3,80 olarak bulunmuştur. Bu parametre numunelerin hava boşluğunu %14'den %8'e indirmek için gerekli enerjiyi temsil ettiğinden düşük *E* kolay sıkıştırılabilirliği, yüksek *E* değeri ise daha zor sıkıştırılabilirliği göstermektedir. G1-H numuneleri için bulunan *E* değeri en küçük olup, homojen numunelerin diğer numunelere göre daha kolay sıkıştırıldığını göstermektedir. E parametresi G1-O ve G1-Y numuneleri için neredeyse eşittir. Kayma direnci eğrileri kullanılarak hesaplanan sıkıştırılabilirlik parametreleri orta ve yüksek seviye segregasyona uğramış numuneler için yakın sonuçlar vermiştir. Kayma direnci ölçümü sırasında her devirde ölçülen en büyük kayma gerilmesi kaydedilmektedir ve bu gerilme birçok parametreye bağlıdır. Agregalar arası temas noktaları ve karışımların stabilitesi gibi etkenler ölçülen kayma mukavemetini etkilediğinden, orta ve yüksek seviye segrege olmuş numunelerin kayma direnci parametrelerinde bariz bir farklılık bulunamamıştır.

Tablo 9. N_d devir sayısında sıkıştırılan karışımların kayma direnci parametreleri

Tasarım	Segregasyon seviyesi	%86 G_{mm}'de N	%92 G_{mm}'de N	%86 G_{mm}'de kayma direnci (kN/mm²)	%92 G_{mm}'de kayma direnci (kN/mm²)	*E*
G1	H	14	48	312,7	346,5	3,72
	O	18	61	320,7	352,9	3,81
	Y	21	72	323,0	350,0	3,80

3.2.2. Sıkışma Enerjisi İndeksi (CEI) Sonuçları

Sıkışma enerjisi indeksi (CEI) sahadaki sıkıştırma sırasında silindirler tarafından yapılan işi temsil etmektedir. Düşük CEI değerleri karışımların daha sıkıştırılabilir olduğunu göstermektedir ve istenen bir durumdur. CEI değerinin düşük olması durumunda hedeflenen yoğunluğa ulaşmak için daha az enerji gerekli olacaktır. CEI indeksi birimsiz olup göreceli olarak hedef yoğunluğa (%92 G_{mm}) ulaşmak için gerekli enerji miktarı göstergesidir.

100 devir sıkıştırma uygulanan G1 numuneleri için hesaplanan CEI değerleri Şekil 10'da verilmiştir. Verilen CEI değerleri her bir segregasyon seviyesi için hazırlanan 6 numunenin ortalama değerleridir. G1-H, G1-O ve G1-Y segregasyon seviyeleri için hesaplanan ortalama CEI değerleri sırasıyla 209, 330 ve 443 olarak hesaplanmıştır. Bu değerler artan agrega segregasyonunun, asfalt karışımının sıkıştırılabilirliğini nasıl zorlaştırdığını açık bir şekilde göstermektedir. Yüksek seviyede segrege olmuş numuneler için hesaplanan CEI değerinin, ön koşulsuz homojen numuneler için hesaplanan değerin iki katından fazla olduğu görülmektedir.

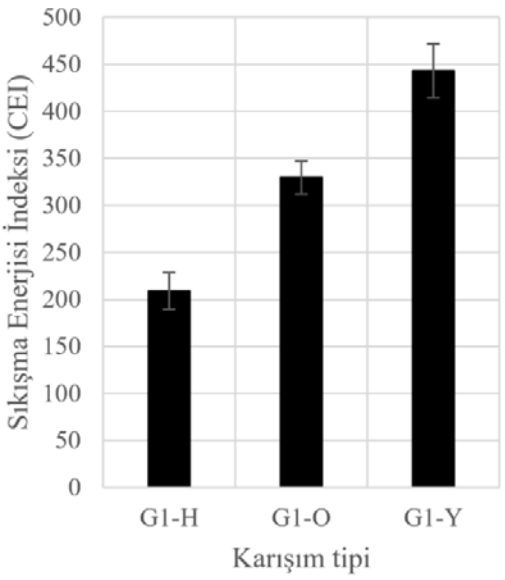

Şekil 10. Farklı segregasyon seviyeleri için CEI değerleri.

Yetersiz sıkıştırmanın, yüksek yaşlanma hızı, tekerlek izi problemleri ve suya karşı daha fazla hassasiyet gibi sonuçları olduğu bilinmektedir. Karışımların sıkıştırılabilirliği; gradasyon, bitüm özellikleri ve miktarı, agrega yapısı ve sıcaklık gibi pek çok parametreye bağlıdır. Bu çalışmada, agrega segregasyonunun laboratuvar ortamında hazırlanan Superpave numuneleri kullanılarak sıkıştırılabilirliği nasıl etkilediği incelenmiştir. Sonuçlar artan segregasyon seviyesi ile sıkışmanın zorlaştığını ve aynı yoğunlukta asfalt betonu elde etmek için segregasyona uğramış numunelerde çok daha fazla sıkıştırma eforu gerektiğini göstermektedir.

4. Sonuç

Bu çalışmada, agrega segregasyonunun asfalt karışımlarının sıkıştırılabilirliği üzerine etkileri laboratuvar ortamında Superpave yöntemi kullanılarak üretilen numunelerle değerlendirilmiştir. Üretilen asfalt karışımı numunelerinin sıkıştırılabilirlikleri; hacimsel özellikler, sıkışma eğrileri, kayma direnci verisi ve CEI indeksi kullanılarak incelenmiştir. Farklı seviyelerde agrega segregasyonunu laboratuvar ortamında simüle etmek amacıyla tasarım gradasyonu, kaba ve ince agrega yoğunluklu iki kısma ayrılarak karışımlar hazırlanmış ve kalıba iki tabaka olarak yerleştirilip sıkıştırılmıştır. Çalışma kapsamında aynı sıkışma eforu altında sıkıştırılan ve aynı hedef yoğunlukta sıkıştırılan homojen, orta seviye segrege ve yüksek seviye segrege numunelerin özellikleri değerlendirilmiştir.

Bu çalışmada, aynı sıkıştırma eforu harcanarak üretilen numuneler ve aynı yoğunlukta sıkıştırılan numunelerin hacimsel sonuçları ve sıkışma eğrilerinden elde edilen veriler, agrega segregasyonunun sıkıştırılabilirliği önemli ölçüde etkilediğini göstermektedir. Homojen, orta ve yüksek seviye segrege asfalt karışımlarına aynı sıkıştırma eforu uygulandığında, segregasyon seviyesi arttıkça numune yükseklikleri ve hava boşluğu miktarı artmaktadır. Buna paralel olarak, artan segregasyon seviyesi ile karışımların sıkıştırılabilirliğini temsil eden CEI indeksi de artmaktadır. Farklı segregasyon seviyesindeki karışımları aynı hedef yoğunluğa sıkıştırmak için yapılan deneylerde, segregasyon seviyesi arttıkça hedef yoğunluğa ulaşmak için uygulanması gereken sıkıştırma devir sayısının artırılması gerektiği görülmüştür. Yüksek seviye segregasyona uğramış bir numuneyi, %4 hava boşluğuna karşılık gelen hedef yoğunlukta sıkıştırmak için homojen numuneye uygulanan sıkıştırma devir sayısının yaklaşık 3 katı sıkıştırma devri uygulanmıştır. Sonuçlar, agrega segregasyonunun asfalt karışımlarının hacimsel özelliklerini önemli ölçüde etkilediğini ve sıkıştırılabilirliğini düşürdüğünü göstermektedir.

Sonraki çalışmalarda, sahadan alınacak karot numuneleri ve laboratuvarda üretilen numuneler kullanılarak segregasyon seviyesine bağlı olarak asfalt betonu performansının değerlendirilmesi önerilmektedir.

Katkı Oranı Beyanı

Yazarların katkı yüzdeleri aşağıda verilmiştir. Yazarlar makaleyi incelemiş ve onaylamıştır.

	A.Ö.Y	M.G.
K	50	50
T	40	60
Y	30	70
VTI	80	20
VAY	70	30
KT	70	30
YZ	80	20
KI	60	40
GR	80	20

K= kavram, T= tasarım, Y= yönetim, VTI= veri toplama ve/veya işleme, VAY= veri analizi ve/veya yorumlama, KT= kaynak tarama, YZ= Yazım, KI= kritik inceleme, GR= gönderim ve revizyon.

Çatışma Beyanı

Yazarlar bu çalışmada hiçbir çıkar ilişkisi olmadığını beyan etmektedirler.

Etik Onay Beyanı

Bu araştırmada hayvanlar ve insanlar üzerinde herhangi bir çalışma yapılmadığı için etik kurul onayı alınmamıştır.

Destek ve Teşekkür Beyanı

Bu çalışma, Ayhan Öner YÜCEL'in doktora tezinden üretilmiştir.

Kaynaklar

AASHTO R35. 2010. Standard practice for superpave volumetric design for asphalt mixtures, american association of state highway and transportation officials. AASHTO, Washington, DC, USA, pp: 154.

Azari H. 2005. Effect of aggregate inhomogeneity on mechanical properties of asphalt mixtures. PhD thesis, University of Maryland at College Park, Maryland, USA, pp: 1-441.

Bahia HU, Friemel TP, Peterson PA, Russell JS, Poehnelt B. 1998. Optimization of constructibility and resistance to traffic: a new design approach for HMA using the superpave compactor. J Assoc Asphalt Paving Technol, 67: 189-232.

Bessa IS, Branco VTFC, Soares JB, Neto JAN. 2015. Aggregate shape properties and their influence on the behavior of hot-mix asphalt. J Mater Civ Eng, 27 (7): 04014212.

Cai X, Wu K, Huang W. 2021. Study on the optimal compaction effort of asphalt mixture based on the distribution of contact points of coarse aggregates. Road Mater Pavement Des, 22 (7): 1594–1615.

Cross SA, Brown ER. 1993. Effect of segregation on performance of hot-mix asphalt. Transp Res Rec, 1417: 117-126.

Cross SA, Hainin MR, Ado-Osei A. 1998. Effects of segregation on mix properties of hot mix asphalt. K-TRAN: KU-96-6, Kansas, USA, pp: 1-117.

Chen MJ, Wong YD. 2017. Evaluation of the development of aggregate packing in porous asphalt mixture using discrete element method simulation. Road Mater Pavement Des, 18 (1): 64–85.

Debao L, Xiaoming H, Changlu G. 2013. Method to determine asphalt film thickness based on actual measurement. Adv Mater Res, 777-780, 140-143.

Dessouky S, Pothuganti A, Walubita LF, Rand D. 2013. Laboratory evaluation of the workability and compactability of asphaltic materials prior to road construction. J Mater Civ Eng, 25 (6): 810–818.

Dubois V, Roche CD La, Burban O. 2010. Influence of the compaction process on the air void homogeneity of asphalt mixtures samples. Constr Build Mater, 24 (6): 885–897.

Gao Y, Huang X, Yu W. 2014. The compaction characteristics of hot mixed asphalt mixtures. J Wuhan Univ Technol Mater Sci Ed, 29 (5): 956–959.

Georgiou P, Plati C. 2021. Microstructure characterisation of field and laboratory roller compacted asphalt mixtures. Road Mater Pavement Des, 22 (4): 942–953.

Guler M, Bahia HU, Bosscher PJ, Plesha ME. 2000. Device for measuring shear resistance of hot-mix asphalt in gyratory compactor. Transp Res Rec, 1723: 16–24.

Gong M, Xiong Z, Deng C, Peng G, Jiang L, Hong J. 2022. Investigation on the impacts of gradation type and compaction level on the pavement performance of semi-flexible pavement mixture. Constr Build Mater, 324: 126562.

Guo R, Zhou F, Nian T. 2022. Analysis of primary influencing factors and indices distribution law of rutting performance of asphalt mixtures. Case Stud Constr Mater, 16: e01053.

Hu T, Yuan J, Zhou X, Liu lu, Ran M. 2022. A two-dimensional entropy-based method for detecting the degree of segregation in asphalt mixture. Constr Build Mater, 347: 128450.

Huanan Y, Ming Y, Guoping Q, Jun C, Hongyu Z, Xiao F. 2021. Gradation segregation characteristic and its impact on performance of asphalt mixture. J Mater Civ Eng, 33 (3): 04020478.

Jiang J, Ni F, Gao L, Yao L. 2017. Effect of the contact structure characteristics on rutting performance in asphalt mixtures using 2D imaging analysis. Constr Build Mater, 136: 426–435.

Jin C, Jue L, Hengwu H, Junfeng Q, Miao Y. 2023. Numerical investigation of aggregate segregation of superpave gyratory compaction and its influence on mechanical properties of asphalt mixtures. J Mater Civ Eng, 35 (3): 04022453.

Jing H, Liu J, Wang Z, Chen H, Zhang X, Yuan L. 2023. X-ray computed tomography analysis of internal voids in steel slag asphalt mixture under freeze–thaw damage and microwave healing process. Constr Build Mater, 377: 131132.

Khedaywi TS, White TD. 1995. Development and analysis of laboratory techniques for simulating segregation. Transp Res Rec, 1492: 36-45, National Research Council, Washington, D.C.

Kwon O, Choubane B, Hernando D, Allick W. 2019. Evaluation of the ımpact of asphalt mix segregation on pavement performance. Transp Res Rec, 2673: 310-316.

Leiva F, West RC. 2008. Analysis of hot-mix asphalt lab compactability using lab compaction parameters and mix characteristics. Transp Res Rec, 2057: 89-98.

Liu H, Yin R, Wu S. 2007. Reducing the compaction segregation of hot mix asphalt. J Wuhan Univ Technol Mater Sci Ed, 22: 132–135.

Ma X, Leng Z, Wang L, Zhou P. 2020. Effect of reclaimed asphalt pavement heating temperature on the compactability of recycled hot mix asphalt. Materials, 13 (16): 3621.

Mahmoud AFF, Bahia H. 2004. Using the gyratory compactor to measure mechanical stability of asphalt mixtures. Wisconsin Highway Research Program 0092-01-02, Wisconsin-Madison, USA, pp: 1-85.

Mallick RB. 1999. Use of superpave gyratory compactor to characterize hot-mix asphalt. Transp Res Rec, 1681: 86–96.

Masad E, Jandhyala VK, Dasgupta N, Somadevan N, Shashidhar N. 2002. Characterization of air void distribution in asphalt mixes using x-ray computed tomography. J Mater Civ Eng, 14 (2): 122-129.

Masad E, Button J. 2004. Implications of experimental measurements and analyses of the internal structure of hot-mix asphalt. Transp Res Rec, 1891: 212–220.

Mohamed EHH, Abd El Halim AO, Kennepohl GJ. 1993. Assessment of the influence of compaction method on asphalt concrete resistance to moisture damage. Constr Build Mater, 7 (3): 149–156.

Onifade I, Jelagin D, Birgisson B, Kringos N. 2016. Towards asphalt mixture morphology evaluation with the virtual specimen approach. Road Mater Pavement Des, 17 (3): 579–999.

Rand DA. 1997. Comparative analysis of Superpave gyratory compactors and TxDOT gyratory compactors. Master Thesis, University of Texas at Austin, Texas, USA.

Roberts FL, Kandhal PS, Brown ER, Lee D-Y, Kennedy TW. 1996. Hot mix asphalt materials, mixture design and construction. Lanham, Md.: Napa Education Foundation, 2nd ed., Napa, USA, pp: 1-585.

Sefidmazgi NR, Tashman L, Bahia H. 2012. Internal structure characterization of asphalt mixtures for rutting performance using imaging analysis. Road Mater Pavement Des, 13 (sup1): 21–37.

Sefidmazgi NR, Teymourpour P, Bahia HU. 2013. Effect of particle mobility on aggregate structure formation in asphalt mixtures. Road Mater Pavement Des, 14 (sup2): 16–34.

Selvam M, NSSP K, Kandasami RK, Singh S. 2023. Assessing the effect of different compaction mechanisms on the internal structure of roller compacted concrete. Constr Build Mater, 365: 130072.

Shi J, Gong H, Cong L, Liang H, Ren M. 2023. Evaluating and quantifying segregation in asphalt pavement construction: A state-of-the-practice survey. Constr Build Mater, 383: 131205.

Stroup-Gardiner M, Brown ER. 2000. Segregation in hot-mix asphalt pavements, Transportation Research Board. Report no: 441, National Research Council, Washington, D.C., USA, pp: 1-95.

Taheri-Shakib J, Al-Mayah A. 2023. A review of microstructure characterization of asphalt mixtures using computed tomography imaging: Prospects for properties and phase determination. Constr Build Mater, 385: 131419.

Tashman L, Masad E, Peterson B, Saleh H. 2001. Internal structure analysis of asphalt mixes to improve the simulation of Superpave gyratory compaction to field conditions (with discussion). J Assoc Asphalt Paving Technol, 2001: 70.

Williams RC, Duncan Jr G, White TD. 1996. Hot-mix asphalt segregation: Measurement and effects. Transp Res Rec, 1543: 97-105.

Xuelian L, Siyu C, Kuiyuan X, Xueying L. 2018. Gradation segregation analysis of warm mix asphalt mixture. J Mater Civ Eng, 30 (4): 04018027.

Yu H, Zhou S, Qian G, Zhang C, Shi C, Yao D, Ge J. 2023. Evaluation of the microscale structure and performance of asphalt mixtures under different design methods. Constr Build Mater, 400: 132810.

Yücel AÖ. 2019. Investigation of the impact of aggregate segregation on rutting resistance of asphalt concrete. PhD thesis, Middle East Technical University, Graduate School of Natural and Applied Sciences, Ankara, Türkiye, pp: 1-212.

Zhang C, Wang H, You Z, Yang X. 2016. Compaction characteristics of asphalt mixture with different gradation type through Superpave Gyratory Compaction and X-Ray CT Scanning. Constr Build Mater, 129: 243–255.

Black Sea Journal of Engineering and Science
doi: 10.34248/bsengineering.1601851

Open Access Journal
e-ISSN: 2619 – 8991

Research Article
Volume 8 - Issue 1: 263-267 / January 2025

K-MEAN CLUSTERING OF HOLSTEIN FRIESIAN DAIRY CATTLE USING GENOMIC BREEDING VALUES

Buğra HOŞGÖNÜL[1]*, Hasan ÖNDER[1]

[1]*Ondokuz Mayıs University, Faculty of Agriculture, Department of Animal Science, 55139, Samsun, Türkiye*

Abstract: Clustering refers to algorithms to uncover such clusters in unlabeled data. Data points belonging to the same cluster exhibit similar features, whereas data points from different clusters are dissimilar to each other. The identification of such clusters leads to segmentation of data points into a number of distinct groups. In this study it was aimed to classify the 492 Holstein Friesian dairy cattle with determining the optimum number of clusters using the genomic breeding values (GBVs) calculated with 13250 SNPs using GBLUP for milk yield (kg), milk fat (%), milk protein (%), milk lactose (%), and milk dry matter (%). Results showed that the optimum number cluster was determined as two for the genomic breeding values. Determining the most appropriate number of clusters, it provides great convenience in the selection of breeding animals after determining the animals that can provide optimum efficiency in the herd or the animals that need to be eliminated from the existing herd. As a result, it can be said that the k-means method can be used successfully in clustering animals for genomic breeding values, but for this, at first, the optimum number of clusters must be determined.

Keywords: K-mean clustering, Breeding value, Genomic selection, Dairy cattle

***Corresponding author:** Ondokuz Mayıs University, Faculty of Agriculture, Department of Animal Science, 55139, Samsun, Türkiye
E mail: honder@omu.edu.tr (H. ÖNDER)
Buğra HOŞGÖNÜL https://orcid.org/0009-0002-9548-3457
Hasan ÖNDER https://orcid.org/0000-0002-8404-8700

Received: December 15, 2024
Accepted: January 08, 2024
Published: January 15, 2025

Cite as: Hoşgönül B, Önder H. 2025. K-mean clustering of Holstein Friesian dairy cattle using genomic breeding values. BSJ Eng Sci, 8(1): 263-267.

1. Introduction

Clustering, as a generic tool for finding groups or clusters in multivariate data, has found wide application in biology, agriculture, psychology and economics (Kodinariya and Makwana, 2013). Cluster analysis encompasses different methods and algorithms for grouping objects of similar kinds into respective categories (Frades and Matthiesen, 2010). Clustering analysis method is one of the main analytical methods in data mining, the method of clustering algorithm will influence the clustering results directly (Na et al., 2010). Clustering is the separation of data with similar characteristics into groups. The general purpose of cluster analysis is to ensure homogeneity within the cluster and heterogeneity between the clusters. In other words, it is desired that the variance within the cluster is low and the variance between the clusters is high (Çolak et al., 2015). It is used to divide units or variables into homogeneous groups by using some measures calculated based on similarities or differences between variables. This allows similar individuals to be collected in the same cluster. Grouping ungrouped data according to their similarities helps the researcher to obtain appropriate usable summarizing information (Kodinariya and Makwana, 2013).

Clustering is the unsupervised, semi supervised, and supervised classification of patterns into groups (Frades and Matthiesen, 2010). Unsupervised learning is done by grouping (clustering) only the elements that have similar properties in the data, without labeling the data set as cause-effect, input-output (Çolak et al., 2015).

One of the main difficulties for cluster analysis is that, the correct number of clusters of different types of datasets is seldom known in practice. However, most of clustering algorithms are designed only to investigate the inherited grouping or partition of data objects according to a known number of clusters. Thus, identifying the number of clusters is an important task for any clustering problem in practice albeit it must be faced with many operational challenges. A tractable way for cluster analysis is to ask the end user to input the number of clusters in advance, which needs the expert domain knowledge over the underlying datasets. On the other hand, many statistical criteria or clustering validity indices have been investigated in the sense of automatically selecting an appropriate number of clusters (Kodinariya and Makwana, 2013).

Today, there are hundreds of clustering methods and they are classified in various ways. According to a widely used classification, clustering methods can be examined in three groups as hierarchical methods, k-mean (partitioning) methods and mixed methods that combine them in various ways (Çolak et al., 2015).

K-mean clustering analysis has been perhaps one of the most widely used segmentation methods for more than 50 years. It has been among the most widely used

methods in almost every field such as economics, customer management, marketing, bioinformatics and engineering research, as well as in informatics applications such as object classification, image segmentation, data mining, and machine learning (Cebeci et al., 2015).

In animal breeding, it is important to separate animals into groups using breeding values determined for more than one character. K-mean clustering is a one of the important tool for this purpose. In this study, we aimed to classify the 492 Holstein Friesian dairy cattle with determining the optimum number of clusters using the genomic breeding values (GBVs) of milk yield (kg), milk fat (%), milk protein (%), milk lactose (%), and milk dry matter (%).

2. Materials and Methods

2.1. Materials

In this study, we used the genomic breeding values (GBVs for 13250 SNPs) of milk yield (kg), milk fat (%), milk protein (%), milk lactose (%), and milk dry matter (%) estimated using GBLUP for 492 Holstein Friesian dairy cattle from a previous published study (Önder et al., 2023).

2.2. K-mean Cluster Analysis and Distance Measures

2.2.1. K-mean cluster analysis

K-mean clustering algorithms are algorithms that divide/partition datasets into k subsets (or clusters). Therefore, one of the most studied issues is the selection of k, which must be known at the very beginning of the analysis, before any algorithm is run. This parameter indicates the number of clusters into which the data set will be clustered, in other words, it indicates the number of clusters present in the data set. A successful or correct clustering depends on the optimal choice of k. Because, regardless of k, partitioning algorithms will produce a valid or invalid clustering result. However, since the aim is to obtain a valid clustering result, finding and using the actual number of clusters or the number closest to it is necessary to ensure accurate results. In other words, the correct selection of k is the main determining factor for a successful cluster analysis.

According to the working mechanism of the k-means algorithm, firstly k objects are randomly selected to represent the center point or mean of each cluster. The remaining objects are included in the clusters to which they are most similar by taking into account their distances from the mean values of the clusters. Then, the mean value of each cluster is calculated and new cluster centers are determined and the distances of the objects to the center are examined again (Na et al., 2010; Kodinariya and Makwana, 2013).

The process of k-means algorithm can be defined as the input and the output that the input is number of desired clusters, k, and a database $D=\{d_1,d_2,...d_n\}$ containing n data objects and the output is a set of k clusters (Na et al., 2010; Cebeci et al., 2015).

The algorithm basically consists of four stages:

The first step is randomly selecting k data objects from dataset D as initial cluster centers (Figure 1).

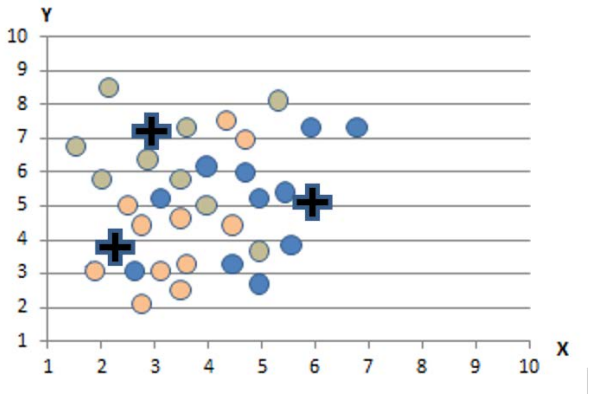

Figure 1. Randomly selected k cluster centers.

The second step is calculating the distance between each data object $d_i(1 <= i <= n)$ and all k cluster centers $c_j(1<=j<=k)$ and assign data object d_i to the nearest cluster.

The step three is determining new centers according to the clustering (or shifting old centers to the new center) (Figure 2).

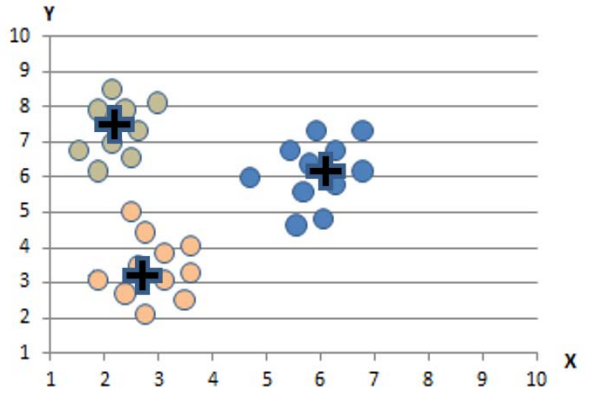

Figure 2. The new centers according to the clustering.

The fourth step is repeating steps two and three until a stable state is reached (Na et al., 2010; Çolak et al., 2015).

2.2.2. Distance measures

K-means is one of the clustering algorithms frequently used in the literature because it is simple and fast. The K-means algorithm divides the data set into k clusters and represents each cluster with a centroid (cluster center). The algorithm assigns the data to the closest centroid by using the squared distances between the data and the centroids.

Most clustering methods are based on the calculation of distances between observation values. Therefore, there is a need for relations that calculate the distance between two points. Euclidean distance can be calculated using Pearson or Manhattan distance formulas for distances between units in a data matrix containing continuous variables (Cebeci et al., 2015).

In the clustering phase, first the distance matrix is obtained. Distance measures can be used directly in clustering units or variables, or they can be used to calculate similarities and differences between units or variables (Figure 3).

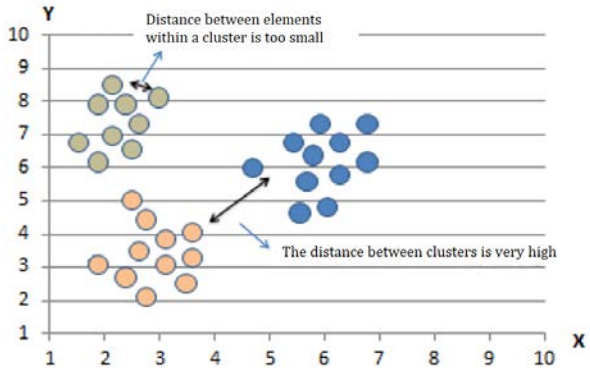

Figure 3. Data points and distances between clusters.

Euclidean distance

Euclidean distance (Equation 1) is a measure that determines the distances between the ith and jth observations in an nxp dimensional data matrix directly in the unit of measurement (Kurnaz and Önder, 2021).

$$d_{(i,j)} = \sqrt{\sum_{k=1}^{p} \left(X_{ik} - X_{jk}\right)^2} \quad (1)$$

here i=1,2,...,n; j=1,2,...,n and k=1,2,...,p. n is the number of units and p is the number of variables.

Pearson distance

Pearson distance (Equation 2) is the Euclidean distance proportional to the variance of the variable. Pearson distance is also called standardized Euclidean distance (Immink et al., 2018).

$$d_{(i,j)} = \sqrt{\sum_{k=1}^{p} \left(X_{ik} - X_{jk}\right)^2 / S_k^2} \quad (2)$$

Manhattan distance

Manhattan distance is a distance type calculated by taking the sum of the absolute distances between units. The Manhattan distance matrix (D_M) elements are calculated as follows (Kurnaz and Önder, 2021).

$$d_{M(i,j)} = \sum_{k=1}^{p} \left(|X_{ik} - X_{jk}|\right) \quad (3)$$

2.2.3. k-mean cluster analysis

For the genomic breeding values (GBVs for 13250 SNPs) of milk yield (kg), milk fat (%), milk protein (%), milk lactose (%), and milk dry matter (%) estimated using GBLUP for 492 Holstein Friesian dairy cattle were given as a small sample in Figure 4.

	A	B	C	D	E	F
1	NO	Milk	Fat	Pro	Lac	DM
2	X1	-761620627737,3250	93418419396,3995	1221379862090,4100	-888807597638,8460	-337628362351,5640
3	X2	-1280510865552,5700	346261253333,2680	1117933713690,1700	-1730445064381,5400	-564502156321,4430
4	X3	-711112554546,64200	313714512418,69700	649898437272,50700	-1293411366237,08000	-168220977207,51900
5	X4	-725803386369,30000	1017073959427,91000	1195837945823,68000	-1090929447420,98000	99357406828,63050
6	X5	-480576929324,79100	74826404622,23070	989828817931,66300	-1280047199605,54000	-193788801592,98200
7	X6	-864713241328,37900	392120314592,03600	1055314867556,73000	-538395630898,36200	-37459224667,76590
8	X7	-623171839016,41400	738436075054,16200	944613005602,30100	-858624793267,75500	50669825524,17770
9	X8	-802025203330,03400	583420057140,17800	461863278397,39200	-901929224436,06200	244452780346,11300

Figure 4. Sample data.

With the breeding values we obtained, the "readr" and "factoextra" libraries were used for K-mean clustering analysis in R software and the code used is given below.

```
library(readr)
library(factoextra)

mydata <- read.delim(file.choose()) #call the data file (txt).

str(mydata)

baru <- mydata[,-1]            # deletion of the first column (animals) from the data.

rownames(baru) <- make.names(mydata$No, unique = TRUE) #determining the animals as clustered objects

databaru <- baru[sample(nrow(mydata)),c(2:5)]

fviz_nbclust(databaru, kmeans, method = "silhouette") # determining the optimum number of cluster

kmeans.awal <- kmeans(databaru,2) # the number (2) is applied number of cluster

kmeans.awal

fviz_cluster(kmeans.awal, databaru) # graphing the clusters
```

3. Results

The optimum number of clusters was determined using the breeding values we obtained and is shown in Figure 5.

According to the results obtained, the optimum number of clusters was determined to be two. In this study, results for three and four clusters were also given in order to show the effects of using different cluster numbers than the optimum number of clusters.

The graphed clusters were given in Figure 6, Figure 7, and Figure 8 for two, three and four clusters, respectively.

Figure 6. K-mean clusters results for two clusters.

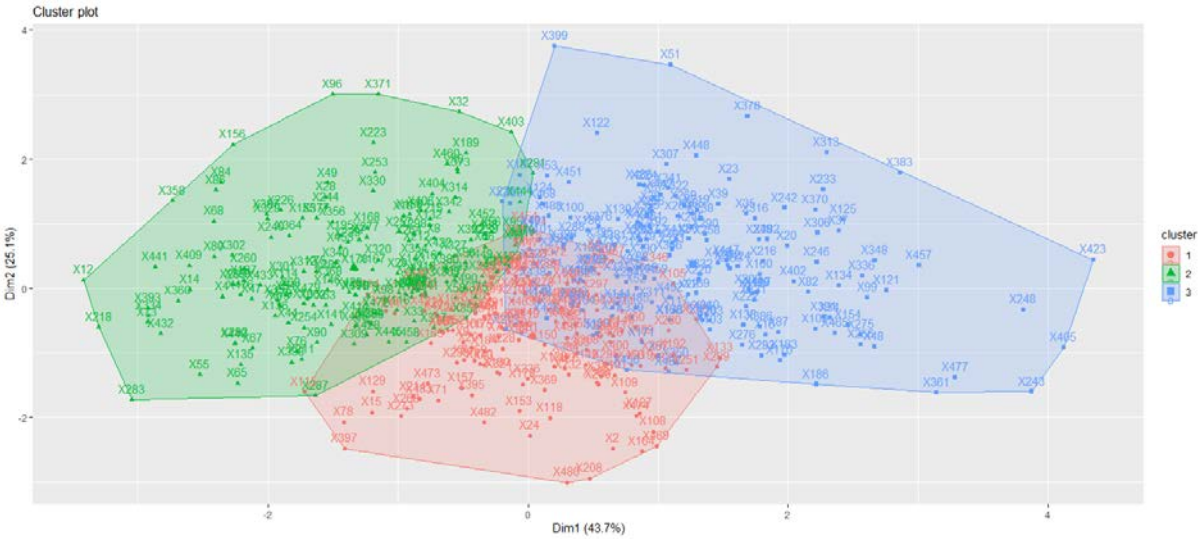

Figure 7. K-mean clusters results for three clusters.

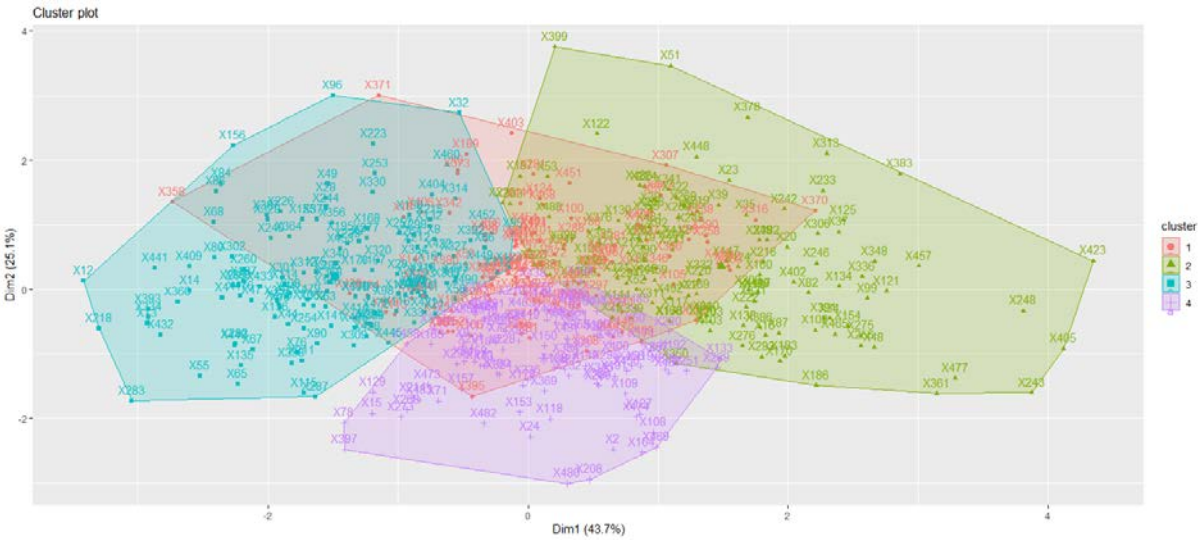

Figure 8. K-mean clusters results for four clusters.

4. Discussion and Conclusion

Results showed that the optimum number cluster was determined as two for the genomic breeding values (GBVs for 13250 SNPs) of milk yield (kg), milk fat (%), milk protein (%), milk lactose (%), and milk dry matter (%) estimated using GBLUP for 492 Holstein Friesian dairy cattle (Figure 5). When the Figure 5 was interpreted, it is understood that the two clusters are not

separated by definition and that some animals are located in the intersection of these two clusters. When we consider the number of clusters of three and four, it was easily understood that that some clusters are located within others and huge intersection of the clusters observed.

According to these results the population can be divided two groups such as high and low combined breeding values. If more than two clusters wanted to use the results is getting unclear. Determining the most appropriate number of clusters, it provides great convenience in the selection of breeding animals after determining the animals that can provide optimum efficiency in the herd or the animals that need to be eliminated from the existing herd. János et al. (2021) indicated in their study, they showed that cluster analysis had a positive effect on the herds they grouped in the breeding, feeding and breeding bull selection of Limousin breed cattle and that it would be beneficial for breeders. Doğan (2002) stated that it would be appropriate to use Cluster Analysis as a method in animal breeding, especially when making selection.

As a result, it can be said that the k-means method can be used successfully in clustering animals for genomic breeding values, but for this, the optimum number of clusters must first be determined.

Author Contributions

The percentages of the authors' contributions are presented below. The authors reviewed and approved the final version of the manuscript.

	B.H.	H.Ö.
C	70	30
D	70	30
S	30	70
DCP	70	30
DAI	70	30
L	70	30
W	70	30
CR	70	30
SR	70	30

C=Concept, D= design, S= supervision, DCP= data collection and/or processing, DAI= data analysis and/or interpretation, L= literature search, W= writing, CR= critical review, SR= submission and revision.

Conflict of Interest

The authors declared that there is no conflict of interest.

Ethical Consideration

Ethics committee approval was not required for this study due to there is no experimental study on research material.

References

Cebeci Z, Yıldız F, Kayaalp GT. 2015. Choosing an optimal k in k-means clustering. 2. Ulusal Yönetim Bilişim Sistemleri Kongresi, October 8-10, Erzurum, Türkiye, pp: 231-242.

Çolak B, Durdağ Z, Erdoğmuş P. 2015. Automatic clustering with k-means. El-Cezeri J Sci Eng, 3(2): 315-323.

Doğan İ. 2002. Selection by Cluster Analysis. Turk J Vet Anim Sci, 26: 47-53.

Frades I, Matthiesen R. 2010. Overview on techniques in cluster analysis. In: Matthiesen R (eds) Bioinformatics Methods in Clinical Research. Methods in Molecular Biology, vol 593. Humana Press. https://doi.org/10.1007/978-1-60327-194-3_5

Janos T, Natasa F, Marton S. 2021. Determining the type of Limousin candidate bulls by cluster analysis. Nat Resour Sust Devel, 11(1): 113-120.

Immink KAS, Cai K, Weber JH. 2018. Dynamic threshold detection based on Pearson distance detection. IEEE Transact Commun, 66(7): 2958-2965.

Kodinariya TM, Makwana PR. 2013. Review on determining number of cluster in k-means clustering. Int J Adv Res Comput Sci Manag Stud, 1(6): 90-95.

Kurnaz B, Önder H. 2021. Distance based regression models. II. International Applied Statistics Conference, June 29 – July 2, Tokat, Türkiye, pp: 120-126.

Na S, Xumin L, Yong G. 2010. Research on k-means clustering algorithm: An improved k-means clustering algorithm. Third International Symposium on Intelligent Information Technology and Security Informatics, April 22, Jian, China, pp: 63-67.

Önder H, Sitskowska B, Kurnaz B, Piwczynski D, Kolenda M, Sen U, Tırınk C, Çanga Boğa D. 2023. Multi-trait single-step genomic prediction for milk yield and milk components for Polish Holstein population. Animals, 13: 3070. https://doi.org/10.3390/ani13193070